REPORT DOCUMENTATION PAGE

1. Recipient's Reference	2. Originator's Reference	3. Further Reference	4. Security Classification of Document
	AGARD-R-709	ISBN 92-835-0355-4	UNCLASSIFIED

5. Originator	Advisory Group for Aerospace Research and Development North Atlantic Treaty Organization 7 rue Ancelle, 92200 Neuilly sur Seine, France

6. Title	SPECIAL COURSE ON STABILITY AND TRANSITION OF LAMINAR FLOW

7. Presented at	an AGARD Special Course at the von Kármán Institute Rhode-Saint-Genèse, Belgium, on 26–30 March 1984.

8. Author(s)/Editor(s)	9. Date
Various	June 1984

10. Author's/Editor's Address	11. Pages
Various	232

12. Distribution Statement	This document is distributed in accordance with AGARD policies and regulations, which are outlined on the Outside Back Covers of all AGARD publications.

13. Keywords/Descriptors

Boundary layer transition	Stability
Laminar flow	Aerodynamics

14. Abstract

The aim of the Special Course on Stability and Transition of Laminar Flows was to present the knowledge of laminar-turbulent transition. Incompressible two-dimensional and compressible flows in transonic, supersonic, and hypersonic regimes were covered, as well as available results for three-dimensional flows.

The course notes consist of material presented and discussed at the Special Course held at the von Kármán Institute, Belgium, on 26–30 March 1984 under the joint sponsorship of the Institute and the AGARD Fluid Dynamics Panel.

AGARD-R-709

AGARD-R-709

AGARD

ADVISORY GROUP FOR AEROSPACE RESEARCH & DEVELOPMENT

7 RUE ANCELLE 92200 NEUILLY SUR SEINE FRANCE

AGARD Report No.709

Special Course on Stability and Transition of Laminar Flow

NORTH ATLANTIC TREATY ORGANIZATION

**DISTRIBUTION AND AVAILABILITY
ON BACK COVER**

NORTH ATLANTIC TREATY ORGANIZATION

ADVISORY GROUP FOR AEROSPACE RESEARCH AND DEVELOPMENT

(ORGANISATION DU TRAITE DE L'ATLANTIQUE NORD)

AGARD Report No.709

SPECIAL COURSE ON STABILITY AND

TRANSITION OF LAMINAR FLOW

THE MISSION OF AGARD

The mission of AGARD is to bring together the leading personalities of the NATO nations in the fields of science and technology relating to aerospace for the following purposes:

— Exchanging of scientific and technical information;

— Continuously stimulating advances in the aerospace sciences relevant to strengthening the common defence posture;

— Improving the co-operation among member nations in aerospace research and development;

— Providing scientific and technical advice and assistance to the North Atlantic Military Committee in the field of aerospace research and development;

— Rendering scientific and technical assistance, as requested, to other NATO bodies and to member nations in connection with research and development problems in the aerospace field;

— Providing assistance to member nations for the purpose of increasing their scientific and technical potential;

— Recommending effective ways for the member nations to use their research and development capabilities for the common benefit of the NATO community.

The highest authority within AGARD is the National Delegates Board consisting of officially appointed senior representatives from each member nation. The mission of AGARD is carried out through the Panels which are composed of experts appointed by the National Delegates, the Consultant and Exchange Programme and the Aerospace Applications Studies Programme. The results of AGARD work are reported to the member nations and the NATO Authorities through the AGARD series of publications of which this is one.

Participation in AGARD activities is by invitation only and is normally limited to citizens of the NATO nations.

PREFACE

Le but de ce Special Course est de présenter, de façon aussi complète que possible, l'état actuel des connaissances sur les phénomènes et sur les moyens de prévision de la transition du laminaire au turbulent.

Une description générale des phénomènes et une analyse de l'influence des facteurs affectant la transition sont d'abord présentées dans le cas des écoulements bidimensionnels de fluide incompressible.

Une étude approfondie de la théorie d'instabilité laminaire est développée ensuite, portant successivement sur les écoulements bidimensionnels incompressible et compressible et sur les couches limites tridimensionnelles.

Une revue spéciale des résultats pour la transition en tridimensionnel est également présentée aussi bien du point de vue de l'instabilité transversale que des problèmes de contamination qui peuvent apparaître sur le bord d'attaque des ailes en flèche.

On considère également les mécanismes non linéaires et le problème des instabilités secondaires.

D'autres aspects importants des problèmes de transition sont enfin examinés, comme la transition dans les couches de cisaillement libre, la réceptivité de la couche limite aux perturbations extérieures, le contrôle d'écoulement laminaire, la simulation visqueuse en soufflerie.

This Lecture Series is sponsored by the Fluid Dynamics Panel of AGARD and implemented by the von Kármán Institute.

R.MICHEL
Lecture Series Director

SPECIAL COURSE STAFF

Special Course Director: Dr R.Michel
Chef du D.E.R.A.T. No.76
Centre d'Etudes et de Recherches de Toulouse
2 Avenue Edouard Belin
B.P. 4025
Toulouse/Cedex
France

LECTURERS

Dr F.Arnal
ONERA/CERT
Département d'Aérothermodynamique
2 Avenue Edouard Belin
31055 Toulouse
France

Dr L.M.Mack
Jet Propulsion Laboratory
California Institute of Technology
4800 Oak Grove Drive
Pasadena
California 91109
USA

Dr D.I.A.Poll
College of Aeronautics
Cranfield Institute of Technology
Cranfield
Bedford MK43 OAL
UK

Dr T.Herbert
Dept. of Engineering Science & Mechanics
Virginia Polytechnic Institute and
    State University
Blacksburg
Virginia 24051
USA

Professor M.V.Morkovin
1104 Lindon Avenue
Oak Park
Illinois 60302
USA

Professor E.Reshotko
Dept. of Mechanics & Aerospace Eng.
Case Western Reserve University
Cleveland
Ohio 44106
USA

LOCAL COORDINATOR

Professor M.Carbonaro
von Kármán Institute for Fluid Dynamics
Chaussée de Waterloo 72
B-1640 Rhode-Saint-Genèse
Belgium

AGARD REPRESENTATIVE

Mr R.H.Rollins II
Fluid Dynamics Panel Executive
7 rue Ancelle
92200 Neuilly-sur-Seine
France

CONTENTS

* Not available at time of printing.

DESCRIPTION AND PREDICTION OF TRANSITION
IN TWO-DIMENSIONAL, INCOMPRESSIBLE FLOW
by
Daniel ARNAL

Office National d'Etudes et de Recherches Aérospatiales (ONERA)
Centre d'Etudes et de Recherches de TOULOUSE
2 avenue Edouard Belin
31055 TOULOUSE Cedex – FRANCE

SUMMARY

This paper deals with a survey of transition problems in two-dimensional, incompressible flows. The first chapter is devoted to a general description of phenomena leading to turbulence under the influence of various factors : free-stream turbulence, sound, pressure gradient, oscillations of the external flow, roughness, suction, wall curvature. Then, linear and non linear stability theories are briefly discussed. This chapter ends with a review of results concerning the structure and growth of turbulent spots and the progressive disappearance of intermittency phenomenon when positive pressure gradients are applied. The second chapter describes practical methods for calculating the transition onset as well as the transition region itself. Methods based on linear stability theory, empirical criteria, intermittency methods and turbulence models are presented successively. Some applications of these techniques are also given.

MAIN NOTATIONS

x	streamwise direction
y	direction normal to the wall
z	spanwise direction
$u(t) = U + \tilde{u}'$	
$v(t) = V + \tilde{v}'$	instantaneous velocities in the x, y, z directions
$w(t) = W + \tilde{w}'$	
U, V, W	mean velocities in the x, y, z directions
$\tilde{u}', \tilde{v}', \tilde{w}'$	fluctuations in the x, y, z directions
u', v', w'	root-mean-square values of $\tilde{u}', \tilde{v}', \tilde{w}'$
$\hat{u}, \hat{v}, \hat{w}$	velocity components describing steady streamwise vortices (GÖRTLER)
$\overline{u'v'}$	Reynolds shear stress : time-averaged value of $\tilde{u}' \tilde{v}'$
p	mean static pressure
t	time
C_f	skin friction coefficient
$H = \delta 1/\theta$	shape factor
$T = \dfrac{(u')_e}{U_e}$ or $\dfrac{(\sqrt{u'^2+v'^2+w'^2})_e}{\sqrt{3}\, U_e}$	free-stream turbulence level
δ	boundary layer thickness
$\delta 1 = \displaystyle\int_o^\delta (1 - \frac{U}{U_e})\,dy$	displacement thickness
$\theta = \displaystyle\int_o^\delta \frac{U}{U_e} (1 - \frac{U}{U_e})\,dy$	momentum thickness
$\Lambda_2 = \dfrac{\theta^2}{\nu} \dfrac{dU_e}{dx}$	POHLHAUSEN's parameter
ν	kinematic viscosity
ρ	density
$Rx = \dfrac{U_e x}{\nu}$	
$R\delta 1 = \dfrac{U_e \delta 1}{\nu}$	Reynolds numbers
$R\theta = \dfrac{U_e \theta}{\nu}$	

Subscripts

cr	critical
e	free-stream
ℓ	laminar
s	separation
t	turbulent
T	transition
∞	upstream

CHAPTER I

GENERAL DESCRIPTION OF TRANSITION

IN TWO-DIMENSIONAL, INCOMPRESSIBLE FLOW

1 - INTRODUCTION

Since the classical experiments performed by Osborne REYNOLDS (1883), the instability of laminar flows and the transition to turbulence have maintained a constant interest in fluid mechanics problems. This interest results from the fact that transition controls important hydrodynamic quantities such as drag or heat transfer. The present paper is devoted to a general survey of transition phenomena, in two-dimensional, incompressible flows.

An overall picture of the boundary layer development is given on figure 1. From the leading edge to a certain distance x_T, the flow remains laminar ; in the zero pressure gradient case, for instance, the shape factor is constant and equal to the BLASIUS value 2.591. At x_T, turbulent structures appear and transition occurs. From x_T to x_E, there is a noticeable change in the boundary layer properties : the process of transition involves a large increase in the momentum thickness θ and a large decrease in the shape factor. As a result, the displacement thickness $\delta 1 = H\theta$ exhibits a more complex evolution. The skin friction coefficient increases from a laminar value to a turbulent one, the latter being in some cases an order of magnitude greater than the former. It is obvious that the location and the extent of the transition depend on a large range of parameters, such as external disturbances, vibrations, pressure gradient, roughness, suction or blowing, wall curvature ...

In fact, two problems have to be studied :

a) What are the mechanisms leading to turbulence ? As long as external perturbations are small, one can observe at first two-dimensional oscillations developing downstream of a certain critical point. After a linear amplification of these waves, three-dimensional and non linear effects become important, leading to secondary instability and then transition. These basic phenomena can be modified or even bypassed by factors more or less controlled.

b) Once the first turbulent structures are created, what will be their subsequent behaviour up to the formation of the turbulent boundary layer ?

Both problems will be examined successively. The influence of some of the aforementioned parameters will also be discussed.

2 - GENERAL DESCRIPTION OF THE MECHANISMS INDUCING TURBULENCE

2.1. Fundamental aspects with zero pressure gradient and low external disturbances level

2.1.1. Linear amplification of small disturbances

The instability leading to transition starts with the growth of two-dimensional disturbances, the existence of which has been first demonstrated by the experiments of SCHUBAUER and SKRAMSTAD /1/. These, now classic, experiments were conducted at the National Bureau of Standards in a subsonic wind tunnel with a very low turbulence level (T $\simeq$ 0.03 10^{-2} in the working section). Figure 2 shows some records delivered by a hot wire set at six streamwise positions, at a constant distance from the wall. The fluctuations are at first almost non existent ; but, when the wire is moved downstream, a regular oscillation appears, with increasing amplitude as the distance increases.

In fact, the existence of small, regular oscillations travelling in the laminar boundary layer was postulated many decades ago by RAYLEIGH (1887) and PRANDTL (1921). Some years later, TOLLMIEN worked out a complete theory of boundary layer instability (1929) and SCHLICHTING calculated the total amplification of the most unstable frequencies (1933). For this reason, the instability waves are often referred as the "TOLLMIEN-SCHLICHTING waves". Nevertheless, the so-called "linear stability theory" received little acceptance, essentially because of a lack of experimental results. The aforementioned experiments of SCHUBAUER and SKRAMSTAD completely revised this opinion by demonstrating the existence of instability waves. Physically, the birth of these waves can be related to the concept of receptivity, introduced by MORKOVIN (1969). The receptivity describes the means by which forced disturbances (sound, external turbulence) enter the boundary layer and their signature in the disturbed flow. If they are small, they will tend to excite the normal modes of the boundary layer ; these normal modes are the TOLLMIEN-SCHLICHTING waves, which constitute free responses of the laminar boundary layer to the disturbance environment.

a) Short survey of the linear stability theory

A complete account of the stability theory is out of the scope of this paper. However, we need to introduce some theoretical elements for a comprehensive study of the experimental results.

The stream function representing a single disturbance is assumed to be of the form :

$$\psi(x, y, t) = \phi(y) \, e^{i(\alpha x - \omega t)} \tag{1}$$

with $\quad \tilde{u}' = \dfrac{\partial \psi}{\partial y} \quad$ and $\quad \tilde{v}' = - \dfrac{\partial \psi}{\partial x} \tag{2}$

It is often assumed that the mean flow is parallel : $V = 0$ and U depends only on y. The introduction of relations (1) and (2) into the continuity and momentum equations allows to obtain the ORR-SOMMERFELD equation, after linearization and elimination of pressure :

$$\varphi^{IV} - 2\alpha^2 \varphi" + \alpha^4 \varphi - iR \left[(\alpha U - \omega)(\varphi" - \alpha^2 \varphi) - \alpha U" \varphi \right] = 0 \qquad (3)$$

The mathematical nature of the two principal parameters α and ω leads to two theories : the spatial theory and the temporal theory. For the moment, we will restrict our purpose to the spatial theory : ω is a real quantity, which represents the circular frequency of the wave and α is complex : $\alpha = \alpha_r + i\alpha_i$. Relation (1) takes the form :

$$\psi(x, y, t) = \varphi(y) \, e^{-\alpha_i x} \, e^{i(\alpha_r x - \omega t)} \qquad (4)$$

φ is a complex amplitude function. The amplification factor α_i determines the degree of amplification or damping and α_r denotes the wave number of the perturbation. If α_i, α_r and ω are made dimensionless with a reference velocity V and a reference length L, the Reynolds number appearing in (3) is equal to V L/ν.

Due to the homogeneous boundary conditions ($\widetilde{u}'$ and $\widetilde{v}'$ must vanish at the wall and in the free stream), the problem is an eigenvalue one. When the mean velocity U(y) is specified, a non zero solution of (3) is obtained for particular combinations of the four real parameters R, α_i, α_r and ω.

The ORR-SOMMERFELD equation was solved by many authors (see /2/ and /3/ for instance). Some results of such computations for the BLASIUS flow are represented on figure 3 where L = $\delta 1$ and V = Ue, so that $\omega = 2\pi f \delta 1/Ue$ (f is the physical frequency). Figure 3a shows some curves of constant amplification rate α_i ; curves of constant wave number α_r are not represented for clarity. In this diagram, curves of constant frequency $F = 2\pi f \nu/Ue^2 = \omega/R$ appear as straight lines through the origin. Stability diagrams are very often plotted in (F, R$\delta 1$) coordinates, as it is the case on figure 3b, which deals only with the curve $\alpha_i = 0$. The locus $\alpha_i = 0$, called the neutral curve, separates the region of stable from that of unstable disturbances. In particular, there is a value of the Reynolds number below which all disturbances decay ; it is the "critical Reynolds number", R$\delta 1_{cr}$, which is slightly greater than 500. Let us notice that computations including non parallel effects (/4/, /5/) give lower value (see figure 3b).

Figure 3 indicates that a single frequency waves travelling in the laminar boundary layer is at first damped, then amplified, and again damped as it leaves the unstable region. An important parameter is the total amplification rate, defined as :

$$\frac{A}{A_o} = \exp \left[\int_{x_o}^{x} - \alpha_i \, dx \right] \qquad (5)$$

A is the wave amplitude and the index o refers to the streamwise position where the wave enters the unstable region.

Two other quantities are of interest :

- The physical wave-length λ of a given wave is obviously related to α_r. At R$\delta 1$ = 2 000, the wavelengths of the unstable frequencies lie between 6 δ and 18 δ. The TOLLMIEN-SCHLICHTING waves are longer compared to the boundary layer thickness.

- The phase velocity c is equal to ω/α_r. For unstable waves at moderate Reynolds numbers, calculations indicate that : $c \simeq 0.2$ to 0.4 Ue.

Similar results may be obtained as regards to temporal theory. In this case, α is real and ω is complex. The stream function is now expressed as :

$$\psi(x, y, t) = \varphi(y) \, e^{\omega_i t} \, e^{i(\alpha x - \omega_r t)}$$

It is clear that the neutral curves are identical in spatial and in temporal theories. As a general rule, GASTER's relation makes possible to convert a temporal to a spatial amplification rate /6/.

In the preceding lines, we considered only two-dimensional waves (i.e. waves, the crests of which travel normally to the main flow). A more general form of the stream function can describe the oblique, three-dimensional waves :

$$\psi(x, y, z, t) = \varphi(y) \, e^{i(\alpha x + \beta z - \omega t)} \qquad (6)$$

These waves are often neglected in two-dimensional problems. In fact, it can be demonstrated that, in the temporal theory, instability appears first for a two-dimensional disturbance (SQUIRE's theorem).

b) Some experimental results
   ̄

We already mentioned that SCHUBAUER and SKRAMSTAD were the first to observe that natural oscillations existed in the laminar boundary layer. In order to make more quantitative comparisons with the theory, they worked then with artificial disturbances : a thin metal strip extending over a width of about 30 cm was placed near the wall and was excited by a magnetic field induced by an alternating current. The so-called "vibrating ribbon" technique made possible to produce two-dimensional disturbances of a prescribed frequency with a controlled initial amplitude. The wave-length, amplification rate, amplitude and phase velocity of the waves were measured with a hot wire anemometer, and the agreement with theoretical results was good.

More recently, ROSS, BARNES, BURNS and ROSS /7/ repeated in some way SCHUBAUER-SKRAMSTAD experiments. Their wind tunnel had also a very low turbulence level (T $\simeq$ 0.03 10^{-2}) and a vibrating ribbon was used to produce instability waves. Typical results are plotted on figures 4 and 5. In figure 4, the experimental distributions of u'/Ue obtained for a given frequency at two values of R$\delta 1$ are compared with JORDINSON's calculations /2/. An interesting feature of these profiles is the existence of a zero-amplitude point, corresponding to a sudden phase shift of 180°. The experimental and theoretical evolutions of the total amplification rate (see relation (5)) are compared in figure 5 for three frequencies : the overall

agreement is reasonable. The points where the curves have a zero slope correspond to $\alpha_i = 0$, that is to say to the neutral curve. The experimental value of the critical Reynolds number was lower than that predicted by the parallel flow assumption theory, but a better agreement was since achieved with the SARIC-NAYFEH calculations /5/ where the non parallel effects are taken into account (figure 3b).

The vibrating ribbon generates waves of a single frequency. In practical situations however, a source of disturbances such as free-stream turbulence will create waves covering a more or less wide range of frequencies and orientations. For this reason, GASTER and GRANT /8/ used a completely different approach : an acoustic pulse was generated by a loudspeaker and transmitted to the boundary layer by a small hole in the flat plate. "This stimulation of the wave system generates a packet of waves, which spreads out as it travels downstream. The initial disturbance excites all possible modes and the wave packet forms through selective amplification and interference of the most unstable waves". Figure 6 shows the growth of two-dimensional waves of various frequencies. Theoretical predictions performed by GASTER /9/ are also given. There is a major difference between figures 5 and 6 : in the present case, all curves are obtained in a single experiment ; on the contrary, each curve shown on figure 5 needs a different experiment.

KNAPP, ROACHE and MUELLER /10/ have used the smoke visualization technique in order to describe the various stages leading to transition. The laminar boundary layer develops in natural conditions $(T \simeq 0.1 \, 10^{-2})$ on an ogive nose cylinder aligned with the free-stream. The upper part of the figure 7 displays the overall smoke pattern as observed with zero pressure gradient (the lower part presents typical records obtained in various experiments). It can be seen that the instability waves take the form of concentrated bands of smoke around the cylinder (left part of the sketch). These "rings" become more distinct as they move down the body, indicating the existence of a strong amplification.

2.1.2. Non linear amplification of disturbances

When the initially weak disturbances reach a certain amplitude, their development begins to deviate from that predicted by the linearized theory : the quadratic terms neglected in this theory are then appreciable and three-dimensional effects appear. The smoke visualizations made by KNAPP et al. indicate that the initially two-dimensional waves are distorted (figure 7) into a series of "peaks" and "valleys". As the flow proceeds downstream, this pattern becomes more and more pronounced.

a) Earlier experimental studies under controlled conditions

The three-dimensional development of the disturbances was studied by KLEBANOFF, TIDSTROM and SARGENT /11/ under controlled conditions. A vibrating ribbon is once again used and thin spacers are placed beneath the ribbon in order to induce a minute periodic variation in the boundary layer thickness in the spanwise direction. Other careful experiments have been carried out by KOVASZNAY, KOMODA and VASUDEVA /12/, who used a technique similar to that of KLEBANOFF et al. : in addition, an array of hot wires provides instantaneous pictures of the flow development.

Figure 8, extracted from /11/, shows the spanwise distributions of the streamwise fluctuation intensity at three streamwise positions. The hot wire is placed at a constant height near the wall. Regions of maximum and minimum amplitude correspond respectively to the "peaks" and "valleys". At $x - x_0 \simeq 7$in., the amplitude measured at the peak position is about six times greater than that measured at the valley position. This observation is illustrated in figure 9, where the amplitudes at peak and valley are plotted as function of the distance from the ribbon.

The distribution of the mean velocity across the boundary layer is also distorted, as it can be seen in figure 10. The considered stations are those indicated on figure 9. At stations C and D, the profiles measured at the peak have developed a point of inflexion, with a progressively greater defect in velocity. On the contrary, the valley position is characterized by a profile somewhat fuller than the BLASIUS one. Measurements of the mean cross-flow velocity W indicate the generation of a system of longitudinal vortices.

In such controlled conditions, the flow remains strictly periodic. For a certain fraction in each cycle of the primary (TOLLMIEN-SCHLICHTING) wave, the instantaneous inflexional form at the peak is more pronounced that the mean one. As a consequence, there is a marked increase in spanwise vorticity. Figure 11 shows the contours of constant $\partial U/\partial y$ (approximate vorticity component in the spanwise direction) measured by KOVASZNAY et al. at the peak position. The abscissa is t/T, where T represents the period in time of the primary wave. With the reservation that a period in time corresponds to a wave-length in space, the plotted curves define a spatial pattern moving towards the right. For the BLASIUS profile, the maximum vorticity is encountered at the wall and is equal to 0.571 when made dimensionless by δ_1 and U_e. Figure 11 indicates that this value is exceeded at $y/\delta \simeq 0.4$ or 0.5 during about a third of the cycle. TANI /13/ suggests that "the spanwise vorticity is convected away from the wall by the induced velocity due to the streamwise vortices. Upon reaching the outer part of the boundary layer ... the vortex tubes constituting the spanwise vorticity are stretched out, until high concentration of vorticity is formed in a thin layer called high-shear layer."

Similar measurements performed off-peak indicate that the vorticity becomes less intense as the valley position is approached. In a plan view, the high-shear layer looks like a blunt-nosed delta /12/.

b) Ordered peak-valley structure in natural conditions

Spanwise variations are also present in natural conditions. KLEBANOFF et al. /11/ reported measurements of the streamwise fluctuation in a direction normal to the main flow : although less regularly spaced than in controlled conditions, a peak-valley system was found to occur. This system is ordered in the sense that peaks follow peaks and valleys follow valleys. The spanwise wave-length is generally somewhat smaller than the streamwise wave-length. It can be noticed that this structure (the so-called K-structure) appears when the maximum rms amplitude of the TOLLMIEN-SCHLICHTING waves approaches one per cent of the free-stream velocity.

The problem is now to give an explanation of the preferred spanwise periodicity. BENNEY and LIN /14/ and BENNEY /15/, /16/ studied theoretically the non linear interaction between a two-dimensional TOLLMIEN-SCHLICHTING wave and a three-dimensional wave with spanwise periodicity. The calculations revealed that this interaction promotes the growth of longitudinal vortices similar to those reported by KLEBANOFF et al., but were unable to estimate the preferred spanwise periodicity.

CRAIK /17/ investigated the interactions of a resonant triad of TOLLMIEN-SCHLICHTING waves. The considered triad involved a two-dimensional wave and two oblique waves propagating at equal and opposite angles to the flow direction, and such that all three waves have the same phase velocity in the downstream direction. The non linear interaction analysis leads to :

$$\frac{1}{A}\frac{dA}{dt} = a_o + a_1 \frac{B^2}{A} + \ldots\ldots$$

$$\frac{1}{B}\frac{dB}{dt} = b_o + b_1 \frac{AB^{\star}}{B} + \ldots\ldots$$

A and B are respectively the amplitudes of the two-dimensional wave and of each oblique wave. $B^{\star}$ is the conjugate amplitude. a_o and b_o are given by the linear stability theory ; an orthogonality condition determines the interaction coefficients a_1 and b_1. The calculations indicate that b_1 is very large. This means that there can be a powerful interaction, leading to a rapid transfer of energy from the primary shear flow to the disturbances, especially to the oblique waves.

CRAIK's model is consistent with some experimental observations, but is inoperative in other cases. As pointed out by HERBERT /18/, the spanwise wave-length seems to depend on unknown details of the experimental set-up.

c) Staggered peak-valley structure in natural and controlled conditions

The peak-valley system described above does not constitute the only one which was encountered. KNAPP, ROACHE and MUELLER /10/ observed that the smoke streaklines formed a staggered peak-valley structure. In this case, peaks follow valleys and valleys follow peaks (figure 12). Let us observe that the smoke visualizations presented in figure 7 do not present this staggered arrangement, because they describe the development of a single wave.

More recently, the staggered structure was studied under controlled conditions (see /19/ for instance) : a vibrating ribbon generates two-dimensional TOLLMIEN-SCHLICHTING waves and three-dimensionality results from very weak background disturbances. In fact, two different types of staggered structures have been observed : one in which λ_z is larger than λ_x (C-type structure) and another in which λ_x is larger than λ_z (H-type structure). As pointed out by SARIC and THOMAS /19/, the important parameter is the maximum value of the primary fluctuation. For amplitudes of the order of 0.3 %, the C-type system appears and is a result of the CRAIK's mechanism /17/. At amplitudes between 0.3 and 0.6 %, the staggered three-dimensional pattern can be explained by the model of HERBERT /18/ and is called the H-type pattern. Larger amplitudes lead to the appearance of the ordered structure studied by KLEBANOFF et al. (K-type structure).

Obviously, a hot wire placed in a flow where staggered peak-valley systems are present will record subharmonics of the primary wave, because the pattern repeats itself with wave length $2\lambda_x$. This mechanism constitutes "the subharmonic route to turbulence" /19/.

2.1.3. The breakdown

The non linear development of disturbances terminates with the "breakdown" phenomenon. The term "breakdown" is used "to describe what appears to be an abrupt change in the character of the wave motion at a peak and the onset of what is believed to be a new instability /11/". This instability is often referred as the secondary instability (HERBERT /18/ calls it the tertiary instability, reserving the secondary instability term to the non linear mechanisms discussed in § 2.1.2.).

As the flow proceeds downstream, the high-shear layer becomes more and more intense, and finally induces the new instability. This is due to the inflexional form of the instantaneous profiles : the linear stability theory predicts that an inflexion point gives rise to important destabilizing effects (see § 2.3.1.). On an $\widetilde{u}'$ signal recorded at $y/\delta \simeq 0.5$ to 0.7, the secondary instability takes the form of a strong negative pulse, the amplitude of which can be 30 to 40 per cent of the free-stream velocity ; its duration is about 1/10th of the primary wave period (figure 7). This signal is called the "spike". In the later development, a second spike will also appear. The maximum root-mean-square value of the longitudinal fluctuation increases abruptly, up to 10 or 15 per cent of Ue.

Figure 13 shows a map of the iso-vorticity contours as measured by KOVASZNAY et al. /12/ at the one spike and double spike stages. HAMA and NUTANT /20/ performed careful visualizations in a water channel by using the hydrogen bubble technique. Examples of results are given in figure 14. A vertical, electrically pulsed wire is placed at a peak position and releases periodically columns of bubbles into a laminar boundary layer. The bubbles lines are convected downstream and are deformed by large stimulated waves and by three-dimensional disturbances. The six photographs cover 40 per cent of the TOLLMIEN-SCHLICHTING period in time and 60 per cent of the wave length. They indicate the development of the sharply kinked lines of bubbles and the final exaggeration of the kink into a spiral.

On the theoretical side, GREENSPAN and BENNEY /21/ calculated the growth of secondary disturbances by a two-dimensional, inviscid, linearized approach. The basic velocity profiles introduced as data in their theory were the instantaneous profiles measured by KOVASZNAY et al.. The main result is that over one half cycle of the primary wave, the amplitude of the most unstable secondary wave increases by a factor of about 10, its frequency being about 8 times that of the primary wave. It is clear that this simple theory contains most of the observed features of breakdown. LANDAHL /22/ made a more ambitious approach on the basis of the

kinematic wave theory for conservative systems. Some of the assumptions he used were criticized by STEWARTSON /23/.

The basic mechanism which was studied for disturbances artificially introduced in the boundary layer is applicable to the case of natural transition : the negative spikes are also observed and are somewhat more numerous at spanwise positions corresponding to the peaks /11/. In their smoke visualizations, KNAPP et al. /10/ observed that within a fraction of a wave-length, the peak-valley system gives rise to a vortex filament, often referred as a "horseshoe vortex" (figure 7). An important difference, however, is that breakdown occurs intermittently rather than continously as in controlled conditions. KNAPP et al. reported that in natural conditions, the smoke waves break down in sets rather than as individuals.

For each cycle of the primary wave, the spikes increase in number and form bunches of high-frequency fluctuations (see $\tilde{u}'$ record in figure 7). This may be interpreted as the shedding of vortices from the nose as well as from the swept-back sides of the delta-shaped high-shear layer. Such vortices have been called "hairpin eddies" by KLEBANOFF et al. /11/. They are highly unstable and break down into smaller vortices, which again break down into smaller vortices. The fluctuations finally take a random character and form a so-called "turbulent spot", the typical arrowhead shape of which is shown in figure 7. A detailed study of the turbulent spots will be given in Section 3.

One has to keep in mind that the non linear phase and the breakdown process occur over a relatively short distance. For typical flat plate conditions, the streamwise extent of linear amplification covers about 75 to 85 per cent of the distance to the beginning of transition. This explains that calculation methods based on linear theory only (e^n methods) give good results for predicting the transition location (see Chapter II).

The fundamental mechanisms which have been described can be more or less modified by a great number of factors such as free-stream turbulence, sound, pressure gradient, suction, wall curvature ... The influence of these factors will now be discussed.

2.2. Influence of sound and free-stream turbulence (zero pressure gradient)

Sound and free-stream turbulence represent two types of external disturbances of very different nature :

– The free-stream turbulence (vorticity-turbulence mode) propagates essentially along streamlines with the local flow velocity. It is a vectorial, three-dimensional quantity, the spectrum of which covers a more or less wide range of frequencies.

– The sound is an irrotational mode of disturbance. In low-speed wind tunnels, it propagates at speeds an order of magnitude faster than the mean flow. It can be considered as monodimensional and the use of a loudspeaker allows to study the effects of a single frequency.

In both cases, when such disturbances enter the laminar boundary layer, they initiate in it two responses : a forced response (solution of a non homogeneous problem, because the outer boundary conditions are non zero) and a free response (solution of an homogeneous equation such as the ORR-SOMMERFELD equation). This problem was called the "receptivity" problem by M.V. MORKOVIN.

2.2.1. Influence of free-stream turbulence

On a theoretical point of view, results concerning the influence of external turbulence are rather scarce. This is due to the three-dimensional and random character of the disturbances. CRIMINALE /24/ studied a non homogeneous form of the ORR-SOMMERFELD equation ; the right-hand side of (3) being replaced by a forcing function $V(x, y, z, t)$. ROGLER /25/ represented the free-stream disturbances by arrays of rectangular vortices, oscillating sheets of vorticity and irrotational fluctuations, and examined their interaction with a boundary layer formed by two straight-line segments. Despite these studies, the linking between imposed disturbances and instability waves is not fully understood.

On an experimental point of view, the results are more numerous. They indicate trends and suggest empirical correlations which may be of interest for practical purposes.

a) Effect of T on transition location

The effect of free-stream turbulence on transition location is shown on figures 15 and 16, where the transition Reynolds number Rx_T is plotted as a function of the external turbulence level T. In figure 15, T is varying from 0 to $3 \cdot 10^{-2}$; the high values of T, such as those used by HALL and HISLOP, are achieved by installing grids just upstream of the test section. Figure 16 shows an enlargement of the previous graph for the lower values of T, say $T < 0.3 \cdot 10^{-2}$. The considered experiments have been carried out in low turbulence wind tunnels, where T is increased by successively removing the damping screens. As T becomes very small, the data of SCHUBAUER-SKRAMSTAD /1/ and those of WELLS /26/ exhibit the same trend, in the sense that Rx_T reaches a constant value. But this value is about $2.8 \cdot 10^6$ for SCHUBAUER-SKRAMSTAD and about $5 \cdot 10^6$ for WELLS. In fact, sound component controls transition when T is very low and the effect of "true" free-stream turbulence can be only observed at values of T greater than $0.1 \cdot 10^{-2}$. (The influence of sound will be examined in § 2.2.2.).

In a general manner, the experimental data seem to collapse onto a single curve. Analytical representations of this curve have been proposed ; they will be discussed in Chapter II. It can be observed that transition moves rapidly upstream when T increases. This effect appears to be very strong : the value of Rx_T corresponding to $T = 0.3 \cdot 10^{-2}$ is about three times greater than that corresponding to $T = 1.5 \cdot 10^{-2}$. On the other side, it is obvious that Rx_T depends not only on the root-mean-square value of the free-stream turbulence, but also on its spectrum. The effect of this latter parameter was studied by MACK /27/.

b) Some detailed experimental results

The rapid decrease in Rx_T indicates that important changes in the laminar boundary layer structure must appear when T increases.

Experiments have been carried out at ONERA/CERT /28/ in a wind tunnel where the natural turbulence was low, but not very low ($T \simeq 0.2 \ 10^{-2}$). The experimental set-up is shown on figure 17, as well as a free-stream turbulence spectrum. The boundary layer develops on a cylinder aligned along the axis of an axisymmetric wind tunnel. The angle of divergence of the slightly conical wall around the cylinder is such that the external velocity is practically constant and equal to 33 m/s.

Profiles of the u'-fluctuation are presented on figure 18 for five stations within the laminar region. At these abscissa, the measured mean velocity profiles are confounded with the BLASIUS solution within the experimental uncertainty. The signal recorded at x = 0.66 m shows that the instantaneous velocity is the sum of an irregular, low frequency oscillation and of a more regular oscillation at a higher frequency. The spectra presented on figure 19 confirm this observation ; they were measured at various streamwise positions, at a constant value of the dimensionless distance from the wall $y/\delta = 0.2$. The low frequency range (f < 200 Hz) represents the boundary layer response to the imposed external fluctuations, whereas the local peak centered around f = 500 - 600 Hz is related to TOLLMIEN-SCHLICHTING waves, that is to say to eigenmodes or natural oscillations. Amplitude profiles corresponding to various frequencies are plotted on figure 20 for x = 0.66 m. As expected, the frequency f = 600 Hz exhibits the classical shape of the TOLLMIEN-SCHLICHTING waves profiles with a zero-amplitude point located at $y/\delta \simeq 0.5$; on the stability diagram, this frequency is placed near the upper branch of the neutral curve, in the region where the greatest amplification factors are encountered.

Other experiments were performed with higher values of T /29/. For this, a grid was inserted at the entrance of the working section. As it can be seen on figure 21, the root-mean-square value of the streamwise fluctuation in the free stream decreased from $T \simeq 0.9 \ 10^{-2}$ (at the stagnation point) to $T \simeq 0.3 \ 10^{-2}$ (at the end of the working section). A power spectrum, measured at x = 0.66 m, is also presented on this figure : the very fine meshes of the grid damp the low frequencies but turbulence is generated for frequencies up to 4 000 Hz and even higher.

Figure 22 shows two samples of u'^2 profiles, with corresponding spectra measured in the boundary layer. At the first station, which is located near the stagnation point, the fluctuation level does not exhibit a large departure from its free-stream value and the spectrum extends over a relatively wide range of frequencies. At the second station (x = 0.66 m), the fluctuation amplitude increases, with a spectrum reduced to lower frequencies, which are stable according to linear stability theory ; the peak related to the TOLLMIEN-SCHLICHTING waves appears at $f \simeq 500 - 600$ Hz, but is not so clearly noticeable.

Experiments were performed with another grid (grid 2), which created a higher free-stream turbulence intensity. In this case, transition moved upstream and occured without the appearance of TOLLMIEN-SCHLICHTING waves, neither on the instantaneous records, nor on the spectra. Such a phenomenon is called "bypass" ; this word means that, for large external disturbances, turbulent spots are triggered without resorting to the linear instability theory.

Some other striking features have to be noted :

. The laminar boundary layer can transport fluctuations of large intensity, as it is illustrated on figure 23, where the maximum value of u'^2 is plotted for the three configurations (no grid, grid 1, grid 2). High intensities (5 or 6 per cent of the external velocity) are encountered in the laminar boundary layer.

. As far as the transition location is concerned, the value of Rx_T measured with grid 1 is somewhat larger than that observed in the no-grid case. This fact strongly disagrees with the simple correlations where Rx_T is a decreasing function of T. In fact, the shape of the turbulence spectrum is not taken into account in such empirical relations.

2.2.2. Influence of sound

The problem is now to study the interference between a laminar boundary layer and a traveling sound wave of a single frequency $\overline{f}$. It will be assumed that the wave propagates in the main flow direction and that its wave-length is infinite. In these conditions, the free-stream velocity is given by :

$$Ue(t) = U_0(1 + N \sin \overline{\omega} t), \text{ with } \overline{\omega} = 2\pi\overline{f} \qquad (7)$$

N is usually close to 10^{-3}.

a) Fundamental aspects (zero pressure gradient)

First of all, it is interesting to know the response of the BLASIUS boundary layer to the imposed external oscillation. An important parameter is the Strouhal number $S = \overline{\omega} x/U_0$. The unsteady laminar boundary layer solutions give the following results /30/ :

$$U(x, y, t) = U_0 \left[f_B'(x, y) + G(x, y, t) \right] \qquad \text{with :} \qquad (8)$$

$$G = N \cos\overline{\omega} t \left[f_B'' + \eta f_B''/2 + 0(S) \right] \quad \text{at small S} \qquad (9)$$

$$G = N \left[\cos\overline{\omega} t - \exp(-\eta) \cos(\overline{\omega} t - \eta) + 0(S^{-1/2}) \right] \text{ at large S} \qquad (10)$$

with $k = (\overline{\omega}/2\nu)^{1/2}$ and $\eta = yk$. f_B' is the classic BLASIUS solution.

When S is small (equation (9)), the unsteady profile is in phase with the free stream. We will assume that this regime corresponds to stable boundary layers. Therefore, our purpose is restricted to large values of S (equation (10)). In this case, the unsteady layer does not grow any longer with x and (8) may be written as :

$$U(x, y, t) = U_0 \left[f_B'(x, y) + N \frac{\Delta U(\eta)}{\Delta U_0} \sin(\overline{\omega}t + \phi(\eta)) \right] \qquad (11)$$

The relative amplitude function $\frac{\Delta U}{\Delta U_0}$ and the lag function ϕ are plotted in figure 24. A double layer structure appears clearly : near the wall, a layer exists in which variations in amplitude and in phase occur (STOKES layer) ; a second layer in phase with the free stream extends in the outer part of the boundary layer. The ratio of the STOKES layer thickness to the steady boundary layer thickness is about $0.6/S^{1/2}$. For $S = 25$, the unsteady effects occur at $y/\delta < 0.12$.

Experiments show that the free response of the boundary layer to the imposed sound disturbance is essentially composed of TOLLMIEN-SCHLICHTING waves having the same frequency.

A careful study of the development of instability waves induced by sound was made by SHAPIRO /31/, /32/. The experiments were performed on a flat plate installed in a low turbulence ($T \simeq 0.04\ 10^{-2}$) subsonic wind tunnel.

The growth of disturbances measured under the presence of acoustic excitation ($f = 500$ Hz) is plotted in figure 25 and compared with the results given by the linear stability theory. Measurements at each station were taken at the position of maximum disturbance amplitude in the boundary layer, for the frequency of the imposed sound field. A standing wave pattern appears for $R\delta1 < 1\ 000$ (the initial amplitude A_0 is the mean value of A in this region) and disappears slowly downstream. In fact, two types of oscillations coexist in the boundary layer : the imposed oscillations (sound) and the natural oscillations (TOLLMIEN-SCHLICHTING waves). If it is assumed that both types of waves have a similar amplitude, then the instantaneous perturbation u' recorded by the hot wire is :

$$\tilde{u}' \simeq \sin\overline{\omega}t + \sin(kx - \omega t), \text{ with } \omega = \overline{\omega} \qquad (12)$$

The mean square value of u' is simply :

$$u'^2 \simeq 1 - \cos kx \qquad (13)$$

which corresponds to the experimental results at the lower values of $R\delta1$. One may notice that the wavelength of the standing wave pattern is the wave length of the TOLLMIEN-SCHLICHTING waves. More elaborate computations of this process were made by THOMAS and LEKOUDIS /33/ and led to the same conclusions. See also works done by MURDOCK /30/ and TAM /34/.

When the TOLLMIEN-SCHLICHTING waves enter the unstable region, their amplitudes become larger than that of the forced oscillations ; the standing wave pattern is less and less visible, and the evolution of the natural waves is well described by the stability theory. In a first approximation, the main effect of the sound takes place near the leading edge ; it is to set an initial condition for the TOLLMIEN-SCHLICHTING oscillations rather than continuously interacting. Further downstream, the sound and the natural waves propagate independently of each other.

Another interesting result of SHAPIRO's work is shown in figure 26. The initial mean amplitude A_0 of the streamwise fluctuation is plotted as a function of the exciting acoustic velocity. "Clearly the relation is not only linear, but essentially one to one, except when the sound level is so low that the excitation is dominated by stream turbulence."

b) Effect of sound on transition location

When the acoustic frequency (or a strong harmonic) falls in the range where TOLLMIEN-SCHLICHTING waves are unstable, the onset of turbulence may be displaced. An example of this effect was already noted in § 2.2.1. a). A hot wire senses both turbulence and sound, and what is called "turbulence intensity" consists of a mixing of both types of disturbances. In SCHUBAUER-SKRAMSTAD experiments, the addition of anti-turbulence screens reduced effectively the true turbulence, but had little effect on the acoustic disturbances, which "assumed the dominant responsibility for transition " /35/. WELLS eliminated the sound sources (sonic throat) and obtained transition Reynolds number of about five millions.

In a later study /36/, SPANGLER and WELLS systematically investigated the effects of acoustic noise fields of discrete frequencies. The evolution of Rx_T against the free-stream disturbance intensity is shown in figure 27. Curve B indicates that high sound levels may be encountered without change in the transition location : in such cases, sound gives rise to TOLLMIEN-SCHLICHTING waves falling outside the dangerous band. If it is not the case, the transition Reynolds number may be dramatically reduced (curves E, D and C). A more quantitative study of these experimental results is difficult, because the sound generator created harmonics, which in some cases, were as strong as the fundamental frequency. (By the way, we can note that SPRANGLER and WELLS studied also the influence of grid-produced turbulence. The results plotted in figure 27 show a stronger effect than the other results /1/, /26/ over the same range of turbulence intensity. This demonstrates one more time that there is not a universal $Rx_T(T)$ curve).

KNAPP et al. /10/ introduced sound into their axisymmetric wind tunnel from a loudspeaker placed ahead of the contraction cone. The sound frequency was that leading to transition in natural conditions. The transition location obviously moved upstream. In addition, all transition regions (two and three-development of the waves, breakdown) were fixed relative to an axial position as in the presence of a vibrating ribbon : for example, all the waves break down at the same streamwise location.

2.3. Combined influence of pressure gradient and free-stream turbulence

2.3.1. Linear stability theory results

In order to clarify the parameters acting on the stability properties, stability calculations were performed by many authors on the similar FALKNER-SKAN profiles. Let us recall that these profiles correspond to external velocity distributions of the form

$$Ue = kx^m \tag{14}$$

In such flows, some important parameters such as the shape factor H or the POHLHAUSEN parameter $\Lambda_2 = \theta^2/\nu.dUe/dx$ remain unchanged in the streamwise direction.

The main result of the stability calculations is that basic velocity profiles with an inflexion point (decelerating flows, $\Lambda_2 < 0$, H > 2.59) are more unstable than those developing in negative pressure gradients (accelerating flows, $\Lambda_2 > 0$, H < 2.59) : the critical Reynolds number decreases rapidly, the amplification factors become very large and, when the Reynolds number goes to infinity, there is always a range of unstable frequencies (inflexional instability). On the contrary, profiles in accelerating flows have a neutral curve which tends to be closed at large Reynolds numbers (viscous instability). The following table /3/ gives some numerical results :

m	H	Λ_2	$R\delta1_{cr}$	
1	2.218	0.0854	12 490	Two-dimensional stagnation point
1/3	2.298	0.0613	7 680	Axisymmetric stagnation point
0	2.591	0	520	BLASIUS profile
− 0.0654	2.963	− 0.0407	138	
− 0.0904	4.032	− 0.0680	67	Separation profile

In a general case, however, the laminar boundary layer does not develop under similarity conditions. This means that at each streamwise position, a given frequency will be placed into a different stability diagram, defined by the local mean velocity profile. On a numerical point of view, stability calculations must be performed step by step.

The strong influence of pressure gradient on stability is illustrated in figure 28, which presents experimental results obtained by SCHUBAUER and SKRAMSTAD in natural conditions /1/. The figure shows oscillograms of the $\tilde{u}$-fluctuation on a flat wall with a non uniform external velocity. The upper half of the diagram indicates that a negative pressure gradient damps out the oscillations, whereas the positive pressure gradient, which succeeds, causes a strong amplification and produces transition.

2.3.2. Practical calculation of the critical Reynolds number

Although the critical point is usually located far upstream the transition onset, it is often useful to calculate it for analyzing experimental results. The most obvious method is to solve the stability equations, but this can lead to complex and time-consuming computations.

For any non similar flow, it is easier to plot the streamwise evolution of the thickness-momentum Reynolds number $R\theta$ for the considered case, and to compare it with the local, "fictitious", critical Reynolds number $R\theta_{crf}$. Figure 29 presents an application of this method. If $R\theta < R\theta_{crf}$, the flow is locally stable. If $R\theta > R\theta_{crf}$, the flow is locally unstable. The true critical abscissa is located at the point where $R\theta = R\theta_{crf}$. For practical applications, it may be assumed that $R\theta_{crf}$ depends on the local shape factor only ; an approximate representation of the stability calculations is the following :

$$R\theta_{crf} = \exp\left[\frac{52}{H} - 14.8\right] \tag{15}$$

In numerical procedures where the local boundary layer equations are solved, it is possible to use the DUNN-LIN /37/, /38/ formulation :

$$R\theta_{crf} = \frac{25 \ U'_o}{c^4} \ , \quad \text{with} \quad U'_o = \left[\frac{\partial(U/Ue)}{\partial(y/\theta)}\right]_{y=0} \tag{16}$$

c is solution of the equation : $- \pi \dfrac{U''_c \ U'_o \ c}{U^3_c} = 0.58$ \hfill (17)

with $U' = \dfrac{\partial(U/Ue)}{\partial(y/\theta)}$, $U'' = \dfrac{\partial^2(U/Ue)}{\partial(y/\theta)^2}$, $U_c = c$

In the example given in figure 29, the pressure gradient is at first negative. Due to the low values of $R\theta$ and to the high values of $R\theta_{crf}$, the boundary layer is stable. Further downstream, the pressure gradient vanishes and then becomes positive. The shape factor increases, the fictitious critical Reynolds number decreases rapidly and the flow enters an unstable region. For such a case, the critical abscissa is close to the maximum velocity point.

2.3.3. Effect of positive pressure gradients

a) Transition without separation

Recently, ARNAL et al. /39/, /40/ performed experiments in decelerating flows. The experimental set-up was already presented in § 2.2.1.. Changing the divergence of the conical wall around the central cylinder made possible to obtain various pressure gradients. Six cases, labelled A, B, C, D, E and F were studied. The corresponding distributions of the external velocity are plotted in figure 30, where U_{ref} refers to the velocity measured at the junction cylinder-ogive. The case A corresponds to the flat plate flow previously mentioned (§ 2.2.1. b)). In the other cases, the boundary layer is subjected to positive pressure gradients. The free-stream turbulence level T is nearly constant from one configuration to another and is equal to about $0.2 \ 10^{-2}$. In any case, the critical abscissa was found to be located near the maximum velocity abscissa, i.e. $x \simeq 0.15$ m.

Figure 31 shows two signals recorded in the case D for which transition starts at $x = 0.44$ m. At $x = 0.35$ m, the signal looks like the one presented in § 2.2.1. b) for the flat plate case : the instability waves are small, compared with the low frequencies fluctuations. At the second station, however, the waves have developed, and the spectrum practically reduces to a single peak at $f = 360$ Hz. The measured evolution of the amplitude profile corresponding to this frequency is plotted in figure 32 and compared with stability calculations, in which the local mean velocity profile (H = 2.96) was introduced. A zero amplitude point, associated with a phase reversal, is always present. Two maxima are visible near the wall, the second one being closely related to the existence of the inflexion point.

Figure 31 indicates that in a decelerating flow, the unstable waves can reach amplitudes larger than in the zero pressure gradient flow (for a given disturbances environment). This confirms the smoke visualization results obtained by KNAPP et al. /10/ : these authors observed that in an adverse pressure gradient, the waves were more clearly visible than in the flat plate case. Similar observations were made by COUSTEIX and PAILHAS /41/, who studied the transition phenomena in a strong positive pressure gradient. More detailed information will be given in Section 3 of this chapter.

As the transition location is approached, the three-dimensional, spanwise variations are weaker than in the flat plate case. The negative spikes become less and less numerous and breakdown tends to be a continuous process.

For a given value of T, the principal effect of a positive pressure gradient is to reduce the transition Reynolds number. Figure 33 shows the evolution of the shape factor as a function of Rx, for the six cases studied at ONERA/CERT. The laminar calculations indicate that transition always occurs before laminar separation. In the following lines, we will define the transition onset as the location where the shape factor exhibits a sudden negative slope. Another presentation of the results is given in figure 34, where the momentum-thickness Reynolds number at the transition onset is plotted as a function of the shape factor at the same location. As it can be expected, the transition Reynolds number decreases rapidly when the pressure gradient intensity increases. This curve does not constitute a transition criterion, but is only a plot of experimental results. The length of the transition region is also reduced, as it will be discussed later.

b) Separation bubbles

When the pressure gradient is very strong, the laminar boundary layer often separates and transition may occur in the separated layer. This intricate problem was studied by many authors (see review by TANI /42/). Recently, detailed measurements were performed at ONERA/CERT by GLEYZES, COUSTEIX and BONNET /43/, /44/, who investigated separation bubbles occuring near the leading edge of an airfoil at incidence, downstream of the suction peak. A first series of experiments was carried out on a 200 mm chord ONERA LC100D profile. Examples of external velocity distributions are presented in figure 35, for a fixed incidence ($\alpha = 7°30$). In any case, laminar separation is present, but due to interactions between viscous and inviscid flows, the velocity distribution depends strongly on the chord Reynolds number R_c. For the so-called short bubbles (here, for $U_\infty > 34$ m/s or $R_c > 0.45 \ 10^6$), the velocity distribution is not far from that obtained at high Reynolds numbers, except in a small domain around the bubble (0.01 m < x < 0.02 m). For $U_\infty < 34$ m/s, a sudden change occurs, corresponding to the bursting of a short bubble in a long bubble. In fact, no discontinuity in the physical size of the separation seems to exist. This can be seen in figure 36, where momentum thickness at 75 % of chord is plotted, versus upstream velocity : there is continuity in θ at the bursting point. Nevertheless, the slope of the curve changes rapidly at this point. On a practical point of view, this figure shows the unfavourable effects of long bubbles, because the momentum thickness is directly related to the drag coefficient of an airfoil.

A study of the short bubbles has then been made on a special model, called "enlarged leading edge". This model corresponds to a 2.5 m chord ONERA D airfoil, truncated and fitted with a blown flap. An important part of the experiments consisted of hot wire and LDA measurements around the separated region. Evolutions of the shape factor obtained with both methods are compared on figure 37, for a configuration where $U_\infty \simeq 13.6$ m/s and $T \simeq 0.4 \ 10^{-2}$. Discrepancies exist in the separated region, due to the presence of backflow close to the wall ; LDA gives more physical values, because it is able to measure negative velocities. The separation and reattachment points are indicated by arrows. The shape factor reaches important values (higher than 8), then decreases rapidly towards turbulent values. High frequency instability waves are recorded in the laminar boundary layer and transition starts at $R\theta_T \simeq 280$.

On the same model, high free-stream turbulence levels were generated by setting a grid at the beginning of the test section. For $T \simeq 2.5 \ 10^{-2}$, transition begins upstream of the theoretical laminar separation point ($R\theta_T \simeq 220$) and no more separated region seems to exist.

2.3.4. Effects of negative pressure gradients

Detailed transition experiments in negative pressure gradients are not numerous. As the flow acceleration acts to stabilize the laminar boundary layer, the lengths required for such studies would be too important in laboratory conditions, except if the free-stream turbulence level is high. In such a case, the external turbulence tends to counteract the favourable effect of the negative pressure gradient. This interplay can be encountered in many practical situations such as turbomachinery and was investigated, for instance, by TURNER /45/ and by BLAIR and WERLE /46/, /47/.

BLAIR and WERLE measured the characteristic parameters of boundary layers developing on a very slightly heated wall. Two accelerating flows were studied. The following expression provides accurate representations of the velocity distributions :

$$Ue = C (A - x)^{-\alpha} \quad (U_e \text{ in m/s and x in m}) \tag{18}$$

where α was close to unity, so that the acceleration parameter $K = \nu/Ue^2.dUe/dx$ was nearly independent of x. Free-stream turbulence levels ranging from 0.7 to 5 per cent were generated through the use of rectangular bar grids.

The experimental evolutions of the shape factor and of the momentum thickness are plotted in figure 38 for two different configurations. The velocity distribution is the same in both cases (C = 89.9, A = 5.08, α = + 1.066, K = $0.2 \ 10^{-6}$), but the free-stream turbulence level is respectively equal to $1 \ 10^{-2}$ (grid 1) and $2 \ 10^{-2}$ (grid 2) at the leading edge of the plate. The overall variation of the shape factor is the same as in positive pressure gradient, except that the laminar values are lower.

Figure 39 compares the streamwise variation of the momentum-thickness Reynolds number to that of the fictitious critical Reynolds number. Experimental positions of the transition onset are indicated by arrows. It appears that the laminar boundary layer remains well below the stability limit. This means that the linear processes are completely "bypassed" for these high turbulence levels.

2.4. Transition in oscillating external flow

This paragraph deals with external flows varying sinusoidally around a mean value U_o, that we will assume independent of x :

$$Ue = U_o(1 + N \sin\overline{\omega}t), \quad \overline{\omega} = 2\pi\overline{f} \tag{19}$$

This is exactly the expression already used in § 2.2.2.. But the amplitude factors are now larger than those representing sound disturbances : typical values are ranged from 0.1 to 0.3, instead of 10^{-3}. At large Strouhal numbers, the amplitude function $\Delta U/\Delta U_o$ and the phase function ϕ within the laminar boundary layer remain the same as those depicted in figure 24. Nevertheless, the velocity profile measured at a fixed station exhibits, during a cycle, large departures from the BLASIUS profile ; an instantaneous reversing flow may even occur near the wall, but this case will not be considered further. Such large values of N are usually achieved, either by a rotating vane /48/, /49/, /50/ or by driving periodically a plate in a steady stream /51/.

2.4.1. An example of periodic transition

Figure 40 presents a series of photographs obtained by OBREMSKI and FEJER /48/ in the following experimental conditions : N = 0.15, U_o = 16.6 m/s, $\overline{f}$ = 12.8 Hz. The upper trace in each photograph represents the oscillating component of the free-stream velocity and the lower trace records the instantaneous velocity at $y/\delta \simeq 0.3$. Six streamwise stations are considered. The second photograph (x = 10 in) shows that small waves (wave packet) are present in the boundary layer near the point of minimum instantaneous velocity. At the 14 in. position, the waves increase in amplitude and turbulent fluctuations appear. Further downstream, the turbulent patches increase in duration and the wave packets disappear. At the last station, the boundary layer is fully turbulent. It is important to note that all phenomena occur during a single cycle of the forced oscillation. Figure 41 summarizes these events in a space-time representation, where the time is made dimensionless with the period of the oscillation. Each photograph in figure 40 corresponds to a vertical cut in this diagram. The unsteady pressure gradients with large amplitude tend to make the phenomenon two-dimensional, as it was already observed in steady positive pressure gradients ; as a consequence, the turbulent patches "appear to extend ribbonlike across the plate and in this differ from the three-dimensional spots in steady boundary layer transition" on a flat plate /48/.

By using conditional sampling techniques, COUSTEIX, HOUDEVILLE and DESOPPER /49/ were able to plot the phase averaged velocity and fluctuation profiles at various instants throughout the cycle (experimental conditions : N = 0.16, U_o = 27 m/s, $\overline{f}$ = 37 Hz). In laminar regime, the shape factor varied typically between 2.7 and 3.5 for Strouhal numbers close to unity. The wave packets were found to occur at instants closely linked with the existence of inflexion points in the instantaneous velocity profiles. Moreover, the waves presented the characteristic features of the TOLLMIEN-SCHLICHTING waves.

This suggests that instability waves appear as free responses to the external disturbances and that their subsequent behaviour depends on the characteristics of the instantaneous profiles. In the aforementioned experiments, the circular frequency ω of the waves was an order of magnitude greater than that of the imposed oscillation, $\overline{\omega}(\omega/\overline{\omega} \simeq 30)$. This enabled OBREMSKI and MORKOVIN /52/ to reconstruct the history of the wave packets by using a quasi steady approach : at each time, the instantaneous velocity profile was introduced as a steady basic profile into the linear stability equations, and the total amplification rate of waves traveling downstream was computed. Figure 42 shows a scheme of the theoretical development of a wave packet : the likeness with the second record presented in figure 40 is striking. Moreover, a good agreement was achieved between the experimental and theoretical values of the most unstable frequencies.

2.4.2. Periodic and aperiodic transition

OBREMSKI and FEJER /48/ measured the transition location for a wide range of the parameters N, $\overline{f}$ and U_0. They deduced the curves reproduced in figure 43, which represent the evolution of the transition Reynolds number as function of N. An intriguing feature is that the experimental data correlate along two distinct, discontinuous curves AA' and BB'. OBREMSKI and FEJER explained this behaviour by introducing the non steady Reynolds number $R_{ns} = L(\Delta U_0/2\pi\nu)$, in which $L = U_0/f$ represents the distance travelled by a free-stream particle in one cycle of imposed oscillation. They stated that, when R_{ns} is lower than a critical value equal to 25 000, the transition Reynolds number is constant and independent of both N and $\overline{f}$ (curve AA'). For higher values of R_{ns}, the transition Reynolds number depends strongly on N, but not on $\overline{f}$ (curve BB'). But, as pointed out by LOEHRKE et al. /35/, this explanation is applicable only for the special natural disturbances which were present in the considered wind tunnel. On the other side, experiments conducted in negative or positive pressure gradients indicate other critical values of R_{ns}.

A more general explanation was developed by OBREMSKI and MORKOVIN /52/. The basic assumption is that the wave packets break down into turbulence if they reach a certain critical threshold, T_r :

- Wave packets which were amplified beyond T_r during the unstable part of a single cycle of the oscillation should correlate according to BB'. Photographs presented in figure 37 as well as experiments performed by COUSTEIX et al. /49/, constitute examples of this mechanism. Transition is said to be periodic.

- It is possible, however, that the wave packets remain below T_r during the unstable part of the first cycle. Quasi steady calculations indicate that the remaining part of this cycle is more stable and the waves will be more or less damped, until they reach the unstable part of the following cycle. In addition, the boundary layer becomes thicker, and the unstable frequency range shifts continuously towards lower frequencies. Such transitions require more than one cycle to develop and are likely to correlate according to AA'. As the breakdown becomes more irregular, this process was termed aperiodic by OBRESMKI and FEJER /48/.

2.4.3. Effects of lower values of $\omega/\overline{\omega}$

All the precedent experiments concerned high ratios of TOLLMIEN-SCHLICHTING frequency ω to driving frequency $\overline{\omega}$. In order to investigate the effects of lower values of $\omega/\overline{\omega}$, it was found useful to generate artificial wave packets by means of a controllable disturber. LOEHRKE (thesis, summarized in /35/) used a resistance heating wire stretched across the span of a flat plate, at $0.1 < y/\delta < 0.3$. Changing the wire temperature led to horizontal oscillations generating wave packets of known frequency and known amplitude. Tests conducted with $\omega/\overline{\omega} > 10$ supported the OBREMSKI-MORKOVIN interpretation of OBREMSKI-FEJER experiments (§ 2.4.2.): the jump from the aperiodic transition to the periodic transition was accomplished by increasing the initial amplitude of the wave packets and not by increasing R_{ns}. At lower values of $\omega/\overline{\omega}$ (in the range 3-5), no evidence of early transition was found. "Rather, one could anticipate less instability, because the TOLLMIEN-SCHLICHTING vorticity interaction has insufficient time to develop during any cycle" /35/.

As the forced oscillation frequency $\overline{\omega}$ rises at constant U_0, the natural instability frequency seems to lock onto the forcing frequency ($\omega/\overline{\omega} = 1$). It is exactly what happens with an acoustic excitation (see § 2.2.1.), except that the values of N are now larger. As in SHAPIRO's experiments, a standing wave pattern is found to occur (LOEHRKE /35/), the wave-length of which being equal to the TOLLMIEN-SCHLICHTING wave-length. But, due to the large amplitude of the forced oscillation, the growth of the unstable waves cannot be computed with a simple steady analysis as in § 2.2.1..

2.5. Influence of wall roughness

In this section, the roughness streamwise position x_k will be characterized by $\delta 1_k$ and θ_k, which represent respectively the displacement and momentum thicknesses of the laminar boundary layer in the absence of roughness. Two other important parameters are the Reynolds number $R\theta_k = Ue\theta_k/\nu$ and the ratio $k/\delta 1_k$, where k is the roughness height.

2.5.1. Two-dimensional roughness

a) Transition process behind a wire normal to the flow

The mechanism by which a two-dimensional roughness induces transition was studied in great detail by KLEBANOFF and TIDSTROM /53/. A cylindrical rod was attached to the surface of a flat plate, with its axis perpendicular to the mean flow direction. Emphasis was placed on measurements within the recovery zone, i.e. "the region in the downstream vicinity of the roughness where the mean flow has been distorted by the presence of the roughness."

Figure 44 shows the evolution of the shape factor versus $x - x_k$, for a case where $k/\delta 1_k = 0.89$ and $R\theta_k = 265$. As it can be expected, the boundary layer separates immediately downstream of the rod ; further downstream, the shape factor decreases and the mean velocity profile returns to the BLASIUS distribution. However, as it will be discussed later, the transition moved forward from its "natural" position. The recovery length is about 40 k.

By introducing a hot wire in the boundary layer, KLEBANOFF and TIDSTROM observed waves of large amplitude. They concluded that, according to linear stability theory, the inflexional velocity profiles encountered in the recovery zone caused a rapid amplification of the instability waves. The disturbances reaching the reattachment location are, then, larger than they would be without roughness and lead to a premature transition. The rod does not introduce new disturbances into the boundary layer, but strongly amplifies the existing perturbations.

HAMA, LONG and HEGARTY /54/ made water-tank observations of the flow pattern behind a wire. Dye injections revealed at first the appearance of spanwise, two-dimensional waves ; as they are swept

downstream, the waves form three-dimensional vortex loops having a well definite wave-length. This peak-valley system leads to the breakdown into turbulence. Transition occurs essentially in the same manner as it would occur on a smooth surface.

b) Movement of the transition location

When increasing the roughness height or the velocity, transition moves gradually upstream. A large amount of experimental work was done for describing this forward movement. An account of these experiments can be found in /55/. An example of correlation proposed by DRYDEN is presented in figure 45. The ratio $Rx_T/(Rx_T)_0$ is plotted as a function of $k/\delta 1_k$, where $(Rx_T)_0$ is the transition Reynolds number in "natural" conditions. Cylindrical wires are used for all experiments, except for those made by QUICK who investigated the effects of flat strips. An additional parameter is the free-stream turbulence level T. It can be seen that appreciable effects occur for roughness elements of height equal to 0.2 to 0.4 $\delta 1_k$, but that the forward movement of the transition is progressive.

2.5.2. Three-dimensional roughness

The effect of a three-dimensional roughness element is very different from that of a two-dimensional element, in the sense that the change in the transition location is more abrupt. This movement is sketched in figure 46, where the transition Reynolds number is plotted as a function of $R_k = U_k k/\nu$. U_k is the laminar velocity at $y = k$ in the absence of roughness. If some three-dimensional roughness element (sphere, small vertical rod) is placed on a flat plate, when increasing the free-stream velocity, the transition Reynolds number is at first unaffected and remains equal to that observed on a smooth surface. When the velocity exceeds some critical value Ue_c, transition moves rapidly forward : a turbulence wedge is formed ; its vertex is located close to the roughness. For spherical roughness elements, the critical value of R_k is about 500 to 600 /55/, /56/.

As pointed out by TANI /57/, no satisfactory explanation has yet been offered for this critical behaviour. Because the separated region is narrow, the mechanism valid for two-dimensional elements (§ 2.5.1.) cannot be put forward. For $Ue < Ue_c$ (subcritical velocity), GREGORY et al. /58/ and MOCHIZUKI /56/ disclosed the existence of two sets of streamwise vortices downstream of a single roughness element (see figure 47, reported in /57/). One is a pair of spiral filaments close behind the roughness, the other is a horseshoe vortex wrapped round the front of the element and trailing downstream. These vortices generate a three-dimensional laminar boundary layer with a cross-flow velocity component ; there is a possibility that transition occurs via a cross-flow instability, as it is the case for rotating disk or swept wing.

For supercritical velocities ($Ue > Ue_c$), a wedge-shaped turbulent region extends downstream of the roughness. SCHUBAUER and KLEBANOFF /59/ examined the turbulence wedge of a sphere by using hot-wire anemometer. They found that the wedge comprises a fully turbulent core beyond which the turbulence is intermittent. Measurements made by MOCHIZUKI /56/ indicate that the vertex angle of the wedge becomes larger in proportion to the velocity ; typical values are ranged from 10° to 15°. This spanwise growth results from the "transverse contamination" process, which takes place for turbulent regions embedded in a laminar boundary layer. The growth of the turbulent spots present another example of such mechanism (section 3). Another striking feature of the turbulence wedge is the presence of streamwise structures close to the wall, which can be related to the stationary vortices arising from cross-flow instability.

2.5.3. Boundary layer tripping

On a practical point of view, the study of roughness effects is important in two aspects. First of all, surface roughnesses such as rivet heads or insects may cause early transition and affect, for instance, aircraft performances. Secondly, boundary layer tripping by rough devices is often used in wind tunnel experiments in order to fix the transition at a given location. In both cases, it is of great significance to be able to estimate the downstream boundary layer behaviour.

Experiments on boundary layer tripping have been carried out at ONERA/CERT in zero, positive and negative pressure gradients /60/, /61/. As an example, we will briefly present some results obtained on a flat plate by using spanwise carborundum bands, in which the grains are glued side by side (maximum possible density). Figure 48 shows a plan view photograph of a carborundum band and a typical evolution of the roughness height in the spanwise direction. This tripping device constitutes in fact a two-dimensional assemblage of three-dimensional elements. In any case, the band width is about 10 $\delta 1_k$; k represents the nominal value of the carborundum grains size.

If one keeps Ue constant but increases k, transition moves progressively upstream towards the roughness location. Figure 49 shows mean velocity and turbulence profiles in a case where the boundary layer is turbulent just downstream of the tripping device ($x_k = 0.148$ m, $R\theta_k = 215$, $k/\delta 1_k = 1.47$). High turbulence intensities are not created on the roughness itself, but rather in the downstream separated region. We believe that the transition mechanisms are not very different from those described by KLEBANOFF-TIDSTROM /53/.

The curve plotted in figure 50 represents the critical grain size required for fixing transition at the roughness location. This critical size depends on $R\theta_k$; it is obviously equal to zero when $R\theta_k$ is equal to the "natural" transition Reynolds number, which is close to 1 000 in the present experiments.

The evolution of the momentum thickness is given in figure 51 for various configurations for which transition is "fixed" at the carborundum band. It is clear that increasing the grain size produces an over-thickness of the boundary layer due to the roughness drag. The step $\Delta\theta$ at the transition location can be expressed as :

$$\Delta\theta = \frac{1}{2} C_D \, k \, (\frac{U_k}{U_e})^2 \tag{20}$$

where the drag coefficient C_D is close to 0.5.

TOTLAND /62/ studied the effects of regularly spaced protrusions made by running a tooth wheel over an adhesive film. He found drag coefficients ranged from 0.10 to 0.70 depending on the shape of the protrusions. Another interesting finding is that a dried thin film of oil flow mixture commonly used in flow visualizations may reduce the transition Reynolds number by roughly 10 %. An overall view of TOTLAND's results is given in figure 52, where the streamwise evolution of $R\theta$ is plotted for various types of roughness.

2.5.4. Distributed roughness

As far as the effects of distributed roughness on transition are concerned, only scant results exist. FEINDT /63/ investigated the influence of sand roughness on the transition Reynolds number, for different pressure gradients and different grain sizes. The measurements were performed in a convergent and a divergent channel of circular cross-section, where T has the relatively high value of 10^{-2}. Figure 53 presents a plot of FEINDT's results as reported by SCHLICHTING /64/ ; the transition Reynolds number is given as a function of Uek/ν. Each curve corresponds to different values of the pressure gradient. It appears that Rx_T steeply decreases for $Uek/\nu > 120$. Below this value, there is no influence of the roughness and transition takes place at the same location as on a smooth surface.

2.6. Influence of suction

In order to illustrate the effects of suction on the flow stability properties, let us consider at first the so-called asymptotic suction profile. This profile is obtained when a continuous suction is applied ; at some distance from the leading edge, the boundary layer becomes independent of the x coordinate and it can be easily demonstrated that :

$$V(y) = - V_0 \quad (V_0 \text{ is the absolute value of the suction velocity})$$
$$U(y) = Ue \left[1 - \exp(V_0 y/\nu)\right] \tag{21}$$

The displacement thickness and the shape factor are equal respectively to $-\nu/V_0$ and 2. Stability calculations presented in /65/ indicate that the critical Reynolds number $R\delta_{1cr}$ is about 42 000. Other numerical results give higher values, of the order of 50 000 (see discussion in /5/). It appears that the asymptotic suction profile possesses a critical Reynolds number which is about one hundred times larger than the one of the BLASIUS profile.

Stability computations were performed for similar and non similar velocity profiles, including the combined effects of pressure gradient and suction /5/, /93/. As a result, the stabilizing effect of suction is evident.

In fact, suction acts in two ways. Firstly, it reduces the boundary layer thickness. Secondly, it creates a velocity profile which is very stable. Both effects are favourable for delaying transition, so that boundary layer suction constitutes the most effective method for viscous drag reduction (see bibliography given in /94/).

Because it is structurally difficult to entirely manufacture a surface of porous material, efforts have been made to discretize suction by slots, perforated surfaces or porous strips.

One of the first wind tunnel experiments concerned with boundary layer control by suction was done by KOZLOV, LEVCHENKO and SHCHERBAKOV /66/. They made detailed mean flow and disturbance measurements over a single slot of a flat plate and showed a significant reduction of the disturbance amplitude in the neighbourhood of the slot. But, as pointed out by SARIC and REED /93/, suction slots are expensive to fabricate and require high mass flow rates, which can lead to instabilities such as separation and backflow. On the other side, perforated surfaces can introduce three-dimensional disturbances into the boundary layer. For these reasons, attention turned to strips of porous material.

Recent experiments were conducted in this way by REYNOLDS and SARIC /67/ on a flat plate equipped with porous suction panels. TOLLMIEN-SCHLICHTING waves are introduced into the laminar boundary layer by a vibrating ribbon and their evolution is studied by hot-wire anemometry. Examples of results are shown in figures 54 and 55. In figure 54, the shape factor variation is plotted for the two cases : with and without suction. When it is present, suction is applied locally by a spanwise porous strip, at the location indicated by an arrow. The abscissa R is proportional to $\sqrt{x}$ and $V_0 = 5.7 \ 10^{-3}$ Ue. As expected, suction leads to a decrease in the shape parameter and the extent of the upstream and downstream influence of the suction strip can be observed. The decrease in H and the suction rate are relatively small, but it must be kept in mind that excessive suction amounts lead to an over-thinned boundary layer, which becomes very sensitive to surface roughness.

Figure 55 shows the evolution of the amplitude of a single frequency disturbance generated by the vibrating ribbon. The suction is intense enough to stop the disturbance growth and cause decay near the suction strip. A good agreement is obtained with the theory of REED and NAYFEH. In a general manner, experiments indicate that suction is more effective when applied at Reynolds numbers close to the lower branch of the neutral curve, than when applied in the region of maximum growth rate.

NAYFEH and EL-HADY /68/ report experiments performed by LACHMANN et al. on a 2.44 m chord model. By using fourteen porous strips, 1.9 cm wide, laminar flow down to 95 % chord was achieved at a chord Reynolds number of $15 \ 10^6$. Flight tests, however, showed difficulties in maintaining smooth joints at the edges of the strips.

2.7. Influence of transverse curvature

The effects of transverse curvature, which occur in boundary layers on axisymmetric bodies, received little attention. To our knowledge, the only available stability calculations are those performed by MORRIS and BYON /69/, who studied the boundary layer developing on a circular cylinder, the axis of which is aligned with the direction of the uniform free-stream.

An important parameter is the ratio $\delta 1/a$, where a is the cylinder radius. Figure 56 shows a comparison between the BLASIUS profile and a profile computed by MORRIS and BYON for $\delta 1/a = 0.3781$. η is a non dimensional distance. It can be seen that the profile subjected to a transverse curvature has a shape factor lower than that of the BLASIUS profile.

With the parallel flow approximation, the stability equation takes the form :

$$\varphi^{IV} + \frac{2\varphi^{III}}{r} - (2\alpha^2 + \frac{3}{r^2})\varphi'' + (\frac{3}{r^3} - \frac{2\alpha^2}{r})\varphi' + (\alpha^4 + \frac{2\alpha^2}{r^2} + \frac{3}{r^4})\varphi$$
$$- i\alpha R \left[(U - \frac{\omega}{\alpha}) (\varphi'' + \frac{\varphi'}{r} - (\alpha^2 + \frac{1}{r^2})\varphi) + (\frac{U'}{r} - U'')\varphi \right] = 0 \tag{22}$$

which reduces to the ORR-SOMMERFELD equation when r (distance to the cylinder axis) goes to infinity.

Figure 57 presents a comparison of neutral curves for the BLASIUS solution and the boundary layer on a cylinder with Reynolds number $U_e a/\nu = 71\ 122$. At all Reynolds numbers, the cylinder boundary layer is more stable than the plane boundary layer : the transverse curvature has a stabilizing influence. It should be observed that the ratios $\delta 1/a$ involved in figure 57 are rather small ($\delta 1/a = 0.014$ for $R\delta 1 = 1\ 000$). Unfortunately, MORRIS and BYON do not give neutral curves for other values of the radius Reynolds number. Increasing $\delta 1/a$ would certainly increase the critical Reynolds number.

Several experiments were conducted on axisymmetric bodies in order to avoid the corner effects (KNAPP et al. /10/, ARNAL et al. /28/). So long as the boundary layer thickness is small compared with the body radius, the plane stability results may be used with confidence.

2.8. Influence of streamwise curvature

For flows developing over a convex surface, centrifugal forces exert a stabilizing effect, in the sense that a displaced fluid element tends to be restored to its equilibrium position. The magnitude of this effect is small : LIEPMANN /70/, /71/ found that on convex surfaces up to $\delta 1/R = 0.0026$, the same TOLLMIEN-SCHLICHTING instability occurs as for the flat plate and the transition Reynolds number remains unchanged.

On the other hand, the destabilizing effect of centrifugal forces on concave walls leads to the formation of pairs of counter-rotating vortices, the axes of which are parallel to the principal flow direction (figure 58). This instability, which was first treated by GÖRTLER /72/, often results in a premature transition.

2.8.1. Theoretical aspects

On a theroretical point of view, it is assumed that a three-dimensional disturbance is superposed on the basic flow. Its form is :

$$(\hat{u}, \hat{v}, \hat{p}) = (f, \varphi, \pi) \cos(\alpha z) A$$
$$\hat{w} = h \sin(\alpha z) A \tag{23}$$

$A = \exp(kt)$ in temporal theory and $A = \exp(\beta x)$ in spatial theory. The earlier works used temporal theory ; SMITH /73/ first formulated the stability problem in terms of spatially growing disturbances. α, β (or k) are real. The amplitude functions f, φ, π and h depend on y only and the transverse wave-length λ is related to the wave number α by $\lambda = 2\pi/\alpha$. The shape of the steady vortices described by (23) is shown in figure 58.

GÖRTLER neglected the boundary layer growth (parallel flow approximation), as well as a number of terms of order δ/R, where R is the radius of curvature of the surface. Relations (23) are substituted into the continuity and the linearized momentum equations ; eliminating the pressure and the cross-flow velocity component yields :

$$(D^2 - \tilde{\alpha}^2 - \sigma)f = \varphi DU$$
$$(D^2 - \tilde{\alpha}^2)(D^2 - \tilde{\alpha}^2 - \sigma)\varphi = -2\tilde{\alpha}^2 G_L^2 fU \tag{24}$$

All quantities are made dimensionless with Ue and a characteristic length L ; $D \equiv d/d(y/L)$, $\tilde{\alpha} = \alpha L$, $\sigma = kL^2/\nu$ and $G_L = (U_eL/\nu).\sqrt{L/R}$. G_L is the GÖRTLER number, which appears in the y-momentum equation.

The above set of equations forms a sixth-order system of homogeneous, linear, ordinary differential equations and is supplemented by homogeneous boundary conditions (f = φ = 0 at y = 0 and for y → ∞). This constitutes an eigenvalue problem for the real parameters ($\tilde{\alpha}$, σ, G_L).

For several basic profiles U(y), GÖRTLER obtained approximate solutions, giving the value of G_L for neutral stability (k = 0) as function of $\tilde{\alpha}$. After GÖRTLER, many attempts were made to correct and supplement his analysis, but these various investigations disagreed often strongly. HERBERT /74/ reviewed these works and compared the resulting neutral curves. This comparison is given in figure 59 for the BLASIUS profile (it is assumed that the effect of curvature on the basic flow can be neglected). The GÖRTLER number G_L

is formed with the reference length $L = \sqrt{\nu x/U_e}$. The discrepancies between the various curves are attributed to three factors :

a) Treatment of the streamwise curvature

Since the local centrifugal force drives the unstable motion, the wall curvature plays a less important role than the overall curvature of the streamlines. GÖRTLER assumed that the streamline curvature is constant at any distance from the wall. Other models were used ; in HÄMMERLIN's calculations /75/, for example, the streamline curvature decays exponentially with y. HERBERT /74/ showed that larger rates of decay of curvature outside the boundary layer, as well as smaller streamwise extent of curvature, stabilized considerably the flow.

b) Boundary layer growth

SMITH /73/ was the first to include the normal velocity terms. HERBERT /74/ stated that the boundary layer growth should be of more importance than for the TOLLMIEN-SCHLICHTING instability.

c) Numerical accuracy

Curves 4, 8 and 9 in figure 59 were deduced from the same set of equations. However, strong discrepancies exist, especially at low $\tilde{\alpha}$. FLORYAN and SARIC /76/ suggest that SMITH's numerical method (curve 4) may not provide sufficient accuracy and that curve 8 is subject to numerical errors.

Recently, FLORYAN and SARIC /76/ developed calculations by using a curvilinear system of coordinates representing streamlines and potential lines of the inviscid flow. The streamwise extent of the curved wall is taken into account, as well as the non parallel effects. Following FLORYAN and SARIC, RAGAB and NAYFEH /77/ employed a coordinate system based on the potential- and streamlines. Both papers give nearly identical results. Figure 60 shows curves of constant growth rate for the BLASIUS flow ; when $\tilde{\alpha}$ goes to zero, the neutral curve appears to asymptotically level off at $G_L \simeq 0.47$ or $G_\theta \simeq 0.25$. In addition, RAGAB and NAYFEH computed neutral stability curves for different FALKNER-SKAN profiles. As it can be expected, favourable pressure gradients are stabilizing, whereas positive pressure gradients are destabilizing, but these effects diminish rapidly as the wave number increases.

NAYFEH /78/ studied the effect of streamwise vortices on TOLLMIEN-SCHLICHTING waves. The basic flow was the sum of a BLASIUS profile and of an additional flow describing steady counter-rotating vortices (GÖRTLER vortices for example). The numerical results showed that such vortices have a strong tendency to amplify three-dimensional TOLLMIEN-SCHLICHTING waves having a spanwise wave-length which is twice that of the vortices.

2.8.2. Experimental studies

A number of experimental studies investigated the influence of steady vortices on the transition process. TANI and co-workers (1962, 1964, 1969) concluded that GÖRTLER vortices affect indirectly the transition by inducing a spanwise variation in boundary layer thickness, at least when the radii of curvature are not very small. They found also that there is at first an exponential growth with x, which diminishes downstream.

WORTMANN /79/ studied the development of instabilities in a water tunnel with curved walls. Using the tellurium method, he determined the direction and relative magnitude of the unsteady velocities. The first step in the transition process is characterized by the classic GÖRTLER vortices pattern, as shown in figure 61a. The strong spanwise deformation of the mean velocity profile appears clearly. Further downstream, a steady second-order instability destroys the symmetry of the vortices (figure 61b) and produces between each vortex pair boundary layer profiles with several points of inflexion. WORTMANN suggested that this instability was caused by secondary vortices, the wave-length of which were twice those of the GÖRTLER vortices. A third-order instability was observed downstream, consisting of regular three-dimensional oscillations (figure 61c). The flow became turbulent a few wave-lengths downstream.

BIPPES and CÖRTLER /80/ conducted experiments on curved walls along which the GÖRTLER vortices were fairly strong. They made flow visualization by using the hydrogen-bubble technique and obtained accurate quantitative information of the flow field. Figure 62 presents the experimental profiles of the three disturbance velocity components, as compared with the eigenfunctions f, φ and h computed by FLORYAN and SARIC /76/. The normal and spanwise velocity perturbations are an order of magnitude smaller than the streamwise velocity perturbation.

Concerning the values of the GÖRTLER number at which transition begins, the experimental results are not numerous. Reference is made again to the work of LIEPMANN /70/, /71/, who investigated the influence of convex and concave curvature on the transition location. The left hand side part of figure 63 shows the evolution of $R\theta$ taken at the transition point, versus the ratio θ/R (reported in /64/). As previously stated, the effect of a convex wall remains very slight. On the other hand, increasing θ/R decreases notably the transition Reynolds number. LIEPMANN found that the transition GÖRTLER parameter $G_{\theta_T} = (R\theta.\sqrt{\theta/R})_T$ is close to 9 at a very low turbulence level, whereas at higher turbulence levels ($T \simeq 0.3\ 10^{-2}$), the value was about 6. It must be emphasized, however, that LIEPMANN's data are restricted to slightly curved walls. FOREST /81/ indicates that measurements on turbine blades give $G_{\theta_T} \simeq 4.5$ for $T \simeq 4\ 10^{-2}$. The dependence on streamwise pressure gradient is certainly small, due to the strong mean velocity profile distorsions introduced by the GÖRTLER vortices. In any case, G_{θ_T} is about two orders of magnitude greater than the critical GÖRTLER number.

3 - THE TRANSITION REGION : TURBULENT SPOTS AND INTERMITTENCY

The major part of this section is devoted to the description of the transition region in steady flow without streamwise pressure gradient (§ 3.1.), because this configuration has attracted a great number of more or less fundamental studies. Although less documented, the influence of positive or negative pressure gradients will be discussed in § 3.2.. Recently, the development of conditional sampling techniques made possible to investigate the flow behaviour in the presence of an external oscillating flows ; typical results are presented in § 3.3..

3.1. The transition region with zero pressure gradient

It has been shown (§ 2.3.) that the breakdown process results in the formation of a turbulent spot exhibiting an arrowhead shape when viewed from above (figure 7). In natural conditions, the spots originate in a more or less random fashion. Once created, they are swept along with the mean flow, growing laterally and axially and finally covering the entire surface. The transition region is defined as the region where the spots grow, overlap and form a turbulent boundary layer.

Experimentally, the transition region may be studied, either in natural or in artificial conditions. In the first case, long-time averaged measurements describe the overall evolution of the boundary layer characteristics from the laminar to the turbulent state. In the second case, turbulent spots are created artificially at fixed positions, at a given frequency ; this enables a more fundamental approach of the phenomena, because the random character of the spots development is suppressed. Both aspects will be successively reviewed.

3.1.1. Natural conditions

A general sketch of the evolution of the boundary layer parameters during transition was given in figure 1. Figure 64 shows more precisely the decrease in the shape factor from the laminar to the turbulent state as measured in the case A of our experiments /82/. Instantaneous signals recorded near the wall are also presented for three stations located respectively at the beginning, in the middle and at the end of the transition region. The successive appearance of turbulent spots, characterized by high frequency fluctuations, and of more regular laminar zones, is called the intermittency phenomenon. By definition, the intermittency factor γ represents the fraction of the total time that the flow is turbulent : in a laminar boundary layer, $\gamma' = 0$ and in a fully turbulent boundary layer, $\gamma = 1$.

Figure 65 presents two instantaneous signals recorded at the same streamwise position but at two distances from the wall, one being near the wall and the other in the middle of the boundary layer thickness. The corresponding power spectra are also given. When y increases, the signature of the spots has at first a rectangular shape and then a triangular one. The leading front of the spots is marked by an abrupt change in velocity (towards higher velocities at y = 0.4 mm, towards lower velocities at y = 2.1 mm), but the return to laminar flow is characterized by a slow, exponential-like variation of the velocity. No peak appears on the spectra.

a) Mean velocity and "turbulence" profiles

The change in the velocity profiles during the transition process is illustrated in figure 66, where the classical measurements of SCHUBAUER and KLEBANOFF /59/ are reported, with the corresponding experimental values of γ. If a pitot tube is moved downstream at a constant height near the wall, it exhibits a marked increase in the total pressure, corresponding to the increase in the mean velocity. This method (the so-called JONES's criterion) allows a rapid determination of the transition region.

Profiles of the longitudinal fluctuation intensity are shown in figure 67. As the transition region is entered, the fluctuation level increases markedly near the wall and reaches values of 15 to 16 per cent of the free-stream velocity (about twice the classical values observed in a fully turbulent boundary layer). A second local maximum appears in the middle of the transition region. Further downstream, the intensity of the first maximum decreases and the profiles look like those measured in a turbulent boundary layer.

The complexity of the transition region comes from the fact that it contains a mixture of two distinct flows, one pertaining to the laminar flow and the other pertaining to the turbulent flow. A convenient methode for studying separately both flows is the conditional sampling technique. Before presenting some results, it is necessary to precise some definitions or notations.

b) Conditional sampling

The first task is to determine a detection signal, D(t), which reflects as well as possible the considered intermittency phenomenon. D(t) may be, for instance, the instantaneous signal to be studied or a time derivative of this signal : ARNAL et al. /82/ used $\left| \partial^2 U / \partial t^2 \right|$ which is very low in laminar regions and very large in turbulent spots due to the presence of high frequency fluctuations. The comparison of D(t) with a threshold level makes possible to obtain the intermittency function I(t), which is 0 in laminar regions and 1 in turbulent regions, and I(t) enables to compute some interesting quantities :

$$\gamma = \overline{I(t)} \qquad \text{Intermittency factor}$$

$$U_t = \overline{I(t)\,u(t)}/\gamma \qquad \text{Turbulent mean velocity}$$

$$U_\ell = \overline{(1 - I(t))\,u(t)}/(1 - \gamma) \qquad \text{Laminar mean velocity}$$

The overbar denotes a time-averaged value.
u'_t (respectively u'_ℓ) are the instantaneous fluctuations around U_t (respectively U_ℓ). It is obvious that relations exist between a quantity and its conditional sampled values inside and outside a turbulent spot :

$$U = \gamma U_t + (1 - \gamma)U_\ell \qquad (25)$$

$$u'^2 = \gamma u_t'^2 + (1 - \gamma) u_\ell'^2 + \gamma(1 - \gamma) (U_t - U_\ell)^2 \qquad (26)$$

Similar relations can be obtained for v'^2, w'^2, $\overline{u'v'}$, u'^3 and so on. U_t, U_ℓ, $u_t'^2$, $u_\ell'^2$ ... are zone averages.

A second type of conditional sampling results is given by the so-called <u>ensemble averages</u>. Let T_t be the total duration of a spot and t the time measured from the beginning of this spot. At a fixed value of t/T_t, we can calculate an arithmetic average of $U(t)$ over a great number of spots, even if these spots are not of equal duration. A statistical picture of a spot is deduced by varying t/T_t from 0 to 1. Such an average will be denoted by $<U_t>$. In the same way, it is possible to obtain ensemble averages for $<U_\ell>$, $<V_t>$, $<V_\ell>$, $<u_t'^2>$, $<u_\ell'^2>$ and so on.

c) Examples of results

Conditional sampling of the instantaneous longitudinal velocity was performed in the zero pressure gradient case, at the three stations indicated in figure 64 /82/. Figure 68 shows the distributions of γ across the boundary layer. γ varies from a constant maximum value close to the wall to zero towards the edge, but it is generally assumed that the γ value near the wall is the characteristic property of importance for the transition region. These maximum values are equal respectively to 0.25, 0.55 and 0.85 for $x = 0.87$ m, 0.94 m and 1.07 m. The streamwise evolution of γ will be discussed in Chapter II, which deals with the prediction methods of the transition region.

Figure 69 presents the zone averaged profiles of the laminar and turbulent mean velocities. According to the observations made on the instantaneous signals, the difference $U_t - U_\ell$ is positive near the wall and becomes negative when the outer edge of the boundary layer is approached.

Relation (26) indicates that the turbulence intensity u'^2 measured by a hot wire (which integrates the square of $\widetilde{u}'$ over a long time) is the sum of three terms : a turbulent term, a laminar term (usually small) and a third term which accounts for the steps between laminar and turbulent mean velocities. These three components are plotted in figure 70 for the station located towards the end of the transition region. As expected, the laminar contribution is very low ; on the contrary, the term $\gamma(1 - \gamma)(U_t - U_\ell)^2$ plays an important role, as it can be seen on the right hand side of the figure, where is plotted the ratio of this term to the global "turbulence" u'^2. Close to the wall, it represents about 40 per cent of u'^2 ; it vanishes at the point where the laminar and turbulent mean velocities are equal and then presents a second maximum, which corresponds to the second maximum observed on the u'^2 profile.

Ensemble averages of the turbulent velocity are presented in figure 71 ; they were computed for various distances from the wall, in the middle of the transition region. In this plot, we assume that the leading interface of the spot appears at the same time for all values of y. This adjustment in time allows to draw ensemble averaged instantaneous profiles during the passage of the spot. Four of these profiles are shown in figure 72. Profile 1 is close to the BLASIUS profile (H = 2.6) ; profile 2 is essentially characterized by an instantaneous increase in the boundary layer thickness and by a decrease in the shape factor. Profile 3 presents high velocities close to the wall. At the end of the spot (or at the beginning of the following laminar region), profile 4 looks like a laminar velocity profile in accelerating flow (H $\simeq$ 2).

3.1.2. Artificially created spots

Different techniques have been used for initiating turbulent spots in a nominally laminar boundary layer :
- electric sparks : MITCHNER /83/, SCHUBAUER-KLEBANOFF /59/, ELDER /84/, WYGNANSKI-SOKOLOV-FRIEDMANN /85/ ...

- small jets of short duration : COLES-BARKER /86/, CANTWELL-COLES-DIMOTAKIS /87/, MATSUI /88/, GAD-EL-HAK - BLACKWELDER-RILEY /89/.

- displacement of a small pin into the boundary layer : COLES-SAVAS /90/ ...

a) Shape of the spots - Propagation velocities

In the following lines, h and b will refer respectively to the height of the spot and to its span ; b = 0 corresponds to the vertical plane of symmetry.

The general shape of a turbulent spot is depicted in figure 73. Figure 73a shows a cross-section of the spot through its vertical plane of symmetry. It has a more or less triangular shape, with a slight overhang at the leading interface. The spot is presented in a (t, y) diagram. When presented in the physical (x, y) coordinates, it would have a more flat shape. In a plan view, the spot presents the well-known arrowhead shape, as it can be seen in figure 73b. The leading edge is swept backwards at an angle θ of about 15°. If the maximum span of the spot is plotted as a function of the streamwise distance, it appears that the spot grows linearly with x. The wedge angle was found approximately equal to 10° or 11° /85/.

Figure 74 is extracted from the work of WYGNANSKI et al.. It shows the spanwise variation of the propagation velocities of the spot. "The propagation velocity U_{TE} of the trailing edge is 0.5 Ue and seems to be independent of the coordinates x, y and z. The propagation velocity U_{LE} of the leading edge is 0.89 Ue on the plane of symmetry only and decreases slowly with increasing z." These values are in agreement with those found by SCHUBAUER-KLEBANOFF, except that the latter authors measured some increase of U_{LE} with y. It is clear, however, that the difference $U_{LE} - U_{TE}$ explains the streamwise spread of the spots.

CANTWELL, COLES and DIMOTAKIS /87/ studied the structure of a spot in its plane of symmetry. They discovered that the mean flow can be fitted to a conical growth law, that is to say the spot can be described by two similarity coordinates, ξ and η :

$$\xi = \frac{x}{U_e t} \quad \text{and} \quad \eta = \frac{y}{U_e t}$$

Thus, they could use their experimental data to construct streamlines and particle paths in the similarity coordinates. These plots revealed the existence of two vortex structures inside the spot.

b) Mean velocity measurements

WYGNANSKI et al. as well as CANTWELL et al. determined the ensemble velocity $\langle U_t \rangle$ as a function of t for various values of y. Figure 75 shows a qualitative comparison between the results of CANTWELL et al. and those obtained in natural conditions. The overall pattern is the same. Moreover, instantaneous profiles measured by WYGNANSKI et al. exhibit an evolution similar of that depicted in figure 72.

WYGNANSKI et al. measured also the two other components of the mean velocity. Figure 76 represents the variations in U and V during the passage of a spot, for $y/h = 0.325$, and at different spanwise locations. The normal velocity V is strongly negative after the leading interface and becomes positive throughout the rest of the spot ; the total variation in V is about $0.03 \, U_e$. This histogram may be interpreted as the signature of a horseshoe vortex. Measurements of the spanwise velocity indicate that W increases with increasing z and reaches a maximum at $z/b > 0.7$ where $W \simeq 0.07 \, U_e$.

c) Structure of the turbulent spots

By using conditional sampling techniques, COLES and BARKER /86/ found that a turbulent spot is essentially a single, large horseshoe vortex structure. WYGNANSKI et al. agreed with this conclusion, but later, CANTWELL et al. concluded that there were in fact two vortex structures associated with the average spot. In fact, as the spot is ever growing, its structure must evolve in time.

This was demonstrated by MATSUI /88/ who studied spots development using the hydrogen bubble technique. Figure 77 shows successive photographs obtained when a bubble generating wire is placed horizontally to the wall. In the first picture, a strong horseshoe vortex and some streamwise vortices are visible. While the spot is travelling downstream, new vortices are created, leading to a marked increase in the spot size. MATSUI concluded that a spot was composed of many small vortices ; the new vortices generated on both sides of the spot explain its lateral growth (cross-contamination process, see below) ; the new vortices generated in the rear part of the spot explain its streamwise growth. GAD-EL-HAK et al. /89/ concluded in the same way ; they stated that a spot is "a random collection of turbulent eddies" and that it grows "by adding more eddies to this collection."

When the spot reaches a certain size, it presents most of the classical turbulent properties. This results was found to apply in natural conditions (gaussian distribution of the u' fluctuation /82/) as well as in controlled conditions (logarithmic velocity distribution near the wall /85/).

d) The growth mechanisms

Entrainment of the non turbulent fluid may occur through two ways :

- by entrainment of the external irrotational fluid ;
- by entrainment of the rotational fluid in the ambient laminar boundary layer.

The first mechanism is similar to that observed in a fully developed turbulent boundary layer. It involves large scale eddies in a "gulping" process and is responsible for the spread of the spot in planes normal to the wall.

The second mechanism is very different from classical entrainment. It is responsible for the spanwise growth of the spot, which is an order of magnitude greater than that normal to the plate : $dh/dx \simeq 0.013$ and $db/dx \simeq 0.18$, where h and b denote characteristic scales of the spot in the y and z directions, respectively /89/. CHARTERS (1943) was the first to note that the transverse growth rate of a turbulent region embedded in a laminar boundary layer is larger than usual entrainment rates. He called this process "transverse contamination" ; GAD-EL-HAK et al. /89/ call it "growth by destabilization" : the turbulent eddies within the approaching spot may induce perturbations into the surrounding unstable laminar boundary layer.

These fluctuations grow up and break down, forming new turbulence without ever being in contact with the older turbulence. The same mechanism explains the spread of a turbulent wedge behind a three-dimensional roughness element (§ 2.5.2.). The vertex angle of the wedge (typically 10° to 15°) is comparable with the maximum angle subtended by the spot measured from its virtual origin (about 10° /85/).

e) Interactions between spots

Up to now, only individual spots have been considered. So, the problem is to examine if the preceding results remain valid when several spots travel downstream together.

ELDER /84/ investigated the degree of interaction between two identical spots placed side by side. It was found that spots grow independently of each other.

A completely different conclusion was given by COLES and SAVAS /90/ who created large arrays of spots : the interaction between neighboring spots cause a strong reduction in the growth rate of each spot, in both the spanwise and streamwise directions. The growth rate normal to the wall, however, is

almost unaffected. The differences with ELDER's findings may be attributed to a greater number of spots and higher values of the Reynolds number.

Another important interaction reported by COLES and SAVAS is the appearance of distinct new regions of turbulence to the rear of the original spots and in the gaps between them. This can be explained by the "transverse contamination" process. What is more striking is that the new turbulent regions grow rapidly in size while the original spots decay and disappear. This "edddy transposition" process occurs especially when substantial regions of laminar flow exist between the spots. Such a phenomenon needs further investigations.

3.2. The transition region in pressure gradients

Due to the lack of results obtained with artificially created spots, all experiments described below were carried out in "natural" conditions.

3.2.1. Effect of a mild positive pressure gradient

Figure 78 compares instantaneous signals recorded near the wall in cases A and B for the experiments performed at ONERA/CERT /91/. Case A is the zero pressure gradient case previously described. In case B, the flow is subjected to a mild positive pressure gradient and transition starts at a value of the shape factor close to 2.8. Both signals were recorded in the middle of the transition region ($\overset{\bullet}{H} \simeq 2$), at the same dimensionless distance from the wall ($y/\theta = 0.4$). The local free-stream velocities are respectively equal to 33 m/s and 28 m/s.

It appears essentially that intermittency is less apparent when transition occurs in an even slight positive pressure gradient. As it has been pointed out in § 2.3., the instability waves exhibit large amplitudes, which make the turbulent spots difficult to distinguish. The conditional sampling techniques are not easy to apply, because the choice of an appropriate detection signal is not obvious.

3.2.2. Effect of a strong positive pressure gradient

In case F, transition starts near the laminar separation point. It is useful to recall that the transition location is defined as the location where H begins to decrease. The signals recorded in the middle of the transition region (figure 79) do not present any trace of turbulent spots and peaks appear on the spectra at the frequency of the instability waves /91/.

The "turbulent" boundary layer developing downstream of the transition region was studied in the same case /91/. Although the shape factor is close to 1.4, the $\tilde{u}'$ fluctuations keep a long time the signature of the laminar instability waves, especially in the outer part of the boundary layer.

The disappearance of turbulent spots in the presence of a strong positive pressure gradient was investigated in detail by COUSTEIX and PAILHAS /92/ who studied the flow development on an ONERA D profile (chord Reynolds number : $3.2 \ 10^5$). Figure 80 shows the streamwise evolution of the shape factor and some examples of $\tilde{u}'$ records. The corresponding turbulence profiles are plotted in figure 81. At x/c = 0.875, the signal contains essentially instability waves ; the root-mean-square value represents about 12 per cent of the free-stream velocity. Further downstream (x/c = 0.925), high frequency fluctuations are superimposed on the primary wave. At the last station, the shape factor has a nearly turbulent value (H = 1.7), but the velocity fluctuation remains practically periodic. Measurements performed with two hot wires displaced in the spanwise direction indicated that the primary oscillation is two-dimensional, at least up to x/c = 0.90. The power spectra reveal that the passage from the "laminar" to the "turbulent" state is accomplished by a progressive appearance of harmonics or subharmonics of the primary wave. These observations agree with visualizations made in water tunnel (WERLE /93/) in the case of leading edge separation bubbles : the instability waves take the form of regular, two-dimensional rollers, which loose progressively their individuality due to the turbulent diffusion process. Peak-valley systems, spikes or spots are never observed. Other experiments /44/ led to the same conclusions.

3.2.3. Effect of a negative pressure gradient

To our knowledge, detailed studies of the transition region have never been made, at least for low free-stream turbulence levels. Some information is available at higher values of T. TURNER /45/ determined the variation of the heat transfer coefficient along a cooled turbine blade ; BLAIR and WERLE /46/ measured the mean velocity and temperature profile along a slightly heated wall. In such cases, transition starts at low Reynolds numbers, but it sometimes extends over large downstream distances : TURNER studied a configuration ($T \simeq 2 \ 10^{-2}$) in which transition occurs at $x \simeq 1.5$ cm but is not terminated at the blade trailing edge (x = 7 cm). Such experiments provide good tests for practical calculation methods (see Chapter II).

3.3. The transition region in oscillating external flow

It was already noted (§ 2.4.) that the turbulent patches appeared as quasi two-dimensional ribbons or belts, extending across the flat plate, provided that the relative amplitude N be large enough (say, N of the order of 0.1).

Let us return now to figure 41, which shows the space-time spreading of wave packets and turbulent regions for a periodic transition. The slopes of the curves marking the limits of the turbulent regions give the propagation velocities of the patches. The average values of OBREMSKI-FEJER /48/ are $0.88 \ U_o$ and $0.51 \ U_o$ for the leading interface and trailing interface speeds, respectively. COUSTEIX et al. /49/ found similar values ($0.89 \ U_o$ and $0.48 \ U_o$). The corresponding propagation speeds of the three-dimensional spots were $0.89 \ U_e$ and $0.50 \ U_e$ on the plane of symmetry (WYGNANSKI et al. /84/, see § 3.1.2.). It appears that the streamwise turbulence spread presents striking similarities for steady and unsteady boundary layers.

Other similarities become more apparent when ensemble velocities are computed. Figure 82 presents ensemble averages of the streamwise velocity at a station where the intermittency factor is close to 0.5 (COUSTEIX et al. /49/). The upper curve represents the evolution in time of the free-stream velocity. As in steady flow, the signature of the turbulent patches manifests itself close to the wall by rectangular velocity steps. Towards the boundary layer edge, the turbulent velocity becomes lower than the laminar one. Figure 83 shows instantaneous velocity and turbulence profiles obtained at the same station at different times during a cycle. As the turbulent region is entered, the increase in the boundary layer thickness is more pronounced than in steady flow (figure 73), but the overall evolution is the same. On the other side, turbulence profiles measured inside the turbulent patches are not far from those measured in a steady turbulent boundary layer.

R E F E R E N C E S

/1/ SCHUBAUER G.B.
SKRAMSTAD H.K.
"Laminar boundary layer oscillations and transition on a flat plate"
Rept. 909 NACA (1948)

/2/ JORDINSON R.
"The flat plate boundary layer. Part 1 – Numerical integration of the
ORR–SOMMERFELD equation"
J. Fluid Mech. Vol. 43, Part 4 (1970)

/3/ OBREMSKI H.J.
MORKOVIN M.V.
LANDAHL M.
"A portfolio of stability characteristics of incompressible boundary
layers"
AGARDograph 134 NATO (1969)

/4/ BARRY M.D.J.
ROSS M.A.S.
"The flat plate boundary layer. Part 2 – The effect of increasing thick-
ness on stability"
J. Fluid Mech. Vol. 43, Part 4 (1970)

/5/ SARIC W.S.
NAYFEH A.H.
"Non parallel stability of boundary layers with pressure gradients and
suction"
AGARD-CP-224 (1977)

/6/ GASTER M.
"A note on the relation between temporally increasing and spatially in-
creasing disturbances in hydrodynamic stability"
J. Fluid Mech. Vol. 14 (1962) 222-224

/7/ ROSS J.A.
BARNES F.H.
BURNS J.G.
ROSS M.A.S.
"The flat plate boundary layer. Part 3 – Comparison of theory with
experiment"
J. Fluid Mech. Vol. 43, Part 4 (1970)

/8/ GASTER M.
GRANT I.
"An experimental investigation of the formation and development of a
wave packet in a laminar boundary layer"
Proc. R. Soc. Lond. 1 347 (1975) 253-269

/9/ GASTER M.
"A theoretical model of a wave packet in the boundary layer on a flat
plate"
Proc. R. Soc. Lond. A 347 (1975) 271-289

/10/ KNAPP C.F.
ROACHE P.J.
MUELLER T.J.
"A combined visual and hot-wire anemometer investigation of boundary
layer transition"
UNDAS-TR-866 CK (1966)

/11/ KLEBANOFF P.S.
TIDSTROM K.D.
SARGENT L.M.
"The three-dimensional nature of boundary layer instability"
J. Fluid Mech. Vol. 12, Part 1 (1962)

/12/ KOVASZNAY L.S.G.
KOMODA H.
VASUDEVA B.R.
"Detailed flow field in transition"
Proc. 1962 Heat Transfer and Fluid Mech. Inst., STANFORD University Press
(1962)

/13/ TANI I.
"Some thoughts on boundary layer transition"
IUTAM Symposium on Laminar-Turbulent Transition, STUTTGART 1979,
Springer Verlag (1980)

/14/ BENNEY D.J.
LIN C.C.
"On the secondary motion induced by oscillations in a shear flow"
Phys. Fluids, 3, (1960) 656-657

/15/ BENNEY D.J.
"A non linear theory for oscillations in a parallel flow"
J. Fluid Mech. Vol. 10 (1961) 209-236

/16/ BENNEY D.J.
"Finite amplitude effects in an unstable laminar boundary layer"
Phys. Fluids, 7, (1964) 319-326

/17/ CRAIK A.D.D.
"Non linear resonant instability in boundary layers"
J. Fluid Mech. Vol. 50, Part 2 (1971)

/18/ HERBERT T.
"Subharmonic three-dimensional disturbances in unstable plane shear flows"
AIAA Paper n° 83-1759 (1983)

/19/ SARIC W.S.
THOMAS A.S.W.
"Experiments on the subharmonic route to turbulence in boundary layers"
IUTAM Symposium on Turbulence and Chaotic Phenomena in Fluids, KYOTO,
(September 1983)

/20/ HAMA F.
NUTANT J.
"Detailed flow-field observations in the transition process in a thick
boundary layer"
Proc. 1963 Heat Transfer and Fluid Mech. Inst., STANFORD University Press

/21/ GREENSPAN H.P.
BENNEY D.J.
"On shear layer instability, breakdown and transition"
J. Fluid Mech. Vol. 15 (1963) 133-153

/22/ LANDAHL M.T.   "Wave mechanics of breakdown"
                            J. Fluid Mech. Vol. 56, Part 4 (1972)

/23/ STEWARTSON K.   "Some aspects of non linear stability theory"
                            Fluid Dynamic Transactions, 7, (1975) 101-128

/24/ CRIMINALE W.O.   "Interaction of the laminar boundary layer with free-stream turbulence"
                            Phys. Fluids Supplement (1967)

/25/ ROGLER H.L.   "The coupling between free-stream disturbances, driver oscillations,
                            forced oscillations and stability waves in a spatial analysis of a
                            boundary layer"
                            AGARD-CP-224 (1977)

/26/ WELLS C.S.   "Effects of free-stream turbulence on boundary layer transition"
                            AIAA Journal, Vol. 5, N° 1 (1967) 172-174

/27/ MACK L.M.   "Transition and laminar instability"
                            Jet Propulsion Laboratory Publication 77-15, PASADENA, CALIFORNIA (1977)

/28/ ARNAL D.   "Recherches sur la transition en écoulement incompressible"
     JUILLEN J.C.   T.P. ONERA N° 1976-146 (1976)

/29/ ARNAL D.   "Contribution expérimentale à l'étude de la réceptivité d'une couche
     JUILLEN J.C.   limite laminaire à la turbulence de l'écoulement général"
                            Rapport Technique OA N° 1/5018 AYD (1978)

/30/ MURDOCK J.W.   "The generation of a TOLLMIEN-SCHLICHTING wave by a sound wave"
                            IUTAM Symposium on Laminar-Turbulent Transition, SUTTGART 1979,
                            Springer Verlag (1980)

/31/ SHAPIRO P.   "The influence of sound upon laminar boundary layer instability"
                            Report N° 83458-83560-1, MASSACHUSETTS Institute of Technology, CAMBRIDGE,
                            MASSACHUSETTS (1977)

/32/ LEEHEY P.   "Leading edge effect in laminar boundary layer excitation by sound"
     SHAPIRO P.   IUTAM Symposium on Laminar-Turbulent Transition, STUTTGART 1979,
                            Springer Verlag (1980)

/33/ THOMAS A.S.W.   "Sound and TOLLMIEN-SCHLICHTING waves in a BLASIUS boundary layer"
     LEKOUDIS S.G.   Phys. Fluids, Vol. 21, N° 11 (1978)

/34/ TAM C.K.W.   "The excitation of TOLLMIEN-SCHLICHTING waves in low subsonic boundary
                            layers by free-stream sound waves"
                            J. Fluid Mech. Vol. 109 (1981) 483-501

/35/ LOEHRKE R.I.   "Review-Transition in non reversing oscillating boundary layers"
     MORKOVIN M.V.   J. of Fluids Engineering (1975)
     FEJER A.A.

/36/ SPANGLER J.G.   "Effect of free-stream disturbances on boundary layer transition"
     WELLS C.S.   AIAA Journal, Vol. 6, N° 3 (1968) 543-545

/37/ DUNN D.W.   "On the stability of the laminar boundary layer in a compressible fluid"
     LIN C.C.   J. of the Aerospace Sciences, Vol. 22 (1955)

/38/ LEES L.   "The stability of the laminar boundary layer in a compressible flow"
                            NACA Report N° 876 (1947)

/39/ ARNAL D.   "Analyse expérimentale de la transition de la couche limite, avec gra-
     JUILLEN J.C.   dient de pression nul et positif"
     MICHEL R.   T.P. ONERA N° 1979-8 (1979)

/40/ JUILLEN J.C.   "Profils de vitesse moyenne et de turbulence mesurés dans une couche
     ARNAL D.   limite de transition, en gradient de pression nul et positif"
                            Rapport Technique OA N° 17/5018 AND (1981)

/41/ COUSTEIX J.   "Etude exploratoire d'un processus de transition laminaire-turbulent au
     PAILHAS G.   voisinage du décollement d'une couche limite laminaire"
                            T.P. ONERA N° 1979-86 (1979)

/42/ TANI I.   "Low-speed flows involving bubble separations"
                            Progress in Aeronautical Science, Vol. 5, Pergamon Press (1964)

/43/ GLEYZES C.   "A calculation method of leading edge separation bubbles"
     COUSTEIX J.   T.P. ONERA N° 1983-10 (1983)
     BONNET J.L.

/44/ BONNET J.L.   "Etude expérimentale de la transition dans les bulbes de décollement
     GLEYZES C.   laminaire au bord d'attaque des profils d'aile"
                            Rapport Technique OA N° 23/5018 AND (1983)

/45/ TURNER A.B.
"Local heat transfer measurements on a gas turbine blade"
J. of Mechanical Engineering Science, Vol. 13, N° 1 (1971)

/46/ BLAIR M.F.
WERLE M.J.
"Combined influence of free-stream turbulence and favourable pressure gradients on boundary layer transition and heat transfer"
UTRC Report R 81-914388-17 (1981)

/47/ BLAIR M.F.
"Influence of free-stream turbulence on boundary layer transition in favourable pressure gradients"
J. of Engineering for Power, Vol. 104 (1982) 743-750

/48/ OBREMSKI H.J.
FEJER A.A.
"Transition in oscillating boundary layer flows"
J. Fluid Mech. Vol. 29, Part 1 (1967)

/49/ COUSTEIX J.
HOUDEVILLE R.
DESOPPER A.
"Transition d'une couche limite soumise à une oscillation de l'écoulement extérieur"
AGARD-CP-224 (1977)

/50/ DESOPPER A.
"Etude expérimentale des couches limites turbulentes et transitionnelles en écoulement pulsé - Essai de prévision théorique"
Thèse de Docteur-Ingénieur soutenue à l'ENSAE (TOULOUSE) (1977)

/51/ KOBASHI Y.
HAYAKAWA M.
"The transition mechanism of an oscillating boundary layer"
IUTAM Symposium on Laminar-Turbulent Transition, STUTTGART 1979, Springer Verlag (1980)

/52/ OBREMSKI H.J.
MORKOVIN M.V.
"Application of a quasi steady stability model to periodic boundary layer flows"
AIAA Journal, Vol. 7, N° 7 (1969) 1298-1301

/53/ KLEBANOFF P.S.
TIDSTROM K.D.
"Mechanism by which a two-dimensional roughness element induces boundary layer transition"
Phys. Fluids, Vol. 15, N° 7 (1972) 1173-1188

/54/ HAMA F.R.
LONG J.D.
HEGARTY J.C.
"On transition from laminar to turbulent flow"
J. of Applied Physics, Vol. 28, N° 4, (1957) 388-394

/55/ DRYDEN H.L.
"Transition from laminar to turbulent flow"
Turbulent Flows and Heat Transfer, High Speed Aerodynamics and Jet Propulsion, C.C. Lin Edition (1959)

/56/ MOCHIZUKI M.
"Smoke observations on boundary layer transition caused by a spherical roughness element"
J. of the Physical Society of JAPAN, Vol. 16, N° 5, (1961) 995-1008

/57/ TANI I.
"Three-dimensional aspects of boundary layer transition"
Proc. Indian Acad. Sci. (Engg. Sci.), Vol. 4, Part 2, (1981) 219-238

/58/ GREGORY N.
WALKER W.S.
"The effect on transition of isolated surface excrescences in the boundary layer"
ARC R and M N° 2779, Part 1 (1951)

/59/ SCHUBAUER G.B.
KLEBANOFF P.S.
"Contribution on the mechanics of boundary layer transition"
Rept. 1289, NACA (1956)

/60/ ARNAL D.
JUILLEN J.C.
OLIVE M.
"Etude expérimentale du déclenchement de la transition par rugosités en écoulement uniforme incompressible"
Rapport Technique OA N° 4/5018 AYD (1979)

/61/ ARNAL D.
JUILLEN J.C.
OLIVE M.
"Etude expérimentale du déclenchement de la transition par rugosités en gradient de pression négatif sur profil d'aile, en incompressible"
Rapport Technique OA N° 5/5018 AYD (1979)

/62/ TOTLAND E.
"An experimental investigation of the effects of different transition devices on boundary layer transition on a flat plate with profiled leading edge"
FFA T.N. AU-1274, Aeron. Res. Inst. SWEDEN (1976)

/63/ FEINDT E.G.
"Untersuchungen über die Abhängigkeit des Umschlages laminar-turbulent von der Oberflachenrauhigkeit und der Druckverteilung"
Jahrbuch 1956 der Schiffbautechnischen Gesellschaft 50, (1957) 180-203

/64/ SCHLICHTING H.
"Boundary layer theory"
6th ed. McGRAW-HILL, NEW YORK (1968) 431-522

/65/ ROSENHEAD L.
"Laminar boundary layers"
OXFORD University Press (1963)

/66/ KOZLOV V.V.
LEVCHENKO V. Ya.
SCHERBAKOV V.A.
"Growth of disturbances in a boundary layer with a suction slot"
(in Russian) Ucheniye Zapiski TsAGI, Vol. 9, N° 2, (1978) 99-105

/67/ REYNOLDS G.A.
SARIC W.S.
"Experiments on the stability of the flat plate boundary layer with suction"
AIAA Paper N° 82-1026 (1982)

/68/ NAYFEH A.H.
EL-HADY N.M.
"An evaluation of suction through porous strips for laminar flow control"
AIAA Paper N° 79-1494 (1979)

/69/ MORRIS P.J.
BYON W.
"The stability of the axisymmetric boundary layer on a circular cylinder"
AIAA Paper N° 82-1012 (1982)

/70/ LIEPMANN H.W.
"Investigations on laminar boundary layer stability and transition on
curved boundaries"
NACA Wartime Report W-107 (1943)

/71/ LIEPMANN H.W.
"Investigation of boundary layer transition on concave walls"
NACA Wartime Report W-87 (1945)

/72/ GÖRTLER H.
"On the three-dimensional instability of laminar boundary layers on
concave walls"
NACA Tech. Memo. 1375 (1954)

/73/ SMITH A.M.O.
"On the growth of TAYLOR-GÖRTLER vortices along highly concave walls"
Quaterly Journal of Applied Mathematics, Vol. 13, N° 3, (1955) 233-262

/74/ HERBERT Th.
"On the stability of the boundary layer along a concave wall"
Archiwum Mechaniki Stosowanej, Vol. 28, N° 5-6 (1976) 1039-1055

/75/ HÄMMERLIN G.
"Über die Stabilität einer kompressiblen Strömung längs einer konkaven
Wand bei verschiedenen Wandtemperaturverhältnissen"
Deutsche Versuchsanstalt für Luftfahrt, Bericht 176 (1961)

/76/ FLORYAN J.M.
SARIC W.S.
"Stability of GÖRTLER vortices in boundary layers"
AIAA Journal, Vol. 20, N° 3 (1982) 316-324 (also AIAA Paper N° 79-1497,
1979)

/77/ RAGAB S.A.
NAYFEH A.H.
"On GÖRTLER instability"
VIRGINIA Polytechnic Institute and State University, BLACKSBURG,
VA 24061 (1979)

/78/ NAYFEH A.H.
"Effect of streamwise vortices on TOLLMIEN-SCHLICHTING waves"
VIRGINIA Polytechnic Institute and State University, BLACKSBURG (1979)

/79/ WORTMANN F.X.
"Visualization of transition"
J. Fluid Mech., Vol. 38, Part 3 (1969)

/80/ BIPPES H.
GÖRTLER H.
"Dreidimensionale Störungen in der Grenzschicht an einer konkaven Wand"
Acta Mechanica, Vol. 14, N° 4, (1972) 251-267

/81/ FOREST A.E.
"Engineering predictions of transitional boundary layers"
AGARD-CP-224 (1977)

/82/ ARNAL D.
JUILLEN J.C.
"Etude de l'intermittence dans une région de transition"
La Recherche Aérospatiale N° 1977-3 (1977)

/83/ MITCHNER M.
"Propagation of turbulence from an instantaneous point disturbance"
J. Aero. Sci. 21 (1954) 350-351

/84/ ELDER J.W.
"An experimental investigation of turbulent spots and breakdown to
turbulence"
J. Fluid Mech., Vol. 9, Part 2 (1960)

/85/ WYGNANSKI I.
SOKOLOV M.
FRIEDMAN D.
"On a turbulent spot in a laminar boundary layer"
J. Fluid Mech., Vol. 78, Part 4 (1976)

/86/ COLES D.
BARKER S.J.
"Some remarks on a synthetic turbulent boundary layer"
Turbulent Mixing in Non Reactive and Reactive Flows, ed. S.N.B. MURTHY,
Plenum, (1975)

/87/ CANTWELL B.
COLES D.
DIMOTAKIS P.
"Structure and entrainment in the plane of symmetry of a turbulent spot"
J. Fluid Mech., Vol. 87, Part 4 (1978)

/88/ MATSUI T.
"Visualization of turbulent spots in the boundary layer along a flat
plate in a water flow"
IUTAM Symposium on Laminar-Turbulent Transition, STUTTGART 1979,
Springer Verlag (1980)

/89/ GAD-EL-HAK M.
BLACKWELDER R.
RILEY J.J.

"A visual study of the growth and entrainment of turbulent spots"
IUTAM Symposium on Laminar-Turbulent Transition, STUTTGART 1979,
Springer Verlag (1980)

/90/ COLES D.
SAVAS O.

"Interactions for regular patterns of turbulent spots in a laminar
boundary layer"
IUTAM Symposium on Laminar-Turbulent Transition, STUTTGART 1979,
Springer Verlag (1980)

/91/ ARNAL D.
JUILLEN J.C.

"Résultats expérimentaux relatifs à l'influence des processus de tran-
sition sur la structure initiale d'une couche limite turbulente"
T.P. ONERA N° 1979-128 (1979)

/92/ WERLE H.
LAVERRE J.

"Techniques de visualisations d'écoulements pariétaux"
T.P. ONERA N° 1977-86 (1977)

/93/ SARIC W.S.
REED H.L.

"Effect of suction and blowing on boundary layer transition"
AIAA Paper N° 83-0043 (1983)

/94/ TUTTLE M.H.
MADDALON D.V.

"Laminar flow control (1976-1982) - A selected, annotated bibliography"
NASA Technical Memorandum 84496 (1982)
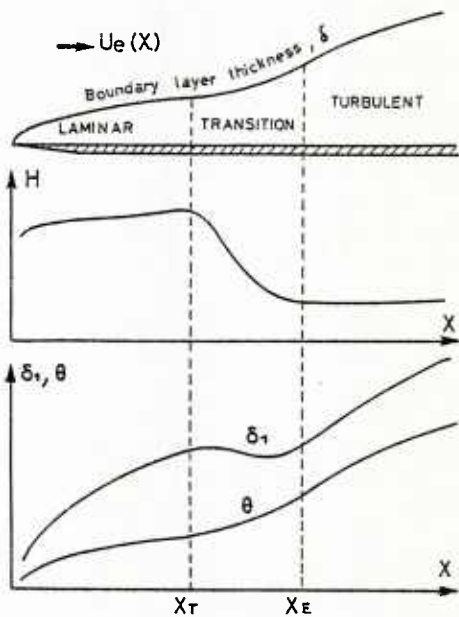
Fig. 1 - Boundary layer development
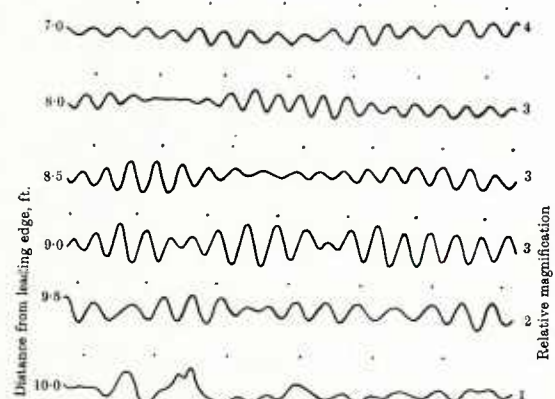
Fig. 2 - Records showing laminar boundary layer
oscillations /1/ - Distance from surface :
0.023 in. Ue = 53 ft/sec.

(a)

(b)
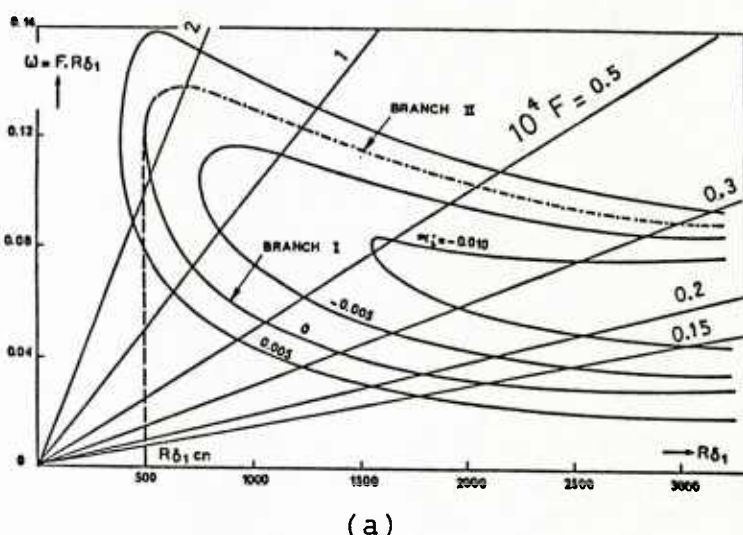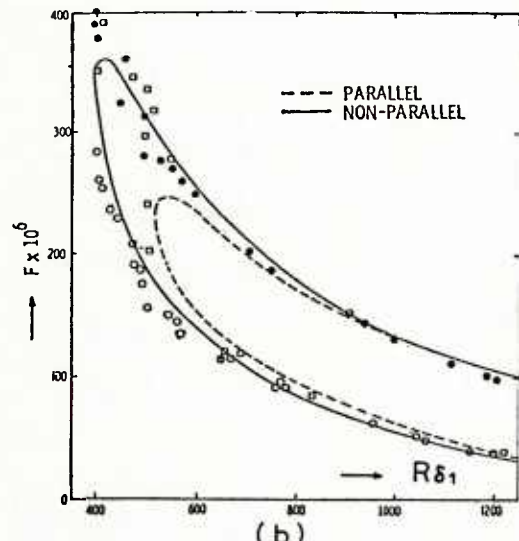
Fig. 3 - Stability diagram for the BLASIUS flow - a) : $(\omega, R\delta_1)$ plane - b) : $(F, R\delta_1)$ plane, in parallel
and non parallel /5/ theories ; ● ■ o □ : experimental /1/ /7/ neutral points
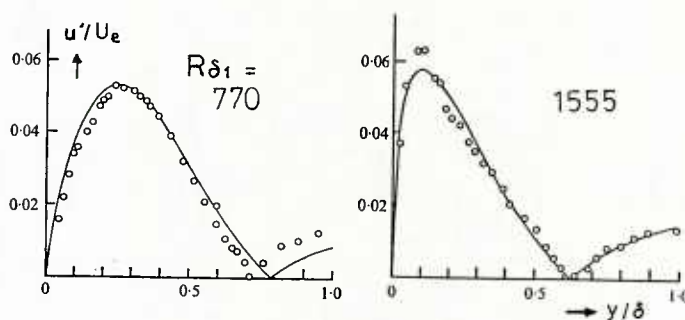
Fig. 4 - Comparison of theoretical /2/ and experimental /7/ pertur-
bation profiles, for $F = 82 \ 10^{-6}$ and two values of $R\delta_1$
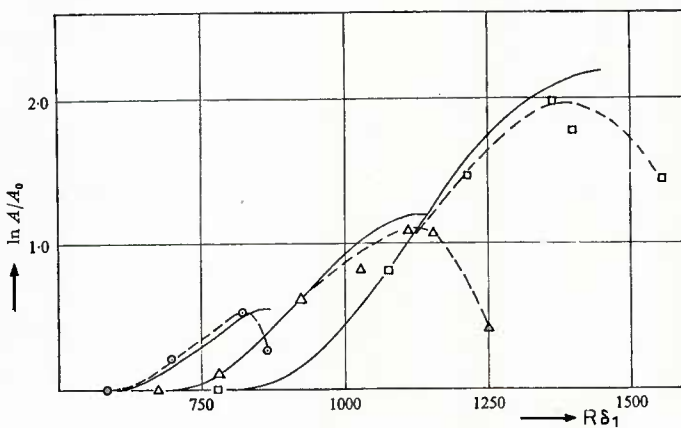
Fig. 5 – Total amplification rates : curves of constant F and varying $R\delta1$.
Total theoretical results /2/ – $\square$ $\triangle$ O experimental results /7/ for F =
$82\ 10^{-6}$, $110\ 10^{-6}$, $157\ 10^{-6}$ respectively
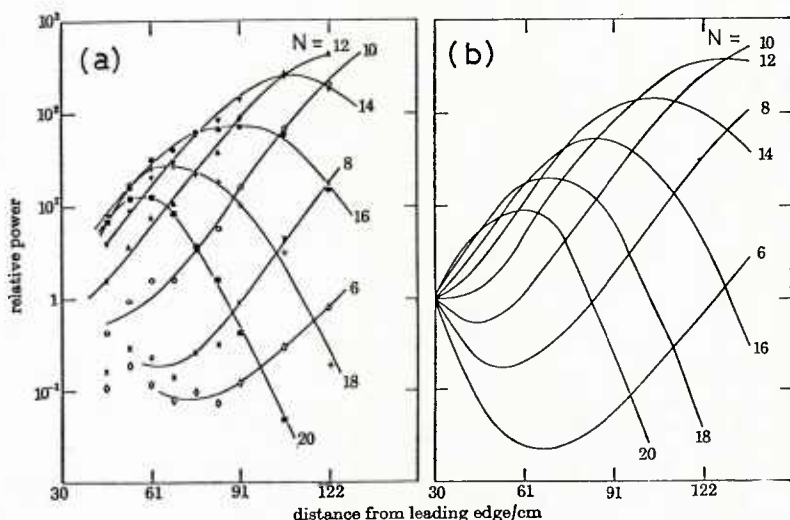
Fig. 6 – Experimental (a) and theoretical (b) growth of two-dimensional
waves /8/ /9/ of various frequencies. N is such that $F = 5.29\ 10^{-6}\ N$.
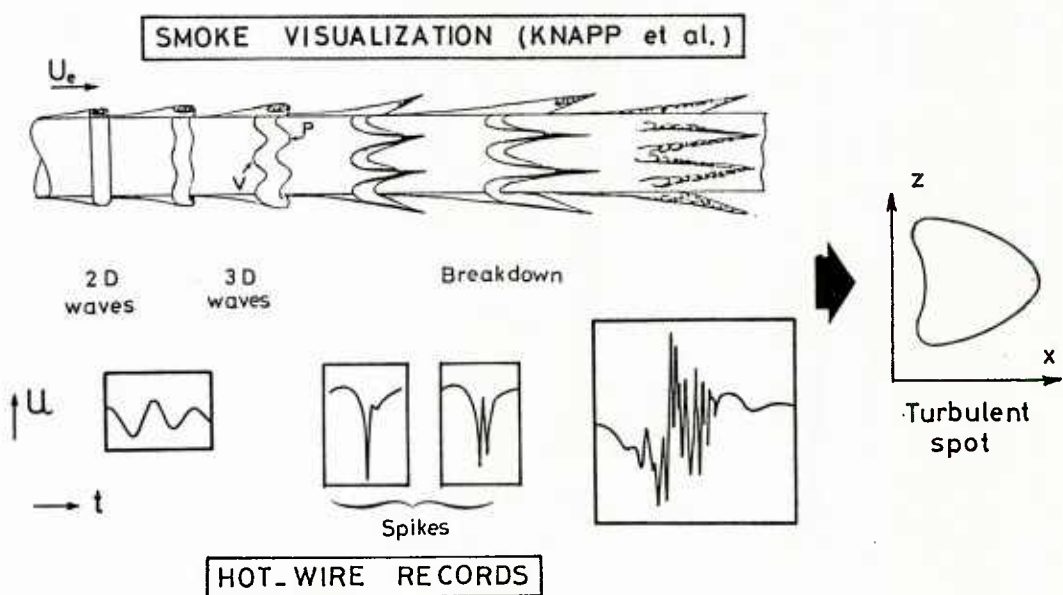
Fig. 7 – Overall picture of the transition process : smoke visualizations /10/ and typical
hot-wire records
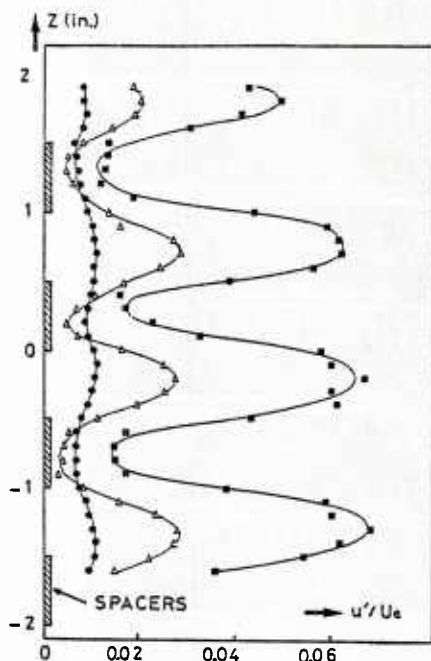
Fig. 8 – Spanwise distributions of u'/Ue at different distances x_1 downstream from vibrating ribbon : ● : x_1 = 3 in. Δ : x_1 = 6 in. ■ : x_1 = 6 in. /11/ – Distance from surface : 0.042 in. U_1/ν = 3.1 10^5 ft^{-1} f = 145 Hz
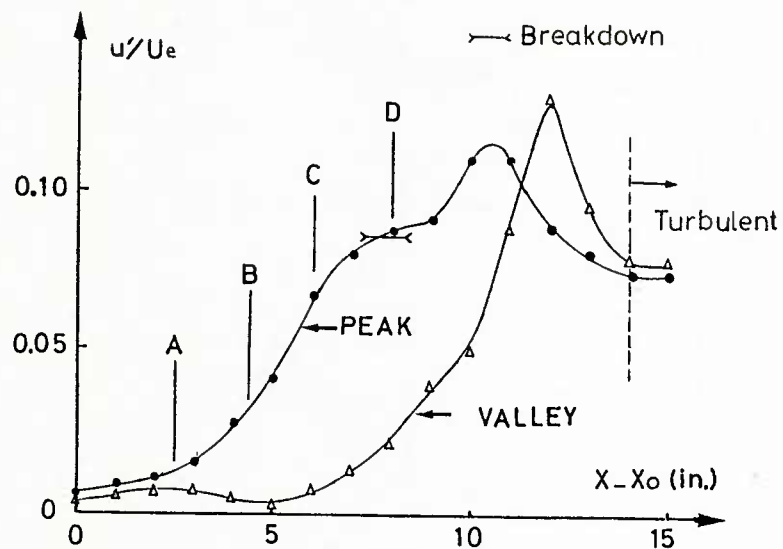
Fig. 9 – Intensity of $\tilde{u}'$-fluctuation at peak and valley positions /11/ – ● : z = – 0.2 in. (peak) – Δ : z = – 0.75 in. (valley). U_1/ν = 3.1 10^{-5} ft^{-1} f = 145 Hz. x_o : reference position, 3 in. downstream from vibrating ribbon
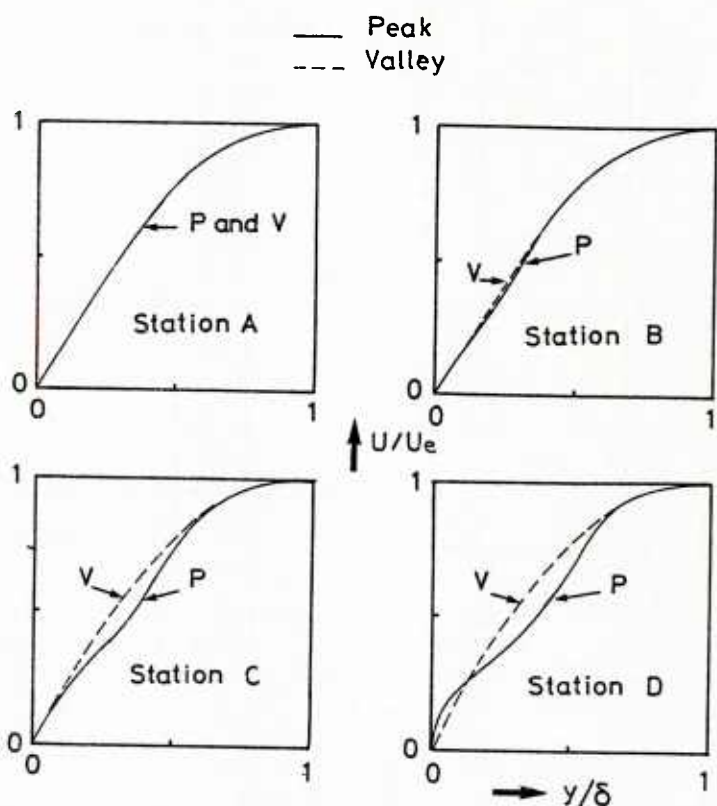
Fig. 10 – Mean velocity distributions at peak (P) and valley (V), at the four stations indicated in figure 9 /11/
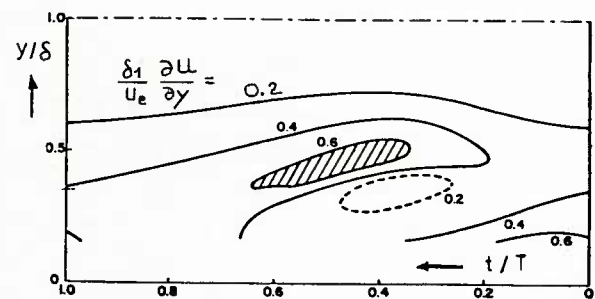
Fig. 11 – Contours of approximate spanwise vorticity at peak position /12/
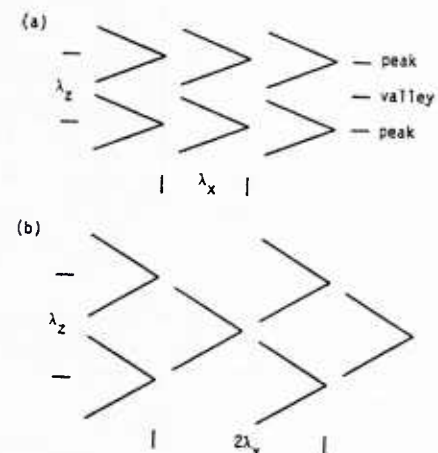
Fig. 12 – Peak-valley patterns – a) Ordered peak-valley structure, K-type b) Staggered peak-valley structure, C-type or H-type
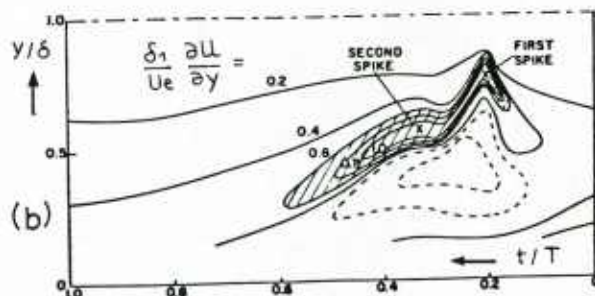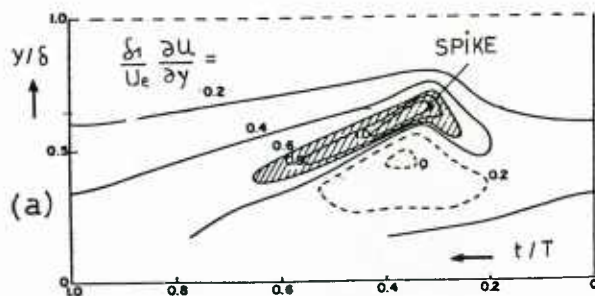
Fig. 13 – Contours of approximate spanwise vorticity at peak position /12/ : one spike stage (a) and double spike stage (b)
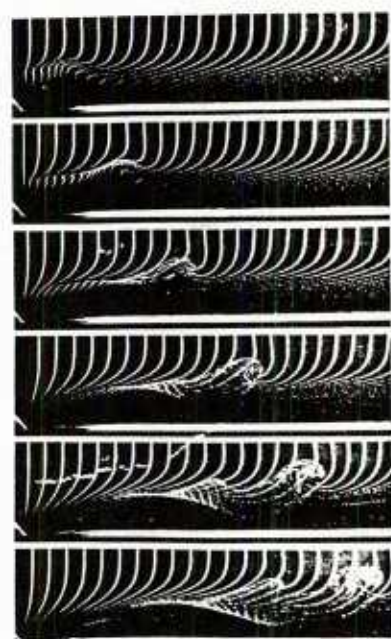
Fig. 14 – Hydrogen bubbles visualization /20/ showing secondary instability of BLASIUS boundary layer
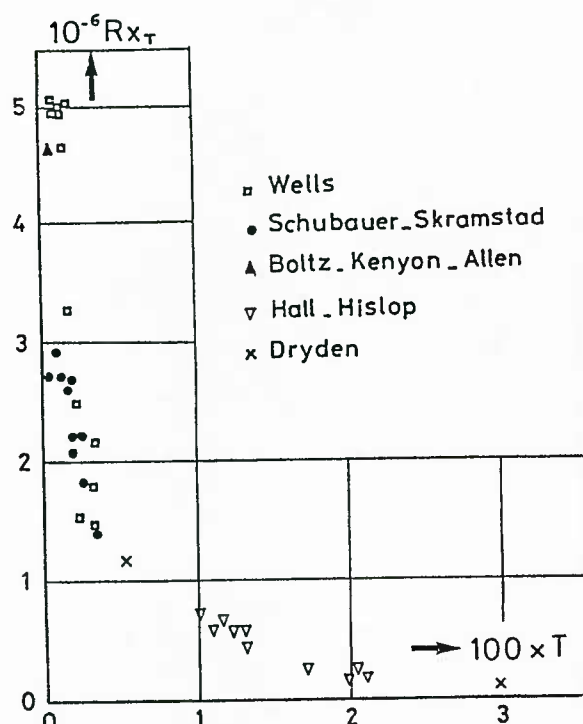
Fig. 15 – Effect of free-stream turbulence on transition Reynolds number : $0 < T < 3 \ 10^{-2}$
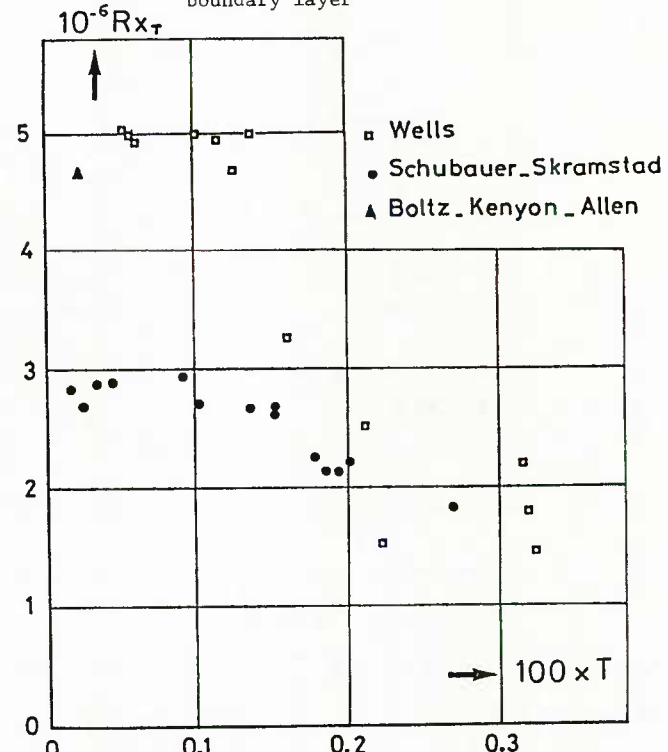
Fig. 16 – Effect of free-stream turbulence on transition Reynolds number for low turbulence intensities

central cylinder
radius = 3 cm – length = 1.2 m
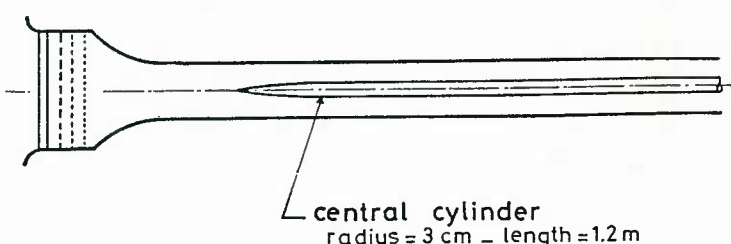
Fig. 17 – Experimental set-up and free-stream turbulence spectrum /28/ – The external velocity distribution is shown in figure 30 (case A)
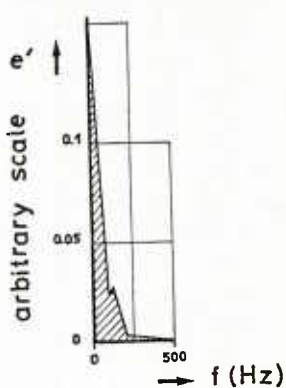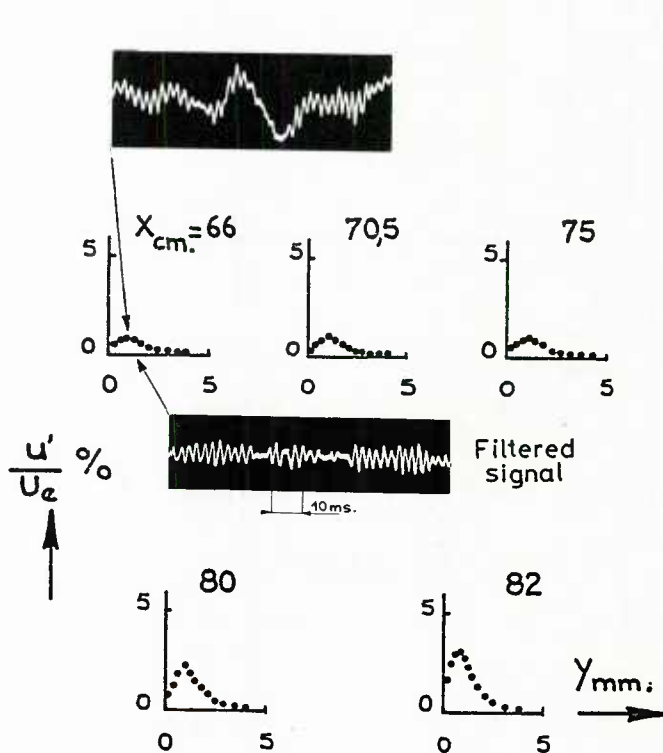
Fig. 18 - Turbulence intensity profiles in a laminar boundary layer. $T \simeq 0.2 \; 10^{-2}$ and $U_e = 33$ m/s
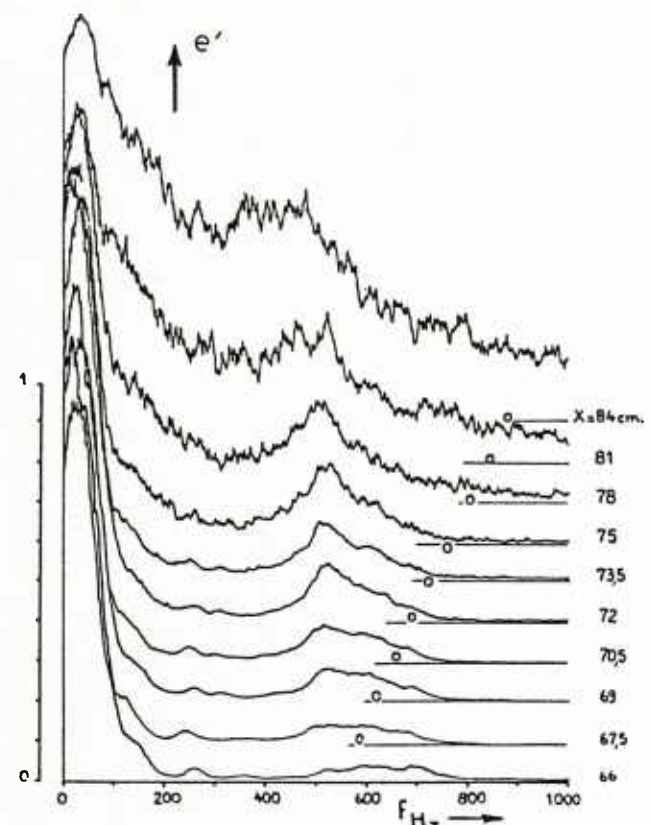
Fig. 19 - Turbulence spectra measured at $y/\delta = 0.2$ for various streamwise stations. The shape factor begins to decrease at $x \simeq 0.84$ m
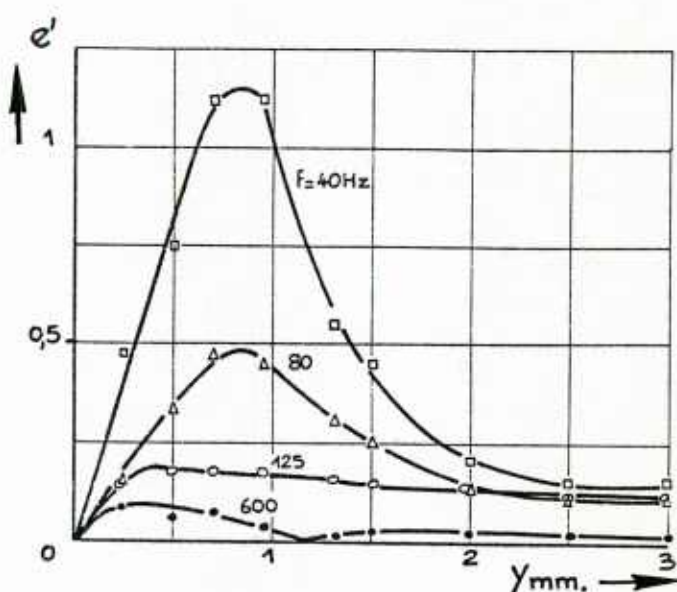
Fig. 20 - Amplitude profiles corresponding to various frequencies, at x = 0.66 m. f = 600 Hz is the central frequency of TOLLMIEN-SCHLICHTING waves
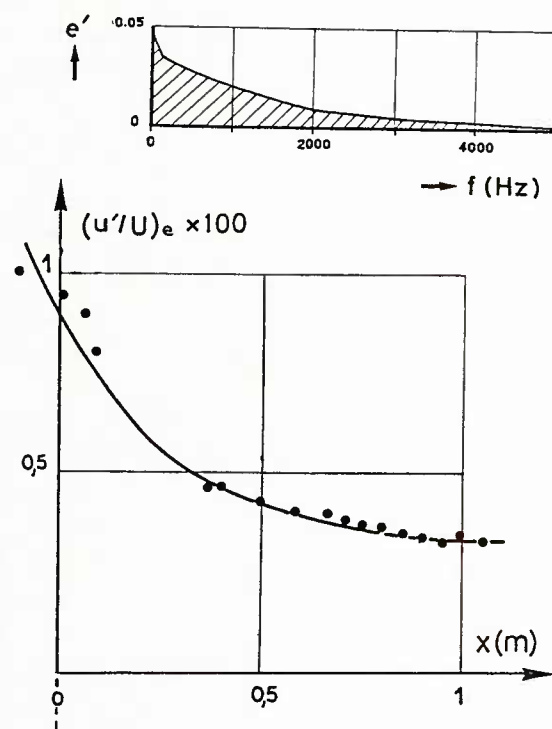

Fig. 21 - Free-stream turbulence intensity generated by grid 1 and free-stream turbulence spectrum measured at x = 0.66 m. The external velocity distribution is shown in figure 30 (case A with U_{ref} = 28 m/s) /29/
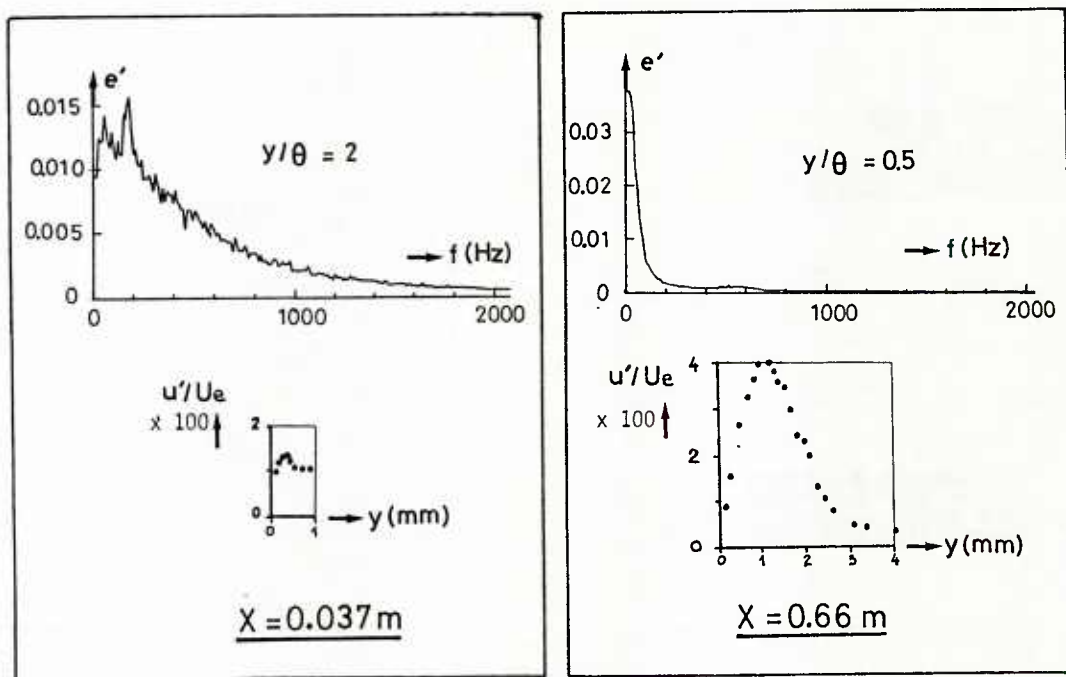
Fig. 22 - Turbulence profiles measured with grid 1 - U_e = 28 m/s
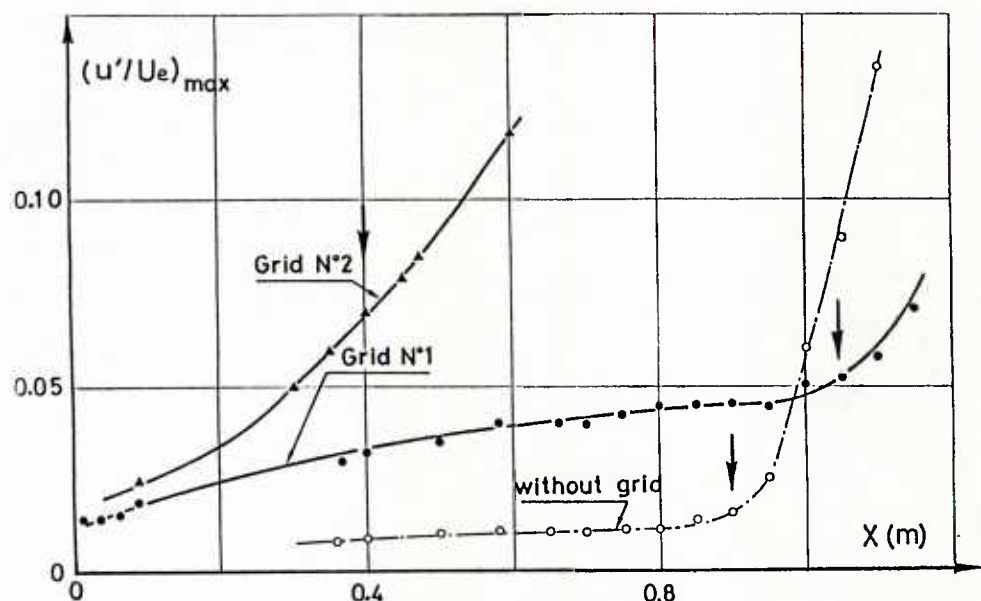

Fig. 23 - Maximum turbulence intensity measured with and without grid. Vertical arrows denote transition onset - U_e = 28 m/s
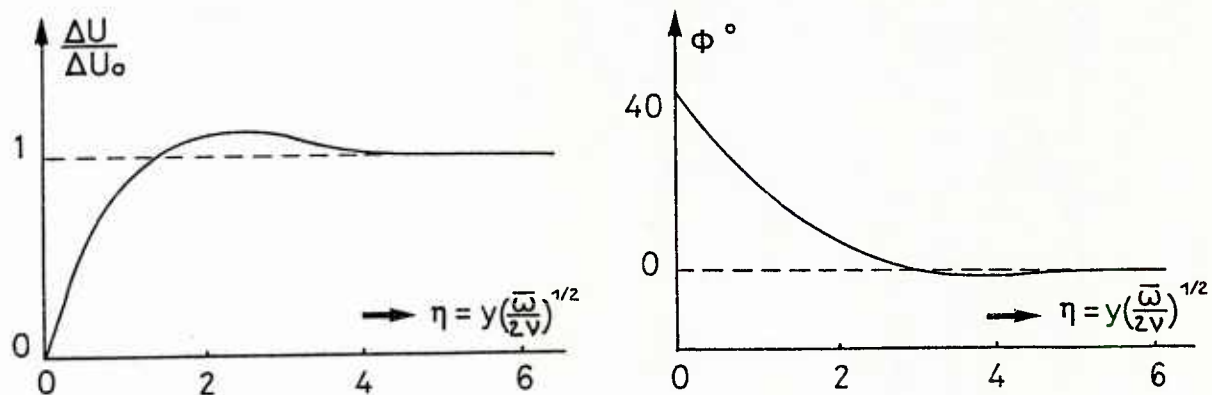


Fig. 24 - Relative amplitude function and lag function
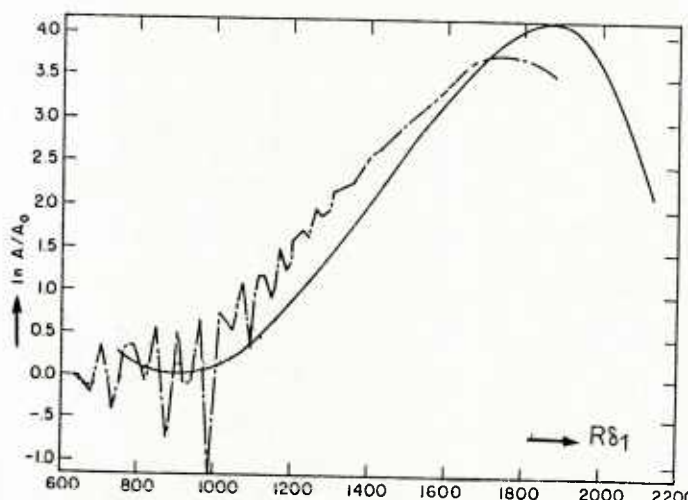
Fig. 25 - Growth of single frequency waves : —— · —— experimental result /31/ /32/ with acoustic excita-
tion, f = 500 Hz and Ue = 29 m/s. —— linear stability theory result for the corresponding value
of $F = 2\pi f\nu/U_e^2 = 56 \cdot 10^{-6}$
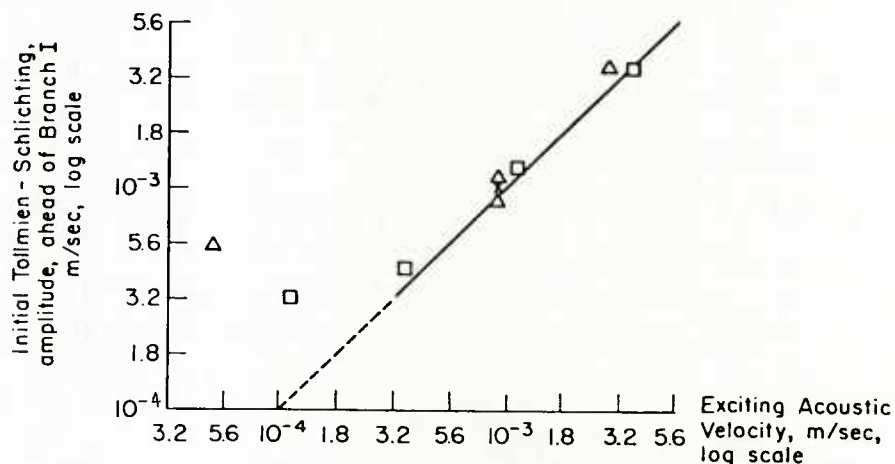
Fig. 26 - Initial mean disturbance wave amplitude as a function of the exciting
sound level : x □ △ experimental results /31/ /32/ for various F. The
line indicates a coupling factor of 1.
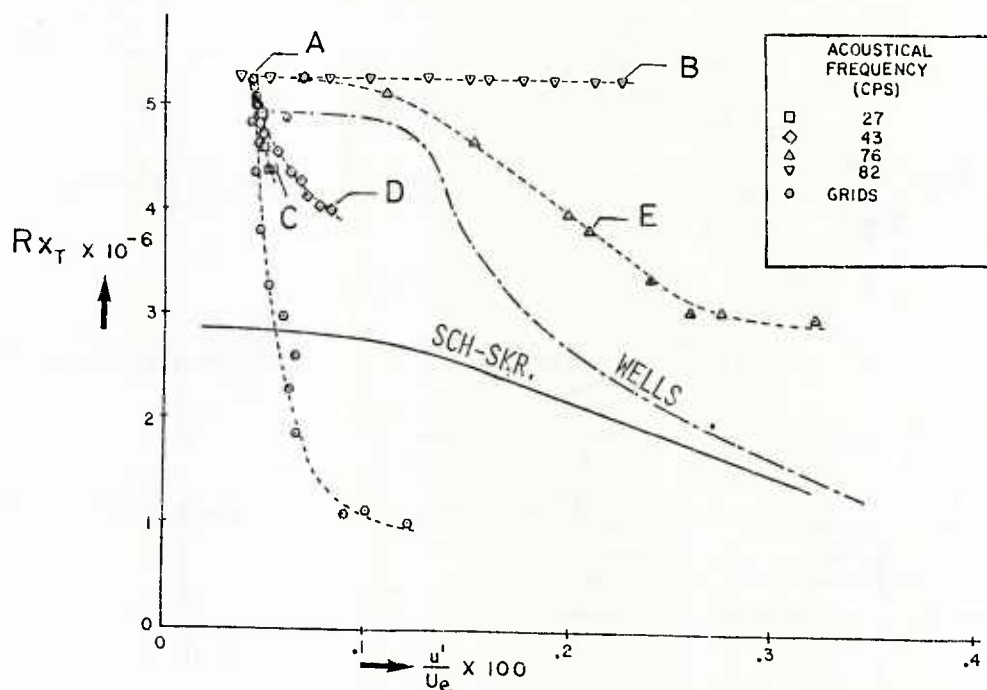
Fig. 27 - Effect of free-stream disturbances (sound and turbulence) on transition Reynolds
number /36/
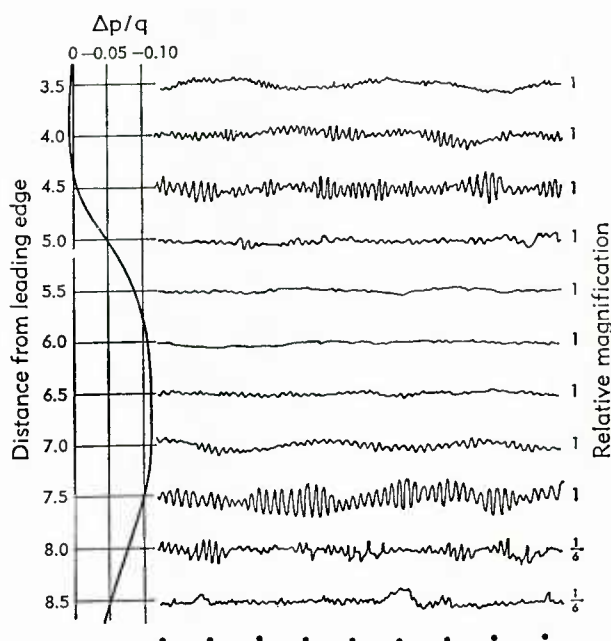
Fig. 28 - Effect of pressure gradient on laminar
boundary layer oscillations /1/. Distance
from surface : 0.021 in. Reference velo-
city : 95 ft/sec.
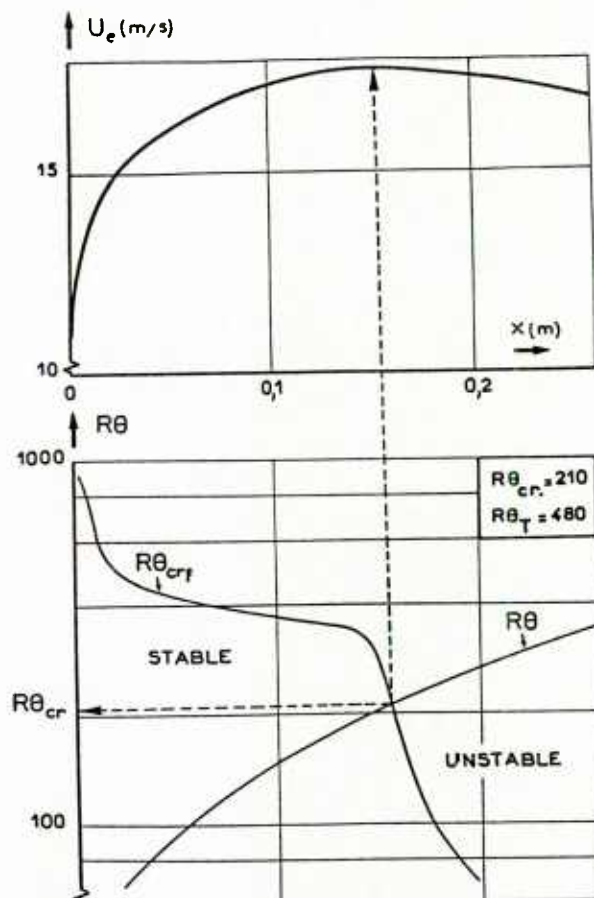
Fig. 29 - Calculation of the critical Reynolds number.
Case E of the experiments performed at
ONERA/CERT /40/ /91/

Configuration	$U_{ref.}$ (m/s)	α (°)
A	33	0,2
B	28	0,7
C	17	✦
D	21	0,9
E	17	✦
F	12	✦

$$Tu = \frac{u'}{U_e} = 0,15\%$$
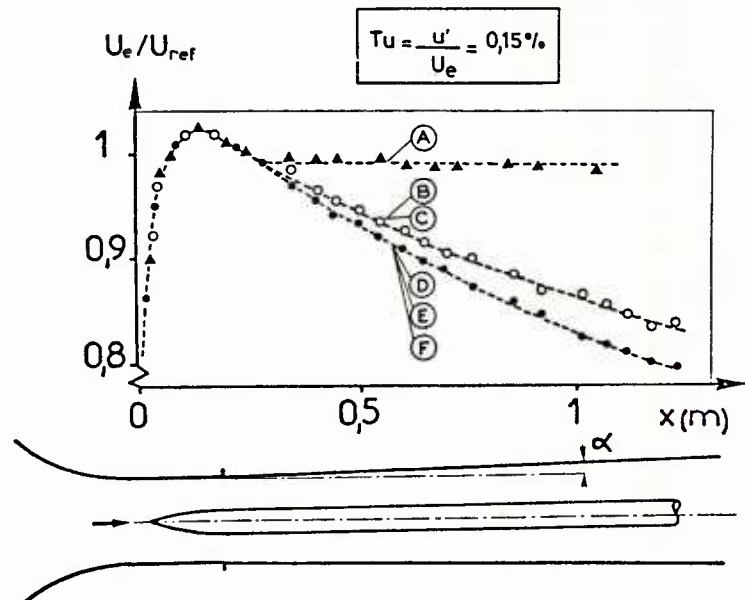
Fig. 30 - External velocity distributions /39/ /40/

x=0,35m y=0,16mm

x=0,425m y=0,15mm
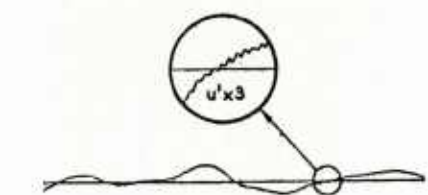
Fig. 31 - Examples of signales recorded
in the case D /39/
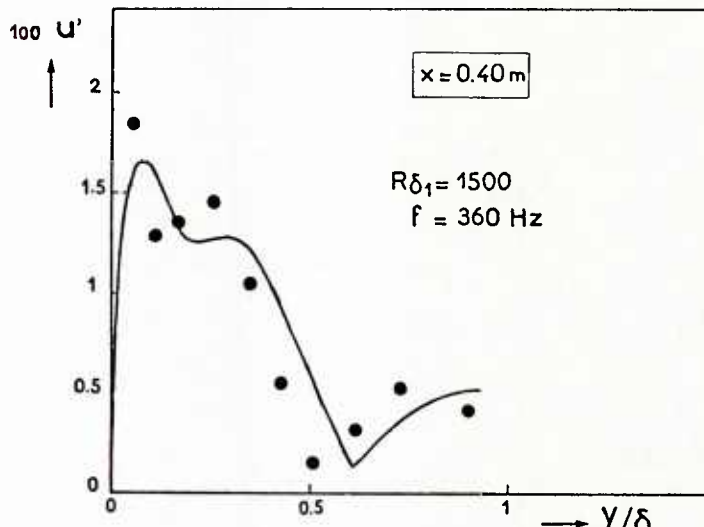
Fig. 32 - Amplitude profiles for f = 360 Hz in case D,
x = 0.40 m : ● experiments /39/ — linear sta-
bility results, see reference /11/ in
Chapter II
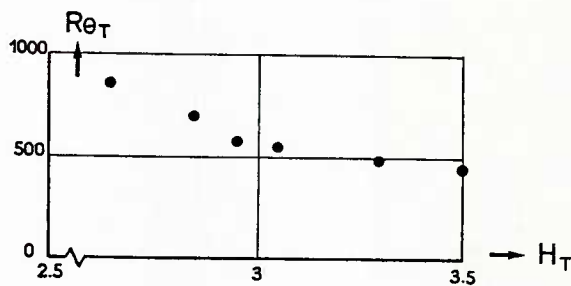
Fig. 34 - Momentum-thickness Reynolds number and
shape factor at the transition onset
/39/ /40/
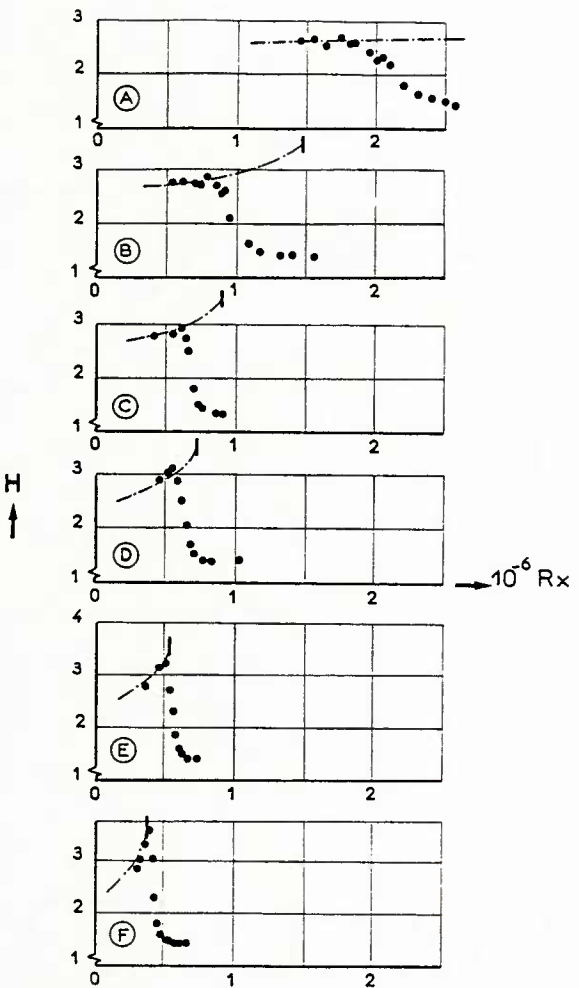
Fig. 33 - Streamwise evolution of the shape factor :
● experiments /39/ /40/ — · — laminar
calculation, with theoretical separation
point
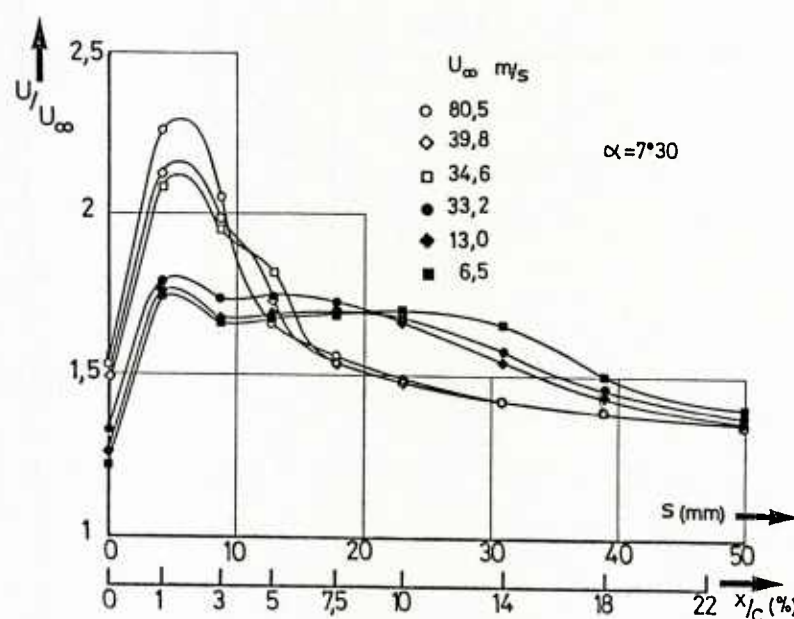
Fig. 35 - LC 100 D profile : velocity distributions in the leading edge region /43/, /44/.
s is the curvilinear distance from stagnation point
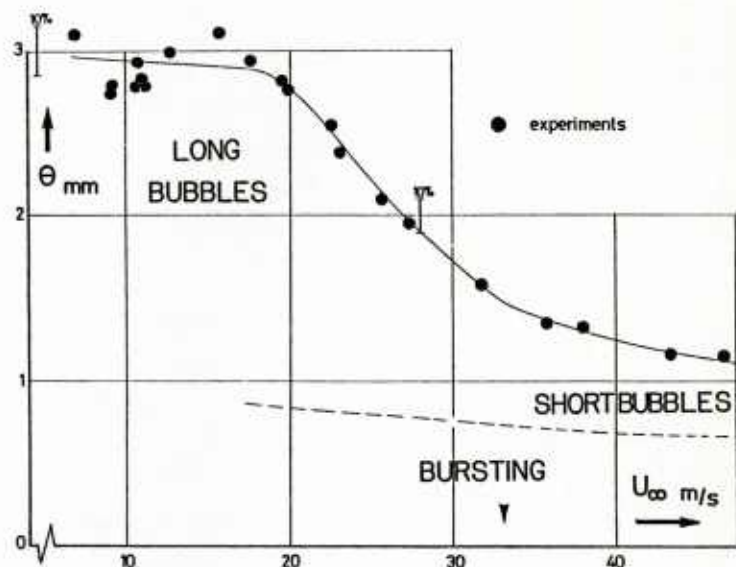
Fig. 36 - LC 100 D profile : momentum thickness at
x/c = 0.75 (α = 7°30) /43/, /44/
---- : calculation with transition at
separation
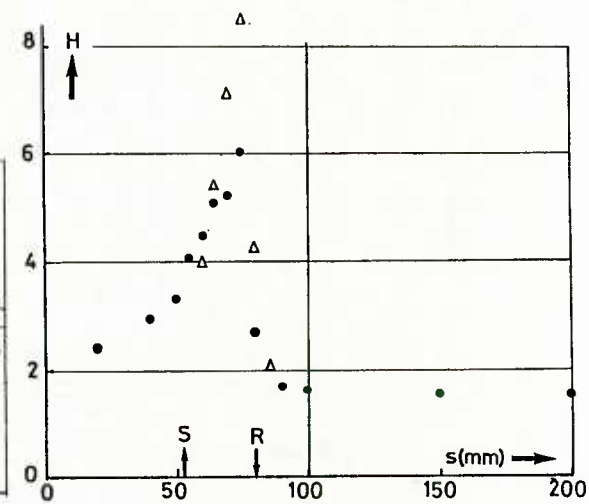
Fig. 37 - Enlarged leading edge : evolution of
the shape factor /43/, /44/
● : hot wire - Δ laser anemometry

Fig. 38 - Experimental evolutions of the shape fac-
tor and of the momentum thickness in acce-
lerating flows /46/ /47/
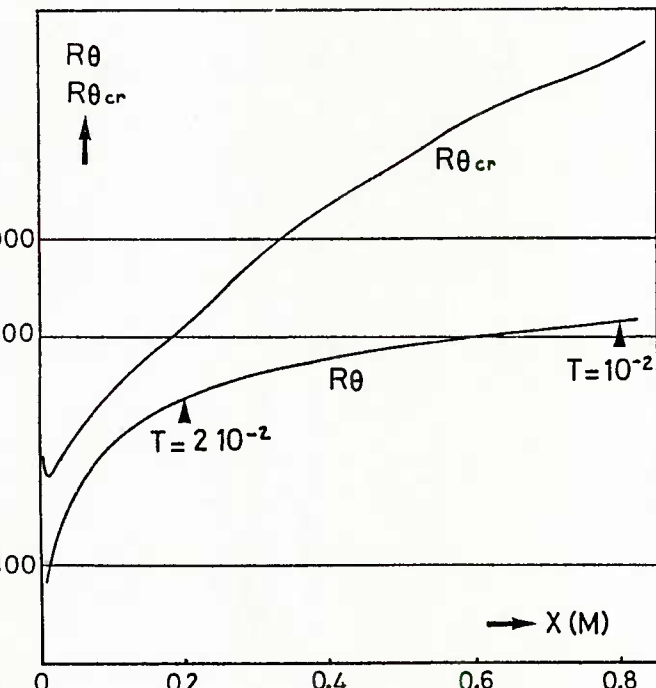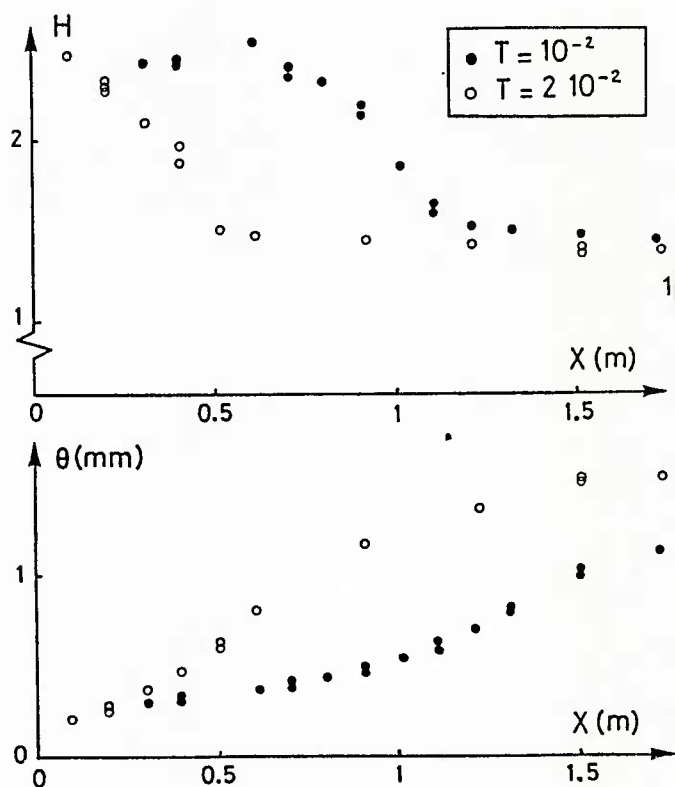
Fig. 39 - Momentum-thickness Reynolds number and
fictitious critical Reynolds number in
accelerating flows /46/ /47/
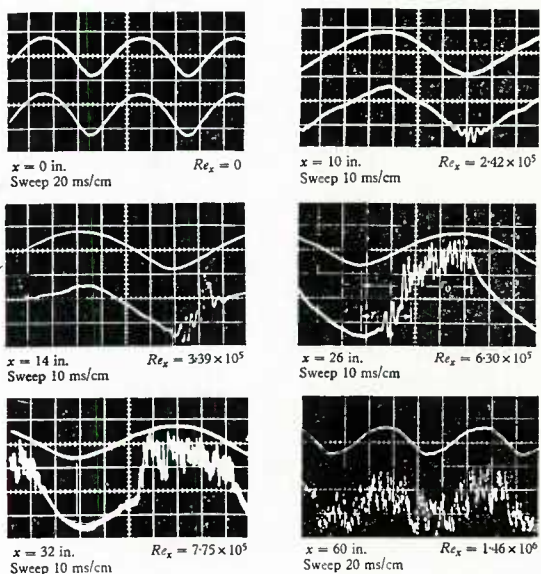
Fig. 40 – Photographs illustrating the initiation and development of a turbulent burst in an oscillating boundary layer /48/
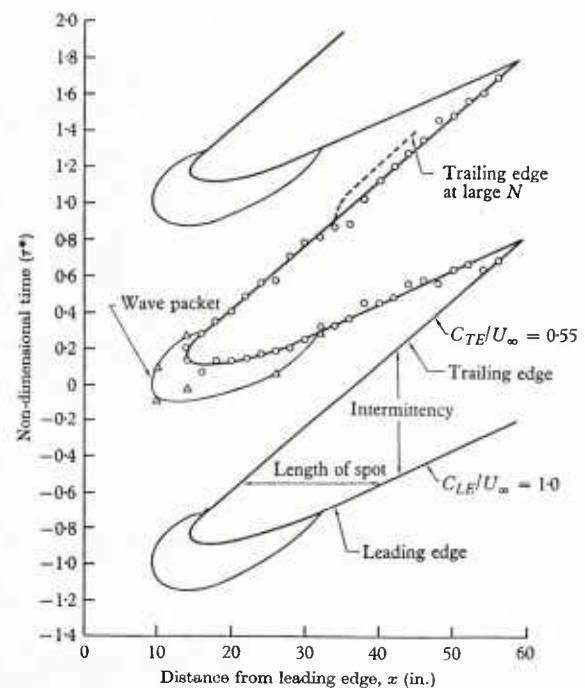
Fig. 41 – Space-time representation of the transition process /48/

N = 0.15   R_ns = 35,000
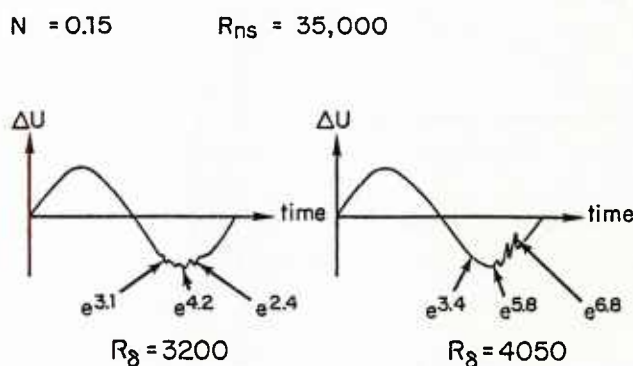
Fig. 42 – Theoretical development of a wave packet, for N = 0.15 /51/
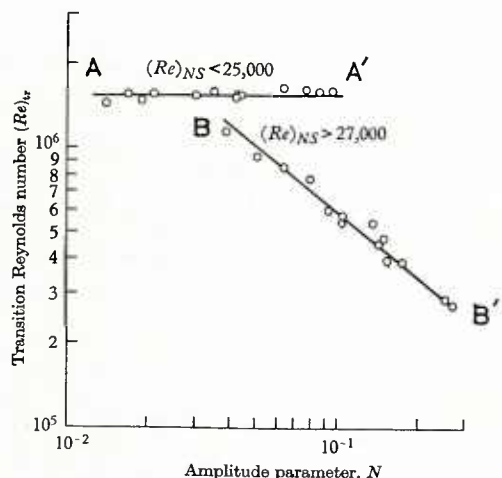
Fig. 43 – Transition Reynolds number as a function of the amplitude parameter /48/.
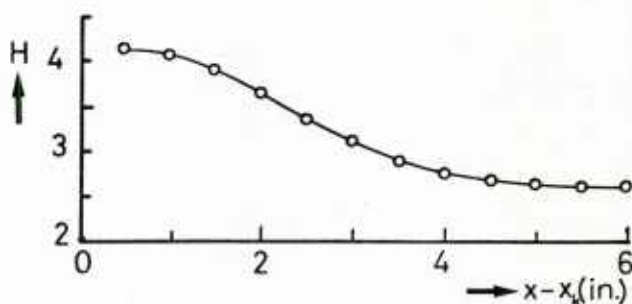
Fig. 44 – Example of shape factor evolution downstream of a cylindrical rod /53/
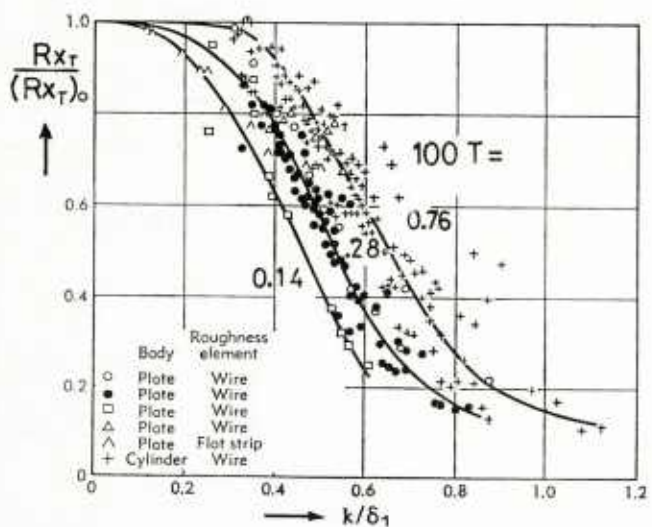
Fig. 45 – Ratio of transition Reynolds number with two-dimensional roughness element to that for smooth plate /55/
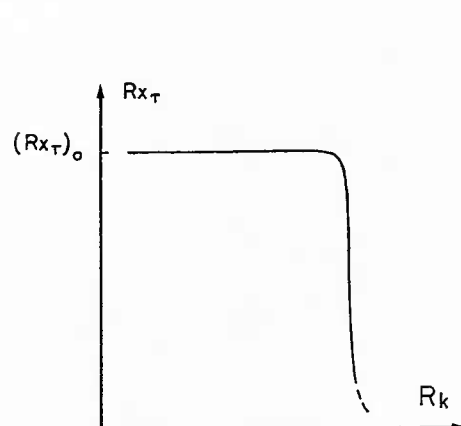
Fig. 46 - Transition Reynolds number as a
function of a Reynolds number
characterizing a three-dimensional
roughness element
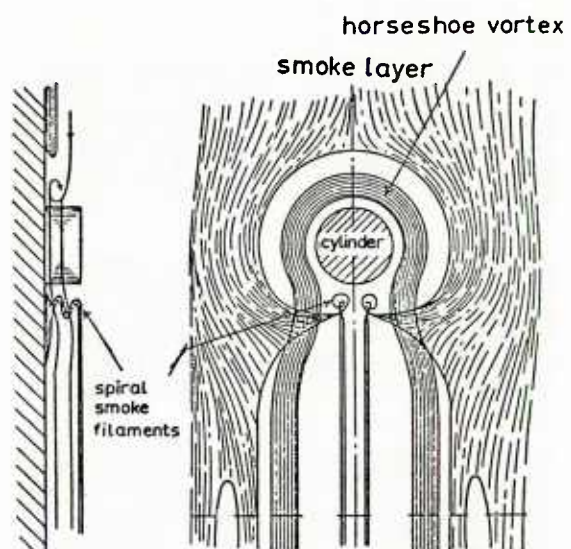
Fig. 47 - Representation of flow past a cylindrical rough-
ness element on a flat plate /58/
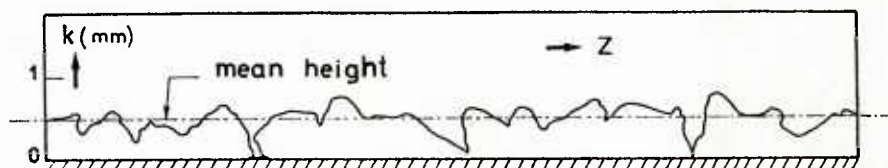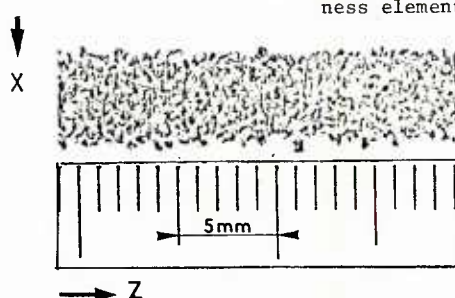
Fig. 48 - Example of carborundum band : plan view photograph and evolution of the
roughness height at a given x /60/
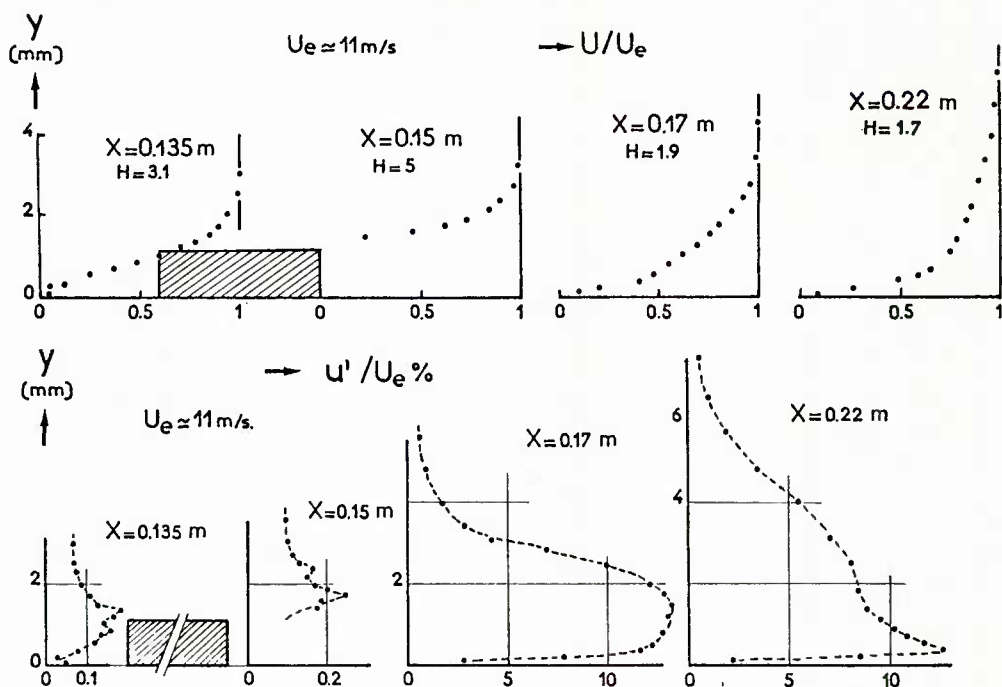
Fig. 49 - Mean velocity and turbulence profiles upstream and downstream of a carborundum band
located at x_K = 0.148 m /60/
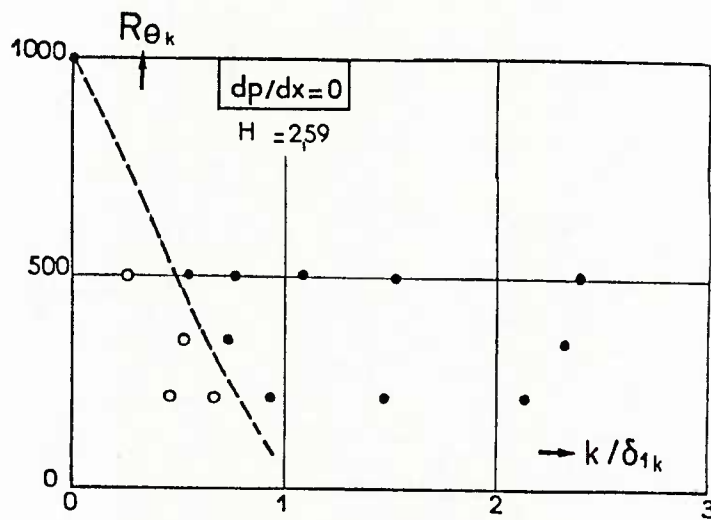
Fig. 50 - Boundary layer tripping with carborundum band : o : transition downstream of the tripping device ● : transition "fixed" on the tripping device /60/
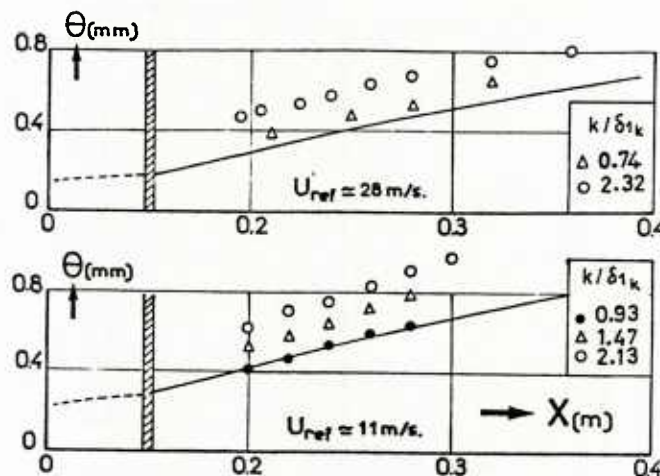
Fig. 51 - Streamwise evolution of the momentum thickness for various roughness heights. --- laminar calculation —— turbulent calculation, with transition at $x = x_k$. $\Delta\theta$ is the difference between experimental and theoretical θ /60/
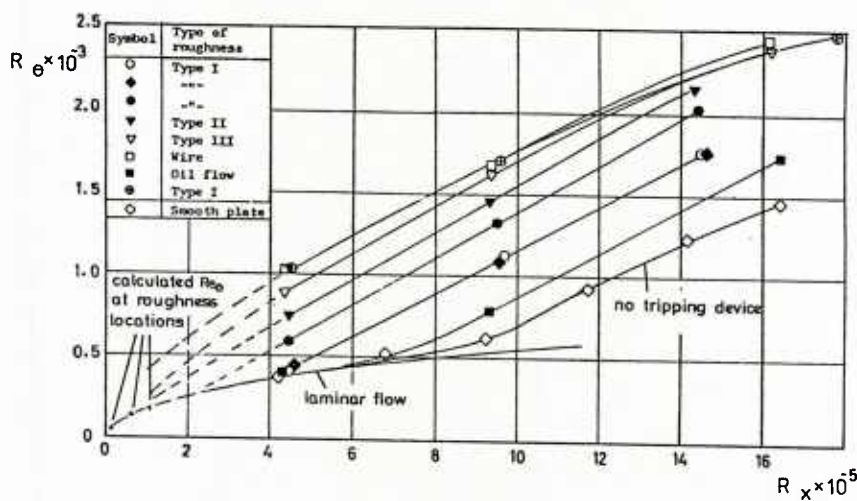
Fig. 52 - Experimental results obtained by TOTLAND /62/
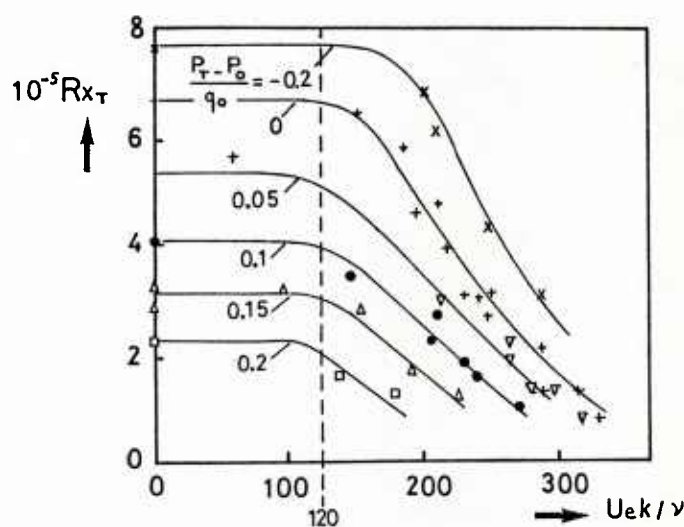
Fig. 53 - Influence of pressure gradient and distributed
roughness on transition Reynolds number /63/.
Ue, P_O and q_O denote velocity, static pressure
and dynamic pressure at the test section entrance
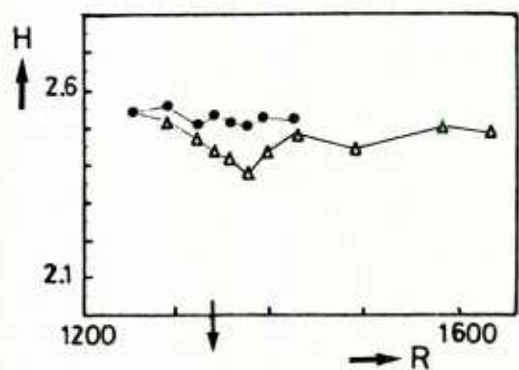
Fig. 54 - Shape factor variation for single
suction-strip configuration /67/ :
● without suction △ with suction
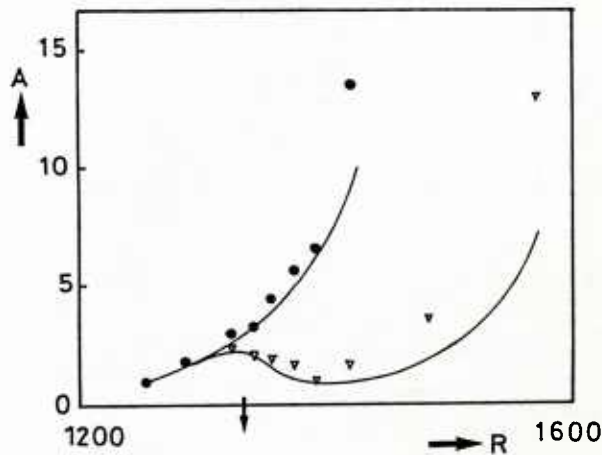
Fig. 55 - Evolution of the disturbance amplitude /67/ :
● experiments without suction ▽ experiments
with suction —— theory
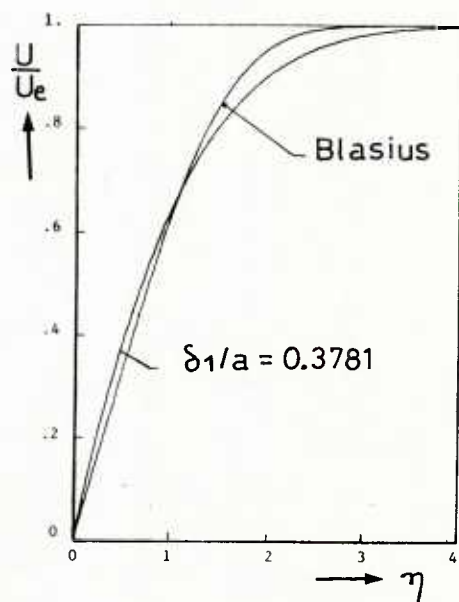
Fig. 56 - Effect of transverse curvature on
boundary layer profile /69/
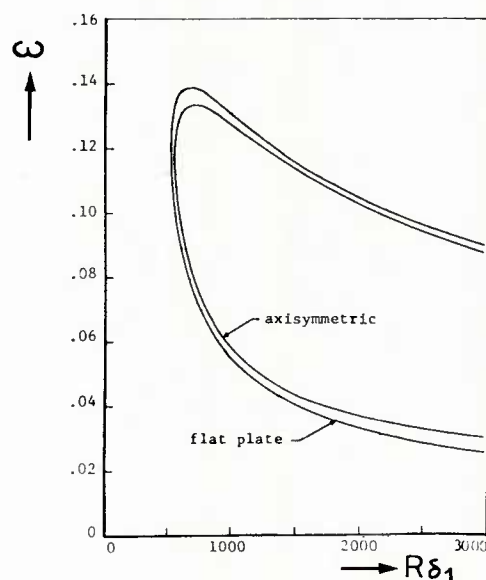
Fig. 57 - Comparison of neutral curves for BLASIUS boundary layer and axisym-
metric boundary layer with $U_e a/\nu = 71\ 122$ /69/
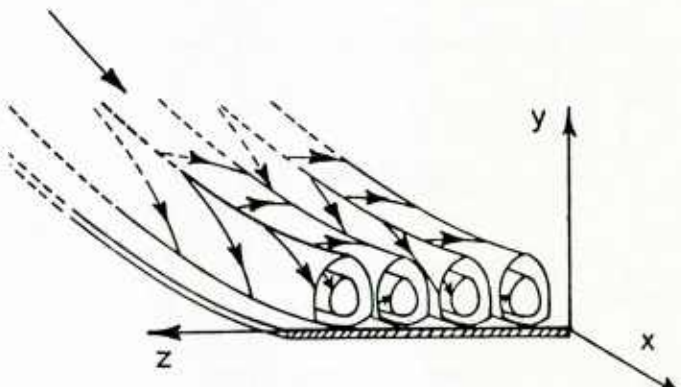
Fig. 58 – GÖRTLER vortices in flow along a concave wall
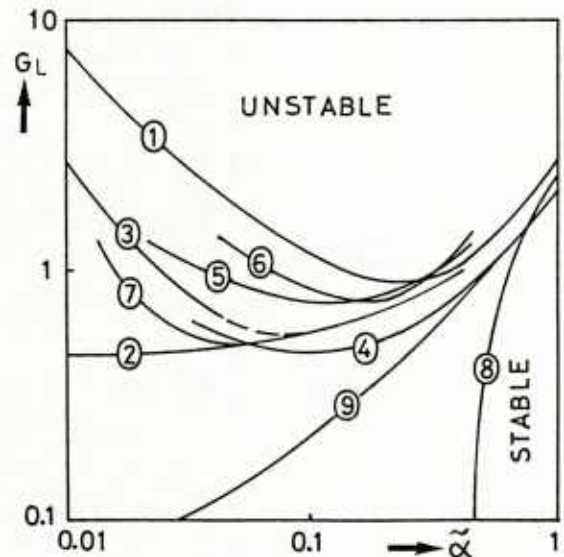
Fig. 59 – Neutral curves obtained from different models or different computation procedures of the GÖRTLER instability /74/. 1 : GÖRTLER; 2,3,5 : HÄMMERLIN ; 4 : SMITH ; 6 : SCHULTZ-GRÜNOW and BEHBAHANI ; 7,8 : KAHAWITA and MERONEY ; 9 : FLORYAN and SARIC
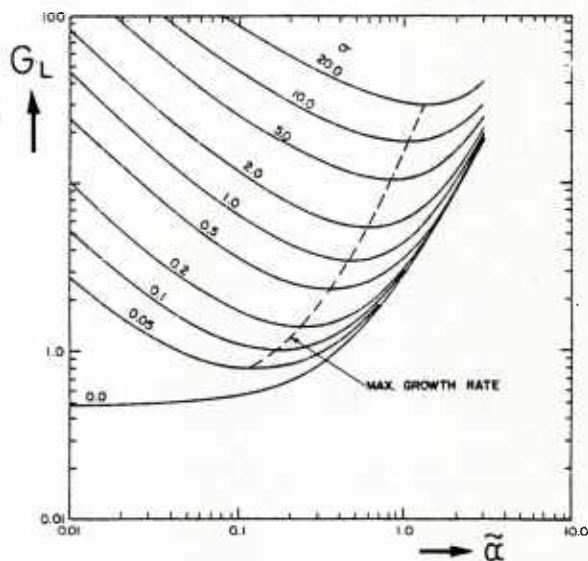
Fig. 60 – Curves of constant growth rate for the BLASIUS flow along a concave wall /77/.
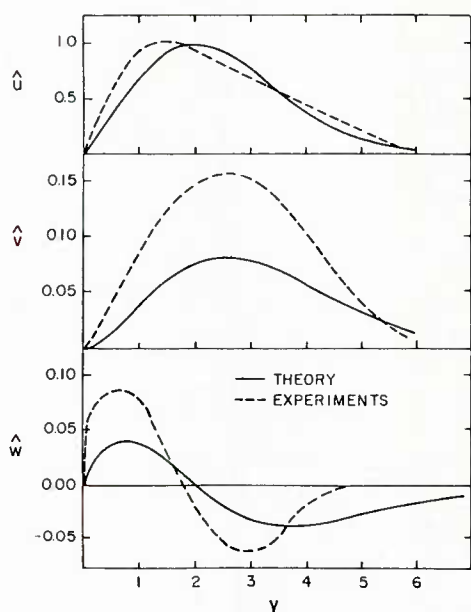
Fig. 62 – Computed /76/ and experimental /80/ profiles of the disturbance velocity components
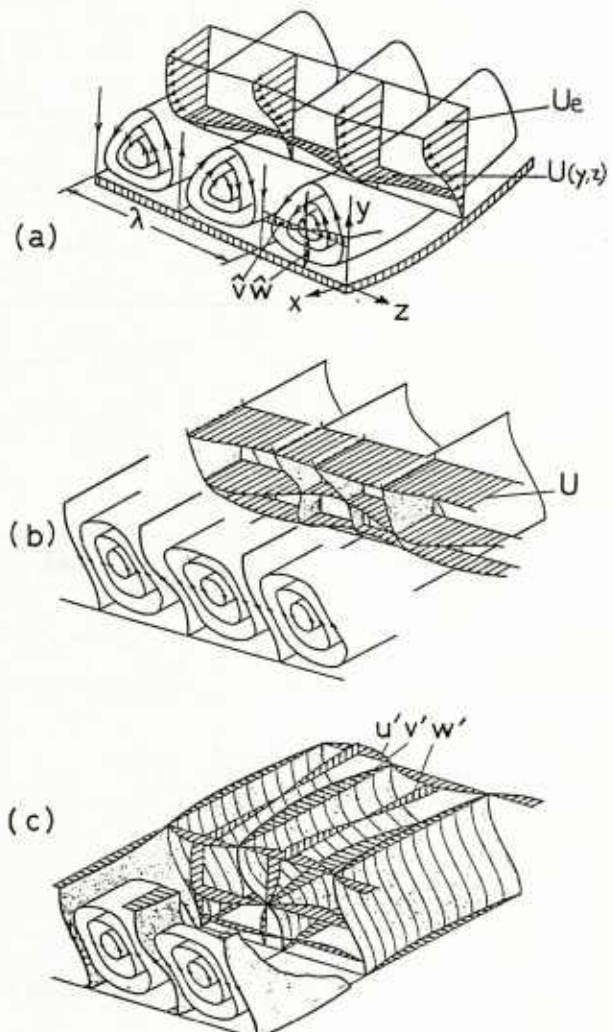
Fig. 61 – Development of instabilities along a concave wall : a) primary instability – b) second-order instability – c) third-order instability (the steady basic flow is suppressed) /79/
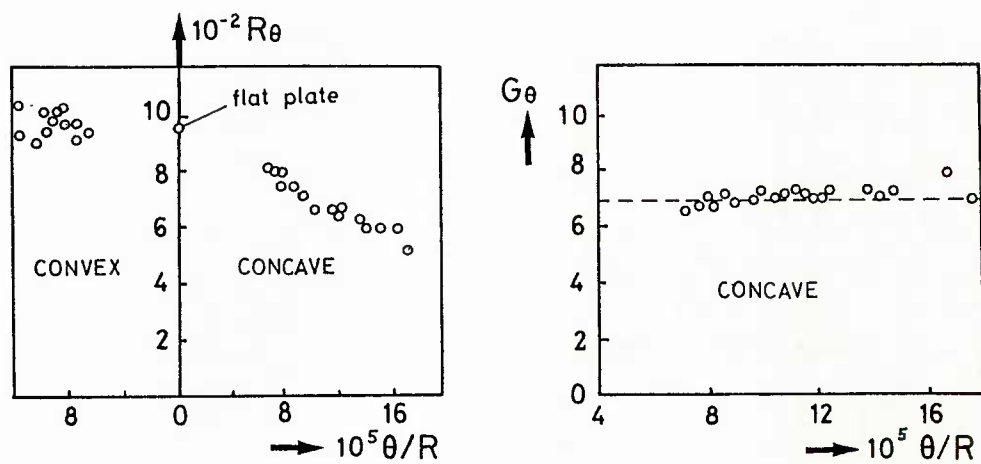
Fig. 63 – Effect of surface curvature on momentum-thickness Reynolds number and on GÖRTLER number at the transition location /70/ /71/
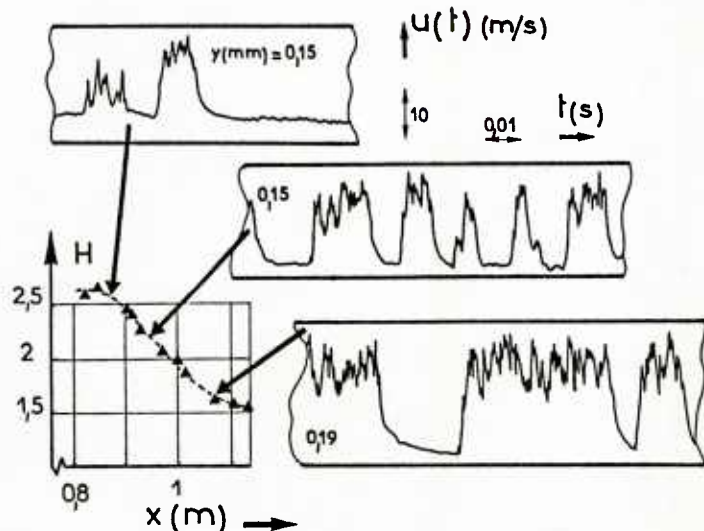
Fig. 64 – Shape factor evolution and typical records in the transition region /82/ – Flat plate case, Ue = 33 m/s
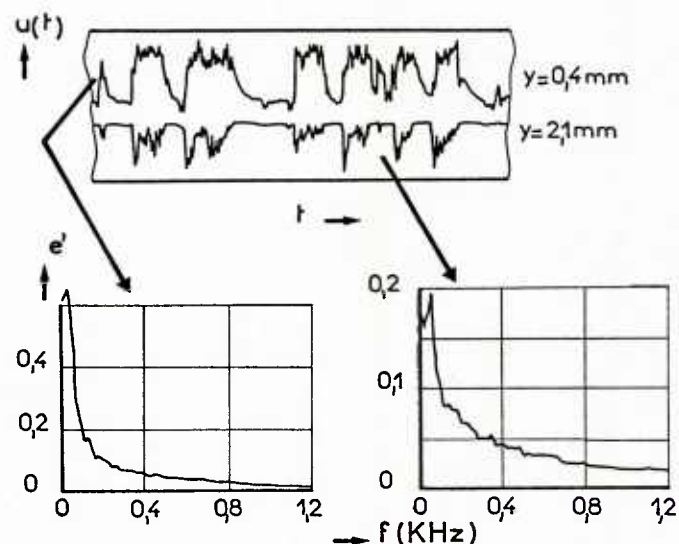
Fig. 65 – Simultaneous signals recorded in the middle of the transition region – Flat plate case, x = 0.94 m
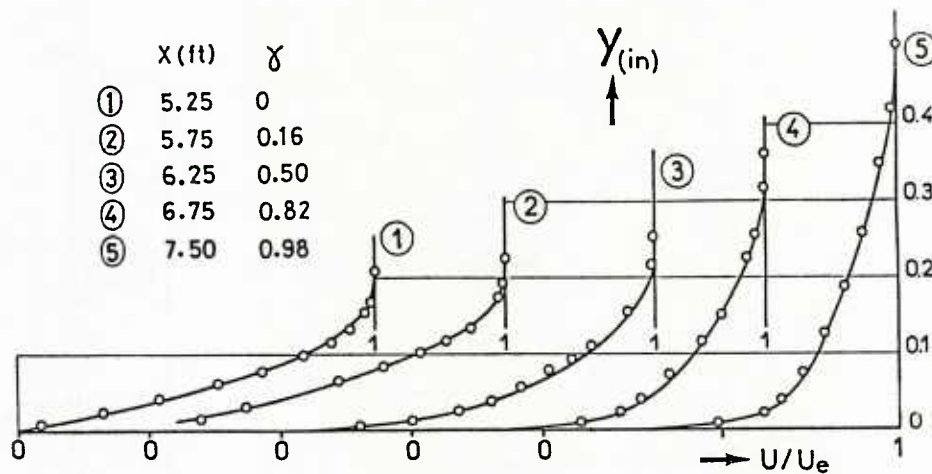
Fig. 66 - Mean velocity profiles through transition region /59/. Ue = 80 ft/s. T = 3 10⁻⁴

X(ft)	γ
① 5.25	0
② 5.75	0.16
③ 6.25	0.50
④ 6.75	0.82
⑤ 7.50	0.98

X(ft)	γ
▽ 5	0
• 5.25	0
▫ 5.75	0.16

▽ 6	0.32
• 6.25	0.50
▫ 6.50	0.70

▽ 6.75	0.82
• 7.50	0.98
▫ 8	1
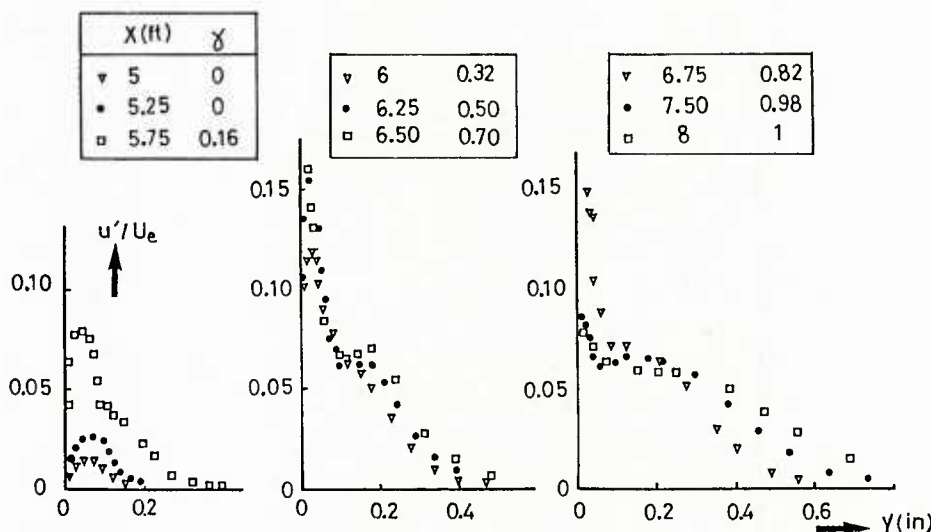
Fig. 67 - Profiles of u'/Ue through transition region /59/. Ue = 80 ft/s. T = 3 10⁻⁴
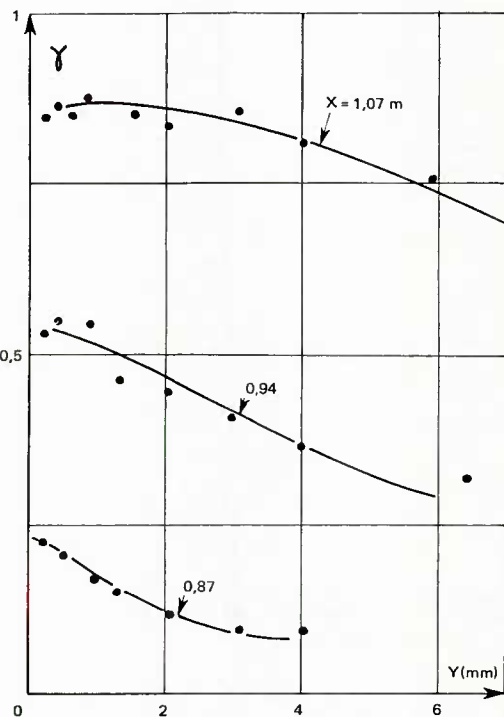
Fig. 68 - Intermittency factor profiles at three streamwise positions /82/
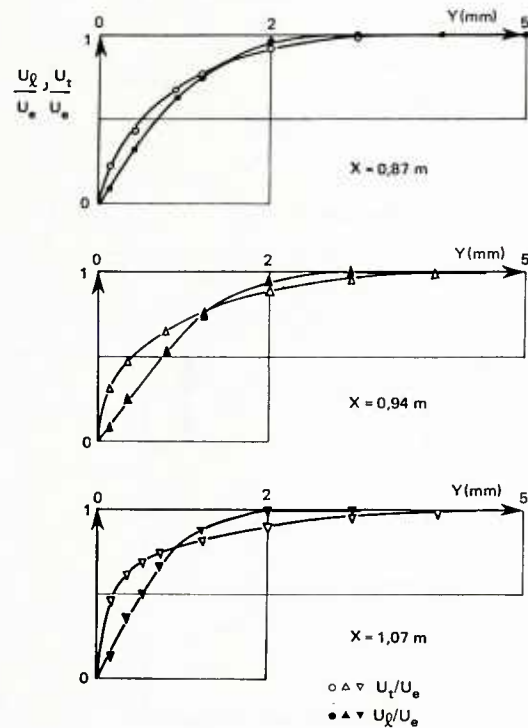
Fig. 69 - Laminar and turbulent mean velocity profiles /82/
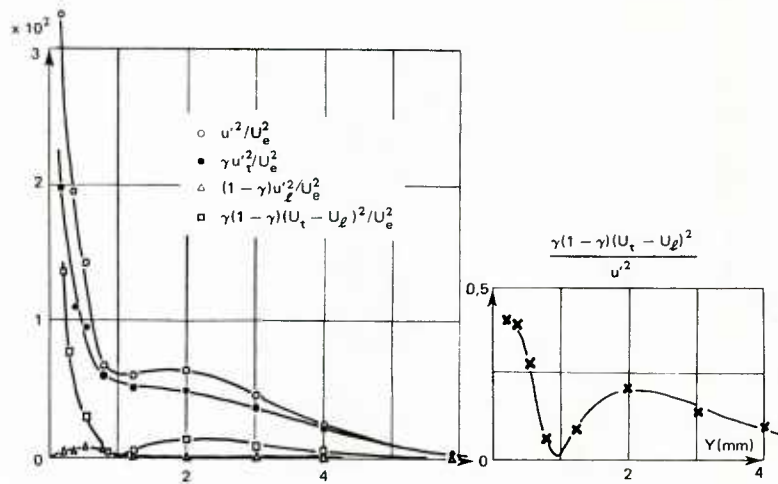
Fig. 70 – The three components of the longitudinal turbulence inten-
sity, x = 1.07 m /82/

Fig. 71 – Ensemble averages of
the turbulent velocity,
x = 0.94 m
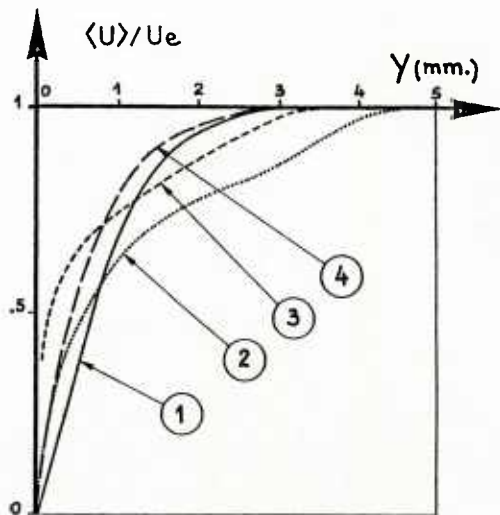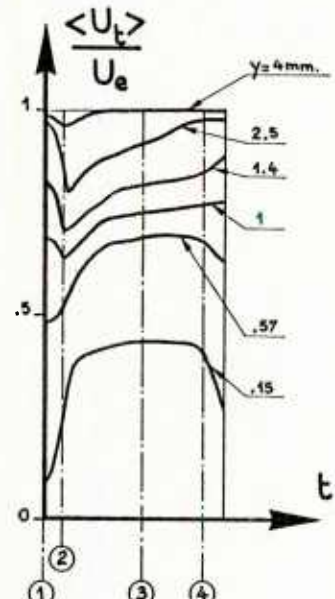
Fig. 72 – Ensemble averaged instantaneous profiles during
the passage of a turbulent spot, x = 0.94 m

Fig. 74 – Spanwise variation of the propagation velocities
of a spot /85/. LE denotes leading edge, TE
denotes trailing edge.
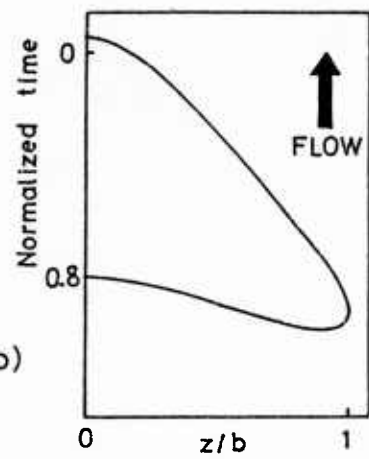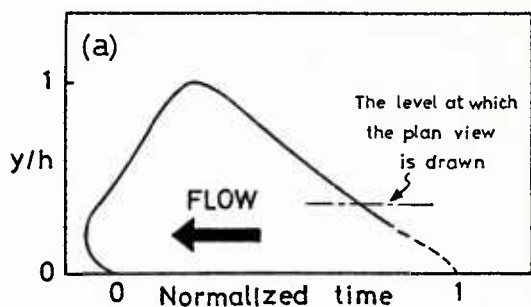
Fig. 73 – Shape of a turbulent spot, after /85/ : a) elevation view ; b) plan view.
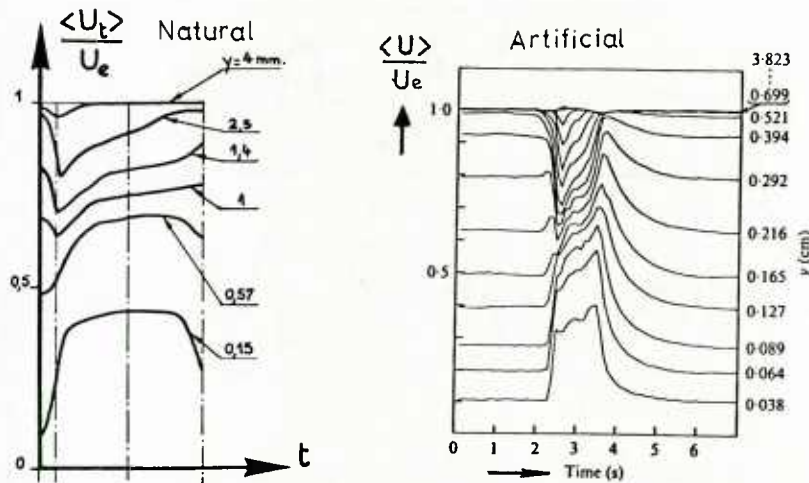
Fig. 75 - Comparison between ensemble velocities $\langle U_t \rangle$ obtained in artificial conditions /87/ and in natural conditions (same as figure 72)
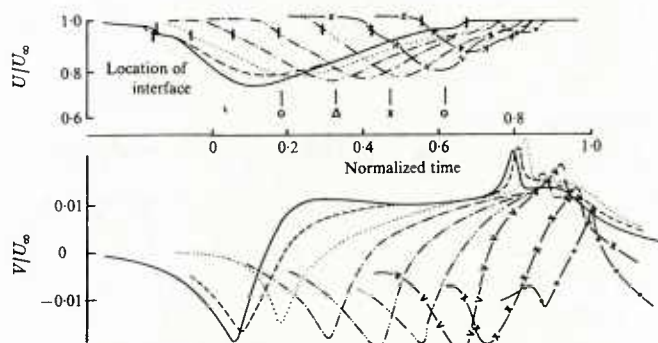
Fig. 76 - Variation of $\langle U_t \rangle$ and $\langle V_t \rangle$ at $y/h = 0.325$ for various values of z/b : ——— :0 ; ——— : 0.118 ; .... : 0.235 ; ——— · ——— : 0.353 ; ——— ·· ——— : 0.471 ; ——— ··· ——— : 0.588 ; ——— V ——— : 0.706 ; ——— X ——— : 0.824 ; ——— 0 ——— : 0.941
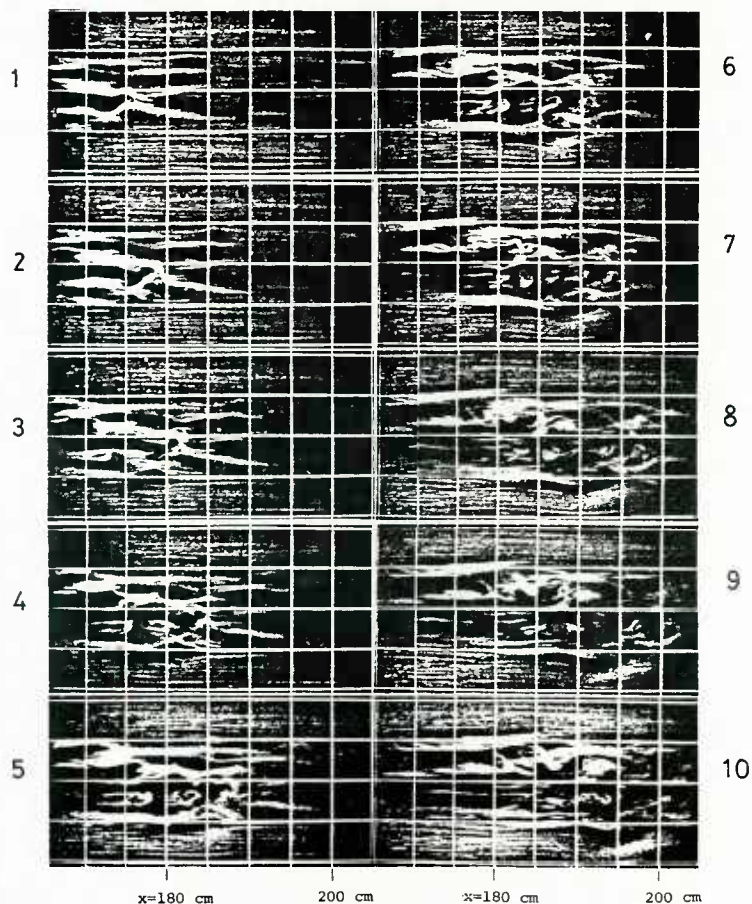
Fig. 77 - Plan view of growth of a turbulent spot, 2 frames/s /88/
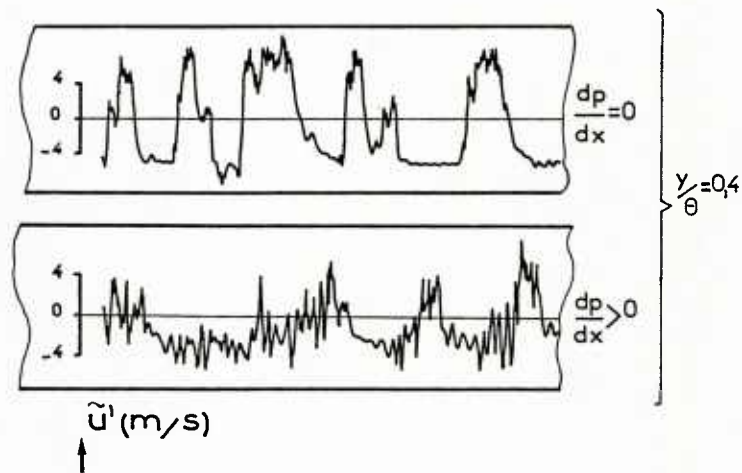
Fig. 78 - Instantaneous signals recorded near the wall in cases A (dP/dx = 0) and
B (mild positive pressure gradient) /91/
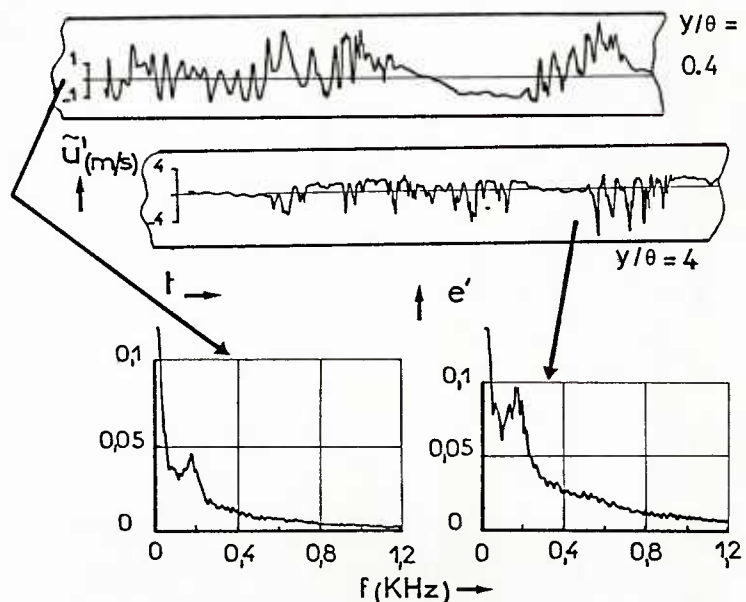
Fig. 79 - Instantaneous signals recorded in case F (strong positive
pressure gradient) /91/
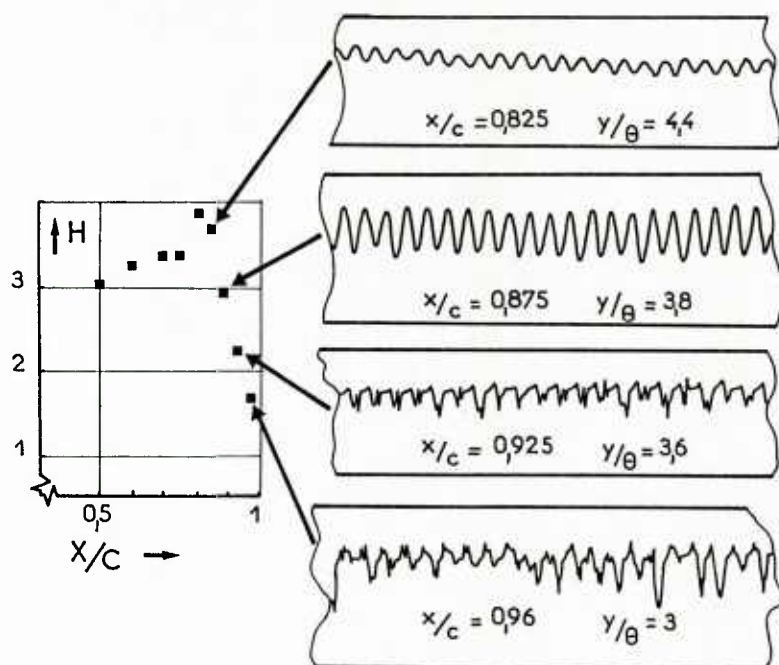
Fig. 80 - Shape factor evolution and typical records in a transition occuring at laminar
separation /92/
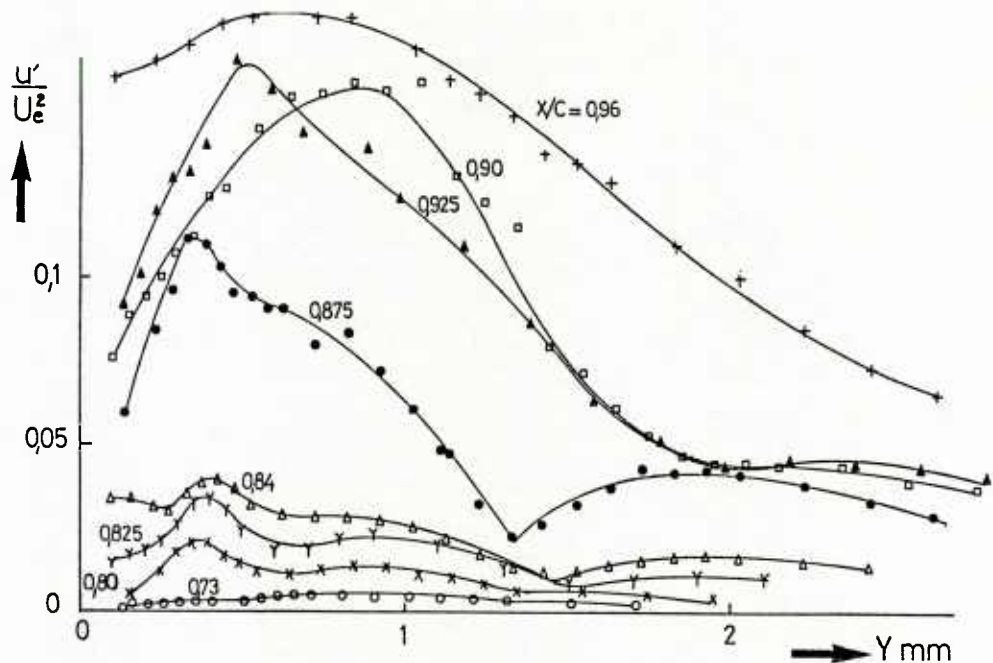
Fig. 81 - Turbulence profiles in laminar and transitional boundary layer /92/
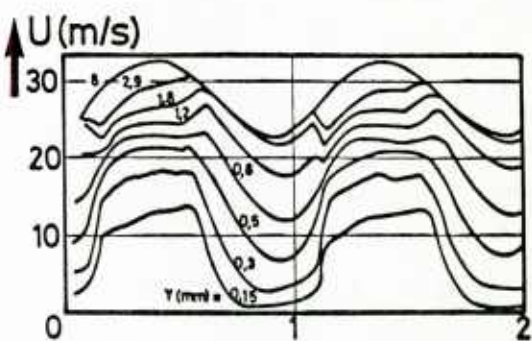
Fig. 82 - Ensemble averages of the streamwise velocity in the transitional region of an oscillating boundary layer /49/. N = 0.16 ; U_O = 27 m/s, $\bar{f}$ = 37 Hz, X = 0.38 m
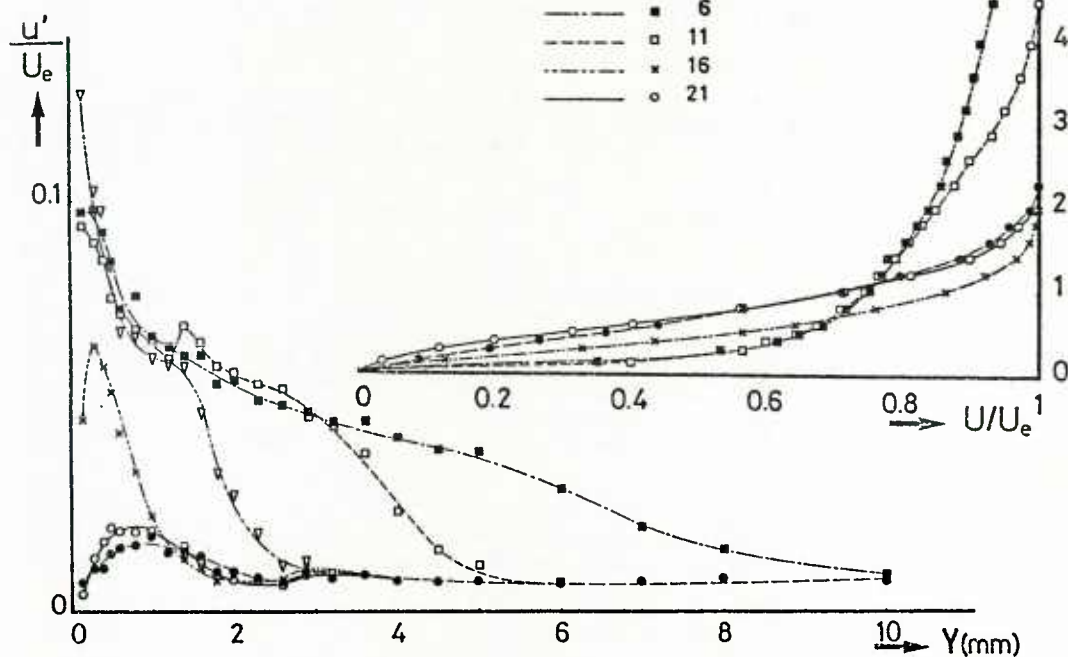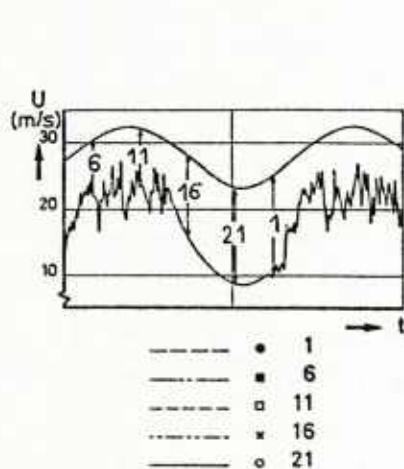
Fig. 83 - Ensemble averages of the mean velocity profiles and of the turbulence profiles /49/. Same conditions as in figure 82.

CHAPTER II

TRANSITION PREDICTION

AT LOW SPEED

1 - INTRODUCTION

The problem considered here is how to predict the position and the extent of the transition in a two-dimensional, incompressible flow developing under the influence of various factors. This prediction is all the more difficult as the fundamental mechanisms of the transition process are far from being fully understood. However, advanced design of aerodynamic vehicles or turbomachinery airfoils needs practical procedures combining acceptable engineering accuracy with simplicity and speed. Most of the methods described in this paper do not claim to represent the intricate physics of the transition process : they only constitute possible short term answers to practical problems.

The first difficulty is to predict the location of the transition onset. For transitions triggered by small amplitude disturbances, the linear stability theory provides us with a useful guideline, even if the non linear phenomena, occuring just before breakdown, are disregarded. But, due to the complexity of the governing equations, simpler empirical correlations have been often used. In the last ten or twenty years, the advent of high speed computers made it possible to solve sets of partial differential equations in which empirical information is able to lead to a "numerical transition". As it will be seen later on, these various techniques are not really antagonist, but rather complementary.

The second problem concerns the boundary layer development from the laminar to the turbulent state. The most obvious way to compute it is to assume that transition is a point-like phenomenon and to overlap the laminar and fully turbulent parameters at this point. Although this crude method may be substantiated in some cases, it does not apply to other configurations : on the pressure side of a turbine blade, for instance, TURNER found that transition extends over 70 per cent of the chord. So, practical methods able to describe the transition region have been developed ; they allow a smooth junction with the more classical turbulent computations and will be discussed at some length.

2 - CALCULATION METHODS BASED ON STABILITY CALCULATIONS

2.1. Stability diagrams and envelope curves

Let us recall that the small, two-dimensional disturbances introduced in the laminar boundary layer are related to a stream function ψ ; using the spatial theory, its expression is :

$$\psi(x, y, t) = \varphi(y) e^{-\alpha_i x} e^{i(\alpha_r x - \omega t)} \tag{1}$$

φ, α_i, α_r and ω represent respectively an amplitude function, an amplification (or damping) coefficient, a wave number and a circular frequency.

Introducing $\widetilde{u}' = \partial\psi/\partial x$ and $\widetilde{v}' = -\partial\psi/\partial x$ into the continuity and linearized NAVIER-STOKES equations, one can obtain the ORR-SOMMERFELD equation :

$$\varphi^{IV} - 2\alpha^2 \varphi'' + \alpha^4 \varphi = iR \left[(\alpha U - \omega)(\varphi'' - \alpha^2 \varphi) - \alpha U'' \varphi \right] \tag{2}$$

with $\alpha = \alpha_r + i\alpha_i$. The Reynolds number R is based on the reference length and on the reference velocity which made all quantities dimensionless. Equation (2) plus boundary conditions constitute an eigenvalue problem which has only solutions if a secular relation of the form :

$$F(\alpha_r, \alpha_i, \omega, R) = 0 \tag{3}$$

is satisfied. For a given mean flow profile U(y), the results of numerical computations can be represented in a (ω, R) diagram ; the neutral curve ($\alpha_i = 0$) separates the region of stable from that of unstable disturbances (figure 1). The critical Reynolds number is defined as the Reynolds number below which all waves are damped.

The total amplification rate of a single frequency is defined as :

$$\frac{A}{A_o} = \exp\left[-\int_{x_o}^{x} \alpha_i dx \right] = \exp\left[-\int_{R_o}^{R} \alpha_i \frac{dx}{dR} dR \right] \tag{4}$$

A is the wave amplitude and the index o refers to the streamwise position where the wave becomes unstable. Figure 2 shows total amplification curves corresponding to various frequencies, obtained for the BLASIUS profile. The dashed line represents the envelope of these curves, which will be called n :

$$n \equiv \underset{\omega}{\text{Max}} \left(\frac{A}{A_o}\right), \text{ at a given x or R} \tag{5}$$

It is obvious that n = 0 for $R = R_{cr}$.

The same type of calculation can be performed for the other similar velocity profiles of the FALKNER-SKAN family. Each profile is characterized by a lot of dimensionless parameters such as :

$$m = \frac{x}{U_e} \frac{dU_e}{dx} \quad , \quad \beta_h = \frac{2m}{m+1} \quad , \quad \Lambda_2 = \frac{\theta^2}{\nu} \frac{dU_e}{dx} \quad , \quad H \text{ (shape factor) ...}$$

For several values of H, the corresponding envelope curves are plotted on figure 3. The stabilizing effect of a negative pressure gradient (H < 2.59) and the destabilizing effect of a positive pressure

gradient (H > 2.59) can be clearly pointed out : as H increases, the critical Reynolds number decreases and the slope $dn/dR\delta 1$ increases.

2.2. LIEPMANN's method

LIEPMANN /1/ was the first who attempted to use the linear stability results for practical applications. He hypothesized that breakdown to turbulence occured when the Reynolds shear stress $\tau = - \rho \overline{u'v'}$ due to unstable waves, became equal to the laminar wall shear stress τ_ℓ :

$$\frac{\tau}{\tau_\ell} = \frac{2}{C_f} \left[\frac{- \overline{u'v'}}{U_e^2} \right] = \frac{2}{C_f} \left[\frac{- \overline{u'v'}}{u' \quad v'} \frac{v'}{u'} \frac{u'^2}{U_e^2} \right] = \frac{2}{C_f} \left[K \, u'^2 \right] \tag{6}$$

At transition, $\left(\dfrac{\tau}{\tau_\ell} \right)_{max} = \dfrac{2}{C_f} \left[K \, A_o^2 \, \left(\dfrac{A}{A_o} \right)^2_{max} \right] = 1$ (7)

The theory provides the values of K and $\left(\dfrac{A}{A_o} \right)_{max}$, but the initial amplitude A_o remains unknown. As it will be seen later, VAN DRIEST and BLUMER developed a simple prediction method based on LIEPMANN's idea.

2.3. e^7, e^8, e^9 and e^n methods

These methods have been developed independently by SMITH and GAMBERONI /2/ and by VAN INGEN /3/. In the general case where the flow is not of a constant β_h-type, these authors calculated at first the laminar boundary layer development ; the second step was to use the stability charts established by PRETSCH for self-similar velocity profiles ; the envelope curve was obtained by computing the growth of waves of different frequencies. SMITH and GAMBERONI compared stability calculations with measured transition points and transition was found to occur when $n \simeq 9$. This means that transition occurs when the most unstable frequency is amplified by a factor e^9. The same result was obtained by VAN INGEN, but with the exponential factor equal to 7 or 8.

More recently, WAZZAN, OKAMURA and SMITH /4/ and JAFFE, OKAMURA and SMITH /5/ improved the original approximate calculation technique, and VAN INGEN extended the method to cases including suction or separation bubbles /6/. As pointed out by MACK /7/, "the method remains essentially as originally developed, and the key to success still lies in a judicious choice of the value of the exponential factor."

Therefore, it seems obvious that a transition criterion should be based on the disturbance amplitude and not on its amplification ratio. The success of the e^9 method is certainly due to the fact that the experimental data were obtained in wind tunnels where the disturbance environment was similar ; in particular, the free-stream turbulence level T was rather low, let say $T \simeq 0.1 \, 10^{-2}$. For higher values of T, the transition Reynolds number decreases rapidly and the e^9 method no longer applies. MACK /7/ suggests an empirical relation between T and the value of n at the transition location :

$$n_T = - 8.43 - 2.4 \, \ell n \, T \tag{8}$$

This relation has been established to fit the experimental results collected by DRYDEN for the flat plate case /8/. For $T < 10^{-3}$, sound disturbances may become the factor controlling transition rather than turbulence and application of (6) may give poor results. If $T = 2.98 \, 10^{-2}$, $n_T = 0$, which means that transition occurs at the critical Reynolds number. If one assumes that the amplitude A reaches a constant value at transition, MACK's relation indicates that the initial amplitude A_o varies as $T^{2.4}$.

An example of application of the so-called e^n method is given on figure 4. It is relative to an experimental case studied at ONERA/CERT, in which the longitudinal pressure gradient is positive : at the transition location, the shape factor is equal to 3 (case C in the experiments reported in /9/, /10/). The figure shows the total amplification curves for five different frequencies. By introducing the experimental value of T ($T \simeq 0.15 \, 10^{-2}$) into relation (8), one obtains $n_T = 7.2$, which corresponds on the envelope curve to $x_T = 0.58$ m. This value is in close agreement with the experimental transition location. Similar comparisons have been made for other cases and are reported in /11/. It appears that MACK's relation can be extended to adverse pressure gradients.

2.4. Amplitude method

MACK /7/ has proposed a more ambitious approach by considering the total perturbation energy Ad^2. The main elements of this theory can be summarized as follows :

. Ad^2 results from the integration of individual energy densities $A^2 = \left(\dfrac{A}{A_o} \right)^2 A_o^2$ over the range of the unstable frequencies taken in the most unstable directions.

. For a given frequency and a given wave orientation, the ratio $\dfrac{A}{A_o}$ is given by the classic results of the linear stability theory and the initial amplitude A_o is related to the free-stream turbulence component having the same frequency and the same orientation ; there is no cross spectral transfer of energy.

. The free-stream turbulence is characterized by its intensity T and a length scale Λ. As a result of some assumptions and simplifications, Ad^2 is found to be a function of T and $R\Lambda = U_e\Lambda/\nu$.

. Transition occurs when $Ad = K \, U_e$. MACK adopted the critical value $K = 0.04$ in order to fit the experimental flat plate data.

A typical result of the amplitude method is that it gives a decrease of 16 % in Rx_T at $T = 0.02 \, 10^{-2}$

as $R\Lambda$ increases from $1\ 10^4$ to $8\ 10^4$. Unfortunately, the validity of this method cannot be exactly checked, due to the lack of experimental information.

3 - TRANSITION CRITERIA

In the following lines, the word criterion can be interpreted as a more or less empirical correlation between boundary layer parameters at the transition onset. These parameters may be some characteristic Reynolds number or a similarity variable, among others. The transition criteria are often used for practical applications, because they are easily introduced in engineering prediction methods such as integral methods. Although the fundamental mechanisms of the transition process do not appear as clearly as in the stability calculations, they provide a fairly acceptable compromise between accuracy and simplicity.

Historically, the first proposed criteria took only into account the pressure gradient effects ; more recently, it was possible to introduce in addition the influence of the free-stream turbulence. Both aspects will be examined successively.

3.1. Pressure gradient effects

In these criteria, the free-stream turbulence level is implicitly assumed to be low.

a) MICHEL /12/, 1951 - For two-dimensional flows over airfoils, MICHEL correlated the values of two Reynolds numbers at transition, $R\theta$ and Rx. This criterion is plotted on figure 5. The mean curve may be fitted by the following expression :

$$R\theta_T = 1.535\ Rx_T^{0.444} \tag{9}$$

For the BLASIUS solution, this relation gives $R\theta_T = 1\ 180$, which is close to the experimental value found by SCHUBAUER-SKRAMSTAD /13/.

b) GRANVILLE /14/, 1953 - GRANVILLE developed a correlation which takes into account two important parameters, namely the stability properties and the flow history :

. The stability of the boundary layer is characterized by the difference in momentum-thickness Reynolds numbers from the neutral stability point to the transition location.

. As the amplification of disturbances depends on the cumulative effect of pressure gradient, an averaged POHLHAUSEN parameter is introduced :

$$\overline{\Lambda}_{2_T} = \frac{1}{x_T - x_{cr}} \int_{x_{cr}}^{x_T} \frac{\theta^2}{\nu} \frac{dU_e}{dx}\ dx$$

This criterion gives a right correlation with available data for transition on airfoils in low turbulence wind tunnels and on wings in flight tests (figure 6).

c) CRABTREE /15/, 1957 - This criterion correlates transition data by using two simple parameters : the momentum-thickness Reynolds number and the local POHLHAUSEN parameter at the transition point (figure 7).

d) Transition criteria in separation bubbles - It was shown (Chapter I) that, if the chord Reynolds number of a given airfoil is small, laminar separation may occur, followed generally by a transitional bubble. An accurate prediction of the transition point is needed in order to compute the downstream effects of the bubble : a delayed transition would cause the bubble not to reattach and the calculation would fail ; on the other hand, with a too early transition, the increase in momentum thickness would be too small and the downstream turbulent calculation would not be significant. In a general way, problems involving separation bubbles are not treated with criteria such as those described above, but rather with specific criteria.

A transition criterion in separation bubbles was established by HORTON /16/ and modified by VINCENT DE PAUL /17/. Once the laminar separation abscissa x_s has been found, it is assumed that there is a sudden transition at a point x_T, defined as follows :

$$x_T - x_s = L, \quad \text{with } \frac{L}{\theta_s} = \frac{K}{R\theta_s} \tag{10}$$

where the subscript s corresponds to the separation point. K is a constant for HORTON ($K = 4\ 10^4$) and a function of $R\theta_s$ for VINCENT DE PAUL.

Another criterion is used by KWON and PLETCHER /18/, where the onset of transition is given by :

$$Rx_T = 1.059\ R\theta_s + 47\ 720$$

3.2. Free-stream turbulence effects with zero pressure gradient

The free-stream turbulence is characterized by its root-mean-square value, defined as :

$$T = \frac{(u')_e}{U_e} \quad \text{or} \quad T = (\sqrt{u'^2 + v'^2 + w'^2})_e / \sqrt{3}\ U_e$$

By reviewing the literature, HALL and GIBBINGS /19/, 1970, concluded that transition occurs when $R\theta$ reaches a value depending on T and given by the empirical expression :

$$R\theta_T = 190 + \exp(6.88 - 103\ T) \tag{11}$$

As concerns the transition length, HALL and GIBBINGS proposed :

$$R\theta_E = 320 + \exp (7.70 - 44.75 \ T) \tag{12}$$

where $R\theta_E$ is the momentum-thickness Reynolds number at the end of the transition region (figure 8).

3.3. Combined effects of pressure gradient and free-stream turbulence

a) VAN DRIEST and BLUMER /20/, 1963 – As the previous ones, the criterion proposed by VAN DRIEST and BLUMER is based on experimental data ; nevertheless, it includes theoretical elements. The authors consider the ratio of the local "turbulent" stress $\rho\ell^2 \ (\partial U/\partial y)^2$ to the local viscous stress $\mu(\partial U/\partial y)$. As ℓ is proportional to y, this ratio is proportional to $y^2/\nu \ . \ \partial U/\partial y$. At transition, it is assumed that :

$$\underset{y}{Max}(\frac{y^2}{\nu} \ \frac{\partial U}{\partial y})_T = \text{constant} = Tr \tag{13}$$

$\frac{y^2}{\nu} \ \frac{\partial U}{\partial y}$ is called the vorticity Reynolds number. For the BLASIUS profile, the maximum of this quantity occurs at $y/\delta \simeq 0.6$; it is approximately the altitude where the breakdown to turbulence has been observed in laboratory experiments. The FALKNER-SKAN similarity profiles and the TAYLOR's relation between pressure fluctuations and velocity fluctuations are then used and Tr is expressed by :

$$\frac{Tr}{R\delta} = A + B\Lambda + CR\delta \ (T)^2 \tag{14}$$

where $\Lambda = \frac{\delta^2}{\nu} \ \frac{dU_e}{dx}$ and $R\delta_T = (\frac{U_e\delta}{\nu})_T$

Tr, A, B and C are adjusted to fit the experimental data :

$$\begin{array}{ll} Tr = 9 \ 860 & B = - \ 0.0485 \\ & \\ A \ = 1 & C \ = \ 3.36 \end{array} \tag{15}$$

Other expressions of this criterion can be deduced from the wedge-flow solutions, where the external velocity is proportional to x^m, where m is a constant ; the most useful correlation is expressed under the form :

$$R\theta_T = f(\Lambda_{2_T}, \ T) \tag{16}$$

Relation (16) is presented on figure 9.

b) DUNHAM /21/, 1972 – Experiments dealing with combined effects of pressure gradient and free-stream turbulence are rather scarce for non zero pressure gradient. However, DUNHAM attempted to correlate the few existing results and proposed :

$$R\theta_T = \left[0.27 + 0.73 \ \exp \ (- \ 80 \ T)\right] \ \left[550 + 680 \ (1 + 100 \ T - 21 \ \Lambda_{2_T})^{-1}\right] \tag{17}$$

A family of curves given by this relation is shown in figure 10. For T = 0 and Λ = 0, the value of $R\theta_T$ is finite and equal to 1 230.

c) SEYB /22/, 1972 – SEYB proposed an empirical correlation which may be expressed as follows :

$$R\theta_T = \frac{1 \ 000}{1.2 + 70 \ T} \ + 10 \ (\frac{0.09 + \Lambda_2}{0.0106 + 3.6 \ T})^{2.62} \tag{18}$$

This relation is valid for $0.1 \ 10^{-2} \leqslant T \leqslant 4 \ 10^{-2}$. If T falls outside this range, $R\theta_T$ is assumed to be equal to the appropriate limit. FOREST /23/ used relation (18) with some modifications.

d) ARNAL, HABIBALLAH and DELCOURT /24/, 1979 – The aim was to obtain a criterion involving the same parameters as those introduced by GRANVILLE, $R\theta_T - R\theta_{cr}$ and Λ_{2_T}. In addition, the free-stream turbulence level T was taken into account. At first, the proposed correlation was established for similarity flows (FALKNER-SKAN family profiles) and then extended to more general configurations.

The criterion starts with the envelope curves of amplitude ratio computed for the FALKNER-SKAN profiles (figure 3). Each curve is characterized by a similarity parameter, such as β_h, H or Λ_2. The POHLHAUSEN parameter $\Lambda_2 = \theta^2/\nu \ . \ dU_e/dx$ will be considered in the following developments. The curves plotted on figure 3 give a relation such as :

$$n \equiv (\ell n \ \frac{A}{A_o})_{max} = n \ (R\delta_1 \ \text{or} \ R\theta, \ \Lambda_2) \tag{19}$$

As the critical Reynolds number is itself a function of Λ_2, equation (19) can be written :

$$n = n \ (R\theta - R\theta_{cr}, \ \Lambda_2) \tag{20}$$

The value of n at the transition location is given by MACK's relation :

$$n_T = - \ 8.43 - 2.4 \ \ell n \ T \tag{21}$$

A combination of (20) and (21) allows to obtain a correlation of the form :

$$R\theta_T - R\theta_{cr} \ (\Lambda_2) = f \ (\Lambda_{2_T}, \ T) \tag{22}$$

Curves corresponding to various values of T are plotted on figure 11. Λ_2 has been replaced by $\overline{\Lambda}_2$, which will be the parameter of interest in practical applications. It can be observed that the proposed criterion coincides practically with the GRANVILLE's one for $T \simeq 0.05 \ 10^{-2}$ to $0.1 \ 10^{-2}$. An analytical expression of the criterion is :

$$R\theta_T - R\theta_{cr} = -206 \exp(25.7 \ \overline{\Lambda}_{2_T}) \left[\ell n(16.8 \ T) - 2.77 \ \overline{\Lambda}_{2_T}\right] \tag{23}$$

$R\theta_{cr}$ is calculated by one of the methods described in Chapter I.

d) <u>Transition criteria in separation bubbles</u> - ROBERTS /25/ extended HORTON's criterion (equation (10)) by assuming that K is a function of T.

Recent calculations were carried out at ONERA/CERT by GLEYZES, COUSTEIX and BONNET /26/ who used a method originally developed by HABIBALLAH /11/ for attached boundary layers. In this method, it is observed that the envelope curves $n(R\theta)$ obtained for similarity profiles can be fitted by straight lines (figure 3) :

$$\frac{dn}{dR\theta} (H, \ R\theta) = S(H)$$

The total amplification is then calculated step by step by the relation :

$$n = \int_{R\theta_{cr}}^{R\theta} S(H) \ dR\theta$$

GLEYZES et al. obtained values of S for separated boundary layers ($H > 4.03$) and assumed that transition occurs when n reaches a critical value given by MACK's relation (equation (21)).

3.4. <u>Remarks and applications</u>

a) Among all the different criteria which take into account the free-stream turbulence level, the criterion proposed by ARNAL et al. gives infinite values of $R\theta_T$ for $T = 0$. On the contrary, the other criteria (VAN DRIEST-BLUMER, DUNHAM, SEYB, HALL-GIBBINGS) give finite values, which are generally adjusted on the SCHUBAUER-SKRAMSTAD experiments for the zero pressure gradient case.

b) Figure 12 presents a comparison between criteria at low values of T, in a $(R\theta_T, \Lambda_{2_T})$ diagram. In the analytical expressions of the VAN DRIEST-BLUMER and DUNHAM criteria, T is set equal to 0. It is always possible to transform any criterion in a criterion involving these variables by the use of similarity relations : for example, MICHEL's correlation $R\theta_T = R\theta_T(Rx_T)$ is converted into a $R\theta_T = R\theta_T(\Lambda_{2_T})$ correlation through the similarity parameter $R\theta/\sqrt{Rx} = f(\Lambda_2)$. The results corresponding to the e^9 method, when it is applied to the similarity profiles, are also plotted on that figure. It appears that large discrepancies exist, especially in positive pressure gradients : for $\Lambda_2 = -0.02$ (H =2.73), the criteria proposed by MICHEL and by CRABTREE give respectively $R\theta_T = 550$ and 1 150. For real and non similarity conditions, however, the differences may be reduced if the criteria are employed in their original formulation. But when the similarity conditions are approached, they will give more and more important discrepancies.

c) An application of DUNHAM's criterion to the experiments carried out at ONERA/CERT is presented in figure 13. The laminar values of $R\theta$ at the beginning of the transition region are plotted as function of the local POHLHAUSEN's parameter. It appears that the experimental value of T ($0.15 \ 10^{-2}$) does not correlate the experimental data. In the case B, for example, the criterion predicts $x_T = 0.8$ m instead of the experimental value $x_T = 0.5$ m. For the cases D, E and F, it does not give any transition point up to the theoretical laminar separation. In a general manner, the use of the local POHLHAUSEN's parameter can lead to large errors at low values of T. The use of a mean parameter seems to be more appropriate.

d) Figure 14 shows the velocity distributions corresponding to two experimental cases : the case F of the ONERA/CERT experiments and a case studied by R. MICHEL on an airfoil /27/. In both experiments, transition occurs at the same value of Λ_2, but the momentum-thickness Reynolds numbers are very different. However, calculations indicate that the critical Reynolds numbers are likewise very different, so that the difference $R\theta_T - R\theta_{cr}$ is nearly the same. This example justifies the use of this parameter in practical criteria, at least for low free-stream turbulence levels.

e) When T becomes large (say $T > 0.5$ or $1 \ 10^{-2}$), the linear stability process is often bypassed. An example of such a phenomenon was studied by BLAIR and WERLE /28/, /29/, who carried out experiments on accelerating flows subject to high free-stream turbulence levels ; the analysis of experimental results revealed that the Reynolds number at the transition onset was lower than the critical Reynolds number (see Chapter I). It is obvious that the criterion developed by ARNAL et al. /23/ (extension of GRANVILLE's criterion) is unable to predict such a transition process, because $R\theta_T$ must be greater than $R\theta_{cr}$: in negative pressure gradients, the critical Reynolds number increases rapidly, as well as the difference $R\theta_T - R\theta_{cr}$ (figure 11). On the contrary, the experimental values of $R\theta_T$ measured at high free-stream turbulence levels are not far from those obtained in zero pressure gradient for the same value of T. This is precisely the trend which is reflected in the criteria proposed by VAN DRIEST-BLUMER, DUNHAM or SEYB. In figure 15, these criteria are applied to a case studied by BLAIR-WERLE ; the experimental values of T and x_T are respectively 10^{-2} and 0.8 m. VAN DRIEST-BLUMER criterion gives $x_T \simeq 0.6$ m, whereas the two other criteria do not indicate any transition. Due to the slow boundary layer thickening, small differences in $R\theta$ can lead to large discrepancies in x, so that these criteria are generally not very accurate in negative pressure gradients.

f) The influence of parameters other than T and the pressure gradient is rarely taken into account in empirical criteria.

Concerning the wall curvature effects, FOREST /22/ correlated the few existing experimental results

by the relation :

$$G\theta_T = 9 \exp(-17.3 \ T)$$

where $G\theta = R\theta \sqrt{\dfrac{\theta}{R}}$ is the GÖRTLER number and $\dfrac{1}{R}$ the wall curvature.

Wall suction (or blowing) results in a decrease (or an increase) of the shape factor. As pointed out by WAZZAN et al. /30/, criteria using POHLHAUSEN's parameter are not adequate : in the zero pressure gradient case, for example, suction will make H decrease and $R\theta_T$ increase, but Λ_2 will remain equal to zero. A possible solution is to use the shape factor as a new parameter instead of Λ_2.

Wall roughness effects are difficult to introduce in practical calculation methods. The experimental results described in Chapter I may be considered as empirical rules for boundary layer tripping purposes.

4 - TRANSITION REGION CALCULATIONS BASED ON INTERMITTENCY METHODS

Let us assume that the transition onset is known. A second objective is to compute the transition region itself, the extent of which may be as long as the laminar region which precedes it. An important parameter characterizing the transitional boundary layer is the intermittency factor γ, which represents the fraction of the total time that the flow is turbulent. The numerical models we will describe in this section are based on the so-called "intermittency method", in which laminar and turbulent quantities are weighted by γ. In fact, experiments show that for strong positive pressure gradients, transition process no more involves turbulent spots and intermittency phenomenon (Chapter I). However, numerical results indicate that the use of an intermittency function can provide satisfactory results. Thus, the first task is to describe the streamwise evolution of the intermittency factor. Computations based on transport equations models do not need the knowledge of γ and will be presented in section 5.

4.1. Evolution of the intermittency factor

SCHUBAUER and KLEBANOFF /31/ measured the streamwise evolution of γ for various flat plate experiments. The length of the transition region varied from one case to another, but the intermittency distribution conserved the shape of the Gaussian integral curve. The standard deviation σ was determined for each experiment, and all data collapsed onto a single curve when γ was plotted as a function of $(x - \bar{x})/\sigma$, where $\bar{x} = x(\gamma = 0.5)$ (figure 16). However, this result does not constitute a calculation method for determining γ, because the values of $\bar{x}$ and σ must be known.

DHAWAN and NARASIMHA /32/ proposed another universal distribution of intermittency for flat plate experiments :

$$\gamma = 1 - \exp\left[-A \ (x - x_T)^2/\lambda^2\right] \tag{24}$$

with $\lambda = x \ (\gamma = 0.75) - x \ (\gamma = 0.25)$

A compatibility relation implies that $A = (\sqrt{\ln 4} - \sqrt{\ln 3/4})^2 = 0.411$. If, for a given experiment, x_T is known, the curve $\gamma(x)$ cannot be determined unless λ is also known. For this, the authors correlated experimental data by the following relation :

$$\frac{U_e \lambda}{\nu} = 5\left(\frac{U_e x_T}{\nu}\right)^{0.8} \tag{25}$$

Under the assumption that turbulent spots appear randomly with a source rate density g, EMMONS /33/ has shown that the intermittency factor at a given point P can be written as :

$$\gamma = 1 - \exp\left(-\int_R g \, dV\right) \tag{26}$$

where R is the influence volume of P, defined by the locus of all points which influence the state of turbulence at point P. By assuming that g can be approximated by a DIRAC's delta function, CHEN and THYSON /34/ obtained an expression valid for plane or axisymmetric flows :

$$\gamma = 1 - \exp\left(-G r_T \left[\int_{r_T}^{r} \frac{dx}{r}\right]\left[\int_{r_T}^{r} \frac{dx}{U_e}\right]\right) \tag{27}$$

r is the body radius and G is a function of Rx_T and Mach number. For plane, incompressible flows, (27) takes the following form :

$$\gamma = 1 - \exp\left[-8.33 \ 10^{-4} Rx_T^{0.66} \ U_e \ \frac{(x - x_T)}{x_T^2} \int_{x_T}^{x} \frac{dx}{U_e}\right] \tag{28}$$

More recently, experiments performed at ONERA/CERT /9/ with zero and positive pressure gradients have shown that the momentum thickness θ_E at the end of the transition region was about twice the momentum thickness θ_T at the transition onset. Therefore, relations of the form :

$$\gamma = f\left(\frac{\theta}{\theta_T}\right) \quad \text{or} \quad \gamma = f\left(\frac{R\theta}{R\theta_T}\right) \tag{29}$$

were adopted. They will be discussed later in more details.

4.2. Local equations in the transition region

At a given point in a transitional boundary layer, an instantaneous signal shows the successive appearance of turbulent spots and of laminar regions. In the following lines, all quantities related to the turbulent spots (respectively to the laminar regions) are denoted by the subscript t (respectively ℓ).

An intermittency function $I(t)$ is introduced ; its value is 1 inside the spots and 0 outside the spots. The intermittency factor γ is the time averaged value of $I(t)$, and the "global" mean velocity U can be expressed as :

$$U = \gamma U_t + (1 - \gamma) U_\ell \qquad (30)$$

Similar relations are valid for the other components for the mean velocity. The root-mean-square value of the longitudinal fluctuation is given by :

$$u'^2 = \gamma u_t'^2 + (1 - \gamma) u_\ell'^2 + \gamma (1 - \gamma)(U_t - U_\ell)^2 \qquad (31)$$

G. VANCOILLIE /35/ deduced a set of equations which apply separately to the turbulent and laminar regions. He assumed that the spots are two-dimensional ($W_\ell = W_t = 0$) and that γ depends on x only. Concerning the mass conservation, the basic equations are :

$$\frac{\partial u(t)}{\partial x} + \frac{\partial v(t)}{\partial y} + \frac{\partial w(t)}{\partial z} = 0 \qquad (32)$$

$$\frac{dI(t)}{dt} = \frac{\partial I(t)}{\partial t} + u(t)\frac{\partial I(t)}{\partial x} + v(t)\frac{\partial I(t)}{\partial y} + w(t)\frac{\partial I(t)}{\partial z} \qquad (33)$$

(32) and (33) are combined and the time average is taken, so that the "zone averaged" continuity equations can be obtained :

$$\frac{\partial \gamma U_t}{\partial x} + \frac{\partial \gamma V_t}{\partial y} = \overline{\frac{dI}{dt}} \qquad (34)$$

$$\frac{\partial (1 - \gamma) U_\ell}{\partial x} + \frac{\partial (1 - \gamma) V_\ell}{\partial y} = -\overline{\frac{dI}{dt}} \qquad (35)$$

Adding /34/ and /35/ yields the continuity equation for the global averaged velocity.

Similar operations lead to the "zone averaged" momentum equations :

$$U_t \frac{\partial U_t}{\partial x} + V_t \frac{\partial U_t}{\partial y} = -\frac{1}{\rho}\frac{dP}{dx} + \frac{\partial}{\partial y}\left(\nu \frac{\partial U_t}{\partial y} - \overline{u_t' v_t'}\right) + \text{additional terms} \qquad (36)$$

$$U_\ell \frac{\partial U_\ell}{\partial x} + V_\ell \frac{\partial V_\ell}{\partial y} = -\frac{1}{\rho}\frac{dP}{dx} + \frac{\partial}{\partial y}\left(\nu \frac{\partial U_\ell}{\partial y} - \overline{u_\ell' v_\ell'}\right) + \text{additional terms} \qquad (37)$$

The additional terms express the interaction at the interface between the turbulent spots and the surrounding laminar flow.

The modelling of the source terms in equations (36), (37) is described in /35/. The final set of equations to be solved is :

$$
\left.
\begin{aligned}
&\frac{\partial U_\ell}{\partial x} + \frac{\partial V_\ell}{\partial y} = 0 \\
&U_\ell \frac{\partial U_\ell}{\partial x} + V_\ell \frac{\partial U_\ell}{\partial y} = -\frac{1}{\rho}\frac{dP}{dx} + \frac{\partial}{\partial y}\left(\nu \frac{\partial U_\ell}{\partial y}\right) - \boxed{300\,\nu\,\frac{U_\ell - U_t}{\delta_1}\,\frac{1}{1-\gamma}\frac{d\gamma}{dx}} \\
&\frac{\partial U_t}{\partial x} + \frac{\partial V_t}{\partial y} = \boxed{\frac{1}{\gamma}(U_\ell - U_t)\frac{d\gamma}{dx}} \\
&U_t \frac{\partial U_t}{\partial x} + V_t \frac{\partial U_t}{\partial y} = -\frac{1}{\rho}\frac{dP}{dx} + \frac{\partial}{\partial y}\left((\nu + \nu_t)\frac{\partial U_t}{\partial y}\right) + \boxed{\frac{U_\ell - U_t}{\gamma}\frac{d\gamma}{dx}} \\
&\qquad\qquad + \boxed{300\,\nu\,\frac{U_\ell - U_t}{\delta_1}\,\frac{1}{\gamma}\frac{d\gamma}{dx}}
\end{aligned}
\right\} \qquad (38)
$$

The eddy viscosity ν_t is calculated with the k-ε model, which gives, in fact, k_t and ε_t, because the transport equations are solved in the turbulent regions only. All source terms are proportional to $d\gamma/dx$, so that a constant value of γ will produce two boundary layers growing independently.

For numerical applications, the curve $\gamma(x)$ is given algebrically. The computer code provides the U_t, U_ℓ, V_t, V_ℓ, k_t and ε_t profiles. In fact, the quantities measured in laboratory experiments are U and u'^2, which are related to the zone averaged quantities by equations (30) and (31). For the purpose of comparison between calculations and experiments, it is assumed that $u_\ell'^2 = 0$ and $u_t'^2 = k_t$, so that u'^2 is calculated by :

$$u'^2 = \gamma k_t + \gamma (1 - \gamma)(U_t - U_\ell)^2 \qquad (39)$$

Examples of results are presented in figure 17. The experiments have been performed at ONERA/CERT on a cylinder with zero pressure gradient /36/. The two considered stations are located in the middle ($\gamma = 0.58$) and towards the end ($\gamma = 0.85$) of the transition region. A remarkable fact is that the numerical model predicts fairly well the complicated shape of the turbulence profiles and especially the existing peak very close to the wall ; the difference between U_t and U_ℓ is very large and the quantity $\gamma(1-\gamma)(U_t-U_\ell)^2$ creates most of the "turbulence" energy.

A similar agreement was obtained with the experiments of SCHUBAUER-KLEBANOFF /31/ and those of WERLE-BLAIR /28/, /29/. The major shortcoming of this method is that the evolution of γ must be prescribed. Moreover, it will be interesting to check its validity in cases involving positive pressure gradients, for which there is a progressive disappearance of the intermittency phenomenon.

4.3. Simpler methods

Many of the practical engineering methods are less sophisticated and work only with the continuity and the momentum equations for the global mean flow :

$$\left.\begin{array}{l} \dfrac{\partial U}{\partial x} + \dfrac{\partial V}{\partial y} = 0 \\[2ex] U\,\dfrac{\partial U}{\partial x} + V\cdot\dfrac{\partial U}{\partial y} = -\dfrac{1}{\rho}\,\dfrac{dP}{dx} + \dfrac{\partial}{\partial y}\,(\nu\,\dfrac{\partial U}{\partial y} - \overline{u'v'}) \end{array}\right\} \tag{40}$$

In the calculation method developed at ONERA/CERT /37/, the turbulent shear stress is expressed by a modified mixing length scheme :

$$-\overline{u'v'} = \gamma\,F^2\,\ell^2\,(\dfrac{\partial U}{\partial y})^2 \tag{41}$$

The mixing length ℓ and the wall damping function F keep the form already used for fully turbulent boundary layers /38/ :

$$\ell = 0.085\,\delta\,\tanh\,(4.823\,\dfrac{y}{\delta}) \tag{42}$$

$$F = 1 - \exp\left[\sqrt{\tau\rho}\,\ell/10.66\,\mu\right] \tag{43}$$

where τ is the total shear stress. The low Reynolds number effects are included in the factor γ, which may be considered, at first sight, as an intermittency factor, because it must increase from zero in laminar flow to unity in turbulent flow. γ is assumed to be a function of θ/θ_T, and first numerical comparisons were performed by considering :

$$\gamma = 1 - \exp\left[-4.5\,(\dfrac{\theta}{\theta_T} - 1)^2\right] \tag{44}$$

Examples of results are given in figure 18 ; comparison is made with an experimental configuration where transition occurs in a mild positive pressure gradient (case D of the ONERA/CERT experiments). The streamwise evolution of γ looks like the one predicted by SCHUBAUER-KLEBANOFF or DAWAN-NARASIMHA (see § 4.1.), but the computed shape factor falls too slowly and the skin friction coefficient is underestimated. A better agreement is achieved when γ is constrained to have an overshoot, well above unity (figure 18). It is clear that γ does not represent the physical intermittency factor ; it is referred as $\tilde{\gamma}$ in figure 18. Nevertheless we keep the assumption that $\tilde{\gamma}$ depends on θ/θ_T only.

In fact, the global shear stress $\overline{u'v'}$ can be expressed as function of the zone-averaged quantities by :

$$\overline{u'v'} = \gamma\,\overline{u_t'\,v_t'} + (1 - \gamma)\,\overline{u_\ell'\,v_\ell'} + \gamma\,(1 - \gamma)\,(U_t - U_\ell)\,(V_t - V_\ell) \tag{45}$$

where γ is the "true" intermittency factor. (45) differs highly from (41), in which the zone averaged mean velocities do not appear. This explains why the multiplicative factor in (41) cannot represent the true intermittency factor.

CEBECI /39/ used an expression similar to (41), the intermittency factor being expressed by the relation (28) proposed by CHEN and THYSON.

FOREST /22/ presented a technique somewhat similar to the previous ones. The shear stress is modelled under the form :

$$-\overline{u'v'} = \gamma\ell_c^2\,(\dfrac{\partial U}{\partial y})^2 + C_T\,T\,U_e\,\ell \tag{46}$$

ℓ is the classical mixing length. ℓ_c is a modified mixing length taking into account the streamlines curvature ($\ell_c = \ell$ on a flat surface). C_T and T represent a correlation factor and the free-stream turbulence level respectively. The "intermittency" factor γ is defined through a lag equation of the form :

$$\dfrac{d\gamma}{dx} = \dfrac{\gamma_e - \gamma}{L} \tag{47}$$

where L is a lag distance. γ_e is expressed as :

$$\gamma_e = 1 - (1 - \gamma_{TS})\,(1 - \gamma_G) \tag{48}$$

γ_G is zero on smooth or convex surfaces. On concave surfaces, it depends on the ratio $G\theta/G\theta_T$, where $G\theta$ represents the GÖRTLER number $R\theta\sqrt{\theta/R}$. The classical intermittency factor was successfully applied to experimental cases involving high turbulence levels and large acceleration effects.

4.4. Integral methods

The intermittency method.can be easily introduced in integral calculation methods, as it was done at ONERA/CERT /24/. The boundary layer development is computed by using the integrated momentum equation (Von KARMAN's equation) and an auxiliary equation (entrainment or mean energy equation). The closure relationships are deduced from self-similarity solutions, and are obviously different in laminar and in turbulent flows.

At a given point in the transition region, the laminar relationships give "fictitious" laminar characteristic parameters, such as the shape factor H_ℓ and the skin friction coefficient $C_{f\ell}$. In the same way, H_t and C_{ft} are obtained from the turbulent relationships. The characteristic parameters of the transitional boundary layer are then expressed as :

$$\left. \begin{aligned} H &= \gamma H_t + (1 - \gamma)\, H_\ell \\ C_f &= \gamma C_{ft} + (1 - \gamma)\, C_{f\ell} \end{aligned} \right\} \tag{49}$$

with $\gamma = 1 - \exp\left(4.5\left(\dfrac{\theta}{\theta_T} - 1\right)\right)$

Figures 19 and 20 present some applications of this technique. In the experiments reported in figure 19, the transition occurs in a positive pressure gradient, with a relatively low free-stream turbulence level. The transition onset is determined with the criterion described in § 3.3.c). Figure 20 shows a comparison with the experiments performed by WERLE-BLAIR in a negative pressure gradient, for two high values of T : $1\ 10^{-2}$ and $2\ 10^{-2}$. The transition position is imposed in the calculation method, because the criterion no longer applies (see § 3.4.e)). In any case, the experimental evolution of the boundary layer parameters in the transition region is fairly well reproduced.

A similar technique was developed by GLEYZES, COUSTEIX and BONNET /26/ for computing short separation bubbles. In this case, a "direct" boundary layer method (the external flow is given) cannot be used, because it leads to a singularity in the vicinity of the zero skin friction point, except if the pressure gradient fills up a compatibility relation. This adjustment is made possible by an inverse mode formulation of the problem : the external velocity is the solution of the boundary layer equations, the distribution of $\delta 1$, for instance, being the input of the calculation. An inviscid calculation must be associated, through a viscous-inviscid interaction procedure.

Figure 21 shows a comparison between experiments and theory, for a case in which $T \simeq 0.4\ 10^{-2}$. The overall agreement is satisfactory. In particular, the validity of the transition criterion described in § 3.3.d) seems good, owing to the correct prediction of either the size of the pressure plateau or the evolution of the shape factor in the vicinity of reattachment.

5 - TRANSITION CALCULATIONS BY TRANSPORT EQUATIONS

During the last two decades, calculation methods using transport equations have been developed and applied to more and more complex turbulent flows. In addition, attempts have been made for extending the range of applications of such methods to the prediction of transition phenomena. For this, additional terms or empirical functions have been introduced in the fully turbulent form of the equations ; they depend usually on the "turbulence Reynolds number" R_t, which represents the ratio of the turbulent shear stress $-\overline{u'v'}$ to the viscous shear stress $\nu\,\dfrac{\partial U}{\partial y}$.

The numerical problem is to solve a set of parabolic partial differential equations with appropriate initial and boundary conditions. These equations are the continuity and momentum equations, plus one, two or more transport equations for turbulent quantities. The calculation starts in laminar flow with specified initial profiles and proceeds step by step in the streamwise direction. If the turbulent quantities are amplified, "transition" may occur, in this sense that the shear stress $-\overline{u'v'}$ becomes large and modifies the mean velocity profile.

These methods present the advantage that a single run is needed for the computation of the laminar, transitional and turbulent boundary layer. A second advantage is that the influence of some important factors acting on the transition processes appears naturally under boundary conditions : the pressure gradient effect is included in the momentum equation, and the free-stream turbulence level represents the value of the turbulent kinetic energy at the boundary layer edge. The major shortcoming, however, is that the set of constants and functions used to describe transition should be regarded as an empirical information and cannot explain (or contain) the fundamental mechanisms.

5.1. Basic equations

The basic equations that govern an incompressible, two-dimensional boundary layer are :

$$\frac{\partial U}{\partial x} + \frac{\partial V}{\partial y} = 0 \tag{50}$$

$$U\,\frac{\partial U}{\partial x} + V\,\frac{\partial U}{\partial y} = U_e\,\frac{dU_e}{dx} + \frac{\partial}{\partial y}\left(\nu\,\frac{\partial U}{\partial y} - \overline{u'v'}\right) \tag{51}$$

The momentum equation (51) contains the double correlation $\overline{u'v'}$, which is an element of the Reynolds stress tensor. The complete equations for the turbulent shear stresses $\overline{u'_i u'_j}$ in a two-dimensional flow can be written as :

$$\underbrace{\frac{D\,\overline{u_i'u_j'}}{Dt}}_{\text{Convection}} = \underbrace{-\,\overline{u_k'u_j'}\,\frac{\partial U_i}{\partial x_k} - \overline{u_k'u_i'}\,\frac{\partial U_j}{\partial x_k}}_{\text{Production}} \underbrace{-\,2\nu\,\overline{\frac{\partial u_i'}{\partial x_k}\frac{\partial u_j'}{\partial x_k}}}_{\text{Dissipation}}$$

$$+\underbrace{\frac{\overline{p'}}{\rho}\left(\frac{\partial u_i'}{\partial x_j} + \frac{\partial u_j'}{\partial x_i}\right)}_{\text{Redistribution}} \underbrace{-\,\frac{\partial}{\partial x_k}\left(\overline{u_i'u_j'u_k'} + \overline{\frac{p'}{\rho}(\delta_{jk}u_i' + \delta_{ik}u_j')} - \nu\,\frac{\partial}{\partial x_k}(\overline{u_i'u_j'})\right)}_{\text{Diffusion}}$$

(52)

By adding the equations for the normal stresses (i = j), one can deduce an equation for the turbulent kinetic energy $k = 1/2\,(\overline{u'^2} + \overline{v'^2} + \overline{w'^2})$:

$$\frac{Dk}{Dt} = -\,\overline{u'v'}\,\frac{\partial U}{\partial y} - 2\nu\,\overline{\left(\frac{\partial u_i'}{\partial x_k}\right)^2} + \frac{\partial}{\partial y}\left(\nu\,\frac{\partial k}{\partial y}\right) + \text{turbulent diffusion} \qquad (53)$$

Due to the boundary layer assumptions, the production terms reduce to $-\,\overline{u'v'}\,\frac{\partial U}{\partial y}$. The redistribution term vanishes by use of the continuity equation. The modelling of the dissipation and diffusion terms is discussed below.

5.2. Earlier methods

a) One-equation model – In fully established turbulent flows, the turbulent kinetic energy equation is commonly used in addition to the classical eddy viscosity formulation :

$$-\,\overline{u'v'} = \nu_t\,\frac{\partial U}{\partial y} \quad\text{with}\quad \nu_t = (2a_1 k)^{1/2}\,L \qquad (54)$$

The dissipation ε is given by :

$$\varepsilon = \frac{(2a_1 k)^{3/2}}{L} \qquad (55)$$

and the turbulent diffusion term is expressed by a gradient formulation :

$$\text{Turbulent diffusion} = \frac{\partial}{\partial y}\left(C_k \nu_t\,\frac{\partial k}{\partial y}\right) \qquad (56)$$

$L = L(y)$ is a length scale which is given analytically. a_1 and C_k are constants. GLUSHKO /40/ extended this model to low Reynolds numbers by assuming that :

$$\left.\begin{aligned}
\nu_t &= h_1\,(2a_1 k)^{1/2}\,L \\
\varepsilon &= 0.63\,\frac{\nu k}{L^2} + h_2\,\frac{(2a_1 k)^{3/2}}{L} \\
\text{Turbulent diffusion} &= \frac{\partial}{\partial y}\left(g C_k \nu_t\,\frac{\partial k}{\partial y}\right)
\end{aligned}\right\} \qquad (57)$$

h_1, h_2 and g are known functions of $R_t \simeq \frac{\sqrt{k}\,L}{\nu}$. They are equal to zero for $R_t = 0$ and tend to unity for large values of R_t. The additional term in the expression of ε becomes negligible in fully turbulent flow.

BECKWITH and BUSHNELL /41/ (1968) used this model in the flat plate case, by starting the calculation in laminar flow. The shape factor remained at first constant and then abruptly decreased at some value of Rx. Multiplying the diffusion term by 3 increased the "transition" Reynolds number (figure 22).

b) DONALDSON's model /42/, 1969 – DONALDSON presented a turbulence model in which the transport equations for $\overline{u'^2}$, $\overline{v'^2}$, $\overline{w'^2}$ and $\overline{u'v'}$ were solved. By modelling the high-order correlations, he introduced a scale length λ, which was not y-dependent. As an example, the $\overline{u'^2}$-equation takes the final form :

(58)
$$\underbrace{\frac{D\overline{u'^2}}{Dt}}_{\text{Conv.}} = \underbrace{-\,2\left(\overline{u'v'}\,\frac{\partial U}{\partial y} + \overline{u'^2}\,\frac{\partial U}{\partial x}\right)}_{\text{Production}} \underbrace{-\,2\nu\,\frac{\overline{u'^2}}{\lambda^2}}_{\text{Diss.}} + \underbrace{\frac{\sqrt{2k}}{\lambda}\left(\frac{2k}{3} - \overline{u'^2}\right)}_{\text{Redistribution}} + \underbrace{\frac{\partial}{\partial y}\left[(\nu + \lambda\,\overline{v'}\,)\,\frac{\partial \overline{u'^2}}{\partial y}\right]}_{\text{Diffusion}}$$

Most of the computational runs were made with initial disturbance profiles looking like the ones illustrated on the picture. Their shape is that of a spike of breadth $\Delta y = 0.2\,\delta$ applied at $y = 0.3\,\delta$. The scale length λ represents the wave-length of the disturbance and remains constant during the run. When the calculation proceeds downstream, the turbulent kinetic energy increases or decreases, depending on the values of λ and of the Reynolds number. This attempt to establish a link with the linear stability theory was interesting, but, on a practical point of view, no direct comparison with experiments was presented.
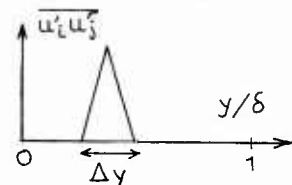
5.3. Two-equation models

These models solve the turbulent kinetic energy equation and a second equation for a turbulent length scale ℓ. More exactly, the second equation describes the behaviour of a combination of k and ℓ, such as $\varepsilon \sim k^{3/2} \ell^{-1}$. In fact, all these models have a similar general form, differing mainly in some empirical coefficients and in the low turbulence approximations.

a) <u>k-ε model</u> – This model retains the k-equation and an equation for the dissipation rate ε. Closure assumptions have been developed by HANJALIC and LAUNDER /43/ for fully turbulent flows ; JONES and LAUNDER /44/ introduced supplementary terms for taking into account the effects of small values of R_t. The final form of the equations for k and ε is as follows :

$$\frac{Dk}{Dt} = - \overline{u'v'} \frac{\partial U}{\partial y} - \varepsilon + \boxed{2\nu \left(\frac{\partial k^{1/2}}{\partial y}\right)^2} + \frac{\partial}{\partial y}\left[(\nu + C_k \nu_t)\frac{\partial k}{\partial y}\right]$$

$$\frac{D\varepsilon}{Dt} = - C_{\varepsilon 1} \frac{\varepsilon}{k} \overline{u'v'} \frac{\partial U}{\partial y} - \boxed{f_2} C_{\varepsilon 2} \frac{\varepsilon^2}{k} + \boxed{2\nu \nu_t \frac{\partial^2 U}{\partial y^2}} + \frac{\partial}{\partial y}\left[(\nu + C_\varepsilon \nu_t)\frac{\partial \varepsilon}{\partial y}\right]$$

$$\left.\right\} \quad (58)$$

with $- \overline{u'v'} = \nu_t \frac{\partial U}{\partial y}$ and $\nu_t = \boxed{f_\mu} (2a_1)^2 \frac{k^2}{\varepsilon}$

The terms set in a frame are those added by JONES and LAUNDER. f_μ and f_2 represent empirical functions of R_t. The two other terms have been introduced in order to obtain a correct evolution of k in the viscous sublayer of a turbulent boundary layer. C_k, C_ε , $C_{\varepsilon 1}$, $C_{\varepsilon 2}$ and a_1 are numerical constants.

b) <u>k-ω model</u> – The transport equation for k appears in this model together with an empirical equation for the turbulent vorticity energy $\omega^2 \simeq k\ell^{-2}$. The turbulence model was at first developed by SAFFMAN and WILCOX /45/ for fully turbulent flows and then extended by WILCOX /46/ to cases involving transition calculations :

$$\frac{Dk}{Dt} = \boxed{f} 2a_1 k \frac{\partial U}{\partial y} - (2a_1)^2 \omega k + \frac{\partial}{\partial y}\left[(\nu + C_k \nu_t)\frac{\partial k}{\partial y}\right]$$

$$\frac{D\omega^2}{Dt} = \alpha_1 \boxed{f} \omega^2 \frac{\partial U}{\partial y} - 2(2a_1)^2 \omega^3 + \frac{\partial}{\partial y}\left[(\nu + (\omega \nu_t)\frac{\partial \omega^2}{\partial y}\right]$$

$$\left.\right\} \quad (59)$$

with $- \overline{u'v'} = (\boxed{\nu} + \nu_t) \frac{\partial U}{\partial y}$ and $\nu_t = \frac{k}{\omega}$

Let us observe that in the k-equation, it was assumed that $- \overline{u'v'} = 2a_1 k$ (production term) and $\varepsilon = (2a_1)^2 \omega k$ (dissipation term). a_1, α_1, C_k and C_ω are constants and f is a given function of $R_t = \frac{k}{\nu \omega}$.

More recently, WILCOX /47/ revised his model in order to develop "an alternative to the e^9 procedure". The boundary layer computation consist of two phases. In the first phase, conventional linear stability calculations are performed until the initial disturbance has been amplified by a factor of e^4. In the second phase, the k-ω^2 model is used and allows to represent non linear processes which ultimately lead to transition ; the initial profiles for k and ω^2, as well as an important parameter included in the low turbulence functions, are deduced from the stability computations. As these profiles are frequency dependent, the spectral effects can be accounted for.

c) <u>k-kℓ model</u> – ARAD, BERGER, ISRAELI and WOLFSHTEIN /48/ extended the NG's turbulence model to the computation of laminar and transitional flows. The turbulence is defined by the kinetic energy k and its scale ℓ, which is expressed as :

$$\ell = \frac{1}{k} \int_0^\infty \frac{E(\tilde{k})}{\tilde{k}} d\tilde{k} \quad , \quad \text{with } k = \int_0^\infty E(\tilde{k}) d\tilde{k} \quad (60)$$

$\tilde{k}$ is the wave number and $E(\tilde{k})$ represents the one-dimensional spectral distribution of the energy. The NG's model describes the behaviour of k and of the product kℓ. When the low Reynolds numbers modifications are included, the governing equations are :

$$\frac{Dk}{Dt} = - \overline{u'v'} \frac{\partial U}{\partial y} - \frac{C_1}{\boxed{f_1}} \frac{k^{3/2}}{\ell} + \frac{\partial}{\partial y}\left[(\nu + C_k \nu_t) \frac{\partial k}{\partial y}\right]$$

$$\frac{D(k\ell)}{Dt} = (C_2 \boxed{f_2} - \frac{C_4}{\boxed{f_4}} \left(\frac{\ell}{y}\right)^6) \ell\nu_t \left(\frac{\partial U}{\partial y}\right)^2 - \frac{C_3}{\boxed{f_3}} k^{3/2} + \frac{\partial}{\partial y}\left[(\nu + C_{k\ell} \nu_t) \frac{\partial (k\ell)}{\partial y}\right]$$

$$\left.\right\} \quad (61)$$

with $\overline{u'v'} = - \nu_t \frac{\partial U}{\partial y}$ and $\nu_t = \boxed{f_\mu} C_\mu \sqrt{k\ell}$

f_1, f_2, f_3, f_4 and f_μ are obviously functions of $R_t = \frac{\sqrt{k\ell}}{\nu}$.

5.4. Other models

a) MacDONALD-FISH model – A somewhat different technique was proposed by MacDONALD and FISH /49/. The basic equations remain of course the continuity and momentum equations, in which the turbulent shear stress is expressed by a mixing length relation :

$$- \overline{u'v'} = \ell^2 \, (\frac{\partial U}{\partial y})^2 \quad \text{with} \quad \frac{\ell}{\delta} = \frac{\ell e}{\delta} \, \tanh(0.4 \, \frac{y}{\delta})\qquad(62)$$

The free-stream mixing length level, ℓe, is calculated by an auxiliary equation. This equation is the turbulent kinetic energy equation integrated across the boundary layer. In this way, there is no partial differential equation to solve for k, but only an ordinary differential equation.

The viscosity effects are accounted for by a multiplicative function $\mathcal{D}$:

$$- \overline{u'v'} = \mathcal{D}^2 \, \ell^2 \, (\frac{\partial U}{\partial y})^2\qquad(63)$$

The damping function $\mathcal{D}$ depends on R_t and on a second parameter in which the wall roughness effects are included.

b) FINSON's model – FINSON solved a five-equation model /50/. The dependent turbulent quantities are the three components of the turbulent kinetic energy $\overline{u'^2}$, $\overline{v'^2}$, $\overline{w'^2}$, the Reynolds stress $\overline{u'v'}$ and the dissipation rate ε. The production, diffusion and dissipation effects are described with approximations commonly used in fully turbulent flows. Some additional terms are introduced for achieving the low Reynolds number behaviour. On the other hand, the closure requirements for the redistribution terms are found to be critical in the transition region. It should be noted that the two-equation model avoid this difficulty, because these terms cancel in the turbulent kinetic energy equation.

In order to take into account the effects of distributed surface roughness, FINSON introduced source or sink terms in the various governing equations. For example, the sink term in the momentum equation is :

$$S = - \frac{1}{2} \, \rho \, U^2 C_D \, D/\ell^2 \qquad \text{(for } y \leqslant k, \text{ the roughness height)}\qquad(64)$$

D is the mean diameter of the roughness elements, ℓ is the mean spacing between elements and $C_D \simeq 0.5$ represents a drag coefficient. Source terms in the transport equations describe the production of turbulence due to the wakes of the roughness elements.

5.5. Examples of numerical results

a) Flat plate flow – Figure 23 shows the influence of T on the transition Reynolds number as computed by many authors : MacDONALD and FISH /49/, ARAD et al. /48/, FINSON /50/ and ARNAL et al. /36/, who used the k-ε model. The hatched area covers the range of experimental data. The overall trend is well reproduced by the calculations ; the FINSON's results, however, exhibit a somewhat more rapid transition movement than that observed.

ARAD et al. studied the influence of the length scale Reynolds number $R_\ell = \dfrac{U_e \ell_\infty}{\nu}$, where ℓ_∞ is the mean value of ℓ outside the boundary layer. The numerical results plotted in figure 24 for $T = 1 \, 10^{-2}$, reveal that the transition Reynolds number decreases when R_ℓ increases (the points in figure 23 have been obtained with $R_\ell = 211$). A systematic study of the influence of ε_e has not been done with the k-ε model.

A fairly good agreement is also achieved when the theoretical evolutions of the boundary layer parameters are compared with the experimental ones ; in particular, the transport equations give a satisfactory estimate of the transition region extent. Nevertheless, important discrepancies appear as concerns the shape of transitional turbulence profiles, as it can be seen in figure 17 ; the turbulence peak near the wall cannot be reproduced, because the intermittency phenomenon is not included in the model.

b) Effect of wall roughness – FEINDT /51/ measured the effect of distributed surface roughness (sandpaper) on the transition location for different flow conditions and roughness heights. In figure 25, a comparison is presented between FEINDT's measurements and calculations performed by MacDONALD and FISH /49/ with $T = 0.75 \, 10^{-2}$. The agreement is correct, but it may be believed that the "roughness function" has been determined in order to fit the experimental results. A reasonable quantitative agreement with FEINDT's data was also obtained by FINSON /50/ and WILCOX /46/.

c) Effect of pressure gradient – The ability of the k-ε model to predict the transition onset has been tested /24/ for the three velocity distributions plotted in figure 26. In all cases, the calculation starts at the stagnation point. For x > 0.15 m, the curves ①, ② and ③ correspond respectively to negative, zero and positive pressure gradients. The free-stream turbulence level is low and identical for the three computational runs.

The table reported in figure 26 presents the numerical values of H and $R\theta$ at the transition location ; they indicate that the transition Reynolds number increases in the adverse pressure gradient. This result is completely at variance with the available experimental results. This strong disagreement is certainly due to the fact that the real transition mechanisms are linked with stability properties, at least for low values of T, and the transport equations could hardly be expected to reproduce linear stability theory. Let us note, however, that BRILEY and MacDONALD /52/ were able to obtain fairly good predictions of incompressible separation bubbles by using the MacDONALD-FISH model /49/.

d) Combined effects of dP/dx and T – TURNER /53/ has reported measurements of the heat transfer distribution on a cooled turbine blade, for three free-stream turbulence levels. For predicting such complex flows, the enthalpy equation is introduced into the computer code. Figure 27 presents a comparison

between experiments and k-ε model calculations /36/ on the pressure side of the airfoil, where the free-stream velocity accelerates rapidly and almost linearly with streamwise distance. The dashed curves represent the results of laminar calculations.

For $T = 0.45 \ 10^{-2}$, the boundary layer remains laminar over the entire length of the blade. For $T = 5.9 \ 10^{-2}$, transition occurs close to the leading edge. At the intermediate turbulence level, transition starts at $x \simeq 1.5$ cm and the numerical results indicate that the boundary layer is not fully turbulent at the trailing edge. In all cases, the calculation reflects well the experimental behaviour. Similar results have been obtained by PRIDDIN (as reported by LAUNDER /54/) and by MacDONALD-FISH /49/, among others.

The analysis of TURNER's data shows that, for the cases where transition exists, the critical Reynolds number is never reached and that the linear stability mechanisms are completely bypassed. This bypass was already encountered in the WERLE-BLAIR experiments (see § 3.4.) which dealt with similar experimental conditions. When the MacDONALD-FISH method is applied to these experiments, rather good results are obtained /28/.

In a general manner, the transport equations give satisfactory results in cases involving large values of T. In such cases, non linear phenomena preponderate and seem to be well described by the transport equations. Moreover, some of these methods have been successfully applied to relaminarizing flows. (The k-ε model was at first modified by JONES and LAUNDER /44/ in order to predict relaminarization). For these reasons, the transport equations models are certainly the most efficient tools for predicting the combined effects of high turbulence levels and of negative pressure gradients (turbomachinery problems).

6 - CONCLUDING REMARKS

Obviously, none of these presented methods is able to predict correctly transition for all practical purposes. All these techniques need the introduction of empirical data, which reduce considerably the range of applications. These data are, for instance, low Reynolds number functions (transport equations) or values of critical amplification rates (e^n methods). Among the many factors acting on stability and transition, two are currently accounted for : the pressure gradient and the free-stream turbulence level ; let us observe, however, that the latter one is only characterized by a rms value and not by its spectrum (except in MACK's amplitude method and in some turbulence models).

At low values of T, methods based on instability theory are certainly the most accurate ones : the pressure gradient effects appear "naturally" through the evolution of the mean velocity profiles. The free-stream turbulence influence is given, for instance, by MACK's relation /8/ which constitutes, in fact, a correlation between the initial perturbation amplitude A_0 and T. The link between A_0 and the external disturbances is the key problem of transition phenomena : recent calculations /55/ /56/ in which the three-dimensional NAVIER-STOKES equations were solved, gave a complete picture of the linear and non linear development of instability waves, but the initial amplitude was imposed.

At high values of T, the laminar instability theory no longer applies and the e^n methods, as well as criteria based on this theory (/24/ /11/) are not valid. To our thinking, the transport equations can provide fairly good results in such situations. Some empirical criteria (DUNHAM, Van DRIEST, SEYB) cover a wide range of free-stream turbulence intensities, but correlations between $R\theta_T$ and a local parameter at the transition point ($\Lambda2_T$ for instance) often lead to large errors, because the boundary layer history is not taken into account.

On the other side, the calculation of the transition region itself does not constitute a crucial problem. It was shown that simple methods give right predictions in very different situations. The inaccuracies of these methods are small as compared with large errors which can arise in the prediction of the transition onset.

R E F E R E N C E S

/1/ LIEPMANN H.W.
"Investigations of laminar boundary layer stability and transition on curved boundaries"
NACA Adv. Conf. Rept. N° 3H30, later W-107 (1943)

/2/ SMITH A.M.O.
GAMBERONI N.
"Transition, pressure gradient and stability theory"
Douglas Aircraft Co. Rept. ES 26 388, EL SEGUNDO, CALIF., (1956)

/3/ VAN INGEN J.L.
"A suggested semi-empirical method for the calculation of the boundary layer transition region"
Univ. of Technology, Dept. of Aero. Eng., Rept UTH-74, DELFT (1956)

/4/ WAZZAN A.R.
OKAMURA T.T.
SMITH A.M.O.
"Spatial and temporal stability charts for the FALKNER-SKAN boundary layer profiles"
DAC 67086, McDonnell Douglas Corp., (1968)

/5/ JAFFE N.A.
OKAMURA T.T.
SMITH A.M.O.
"Determination of spatial amplification factors and their application to predicting transition"
AIAA Journal, Vol. 8, N° 2, (1970) 301-308

/6/ VAN INGEN J.L.
"Transition, pressure gradient, suction, separation and stability theory"
AGARD-CP-224 (1977)

/7/ MACK L.M.
"Transition and laminar instability"
Jet Propulsion Laboratory Publication 77-15, PASADENA, CALIFORNIA (1977)

/8/ DRYDEN H.L.
"Transition from laminar to turbulent flow"
Turbulent Flows and Heat Transfer, High Speed Aerodynamics and Jet Propulsion, C.C. Lin Editor (1959)

/9/ ARNAL D.
JUILLEN J.C.
MICHEL R.
"Analyse expérimentale de la transition de la couche limite, avec gradient de pression nul et positif"
T.P. ONERA N° 1979-8 (1979)

/10/ JUILLEN J.C.
ARNAL D.
"Profils de vitesse moyenne et de turbulence mesurés dans une couche limite de transition, en gradient de pression nul et positif"
Rapport Technique OA N° 17/5018 AND (1981)

/11/ HABIBALLAH M.
"Analyse de l'instabilité des couches limites laminaires et prévision de la transition du régime laminaire au régime turbulent"
Thèse de Docteur-Ingénieur soutenue à l'ENSAE (TOULOUSE) (1981)

/12/ MICHEL R.
"Détermination du point de transition et calcul de la traînée des profils d'aile en incompressible"
ONERA Publication N° 58 (1952)

/13/ SCHUBAUER G.B.
SKRAMSTAD H.K.
"Laminar boundary layer oscillations and transition on a flat plate"
Rept. 909 NACA (1948)

/14/ GRANVILLE P.S.
"The calculation of the viscous drag of bodies of revolution"
David Taylor Model Basin Report 849 (1953)

/15/ CRABTREE L.F.
"Prediction of transition in the boundary layer on an aerofoil"
Journal of the Royal Aeronautical Society (1958)

/16/ HORTON H.P.
"A semi-empirical theory for the growth and bursting of laminar separation bubbles"
ARC, CP N° 1073 (1969)

/17/ VINCENT DE PAUL M.
"Prévision du décrochage d'un profil d'aile en écoulement incompressible"
AGARD-CP-102 (1972)

/18/ KWON O.K.
PLETCHER R.H.
"Prediction of incompressible separated boundary layer including viscous-inviscid interaction"
AIAA Paper A 79-38909 (1979)

/19/ HALL D.J.
GIBBINGS J.C.
"Influence of free-stream turbulence and pressure gradient upon boundary layer transition"
J. Mechanical Engineering Science, Vol. 14, N° 2 (1972)

/20/ VAN DRIEST E.R.
BLUMER C.B.
"Boundary layer transition : free-stream turbulence and pressure gradient effects"
AIAA Journal, Vol. 1, N° 6 (1963)

/21/ DUNHAM J.
"Predictions of boundary layer transition on turbomachinery blades"
AGARD Meeting Boundary Layer in Turbomachines, PARIS (1972)

/22/ SEYB N.J.
"The role of boundary layers in axial flow turbomachines and the prediction of their effects"
ROLLS-ROYCE Limited, BRISTOL Engine Division (1971)

/23/ FOREST A.E.
"Engineering predictions of transitional boundary layers"
AGARD-CP-224 (1977)

/24/ ARNAL D.
HABIBALLAH M.
DELCOURT V.
"Synthèse sur les méthodes de calcul de la transition développées au DERAT"
Rapport Technique OA N° 11/5018 AYD (1980)

/25/ ROBERTS W.B.
"Calculation of laminar separation bubbles and their effect on airfoil performance"
AIAA 17th 79-0285 (1979)

/26/ GLEYZES C.
COUSTEIX J.
BONNET J.L.
"A calculation method of leading edge separation bubbles"
T.P. ONERA N° 1983-10 (1983)

/27/ MICHEL R.
"Etude expérimentale de la transition sur différents profils d'aile"
Note Technique ONERA 1/1578 A (1951)

/28/ BLAIR M.F.
WERLE M.J.
"Combined influence of free-stream turbulence and favourable pressure gradients on boundary layer transition and heat transfer"
UTRC Report R 81-914388-17 (1981)

/29/ BLAIR M.F.
"Influence of free-stream turbulence on boundary layer transition in favourable pressure gradients"
J. of Engineering for Power, Vol. 104, (1982) 743-750

/30/ WAZZAN A.R.
GAZLEY C.
SMITH A.M.O.
"H-Rx method for predicting transition"
AIAA Journal, Vol. 19, N° 6 (1981) 810-812

/31/ SCHUBAUER G.B.
KLEBANOFF P.S.
"Contribution on the mechanics of boundary layer transition"
Rept. 1289, NACA, (1956)

/32/ DHAWAN S.
NARASIMHA R.
"Some properties of boundary layer flow during the transition from laminar to turbulent motion"
J. Fluid Mech., Vol. 3, Part 4 (1958)

/33/ EMMONS H.W.
"The laminar-turbulent transition in a boundary layer - Part I"
J. Aero. Sci., 18, (1951) 490-498

/34/ CHEN K.K.
THYSON N.A.
"Extension of EMMONS' spot theory to flows on blunt bodies"
AIAA Journal, Vol. 9, N° 5, (1971) 821-825

/35/ VANCOILLIE G.
"A turbulence model for the numerical simulation of the transition zone in a boundary layer"
Laboratory of Machines and Machine Construction, GENT, BELGIUM (1983)

/36/ ARNAL D.
JUILLEN J.C.
"Etude expérimentale et théorique de la transition de la couche limite"
T.P. ONERA N° 1976-146 (1976)

/37/ COUSTOLS E.
"Stabilité et transition en écoulement tridimensionnel : cas des ailes en flèche"
Thèse de Docteur-Ingénieur soutenue à l'ENSAE (TOULOUSE) (1983)

/38/ MICHEL R.
QUEMARD C.
DURANT R.
"Application d'un schéma de longueur de mélange à l'étude des couches limites turbulentes d'équilibre"
Note Technique ONERA N° 154 (1969)

/39/ CEBECI T.
"Wall curvature and transition effects in turbulent boundary layers"
AIAA Journal, Vol. 9, N° 9 (1971) 1868-1870

/40/ GLUSHKO G.S.
"Turbulent boundary layer on a flat plate in an incompressible fluid"
Bull. Acad. Sci. USSR, Mech. Ser., N° 4, (1965) 13-23

/41/ BECKWITH I.E.
BUSHNELL D.M.
"Calculation of mean and fluctuating properties of the incompressible turbulent boundary layer"
AFOSR-IFP- Conference on Turbulent Boundary Layer Prediction, Vol. 1, STANFORD (1968)

/42/ DONALDSON C. du P.
"A computer study of an analytical model of boundary layer transition"
AIAA Journal, Vol. 7, N° 2, (1969) 271-278

/43/ HANJALIC K.
LAUNDER B.E.
"A Reynolds stress model of turbulence and its application to thin shear flows"
J. Fluid Mech., Vol. 52, Part 4 (1972)

/44/ JONES W.P.
LAUNDER B.E.
"The prediction of laminarization with a two-equation model of turbulence"
Int. J. of Heat and Mass Transfer, Vol. 15, N° 2, (1972) 301-314

/45/ SAFFMAN P.G.
        WILCOX D.C.

"Turbulence model predictions for turbulent boundary layers"
AIAA Journal, Vol. 12, N° 4 (1974)

/46/ WILCOX D.C.

"Turbulence model transition predictions : effects of surface roughness
and pressure gradient"
AIAA Paper N° 75-857 (1975)

/47/ WILCOX D.C.

"Development of an alternative to the e^9 procedure for predicting
boundary layer transition"
AIAA Paper N° 80-0278 (1980)

/48/ ARAD E.
        BERGER M.
        ISRAELI M.
        WOLFSHTEIN M.

"Numerical calculation of transitional boundary layers"
Int. J. for Numerical Methods in Fluids, Vol. 2, (1982) 1-23

/49/ McDONALD H.
        FISH R.W.

"Practical calculations of transitional boundary layers"
AGARDograph N° 164, Boundary Layers in Turbomachines (1972)

/50/ FINSON M.L.

"On the application of second-order closure models to boundary layer
transition"
AGARD-CP-224 (1977)

/51/ FEINDT E.G.

"Untersuchungen über die Abhängigkeit des Umschlages laminar-turbulent
von der Oberflachenrauhigkeit und der Druckverteilung"
Jahrbuch 1956 der schiffbautechnischen Gesellschaft 50, (1957) 180-203

/52/ BRILEY W.R.
        McDONALD H.

"Numerical prediction of incompressible separation bubbles"
J. Fluid Mech., Vol. 69, Part 4 (1975)

/53/ TURNER A.B.

"Local heat transfer measurements on a gas turbine blade"
J. of Mechanical Engineering Science, Vol. 13, N° 1 (1971)

/54/ LAUNDER B.E.

"Progress in the modelling of turbulent transport"
VKI Lecture Series 76 (1975)

/55/ WRAY A.
        HUSSAINI M.Y.

"Numerical experiments in boundary layer stability"
AIAA Paper N° 80-0275 (1980)

/56/ KLEISER L.
        SCHUMANN U.

"Spectral simulation of the laminar-turbulent transition process in
plane POISEUILLE flow"
Symposium on Spectral Methods for Partial Differential Equations,
ICASE, NASA Langley Research Center (1982)
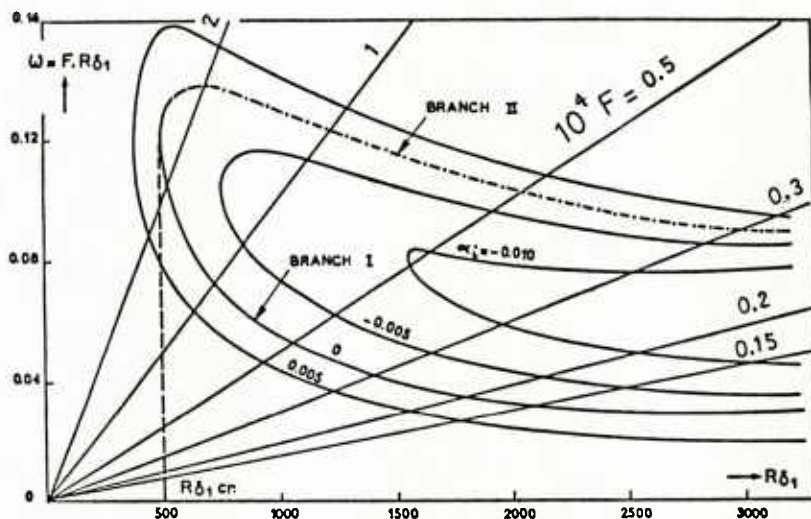
Fig. 1 - Stability diagram for BLASIUS flow
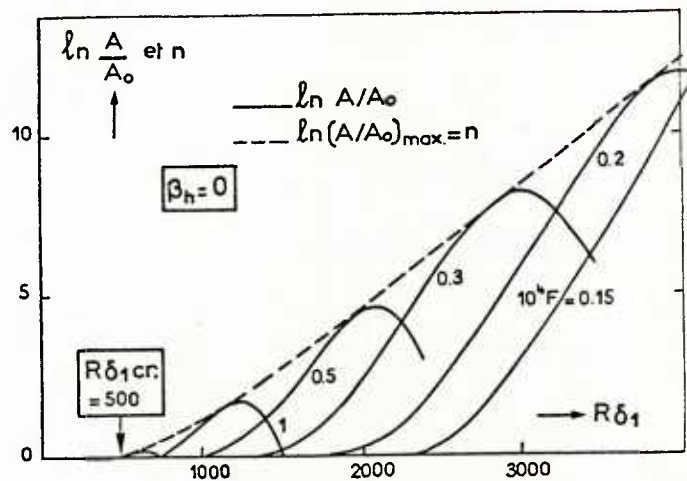
Fig. 2 - Total amplification curves for various frequencies and envelope curve (flat plate)
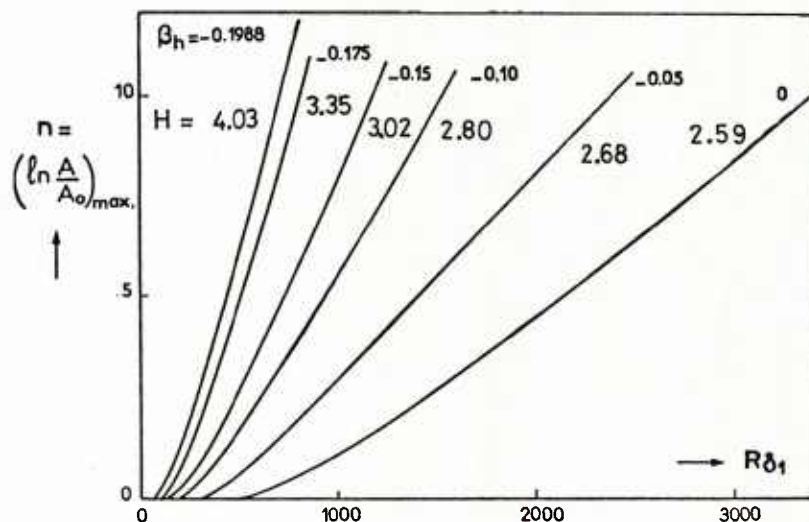
Fig. 3 - Envelope curves for FALKNER-SKAN similarity profiles
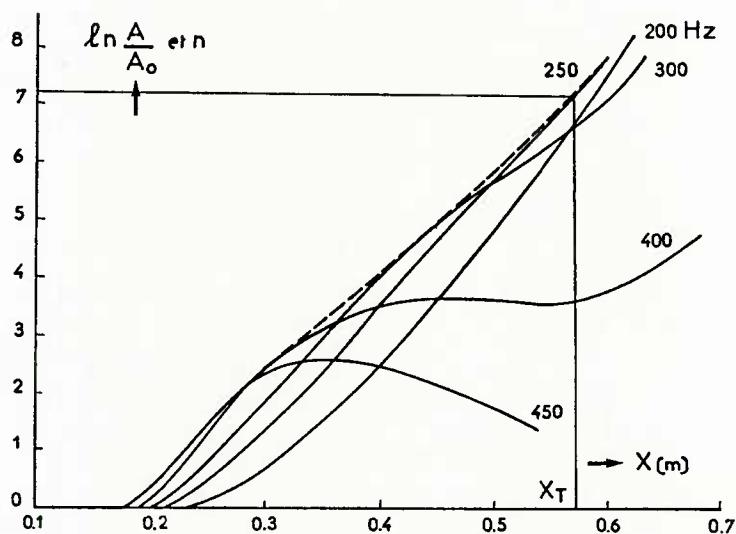
Fig. 4 – Example of application of the e^n method. Case C of the experiments reported in /9/ /10/

• Experiments
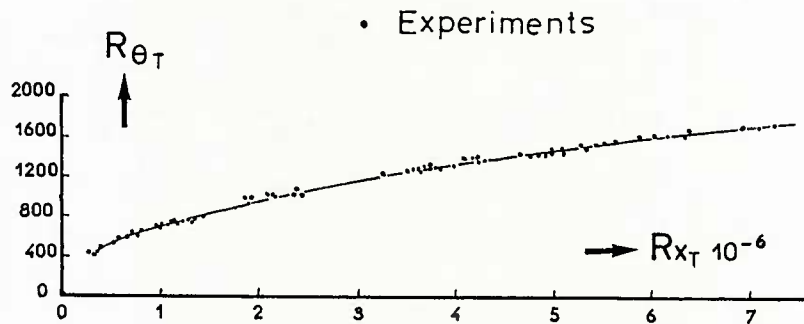
Fig. 5 – Criterion proposed by MICHEL /12/

△ ▼ ●
□ ■ Experiments

$(Re_T - Re_{cr.}) \cdot 10^{-3}$

$\overline{\Lambda_{2_T}} \cdot 10^2$
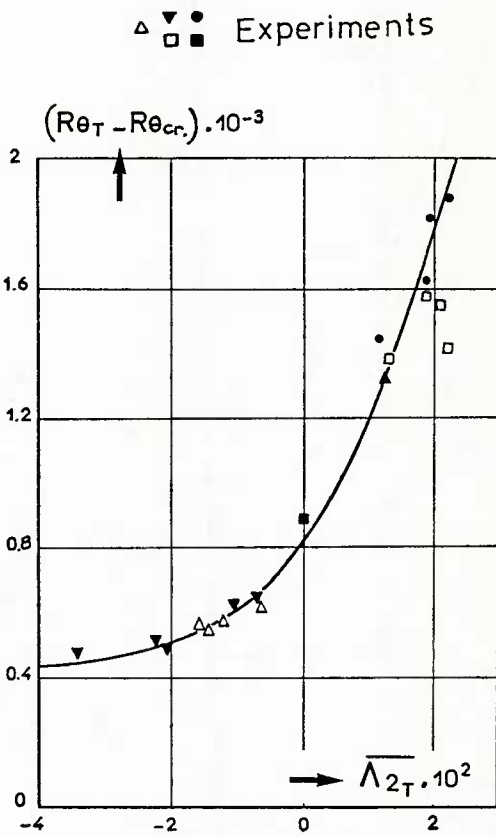
Fig. 6 – Criterion proposed by GRANVILLE /14/

$R_{\theta_T} \cdot 10^3$

Laminar separation

$\Lambda_{2_T} = \dfrac{\theta^2}{\nu} \cdot \dfrac{du_e}{dx}$
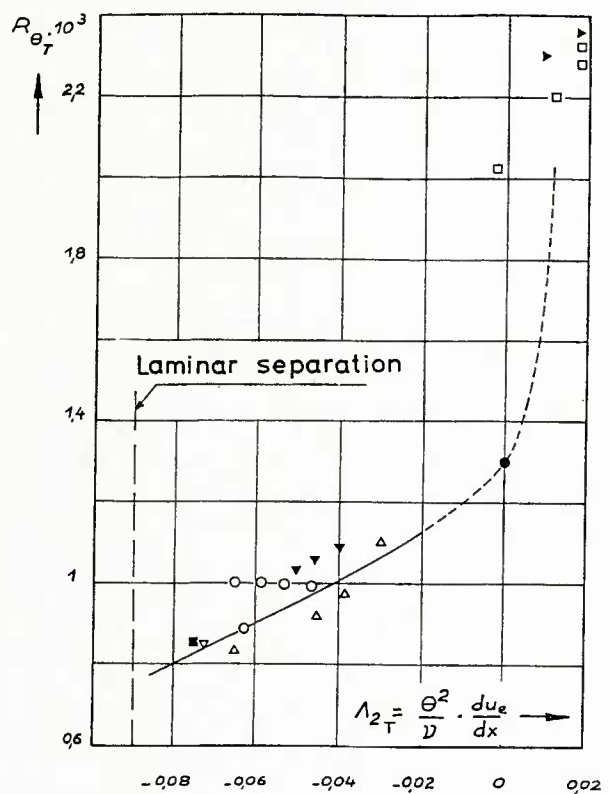
Fig. 7 – Criterion proposed by CRABTREE /15/
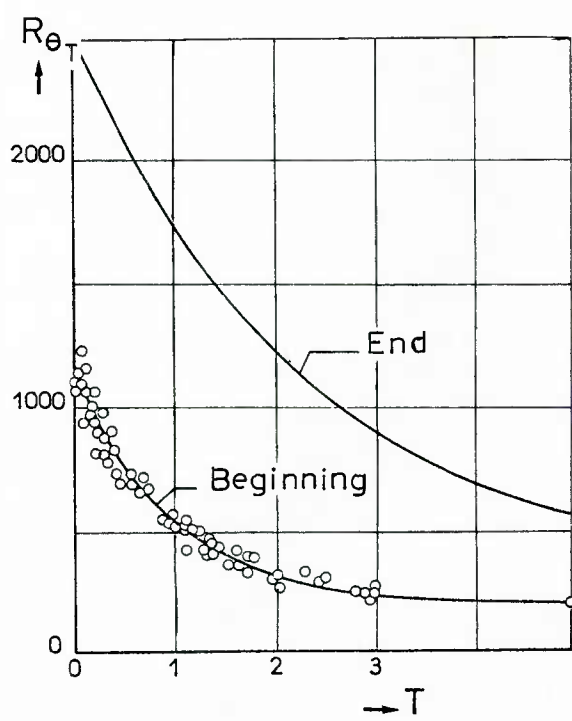
Fig. 8 – Criterion proposed by HALL and GIBBINGS [19]
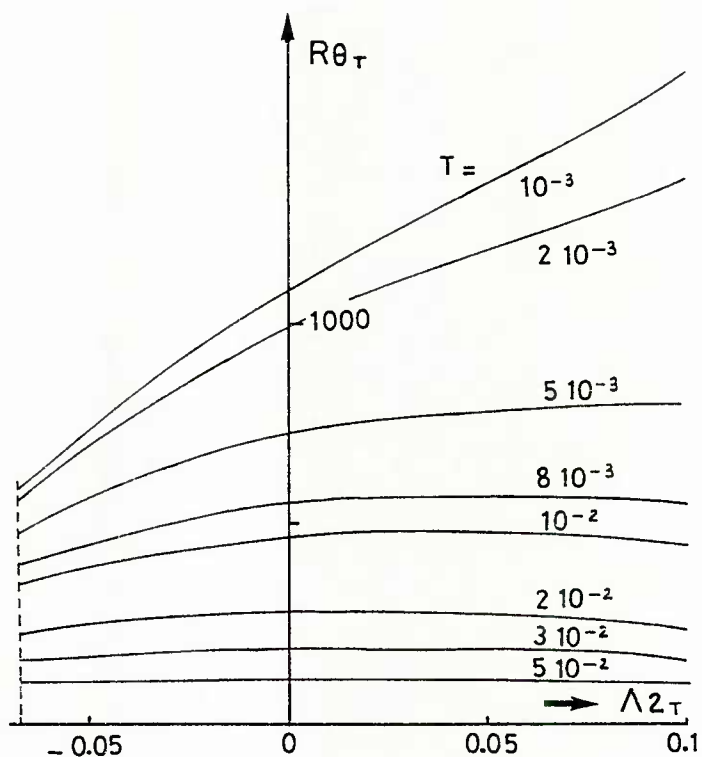
Fig. 9 – Criterion proposed by Van DRIEST and BLUMER [20]
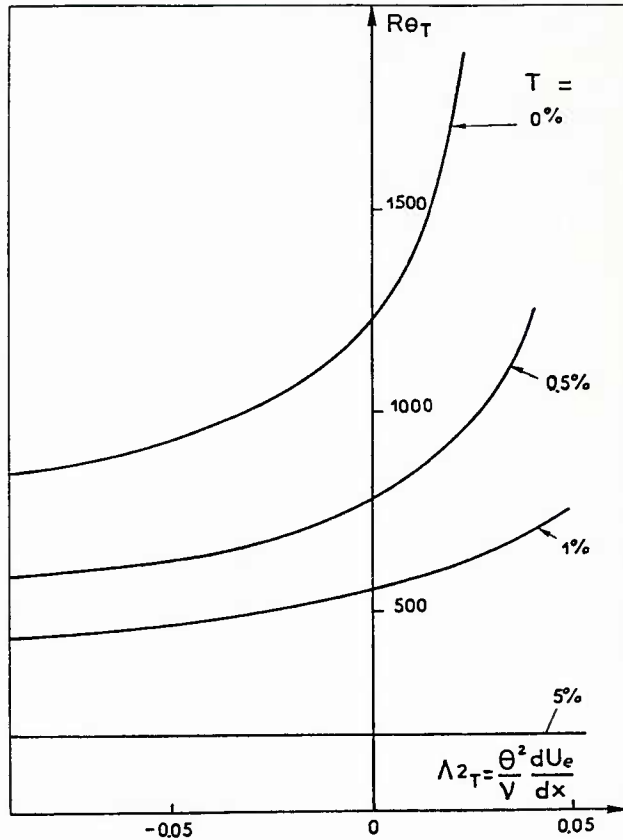
Fig. 10 – Criterion proposed by DUNHAM [21]
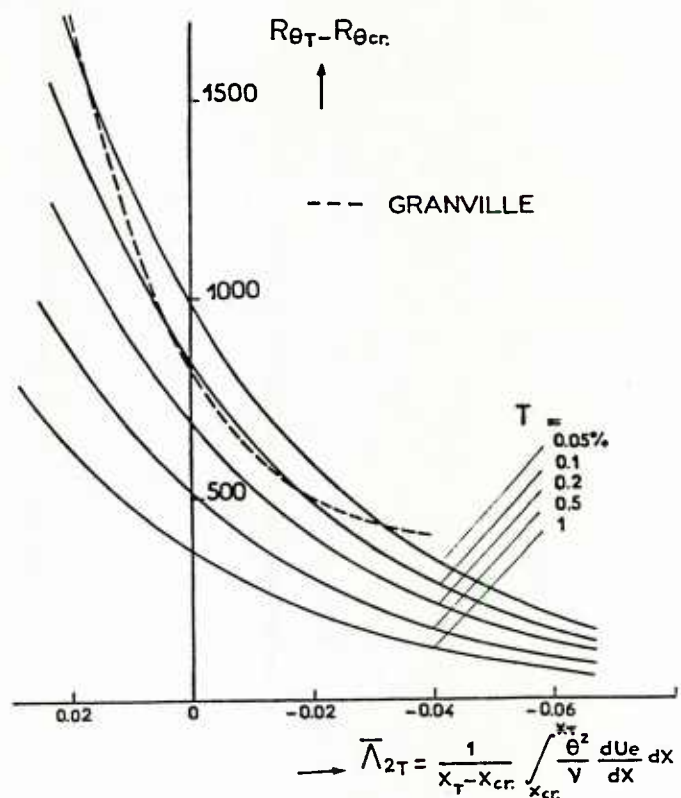
Fig. 11 – Criterion proposed by ARNAL, HABIBALLAH and DELCOURT [24]
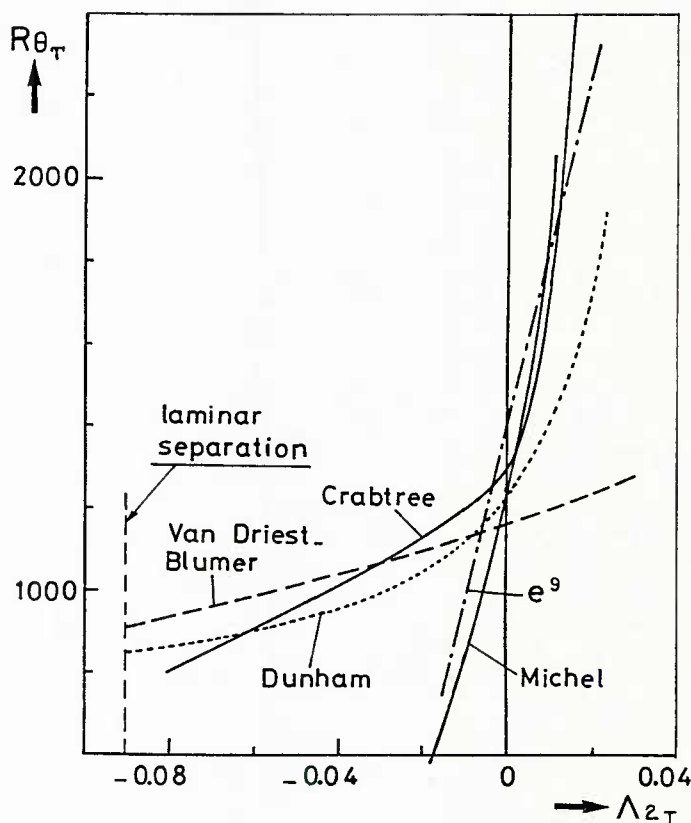
Fig. 12 - Comparison between some criteria at low values of T
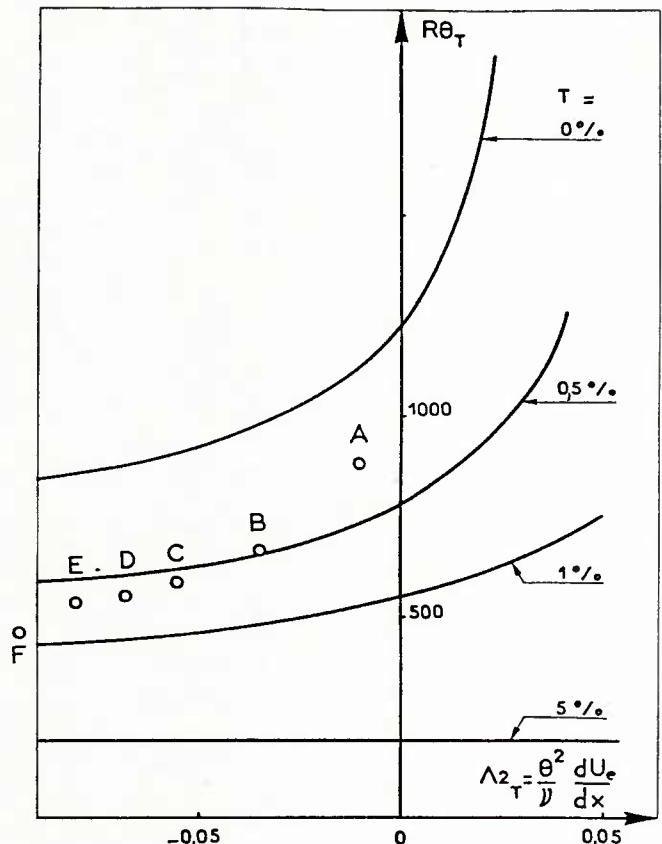
Fig. 13 - Application of DUNHAM's criterion to the experiments performed at ONERA/CERT /9/ /10/
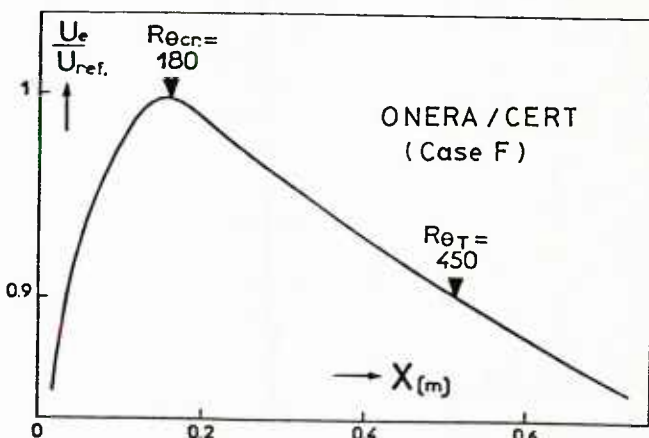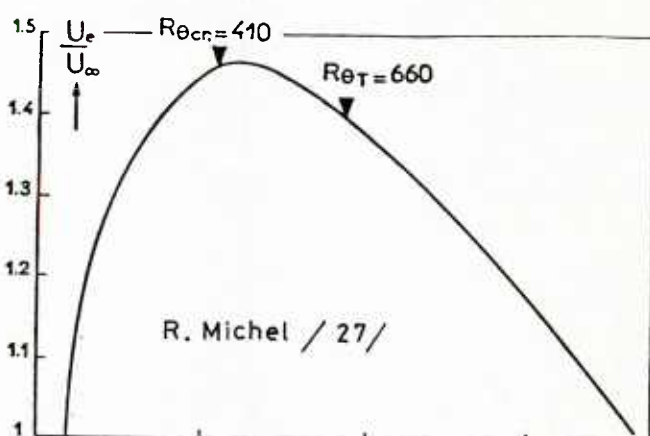
Fig. 14 - Free-stream velocity distributions for two experimental cases
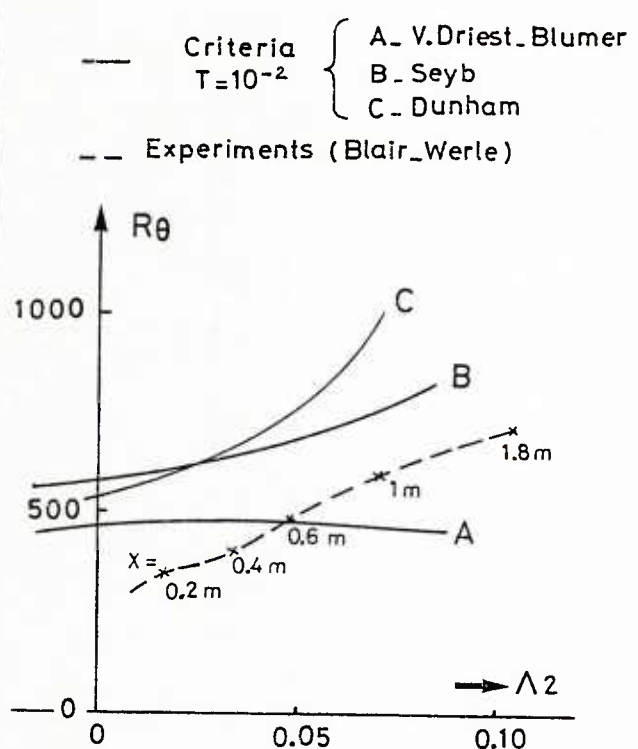
Fig. 15 - Application of three criteria /20/ /21/ /22/ to an experimental case studied by BLAIR and WERLE /28/ /29/. Experimental transition is located at x = 0.8 m
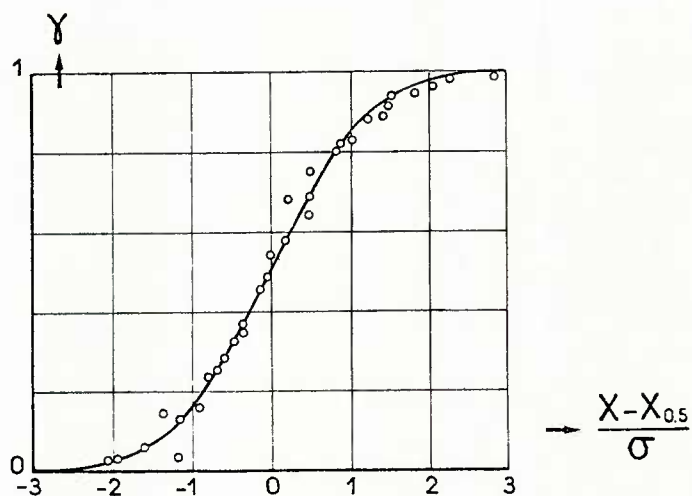
Fig. 16 — Distribution of the intermittency factor in the transition
region (flat plate) : o experiments /31/ ——— Gaussian curve

$$X = 1.035 \text{ m}$$
$$\gamma = 0.58$$

$$X = 1.135 \text{ m}$$
$$\gamma = 0.85$$
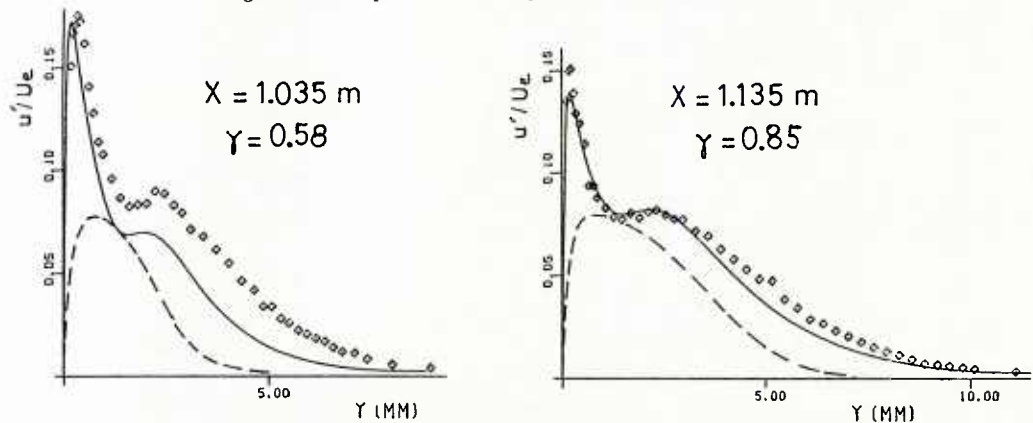
Fig. 17 — Turbulence intensity profiles in the transition region (flat plate) : ◇ experiments /36/
——— calculations of VANCOILLIE /35/ ———— calculations of ARNAL and JUILLEN using k-ε
model /36/
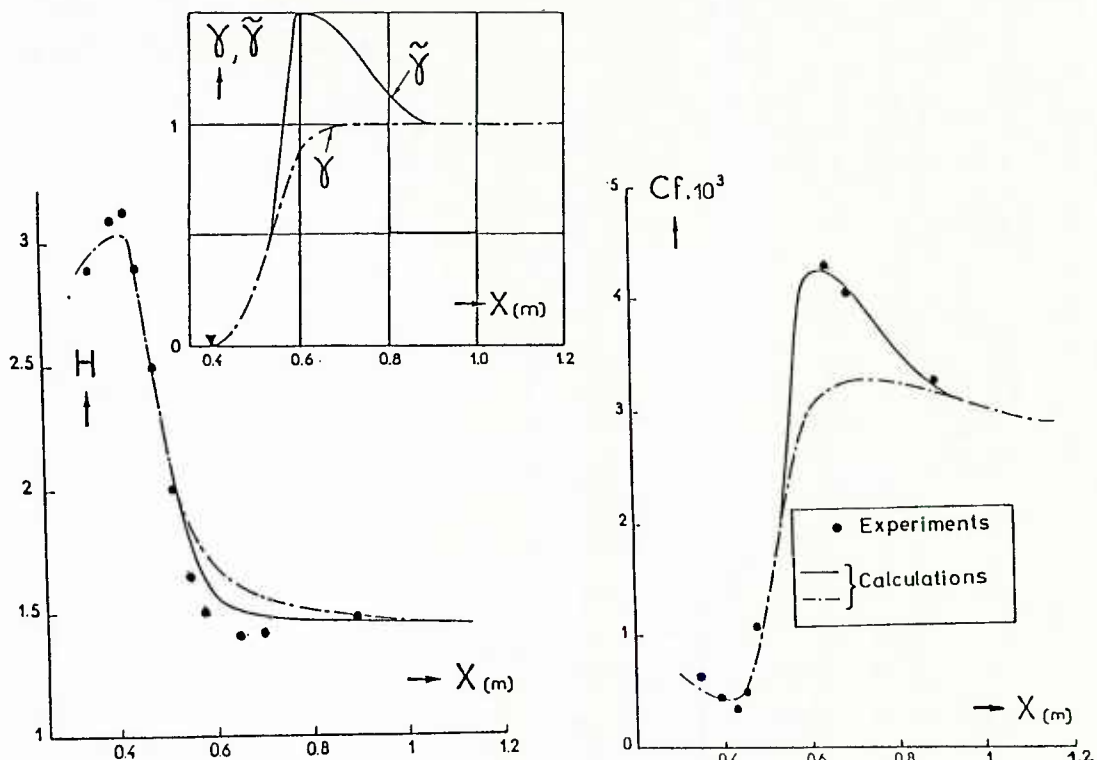
Fig. 18 — Application of an intermittency method to a transition occuring in positive pressure
gradient /9/ /10/ /37/
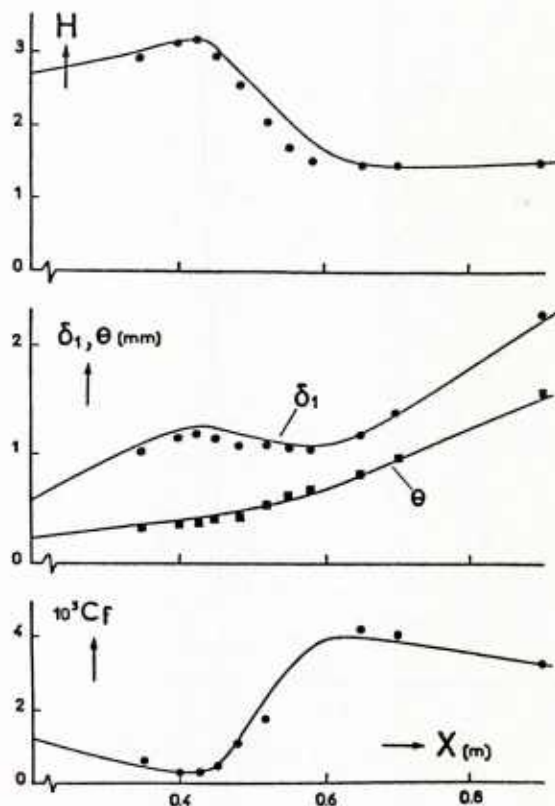
Fig. 19 – Boundary layer transition in positive
pressure gradient. o●■: experiments
/9/ /10/, case D, T ≃ 0.15 10⁻² ;
—— calculation (integral method)
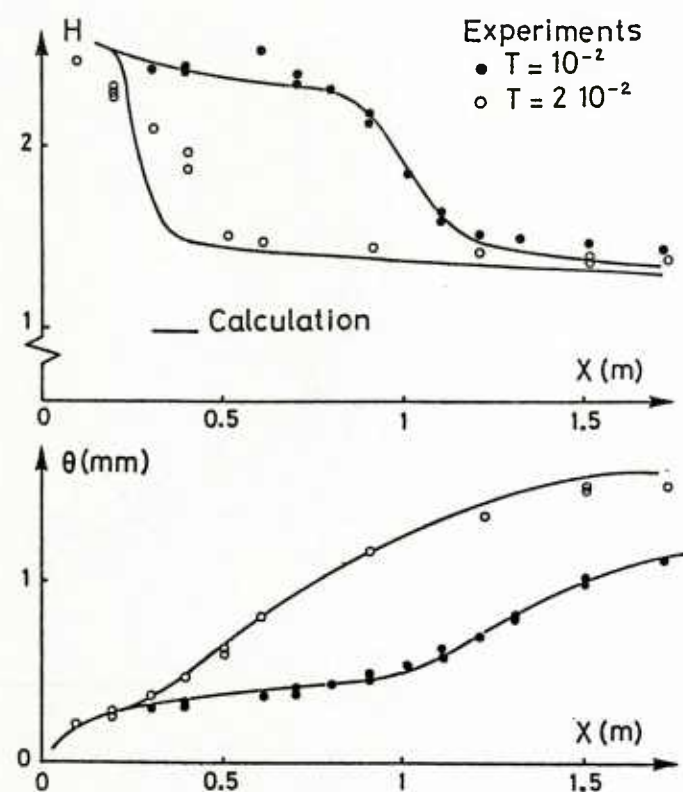
Fig. 20 – Boundary layer transition in negative pres-
sure gradient. o● : experiments /28/ /29/,
T = 1 and 2 10⁻² ; —— calculation (inte-
gral method)
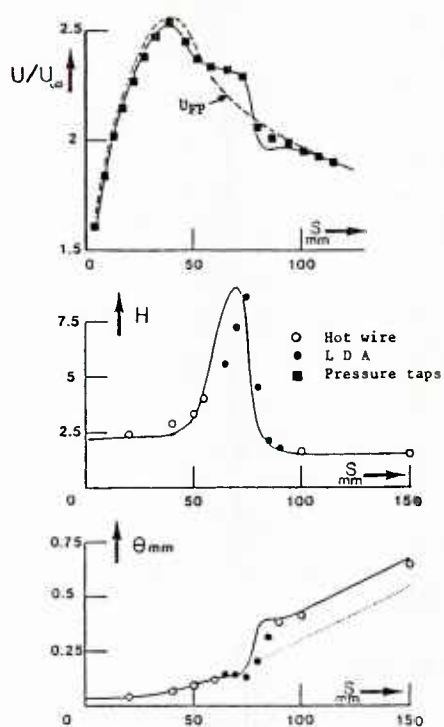
Fig. 21 – Boundary layer transition in a separation bubble.
■ ●o : experiments /26/, T = 0.4 10⁻²; —— cal-
culation (integral method /26/). U$_{FP}$ denotes
inviscid free-stream velocity distribution.
.... : momentum thickness computed by assuming
transition at separation point.
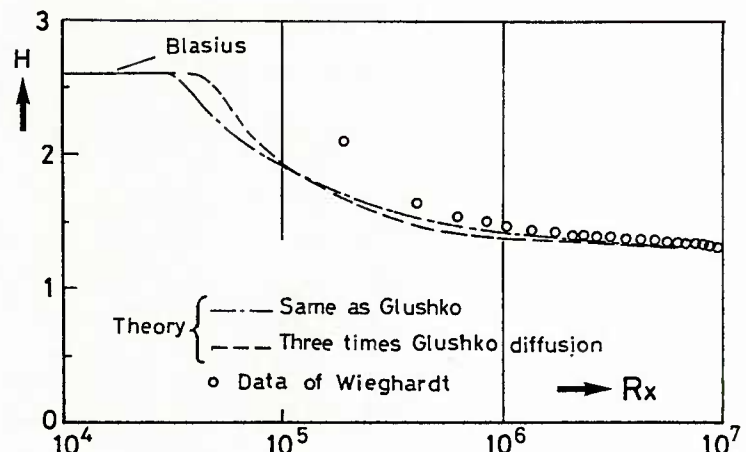
Fig. 22 – Experimental and computed /41/ evolutions of the
shape factor in zero pressure gradient
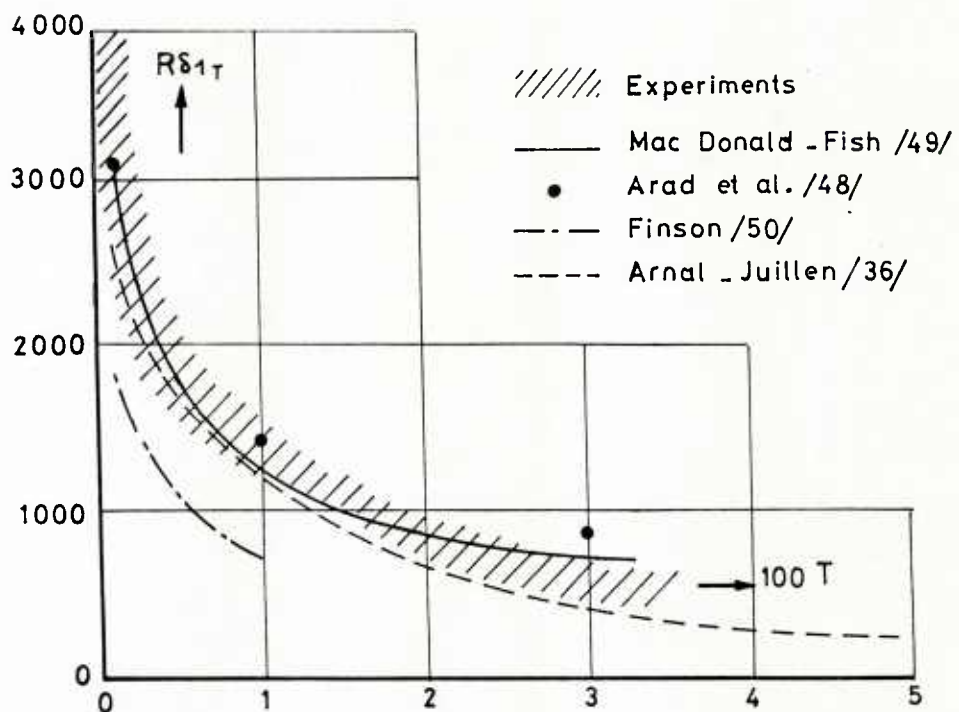
Fig. 23 - Experimental and computed /36/ /48/ /49/ /50/ transition Reynolds numbers as a function of T (flat plate)
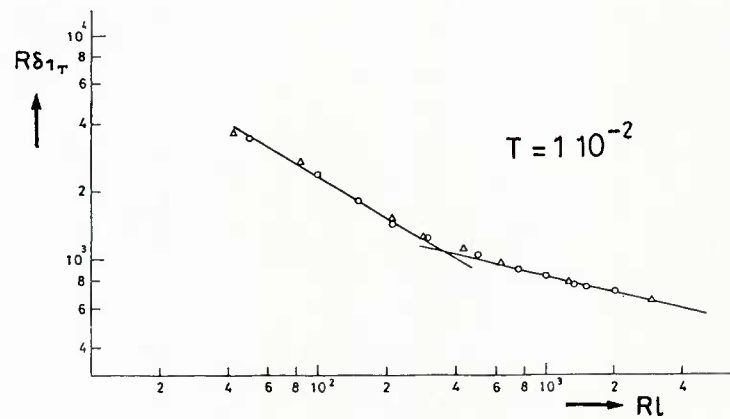
Fig. 24 - Theoretical transition Reynolds number as a function of the free-stream disturbances scale /48/ (flat plate)
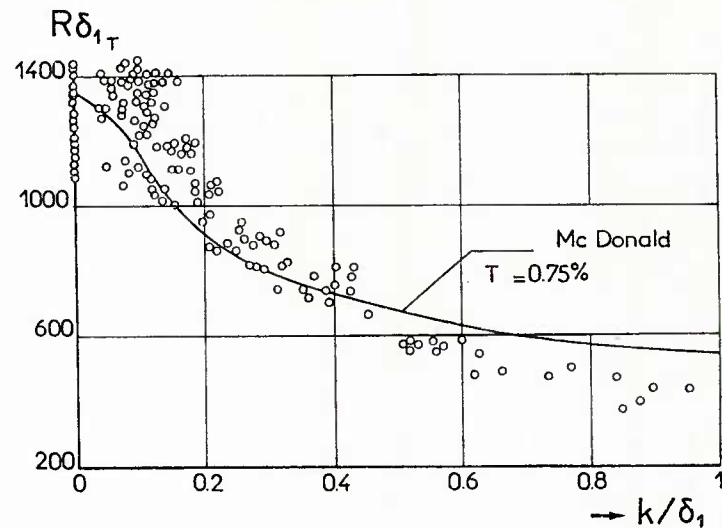
Fig. 25 - Effect of distributed surface roughness upon transition Reynolds number. o : experiments /51/ ; —— : calculation /49/
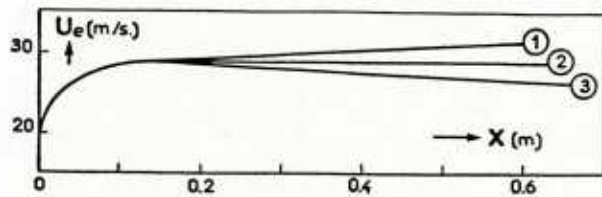
Fig. 26 – Effect of pressure gradient upon transition Reynolds number : k-ε model predictions /24/
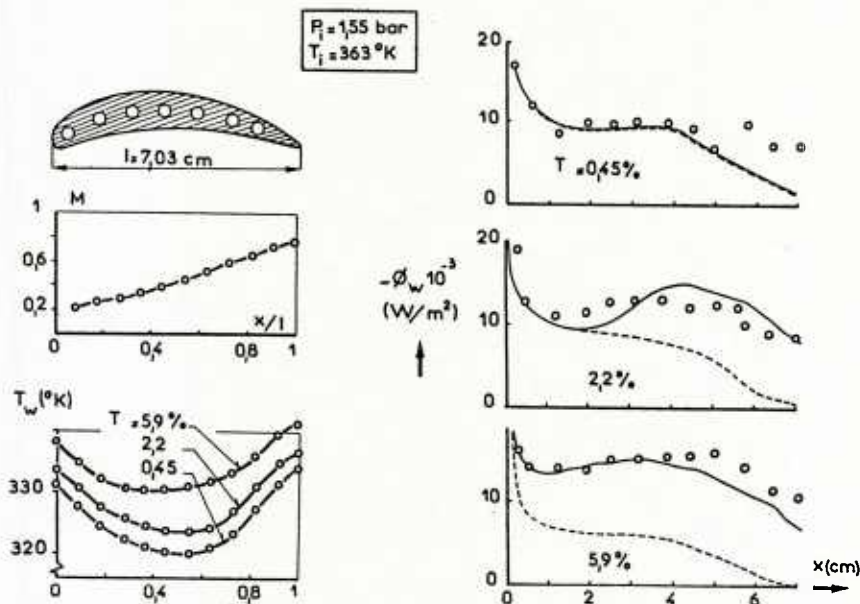
Fig. 27 – Combined effects of negative pressure gradient and of high free-stream turbulence level. Left-hand side : geometry, Mach number and temperature distributions. Right-hand side : evolution of the wall heat flux ϕ_W ; o : experiments /53/ ; —— k-ε model predictions /36/ ; --- : laminar calculations

BOUNDARY-LAYER LINEAR STABILITY THEORY

by

Leslie M. Mack
Jet Propulsion Laboratory
California Institute of Technology
Pasadena, California 91109
U.S.A.

1. INTRODUCTION

1.1 Historical background

Most fluid flows are turbulent rather than laminar and the reason why this is so has been the object of study by several generations of investigators. One of the earliest explanations was that laminar flow is unstable, and the linear instability theory was first developed to explore this possibility. Such an approach tells nothing about turbulence, or about the details of its initial appearance, but it does explain why the original laminar flow can no longer exist. A series of early papers by Rayleigh (1880, 1887,1892,1895,1913) produced many notable results concerning the instability of inviscid flows, such as the discovery of inflectional instability, but little progress was made toward the original goal. Viscosity was commonly thought to act only to stabilize the flow, and flows with convex velocity profiles thus appeared to be stable. In a review of 30 years of effort, Noether (1921) wrote: "The method of small disturbances, which can be considered essentially closed, has led to no useful results concerning the origin of turbulence."

Although Taylor (1915) had already indicated that viscosity can destabilize a flow that is otherwise stable, it remained for Prandtl (1921), in the same year as Noether's review paper, to independently make the same discovery as Taylor and set in motion the investigations that led to a viscous theory of boundary-layer instability a few years later [Tollmien (1929)]. A series of papers by Schlichting (1933a, 1933b,1935,1940), and a second paper by Tollmien (1935) resulted in a well-developed theory with a small body of numerical results. Any expectation that instability and transition to turbulence are synonomous in boundary layers was dashed by the low value of the critical Reynolds number Re_{cr}, i.e. the x Reynolds number at which instability first appears. Tollmien's value of Re_{cr} for the Blasius boundary layer was 60,000, and even in the high turbulence wind tunnels of that time, transition was observed to occur between $Re_t = 3.5 \times 10^5$ and 1×10^6. In what can be considered the earliest application of linear stability theory to transition prediction, Schlichting (1933a) calculated the amplitude ratio of the most amplified frequency as a function of Reynolds number for a Blasius boundary layer, and found that this quantity had values between five and nine at the observed Re_t.

Outside of Germany, the stability theory received little acceptance because of the failure to observe the predicted waves, mathematical obscurities in the theory, and also a general feeling that a linear theory could not have anything useful to say about the origin of turbulence, which is inherently nonlinear. A good idea of the low repute of the theory can be gained by reading the paper of Taylor (1938) and the discussion on this subject in the Proceedings of the 5th Congress of Applied Mechanics held in 1938. It was in this atmosphere of disbelief that one of the most celebrated experiments in the history of fluid mechanics was carried out. The experiment of Schubauer and Skramstad (1947), which was performed in the early 1940's but not published until some years later because of wartime censorship, completely reversed the prevailing opinion and fully vindicated the Göttingen proponents of the theory. This experiment unequivocally demonstrated the existence of instability waves in a boundary layer, their connection with transition, and the quantitative description of their behavior by the theory of Tollmien and Schlichting. It made an enormous impact at the time of its publication, and by its very completeness seemed to answer most of the questions concerning the linear theory. To a large extent, subsequent experimental work on transition went in other directions, and the possibility that linear theory can be quantitatively related to transition has not received a decisive experimental test. On the other hand, it is generally accepted that flow parameters such as pressure gradient, suction and heat transfer qualitatively affect transition in the manner predicted by the linear theory, and in particular that a flow predicted to be stable by the theory should remain laminar. This expectation has often been deceived. Even so, the linear theory, in the form of the e^9, or N-factor, method first proposed by Smith and Gamberoni (1956) and Van Ingen (1956), is today in routine use in engineering studies of laminar flow control [see, e.g., Hefner and Bushnell (1979)]. A good introduction to the complexities of transition and the difficulties involved in trying to arrive at a rational approach to its prediction can be found in three reports by Morkovin (1969,1978,1983), and a review article by Reshotko (1976).

The German investigators were undeterred by the lack of acceptance of the stability theory elsewhere, and made numerous applications of it to boundary layers with pressure gradients and suction. This work is summarized in Schlichting's book (1979). We may make particular mention of the work by Pretsch (1942), as he provided the only large body of numerical results for exact boundary-layer solutions before the advent of the computer age by calculating the stability characteristics of the Falkner-Skan family of velocity profiles. The unconvincing mathematics of the asymptotic theory was put on a more solid foundation by Lin (1945) and Wasow (1948), and this work has been successfully continued by Reid and his collaborators [Lakin, Ng and Reid (1978)].

When in about 1960 the digital computer reached a stage of development permitting the direct solution of the primary differential equations, numerical results were obtained from the linear theory during the next ten years for many different boundary-layer flows: three-dimensional boundary layers [Brown (1959), following the important theoretical contribution of Stuart in Gregory et al. (1955)]; free-convection boundary layers [Kurtz and Crandall (1962) and Nachtsheim (1963)]; compressible boundary layers [Brown (1962) and Mack (1965,1969)]; boundary layers on compliant walls [Landahl and Kaplan (1965)]; a recomputation of Falkner-Skan flows [Wazzan, Okamura and Smith (1968)]; unsteady boundary layers

[Obremski, Morkovin and Landahl (1969)]; and heated-wall water boundary layers [Wazzan, Okamura and Smith (1968)]. More recent work has focussed on three-dimensional boundary layers in response to the renewed interest in laminar-flow control for swept wings [Srokowski and Orszag (1977), Mack (1977,1979a,1979b,1981), Nayfeh (1980a,1980b), Cebeci and Stewartson (1980a,1980b), Lekoudis (1979,1980)]. A notable contribution to linear stability theory that stands somewhat apart from the principal line of development has been provided by Gaster (1968,1975,1978,1981a,1981b,1982a,1982b) in a series of papers on the wave packets produced by a pulsed point source in a boundary layer. Gaster's work on this problem also includes a major stability experiment [Gaster and Grant (1975)].

There are a number of general references that are helpful to anyone interested in the linear theory. Review articles are by Schlichting (1959), Shen (1954), Stuart (1963) and Reid (1965). Books are by Lin (1955), Betchov and Criminale (1967), and Drazin and Reid (1981). Schlichting's book on boundary-layer theory (1979) contains two chapters on stability theory and transition, and Monin and Yaglom's book on turbulence (1971) contains a lengthy chapter on the same subject, as does the book by White (1974) on viscous flow theory. Reviews of transition have been given by Dryden (1959), Tani (1969,1981), Morkovin (1969,1978,1983), and Reshotko (1976). An extensive discussion of both stability theory and transition, not all at high speeds in spite of the title, may be found in the recorded lectures of Mack and Morkovin (1971).

1.2 Elements of stability theory

Before we get into the main body of the subject, a brief introduction is in order to orient those who are new to this field. The stability theory is mainly concerned with individual sine waves propagating in the boundary layer parallel to the wall. These waves are waves of vorticity and are commonly referred to as Tollmien-Schlichting waves, or TS waves, or simply as instability waves. The amplitudes of the waves, which vary through the boundary layer and die off exponentially in the freestream, are small enough so that a linear theory may be used. The frequency of a wave is ω and the wavenumber is $k = 2\pi/\lambda$, where is the wavelength. The wave may be two-dimensional, with the lines of constant phase normal to the freestream direction (and parallel to the wall), or it may be oblique, in which case the wavenumber is a vector k at an angle ψ to the freestream direction with streamwise (x) component α and spanwise (z) component β. The phase velocity c is always less than the freestream velocity U_1, so that at some point in the boundary layer the mean velocity is equal to c. This point is called the critical point, or critical layer, and it plays a central role in the mathematical theory. The wave amplitude usually has a maximum near the critical layer.

At any given distance from the origin of the boundary layer, or better, at any given Reynolds number $Re = U_1 x/\nu$, where ν is the kinematic viscosity, an instability wave of frequency ω will be in one of three states: damped, neutral, or amplified. The numerical results calculated from the stability theory are often presented in the form of diagrams of neutral stability which show graphically the boundaries between regions of stability and instability in ω,Re space or k,Re space. There are two general kinds of neutral-stability diagrams to be found, as shown in Fig. 1.1 for a two-dimensional wave in a two-dimensional boundary layer. In this figure, the dimensionless wavenumber $\alpha\delta$ is plotted against R_δ, the Reynolds number based on the boundary-layer thickness δ. Waves are neutral at those values of $\alpha\delta$ and R_δ which lie on the contour marked neutral; they are amplified inside of the contour, and are damped everywhere else. With a neutral-stability curve of type (a), all wavenumbers are damped at sufficiently high Reynolds numbers. In this case, the mean flow is said to have viscous instability. Since decreasing Reynolds number, or increasing viscosity, can lead to instability, it is apparent that viscosity does not act solely to damp out waves, but can actually have a destabilizing influence. The incompressible flat-plate (Blasius) boundary layer, and all incompressible boundary layers with a favorable pressure gradient, are examples of flows which are unstable only through the action of viscosity. With a neutral-stability curve of type (b), a non-zero neutral wavenumber $(\alpha\delta)_s$ exists at $Re \to \infty$, and wavenumbers smaller than $(\alpha\delta)_s$ are unstable no matter how large the Reynolds number becomes. A mean flow with a type (b) neutral-stability curve is said to have inviscid instability. The boundary layer in an adverse pressure gradient is an example of a flow of this kind.

In both cases (a) and (b), all waves with $\alpha\delta$ less than the peak value on the neutral-stability curve are unstable for some range of Reynolds numbers. The Reynolds number Re_{cr} below which no amplification is possible is called the minimum critical Reynolds number. It is often an objective of stability theory to determine Re_{cr}, although it must be cautioned that this quantity only tells where instability starts, and cannot be relied upon to indicate the relative instability of various mean flows further downstream. It is definitely not proper to identify Re_{cr} with the transition point.

A wave which is introduced into a steady boundary layer with a particular frequency will preserve that frequency as it propagates downstream, while the wavenumber will change. As shown in Fig. 1.1, a wave of frequency ω which passes through the unstable region will be damped up to $(Re)_L$, the first point of neutral stability. Between $(Re)_L$ and $(Re)_U$, the second neutral point, it will be amplified; downstream of $(Re)_U$ it will be damped again. If the amplitude of a wave becomes large enough before $(Re)_U$ is reached, then the nonlinear processes which eventually lead to transition will take over, and the wave will continue to grow even though the linear theory says it should damp.

The theory can be used to calculate amplification and damping rates as well as the frequency, wavenumber and Reynolds number of neutral waves. For example, it is possible to compute the amplification rate as a function of frequency at a given Re. The neutral-stability curve only identifies the band of unstable frequencies, but the amplification rate tells how fast each frequency is growing, and which frequency is growing the fastest. Even more useful than the amplification rate is the amplitude history of a wave of constant frequency as it travels through the unstable region. In the simplest form of the theory, this result can be calculated in the form of a ratio of the amplitude to some initial amplitude once the amplification rates are known. Consequently, it is possible to identify, given some initial disturbance spectrum, the frequency whose amplitude has increased the most at each Reynolds number. It is presumably one of these frequencies which, after it reaches some critical amplitude, triggers the whole transition process.

We have divided the following material into three major parts: the incompressible stability theory is in Part A, the compressible stability theory is in Part B, and three-dimensional stability theory, both incompressible and compressible, is in Part C. The field of laminar instability is a vast one, and many topics that could well have been included have been left out for lack of space. We have restricted ourselves strictly to boundary layers, but even here have omitted all flows where gravitational effects are important, low-speed boundary layers with wall heating or cooling, and the important subject of Görtler instability. Within the topics that have been included, we give a fairly complete account of what we consider to be the essential ideas, and of what is needed to understand the published literature and make intelligent use of a computer program for the solution of boundary-layer stability problems. Attention is concentrated principally on basic ideas, but also on the formulations which are incorporated into computer codes based on the shooting-method of solving the stability equations. Only selected numerical results are included, and these have been chosen for their illustrative value, and not with any pretension to comprehensive coverage. Numerous references are given, but the list is by no means complete. In particular, a number of USSR references have not been included because of my unfamiliarity with the Russian language. Much use has been made of a previous work [Mack (1969)], which is still the most complete source for compressible boundary-layer stability theory.

PART A. INCOMPRESSIBLE STABILITY THEORY

2. FORMULATION OF INCOMPRESSIBLE STABILITY THEORY

2.1 Derivation of parallel-flow stability equations

The three-dimensional (3D) Navier-Stokes equations of a viscous, incompressible fluid in Cartesian coordinates are

$$\frac{\partial \bar{u}_i^*}{\partial t^*} + \bar{u}_j^* \frac{\partial \bar{u}_i^*}{\partial x_j^*} = -\frac{1}{\rho^*} \frac{\partial \bar{p}^*}{\partial x_i^*} + \nu^* \nabla^2 \bar{u}_i^* \; , \tag{2.1a}$$

$$\frac{\partial \bar{u}_i^*}{\partial x_i^*} = 0 \; , \tag{2.1b}$$

where $\bar{u}_i^* = (\bar{u}^*, \bar{v}^*, \bar{w}^*)$, $x_i^* = (x^*, y^*, z^*)$, and $i, j = (1,2,3)$ according to the summation convention. The asterisks denote dimensional quantities, and overbars denote time-dependent quantities. The velocities $\bar{u}^*$, $\bar{v}^*$, $\bar{w}^*$ are in the x^*, y^*, z^* directions, respectively, where x^* is the streamwise and z^* the spanwise coordinate; $\bar{p}^*$ is the pressure; ρ^* is the density; ν^* is the kinematic viscosity μ^*/ρ^*, with μ^* the viscosity coefficient. Equations (2.1a) are the momentum equations, and Eq. (2.1b) is the continuity equation. We first put the equations in dimensionless form with the velocity scale U_r^*, the length scale L^*, and the pressure scale $\rho^* U_r^{*2}$. Both L^* and U_r^* are unspecified for the present. The Reynolds number is defined as

$$R = U_r^* L^* / \nu^*. \tag{2.2}$$

The dimensionless equations are identical to Eqs. (2.1) except that ν^* is replaced by $1/R$, and ρ^* is absorbed into the pressure scale.

We next divide each flow variable into a steady mean-flow term (denoted by an upper-case letter) and an unsteady small disturbance term (denoted by a lower-case letter):

$$\bar{u}_i(x,y,z,t) = U_i(x,y,z) + u_i(x,y,z,t) \; ,$$

$$\bar{p}(x,y,z,t) = P(x,y,z) + p(x,y,z,t) \; . \tag{2.3}$$

When these expressions are substituted into Eqs. (2.1), the mean-flow terms subtracted out, and the terms which are quadratic in the disturbances dropped, we arrive at the following dimensionless linearized equations for the disturbance quantities:

$$\frac{\partial u_i}{\partial t_j} + u_j \frac{\partial U_i}{\partial x_j} + U_j \frac{\partial u_i}{\partial x_j} = -\frac{\partial p}{\partial x_i} + \nu \nabla^2 u_i \; , \tag{2.4a}$$

$$\frac{\partial u_i}{\partial x_i} = 0 \; . \tag{2.4b}$$

For a truly parallel mean flow, of which a simple two-dimensional example is a fully-developed channel flow, the normal velocity V is zero and U and W are functions only of y. The parallel-flow equations, when written out, are

$$\frac{\partial u}{\partial t} + U \frac{\partial u}{\partial x} + W \frac{\partial u}{\partial z} + v \frac{dU}{dy} = -\frac{\partial p}{\partial x} + \nu \nabla^2 u \; , \tag{2.5a}$$

$$\frac{\partial v}{\partial t} + U \frac{\partial v}{\partial x} + W \frac{\partial v}{\partial z} = -\frac{\partial p}{\partial y} + \nu \nabla^2 v \; , \tag{2.5b}$$

$$\frac{\partial w}{\partial t} + U \frac{\partial w}{\partial x} + W \frac{\partial w}{\partial z} + v \frac{dW}{dy} = -\frac{\partial p}{\partial z} + \nu \nabla^2 w \; , \tag{2.5c}$$

$$\frac{\partial u}{\partial x} + \frac{\partial v}{\partial y} + \frac{\partial w}{\partial z} = 0 \; . \tag{2.5d}$$

These equations are in separable form, i.e., they permit the normal-mode solutions

$$[u,v,w,p]^T = [\hat{u}(y),\hat{v}(y),\hat{w}(y),\hat{p}(y)]^T \exp[i(\alpha x+\beta z-\omega t)] \qquad (2.6)$$

where α and β are the x and z components of the wavenumber vector $\vec{k}$, ω is the frequency, and $\hat{u}(y)$, $\hat{v}(y)$, $\hat{w}(y)$ and $\hat{p}(y)$ are the complex functions, or eigenfunctions, which gives the mode structure through the boundary layer, and are to be determined by the ordinary differential equations given below. It is a matter of convenience to work with complex normal modes; the physical solutions are the real parts of Eqs. (2.6). The normal modes are travelling waves in the x,z plane, and in the most general case, α, β and ω are all complex. If they are real, the wave is of neutral stability and propagates in the x,z plane with constant amplitude[1] and phase velocity $c = \omega/k$, where $k = (\alpha^2+\beta^2)^{1/2}$ is the magnitude of $\vec{k}$. The angle of $\vec{k}$ with respect to the x axis is $\psi = \tan^{-1}(\beta/\alpha)$. If any of α, β, ω are complex, the amplitude will change as the wave propagates.

When Eqs. (2.6) are substituted into (2.5), we obtain the following ordinary differential equations for the modal functions:

$$i(\alpha U+\beta W-\omega)\hat{u} + DU\hat{v} = -i\alpha\hat{p} + \frac{1}{R}[D^2 - (\alpha^2+\beta^2)]\hat{u} , \qquad (2.7a)$$

$$i(\alpha U+\beta W-\omega)\hat{v} = -D\hat{p} + \frac{1}{R}[D^2 - (\alpha^2+\beta^2)]\hat{v} , \qquad (2.7b)$$

$$i(\alpha U+\beta W-\omega)\hat{w} + DW\hat{v} = -i\beta\hat{p} + \frac{1}{R}[D^2 - (\alpha^2+\beta^2)]\hat{w} , \qquad (2.7c)$$

$$\alpha\hat{u} + \beta\hat{w} + D\hat{v} = 0 , \qquad (2.7d)$$

where $D = d/dy$. For a boundary layer, the boundary conditions are that at the wall the no-slip condition applies,

$$\hat{u}(0) = 0, \quad \hat{v}(0) = 0, \quad \hat{w}(0) = 0 , \qquad (2.8a)$$

and that far from the wall all disturbances go to zero,

$$\hat{u}(y) \to 0, \quad \hat{v}(y) \to 0, \quad \hat{w}(y) \to 0 \text{ as } y \to \infty . \qquad (2.8b)$$

Since the boundary conditions are homogeneous, we have an eigenvalue problem, and solutions of Eqs. (2.7) that satisfy the boundary conditions will exist only for particular combinations of α, β and ω. The relation for the eigenvalues, usually called the dispersion relation, can be written as

$$\omega = \Omega(\alpha,\beta) . \qquad (2.9)$$

There are six real quantities in Eq. (2.9); any two of them can be solved for as eigenvalues of Eqs. (2.7) and (2.8), and the other four have to be specified. The evaluation of the dispersion relation for a given Reynolds number and boundary-layer profile (U,W) is the principal task of stability theory. The eigenvalues, along with the corresponding eigenfunctions $\hat{u}$, $\hat{v}$, $\hat{w}$ and $\hat{p}$, give a complete specification of the normal modes. The normal modes, which are the natural modes of oscillation of the boundary layer, are customarily called Tollmien-Schlichting (TS) waves, or instability waves.

2.2 Non-parallel stability theory

Except for the asymptotic suction boundary layer, most boundary layers grow in the downstream direction, and even for a wave of constant frequency α, β, $\hat{u}$, $\hat{v}$, $\hat{w}$ and $\hat{p}$ are all functions of x (and z in a general 3D boundary layer). What we have to deal with is a problem of wave propagation in a nonuniform medium. Since the complete linearized equations (2.4) are not separable, they do not have the normal modes of Eq. (2.6) as solutions. The most straightforward approach is to simply set the non-parallel terms to zero on the grounds that the boundary-layer growth is small over a wavelength, and it is the local boundary-layer profile that will determine the local wave motion. This approach, called the quasi- or locally-parallel theory, has been almost universally adopted. It retains the parallel-flow normal modes as local solutions, but is, of course, an extra approximation beyond linearization and leaves open the question of how important the admittedly slow growth of the boundary layer really is. It also makes for difficulties in comparisons between theory and experiment.

The first complete non-parallel theories were developed independently by (in order of journal publication date) Bouthier (1972,1973), Gaster (1974) and Saric and Nayfeh (1975). Gaster used the method of successive approximations; the others used the method of multiple scales. There has been considerable controversy on this subject, mainly because of the way in which Saric and Nayfeh (1975,1977) chose to present their numerical results, but it is now generally agreed that the three theories are equivalent. Gaster's calculations of neutral-stability curves for the Blasius boundary layer have since been verified to be correct by Van Stijn and Van de Vooren (1983), and have the additional virtue of being based on quantities that can be measured experimentally. The calculations show the non-parallel terms to have little effect on local instability except at very low Reynolds numbers. However, this does not mean that non-parallel effects can be neglected when dealing with waves over distances of many wavelengths.

In the multiple-scale theory, in addition to the usual "fast" x scale over which the phase changes, there is a "slow" x scale, $x_1 = \varepsilon x$, where ε is a small quantity identified with $1/R$. The slow scale governs the boundary-layer growth, the change of the eigenfunctions, and a small additional amplitude modulation. The disturbances are expressed in the form

$$u = u^{(0)} + \varepsilon u^{(1)} + \ldots , \qquad (2.10)$$

---

1. The term amplitude will always refer to the peak or rms amplitude, never to the instantaneous amplitude.

with similar expressions for v, w and p. The mean flow is given by

$$U(x,y) = U^{(0)}(x_1) + \ldots ,$$

$$W(x,y) = W^{(0)}(x_1) + \ldots , \qquad (2.11)$$

$$V(x,y) = \varepsilon V^{(0)}(x_1) + \ldots .$$

Here the mean boundary layer is independent of z, and this is the only kind of boundary layer that we will consider in this work. Examples are 2D planar boundary layers and the boundary layers on a rotating disk, on a cone at zero incidence, and on an infinite-span swept wing.

When Eqs. (2.11) are substituted into Eqs. (2.4) and equal powers of ε collected, the zeroth-order equations for $u^{(0)}$, $v^{(0)}$, $w^{(0)}$ and $p^{(0)}$ are identical to the parallel-flow equations (2.5). The normal modes, however, have the more general form

$$u^{(0)}(x,y,z,t) = A(x_1)\hat{u}^{(0)}(x_1,y)\exp[i\theta^{(0)}(x,z,t)] , \qquad (2.12)$$

where the phase function is

$$\theta^{(0)}(x,z,t) = \int^x \alpha^{(0)}(x_1)dx + \beta^{(0)}(x_1)z - \omega^{(0)}(x_1)t , \qquad (2.13)$$

and $A(x_1)$ is a complex amplitude modulation function. The dispersion relation also becomes a function of x_1:

$$\omega^{(0)} = \Omega^{(0)}(\alpha^{(0)},\beta^{(0)};x_1) . \qquad (2.14)$$

The non-parallel theories as developed by Bouthier, Gaster, and Saric and Nayfeh calculate the dispersion relation only to zeroth order, just as in the quasi-parallel theory. The next order (ε^1) enters only as a solvability condition of the first-order equations. This condition determines the function $A(x_1)$.

We shall use only the quasi-parallel theory in the remainder of this work. Consequently, all of the zeroth-order quantities are calculated as functions of x in accordance with Eqs. (2.12), (2.13) and (2.14). However, the quasi-parallel theory cannot determine the quantity $A(x_1)$, and this is simply set equal to the initial amplitude A_0. In the non-parallel theory, the product $A\hat{u}$ is a unique quantity, independent of the normalization of the eigenfunction $\hat{u}$, that gives a precise meaning to the amplitude of the flow variable $\hat{u}$ as a function of y and permits direct comparisons of theory and experiment. In the quasi-parallel theory, only the contribution to the amplitude that comes from the imaginary parts of α,β and ω can be accounted for. The corrections due to the function $A(x_1)$ and the x dependence of the eigenfunctions are outside of the scope of the theory. This lack of physical reality in the quasi-parallel theory introduces an uncertainty in the calculation of wave amplitude and complicates comparisons with experiment. More on the use of the quasi-parallel theory can be found in Section 2.6.

2.3 Temporal and spatial theories

If α and β are real, and ω is complex, the amplitude will change with time; if α and β are complex, and ω is real, the amplitude will change with x. The former case is referred to as the temporal amplification theory; the latter as the spatial amplification theory. If all three quantities are complex, the disturbance will grow in space and time. The original, and for many years the only, form of the theory was the temporal theory. However, in a steady mean flow the amplitude of a normal mode is independent of time and changes only with distance. The spatial theory, which was introduced by Gaster (1962,1963,1965), gives this amplitude change in a more direct manner than does the temporal theory.

2.3.1 Temporal amplification theory

With $\omega = \omega_r + i\omega_i$ and α and β real, the disturbance can be written

$$u(x,y,z,t) = \hat{u}(y)\exp(\omega_i t)\exp[i(\int^x \alpha dx + \beta z - \omega_r t)] . \qquad (2.15)$$

The magnitude of the wavenumber vector $\vec{k}$ is

$$k = (\alpha^2 + \beta^2)^{1/2} , \qquad (2.16)$$

and the angle between the direction of $\vec{k}$ and the x axis is

$$\psi = \tan^{-1}(\beta/\alpha) . \qquad (2.17)$$

The phase velocity c, which is the velocity with which the constant-phase lines move normal to themselves, has the magnitude

$$c = \omega_r/k , \qquad (2.18)$$

and is in the direction of $\vec{k}$. If A represents the magnitude of $\hat{u}$ at some particular y, say the y for which $\hat{u}$ is a maximum, then it follows from Eq. (2.15) that

$$(1/A)(dA/dt) = \omega_i . \qquad (2.19)$$

We can identify ω_i as the temporal amplification rate. Obviously A could have been chosen at any y, or for another flow variable besides u, and Eq. (2.19) would be the same. It is this property that enables us to talk about the "amplitude" of an instability wave in the same manner as the amplitude of a water wave, even though the true wave amplitude is a function of y and the particular flow variable selected.

We may distinguish three possible cases:

$$\omega_i < 0 \qquad \text{damped wave ,}$$

$$\omega_i = 0 \qquad \text{neutral wave ,} \qquad\qquad (2.20)$$

$$\omega_i > 0 \qquad \text{amplified wave .}$$

The complex frequency may be written

$$\omega = k\tilde{c} = k(\tilde{c}_r + i\tilde{c}_i) . \qquad\qquad (2.21)$$

The real part of $\tilde{c}$ is equal to the phase velocity c, and $k\tilde{c}_i$ is the temporal amplification rate. The quantity $\tilde{c}$ appears frequently (as c) in the literature of stability theory. However, it cannot be used in the spatial theory, and since general wave theory employs only $\vec{k}$ and ω, with the phase velocity being introduced as necessary, we shall adopt the same procedure.

2.3.2 Spatial amplification theory

In the spatial theory, ω is real and the wavenumber components α and β are complex. With

$$\alpha = \alpha_r + i\alpha_i , \qquad \beta = \beta_r + i\beta_i , \qquad\qquad (2.22)$$

we can write the normal modes in the form

$$u(x,y,z,t) = \hat{u}(y)\exp[-(\int^x \alpha_i dx + \beta_i z)]\exp[i(\int^x \alpha_r dx + \beta_r z - \omega t)] . \qquad (2.23)$$

By analogy with the temporal theory, we may define a real wavenumber vector $\vec{k}$ with magnitude

$$k = (\alpha_r^2 + \beta_r^2)^{1/2} . \qquad\qquad (2.24)$$

The angle between the direction of $\vec{k}$ and the x axis is

$$\psi = \tan^{-1}(\beta_r/\alpha_r) , \qquad\qquad (2.25)$$

and the phase velocity is

$$c = \omega/k . \qquad\qquad (2.26)$$

It follows from Eq. (2.23) that

$$(1/A)dA/dx = -\alpha_i , \qquad\qquad (2.27)$$

and we can identify $-\alpha_i$ as the amplification rate in the x direction. In like manner $-\beta_i$ is the amplification rate in the z direction. Indeed, the spatial amplification rate is a vector like the wavenumber vector with magnitude

$$|\sigma| = (\alpha_i^2 + \beta_i^2)^{1/2} , \qquad\qquad (2.28)$$

and angle

$$\bar{\psi} = \tan^{-1}(-\beta_i/-\alpha_i) \qquad\qquad (2.29)$$

with respect to the x axis. The amplification rate $-\beta_i$ is at this point a free parameter, and its selection is left for future consideration.

For the special boundary layers to be considered in this work (see p. 5), we define a spatial wave to be amplified or damped according to whether its amplitude increases or decreases in the x direction. Therefore, the three possible cases which correspond to Eq. (2.20) are:

$$-\alpha_i < 0 \qquad \text{damped wave ,}$$

$$-\alpha_i = 0 \qquad \text{neutral wave ,} \qquad\qquad (2.30)$$

$$-\alpha_i > 0 \qquad \text{amplified wave .}$$

2.3.3 Relation between temporal and spatial theories

A laminar boundary layer is a dispersive medium for the propagation of instability waves. That is, different frequencies propagate with different phase velocities, so that the individual harmonic components in a group of waves at one time will be dispersed (displaced) from each other at some later time. In a conservative system, where energy is not exchanged between the waves and the medium, an overall quantity such as the energy density or amplitude propagates with the group velocity. Furthermore, the group velocity can be considered a property of the individual waves, and to follow a particular normal mode we use the group velocity of that mode. Because of damping and amplification, instability waves in a boundary layer do not constitute a conservative system, and the group velocity is in general complex. However, some of the ideas of conservative systems are still useful. If we consider an observer moving at the group velocity of a normal mode, the wave in the moving frame of reference will appear to undergo temporal amplification, while in the frame at rest it undergoes spatial amplification.

Thus we can write

$$d/dt = C_r d/dx_g \ , \qquad (2.31)$$

where in this argument C_r is the magnitude of $\vec{C}_r$, the real part of the group velocity vector $\vec{C}$, and x_g is the coordinate in the direction of $\vec{C}_r$. Therefore, if ω_i is the temporal amplification rate, the spatial amplification rate in the direction parallel to $\vec{C}_r$ is immediately given to be

$$-(\alpha_i)_g = \omega_i/C_r \ . \qquad (2.32)$$

The problem of converting a temporal to a spatial amplification rate was first encountered by Schlichting (1933a), who used the two-dimensional version of Eq. (2.32) without comment. The same relation was also used later by Lees (1952), and justified on intuitive grounds, but the first mathematical derivation was given by Gaster (1962) for the 2D case, and the relation bears his name. Gaster's derivation is straightforward and can be generalized to three dimensions with the result given above in Eq. (2.32). It is essential to note that the Gaster relation is only an approximation that is valid for small amplification rates. Within the approximation, the frequency and wavenumber of the spatial wave are the same as for the temporal wave. If we use the complex group velocity in the above derivation, we arrive at the separate transformations for constant frequency and constant wavenumber obtained by Nayfeh and Padhye (1979) from another point of view. In this approach, Eq. (2.32) corresponds to a transformation of constant wavenumber.

We can also make use of Eq. (2.32) to arrive at a useful result for spatial waves. The same argument that led to Eq. (2.32) also applies to a component of the group velocity. Therefore,

$$-(\alpha_i)_{\bar{\psi}} = \omega_i/C_r \cos(\bar{\psi} - \phi_r) \ , \qquad (2.33)$$

where $-(\alpha_i)_{\bar{\psi}}$ is the spatial amplification rate in the arbitrary direction $\bar{\psi}$. The quantity ϕ_r is the real part of the complex group velocity angle ϕ defined by

$$C_x = C \cos\phi \ , \qquad C_z = C \sin\phi \ , \qquad (2.34)$$

where C_x and C_z are the complex x and z components of $\vec{C}$, and C is the complex magnitude of $\vec{C}$. Eliminating ω_i/C_r by Eq. (2.32), we arrive at

$$(\alpha_i)_{\bar{\psi}} = (\alpha_i)_g/\cos(\bar{\psi} - \phi_r) \ . \qquad (2.35)$$

This relation, which may appear rather obvious, is not a general relation valid for two arbitrary angles. It is only valid when one of the two angles is ϕ_r. When both angles are arbitrary, a more complicated relation exists and has been derived by Nayfeh and Padhye (1979). There is also a small change in $\vec{k}$ unless the group-velocity angle is real. We might close this subject by noting that while the various Nayfeh-Padhye transformation formulas use the complex group-velocity, they too are not exact because the group velocity is considered to be constant in the transformation. We recommend to the interested reader to examine the instructive numerical examples given by Nayfeh and Padhye.

2.4 Reduction to fourth-order system

Equations (2.7) constitute a sixth-order system for the variables $\hat{u}$, $\hat{v}$, $\hat{w}$, $\hat{p}$, $D\hat{u}$, $D\hat{w}$, as can be shown by rewriting them as six first-order equations. This system may be reduced to fourth order for the determination of eigenvalues. One approach is to multiply Eq. (2.7a) by α and Eq. (2.7c) by β and add, and then multiply Eq. (2.7c) by α and Eq. (2.7a) by β and subtract, to arrive at the following system of equations for the variables $\alpha\hat{u}+\beta\hat{w}$, $\hat{v}$, $\alpha\hat{w}-\beta\hat{u}$, and $\hat{p}$:

$$i(\alpha U+\beta W-\omega)(\alpha\hat{u}+\beta\hat{w}) + (\alpha DU+\beta DW)\hat{v} = -i(\alpha^2+\beta^2)\hat{p} + \frac{1}{R}[D^2 - (\alpha^2+\beta^2)](\alpha\hat{u} + \beta\hat{w}), \qquad (2.36a)$$

$$i(\alpha U+\beta W-\omega)\hat{v} = -D\hat{p} + \frac{1}{R}[D^2 - (\alpha^2+\beta^2)]\hat{v} \ , \qquad (2.36b)$$

$$i(\alpha U+\beta W-\omega)(\alpha\hat{w}-\beta\hat{u}) + (\alpha DW-\beta DU)\hat{v} = \frac{1}{R}[D^2 - (\alpha^2+\beta^2)](\alpha\hat{w}-\beta\hat{u}) \ , \qquad (2.36c)$$

$$i(\alpha\hat{u}+\beta\hat{w}) + D\hat{v} = 0 \ , \qquad (2.36d)$$

where Eqs. (2.7b) and (2.7d) have been duplicated for convenience as Eqs. (2.36b) and (2.36d). The point to note is that Eqs. (2.36a), (2.36b) and (2.36d) are a fourth-order system for the dependent variables $\alpha\hat{u}+\beta\hat{w}$, $\hat{v}$ and $\hat{p}$. The fourth variable of this system is $\alpha D\hat{u}+\beta D\hat{w}$. The dependent variable $\alpha\hat{w}-\beta\hat{u}$ appears only in Eq. (2.36c). Therefore, we may determine the eigenvalues from the fourth-order system, and if subsequently the eigenfunctions $\hat{u}$ and $\hat{w}$ are needed, they are obtained by solving the second-order equation (2.36c).

2.4.1 Transformations to 2D equations - temporal theory

The above equations are the ones that we will use, but they also offer a basis to discuss some transformations that have been used in the past. If α and β are real, the interpretation of the equations is evident. Equation (2.36a) is the momentum equation in the direction parallel to $\vec{k}$, and Eq. (2.36c) is the momentum equation in the direction normal to $\vec{k}$ in the x,z plane. Indeed, if we use the transformations

$$\tilde{\alpha}\tilde{U} = \alpha U + \beta W \quad , \qquad \tilde{\alpha}\tilde{W} = \alpha W - \beta U \quad , \tag{2.37a}$$

$$\tilde{\alpha}\tilde{u} = \alpha\hat{u} + \beta\hat{w} \quad , \qquad \tilde{\alpha}\tilde{w} = \alpha\hat{w} - \beta\hat{u} \quad , \tag{2.37b}$$

$$\tilde{\alpha}^2 = \alpha^2 + \beta^2 \quad , \tag{2.37c}$$

and leave ω, R, $\hat{v}$ and $\hat{w}$ unchanged, Eqs. (2.36) become

$$i(\tilde{\alpha}\tilde{U} - \omega)\tilde{u} + D\tilde{U}\hat{v} = i\tilde{\alpha}\hat{p} + \frac{1}{R}[D^2 - \tilde{\alpha}^2]\tilde{u} \quad , \tag{2.38a}$$

$$i(\tilde{\alpha}\tilde{U} - \omega)\hat{v} \quad\quad = -D\hat{p} + \frac{1}{R}[D^2 - \tilde{\alpha}^2]\hat{v} \quad , \tag{2.38b}$$

$$i(\tilde{\alpha}\tilde{U} - \omega)\tilde{w} + D\tilde{W}\hat{v} = \quad\quad \frac{1}{R}[D^2 - \tilde{\alpha}^2]\tilde{w} \quad , \tag{2.38c}$$

$$i\tilde{\alpha}\tilde{u} + D\hat{v} = 0 \quad . \tag{2.38d}$$

These transformed equations are of the form of Eqs. (2.7) for a two-dimensional wave ($\beta = 0$) in a two-dimensional boundary layer ($W=0$) except for the presence of Eq. (2.38c). We may observe from Eq. (2.7c) that even with $\beta = 0$, a $\hat{w}$ velocity component will exist whenever there is a W because of the vorticity production term $DW\hat{v}$.

Thus in a 3D boundary layer with velocity profiles (U,W) at Reynolds number R, the eigenvalues of an oblique <u>temporal</u> wave can be obtained from the eigenvalues of a 2D wave of the same frequency in a 2D boundary layer at the same Reynolds number with the velocity profile of the 3D boundary layer in the direction of the wavenumber vector. The key result that it is the latter velocity profile that governs the instability was obtained by Stuart [Gregory et al. (1955)] in his classic study of the stability of three-dimensional boundary layers, and by Dunn and Lin (1955) [see also Lin (1955)] in their study of the stability of compressible boundary layers. We shall refer to this velocity profile as the directional profile.

A slightly different transformation was employed by Squire (1933) and bears his name. Squire's original transformation was for a 2D boundary layer and the Orr-Sommerfeld equation (see Section 2.5.1), but a generalization valid for a 3D boundary layer is

$$\tilde{U} = U + W\tan\psi \quad , \qquad \tilde{W} = W - U\tan\psi \quad , \tag{2.39a}$$

$$\tilde{u} = \hat{u} + \hat{w}\tan\psi \quad , \qquad \tilde{w} = \hat{w} - \hat{u}\tan\psi \quad , \tag{2.39b}$$

$$\tilde{\alpha} = \alpha^2 + \beta^2 \quad , \quad \tilde{\omega}/\tilde{\alpha} = \omega/\alpha \quad , \quad \tilde{\alpha}\tilde{R} = \alpha R \quad , \tag{2.39c}$$

$$\tilde{p}/\tilde{\alpha}^2 = p/\alpha^2 \quad , \quad \tilde{v}/\tilde{\alpha} = v/\alpha \quad . \tag{2.39d}$$

When Eqs. (2.39) are substituted into Eqs. (2.36), the resultant equations are the same as Eqs. (2.38) except that ω, R, $\hat{v}$ and $\hat{p}$ are replaced by the corresponding tilde quantities. Thus the transformed equations, except for the $\tilde{w}$ equation which does not enter the eigenvalue problem, are again in 2D form, but now the Reynolds number has also been transformed to the new coordinate system. This transformation relates the eigenvalues of an oblique <u>temporal</u> wave of frequency ω in a 3D boundary layer with velocity profiles (U,W) at Reynolds number R to a 2D wave of frequency $\omega/\cos\psi$ in a 2D boundary layer at Reynolds number $R\cos\psi$ with velocity profile $U + W\tan\psi$. It can be interpreted as the same rotation of coordinates as in the transformation of Eq. (2.37) plus the redefinition of the reference velocity from U_r^* to $U_r^*\cos\psi$.

For a 3D boundary layer, the generalized Squire transformation is merely a different way of doing what has already been accomplished by Eqs. (2.36). However, for a two-dimensional boundary layer ($W=0$), which was the case considered by Squire, $\tilde{U} = U$ and the dimensionless velocity profile is unchanged by the transformation. This means that numerical stability results for oblique temporal waves can be immediately obtained from known results for 2D waves in the same velocity profile. Furthermore, since $\tilde{R} = R\cos\psi$, the smallest Reynolds number at which a wave of any frequency becomes unstable (minimum critical Reynolds number) must always occur for a 2D wave. This is the celebrated Squire theorem. It applies only to the minimum critical Reynolds number and not to the critical Reynolds number of a particular frequency, for which instability may well occur first for an oblique wave. It should also be noted that the theorem applies only to a self-similar boundary layer where the velocity profile is independent of R.

2.4.2 Transformations to 2D equations - spatial theory

When α and β are complex, the interpretation of the transformation equations (2.37) as a rotation of coordinates is lost, because the transformed velocity profiles are complex. There is one exception, however. In general, the quantity $\alpha/\tilde{\alpha}$, which for a temporal wave is $\cos\psi$, is complex. However, if $\alpha_i/\beta_i = \alpha_r/\beta_r$, that is if the spatial amplification rate vector is parallel to the wavenumber vector, $\alpha/\tilde{\alpha}$ is still real and equal to $\cos\psi$. Thus it would appear that the eigenvalues of a spatial wave could still be calculated from the 2D equations in the tilde coordinates. Unfortunately, this expectation is not correct. When α and β are real,

$$\alpha = \tilde{\alpha}\cos\psi \quad , \tag{2.40}$$

but there is no justification for applying Eq. (2.40) separately to the real and imaginary parts of a complex α when $\alpha/\tilde{\alpha}$ is complex. We are able, however, to derive the correct transformation rule from Eq. (2.35). With $\tilde{\psi} = \psi$ and $\tilde{\alpha}_i = (\alpha_i)_\psi$,

$$(-\alpha_i)_g = -\tilde{\alpha}_i\cos(\psi - \phi_r) \quad , \tag{2.41a}$$

and with $\psi = 0$,

$$-\alpha_1 = (-\alpha_1)_g / \cos\phi_r \quad . \tag{2.41b}$$

Eliminating $(-\alpha_1)_g$, we obtain

$$-\alpha_1 = -\tilde{\alpha}_1 \cos(\psi - \phi_r)/\cos\phi_r \quad . \tag{2.41c}$$

Consequently, Eq. (2.40) can be used for α_1 only when the real part of the group-velocity angle is zero. There is also a small shift in the wavenumber vector whenever $\phi_1 \neq 0$.

An alternative procedure for spatial waves is to use the equations that result from the transformations of Eq. (2.39), but to not invoke Eq. (2.40) when $\alpha/\tilde{\alpha}$ is complex. The quantities R and $\tilde{\omega}$ are complex, as are $\tilde{U}$ and $\tilde{W}$ for a 3D boundary layer, but this causes no difficulty in a numerical solution. Such a procedure, which amounts to a generalized complex Squire transformation, was incorporated into the JPL viscous stability code VSTAB/VSP. The approach with Eqs. (2.36), which has the advantage that no transformations are needed in determining the eigenvalues, is used in the newer JPL stability codes VSTAB/3D, VSTAB/AF and SFREQ/EV. It should be noted that even in the spatial theory, the governing <u>real</u> velocity profile is the profile in the direction of $\vec{k}$.

2.5 Special forms of the stability equations

2.5.1 Orr-Sommerfeld equation

A single fourth-order equation can be derived from Eqs. (2.36) by eliminating $\alpha\hat{u}+\beta\hat{w}$ from Eq. (2.36a) by (2.36d), and, after differentiation eliminating $D\hat{p}$ by (2.36b). The result is

$$[D^2 - (\alpha^2+\beta^2)]^2\hat{v} = iR\{(\alpha U+\beta W-\omega)[D^2 - (\alpha^2+\beta^2)] - (\alpha D^2 U+\beta D^2 W)\}\hat{v} \quad , \tag{2.42}$$

with the boundary conditions

$$\hat{v}(0) = 0, \qquad D\hat{v}(0) = 0 \quad ,$$

$$\hat{v}(y) \rightarrow 0, \qquad D\hat{v}(y) \rightarrow 0 \quad \text{as } y \rightarrow \infty \quad . \tag{2.43}$$

When $W=0$, Eq. (2.42) reduces to the equation for a 2D boundary layer obtained by Squire (1933). When in addition $\beta = 0$,

$$(D^2 - \alpha^2)^2 \hat{v} = iR[(\alpha U-\omega)(D^2 - \alpha^2) - \alpha D^2 U]\hat{v} \quad . \tag{2.44}$$

This is the Orr-Sommerfeld equation and is the basis for most of the work that has been done in incompressible stability theory. It is often derived from the vorticity equation, in which case $\hat{v}$ is the eigenfunction of the stream function. The Orr-Sommerfeld equation is valid for a two-dimensional wave in a two-dimensional boundary layer. However, the generalized Squire transformation, Eq. (2.39), reduces the 3D equation (2.42) to Eq. (2.44) in the tilde coordinates. Consequently, for 3D boundary layers all oblique temporal waves can be obtained by solving a 2D problem for the renormalized velocity profile in the direction of the wavenumber vector, and when the boundary layer is two-dimensional, for the same velocity profile. The 2D Orr-Sommerfeld equation and the same transformation can also be used for spatial oblique waves, but in this case R is complex, and for a 3D boundary layer so is $\tilde{U}$. The inviscid form of the complex Squire transformation was used by Gaster and Davey (1968) for an unbounded 2D shear flow, and the complete viscous form by Gaster (1975) for a Blasius boundary layer. When one is not trying to make use of previously computed two-dimensional eigenvalues, it is perhaps simpler to use Eq. (2.42) to calculate 3D eigenvalues as needed, thus avoiding transformations in R and ω.

2.5.2 System of first-order equations

There are a number of stability problems that cannot be reduced to a fourth-order system, and therefore are not governed by the Orr-Sommerfeld equation. A more flexible approach is to work from the outset with a system of first-order equations. With the definitions

$$Z_1 = \alpha\hat{u} + \beta\hat{w}, \quad Z_2 = \alpha D\hat{u} + \beta D\hat{w}, \quad Z_3 = \hat{v}, \quad Z_4 = \hat{p} \quad ,$$

$$Z_5 = \alpha\hat{w} - \beta\hat{u}, \quad Z_6 = \alpha D\hat{w} - \beta D\hat{u} \quad , \tag{2.45}$$

Eqs. (2.36) can be written as six first-order equations:

$$DZ_1 = Z_2 \quad , \tag{2.46a}$$

$$DZ_2 = [\alpha^2+\beta^2+iR(\alpha U+\beta W-\omega)]Z_1 + R(\alpha DU+\beta DW)Z_3 + iR(\alpha^2+\beta^2)Z_4 \quad , \tag{2.46b}$$

$$DZ_3 = -iZ_1 \quad , \tag{2.46c}$$

$$DZ_4 = -(i/R)Z_2 - [i(\alpha U+\beta W-\omega) + (\alpha^2+\beta^2)/R] Z_3 \quad , \tag{2.46d}$$

$$DZ_5 = Z_6 \quad , \tag{2.46e}$$

$$DZ_6 = (\alpha DW-\beta DU)RZ_3 + [\alpha^2+\beta^2+iR(\alpha U+\beta W-\omega)]Z_5 \quad . \tag{2.46f}$$

The boundary conditions are

$$Z_1(0) = 0 \ , \qquad Z_3(0) = 0 \ , \qquad Z_5(0) = 0 \ ,$$

$$Z_1(y) \rightarrow 0 \ , \qquad Z_3(y) \rightarrow 0 \ , \qquad Z_5(y) \rightarrow 0 \ \text{as } y \rightarrow \infty \quad . \tag{2.47}$$

The fact that the first four of Eqs. (2.46) do not contain Z_5 or Z_6 confirms that eigenvalues can be obtained from a fourth-order system even though the stability equations constitute a sixth-order system. It is only the determination of all the eigenfunctions that requires the solution of the full sixth-order system. The above formulation is applicable when α and β are complex as well as real, and to 3D as well as 2D boundary layers. Only the transformations of Eq. (2.37b) enter in this formulation, and then only in the definitions of the dependent variables Z_1, Z_2, Z_5 and Z_6. No transformations are involved in the determination of the eigenvalues. Another point to note is that only the first derivatives of U and W appear in Eqs. (2.46) instead of the second derivatives which are present in the Orr-Sommerfeld equation.

2.5.3 Uniform mean flow

In the freestream, the mean flow is uniform and Eqs. (2.46) have constant coefficients. Therefore, the solutions are of the form

$$Z^{(i)}(y) = A^{(i)} \exp(\lambda_i y) , \qquad (i=1,6) , \qquad (2.48)$$

where the $Z^{(i)}$ are the six-component solution vectors, the λ_i are the characteristic values (the term eigenvalue is reserved for the α, β, ω which satisfy the dispersion relation), and the $A^{(i)}$ are the six-component characteristic vectors [not to be confused with the wave amplitude A in Eq. (2.12)]. The characteristic values occur in pairs, and are easily found to be

$$\lambda_{1,2} = \mp(\alpha^2+\beta^2)^{1/2} , \qquad (2.49a)$$

$$\lambda_{3,4} = \mp[\alpha^2+\beta^2+iR(\alpha U_1+\beta W_1-\omega)]^{1/2} , \qquad (2.49b)$$

$$\lambda_{5,6} = \lambda_{3,4} , \qquad (2.49c)$$

where U_1 and W_1 are the freestream values of U(y) and W(y). Only the upper signs satisfy the boundary conditions at $y \to \infty$. The components of the characteristic vector $A^{(1)}$ are

$$A_1^{(1)} = -i(\alpha^2+\beta^2)^{1/2} , \qquad (2.50a)$$

$$A_2^{(1)} = i(\alpha^2+\beta^2) , \qquad (2.50b)$$

$$A_3^{(1)} = 1 , \qquad (2.50c)$$

$$A_4^{(1)} = i(\alpha U_1+\beta W_1-\omega)/(\alpha^2+\beta^2)^{1/2} , \qquad (2.50d)$$

$$A_5^{(1)} = 0 , \qquad A_6^{(1)} = 0 . \qquad (2.50e,f)$$

For real α, β and ω this solution is the linearized potential flow over a wavy wall moving in the direction of the wavenumber vector with the phase velocity ω/k. It can be called the inviscid solution, although this designation is valid only in the freestream.

The components of the characteristic vector $A^{(3)}$ are

$$A_1^{(3)} = 1 , \qquad (2.51a)$$

$$A_2^{(3)} = [\alpha^2+\beta^2+iR(\alpha U_1+\beta W_1-\omega)]^{1/2} , \qquad (2.51b)$$

$$A_3^{(3)} = 1/[\alpha^2+\beta^2-iR(\alpha U_1+\beta W_1-\omega)]^{1/2} , \qquad (2.51c)$$

$$A_4^{(3)} = 0 , \qquad A_5^{(3)} = 0 , \qquad A_6^{(3)} = 0 . \qquad (2.51d,e,f)$$

This solution represents a viscous wave and can be called the first viscous solution.

The characteristic vector $A^{(5)}$ is a second viscous solution, and its components are

$$A_1^{(5)} = 0 , \qquad A_2^{(5)} = 0 , \qquad (2.52a,b)$$

$$A_3^{(5)} = 0 , \qquad A_4^{(5)} = 0 , \qquad (2.52c,d)$$

$$A_5^{(5)} = 1 , \qquad (2.52e)$$

$$A_6^{(5)} = -[\alpha^2+\beta^2+iR(\alpha U_1+\beta W_1-\omega)]^{1/2} . \qquad (2.52f)$$

The three linearly independent solutions $A^{(1)}$, $A^{(3)}$ and $A^{(5)}$ are the key to the numerical method that we will use to obtain the eigenvalues, as they provide the initial conditions for the numerical integration.

We can observe that the second viscous solution can also be valid in the boundary layer as a pure mode if Z_1, Z_3 and Z_4 are all zero. This follows from Eqs. (2.46). In the notation of Eq. (2.37b), the only non-zero flow variable, Z_5, is $\tilde{\alpha}\tilde{w}$, where in the temporal theory $\tilde{w}$ is the eigenfunction of the fluctuation velocity normal to $\tilde{k}$. But since $\eta = \partial w/\partial x - \partial u/\partial z$ is the fluctuation vorticity component normal to the wall, Z_5 is also $-i\hat{\eta}$, where $\hat{\eta}$ is the eigenfunction of η. This interpretation is valid for both the temporal and spatial theories. The eigensolutions of the second-order equation (2.46f) with $Z_3 = 0$ satisfy the boundary condition $\hat{\eta}(0) = 0$ and give the vorticity modes in the boundary layer. These modes were first considered by Squire (1933), and were proven by him to be always stable. Recently it was shown by Herbert (1983a,1983b) that the Squire modes provide an important mechanism of subharmonic secondary instability at low, but finite, amplitudes of a primary 2D instability wave.

2.6 Wave propagation in a growing boundary layer

We have already discussed some aspects of this problem in Section 2.2, and we have chosen to use the quasi-parallel rather than the non-parallel theory. In the quasi-parallel theory, the normal-mode solutions are of the form

$$u(x,y,z,t) = A_0 \hat{u}(y;x) \exp[i\Theta(x,y,z,t)] \ , \tag{2.53}$$

with similar expressions for the other flow variables. The slowly varying amplitude $A(x)$ of the non-parallel solution Eq. (2.12) has been set equal to the constant A_0, and

$$\Theta(x,z,t) = \int^x \alpha(x)dx + \beta(x_1)z - \omega(x_1)t \ . \tag{2.54}$$

Equation (2.54) is the same as Eq. (2.13). We have left β and ω as functions of the slow scale x_1 in order to make it clear that $\partial\Theta/\partial x = \alpha$, just as for strictly parallel flow. The eigenvalues α, β and ω satisfy the local dispersion relation Eq. (2.14), and the eigenfunction $\hat{u}(y;x)$ is also a slowly varying function of x. Consequently, at each x a different eigenvalue problem has to be solved because of the change in the boundary-layer thickness, or velocity profiles, or, as is usually the case, both. The problem we must resolve is how to "connect" the possible eigenvalues at each x so that they represent a continuous wave train propagating through the growing boundary layer.

In a steady boundary layer, which is the only kind that we shall consider, the dimensional frequency of a normal mode is constant. For a 2D wave in a 2D boundary layer, $\beta = 0$, and the complex wavenumber α in the spatial theory, or the real wavenumber α and the imaginary part of the frequency ω_i in the temporal theory, are obtained as eigenvalues for the local boundary-layer profiles. The only problem here is the relatively minor one of calculating the wave amplitude as a function of x from the amplification rate, and we shall discuss this in Section 2.6.2.

2.6.1 Spanwise wavenumber

When the wave is oblique, $\beta \neq 0$, and it is not obvious how to proceed. According to the dispersion relation, α is a function of β as well as of x. How do we choose β at each x? The answer is provided by the same procedure as used in conservative wave theory. When we differentiate Eq. (2.54) with respect to x (not x_1) and z, we obtain

$$\partial\Theta/\partial x = \alpha, \ \partial\Theta/\partial z = \beta, \tag{2.55a}$$

or

$$\mathrm{grad}\,\Theta = \vec{k}_c \ , \tag{2.55b}$$

where $\vec{k}_c$ is the _complex_ vector wavenumber. Thus it follows directly that

$$\vec{\nabla} \times \vec{k}_c = 0 \ , \tag{2.55c}$$

and $\vec{k}_c$ is irrotational. This condition is a generalization to a nonconservative system of the well-known result for the real wavenumber vector in conservative kinematic wave theory.

In the boundary layers we will consider here, the mean flow is independent of z. Consequently, if we restrict ourselves to spatial waves of constant β at the initial x, they can be represented by a single normal mode because the eigenvalue α will also be independent of z. Therefore, according to Eq. (2.55c) the sought-after downstream condition on β is

$$\beta = \mathrm{const.} \tag{2.56}$$

One caution is that if the reference length L^* is itself a function of x, as it will be if $L^* = \delta^*$ for example, the argument has to be slightly modified and Eq. (2.56) refers to β^* rather than to β.

It still remains to specify the initial value of β. Naturally occurring instability waves in a boundary layer will be a superposition of normal modes, with a spectrum over both ω and β that will depend on the particular origin of the waves. It is probably only in a controlled experiment with a suitable wavemaker that a single normal mode can be excited. For example, the vibrating ribbon first used by Schubauer and Skramstad (1947) in their celebrated experiment excites a spatial 2D normal mode with the frequency of the ribbon. It is also possible to conceive of wavemakers that excite single oblique normal modes in boundary layers which are independent of z. Such normal modes will have an initial β_r which matches that of the wavemaker, and, because the wave can grow only in x, the initial β_i must be zero. These normal modes are well-suited for use in stability calculations for the estimation of the location of transition. In the calculations, β_r is assigned as a parameter, β_i is zero, and Eq. (2.56) controls the downstream values of β_r. Not only do these normal modes represent physical waves that can be produced by a suitable wavemaker, but they are also convenient to use in all calculations of normal modes, such as transition prediction, where we are interested in the largest possible growth of any normal mode, or the point-source calculations of Section 7. In earlier work on two-dimensional planar boundary layers, some results from which will appear in later Sections, the angle ψ was chosen as the parameter to hold constant, rather than β_r, as the wave propagates downstream. Although α_r is nearly constant in such boundary layers, it changes enough so that the assumption of constant ψ is not equivalent to Eq. (2.56). In the work on three-dimensional boundary layers presented in Sections 13 and 14, Eq. (2.56) is applied to the spanwise wavenumbers, but the direction of the spatial amplification rate is either parallel to the local potential flow, or, occasionally, in the direction of the real part of the group-velocity angle.

2.6.2 Some useful formulas

It is worthwhile at this point to list some formulas that will be of use for stability calculations in growing boundary layers. Only 2D boundary layers are considered here; 3D boundary layers are taken up separately in Part C. First, we choose as the length scale,

$$L^* = [\nu^* x^* / U_1^*(x^*)]^{1/2} \ , \tag{2.57}$$

which is the usual length scale of the Falkner-Skan family of boundary layers, and of many nonsimilar boundary-layer solutions. Other length scales that have been used are the boundary layer thickness, the displacement thickness, and the inverse unit Reynolds number. The velocity scale is $U_1^*(x^*)$, the local velocity at the edge of the boundary layer. With these choices, the Reynolds number in the stability equations is

$$R = U_1^*(x^*) \ L^* / \nu^* = (U_1^* x^* / \nu^*)^{1/2} = Re^{1/2} \ . \tag{2.58}$$

The dimensionless coordinate normal to the wall,

$$y = (y^*/x^*)R \ , \tag{2.59}$$

is the usual independent variable of boundary-layer theory.

The dimensionless quantities α, β, ω, R and y referenced to L^* may be converted to other length scales, such as displacement or momentum thickness, by multiplying by the dimensionless (with respect to L^*) displacement or momentum thickness. The latter quantities are almost always obtained as part of a boundary-layer calculation. To convert α, β and ω to dimensionless quantities based on the inverse unit Reynolds number ν^*/U_1^*, it is only necessary to divide α, β and ω by R.

The dimensional circular frequency ω^* of a normal mode is constant as the wave travels downstream, but the dimensionless frequency

$$\omega = \omega^* L^* / U_1^* \ , \tag{2.59}$$

is a function of x. It has become almost standard to use

$$F = \omega^* \nu^* / U_1^{*2} = \omega / R \tag{2.60}$$

in place of ω as the dimensionless frequency. However, F is also a function of x for anything but a flat-plate boundary layer. For the Falkner-Skan family of velocity profiles, the dimensionless velocity gradient,

$$m = (x^*/U_1^*)(dU_1^*/dx^*) \ , \tag{2.61}$$

is constant and related to the usual Hartree parameter β_h (the subscript h is used to avoid confusion with the wavenumber component β), by

$$\beta_h = 2m/(m+1) \ . \tag{2.62}$$

The variable dimensionless frequency for constant ω^* is

$$F(R) = F(R_0)(R_0/R)^{4m/(m+1)} \ , \tag{2.63}$$

where R_0 is the Reynolds number at the initial x station. When a stability code can handle several frequencies at once, it is more convenient to use some fixed velocity as the reference velocity so that F will remain constant for each frequency. For the nonsimilar boundary layers on airfoils, the JPL stability codes use the velocity in the undisturbed freestream.

With L^* a function of x^*, the irrotationality condition Eq. (2.56) applies to the dimensional spanwise wavenumber. For the Falkner-Skan family, the dimensionless β for constant β^* is given by

$$\beta(R)/\beta(R_0) = (R/R_0)^{(1-m)/(1+m)} \ . \tag{2.64}$$

We note that for a Blasius boundary layer (m=0), β increases linearly with R. The dimensional wavenumber α_r^* is almost, but not quite, constant, because there is a small increase in the phase velocity with increasing R. As a result, the wave angle ψ __increases__ as the wave travels downstream. This increase is at most a few degrees for a planar boundary layer. However, on an axisymmetric body, it is the circumferential wavenumber per radian that is constant. Thus, neglecting the small decrease in α_r^*, $\tan\psi$ is inversely proportional to the radius. For instance, on a cone, where the radius is increasing, an oblique wave is rapidly converted to a nearly 2D wave as it travels downstream; on a body with decreasing radius, the effect is reversed.

2.6.3 Wave amplitude

In the quasi-parallel theory, the amplitude ratio of a spatial normal mode of frequency ω^* with $\beta_i = 0$ is obtained from the imaginary part of the phase function Eq. (2.54):

$$\ln(A/A_0) = -\int_{x_0^*}^{x^*} \alpha_i^* dx^* \tag{2.65}$$

in accord with Eq. (2.27). Here A_0 is the amplitude at the initial station x_0^*, and the integral is evaluated with constant ω^* and β^*. If x_0^* is the start of the instability region for the frequency ω^*, $\ln(A/A_0)$ is the N factor that is the basis of the e^N method of transition prediction. As discussed in Section 2.2, A may represent any flow variable at any y location. It may be helpful to think of A as, say, the maximum value of $|\hat{u}|$ in the boundary layer, as this is a quantity that can be determined experimentally. Along with the amplitude, the time-independent phase relative to the initial phase at x_0^*, z_0^* is

$$\chi(x) - \chi(x_0) = \int_{x_0^*}^{x^*} \alpha_r^* dx^* + \beta_r^* (z^* - z_0^*) \ . \tag{2.66}$$

The phase is a vital quantity in superposition calculations (Section 7), but otherwise it is usually not computed.

For the Falkner-Skan family, the amplitude ratio in terms of R is

$$\ln(A/A_0) = - [2/(m+1)]\int_{R_0}^{R} \alpha_i dR , \qquad (2.67)$$

where the integrand α_i is calculated as an eigenvalue with the F of Eq. (2.63) and the β of Eq. (2.64). For a nonsimilar boundary layer, $U_1^*(x^*)$ is not an analytical function, and the integration has to be with respect to x^*. A formula that is used in the JPL stability codes is

$$\ln(A/A_0) = -R_c\int_{(x_c)_0}^{x_c} (\alpha_i/R)(U_1^*/U_\infty^*)dx_c , \qquad (2.68)$$

where α_i is based on the local L^*; U_∞^* is the velocity of the undisturbed freestream; x_c is x^*/c_h^*, where c_h^* is the chord; $R_c \equiv U_\infty^* c_h^*/\nu^*$ is the full chord Reynolds number; and the integral is again evaluated for constant ω^* and β^*.

3. INCOMPRESSIBLE INVISCID THEORY

The system of first-order equations (2.46), or the Orr-Sommerfeld equation in either 2D or 3D form, Eq. (2.42) or (2.44), governs the motion of linear waves at finite Reynolds numbers. With the highest derivative of $\hat{v}$ in the Orr-Sommerfeld equation multiplied by 1/R, which is usually a small quantity, it is apparent that mathematical and numerical methods of some complexity are required to obtain the eigenvalues and eigenfunctions. On the other hand, if viscosity is considered to act only in the establishment of the mean flow, but to have a negligible effect on the instability waves, the equations take on a much simpler form. For example, the 2D Orr-Sommerfeld equation reduces to

$$[(\alpha U - \omega)(D^2 - \alpha^2) - \alpha D^2 U]\hat{v} = 0 . \qquad (3.1)$$

This is the fundamental equation of the inviscid stability theory, and is usually referred to as the Rayleigh equation. It is of second order and so only the two boundary conditions

$$\hat{v}(0) = 0 , \quad \hat{v}(y) \rightarrow 0 \text{ as } y \rightarrow \infty , \qquad (3.2)$$

can be satisfied. The normal velocity at the wall is zero, but the no slip condition is not satisfied.

The inviscid theory has dealt largely with 2D temporal waves. Since all of the essential ideas are included within this framework, we shall adopt the same procedure in this Section. The Rayleigh equation (3.1) has a singularity at $y = y_c$ where $\alpha U = \omega$. This singularity is of great importance in the theory, and is called the critical layer, or critical point. It does not occur in the Orr-Sommerfeld equation, but even so the Rayleigh equation is simpler to work with than the Orr-Sommerfeld equation, and an extensive inviscid stability theory has been developed over the past 100 years. The early work was mainly by Rayleigh (1880,1887,1892,1895,1913), but a great number of authors have made contributions in more recent times. An excellent review of the subject may be found in the article by Drazin and Howard (1966). Only those aspects of the theory which are necessary for a general understanding, and have relevance to boundary-layer flows, will be taken up in this Section. We also restrict ourselves to boundary layers with monotonic velocity profiles. These profiles have only a single critical layer. We defer until Section 12 the discussion of the important directional velocity profiles of 3D boundary layers which have two critical layers.

The inviscid theory has been used for two purposes. One is to provide two of the four independent solutions that are needed in the asymptotic viscous theory. The other is as an inviscid stability theory per se. We shall not discuss the asymptotic theory, so it is only the second use that is of interest here. Not many numerical results have been worked out from the inviscid theory for incompressible boundary layers. However, one of the two chief instability mechanisms is inviscid in nature, so that some knowledge of the theory is essential for an understanding of boundary-layer instability. The presentation here will also serve as a necessary prelude to compressible stability theory, where the inviscid theory has a larger role to play.

3.1 Inflectional instability

3.1.1 Some mathematical results

There are a number of general mathematical results that can be established in the inviscid theory, in contrast to the viscous theory where few such results are known. We shall give two which demonstrate that no unstable or neutral temporal waves can exist unless the velocity profile has a point of inflection. The first result concerns unstable waves. If we multiply Eq. (3.1) by $\hat{v}^*$, the complex conjugate of $\hat{v}$, and then subtract the complex conjugate of the resultant equation, we obtain

$$D(v^*D\hat{v} - \hat{v}D\hat{v}^*) - 2i\omega_i D^2 U|\hat{v}|^2/|\alpha U - \omega|^2 = 0 . \qquad (3.3)$$

The first term of Eq. (3.3) can be made more meaningful by relating it to the Reynolds stress, which, in dimensionless form, is

$$\tau = -(\alpha/2\pi)\int_0^{2\pi/\alpha} uv \, dx . \qquad (3.4)$$

If we recall the necessity of first taking the real parts of u and v before multiplying, and make use of the continuity equation, we obtain

$$D\tau = \omega_i D^2 U \langle v^2 \rangle / |\alpha U - \omega|^2 , \qquad (3.5)$$

where $(1/2)|\hat{v}|^2\exp(2\omega_i t)$ has been replaced by $\langle v^2\rangle$, the average over a wavelength of the square of the velocity fluctuation v.

Eq. (3.5) is a special case of a formula derived by Foote and Lin (1950) [see also Lin (1954,1955)]. When Eq. (3.5) is integrated from y = 0 to infinity, the Reynolds stress at the wall and in the freestream is zero by the boundary conditions. Therefore, since $D^2U = 0$ in the freestream,

$$\omega_i\int_0^{y_\delta}(\langle v^2\rangle D^2U/|\alpha U-\omega|^2)dy = 0 ,\qquad(3.6)$$

where y_δ is the dimensionless boundary-layer thickness. It follows from Eq. (3.6) that if $\omega_i \neq 0$, D^2U must change sign somewhere in the interval $0<y<y_\delta$. Consequently, it has been proven that the velocity profile must have a point of inflection for there to be an unstable wave. This result was first obtained by Rayleigh. Later, Fjortoft (1950) strengthened Rayleigh's necessary condition to $D^2U(U-U_s) < 0$ somewhere in the flow, where U_s is the mean velocity at the inflection point. This condition is equivalent to requiring that the modulus of DU have a maximum for there to be instability. It is always satisfied in a boundary layer with an inflection point, because $DU \to 0$ as $y \to \infty$ and $|DU|$ cannot only have a minimum. It was subsequently proven by Tollmien (1935) that for most of the profiles which occur in boundary layers, including 3D boundary layers, the condition $D^2U = 0$ is also sufficient. Another result of Rayleigh, for which the proof will not be given, established that the phase velocity of an unstable wave always lies between the maximum and minimum values of U. This result was later generalized by Howard (1961) into an elegant semicircle theorem which relates both ω_r/α and ω_i/α to the maximum and minimum values of U.

The second result concerns neutral waves. It follows from Eq. (3.5) that with $\omega_i = 0$, the Reynolds stress must be constant everywhere except for a possible discontinuity at the critical layer y_c. When Eq. (3.5) is integrated across the boundary layer, the only contribution to the integral comes from the immediate neighborhood of y_c. Hence,

$$\tau(y_c+0)-\tau(y_c-0) = -(D^2U/DU)_c\langle v^2\rangle \lim_{\omega_i\to 0}\int_{U(y_c-0)}^{U(y_c+0)}\{\omega_i/[(\alpha U-\omega_r)^2+\omega_i^2]\}dU.\qquad(3.7)$$

The integration variable has been changed from y to U. In the limit of $\omega_i \to 0$, the integrand of Eq. (3.7) acts as a delta function, and the intgegral has a value of π/α. Consequently,

$$\tau(y_c+0)-\tau(y_c-0) = (\pi/\alpha)(D^2U/DU)_c\langle v_c^2\rangle.\qquad(3.8)$$

Since $\tau(y_c+0)$ and $\tau(y_c-0)$ are both zero by the boundary conditions, D^2U_c must also be zero, and it has been proven that a wave of neutral stability can exist only when the velocity profile has a point of inflection. Furthermore, $\omega_r/\alpha = U_c$ and the phase velocity of a neutral wave is equal to the mean velocity at the inflection point.

The chief analytical feature of the Rayleigh equation (3.1) is the singularity at $\alpha U = \omega$. Since ω is in general complex, so is y_c. Of course the mean velocity U is real in the physical problem, but it may be analytically continued onto the complex plane by a power-series expansion of U or by some other method. Two approaches to obtaining analytical solutions of the inviscid equation are the power series in α^2 used by Heisenberg (1924) and Lin (1945), and the method of Frobenius used by Tollmien (1929). The two solutions obtained by Tollmien are

$$\hat{v}_1(y) = (y-y_c)P_1(y-y_c) ,\qquad(3.9a)$$

$$\hat{v}_2(y) = P_2(y-y_c) + (D^2U/DU)_c(y-y_c)P_1(y-y_c)\log(y-y_c) ,\qquad(3.9b)$$

where

$$P_1(y-y_c) = 1 + (D^2U/2DU)_c(y-y_c) + (1/6)[D^3U/DU)_c + \alpha^2](y-y_c)^2 + \dots,$$

$$P_2(y-y_c) = 1 + [(D^3U/2DU)_c - (D^2U/DU^2)_c + (1/2)\alpha^2](y-y_c)^2 + \dots$$

$$(3.10)$$

The first solution is regular, but $\hat{v}_2$ is not in general regular near y_c because of the logarithmic term. However, for a neutral wave D^2U_c is zero, and in this one case $\hat{v}_2$ is also regular.

To summarize what we have learned in this section, for a velocity profile without an inflection point, (e.g., the Blasius boundary layer), there can be neither unstable nor neutral waves (save for the trivial solution $\alpha = 0$, $\omega = 0$). When there is an inflection point, a neutral wave with a phase velocity equal to the mean velocity at the inflection point can exist, and in boundary layers unstable waves with phase velocities between 0 and 1 can and will exist.

3.1.2 Physical interpretations

The mathematical theory is complete in itself, and with the use of the Reynolds stress also makes the physical consequences of an inflection point clear. However, there have been attempts to formulate physical arguments that in some manner bring in the concept of negative stiffness, which is the way in which one usually thinks about unstable wave motions. The first of these was by Taylor (1915), and appeared as an addendum to a major paper in which he developed his vorticity transfer theory. He applied this theory to deriving an expression for the vertical transfer of disturbance momentum, which immediately showed that if D^2U is of the same sign everywhere, the disturbance momentum can only increase or decrease everywhere, a situation incompatible with the inviscid boundary conditions. However, if D^2U changes sign, then momentum can be transferred from one place to another without affecting the boundaries, thus permitting instability. Later arguments made use of vorticity concepts. The most detailed is by Lin (1945,1955), and is supported by a considerable mathematical development. Lighthill (1963, p. 92) gives a very helpful presentation with three diagrams, and finally Gill (1965) has constructed an argument that makes use of Kelvin's (1880) cat's eye diagram of the streamlines in the vicinity of an inflection point to demonstrate that only a maximum in DU can cause instability. All of these presentations are worth careful study.

3.2 Numerical integration

The analytical methods are not adequate for producing numerical solutions of the Rayleigh equation except in certain special cases. Only direct numerical integration of Eq. (3.1) can produce solutions accurately and quickly for the great variety of velocity profiles encountered in practice. There are at least two methods available. In the first, which was developed by Conte and Miles (1959), the integration is restricted to the real axis and is carried past the critical point by the Tollmien solutions. In the second method, which was developed by Zaat (1958), the solution is produced entirely by numerical integration, and the critical point is avoided by use of an indented contour in the complex plane. It is as easy to perform the numerical integration along such a contour as along the real axis, provided the analytic continuation of U away from the real axis is available. This approach, except for a difference in the method of analytic continuation, was used by Mack (1965a) to integrate the compressible inviscid equations. It was later extended to incompressible flow, and is incorporated into the JPL inviscid stability code ISTAB.

For numerical integration, Eq. (3.1) is replaced by the two first-order equations for $\hat{v}$ and $\hat{p}$ which follow from Eqs. (2.36) when $R \to \infty$:

$$D\hat{v} = [\alpha/(\alpha U - \omega)](DU\hat{v}+i\alpha\hat{p}) , \qquad (3.11a)$$

$$D\hat{p} = -i(\alpha U-\omega)\hat{v} . \qquad (3.11b)$$

The solutions in the freestream, where $U = 1$ and $DU = 0$, are

$$\hat{v} = \exp(-\alpha y) , \qquad (3.12a)$$

$$\hat{p} = -i(1-\omega/\alpha)\exp[-\alpha y] , \qquad (3.12b)$$

where we have chosen the normalization to agree with Eqs. (2.50). These expressions provide the initial values for the numerical integration to start at some $y = y_1 > y_\delta$. For chosen values of α and $\omega_r + i\omega_i$, the integration proceeds from y_1 to the wall along the real y axis and an indented rectangular contour around the critical point when necessary. The velocity U is continued on to the indented contour by a power-series expansion in $y - y_c$. The necessary derivatives of U are obtained from the boundary-layer equations. A Newton-Raphson search procedure, in which any two of α, ω_r, ω_i are perturbed, is used to find the eigenvalues, i.e., an α and $\omega_r + i\omega_i$ for which the boundary condition $\hat{v}(0) = 0$ is satisfied. If α is held constant, then the Cauchy-Riemann equations can be used to eliminate one perturbation because the function $\Omega(\alpha)$ in the dispersion relation is analytic.

3.3 Amplified and damped inviscid waves

3.3.1 Amplified and damped solutions as complex conjugates

In the use of the inviscid theory in the asymptotic viscous theory, the choice of the branch of the logarithm in Eq. (3.9b) constitutes a major problem. This same difficulty also shows up in the inviscid theory itself, but in a much less obvious manner. Since $DU > 0$ for the type of boundary layer we are considering in this Section, it follows that for an amplified wave ($\omega_i > 0$) the critical layer lies above the real y axis [$(y_c)_i > 0$]; for a damped wave ($\omega_i < 0$) it is below the real axis [$(y_c)_i < 0$]. For a neutral wave ($\omega_i = 0$), the critical layer is on the real axis, but since $D^2U_c = 0$ the logarithmic term drops out of Eq. (3.9b) and the solution is regular. With the critical layer located off the real axis for amplified and damped waves, it would seem that there is nothing to hinder integration along the real axis. Indeed, it can be seen by manipulating the inviscid equation (3.1) that if $\hat{v}_r + i\hat{v}_i$ is a solution for $\omega_r + i\omega_i$, then $\hat{v}_r - i\hat{v}_i$ is a solution for $\omega_r - i\omega_i$. Thus amplified and damped solutions are complex conjugates, and the existence of one implies the existence of the other. From this point of view, the criterion for instability is that ω is complex, and the only stability is neutral stability with ω real. Since Eq. (3.6) applies for $\omega_i < 0$ as well as for $\omega_i > 0$, neither amplified nor damped waves can exist unless there is an inflection point. The Blasius boundary layer has no inflection point (except at y = 0), and according to this argument no inviscid waves are possible, amplified, damped or neutral (except for $\alpha = 0$, $\omega = 0$). But viscous solutions certainly exist; what happens to these solutions in the limit as $R \to \infty$?

3.3.2 Amplified and damped solutions as $R \to \infty$ limit of viscous solutions

The clarification of this point is due to Lin (1945), who showed that if the inviscid solutions are regarded as the infinite Reynolds limit of viscous solutions, a consistent inviscid theory can be constructed in which damped solutions exist that are not the complex conjugates of amplified solutions. To achieve this result, integration along the real axis is abandoned for damped waves. Instead, the path of integration is taken under the singularity just as it is for the inviscid solutions that are used in the asymptotic viscous theory, and $\ln(y - y_c) = \ln|y - y_c| - i\pi$ for $y < y_c$. For damped waves, the effect of viscosity is present even in the limit $R \to \infty$, and a completely inviscid solution cannot be valid along the entire real axis. Lin's arguments were physical and heuristic, but a rigorous justification was given by Wasow (1948).

It is also possible to arrive at Lin's result from a strictly numerical approach. In Section 3.2, no mention was made of how to indent the contour of integration. The two possibilities are shown in Fig. 3.1. For an inviscid neutral solution ($\omega_i = 0$), $\hat{v}$ is purely imaginary and $\hat{p}$ is real. It makes no difference if the contour is indented below the real axis, as in Fig. 3.1a, or above, as in Fig. 3.1b. The same eigenvalue α is obtained in either case. If $\omega_i \neq 0$, the integration can be restricted to the real axis. However, unless $D^2U = 0$ somewhere in the boundary layer, there are no amplified solutions, or their complex conjugates the damped solutions. But if we use contour (a) for damped waves, and contour (b) for amplified waves, both solutions exist even with $D^2U \neq 0$. Some eigenvalues computed for the Blasius velocity profile are given in Table 3.1, where the eigenvalues have been made dimensionless by reference to L^* [Eq. (2.57)], which enters the inviscid problem through the boundary-layer similarity

variable $y = y^*/L^*$. As can be verified from Eqs. (3.11), the solutions with $\omega_r - i\omega_i$ and contour (a) are related to the solutions with $\omega_r + i\omega_i$ and contour (b) by

$$\hat{\varphi}^{(a)} + i\hat{\varphi}^{(a)} = \hat{\varphi}^{(b)} - i\hat{\varphi}^{(b)} ,$$

$$\hat{\beta}^{(a)} + i\hat{\beta}^{(a)} = -\hat{\beta}^{(b)} + i\hat{\beta}^{(b)} .$$

(3.13)

Table 3.1 Inviscid eigenvalues of Blasius velocity profile
computed with indented contours.

Contour	α	ω_r	$\omega_i \times 10^3$
(a)	0.128	0.0333	−2.33
(b)	0.128	0.0333	2.33
(a)	0.180	0.0580	−6.80
(b)	0.180	0.0580	6.80

Which option do we pick, (a) or (b)? Since the neutral-stability curve for the Blasius profile is of the type shown in Fig. 1.1a, waves of all wavenumbers are damped in the limit $R \to \infty$. Consequently, if the inviscid solutions are required to be the $R \to \infty$ limit of viscous solutions, it is evident that contour (a) must be used, just as in the asymptotic theory and in agreement with Lin. Without an inflection point, there are no inviscid amplified solutions. For a velocity profile with $D^2U = 0$ at y_s, where the subscript s refers to the inflection point, both amplified and damped waves exist for each contour, unlike the Blasius case. The neutral wavenumber is α_s, and can be obtained with either contour. With contour (a), the wavenumbers of the amplified waves are located below α_s, and the wavenumbers of the damped waves are located above α_s; contour (b) gives the opposite results. Comparison with the viscous neutral-stability curve, which is of the type shown in Fig. 1.1b, shows that contour (b) must be rejected in this case also.

The damped solutions with contour (a) do not exist everywhere on the real axis. According to Lin (1955, p. 136), there is an _interval_ of the real axis in the vicinity of the critical layer where viscosity will always have an effect even in the limit of $R \to \infty$, and where the inviscid solution is not a valid asymptotic approximation to the viscous solution. In the final paragraph of his book, Lin remarked that in this interval the viscous solution has an oscillatory behavior. This remark was confirmed analytically by Tatsumi and Gotoh (1971), and verified numerically by Davey (1981) at an extremely high Reynolds number using the compound matrix method.

As a numerical example of damped inviscid eigenvalues, Fig. 3.2 gives $-\omega_i$, the temporal damping rate, as a function of α for the Blasius velocity profile. The calculation was performed along an indented contour of type (a). The inviscid damping rates are, for the most part, much larger than the viscous amplification rates. That damped inviscid eigenvalues calculated with a type (a) contour are the $R \to \infty$ limit of viscous eigenvalues was confirmed numerically by Davey in the paper mentioned in the preceding paragraph. For $\alpha = 0.179$, the inviscid eigenvalue is $\omega/\alpha = 0.32126-0.036711$; the viscous eigenvalue computed by Davey at $R = 1 \times 10^6$ is $\omega/\alpha = 0.32166-0.036291$.

4. NUMERICAL TECHNIQUES

4.1 Types of methods

Since the early 1960's, the asymptotic theories developed by Tollmien (1929) and Lin (1945) have been largely superseded as a means of producing numerical results in favor of direct solutions of the governing differential equations on a digital computer. The numerical methods that have been employed fall roughly into three categories: (1) finite-difference methods, used first by Thomas (1953) in his pioneering numerical work on plane Poiseuille flow, and later by Kurtz (1961), Osborne (1967), and Jordinson (1970), among others; (2) spectral methods, used first by Gallagher and Mercer (1962) for Couette flow with Chandrasekhar and Reid functions, and later improved by Orszag (1971) with the use of Chebyshev polynomials; and (3) shooting methods, used first by Brown and Sayre (1954). All of these methods have advantages and disadvantages which show up in specialized situations, but they are all equally able to do the routine eigenvalue computations required in transition-prediction calculations. However, a shooting method has been used for almost all of the numerical results given in the present lectures, and it is this method that will be described here.

4.2 Shooting methods

After the early work of Brown (1954,1959,1960, 1961, 1962), computer codes for boundary-layer problems that were also based on shooting methods were developed by Nachtsheim (1963), Mack (1965a), Landahl and Kaplan (1965), Radbill and Van Driest (1966), Wazzan, Okamura and Smith (1968), Davey (1973), and Cebeci and Stewartson (1979), among others. Most of these codes solve the Orr-Sommerfeld equation; exceptions are the compressible stability code of Brown (1961), and the codes of Mack (1965a), which were also originally developed for compressible flow and only later extended to incompressible flow. Almost all of the codes have the feature that the numerical integration proceeds from the freestream to the wall. The exceptions are the codes of Brown and of Nachtsheim (1963), where the integration proceeds in the opposite direction [in a later report on plane Poiseuille flow, Nachtsheim (1964) used a method that integrates in both directions].

Various integrators have been used to implement the shooting method. Perhaps the most common is some form of the Runge-Kutta method, but the Adams-Moulton and Keller box method have also been used. One choice that has to be made is whether to use a fixed or variable step-size integrator. The latter is better in principle, but it adds to the computational overhead, and thus to the expense, and it may be as difficult to construct a proper error test and then choose the error limits as it is to select the proper fixed step size. It must also be remembered that the variable step-size methods do not really address the

right problem. What we are interested in is a certain accuracy of the eigenvalues and eigenfunctions, not in the per-step truncation error of the independent solutions, which is what the variable step-size methods control. These methods seem to require more integration steps than fixed step-size methods, which adds to the expense, and the only compensation is to relieve the user of the need to select the step size. The JPL viscous stability codes have used a fixed step-size fourth-order Runge-Kutta integrator for many years without ever encountering a problem that required a variable step-size integrator. A severe test of any integrator is to calculate the discrete eigenvalue spectrum, because the higher viscous modes have rapidly oscillating eigenfunctions. The fixed step-size integrator had little difficulty in calculating a number of additional temporal modes for plane Poiseuille flow, and its ultimate failure in a portion of the complex ω/α plane for Blasius flow was caused by a round-off error problem that apparently cannot be cured by any of the usual methods [Mack (1976), p. 501].

The early applications of shooting methods suffered from the problem of parasitic error growth. This growth arises because of the presence of a rapidly growing solution in the direction of integration that is associated with the large characteristic value λ_3 in the freestream, which the numerical round-off error will follow. The parasitic error eventually completely contaminates the less rapidly growing solution, associated with the characteristic value λ_1 in the freestream. The essential advance in coping with this problem, which had previously limited numerical solutions to moderate Reynolds numbers, was made by Kaplan (1964). The Kaplan method "purifies" the contaminated solution by filtering out the parasitic error whenever it becomes large enough to destroy the linear independence of the solutions. An illuminating presentation and application of the Kaplan method may be found in Betchov and Criminale (1967). Three recent methods that cope exceptionally well with the contamination problem are the Riccati method [Davey (1977,1979)], the method of compound matrices of Ng and Reid (1979,1980), and the method of order reduction [Van Stijn and Van de Vooren (1982)].

4.3 Gram-Schmidt orthonormalization

A widely used method, that was originally developed for systems of linear differential equations by Godunov (1961) and Bellman and Kalaba (1965) and applied to the boundary-layer stability problem by Radbill and Van Driest (1966) and Wazzan, Okamura and Smith (1968), is that of Gram-Schmidt orthonormalization. This method has the advantage that it is easier to generalize to higher-order systems than is the Kaplan filtering technique. However, the geometrical argument often adduced in its support, that this procedure preserves linear independence by keeping the solution vectors orthogonal, cannot be correct because the solution vector space does not have a metric. In such vector spaces, vectors are either parallel or non-parallel; the concept of orthogonality does not exist. Instead, the orthonormalization method works on exactly the same basis as Kaplan filtering: the "small" solution is replaced by a linear combination of the "small" and "large" solutions which is itself constrained to be "small."

For the simplest case of a two-dimensional wave in a two-dimensional boundary layer, there are two solutions, $Z^{(1)}$ and $Z^{(3)}$, each consisting of four components. In the freestream, $Z^{(1)}$ is the inviscid and $Z^{(3)}$ the viscous solution. Although this identification is lost in the boundary layer, $Z^{(3)}$ continues to grow more rapidly with decreasing y than does $Z^{(1)}$. The parasitic error will follow $Z^{(3)}$, and when the difference in the "magnitudes" of $Z^{(3)}$ and $Z^{(1)}$ as defined by an arbitrarily assigned metric becomes sufficiently large, $Z^{(1)}$ will no longer be independent of $Z^{(3)}$. Well before this occurs, the Gram-Schmidt orthonormalization algorithm is applied. The "large" solution $Z^{(3)}$ is normalized component by component to give the new solution

$$S^{(3)} = Z^{(3)}/\{Z^{(3)*}Z^{(3)}\}^{1/2} , \qquad (4.1)$$

where an asterisk refers to a complex conjugate and $\{\}$ to a scalar product. The metric adopted for the vector space is the usual Euclidian norm. The scalar product of $Z^{(1)}$ and $S^{(3)}$ is used to form the vector

$$S^{(1)} = [Z^{(1)*} - (S^{(3)*}Z^{(1)})S^{(3)}]/(\bar{S}^{(1)*}\bar{S}^{(1)})^{1/2} , \qquad (4.2)$$

which replaces $Z^{(1)}$, and where $\bar{S}$ refers to the quantity in the numerator.

The numerical integration continues with $S^{(1)}$ and $S^{(3)}$ in place of $Z^{(1)}$ and $Z^{(3)}$, and when in turn $|S^{(3)}|$ exceeds the set criterion of, say, 10^5 with single precision arithmetic and a 36 bit computer word, the orthonormalization is repeated. With homogeneous boundary conditions at the wall, it makes no difference in the determination of the eigenvalues whether the $Z^{(i)}$ or $S^{(i)}$ are used. A linear combination of the two solutions satisfies the $\hat{u}(0)=0$ boundary condition, but the $\hat{v}(0)=0$ boundary condition will in general not be satisfied unless α, β and ω satisfy the dispersion relation.

Although the orthonormalization procedure has no effect on the method of determining eigenvalues, it does complicate the calculation of the eigenfunctions. The solution vectors of the numerical integration are linear combinations of the original solution vectors $Z^{(1)}$ and $Z^{(3)}$, and it is necessary to "unravel" these combinations. Two well-known applications of orthonormalization have been given by Conte (1966) and by Scott and Watts (1977). The latter authors incorporated their method in the general purpose code SUPORT that has been used in several stability investigations. A different procedure from either of these was worked out for the JPL stability codes (1971), and is readily applicable to any order of differential equations.

4.4 Newton-Raphson search procedure

The Newton-Raphson method has been found to be satisfactory for obtaining the eigenvalues. The boundary condition on $Z^{(1)}$ (or $S^{(1)}$) is satisfied at the conclusion of each integration by a linear combination of the two solutions at y=0. In the spatial theory with ω and β fixed, the guess value of α_r is perturbed by a small amount and the integration repeated. Because $\hat{v}(0)$ is an analytic function of the complex variable α, the Cauchy-Riemann equations

$$\partial \hat{v}_i(0)/\partial \alpha_i = \partial \hat{v}_r(0)/\partial \alpha_r \ ,$$

$$\partial \hat{v}_r(0)/\partial \alpha_i = -\partial \hat{v}_i(0)/\partial \alpha_r \ ,$$

(4.3)

can be applied to eliminate the need for a second integration with α_i perturbed. We may note that $\hat{v}(0)$ is an analytic function of α even after orthonormalization with the usual definition of the scalar product, remarks to the contrary in the literature notwithstanding.

The corrections $\delta\alpha_r$ and $\delta\alpha_i$ to the initial guesses α_r and α_i are obtained from the residual $\hat{v}(0)$ and the numerical (linear) approximations to the partial derivatives by

$$[\partial\hat{v}_r(0)/\partial\alpha_r]\delta\alpha_r - [\partial\hat{v}_r(0)/\partial\alpha_i]\delta\alpha_i = -\hat{v}_r(0) \ ,$$

$$[\partial\hat{v}_i(0)/\partial\alpha_r]\delta\alpha_r - [\partial\hat{v}_i(0)/\partial\alpha_i]\delta\alpha_i = -\hat{v}_i(0) \ .$$

(4.4)

The corrected α_r and α_i are used to start a new iteration, and the process continues until $\delta\alpha_r$ and $\delta\alpha_i$ have been reduced below a preset criterion.

5. VISCOUS INSTABILITY

5.1 Kinetic-energy equation

The approach to instability theory based on the energy equation was originated by Reynolds (1895), and has proven to be especially helpful in the nonlinear theory. An extended account of recent work has been given by Joseph (1976). In the linear theory, the eigenmodes of the Orr-Sommerfeld equation already supply us with complete information on the instability characteristics of any flow, so the energy method is mainly useful as an aid to our physical understanding. We start by defining

$$e = (1/2)(u^2 + v^2)$$

(5.1)

to be the kinetic energy of a small 2D disturbance. When we multiply the dimensionless x and y parallel-flow momentum equations by u and v, respectively, and add, we obtain

$$(\frac{\partial}{\partial t} + U\frac{\partial}{\partial x})e + uv\frac{dU}{dy} = -u\frac{\partial p}{\partial x} - v\frac{\partial p}{\partial y} + \frac{1}{R}(u\nabla^2 u + v\nabla^2 v) \ .$$

(5.2)

If we integrate Eq. (5.2) from y=0 to infinity and average over a wavelength, we find, for a temporal disturbance,

$$\frac{\partial E}{\partial t} = \int_0^\infty \tau\frac{dU}{dy}dy - \frac{1}{R}\int_0^\infty \langle\zeta^2\rangle dy \ ,$$

(5.3)

where E is the total disturbance kinetic energy per wavelength, $\tau = -\langle uv\rangle$ is the Reynolds stress, and

$$\zeta = \partial u/\partial y - \partial v/\partial x$$

(5.4)

is the z-component of the fluctuation vorticity. A derivation of Eq. (5.3) may be found in the review article of Prandtl (1934, p. 180). The last term can be rewritten as

$$\int_0^\infty \langle\zeta^2\rangle dy = 2\int_0^\infty \langle\left(\frac{\partial u}{\partial x}\right)^2 + \left(\frac{\partial v}{\partial y}\right)^2\rangle dy + \int_0^\infty \langle\left(\frac{\partial u}{\partial y} + \frac{\partial v}{\partial x}\right)^2\rangle dy \ ,$$

(5.5)

which is more readily identified as the viscous dissipation. It is customary to write Eq. (5.3) as

$$\partial E/\partial t = \bar{P} - \bar{D} \ ,$$

(5.6)

where

$$\bar{P} = \int_0^\infty \tau(dU/dy)dy$$

(5.7a)

is the total energy production term over a wavelength, and

$$\bar{D} = \int_0^\infty \langle\zeta^2\rangle dy$$

(5.7b)

is the viscous dissipation. A disturbance will amplify, be neutral, or damp depending on whether P is greater than, equal to, or less than D. Consequently, there can only be instability if τ is sufficiently positive over enough of the boundary layer so that the production term can outweigh the dissipation term.

5.2 Reynolds stress in the viscous wall region

The inviscid theory gives the result that a flow with a convex velocity profile, of which the Blasius boundary layer is an example, can support only damped instability waves. Originally the prevailing view was that a flow that is stable in the absence of viscosity can only be more stable when viscosity is present. We see from Eq. (3.8) that in a Blasius boundary layer, where $D^2U<0$, a wave of any phase velocity less than the freestream velocity creates a positive Reynolds stress for $y<y_c$. Therefore, the only way an instability wave can exist is if viscosity causes a positive Reynolds stress to build up near the wall. It was this possibility that Taylor (1915) recognized, but his observation went unnoticed. A few years later Prandtl (1921) was led to the same idea, and calculated the Reynolds stress near the wall from a simple mathematical model.

It is of interest to note that Prandtl was moved to investigate the possibility of viscous instability by an experiment in which he saw, or thought he saw, amplifying instability waves in a flow that was supposed to be stable. In view of the importance of this discovery, we shall quote a few lines from his paper:

"Previous mathematical investigations on the origin of turbulence have led to the opinion that small disturbances of a viscous, laminar flow between two walls are always damped... In order to learn how turbulence actually originates, I had built at Göttingen an open channel...and observed the flow by the Ahlborn method (sprinkled lycopodium powder)... Wave forms with slowly increasing amplitude were occasionally observed... These waves of increasing amplitude contradicted the dogma of the stability of laminar motion with respect to small disturbances, so that at first I tended to believe that I had not seen this infrequent phenomenon completely right."

"We now applied ourselves to the theoretical treatment, and, to anticipate a little, we found, contrary to the dogma, an instability of the small disturbances."

Prandtl's argument was later refined by Lin (1954,1955), but we shall follow essentially the original derivation here. An inviscid wave is assumed to exist in the boundary layer, and viscosity to act only in a narrow region near the wall. To simplify the analysis, U(y) is taken to be zero in this region. With this assumption, the 2D dimensionless, parallel-flow x momentum equation simplifies to

$$\frac{\partial u}{\partial t} = -\frac{\partial p}{\partial x} + \frac{1}{R}\frac{\partial^2 u}{\partial y^2} , \qquad (5.8)$$

where the terms vDU and $\partial^2 u/\partial x^2$ have been dropped. Outside of the wall viscous region, Eq. (5.8) reduces

$$\frac{\partial u}{\partial t} = -\frac{\partial p}{\partial x} . \qquad (5.9)$$

The disturbance velocity u consists of two parts: an inviscid part u_i that satisfies Eq. (5.9), and a viscous part u_v that satisfies the difference between Eqs. (5.8) and (5.9). It is the total velocity $u=u_i + u_v$ that satisfies the no-slip boundary condition. Hence,

$$\frac{\partial u_v}{\partial t} = \frac{1}{R}\frac{\partial^2 u_v}{\partial y^2} . \qquad (5.10)$$

The solution of Eq. (5.10) for ω real is

$$u_v(y) = -u_i(0) \exp[-(1-i)(\omega R/2)^{1/2}y]\exp[i(\alpha x-\omega t)] , \qquad (5.11)$$

where the boundary conditions

$$u(0) = u_i(0) + u_v(0) \text{ and } u(y) \to u_i(y) \text{ as } y \to \infty \qquad (5.12)$$

have been applied.

The additional longitudinal disturbance velocity u_v, which is needed to satisfy the no-slip condition, induces, through the continuity equation, an additional normal disturbance velocity

$$v_v(y) = -\int_0^y (\partial u_v/\partial y)dy , \qquad (5.13)$$

which yields, upon substitution of Eq. (5.11),

$$v_v(y) = (1-i)\alpha u_i(0)[1/(2\omega R)^{1/2}]\{\exp[-(1-i)(\omega R/2)^{1/2}y]-1\}\exp[i(\alpha x-\omega t)] . \qquad (5.14)$$

Outside of the viscous region ($y\to\infty$) v_v is independent of y and u_v is zero. From Eq. (5.14),

$$v_v(\infty) = -(1-i)[\alpha u_i(0)/(2\omega R)^{1/2}]\exp[i(\alpha x-\omega t)] . \qquad (5.15)$$

The consequences of Eq. (5.15) for the Reynolds stress are as follows. For an inviscid neutral disturbance, u and v are 90° out of phase [see Eqs. (2.50a) and (2.50c)] and τ is zero. However, for any other disturbance u and v are correlated, and there is a Reynolds stress. Since u_v is zero outside of the wall viscous layer, it can contribute nothing to τ there. However, v_v persists for some distance outside of the wall layer, and since it is shifted 135° with respect to u, it will produce a Reynolds stress. This Reynolds stress must equal the Reynolds stress set up by the disturbance in the vicinity of the critical layer, and which, in the absence of viscosity, would extend to the wall. We have already derived a formula for this stress in Section 3.1 [Eq. (3.8)].

The formula for the Reynolds stress at the edge of the wall viscous region can be derived from Eq. (5.15). We find

$$\tau_e = -\langle u_i v_v \rangle = (1/2)[\alpha/(2\omega R)^{1/2}][u_i(0)]^2 . \qquad (5.16)$$

If the ratio $\tau_e/\langle v_v^2 \rangle$ is formed, we have

$$\tau_e/\langle v_v^2 \rangle = (1/2\alpha)(2/\omega R)^{1/2} . \qquad (5.17)$$

A general expression for τ in the wall viscous region can be obtained from Eqs. (5.11) and (5.14), and this expression would give the increase of τ from zero at the wall to the value given by Eq. (5.17) at the edge of the viscous region. However, Eq. (5.17) establishes the essential result that τ is positive, and thus viscosity acts as Taylor thought it would, and builds up a Reynolds stress to match the inviscid Reynolds stress, or, in Taylor's precise view, permits the momentum of the disturbance to be absorbed at the wall. According to Eq. (5.7a), with a positive stress energy will be transferred from the mean flow to the disturbance. Consequently, the wall viscous region, which is formed to satisfy the no-slip boundary condition for the disturbance, has the effect of creating a Reynolds stress which acts to destabilize the flow. This mechanism must be present to some extent for all disturbances, but whether a particular disturbance is actually amplified or damped will depend on the magnitude and distribution of the Reynolds stress through the entire boundary layer, and on the magnitude of the dissipation term.

As a note of caution, it must be recalled that the preceding analysis rests on the neglect of U in the wall viscous region. Therefore, we can expect the results to be valid only at high values of R, when the wall viscous region is thin compared to the boundary-layer thickness, and when the critical layer is outside of the wall viscous region.

6.   NUMERICAL RESULTS - 2D BOUNDARY LAYERS

In this Section, we shall present a number of numerical results which have been chosen to illustrate important aspects of the theory, as well as to give an idea of the numerical magnitudes of the quantities we have been discussing in the previous Sections.

6.1 Blasius boundary layer

The Blasius boundary layer, because of its simplicity, has received the most attention. The uniform external flow means that not only is the boundary-layer self similar, but there is only a single parameter, the Reynolds number. As there is no inflection point in the velocity profile, the only instability is viscous instability. Thus we are able to study this form of instability without the competing influence of any other mechanism of instability.

The first result of importance is the parallel-flow neutral stability curve for 2D waves, which is shown in Fig. 6.1 as three separate curves for: (a) the dimensionless frequency F [Eq. (2.60)]; (b) the dimensionless wavenumber α based on L^* [Eq. (2.57)]; and (c) the dimensionless phase velocity c based on U_1^*. Normal modes for which F, α and c lie on the curves are neutral; those for which F, α and c lie in the interior of the curves are unstable; everywhere else the normal modes are damped. The neutral-stability curves are a convenient means of identifying at each Reynolds number the F, α and c bands for which a wave is unstable. Figure 6.1a also contains two additional curves which give the frequencies of the maximum spatial amplification rate and of the maximum amplitude ratio A/A_0, where A_0 is the amplitude at the lower-branch neutral point of the frequency in question. Both maxima are with respect to frequency at constant Reynolds number. We have used σ in Fig. 6.1a to denote $-\alpha_i$, the spatial amplification rate in the streamwise direction, and will continue to do so in the remainder of this document. The corresponding wavenumbers for the additional curves are given in Fig. 6.1b. The ratio of wavelength to boundary-layer thickness is $2\pi/\alpha_r y_\delta$, and y_δ, the y [Eq. (2.59)] for which U = 0.999, is equal to 6.01. Consequently, the unstable waves at R = 1000 have wavelengths between $5.5\delta(19.4\delta^*)$ and $14.1\delta(49.2\delta^*)^1$. According to Fig. 6.1c, the unstable phase velocities at this Reynolds number are between $0.282U_1^*$ and $0.335U_1^*$.

We must keep in mind that the neutral curves of Fig. 6.1 have been calculated from the quasi-parallel theory, which does not distinguish between flow variables or location in the boundary layer. All of the non-parallel neutral curves calculated by Gaster (1974) define a slightly greater unstable zone, with the greatest differences coming at the lowest Reynolds numbers as might be expected. The difficulties involved in making accurate measurements of wave growth at low Reynolds numbers have so far precluded the experimental determination of what can be regarded as an unequivocally "correct" neutral-stability curve for any flow variable.

The next quantity to examine is the dimensionless spatial amplification rate σ based on L^*. This amplification rate is shown in Fig. 6.2 for 2D waves as a function of the dimensionless frequency F at the two Reynolds numbers R = 600 and 1200. From the definition of the amplification rate in Eq. (2.27), the fractional change in amplitude over a distance equal to one boundary-layer thickness is σy_δ. Thus the most unstable wave of frequency $F = 0.33 \times 10^{-4}$ at R = 1200 grows by 4.0% over a boundary-layer thickness. The amplification rate based on ν^*/U_1^*, $\hat{\sigma} = \sigma/R$, gives the fractional wave growth over a unit increment in Re. Thus this same wave grows by 5.6% over an increment in Re of 10,000.

The maximum amplification rates σ_{max} and $\hat{\sigma}_{max}$, where the maxima are with respect to frequency (or wavenumber) at constant Reynolds number, are shown in Fig. 6.3 as functions of Reynolds number. The amplification rate $\hat{\sigma}$, which gives the wave growth per unit of Reynolds number, peaks at the low Reynolds number of R = 630. The amplification rate σ, which is proportional to the wave growth per boundary-layer thickness, does not peak until R = 2740 [calculated by Kümmerer (1973)]. The dimensional amplification rate is proportional to $\hat{\sigma}$ for a fixed unit Reynolds number. Figure 6.3 shows that the decline in the dimensional amplification rate with increasing x-Reynolds number is almost counteracted by the increase in the boundary-layer thickness. Viscous instability, if characterized by σ, persists to extremely high Reynolds numbers. However, if the measure of viscous instability is taken to be the wave growth over a fixed x^* increment as expressed by $\hat{\sigma}$, then by this criterion the maximum viscous instability occurs at low Reynolds number.

The logarithm of the amplitude ratio, A/A_0, is shown in Fig. 6.4 for 2D waves as a function of R for a number of frequencies F. The envelope curve, which gives the maximum amplitude ratio possible at any Reynolds number, is also shown in the figure along with the corresponding frequencies. It is this type of diagram that is used in engineering studies of boundary-layer transition. When $\ln(A/A_0)$, which is often called the N factor, reaches some predetermined value, say nine as suggested by Smith and Gamberoni (1956), or ten as suggested by Jaffe, Okamura and Smith (1970), transition is considered to take place, or at least to start.

The distribution of the logarithm of the amplitude ratio with frequency is shown in Fig. 6.5 for several Reynolds numbers. This figure illustrates the filtering action of the boundary layer. The simultaneous narrowing of the bandwidth of unstable frequencies and the large increase in amplitude ratio as the Reynolds number increases means that an initial uniform power spectrum of instability waves tends to a spectrum at high Reynolds numbers that has a sharp peak at the most amplified frequency. The inset in Fig. 6.5 gives the bandwidth, defined as the frequency range over which the amplitude ratio is within 1/e of the peak value, as a function of Reynolds number.

---

1. δ is the dimensional boundary-layer thickness, y_δ is the dimensionless boundary-layer thickness δ/L^*, and, in accord with the standard notation, δ^* is the dimensional displacement thickness.

The Squire theorem (Section 2.4.1) has told us that it is a 2D wave that first becomes unstable. Furthermore, at any Reynolds number it is a 2D wave that has the maximum amplification rate and also the maximum amplitude ratio. Thus the envelope curve of amplitude ratio when all oblique waves are considered as well as 2D waves is still as shown in Fig. 6.4 However, for a given frequency the 2D wave is not necessarily the most unstable, as is shown in Fig. 6.6. In this figure, the spatial amplification rate σ, calculated with $\bar{\psi} = 0$, is plotted against the wave angle ψ for three frequencies at R = 1200. At this Reynolds number, the maximum amplification rate occurs for $F = 0.33 \times 10^{-4}$. Above this frequency, 2D waves are certainly the most unstable. However, below about $F = 0.26 \times 10^{-4}$ an oblique wave is the most unstable, and the wave angle of the maximum amplification rate increases with decreasing frequency.

In the calculations for Fig. 6.6, the complex wavenumber was obtained as a function of the spanwise wavenumber β_r with $\beta_i = 0$ and the frequency real and constant. Thus the complex group-velocity angle ϕ can be readily obtained from $\partial\alpha/\partial\beta_r$ $(= -\tan\phi)$, and the results are given in Fig. 6.7 for $F \times 10^4 = 0.20$ and 0.30. The real part of ϕ is limited to less than 10°, and ϕ_i can be either plus or minus. It is evident that at the maximum of σ, where $\partial\alpha/\partial\beta_r$ is real, ϕ_i must be zero. With the group-velocity angle known, the accuracy of the simple relation Eq. (2.35) for σ as a function of ψ can be checked. We choose $F = 0.20 \times 10^{-4}$ and $\psi = 45^\circ$ in order to have ϕ real. Table 6.1 gives k, the wavenumber; $\bar{\sigma}$, the amplification rate parallel to $\bar{\psi}$ (both of these are calculated as an eigenvalue); $\sigma(\bar{\psi})$, the component of $\bar{\sigma}$ in the x direction for the specified $\bar{\psi}$; and $\sigma(0)$, the amplification rate in the x direction for $\bar{\psi} = 0$ as calculated from Eq. (2.41c), the spatial-theory replacement for the Squire transformation derived from Eq. (2.35), but with ψ replaced by $\bar{\psi}$. In the latter calculation we have used $\phi_r = 9.65^\circ$, the value obtained with $\bar{\psi} = 0$. The transformation works very well; the small discrepancies from the correct $\bar{\psi} = 0$ value are due to ϕ_r being a weak function of $\bar{\psi}$ instead of constant as assumed in the derivation.

Table 6.1 Effect of $\bar{\psi}$ on amplification rate and test of transformation rule. $F = 0.20 \times 10^{-4}$, R = 1200, $\psi = 45^\circ$.

$\bar{\psi}$	k	$\bar{\sigma} \times 10^3$	$\sigma(\bar{\psi}) \times 10^3$ eigenvalue	$\sigma(0) \times 10^3$ transformation
0.0	0.1083	3.201	3.201	3.201
9.7	0.1083	3.156	3.111	3.201
15.0	0.1083	3.170	3.062	3.201
30.0	0.1083	3.368	2.916	3.203
45.0	0.1083	3.873	2.739	3.204
60.0	0.1083	4.955	2.478	3.207
75.0	0.1083	7.601	1.967	3.216

We observe in Table 6.1 that the real Squire transformation, which is the $\sigma(\bar{\psi})$ entry for $\bar{\psi} = \psi$, is in error by 14.4%, whereas the correct transformation is in error by only 0.1%. When the same calculation is repeated for the other frequency of Fig. 6.7, $F = 0.30 \times 10^{-4}$, for which $\phi_i = -2.48^\circ$ at $\psi = 45^\circ$ instead of 0° as for the frequency of the Table, equally good results are obtained for $\sigma(0)$ from the transformation. However, k is no longer constant, but increases with $\bar{\psi}$; for $\bar{\psi} = 75^\circ$ it is 0.4% larger than at $\bar{\psi} = 0^\circ$. Nayfeh and Padhye (1979) provide a formula for this change.

In Fig. 6.8, $\ln(A/A_0)$ is given at several Reynolds numbers for $F = 0.20 \times 10^{-4}$ as calculated with the irrotationality condition, Eq. (2.64), applied to the wavenumber vector. The abscissa is the initial wave angle at R = 900. The change in the wave angle from R = 900 to 1900 is 1.7° for the wave that has an initial wave angle of 45°. This figure shows that the greater amplification rate of oblique waves in the instability region near the lower branch of the neutral curve translates into an amplitude ratio that is greater than the 2D value. However, $\ln(A/A_0)$ for an oblique wave is never more than 0.35 greater than the 2D value. Figure 6.8 also shows that just as the frequency bandwidth narrows with increasing R, so does the bandwidth in spanwise wavenumber. Although at the lower Reynolds numbers the response extends to large wave angles, at R = 1900 the amplitude ratio is down to 1/e of its 2D value at $\psi = 37^\circ$, and on the envelope curve this angle will be still smaller. For example, the 1/e amplitude for $F = 0.60 \times 10^{-4}$ at the envelope-curve Reynolds number (R = 900) occurs at $\psi = 29^\circ$; for $F = 0.30 \times 10^{-4}$, at $\psi = 26^\circ$. Even so, it is necessary when thinking about wave amplitudes in the boundary layer to keep in mind that both a frequency band and spanwise-wavenumber band must be considered, not just a 2D wave.

So far we have only been considering the eigenvalues and not the eigenfunctions. The eigenfunctions give the possibility of penetrating further into the physics of instability, and we shall take them up briefly at this point. Eigenfunctions are readily obtained with any of the current numerical methods, but were difficult to compute with the old asymptotic theory. The first eigenfunctions were obtained by Schlichting (1935), and the good agreement of the measurements of Schubauer and Skramstad (1947) with these calculations was a key factor in establishing the validity of the linear stability theory. The problem now is more one of finding a reasonable way to present the great mass of numerical data that can be computed, and to extract useful information from this data. Some progress has been made in the latter direction by Hama, Williams and Fasel (1980). For different amplitudes of 2D waves, these authors calculated streamline pattens, contours of constant total vorticity, Reynolds stress and all terms of the local spatial energy balance.

Figure 6.9 gives the amplitude of the eigenfunction $\hat{u}$ of the streamwise velocity fluctuation u at R = 800, 1200 and 1600 for the 2D wave of frequency $F = 0.30 \times 10^{-4}$. The corresponding phases are given in Fig. 6.10. As may be seen from Fig. 6.1a, these Reynolds numbers are, respectively, just below the lower branch of the neutral-stability curve, near the maximum of σ, and on the envelope curve of the amplitude ratio. The eigenfunction normalization of Figs. 6.9 and 6.10 is $\hat{p}(0) = (2^{-1/2}, 0)$. The eigenfunctions have not been renormalized to, say, a constant peak amplitude as is often done, in order to emphasize that in the quasi-parallel theory the normalization is completely arbitrary. Nothing can be learned as to the

effect of the variability of the eigenfunction with Reynolds number on the wave amplitude within the framework of this theory. Attempts have been made to do this, and plausible looking results obtained, but this approach is without theoretical justification. It has already been pointed out in Section 2.2 that the meaningful quantity for the amplitude modulation is the product of $A(x_1)$ and the eigenfunction, and this product, which has a fixed value regardless of the normalization of the eigenfunction, can only be calculated from the nonparallel theory.

For the wave of Fig. 6.9, the critical layer is at about y = 0.15 and varies only slightly with Reynolds number. Thus the location of the amplitude peak, which is a strong function of R, is only coincidentally at the critical point. As R increases, the viscous layer near the wall becomes thinner as expected. The characteristic phase change of approximately 180° in the outer part of the boundary layer has nothing to do with the 180° phase change at the critical layer in the inviscid solution [Eq. (3.9b)], but is a kinematical consequence of a wave with zero amplitude at both the wall and at $y \rightarrow \infty$. At some y_m greater than the y of maximum amplitude, where viscosity has little influence, the slope of the streamlines relative to the phase velocity has a maximum. Thus the velocity-streamtube area relation changes sign, and at all $y > y_m$ the u fluctuation from this effect is opposite in sign to the fluctuation that arises from the wavy motion in a monotonically increasing velocity profile. At some $y_b > y_m$, these two effects can exactly balance for a neutral inviscid wave, and almost balance for nonneutral, viscous waves. For the latter, as shown in Fig. 6.10, there is a nearly 180° shift in the phase of $\hat{u}$. The fact that the phase can either advance or retreat in this region was first noted by Hama et al (1980), and its significance, if any, is unknown.

It was shown in Section 5.1 that the kinetic energy of a 2D instability wave is produced by the term $\tau dU/dy$, where τ is the Reynolds stress built up by the action of viscosity. Reynolds stress distributions have been given by Jordinson (1970) and Kümmerer (1973), among others. The energy production term is shown in Fig. 6.11 for the frequency and three Reynolds numbers of Figs. 6.9 and 6.10. The peak production does not occur at the critical layer at any of the three Reynolds numbers. We see that energy production is by no means limited to the region between the wall and the critical layer, as might be expected from the simple theory of Section 5. At R = 1200, where the amplification rate is near its maximum, there is significant energy production over about half of the boundary-layer thickness. In these examples, the Reynolds stress is positive except for the slightly dampled wave at R = 800, where there is a small negative contribution over the outer 70% of the boundary layer. The damping at R = 800 is due to viscous dissipation, not to a negative production term. Hama et al (1980) give an example at low Reynolds number where the production term is negative over the entire boundary layer.

6.2 Falkner-Skan boundary layers

The influence of pressure gradient on boundary-layer stability can be studied conveniently by means of the Falkner-Skan family of self-similar boundary layers, where the Hartree parameter β_h [Eq. (2.62)] serves as a pressure-gradient parameter. The range of β_h is from -0.19883774 (separation profile) through 0 (Blasius profile) to 1.0 (2D stagnation-point profile). Extensive numerical calculations for Falkner-Skan profiles have been carried out by Wazzan, Okamura and Smith (1968; see also Obremski et al. (1969)], and by Kümmerer (1973). Figure 6.12, taken from Mack (1978), gives the influence of β_h on the N-factor envelope curve. It is clear that a favorable pressure gradient ($\beta_h > 0$) stabilizes the boundary layer, and an adverse pressure gradient ($\beta_h < 0$) destabilizes it. The strong instability for adverse pressure gradients is caused by an inflection point in the velocity profile that moves away from the wall as β_h becomes more negative. The adverse pressure gradient Falkner-Skan boundary layers are particularly instructive because they provide us with examples of boundary layers with both viscous and inflectional instability.

The amplification rate $\hat{\sigma}$ is unsuitable for studying inflectional instability, which is basically an inviscid phenomenon, as it is zero at $R \rightarrow \infty$ regardless of whether the boundary layer is stable or unstable in the inviscid limit. The calculations of Kümmerer (1973) include both σ and $\hat{\sigma}$ and show that the maximum amplification rate σ_{max} moves from R = 2740 for the Blasius boundary layer to $R \rightarrow \infty$ as β_h decreases from zero. When σ_{max} is at $R \rightarrow \infty$, which occurs before β_h reaches the separation value, we can say that the boundary layer is dominated by inflectional instability. In these cases, viscosity acts primarily to damp out the disturbances just as envisioned by the early investigators. When we take up compressible boundary layers in Part B, we shall encounter another example where the dominant instability changes from viscous to inflectional as a parameter (the freestream Mach number) varies.

The frequencies along the envelope curves of Fig. 6.12 are given in Fig. 6.13. We may observe that in boundary layers with favorable pressure gradients, where viscous instability is the only source of instability, it is low frequency waves which are the most amplified. On the contrary, for boundary layers with adverse pressure gradients, where inflectional instability is dominant, it is high-frequency waves which are the most amplified.

In a natural disturbance environment, a wide spectrum of normal modes may be expected to exist in the boundary layer. It is helpful to know the sharpness of the response in estimating when the disturbance amplitude is large enough to initiate transition. A measure of this quantity is given in Fig. 6.14, where a frequency bandwidth of the 2D waves along the envelope curve, expressed as a fraction of the most amplified frequency, is shown for the Falkner-Skan family. This bandwidth is not identical to the one in the inset of Fig. 6.5, as it gives only the frequency range less than the most amplified frequency for which the amplitude ratio is within 1/e of the peak value. The filtering action of the boundary layer is again evident in the narrowing of the bandwidth with increasing Reynolds number for a given boundary layer, and we see that the more unstable adverse pressure-gradient boundary layers have the strongest filtering action.

6.3 Non-similar boundary layers

The self-similar boundary layers are useful for illustrating basic instability mechanisms, but in practice boundary layers are non-similar. A computer code to perform stability calculations for non-similar boundary layers is more complicated than for self-similar boundary layers, but only because of the

necessity of calling up a different velocity profile at each Reynolds number, or of interpolating between different profiles. The stability calculations themselves are the same as in any Reynolds number dependent boundary layer. The eigenvalues are calculated as a function of Reynolds number, and then can be subsequently used to calculate N factors, or for any other purpose, exactly as if the boundary layer were self-similar. Such calculations have been done on a routine basis as least as far back as the paper of Jaffe, Okamura and Smith (1970).

6.4 Boundary layers with mass transfer

Suction stabilizes a boundary layer, and blowing destabilizes it. This result was established by the early investigators, and extensive stability calculations were carried out with the asymptotic theory. Suction can stabilize a boundary layer with or without an inflection point. The stability mechanism is similar to the action of a pressure gradient. Suction gives a "fuller" velocity profile, just as does a favorable pressure gradient; blowing gives a velocity profile with an inflection point, just as does an adverse pressure gradient. Suction is the primary method proposed for laminar flow control on aircraft, where it has been investigated mainly in connection with three-dimensional boundary layers. A summary account of early work on this subject may be found in the book of Schlichting (1979). More recent work is primarily associated with Pfenninger, and a summary account of the vast body of work on this subject carried out by him and his co-workers may be found in the Lecture Notes of an AGARD/VKI Special Course [Pfenninger (1977)].

6.5 Boundary layers with heating and cooling

Heating an air boundary layer destabilizes it, and cooling stabilizes it. The proper calculation of this effect requires the compressible stability theory which is given in Part B. An example for a low-speed boundary layer may be found in Section 10.3.

For a water boundary layer, the effect is the opposite, and heating the wall has been extensively studied as a means of stabilization. This mechanism of stabilization is solely through the effect on the viscosity, and can be studied with the incompressible stability theory provided only that the viscosity is taken to be a function of temperature. The initial work on this subject was by Wazzan, Okamura and Smith (1968b).

6.6 Eigenvalue spectrum

An arbitrary disturbance cannot be represented by a single normal mode, or by a superposition of normal modes. These modes represent only a single member of an entire eigenvalue spectrum, and it is this spectrum that is required for an arbitrary disturbance. It can be proved that for a bounded shear flow, such as plane Poiseuille flow, the eigenvalue spectrum is discrete and infinite [Lin (1961)]. That is, for a given wavenumber and Reynolds number, there is an infinite discrete sequence of complex frequencies whose eigenfunctions satisfy the boundary conditions. Each element of the sequence constitutes a mode. This is the more precise meaning of the term mode; what we have called the normal modes all belong to the first, or least stable, of these more general modes. To distinguish between the two usages of the term mode, we shall refer to the discrete sequence as the viscous modes. Only the first viscous mode can be unstable; all of the others are heavily damped, which is the reason why they are unimportant in almost all practical stability problems. Calculations of the discrete temporal eigenvalue spectrum of plane Poiseuille flow have been carried out by Grosch and Salwen (1968), Orszag (1971), and Mack (1976).

It was long believed that the eigenvalue spectrum of boundary-layer flows is also discrete. However, a calculation by Jordinson (1971) for a single value of α and R uncovered only a finite discrete spectrum for the Blasius boundary layer. These calculations were in some error numerically, but a later investigation by Mack (1976), which worked out the correct temporal spectrum, confirmed the conclusion of Jordinson. As shown in Fig. 6.15, at $\alpha = 0.179$, R = 580, the case considered by Jordinson, there are only seven viscous modes. Mode 1 is amplified; Modes 2-7 are strongly damped. In Fig. 6.15, the eigenvalues are shown in complex c space, rather than ω space, because $c_r = 1.0$ has a special significance in this problem.

Although the number of discrete modes is a function of both wavenumber and Reynolds number, the number remains finite and comparatively small. It was shown by Mack (1976) on the basis of numerical examples with finite-width channels in which the upper boundary moved to $y \to \infty$, and with polynomial velocity profiles of various orders, that both the semi-infinite flow interval and the continuity of the velocity profile at the edge of the boundary layer, are responsible for the non-existence of the infinite part of the discrete spectrum of bounded flows. As a finite discrete spectrum is still unable to represent an arbitrary disturbance, where are the missing eigenvalues?

It is a not uncommon occurrence in eigenvalue problems to have only a finite discrete spectrum. The remaining part of the spectrum is then a continuous spectrum. An example is the inviscid stability equation, which has a continuous spectrum associated with the singularity at the critical layer. It was already suggested by Jordinson (1971) that the discrete viscous spectrum is supplemented by a continuous spectrum along the $c_r = 1$ axis. The proof by Lin (1961) that a viscous continuous spectrum cannot exist for a bounded flow does not apply to an unbounded flow. Mack (1976) supported Jordinson's expectation by means of a few numerical calculations of continuous-spectrum eigenvalues, and also showed that the continuous spectrum is always damped because of the restriction $c_i < -\alpha/R$. A more complete and definitive study of the continuous spectrum was subsequently carried out by Grosch and Salwen (1978), who are responsible for clarifying many aspects of this problem. Also a paper by Murdock and Stewartson (1977) must be mentioned. Results for the discrete spatial spectrum of the Blasius boundary layer have been given by Corner, Houston and Ross (1976).

7. HARMONIC POINT SOURCES OF INSTABILITY WAVES

7.1 General remarks

In the previous Sections, we have been considering the behavior of the individual normal-mode solutions of the linearized, quasi-parallel stability equations. This primary attention to the normal modes has been the usual course in most theoretical and experimental work on boundary-layer stability. The fundamental stability experiments of Schubauer and Skramstad (1947) in low-speed flow, and of Kendall (1967) in high-speed flow were both designed to produce a particular normal mode. Even the much used e^N method of transition prediction is based on the amplitude ratio of the most amplified normal mode. In most actual flow situations, however, a spectrum of instability waves is present. If the boundary layer were truly parallel, the most unstable mode would eventually be the dominant one, and all of the other modes would be of negligible importance. As boundary layers found in practice are not parallel, the changing Reynolds number means that the identity of the most unstable mode also changes as the wave system moves downstream, and no single mode can grow indefinitely. Disturbance energy will always be distributed over a finite bandwidth. If the modes all come from a single source, or are otherwise phase related, then interference effects will cause the evolution of the wideband amplitude to further depart from the amplitude evolution of a single normal mode. This difference was vividly demonstrated in the experiment of Gaster and Grant (1975), where the amplitude at the center of a wave packet produced by a pulsed point source changed little with increasing distance from the source, even though the amplitude of the most amplified normal mode was increasing several times.

The wave-packet problem was treated first by Criminale and Kovasnay (1962) and by Gaster (1968). Neither the straight wave fronts of the former, nor the caustic of the latter, were observed experimentally, because in each case approximations that were needed to produce numerical results turned out not to be valid. Later, Gaster (1975) obtained results in good agreement with experiment by replacing the method of steepest descent used earlier by direct numerical integration. He was also able to demonstrate the validity of the method of steepest descent for a 2D wave packet in a strictly parallel flow by exact calculation of the necessary eigenvalues [Gaster (1981b,1982a)]. Finally, he showed how to extend this method to a growing boundary layer [Gaster (1981a,1982b)], where the mean flow downstream of the source is a function of Reynolds number.

In this Section, we shall examine a simpler problem than the wave packet, namely the stationary wave pattern produced by a harmonic point source. This wave motion has the same number of space dimensions as a 3D wave packet, but is really a 2D wave propagation problem that is closely related to Gaster's 2D wave packets. The propagation space here is x,z, the plane of the flow, rather than x,t as in the latter problem. The fact that the wave motion is two dimensional makes it possible to obtain detailed numerical results both by numerical integration and by Gaster's (1981a,1982b) extension of the method of steepest descent for a growing boundary layer [Mack and Kendall (1983)]. In the point-source problems, no attempt is made to find a complete mathematical solution. Instead it is merely assumed, following Gaster (1975), that the source produces a continuous spectrum of the least stable normal modes. For a pulsed 2D (line) source, the spectrum is over frequency; for a pulsed 3D (point) source, the spectrum is over frequency and spanwise wavenumber; for a harmonic point source, the spectrum is over spanwise wavenumber. It is usually, but not always, assumed that the spectral densities are uniform ("white noise" spectra).

The solution for a harmonic point source is obtained by evaluating the integral for the complex amplitude over all possible spanwise wavenumbers. The most straightforward method is to use direct numerical integration; a second method is to evaluate the integral asymptotically by the method of steepest descent as was done for parallel flows by Cebeci and Stewartson (1980a,1980b), and, in more detail, by Nayfeh (1980a,1980b). Some numerical results for Blasius flow were cited by Cebeci and Stewartson (1980b), but within the framework of the e^N method of transition prediction. Only the exponential term of the amplitude was evaluated, and the saddle-point condition was the one for parallel flow.

Experiments on the harmonic point source have been carried out by Gilev, Kachanov and Kozlov (1981), and by Mack and Kendall (1983). In these experiments, extensive hot-wire measurements of amplitude and phase were made in the downstream and spanwise directions in a Blasius boundary layer. In Gilev et al. (1981), a Fourier analysis of the data yielded the oblique normal modes, but no comparisons with theory were made. One significant result was the mapping out of the lines of constant phase in the x,z plane as shown in Fig. 7.1. At least three distinct regions can be identified in this figure. Close to the source, the curvature is convex, and far away it is concave. In an intemediate region, a "dimple" appears at the center line. A region of concave curvature gradually extends outward to encompass the entire outer portion of the wave pattern, while the dimple spreads, flattens and finally disappears. All of these features are duplicated in the wave pattern calculated by numerical integration [Mack and Kendall (1983)].

Figure 7.1 shows that there is a maximum inclination of each constant-phase line that is much less than the maximum wave angle of unstable normal modes. This feature follows directly from the method of steepest descent, where the saddle-point condition limits the Reynolds-number dependent maximum wave angle to $40°$-$45°$. This restriction was noted in unpublished calculations by Mack and by Padhye and Nayfeh (private communication), as well as by Cebeci and Stewartson (1980b).

In the quasi-parallel theory, amplitude is defined as the integral of the spatial amplification rate, and is not identified with any particular flow variable or distance y from the wall. In the Gaster-Grant (1975) experiment, amplitude was measured at the outer peak of the amplitude distribution; in Gilev et al. (1981) at a fixed y^*/δ in the boundary layer, and also at a fixed y^* just outside of the boundary layer; and in Mack and Kendall (1983), at the inner peak of the amplitude distribution. A comparison of the calculated amplitudes with the measurements thus demonstrates whether the amplitude of the quasi-parallel theory has any relevance to point-source problems. Exact correspondence can hardly be expected, if for no other reason than the fact that the disturbance energy is distributed over an ever increasing boundary-layer thickness as the waves move downstream.

The integral over all spanwise wavenumbers for the dimensional velocity fluctuation u_t (the subscript t denotes time dependence) from a source of frequency ω^* located at x_s^*, z_s^* is

$$u_t^*(x^*,z^*,t^*) = \exp(-i\omega^* t^*)\int_{-\infty}^{\infty} g^*(\beta^*)\exp[i\chi(\beta^*;x^*,z^*)]d\beta^* , \quad (7.1)$$

where $g^*(\beta^*)$ is the (complex) amplitude distribution function of dimensions velocity x length, the frequency is real,

$$\chi(x^*,z^*) = \int_{x_s^*}^{x^*} \alpha^*(x^*;\beta^*,\omega^*)dx^* + \beta^*(z^*-z_s^*) \quad (7.2)$$

is the time-independent part of the phase, and the wavenumber components α^* and β^* are complex. The eigenfunctions are ignored so that u_t is independent of y^*, and u_t could equally well be considered as any other flow variable. This integral will be evaluated below by direct numerical integration, and by an adaptation of Gaster's (1981a,1982b) asymptotic method.

7.2 Numerical integration

We place the source at $z_s^* = 0$, drop the time factor, and define the dimensionless variables

$$\hat{\alpha} = \alpha^* \nu^*/U_1^* , \qquad \hat{\beta} = \beta^* \nu^*/U_1^* ,$$

$$\hat{x} = U_1^* x^*/\nu^* , \qquad \hat{z} = U_1^* z^*/\nu^* , \quad (7.3)$$

$$u = u^*/U_1^* , \qquad g = 2\pi g^*/\nu^* ,$$

where u^* is the time-independent part of u_t^*, and the reference velocity is the freestream velocity U_1^*. We have chosen the inverse unit Reynolds number ν^*/U_1^* as the reference length so that $\hat{\beta}$, as well as $\hat{\beta}$ will satisfy the irrotationality condition in the simplest form, Eq. (2.56). With these choices, the dimensionless $\hat{x}$ and $\hat{z}$ are the usual x and z Reynolds numbers. The reason for the normalization constant 2π in the definition of g will appear in Section 7.4. With the definitions of Eqs. (7.2), Eq. (7.1) becomes

$$u(\hat{x},\hat{z};F) = (1/2\pi)\int_{-\infty}^{\infty} g(\hat{\beta})\exp[i\chi(\hat{\beta};\hat{x},\hat{z})]d\hat{\beta} . \quad (7.4)$$

With $z_s^* = 0$, the phase is

$$\chi(\hat{\beta};\hat{x},\hat{z}) = \int_{\hat{x}_s}^{\hat{x}} \hat{\alpha}d\hat{x} + \hat{\beta}\hat{z} . \quad (7.5)$$

We take $\hat{\beta}$ to be real for convenience, which means that we are going to sum over spatial normal modes of the type we have been using all along. If we write

$$\chi = \chi_{xr} + i\chi_i + \hat{\beta}\hat{z} , \quad (7.6a)$$

where

$$\chi_{xr} = \int_{\hat{x}_s}^{\hat{x}} \hat{\alpha}_r d\hat{x} , \qquad \chi_i = \int_{\hat{x}_s}^{\hat{x}} \hat{\alpha}_i d\hat{x} , \quad (7.6b)$$

the real and imaginary parts of u are

$$u_r(\hat{x},\hat{z}) = (1/\pi)\int_0^{\pi} g(\hat{\beta})\exp(-\chi_i)\cos\chi_{xr}\cos(\hat{\beta}\hat{z})d\hat{\beta} , \quad (7.7a)$$

and

$$u_i(\hat{x},\hat{z}) = (1/\pi)\int_0^{\pi} g(\hat{\beta})\exp(-\chi_i)\sin\chi_{xr}\cos(\hat{\beta}\hat{z})d\hat{\beta} . \quad (7.7b)$$

We have taken advantage of the symmetry in $\hat{\beta}$ of $g(\hat{\beta})$, χ_{xr} and χ_i to restrict the interval of integration to the positive $\hat{\beta}$ axis. Equations (7.7) are the specific integrals to be evaluated by numerical integration. It is convenient to present the numerical results in terms of the peak, or envelope, amplitude

$$A(\hat{x},\hat{z}) = (u_r^2 + u_i^2)^{1/2} , \quad (7.8a)$$

and the local phase

$$\theta(\hat{x},\hat{z}) = \tan^{-1}(u_i/u_r) . \quad (7.8b)$$

Both of these quantities can be measured experimentally.

The numerical integration of Eqs. (7.7) proceeds as follows: With the dimensionless frequency F equal to the frequency of the source, the phase integrals χ_{xr} and χ_i of Eq. (7.6b) are evaluated as functions of $\hat{x}$ with constant $\hat{\beta}$ for a band of spanwise wavenumbers from the eigenvalues $\hat{\alpha}(\hat{x};\hat{\beta},F)$. The Fourier cosine integrals are evaluated at enough $\hat{z}$ stations at each $\hat{x}$ to resolve the wave pattern. Highly oblique waves are damped, with the damping rate increasing with increasing obliquity. Consequently, the integrals of Eq. (7.7) will always converge for $\hat{x} > \hat{x}_s$ if large enough values of $\hat{\beta}$ are used. At $\hat{x} = \hat{x}_s$, $\chi = \hat{\beta}\hat{z}$ and $g(\hat{\beta})$ is the Fourier cosine transform of $u_r(\hat{z})$. In particular, if $g(\hat{\beta}) = 1$, then u_r is a δ-function in $\hat{z}$; if $g(\hat{\beta})$ is a Gaussian, then so is u_r.

7.3 Method of steepest descent

The method of numerical integration is straightforward, but requires the evaluation of a few hundred eigenvalues for good resolution of the wave pattern. A different approach is to evaluate the integral of Eq. (7.4) asymptotically by the method of steepest descent, or saddle-point method. This method allows

certain results to be obtained with fewer calculations, and also has the advantage that the dominant wave at each $\hat{x},\hat{z}$ seems to correspond directly to what is observed.

Equation (7.4), with $g(\hat{\beta}) = 1$, is written

$$u(\hat{x},\hat{z}) = \lim_{\hat{x}\to\infty} (1/2\pi)\int_C \exp[(\hat{x}-\hat{x}_s)\Phi(\hat{\beta})]d\hat{\beta} \quad , \tag{7.9}$$

where C is the contour of steepest descent in the complex $\hat{\beta}$ plane, and

$$(\hat{x}-\hat{x}_s)\,\Phi = i\int_{\hat{x}_s}^{\hat{x}} \hat{\alpha}(\hat{x};\hat{\beta})d\hat{x} + i\hat{\beta}(\hat{x}-\hat{x}_s) \quad . \tag{7.10}$$

The limit $\hat{x}\to\infty$ is taken with $\hat{z}/(\hat{x}-\hat{x}_s)$ held constant. The condition for the saddle point $\hat{\beta}_c$ is

$$\partial\Phi/\partial\hat{\beta} = 0 \quad , \tag{7.11}$$

which is equivalent to the two real conditions

$$\int_{\hat{x}_s}^{\hat{x}} (\partial\hat{\alpha}/\partial\hat{\beta})_r d\hat{x} = -\hat{z} \quad , \tag{7.12a}$$

$$\int_{\hat{x}_s}^{\hat{x}} (\partial\hat{\alpha}/\partial\hat{\beta})_i d\hat{x} = 0 \quad . \tag{7.12b}$$

These integrals are evaluated with the complex $\hat{\beta}$ held constant, so that we are dealing with spatial waves that satisfy the generalized irrotationality condition of kinematic wave theory.

The saddle-point conditions of Eq. (7.12) are of the same type as introduced by Gaster (1981a,1982b) for a 2D wave packet in a growing boundary layer. Usually the saddle-point method is applied to problems where the wave-propagation medium (here the boundary layer) is independent of $\hat{x}$, but Gaster demonstrated the correctness of the present procedure when the medium is a function of $\hat{x}$. In a strictly parallel flow, the boundary layer meets the more restricted requirement of $\hat{x}$ independence, and the saddle-point conditions simplify to

$$(\partial\hat{\alpha}/\partial\hat{\beta})_r = -\hat{z}/(\hat{x}-\hat{x}_s) \quad , \tag{7.13a}$$

$$(\partial\hat{\alpha}/\partial\hat{\beta})_i = 0 \quad . \tag{7.13b}$$

For a constant-frequency wave,

$$(\partial\hat{\alpha}/\partial\hat{\beta}) = -(\partial\omega/\partial\hat{\beta})/(\partial\omega/\partial\hat{\alpha}) = -\tan\phi \quad , \tag{7.14}$$

where ϕ is the complex angle of the group-velocity vector, and we see that the parallel-flow saddle-point condition is equivalent to requiring the group-velocity angle to be real. Consequently, the observed wave pattern in a parallel flow consists of waves of constant complex spanwise wavenumber $\hat{\beta}_c$ moving along group-velocity trajectories in the real $\hat{x},\hat{z}$ plane. This saddle-point condition has been applied to a growing boundary layer by Cebeci and Stewartson (1980a,1980b) and by Nayfeh (1980a,1980b). This procedure can yield satisfactory results in a restricted region of the $\hat{x},\hat{z}$ plane, but cannot be valid everywhere as the correct asymptotic representation of Eq. (7.9) is in terms of Eq. (7.12) saddle points rather than Eq. (7.18) saddle points. The "rays" defined by Eq. (7.12) are not physical rays in the usual sense. For a complex $\hat{\beta}_c$ that satisfies Eq. (7.12), $\hat{z}$ is complex at all $\hat{x}>\hat{x}_s$ except at the final, or observation, point. The trajectory that is traced out in the $\hat{x},\hat{z}$ plane by satisfying Eq. (7.12) at successive $\hat{x}>\hat{x}_s$ for the same $(\hat{\beta}_c)_r$ has a different $(\hat{\beta}_c)_i$ at each point. In a parallel flow, a single normal mode defines as entire ray; here a single normal mode defines only a single point.

With Φ expanded in a power series in $\hat{\beta}-\hat{\beta}_c$, and with only the first nonzero term retained (assuming it is the second derivative), Eq. (7.9) becomes

$$u = (1/2\pi)\exp[(\hat{x}-\hat{x}_s)\Phi(\hat{\beta}_c)] \int_C \exp[1/2(\partial^2\Phi/\partial\hat{\beta}^2)_{\hat{\beta}_c}(\hat{x}-\hat{x}_s)(\hat{\beta}-\hat{\beta}_c)^2]d\hat{\beta} \quad . \tag{7.15}$$

We write

$$(\partial^2\Phi/\partial\hat{\beta}^2)_{\hat{\beta}_c} = \hat{D}\exp(i\theta_d) \quad , \tag{7.16a}$$

$$\hat{\beta}-\hat{\beta}_c = \pm is\exp(i\theta_s) \quad , \tag{7.16b}$$

where s is the path length measured from the saddle point, and θ_s is its inclination. With the contour C selected to pass through $\hat{\beta}_c$ from left to right at the constant angle $\theta_s = -\theta_d/2$, the final result is

$$u(\hat{x},\hat{z}) = [(1/2\pi)(\hat{x}-\hat{x}_s)D]^{1/2}\exp[(\hat{x}-\hat{x}_s)\Phi(\hat{\beta}_c)]\exp[i(\pi/4-\theta_d/2)] \quad . \tag{7.17}$$

Replacing $\hat{D}$, $\hat{x}$, $\hat{\alpha}$ and $\hat{\beta}$ by D, R, α and β, where the reference length is L^* of Eq. (2.57), we obtain

$$u(R,\hat{z}) = (2/\pi D)^{1/2}\exp(-\chi_i + i\chi_r) \quad , \tag{7.18}$$

where

$$D = 2\left|\int_{R_s}^{R} R^2(\partial^2\alpha/\partial\beta^2)dR\right| \quad , \tag{7.19}$$

$$\chi_r = 2\int_{R_s}^{R} \alpha_r(R;\beta_c)dR + (\beta_c)_r\hat{z}/R + \pi/4 - \theta_d/2 \quad , \tag{7.20a}$$

$$\chi_i = 2\int_{R_s}^{R} \alpha_i(R;\beta_c)dR + (\beta_c)_i\hat{z}/R \quad , \tag{7.20b}$$

and θ_d is the argument of the complex integral in Eq. (7.19). We continue to use $\hat{z}$ for the z-Reynolds number.

In these variables the saddle-point conditions are

$$2\int_{R_s}^{R} (\partial\alpha/\partial\beta)_r R dR = -\hat{z} \quad , \tag{7.21a}$$

$$\int_{R_s}^{R} (\partial\alpha/\partial\beta)_i R dR = 0 \quad . \tag{7.21b}$$

With the parallel-flow saddle-point conditions of Eqs. (7.13), Eq. (7.18) is still valid, but D and θ_d have different meanings. With $\partial^2\hat{\alpha}/\partial\beta^2$ constant,

$$D = [R(R^2-R_s^2)(\partial^2\alpha/\partial\beta^2)]^{1/2} \quad , \tag{7.22}$$

and θ_d is the argument of $\partial^2\hat{\alpha}/\partial\beta^2$ rather than of its integral.

For a given R and $\hat{z}$, a double iteration procedure is needed to find the complex $\hat{\beta}_c$ that satisfies Eq. (7.12). As each iteration involves the recalculation of eigenvalues and $\partial^2\hat{\alpha}/\partial\beta^2$ from R_s to R, the computational requirements are large. If only R is given, then an iteration of $\hat{\beta}_r$ for a sequence of $\hat{\beta}_r$ will produce the wave pattern at that R with much less computation, but the specific $\hat{z}$ at which the amplitude and phase are calculated will not be known in advance. Or, both $\hat{\beta}_r$ and $\hat{\beta}_i$ can be specified, and R advanced until the integral in Eq. (7.12b) changes sign. This will not always happen, but when it does, a saddle point and its location in the R,$\hat{z}$ plane are obtained without iteration.

Because of the iteration requirement, the saddle-point method is less suited than numerical integration to the detailed calculation of the entire wave pattern, but it can more readily produce results at just a few locations. Its greatest advantage, however, is that along the centerline (z = 0) the amplitude and phase can be obtained at a specified R without iteration, and a single integration pass from R_s to R produces results at all intermediate R at which eigenvalues are calculated. This is possible because the saddle point is at $\beta = 0$ all along the centerline, and only Eq. (7.19) has to be used, and not Eqs. (7.12). We can also note that there is no real saving by using the approximate Eq. (7.22) in place of Eq. (7.19), because $\partial^2\alpha/\partial\beta^2$ has to be calculated in any case, and only the numerical integration of this derivative is eliminated.

7.4 Superposition of point sources

We can imagine sources of instability waves to occur not just as single point sources, but as multiple point sources and as distributed sources. For several discrete sources, the formulas of the preceding Section apply, and we just have to add the contributions from the various sources. We can use this same approach for distributed sources: The distributed source is represented by discrete, closely spaced, infinitesimal point sources. In this Section, we apply this idea to line sources.

We replace the function $g^*(\beta^*)$ in Eq. (7.1) with a more general function

$$g^*(\beta^*,x_s^*,z_s^*) = (1/2\pi)u_s^*(x_s^*,z_s^*)\Delta\xi_s^* g(\hat{\beta}) \quad , \tag{7.23}$$

where u_s^*, the source strength, has the same dimensions as u_t^*, and ξ_s^* is the arc length along the source. We substitute Eq. (7.23) into Eq. (7.1) without the time factor, use the definitions of Eq. (7.3), and arrive at

$$\Delta u(\hat{x},\hat{z}) = (1/2\pi)u_s\Delta\xi_s\int_{-\infty}^{\infty} g(\hat{\beta})\exp(i\chi)d\hat{\beta} \tag{7.24a}$$

for the contribution to u at $\hat{x},\hat{z}$ of an infinitesimal line source at $\hat{x}_s,\hat{z}_s$. In Eq. (7.24a), $u_s = u_s^*/U_1^*$, $\xi_s = \xi_s^* U_1^*/\nu^*$, and

$$\chi(\beta;\hat{x},\hat{z}) = \int_{\hat{x}_s}^{\hat{x}} \hat{\alpha}d\hat{x} + \hat{\beta}(\hat{z}-\hat{z}_s) \quad . \tag{7.24b}$$

A finite-length source which extends from s1 = $(\hat{x}_s,\hat{z}_s)_1$ to s2 = $(\hat{x}_s,\hat{z}_s)_2$ will produce at $\hat{x},\hat{z}$ the velocity

$$u(\hat{x},\hat{z}) = (1/2\pi)\int_{s1}^{s2} u_s d\xi_s\int_{-\infty}^{\infty} g(\hat{\beta})\exp(i\chi)d\hat{\beta} \quad , \tag{7.25}$$

where the ξ_s integration proceeds along the line source.

As the simplest possible example, we apply Eq. (7.25) to a 2D infinite-length line source, i.e., a source which extends from $\hat{z} \to -\infty$ to $+\infty$ at a constant $\hat{x}_s$. With $g(\hat{\beta}) = 1$, so that all oblique normal modes have the same initial amplitude and phase, we obtain

$$u(\hat{x},\hat{z}) = (1/2\pi)\int_{-\infty}^{\infty} u_s d\hat{z}_s\int_{-\infty}^{\infty} \exp(i\chi)d\hat{\beta} \quad . \tag{7.26}$$

The integral over $\hat{z}_s$ must converge because the $\hat{\beta}$ integral is just the point-source solution Eq. (7.3). A physical interpretation of Eq. (7.26) is that Eq. (7.3) can be regarded as either the distribution of u with respect to $\hat{z}$ at the observation station $\hat{x}$ due to a single source at $\hat{x}_s,0$, or as the variation of u at the single observation point $\hat{x},0$ as the point source at $\hat{x}_s$ moves from $\hat{z}_s \to -\infty$ to $\hat{z} \to +\infty$. Consequently, if the point-source solution is weighted by u_s and integrated with respect to $\hat{z}_s$, the resultant amplitude and phase must be that produced by an infinite-length spanwise line source.

At $\hat{x}=\hat{x}_s$, the phase function χ reduces to $\hat{\beta}(\hat{z}-\hat{z}_s)$ and Eq. (7.26) becomes

$$u(\hat{x}_s,\hat{z}) = (1/2\pi)\int_{-\infty}^{\infty} u_s d\hat{z}_s\int_{-\infty}^{\infty} \cos[\hat{\beta}(\hat{z}-\hat{z}_s)]d\hat{\beta} \quad . \tag{7.27}$$

We recognize the $\hat{\beta}$ integral as the Dirac δ-function:

$$\cos[\hat{\beta}(\hat{z}-\hat{z}_s)]d\hat{\beta} = 2\pi\,\delta(\hat{z}-\hat{z}_s) \quad, \tag{7.28}$$

Therefore, $u(\hat{x}_s,\hat{z}) = u_s$ as it should, and we see the reason for the factor 2π in the definition of the function g in Eqs. (7.3) and (7.23). Thus when applied to an infinite-length line source of constant amplitude A_s and of constant phase, Eq. (7.25) must yield the amplitude ratio A/A_s of a 2D normal mode. This property of the point-source solution offers a convenient check on numerical results. Furthermore, if $u_s = A_s\sin(\hat{\beta}_s\hat{z}_s)$ (standing wave) or $A_s\exp(i\hat{\beta}_s\hat{z}_s)$ (travelling wave), Eq. (7.25) will give the amplitude ratio of an oblique normal mode of spanwise wavenumber $\hat{\beta}_s$. Applications of Eq. (7.25) to finite-length 2D and oblique line sources have been given by Mack (1984a).

7.5 Numerical and experimental results

The wave pattern behind a harmonic point source of frequency $F = 0.60 \times 10^{-4}$ located at $R_s = 485$ has been worked out in detail by Mack and Kendall (1983). We shall quote a few results here. Figure 7.2 gives the centerline amplitude distribution downstream of the source as calculated by numerical integration from Eq. (7.7) with $\hat{g}(\hat{\beta}) = 1$. The amplitude distribution of the 2D normal mode is shown for comparison, where A_0 has been chosen to equal the amplitude at $R = 630$. The initial steep drop in the amplitude is reversed near the lower branch of the 2D neutral-stability curve, but this first minimum is followed by a broad second minimum before the sustained amplitude growth gets under way. The peak amplitude occurs at the upper-branch location of $R = 1050$. However, the magnitude of the peak amplitude is less than half of the normal-mode amplitude. The reduction in amplitude is due to the sideways spreading of the wave energy in the point-source problem.

The wave energy also spreads in the y direction because of the growth of the boundary layer. This effect is not included in the calculation because of the use of parallel-flow eigenvalues, even though the correct Reynolds-number dependent eigenvalue have been used. In the point-source wave-packet problem, Gaster (1975) found that the boundary-layer growth could not be ignored, and he introduced a correction based on a simple energy argument. With the assumption that the wave energy is proportional to the square of the amplitude, A^2 would be constant in the absence of damping or amplification or sideways spreading. This argument suggests that the amplitude from Eq. (7.7) be multiplied by $R^{-1/2}$ to correct for boundary-layer growth, and the result is shown in Fig. 7.2. This correction is sizeable, and if correct cannot be neglected.

A characteristic feature of experimental phase measurements on the centerline is that if the phase is extrapolated backwards to zero the apparent location of the source is downstream of the actual source location. Figure 7.3 demonstrates why this is so. The phase initially rises at a slower rate, and it is only after an adjustment in the region where amplification starts that the phase then increases at the faster rate of the measurements.

The centerline amplitude distribution has also been calculated from Eq. (7.18) of the extended saddle-point method. Starting at about $R = 650$, the saddle-point results are virtually identical with those obtained from numerical integration in both amplitude and phase. Even the parallel-flow saddle-point method gives a good result to about the region of maximum amplitude, after which there is a slight departure. Consequently, Eq. (7.18) gives us a way to obtain the centerline amplitude accurately everywhere except quite close to the source with only a little more calculation than is needed to obtain the normal-mode A/A_0.

The important question now is whether or not the amplitude distribution of Fig. 7.2 has anything to do with an experimentally determined amplitude. The answer is given in Fig. 7.4 [Mack and Kendall (1983)]. For the same conditions as the calculations, a hot-wire anemometer was moved downstream in a Blasius boundary layer. At each Reynolds number station, the maximum fluctuation amplitude in the boundary layer was determined by a vertical traverse of the hot wire. The source strength was well within the range for which the response at the hot wire varied linearly with the source amplitude. The amplitude in Fig. 7.4 is the actual measured amplitude expressed as a fraction of the freestream velocity. The level of the calculated amplitude has been adjusted accordingly. The calculated amplitude increases more rapidly than in the experiment, but the Gaster correction for boundary-layer growth makes the two amplitude distributions identical up to about $R = 890$, where the measurements depart abruptly from the theory. This disagreement was traced to a favorable pressure gradient on the flat plate that started precisely at the point of departure. The good agreement in this one example of the calculation with the Gaster growth correction and the measurement in the zero pressure-gradient region, while hardly conclusive, does suggest that when dealing with wave motion over many wavelengths, the growth at the boundary layer cannot be neglected.

The off-centerline wave pattern is of considerable complexity, as shown by Gilev et al (1981). The peak amplitude occurs initially off centerline, and it is only well downstream of the source that it is found on the centerline. A typical calculated spanwise amplitude and phase distribution is shown in Fig. 7.5. The complex evolution of the phase that appears in Fig. 7.1 is reproduced quite closely by Eq. (7.7), but the calculated off-centerline amplitude is less exact. Indeed, the saddle-point method, even in its extended form, fails to give off-centerline amplitude peaks of sufficient magnitude, and only agrees well with the numerical-integration results after these peaks have disappeared. The parallel-flow saddle-point method fails badly in calculating the off-centerline wave pattern. The difficulty of correctly computing the amplitude with the present methods is probably related to the complicated nature of the eigenfunctions, which in much of the wave pattern bear little resemblance to conventional normal-mode eigenfunctions. In order for amplitude calculations to agree as well with experiment as do the phase calculations, it will be necessary to include the eigenfunctions in the calculations. However, even with this limitation, the numerical-integration method does remarkably well in reproducing the measured wave pattern, and provides another example of the utility of linear stability theory in dealing with point-source problems.

PART B. COMPRESSIBLE STABILITY THEORY

8. FORMULATION OF COMPRESSIBLE STABILITY THEORY

8.1 Introductory remarks

The theory of the stability of a compressible laminar boundary layer differs sufficiently from the incompressible theory to warrant being treated as a separate subject. The basic approach and many of the ideas are the same, and for this reason the incompressible theory can be regarded as an indispensable prelude to the study of the compressible theory. For example, all of the material in Sections 2.2, 2.3 and 2.6 applies also to the compressible theory. The motivation for the study of the stability of compressible boundary layers is the problem of transition to turbulence, just as it is for the incompressible theory. However, the relation of stability to transition is even more of an open question than at low speeds. Experiments have been performed that firmly establish the existence of instability waves in supersonic and hypersonic boundary layers [Laufer and Vrebalovich (1960), Kendall (1967,1975)], but there are none that really demonstrate when, and under which circumstances, transition is actually caused by linear instability. A series of stability experiments with "naturally" occurring transition in wind tunnels has been carried out by Demetriades (1977) and Stetson et al. (1983,1984), but many of their observations have yet to be reconciled with theory. Mention must also be made of the remarkable flight experiment by Dougherty and Fisher (1980) that is probably the best evidence to date that transition in a low-disturbance environment at supersonic speeds is caused by laminar instability. For further information on the intricacies of transition at supersonic and hypersonic speeds, we recommend a study of the report by Morkovin (1969).

The first attempt to develop a compressible stability theory was made by Küchemann (1938). Viscosity, the mean temperature gradient and the curvature of the velocity profile were all neglected. The latter two assumptions later proved to have been too restrictive. The most important theoretical investigation to date of the stability of the compressible boundary layer was carried out by Lees and Lin (1946). They developed an asymptotic theory in close analogy to the incompressible asymptotic theory of Lin (1945), and, in addition, gave detailed consideration to a purely inviscid theory. The Rayleigh theorems were extended to compressible flow, and the energy method was used as the basis for a discussion of waves moving supersonically with respect to the freestream. The quantity $D(\rho DU)$, where $D = d/dy$, was found to play the same role in the inviscid compressible theory as does D^2U in the incompressible theory. As a consequence, the flat-plate compressible boundary layer is unstable to purely inviscid waves, quite unlike the incompressible Blasius boundary layer where the instability is viscous in origin.

The close adherence of Lees and Lin to the incompressible theory, and the inadequacy of the asymptotic theory except at very low Mach numbers, meant that some major differences between the incompressible and compressible theories were not uncovered until extensive calculations had been carried out on the basis of a direct numerical solution of the differential equations. In the incompressible theory, it is possible to make substantial progress by ignoring three-dimensional waves, because a 2D wave will always have the largest amplitude ratio at any Reynolds number. This is no longer true above about a Mach number of 1.0. A second notable difference is that in the incompressible theory there is a unique relation between the wavenumber and phase velocity, whereas in the compressible theory there is an infinite sequence of wavenumbers for each phase velocity whenever the mean flow relative to the phase velocity is supersonic [Mack (1963,1964,1965,1969), Gill (1965)]. These additional solutions are called the higher modes. They are of practical importance for boundary layers because it is the first of the additional solutions, the second mode, that is the most unstable according to the inviscid theory. Above about $M_1 = 4$, it is also the most unstable at almost all finite Reynolds numbers.

Subsequent to the work of Lees and Lin, a report of Lees (1947) presented neutral-stability curves for insulated-wall flat plate boundary layers up to $M_1 = 1.3$, and for cooled-wall boundary layers at $M_1 = 0.7$. This report also included the famous prediction that cooling the wall acts to stabilize the boundary layer. However, this prediction must be considerably modified because of the existence of the higher modes. These modes require for their existence only a region of supersonic relative flow, and thus cannot be eliminated by cooling the wall. Indeed, they are actually <u>destabilized</u> by cooling [Mack (1965,1969)].

8.2 Linearized parallel-flow stability equations

A comprehensive account of the compressible stability theory must start with the derivation of the governing equations from the Navier-Stokes equations for a viscous, heat conducting, perfect gas, which in dimensional form are

$$\frac{\partial \bar{u}_i^*}{\partial t^*} + \bar{u}_j^* \frac{\partial \bar{u}_i^*}{\partial x_j^*} = \frac{1}{\bar{\rho}^*} \frac{\partial \bar{\tau}_{ij}^*}{\partial x_j^*} \quad , \tag{8.1a}$$

$$\frac{\partial \bar{\rho}^*}{\partial t^*} + \frac{\partial}{\partial x_j^*}(\bar{\rho}^* \bar{u}_j^*) = 0 \quad , \tag{8.1b}$$

$$\bar{\rho}^* c_v^* (\frac{\partial \bar{T}^*}{\partial t^*} + \bar{u}_j^* \frac{\partial \bar{T}^*}{\partial x_j^*}) = \frac{\partial}{\partial x_j^*}(\bar{\kappa}^* \frac{\partial \bar{T}^*}{\partial x_j^*}) + \bar{\tau}_{ij}^* \bar{e}_{ij}^* \quad , \tag{8.1c}$$

$$\bar{p}^* = \bar{\rho}^* R^* \bar{T}^* \quad , \tag{8.1d}$$

where

$$\bar{e}_{ij}^* = \frac{1}{2}(\frac{\partial \bar{u}_i^*}{\partial x_j^*} + \frac{\partial \bar{u}_j^*}{\partial x_i^*}) \quad , \tag{8.2a}$$

$$\bar{\tau}_{ij}^* = 2\bar{\mu}^* \bar{e}_{ij}^* + [\frac{2}{3}(\bar{\lambda}^* - \bar{\mu}^*)\bar{e}_{KK}^* - \bar{p}^*]\delta_{ij} \quad . \tag{8.2b}$$

Again asterisks denote dimensional quantities, overbars time-dependent quantities, and the summation convention has been adopted as in Section 2. The equations are, respectively, of momentum, continuity, energy and state. The quantities which did not appear in the incompressible equations are T^*, the temperature; κ^*, the coefficient of thermal conductivity; R^*, the gas constant; c_v, the specific heat at constant volume, which will be assumed constant; and $\bar{\lambda}^*$, the coefficient of second viscosity (= 1.5 x bulk viscosity coefficient).

The stability equations are obtained from the Navier-Stokes equations by the same procedure that was used for incompressible flow in Section 2.1. First, all quantities are divided into mean flow and fluctuation terms. With primes used to denote fluctuations of the transport coefficient,

$$\bar{u}^* = U^* + u^* , \qquad \bar{p}^* = P^* + p^* ,$$

$$\bar{T}^* = T^* + \theta^* , \qquad \bar{\rho}^* = \rho^* + r^* , \tag{8.3}$$

$$\bar{\mu}^* = \mu^* + \mu'^* , \quad \bar{\kappa}^* = \kappa^* + \kappa'^* , \quad \bar{\lambda}^* = \lambda^* + \lambda'^* .$$

where the first variable on each RHS is a steady mean-flow quantity, and the second is an unsteady fluctuation.

Next, the equations are linearized, the mean-flow terms are subtracted out, and, finally, the parallel-flow assumption is made. The resulting equations are then made dimensionless with respect to the local freestream velocity U_1^*, a reference length L^*, and the freestream values of all state variables (including the pressure). Both viscosity coefficients are referred to μ_1^*, and κ^* is referred to $c_p \mu_1^*$, where c_p^* is the specific heat at constant pressure. The transport coefficients are functions only of temperature, so that their fluctuations can be written

$$\mu' = (d\mu/dT)\theta, \qquad \kappa' = (d\kappa/dT)\theta, \qquad \lambda' = (d\lambda/dT)\theta . \tag{8.4}$$

Therefore, μ, κ and λ in the following equations, along with ρ, are mean-flow quantities, not fluctuations. The dimensionless, linearized x-momentum equation is

$$\rho(\frac{\partial u}{\partial x} + U\frac{\partial u}{\partial x} + v\frac{dU}{dy} + W\frac{\partial u}{\partial z}) = -\frac{1}{\gamma M_1^2}\frac{\partial p}{\partial x}$$

$$+ \frac{1}{R}[2\mu\frac{\partial^2 u}{\partial x^2} + \mu(\frac{\partial^2 u}{\partial y^2} + \frac{\partial^2 u}{\partial z^2} + \frac{\partial^2 v}{\partial x\partial y} + \frac{\partial^2 w}{\partial x\partial z})$$

$$+ \frac{2}{3}(\lambda-\mu)(\frac{\partial^2 u}{\partial x^2} + \frac{\partial^2 v}{\partial x\partial y} + \frac{\partial^2 w}{\partial x\partial z}) + \frac{d\mu}{dT}\frac{dT}{dy}(\frac{\partial u}{\partial y} + \frac{\partial v}{\partial x})$$

$$+ \frac{d\mu}{dT}(\frac{d^2 U}{dy^2}\theta + \frac{dU}{dy}\frac{\partial\theta}{\partial y}) + \frac{d^2\mu}{dT^2}\frac{dT}{dy}\frac{dU}{dy}\theta] . \tag{8.5a}$$

The y-momentum equation is

$$\rho(\frac{\partial v}{\partial t} + U\frac{\partial v}{\partial x} + W\frac{\partial v}{\partial z}) = -\frac{1}{\gamma M_1^2}\frac{\partial p}{\partial y} + \frac{1}{R}[2\mu\frac{\partial^2 v}{\partial y^2}$$

$$+ \mu(\frac{\partial^2 v}{\partial x^2} + \frac{\partial^2 v}{\partial z^2} + \frac{\partial^2 u}{\partial x\partial y} + \frac{\partial^2 w}{\partial y\partial z}) + \frac{2}{3}(\lambda-\mu)(\frac{\partial^2 u}{\partial x\partial y} + \frac{\partial^2 v}{\partial y^2}$$

$$+ \frac{\partial^2 w}{\partial y\partial z}) + \frac{d\mu}{dT}(2\frac{dT}{dy}\frac{\partial v}{\partial y} + \frac{dU}{dy}\frac{\partial\theta}{\partial x} + \frac{dW}{dy}\frac{\partial\theta}{\partial z})$$

$$+ \frac{2}{3}(\frac{d\lambda}{dT} - \frac{d\mu}{dT})\frac{dT}{dy}(\frac{\partial u}{\partial x} + \frac{\partial v}{\partial y} + \frac{\partial w}{\partial z})] . \tag{8.5b}$$

The z-momentum equation is

$$\rho(\frac{\partial w}{\partial t} + U\frac{\partial w}{\partial x} + v\frac{dW}{dy} + W\frac{\partial w}{\partial z}) = -\frac{1}{\gamma M_1^2}\frac{\partial p}{\partial z}$$

$$+ \frac{1}{R}[2\mu\frac{\partial^2 w}{\partial z^2} + \mu(\frac{\partial^2 w}{\partial y^2} + \frac{\partial^2 w}{\partial x^2} + \frac{\partial^2 v}{\partial y\partial z} + \frac{\partial^2 u}{\partial x\partial z})$$

$$+ \frac{2}{3}(\lambda-\mu)(\frac{\partial^2 w}{\partial z^2} + \frac{\partial^2 v}{\partial y\partial z} + \frac{\partial^2 u}{\partial x\partial z}) + \frac{d\mu}{dT}\frac{dT}{dy}(\frac{\partial w}{\partial y} + \frac{\partial v}{\partial z})$$

$$+ \frac{d\mu}{dT}(\frac{d^2 W}{dy^2}\theta + \frac{dW}{dy}\frac{\partial\theta}{\partial y}) + \frac{d^2\mu}{dT^2}\frac{dT}{dy}\frac{dW}{dy}\theta] . \tag{8.5c}$$

The continuity equation is

$$\frac{\partial r}{\partial t} + \rho \left(\frac{\partial u}{\partial x} + \frac{\partial v}{\partial y} + \frac{\partial w}{\partial z}\right) + v \frac{d\rho}{dy} + U \frac{\partial r}{\partial x} + W \frac{\partial r}{\partial z} = 0 . \tag{8.5d}$$

The energy equation is

$$\rho\left(\frac{\partial \theta}{\partial t} + U \frac{\partial \theta}{\partial x} + v \frac{dT}{dy} + W \frac{\partial \theta}{\partial z}\right) = -(\gamma-1)\left(\frac{\partial u}{\partial x} + \frac{\partial v}{\partial y} + \frac{\partial w}{\partial z}\right)$$

$$+ \frac{\gamma\mu}{\sigma R} \left[\left(\frac{\partial^2 \theta}{\partial x^2} + \frac{\partial^2 \theta}{\partial y^2} + \frac{\partial^2 \theta}{\partial z^2} + \frac{1}{\kappa}\frac{d\kappa}{dT}\frac{d^2 T}{dy^2}\theta + \frac{2}{\kappa}\frac{d\kappa}{dT}\frac{dT}{dy}\frac{\partial \theta}{\partial y}\right.\right.$$

$$+ \frac{1}{\kappa}\frac{d^2\kappa}{dT^2}\left(\frac{dT}{dy}\right)^2 \theta\right] + \gamma(\gamma-1)M_1^2 \frac{1}{R}\left[2\mu\frac{dU}{dy}\left(\frac{\partial u}{\partial y} + \frac{\partial v}{\partial x}\right)\right.$$

$$+ 2\mu\frac{dW}{dy}\left(\frac{\partial v}{\partial z} + \frac{\partial w}{\partial y}\right) + \frac{d\mu}{dT}\left(\frac{dU}{dy}\right)^2\theta + \frac{d\mu}{dT}\left(\frac{dW}{dy}\right)^2\theta\right] . \tag{8.5e}$$

The equation of state is

$$p = r/\rho + \theta/T . \tag{8.5f}$$

Previously undefined quantities which appear in these equations are M_1, the local Mach number at the edge of the boundary layer; γ, the ratio of specific heats; and $\sigma = c_p \mu^*/\kappa^*$, the Prandtl number, which is a function of temperature. Equations (8.5) are the compressible counterparts of the incompressible stability equations (2.5), and are valid for a 3D disturbance in a 3D mean flow. It should be noted that unlike most compressible stability analyses, Eq. (8.5e), the energy equation, is valid for a variable Prandtl number. The constant Prandtl number form is recovered by replacing κ with μ in the three terms in which it occurs.

The boundary conditions at $y = 0$ are

$$u(0) = 0, \quad v(0) = 0, \quad w(0) = 0, \quad \theta(0) = 0 . \tag{8.6a}$$

The boundary conditions on the velocity fluctuations are the usual no-slip conditions, and the boundary condition on the temperature fluctuation is suitable for a gas flowing over a solid wall. For almost any frequency, it is not possible for the wall to do other than to remain at its mean temperature. The only exception is for a stationary, or near stationary, crossflow disturbance, when $\theta(0) = 0$ is replaced by $D\theta(0) = 0$. The boundary conditions at $y \to \infty$ are

$$u(y), \quad v(y), \quad w(y), \quad p(y), \quad \theta(y) \text{ are bounded as } y \to \infty . \tag{8.6b}$$

This boundary condition is less restrictive that requiring all disturbances to be zero at infinity, but in supersonic flow waves may propagate to infinity and we wish to include those that do so with constant amplitude.

8.3 Normal-mode equations

We now specialize the disturbances to normal modes as in Section 2.3:

$$[u,v,w,p,r,\theta]^T = [\hat{u}(y),\hat{v}(y),\hat{w}(y),\hat{p}(y),\hat{r}(y),\hat{\theta}(y)]^T \exp[i(\int\alpha dx + \beta dz - \omega t)] , \tag{8.7}$$

where we have adopted the quasi-parallel form of the complex phase function. The normal modes may grow either temporally or spatially or both, depending on whether ω or $\tilde{k}$, or both, are complex. The discussion in Section 2.3 applies to the compressible theory just as well as to the incompressible theory.

When Eqs. (8.7) are substituted into Eqs. (8.5), and the same linear combinations of the x and z momentum equations formed as in Section (2.4) for the variables

$$\tilde{\alpha}\tilde{u} = \alpha\hat{u} + \beta\hat{w} , \qquad \tilde{\alpha}\tilde{w} = \alpha\hat{w} - \beta\hat{u} , \tag{8.8}$$

we obtain a system of equations which are the compressible counterparts of Eqs. (2.36). The momentum equation in the direction parallel to the wavenumber vector $\tilde{k}$ is

$$\rho[i(\alpha U + \beta W - \omega)\tilde{\alpha}\tilde{u} + (\alpha DU + \beta DW)\hat{v}] = -i(\alpha^2+\beta^2)(\hat{p}/\gamma M_1^2)$$

$$+ \frac{\mu}{R}[\tilde{\alpha}D^2\tilde{u} + (\alpha^2+\beta^2)(iD\hat{v} - 2\tilde{\alpha}\tilde{u})] + \frac{2}{3}\frac{\lambda-\mu}{R}(\alpha^2+\beta^2)(iD\hat{v} - \tilde{\alpha}\tilde{u})$$

$$+ \frac{1}{R}\{\frac{d\mu}{dT}(\alpha D^2 U + \beta D^2 W)\hat{\theta} + (\frac{d\mu}{dT}D\hat{\theta} + \frac{d^2\mu}{dT^2}DT\hat{\theta})(\alpha DU + \beta DW)$$

$$+ \frac{d\mu}{dT}DT[\tilde{\alpha}D\tilde{u} + i(\alpha^2+\beta^2)\hat{v}]\} . \tag{8.9a}$$

The y momentum equation is

$$i\rho(\alpha U + \beta W - \omega)\hat{v} = -D\hat{p}/\gamma M_1^2 + \frac{\mu}{R}[2D^2\hat{v} + i\tilde{\alpha}D\tilde{u} - (\alpha^2+\beta^2)\hat{v}]$$

$$+ \frac{2}{3}\frac{\lambda-\mu}{R}(D^2\hat{v} + i\tilde{\alpha}\tilde{u}) + \frac{1}{R}[i\frac{d\mu}{dT}(\alpha DU + \beta DW)\hat{\theta} + 2\frac{d\mu}{dT}DTD\hat{v}$$

$$+ \frac{2}{3}\frac{d}{dT}(\lambda-\mu)DT(D\hat{v} + i\tilde{\alpha}\tilde{u})] . \tag{8.9b}$$

The momentum equation in the direction normal to $\vec{k}$ is

$$\rho\,[i(\alpha U+\beta W-\omega)\tilde{\alpha}\tilde{w} + (\alpha DW-\beta DU)\hat{v}] = \frac{\mu}{R}\,[\tilde{\alpha}D^2\tilde{w} - (\alpha^2+\beta^2)\tilde{\alpha}\tilde{w}]$$
$$+ \frac{1}{R}\,[\frac{d\mu}{dT}\,DT\,\tilde{\alpha}D\tilde{w} + \frac{d\mu}{dT}\,(\alpha D^2W-\beta D^2U)\hat{\theta} + (\frac{d\mu}{dT}\,D\hat{\theta} + \frac{d^2\mu}{dT^2}\,DT\,\hat{\theta}\,)(\alpha DW-\beta DU)]\quad. \tag{8.9c}$$

The continuity equation is

$$i\,(\alpha U+\beta W-\omega)\hat{r} + \rho(D\hat{v}+i\tilde{\alpha}\tilde{u}) + D\rho\,\hat{v} = 0\quad. \tag{8.9d}$$

The energy equation is

$$\rho\,[i\,(\alpha U+\beta W-\omega)\hat{\theta} + DT\,\hat{v}] = -\,(\gamma - 1)\,(D\hat{v}+i\tilde{\alpha}\tilde{u})$$
$$+ \frac{\gamma\mu}{\sigma R}\,\{D^2\hat{\theta} - (\alpha^2+\beta^2)\hat{\theta} + \frac{1}{\kappa}\,[\frac{d\kappa}{dT}\,D^2T + \frac{d^2\kappa}{dT^2}\,(DT)^2]\hat{\theta} + \frac{1}{\kappa}\,\frac{d\kappa}{dT}\,DT\,D\hat{\theta}\}$$
$$+ \gamma(\gamma - 1)M_1^2\,\frac{1}{R}\,\{i2\mu(\alpha DU+\beta DW)\hat{v} + \frac{d\mu}{dT}\,(DU^2+DW^2)\hat{\theta}\}$$
$$+ \frac{2\mu}{\alpha^2+\beta^2}\,[(\alpha DU+\beta DW)\tilde{\alpha}D\tilde{u} + (\alpha DW-\beta DU)\tilde{\alpha}D\tilde{w}]\}\quad. \tag{8.9e}$$

The equation of state is

$$\hat{p} = \hat{r}/\rho + \hat{\theta}/T\quad. \tag{8.9f}$$

To reiterate, in these equations the eigenfunctions of the fluctuations are functions only of y and are denoted by a caret or a tilde; the mean-flow velocities U and W are also functions of y, as are the other mean-flow quantities: density ρ $(= 1/T)$, temperature T, viscosity coefficients μ and λ, thermal conductivity coefficient κ, and Prandtl number. The specific heats are constant. The reference velocity for U and W is the same as for R and M_1, and the reference length for y is the same as in R.

8.4 First-order equations

8.4.1 Eighth-order system

Equations (8.9) are the basic equations of the compressible stability theory, but are not yet in a form suitable for numerical computation. For this purpose we need a system of first-order equations as in Section 2.5.2. With the dependent variables defined by

$$Z_1 = \alpha\hat{u} + \beta\hat{w}\ ,\qquad Z_2 = DZ_1\ ,\qquad Z_3 = \hat{v}\ ,$$
$$Z_4 = \hat{p}/\gamma M_1^2\ ,\qquad Z_5 = \hat{\theta}\ ,\qquad Z_6 = D\hat{\theta}\ , \tag{8.10}$$
$$Z_7 = \alpha\hat{w} - \beta\hat{u}\ ,\qquad Z_8 = DZ_7\ ,$$

Equations (8.9) can be written as eight first-order differential equations

$$DZ_i(y) = \sum_{j=1}^{8} a_{ij}(y)\,Z_j(y)\ ,\qquad (i = 1,\,8)\ , \tag{8.11}$$

and the fact that this reduction is possible proves that Eqs. (8.9) constitute an eighth-order system. The lengthy equations for the matrix elements are listed in Appendix 1.

The boundary conditions are

$$Z_1(0) = 0\ ,\qquad Z_3(0) = 0\ ,\qquad Z_5(0) = 0\ ,\qquad Z_7(0) = 0\ ,$$
$$Z_1(y)\ ,\qquad Z_3(y)\ ,\qquad Z_5(y)\ ,\qquad Z_7(y)\ \text{bounded as}\ y \to \infty\ . \tag{8.12}$$

8.4.2 Sixth-order system

Equations (8.11) can be solved by the same numerical techniques as used for the fourth-order system of the incompressible theory. However, the fact that there are 16 real equations and four independent solutions means that the computer time required to calculate an eigenvalue is increased by several times. It is therefore important to know if it is possible to make use of a system of lesser order, as in the incompressible theory where the original sixth-order system could be reduced to fourth order for the determination of eigenvalues. We note that for a 2D wave in a 2D boundary layer, the system already is of only sixth order, as there can be no velocity component, either mean or fluctuating, in the z direction. Is there an exact reduction available from eighth to sixth order? The answer, unfortunately, as mentioned by Dunn and Lin (1955) and explicitly demonstrated by Reshotko (1962), is no.

The theory of Dunn and Lin (1955) achieved the reduction to sixth order by an order of magnitude argument valid for large Reynolds numbers. The motivation was to put the equations in a form where an improved 2D asymptotic theory could be applied to oblique waves in a 2D boundary layer. However, neither this theory, nor direct numerical solutions of the Dunn-Lin sixth-order system of equations, turned out to give adequate numerical results above a low supersonic Mach number.

We may observe from the coefficient matrix of Eq. (8.11) listed in Appendix 1 that the only term that couples the first six equations to the last two is a_{68}. This coefficient comes from the last term of the energy equation (8.9e), and is one of four dissipation terms. It is the product of the gradient of the mean velocity normal to $\vec{k}$ and the gradient of the fluctuation velocity in the same direction. It was proposed by Mack (1969) to simply set this term equal to zero, and use the resultant sixth-order system for the calculation of eigenvalues. The numerical evidence, as discussed further in Section 10.4, is that except near the critical Reynolds number this approximation gives amplification rates within a few percent

of those obtained from the full eighth-order system, and is most accurate at higher Mach numbers.

8.6 Uniform mean flow

In the freestream $U = U_1$, $W = W_1$, $T = 1$, $\mu = 1$, $\kappa = 1/\sigma_1$, all y derivatives of mean-flow quantities are zero, and Eqs. (8.11) reduce to a system of equations with constant coefficients. In spite of the greater complexity of these equations compared to those for incompressible flow, we are still able to arrive at analytical solutions. The lengthy derivation is given in Appendix 2 [Mack (1965a)]. The exact freestream solutions are the ones to use to calculate the initial values for a numerical integration of Eqs. (8.11), but they do not lend themselves to a ready physical interpretation. For this purpose, we examine the limit of large Reynolds number. The characteristic values simplify to

$$\lambda_{1,2} = \mp [\alpha^2 + \beta^2 - M_1^2(\alpha U_1 + \beta W_1 - \omega)^2]^{1/2} , \tag{8.13a}$$

$$\lambda_{3,4} = \mp [iR(\alpha U_1 + \beta W_1 - \omega)]^{1/2} , \tag{8.13b}$$

$$\lambda_{5,6} = \mp [i\sigma R(\alpha U_1 + \beta W_1 - \omega)]^{1/2} , \tag{8.13c}$$

$$\lambda_{7,8} = \lambda_{3,4} . \tag{8.13d}$$

We can now identify our solutions as, in order, the inviscid solution, the first viscous velocity solution, a viscous temperature solution, which is new and does not appear in the incompressible theory, and the second viscous velocity solution. We shall only use the upper signs in what follows, as these are the solutions which enter the eigenvalue problem.

The components of the characteristic vector of the inviscid solution are

$$A_1^{(1)} = -i(\alpha^2 + \beta^2)^{1/2} , \tag{8.14a}$$

$$A_3^{(1)} = [\alpha^2 + \beta^2 - M_1^2(\alpha U_1 + \beta W_1 - \omega)^2]^{1/2}/(\alpha^2 + \beta^2)^{1/2} \tag{8.14b}$$

$$A_4^{(1)} = i(\alpha U_1 + \beta W_1 - \omega)/(\alpha^2 + \beta^2)^{1/2} , \tag{8.14c}$$

$$A_5^{(1)} = i(\gamma-1)M_1^2(\alpha U_1 + \beta W_1 - \omega)/(\alpha^2 + \beta^2)^{1/2} . \tag{8.14d}$$

The normalization has been changed to correspond to the incompressible solutions of Eq. (2.50). It can be noted that these expressions are correct when we set $M_1 = 0$.

The components of the characteristic vector corresponding to the first viscous velocity solution are

$$A_1^{(3)} = 1 , \tag{8.15a}$$

$$A_3^{(3)} = i/[iR(\alpha U_1 + \beta W_1 - \omega)]^{1/2} , \tag{8.15b}$$

$$A_4^{(3)} = 0 , \quad A_5^{(3)} = 0 . \tag{8.15c}$$

This solution is identical to the λ_3 incompressible solution only in the limit of large Reynolds numbers.

The components of the characteristic vector corresponding to the viscous temperature solution are

$$A_1^{(5)} = 0 , \tag{8.16a}$$

$$A_3^{(5)} = -i(\alpha U_1 + \beta W_1 - \omega)^{1/2}/(i\sigma R)^{1/2} , \tag{8.16b}$$

$$A_4^{(5)} = 0 , \quad A_5^{(5)} = 1 , \tag{8.16c}$$

The components of the characteristic vector corresponding to the second viscous velocity solution are

$$A_1^{(7)} = 0 , \quad A_3^{(7)} = 0 , \quad A_4^{(7)} = 0 , \quad A_5^{(7)} = 0 , \tag{8.17a}$$

$$A_7^{(7)} = 1 , \tag{8.17b}$$

$$A_8^{(7)} = -[\alpha^2 + \beta^2 + iR(\alpha U_1 + \beta W_1 - \omega)]^{1/2} . \tag{8.17c}$$

This solution is exact and is the same spanwise viscous wave solution as in incompressible flow.

We may observe that the viscous velocity solutions have only fluctuations of velocity, not of pressure or temperature. The velocity fluctuations in the x,z plane are in the direction of $\vec{k}$ for the first solution, and are normal to $\vec{k}$ for the second solution which is periodic only in time. The viscous temperature solution has no velocity fluctuations in the x,z plane, or pressure fluctuations. We may regard these solutions as the responses to sources of $\tilde{u}$, $\tilde{w}$ and $\tilde{\theta}$, and to emphasize this fact the respective solutions have been normalized to make these quantities unity. The second viscous velocity solution still has the interpretation of a normal vorticity wave, as in incompressible flow, but this wave cannot exist as a pure mode in the boundary layer (Squire mode) because of the a_{68} dissipation term that couples the latter two of Eqs. (8.11) to the first six equations.

9. COMPRESSIBLE INVISCID THEORY

9.1 Inviscid equations

In compressible flow, even flat-plate boundary layers have inviscid instability, and this instability increases with increasing Mach number. Therefore, the inviscid theory is much more useful in arriving at

an understanding of the instability of compressible boundary layers than it is at low speeds. Indeed the initial detailed numerical working out of the viscous theory [Mack (1969)] was greatly facilitated by the insight offered by the inviscid theory. In the limit of infinite Reynolds number, Eqs. (8.9) reduce to

$$\rho[i(\alpha U+\beta W-\omega)\tilde{\alpha}\tilde{u} + (\alpha DU+\beta DW)\hat{v}] = -i(\alpha^2+\beta^2)(\hat{p}/\gamma M_1^2) . \tag{9.1a}$$

$$i\rho(\alpha U+\beta W-\omega)\hat{v} = -D\hat{p}/\gamma M_1^2 , \tag{9.1b}$$

$$i(\alpha U+\beta W-\omega)\tilde{\alpha}\tilde{w} + (\alpha DW-\beta DU)\hat{v} = 0 , \tag{9.1c}$$

$$i(\alpha U+\beta W-\omega)\hat{r} + \rho(D\hat{v}+i\tilde{\alpha}\tilde{u}) + D\rho\ \hat{v} = 0 , \tag{9.1d}$$

$$\rho[i(\alpha U+\beta W-\omega)\hat{\theta} + DT\ \hat{v}] = -(\gamma-1)(D\hat{v}+i\tilde{\alpha}\tilde{u}) , \tag{9.1e}$$

$$\hat{p} = \hat{r}/\rho + \hat{\theta}/T . \tag{9.1f}$$

We note that the $\tilde{w}$ momentum equation, Eq. (9.1c), and the energy equation, Eq. (9.1e), are decoupled from the other equations. Therefore we can eliminate $\tilde{\alpha}\tilde{u}$ and $\hat{r}$ from the latter to arrive at the following two first-order equations for $\hat{v}$ and $\hat{p}$:

$$(\alpha U+\beta W-\omega)D\hat{v} = (\alpha DU+\beta DW)\hat{v} + i(\alpha^2+\beta^2)[T - M_1^2(\alpha U+\beta W-\omega)/(\alpha^2+\beta^2)](\hat{p}/\gamma M_1^2) \tag{9.2a}$$

$$D(\hat{p}/\gamma M_1^2) = -i\rho(\alpha U+\beta W-\omega)\hat{v} . \tag{9.2b}$$

These equations are the 3D compressible counterparts of Eqs. (3.12). The boundary conditions are

$$\hat{v}(0) = 0 , \qquad \hat{v}(y) \text{ is bounded as } y \to \infty. \tag{9.3}$$

The inviscid equations can be written in a simplified form if we introduce the Mach number

$$\bar{M} = (\alpha U+\beta W-\omega)M_1/(\alpha^2+\beta^2)^{1/2}T^{1/2} \tag{9.4}$$

For a temporal neutral wave, $\bar{M}$ is real and is the local Mach number of the mean flow in the direction of the wavenumber vector $\vec{k}$ relative to the phase velocity ω_r/k. In all other cases, $\bar{M}$ is complex, but even so we shall refer to it as the relative Mach number. In terms of $\bar{M}$, Eqs. (9.2) simplify to

$$D[\hat{v}/(\alpha U+\beta W-\omega)] = i(1-\bar{M}^2)(\hat{p}/\gamma\bar{M}^2) , \tag{9.5a}$$

$$D\hat{p} = -i\gamma\bar{M}^2(\alpha^2+\beta^2)\hat{v}/(\alpha U+\beta W-\omega) . \tag{9.5b}$$

We observe that these equations are identical to two-dimensional equations ($\beta = 0$) when written in the tilde variables of Eq. (2.37). Therefore, inviscid instability is governed by the mean flow in the direction of $\vec{k}$, just as for incompressible flow. Either Eqs. (9.5) or (9.2) can be used for numerical integration, but the latter have the advantage that $\hat{v}$ is a better behaved function near the critical point than is $\hat{v}/(\alpha U+\beta W-\omega)$.

Equation (9.5a) is the familiar linearized pressure-area relation of one-dimensional flow. The quantity $\hat{v}/(\alpha U+\beta W-\omega)$ is the amplitude function of the streamtube area change. The other flow variables can be written in a similar manner as

$$\tilde{u} = i[D\tilde{U}\frac{\hat{v}}{\tilde{\alpha}\tilde{U}-\omega} + \frac{1}{\tilde{\alpha}}(\tilde{\alpha}\tilde{U}-\omega)\frac{1}{1-\bar{M}^2}D\left(\frac{\hat{v}}{\tilde{\alpha}\tilde{U}-\omega}\right)] , \tag{9.6a}$$

$$\hat{\theta} = i[DT\frac{\hat{v}}{\tilde{\alpha}\tilde{U}-\omega} - (\gamma-1)T\frac{1}{1-\bar{M}^2}D\left(\frac{\hat{v}}{\tilde{\alpha}\tilde{U}-\omega}\right)] , \tag{9.6b}$$

$$\hat{r} = i[D\rho\frac{\hat{v}}{\tilde{\alpha}\tilde{U}-\omega} - \rho\frac{\bar{M}^2}{1-\bar{M}^2}D\left(\frac{\hat{v}}{\tilde{\alpha}\tilde{U}-\omega}\right)] , \tag{9.6c}$$

$$\tilde{w} = iD\tilde{W}\frac{\hat{v}}{\tilde{\alpha}\tilde{U}-\omega} , \tag{9.6d}$$

where we have used the tilde variables for simplicity. When the second terms of these equations are written with $\hat{p}$ in place of $\hat{v}/(\tilde{\alpha}\tilde{U}-\omega)$, they can be readily recognized as the linearized momentum equation, the isentropic temperature-pressure relation, and the isentropic density-pressure relation, respectively. The first terms are in the nature of source terms, and arise from the combination of a vertical fluctuation velocity and a mean shear. Because Eq. (9.6d) is an equation for the vertical vorticity component $\tilde{\alpha}\tilde{w}$, only the source term is present.

A manipulation of Eqs. (9.1) leads to a single second-order equation for $\hat{v}$:

$$D\{[(\tilde{\alpha}\tilde{U}-\omega)D\hat{v}-\tilde{\alpha}DU\hat{v}]/(1-\bar{M}^2)\} - (\alpha^2+\rho^2)(\tilde{\alpha}\tilde{U}-\omega)\hat{v} = 0 , \tag{9.7}$$

This equation, which in 2D form was used by Lees and Lin (1946), is the 3D compressible counterpart of the Rayleigh equation. A second-order equation for $\hat{v}/(\tilde{\alpha}\tilde{U}-\omega)$ follows directly from Eq. (9.5):

$$D^2[\hat{v}/(\tilde{\alpha}\tilde{U}-\omega)] + D\{\ln[\bar{M}^2/(1-\bar{M}^2)]\}D[\hat{v}/(\tilde{\alpha}\tilde{U}-\omega)] - \tilde{\alpha}^2(1-\bar{M}^2)[\hat{v}/(\tilde{\alpha}\tilde{U}-\omega)] = 0 . \tag{9.8}$$

The corresponding equation for $\hat{p}$ is

$$D^2\hat{p} - D[\ln(\bar{M}^2)]D\hat{p} - (\alpha^2+\beta^2)(1-\bar{M}^2)\hat{p} = 0 \ . \tag{9.9}$$

9.2 Uniform mean flow

In the freestream, Eq. (9.9) reduces to

$$D^2\hat{p} - (\alpha^2+\beta^2)(1-\bar{M}_1^2)\hat{p} = 0 \ . \tag{9.10}$$

The solution which satisfies the boundary condition at infinity is

$$\hat{p}/\gamma M_1^2 = i[(\alpha U+\beta W-\omega)/(\alpha^2+\beta^2)^{1/2}]\exp[-(\alpha^2+\beta^2)^{1/2}(1-\bar{M}_1^2)^{1/2}y] \ , \tag{9.11}$$

which agrees with Eq. (8.14c). Equations (9.11) and (8.14b) provide the initial values for the numerical integration.

The freestream solutions may be classified into three groups: subsonic waves with $\bar{M}_1^2 < 1$; sonic waves with $\bar{M}_1^2 = 1$; and supersonic waves with $\bar{M}_1^2 > 1$. Neutral supersonic waves are Mach waves of the relative flow, and can exist as either outgoing or incoming waves. True instability waves, which must satisfy the boundary condition at $y = 0$ as well as infinity, are almost all subsonic, but eigenmodes which are supersonic waves of the outgoing family in the freestream have been found for highly cooled boundary layers [Mack (1969)]. A combination of incoming and outgoing waves permits the boundary condition at $y = 0$ to be satisfied for any combination of α, β and ω, as pointed out by Lees and Lin (1946). It is when only one family of waves is present that we have an eigenvalue problem. The combination of both families is the basis of the forcing theory presented in Section 11.

9.3 Some mathematical results

The detailed study of the two-dimensional inviscid theory carried out by Lees and Lin (1946) established a number of important results for temporal waves. Lees and Lin classified all instability waves as subsonic, sonic, or supersonic, depending on whether the relative _freestream_ Mach number $\bar{M}_1$ is less than, equal to, or greater than one. Their chief results are:

(i) The necessary and sufficient condition for the existence of a _neutral_ subsonic wave is that there is some point $y_s > y_0$ in the boundary layer where

$$D(\rho DU) = 0 \ , \tag{9.12}$$

and y_0 is the point at which $U = 1 - 1/M_1$. The phase velocity of the neutral wave is c_s, the mean velocity at y_s. This necessary condition is the generalization of Rayleigh's condition for incompressible flow that there must be a point of inflection in the velocity profile for a neutral wave to exist. The point y_s, which plays the same role in the compressible theory as the inflection point in the incompressible theory, is called the generalized inflection point. The proof of sufficiency given by Lees and Lin requires $\bar{M}$ to be everywhere subsonic.

(ii) A sufficient condition for the existence of an _unstable_ wave is the presence of a generalized inflection point at some $y > y_0$, where y_0 is the point at which $U = 1 - 1/M_1$. The proof of this condition also requires $\bar{M}$ to be subsonic.

(iii) There is a neutral sonic wave with the eigenvalues $\alpha = 0$, $c = c_0 = 1 - 1/M_1$.

(iv) If $\bar{M}^2 < 1$ everywhere in the boundary layer, there is a unique wavenumber α_s corresponding to c_s for the neutral subsonic wave.

Lees and Lin obtained these results by a direct extension of the methods of proof used for incompressible flow. The necessary condition for a neutral subsonic wave was derived from the discontinuity of the Reynolds stress $\tau = -\langle uv \rangle$ at the critical point y_c. As in incompressible flow, τ is constant for a neutral inviscid wave except possibly at the critical point. For $\omega_i = 0$,

$$\tau(y_c+0) - \tau(y_c-0) = (\pi/\alpha)[D(\rho DU)/DU]_c \langle v_c^2 \rangle \ . \tag{9.13}$$

Equation (9.13) is the same as Eq. (3.9) in the incompressible theory except that $D(\rho DU)$ appears in place of D^2U. Since τ is zero at the wall and in the freestream by the boundary conditions for a subsonic wave, it follows that $D(\rho DU)$ must be zero at y_c. We may also note that for a neutral supersonic wave, where $c < c_0$ and $\tau(y_c+0) = (\alpha^2/2)(\bar{M}_1^2-1)^{1/2}$ from the freestream solutions, the discontinuity at the critical point must equal this value of τ and the phase velocity must be other than U_s.

At this point we can examine the numerical consequences of the finding that neutral and unstable waves depend on the existence of a generalized inflection point. For the Blasius boundary layer, D^2U is negative everywhere except at $y = 0$. However, for a compressible boundary layer on an insulated flat plate, $D(\rho DU)$ is always zero somewhere in the boundary layer. Consequently, all such boundary layers are unstable to inviscid waves. Figure 9.1 shows that c_s, the mean velocity at the generalized inflection point and thus the phase velocity of the neutral subsonic wave, increases with increasing freestream Mach number M_1 in accordance with the outward movement of the generalized inflection point. If we recall from Section 6 that inviscid instability increases for the adverse pressure-gradient Falkner-Skan profiles as the inflection point moves away from the wall, we can expect in this instance that inviscid instability will increase with increasing Mach number. Figure 9.1 also includes both c_0, the phase velocity of a neutral sonic wave, and the phase velocity for which $\bar{M} = -1$ at the wall. In the exact numerical solutions of the boundary-layer equations which were used for Fig. 9.1, the wall is insulated and the freestream temperature T_1 is characteristic of wind-tunnel conditions. The stagnation temperature is held constant

at 311°K until, with increasing M_1, T_1^* drops to 50°K. For higher Mach numbers, T_1^* is held constant at 50°K.

For a wave to be subsonic relative to the freestream, and hence have vanishing amplitude at $y \to \infty$ even when neutral, c must be greater than c_0. It is often said that only subsonic waves are considered in stability theory, but this statement is not entirely correct. It is true that the neutral subsonic wave with eigenvalues α_s, c_s can only exist when $c_s > 1 - 1/M_1$. However, this does not rule out amplified and damped waves with $c < 1 - 1/M_1$, or even neutral supersonic waves with a c different from c_s. Examples of such waves have been found, all of which satisfy the boundary conditions at infinity and so are solutions of the eigenvalue problem. For $\omega_i \neq 0$, the amplitudes of outgoing amplified and incoming damped waves vanish at infinity regardless of the value of c; for neutral waves, the amplitude will only be bounded at infinity when $c < c_0$. What does turn out to be true is that the most unstable waves are always subsonic. Furthermore, for one class of waves, the amplified first-mode waves, the phase velocity is always between c_0 and c_s. This result has important consequences.

9.4 Methods of solution

The methods for obtaining solutions of the inviscid equations for boundary-layer profiles have been patterned after corresponding methods in incompressible flow. Lees and Lin (1946) developed power-series solutions in α^2, and also used the generalizations of Tollmien's incompressible solutions

$$\hat{v}_1(y) = (y-y_c)P_1(y-y_c) , \tag{9.14a}$$

$$\hat{v}_2(y) = P_2(y-y_c) + (T^2/DU^3)_c [D(\rho DU)]_c \hat{v}_1(y)\ln(y-y_c), \quad y > y_c. \tag{9.14b}$$

For $y < y_c$, $\ln(y-y_c) = \ln|y-y_c| - i\pi$ as for incompressible flow. The leading terms of P_1 and P_2 are DU_c and T_c/DU_c, respectively, so that $\hat{v}_1$ and $\hat{v}_2$ are normalized here in a different manner than in Section 3.1. These solutions have been worked out in more detail by Reshotko (1960). Both $\hat{v}$ and $\hat{u}$ have the same analytical behavior as in incompressible flow. What is new here is the temperature fluctuation, which, according to Reshotko, has the behavior

$$\hat{\theta} \simeq 1/(y-y_c) + (T/DU)_c[D(\rho DU)]_c\ln(y-y_c) + \ldots . \tag{9.15}$$

Hence, even for a neutral subsonic wave, where $[D(\rho DU)]_c = 0$ and $\hat{v}$ and $\hat{u}$ are both regular, $\hat{\theta}$ has a singularity at y_c.

Two methods have been devised for the numerical integration of the inviscid stability equations. The first method [Lees and Reshotko (1962)] transforms the second-order linear equation into a first-order nonlinear equation of the Riccati type. This equation is solved by numerical integration except for the region around the critical point, where the power series in $y-y_c$ are used. The second method [Mack (1965a)] is a generalization to compressible flow of Zaat's (1958) method. This method has already been described in Section 3.2. For neutral and damped solutions, the contour of integration is indented under the singularity, just as for incompressible flow.

9.5 Higher modes

9.5.1 Inflectional neutral waves

Although the Lees-Lin proof for neutral subsonic waves that α_s is a unique function of c_s was dependent on $\bar{M}^2 < 1$, and although Lees and Reshotko (1962) mentioned the possibility that α_s may not be unique for $\bar{M}^2 > 1$, no serious consideration was given to the possibility of multiple solutions until the extensive numerical work of Mack (1963,1964,1965b) brought them to light. Similar multiple solutions were found independently at about the same time by Gill (1965, paper presented in 1964) in his study of "top-hat" jets and wakes. With the benefit of hindsight, it is actually rather easy to demonstrate their existence. The inviscid equations for $\hat{v}/(\tilde{\alpha}\tilde{U}-\omega)$ and $\hat{p}$, Eqs. (9.8) and (9.9), quite evidently have a different analytical character depending on whether $\bar{M}^2$ is less than or greater than unity. It is instructive, as suggested by Lees [private communication (1964)], to consider α^2 large enough so that the first-derivative term can be neglected. Then Eq. (9.8) reduces to

$$D[\hat{v}/(\tilde{\alpha}\tilde{U}-\omega)] - \tilde{\alpha}^2(1-\bar{M}^2)[\hat{v}/(\tilde{\alpha}\tilde{U}-\omega)] = 0 . \tag{9.16}$$

When $\bar{M}^2 < 1$, the solutions of Eq. (9.16) are elliptic, and it is under this circumstance that Lees and Lin proved the uniqueness of α_s. However, when $\bar{M}^2 > 1$, Eq. (9.16) becomes a wave equation, and as in all problems governed by a wave equation, we can expect there to be an infinite sequence of wavenumbers that will satisfy the boundary conditions. We may note that for a subsonic wave (this terminology still refers to the freestream) and the usual sort of boundary-layer profiles, the relative supersonic region occurs below the critical point where $\bar{M} < 0$.

If y_a is the y where $\bar{M}^2 = 1$, approximate solutions of Eq. (9.16) of the WKB type are

$$\hat{v}/(\tilde{\alpha}\tilde{U}-\omega) = \pm \sin[\tilde{\alpha}_{sn}\int_0^y (\bar{M}^2-1)^{1/2}dy] , \quad y < y_a , \tag{9.17a}$$

$$\hat{v}/(\tilde{\alpha}\tilde{U}-\omega) = - i\exp[-\tilde{\alpha}_{sn}\int_{y_a}^y (1-\bar{M}^2)^{1/2}dy], \quad y > y_a , \tag{9.17b}$$

where Eq. (9.17a) follows from the boundary condition $\hat{v}(0) = 0$. We have written $\tilde{\alpha}_s$ as $\tilde{\alpha}_{sn}$. The subscript s denotes a neutral subsonic solution as before; the subscript n refers to the multiple solutions. The constant in Eq. (9.17b) is chosen as $-i$ to make $\hat{p}$ real and positive for $y > y_a$. Either sign is possible for $y > y_a$. Since $\hat{p}$ is continuous and finite at $y = y_a$, $D[\hat{v}/(\tilde{\alpha}\tilde{U}-\omega)]$, from Eq. (9.5a), must go to zero as $y \to y_a$ as does $\bar{M}^2-1$. The derivative of $\hat{v}/(\tilde{\alpha}\tilde{U}-\omega)$ gives a factor $(\bar{M}^2-1)^{1/2}$, and the required additional factor of $(\bar{M}^2-1)^{1/2}$ can only come from the cosine having a zero at y_a. Consequently,

$$\cos[\tilde{\alpha}_{sn}\int_{0}^{y_a} (\overline{M}^2-1)^{1/2}dy] = 0 \ , \qquad (9.18a)$$

and

$$\tilde{\alpha}_{sn}\int_{0}^{y_a} (\overline{M}^2-1)^{1/2}dy = (n-\tfrac{1}{2}) \quad , \quad n = 1,2,3,\ldots . \qquad (9.18b)$$

Equation (9.18b) is the final result, and demonstrates that there is an infinite sequence of discrete neutral wavenumbers with the phase velocity c_s. The difference between adjacent values of $\tilde{\alpha}_{sn}$ is

$$\tilde{\alpha}_{s(n+1)} - \tilde{\alpha}_{sn} = \pi\left(\int_{0}^{y_a} (\overline{M}^2-1)^{1/2}dy\right)^{-1} . \qquad (9.19)$$

We may also observe that according to Eq. (9.18b), the sequence of values of $2\tilde{\alpha}_{sn}/\pi$ is 1,3,5,7,.... This result was first noted and given a physical explanation by Morkovin [private communication (1982)]. Because Eq. (9.16) is only approximate, the magnitude of $\tilde{\alpha}_{sn}$, the difference formula, and the ratio sequence are not expected to be numerically correct. However, as we shall see below, with an important exception they are either correct, or approximately correct.

When the numerical integration of Eqs. (9.2) is carried out for 2D waves with $c = c_s$ and $\omega_i = 0$ for the insulated-wall flat-plate boundary layers described in Section 9.3, the α_{sn} which are found by the eigenvalues search procedure are shown in Fig. 9.2. The solution for each n will be referred to as a mode: n = 1 is the first mode, n = 2 the second mode, etc. The wavenumbers of the first mode were first computed by Lees and Reshotko (1962). With $c = c_s$, a y_a where $\overline{M}^2 = 1$ occurs first at $M_1 = 2.2$ ($y_a = 0$). With increasing M_1, the relative sonic point y_a moves out into the boundary layer, and α_{sn} varies in inverse proportion to y_a as required by Eq. (9.18b). No higher modes with $c = c_s$ could be found numerically for $M_1 < 2.2$, in agreement with the theory given above.

A prominent feature of Fig. 9.2 is that the upward sloping portion of the first-mode curve between M_1 = 2 and 4.5 is in a sense continuous through the other modes, i.e., there is a Mach number range for each mode where the α_{sn} vs. M_1 curve has a positive slope. The end point of this region for one mode is close to the starting point of a similar region for the next higher mode. The approach becomes closer as M_1 increases. The significance of these intervals of positive slope is that they provide the exceptions to the correctness, or approximate correctness, of the results given by, or deduced from, Eqs. (9.18b). Indeed we could well identify these modes as the "exceptional" modes.

With the wavenumbers of the multiple neutral waves established, the next step is to examine the eigenfunctions. For this purpose, the eigenfunction $\hat{p}/\gamma M_1^2$ is shown in Fig. 9.3 for the first six modes at $M_1 = 10$. The first thing to note is that the number of zeroes in $\hat{p}$ is one less than the mode number n. For example, the second mode has one zero, and $\hat{p}(0)$ is 180° out of phase with $\hat{p}(\delta)$; the third mode has two zeroes and $\hat{p}(0)$ is in phase with $\hat{p}(\delta)$. The number of zeroes in $\hat{p}(y)$ is the surest identification of the mode under consideration. By keeping track of the phase difference between $\hat{p}(0)$ and $\hat{p}(\delta)$, it is possible to determine when there is a change from one mode to another.

The appearance of the eigenfunctions in Fig. 9.3 confirms the simple theory given above: there is an infinite sequence of periodic solutions in the supersonic relative flow region which can satisfy the boundary conditions. The magnitude of $\hat{p}(0)$ is a minimum for the fourth mode [$\hat{p}(\delta)$ is the same for all modes]. Since the fourth mode at $M_1 = 10$ is on the upward sloping portion of the eigenvalue curve in Fig. 9.2, this is another indication of the special nature of such neutral solutions. For other modes, $\hat{p}(0)/\hat{p}(\delta)$ tends to become large away from n = 4, and tends to infinity as $n \to \infty$.

There is one important difference between the simple theory and Fig. 9.3. According to the theory, $\hat{p}(\delta)$ is positive for all modes; there are no zeroes in the interval $y > y_a$, and the number of zeroes in $y < y_a$ increases by one for each successive mode. We see from Fig. 9.3 that $\hat{p}(\delta)$ is negative for n > 4, and the number of zeroes in $y < y_a$ is the same for n = 5 as for n = 4. The total number of zeroes increases by one from n = 4 to n = 5 only because of the zero in $y > y_a$. However, we note that the progression of zeroes is correct in the supersonic region if we exclude the mode n = 4. This "exceptional" mode is extraneous to the simple theory, and preserves something of a first-mode character which probably betrays a different physical origin from the other modes. Indeed, the other higher modes are nothing more than sound waves which reflect back and forth between the wall and the sonic line of the relative flow at $y = y_a$ as first suggested by Lees and Gold (1964). Morkovin's theory is based on this idea, and its duplication of the wavenumber ratio sequence 1,3,5,... attests to its correctness. The "exceptional" modes are not part of this theory; they are perhaps vorticity waves associated with the generalized inflection point as are incompressible and low Mach number first-mode waves. In this view, the modes which have been identified in Figs. 9.2 and 9.3 as first-mode waves for $M_1 > 5$ are not first-mode waves at all; this distinction is reserved for the modes whose wavenumbers increase monotonically with increasing M_1. However, we shall continue to refer to n = 1 as the first mode.

9.5.2 Noninflectional neutral waves

A further consequence of a region of supersonic relative flow in the boundary layer is the existence of a class of neutral waves which is completely different from anything encountered in the incompressible theory. These waves are characterized by having phase velocities in the range $1 \lesssim c \lesssim 1 + 1/M_1$. For each phase velocity there is an infinite sequence of wavenumbers, just as for the inflectional neutral waves. A wave with c = 1 is at rest with respect to the freestream; a wave with $c = c_{02} = 1 + 1/M_1$ propagates downstream relative to U_1^* with the freestream speed of sound. The Lees-Lin neutral sonic wave propagates upstream relative to U_1^* with the freestream speed of sound.

All of the $1 \lesssim c \lesssim 1 + 1/M_1$ waves are subsonic waves, and, because $D(\rho DU) = 0$ in the freestream, there is no discontinuity in the Reynolds stress and the necessary condition for the existence of a subsonic neutral wave is satisfied. Unlike the inflectional neutral waves, $D(\rho DU)$ does not have to be zero in the boundary layer, and the $1 \lesssim c \lesssim 1 + 1/M_1$ waves exist for any boundary layer subject only to

the requirement that $\bar{M}^2 > 1$ somewhere. The importance of the $c=1$ neutral waves is that in the absence of an interior generalized inflection point they are accompanied by a neighboring family of unstable waves with $c < 1$. Consequently, a compressible boundary layer is unstable to inviscid waves whenever $\bar{M}^2 > 1$, regardless of any other feature of the velocity and temperature profiles.

If we examine the inviscid equations (9.2), we see that when $c > 1$ they are no longer singular; i.e., there is no critical layer. Even when $c = 1$, and the critical layer is in a sense the entire freestream, Eq. (9.2a) is still not singular because $DU/(U-1)$ and $\hat{p}(y)/(U-1)$ both have finite limits as $y \to y_\delta$. We call this class of solutions the noninflectional neutral waves. These waves persist to low subsonic Mach numbers, because, except at $M_1 = 0$, it is always possible to find a c large enough so that $\bar{M} = -1$ somewhere in the boundary layer.

The approximate theory of the preceding Section applies to the noninflectional neutral waves just as well as to the inflectional neutral waves provided the initialization is changed for $c = 1$ to make $\hat{v}/(\alpha U - \omega)$ finite in the freestream. This change is needed because with $c = 1$ the wave motion is confined to the boundary layer and $\hat{v}$ must be zero for $y > y_\delta$. An infinite sequence of wavenumbers is obtained with the spacing given by Eq. (9.19), but since c is different from c_s the numerical values are not the same as for the inflectional waves. The wavenumbers obtained from the numerical integration with $c = 1$ are shown in Fig. 9.4 as functions of Mach number. These wavenumbers are denoted by α_{1n}, where the first subscript refers to $c = 1$, and the second is the mode number. There is now no portion of any wavenumber curve with a positive slope, and the spacing agrees reasonably well with the approximate formula. The discrepancy is about 10% for the first two modes, and decreases to about 1% for the fifth and sixth modes.

The eigenfunctions $\hat{p}(y)$ of the first six modes of the noninflectional neutral waves with $c = 1$ at $M_1 = 10$ are shown in Fig. 9.5. Here the ratio $\hat{p}(y)/\hat{p}(0)$ is plotted, rather than $\hat{p}(y)$ with $\hat{p}(\delta)$ fixed as in Fig. 9.3. The appearance of these eigenfunctions is in complete accord with the simple theory, unlike the inflectional neutral waves where the modes on the upward sloping portions of the wavenumber curves interrupt the orderly sequence, and where an outer zero appears in the eigenfunctions for $n > 4$.

The numerical results for $1 < c < 1 + 1/M_1$ are similar to those presented for $c = 1$. Since these waves have no neighboring unstable or damped waves, they are of less importance in the inviscid theory than the other neutral waves. Consequently, these waves will not be considered further, and the term noninflectional neutral wave will refer only to a $c = 1$ wave. However, we might mention that the viscous counterparts of the $c > 1$ waves, which are damped rather than neutral, do have a role to play in certain cases.

9.6 Unstable 2D waves

A detailed discussion of the eigenvalues of amplified and damped waves as a function of Mach number for the first few modes has been given by Mack (1969). What we are mainly interested in here is the maximum amplification rate of the various modes, and this is shown in Fig. 9.6, where the maximum temporal amplification rate is given as a function of Mach number up to $M_1 = 10$. The corresponding frequencies are shown in Fig. 9.7. We see from Fig. 9.6 that below about $M_1 = 2.2$ the family of boundary layers we are considering is virtually stable to inviscid 2D waves, and that above $M_1 = 2.2$ the second mode is the most unstable mode. The latter result holds for 2D waves in all boundary layers that have been studied, and is one of the features that makes supersonic stability theory so different from the incompressible theory. Not only is there more than one mode of instability, but it is one of the additional modes that is the most unstable. Above $M_1 = 6.5$, the first mode is not even the second most unstable mode. The second-mode amplification rates can be appreciable. At $M_1 = 5$, the amplitude growth over a boundary-layer thickness is about double what is possible in a Blasius boundary layer at the Reynolds number of the maximum amplification rate, and about 25% of the maximum growth in a Falkner-Skan separation boundary layer.

9.7 Three-dimensional waves

In the detailed study of the eigenvalues of unstable 2D first-mode waves [Mack (1969)], it was noted that the phase velocity is always between c_o and c_s. These two velocities are almost identical near $M_1 = 1.6$, which suggests why boundary layers near that Mach number are almost stable even though the generalized inflection point has moved out to $U_s = 0.38$. The inflection point is a fixed feature of the boundary layer profile, and so is independent of the wave orientation. The phase velocity c_s of a 3D wave is $U_s \cos\psi$, and the phase velocity c_o is $(1-1/\bar{M}_1)\cos\psi$, where $\bar{M}_1 = M_1 \cos\psi$. Thus as the wave angle ψ increases from zero, c_o decreases more than by $\cos\psi$, and the difference $c_s - c_o$ increases. Consequently, we can expect the first mode to become more unstable. At the same time the thickness of the supersonic relative flow region, where one exists, will decrease along with $\bar{M}_1$ and we shall not be surprised to find that the higher modes become more stable.

Figure 9.8 shows the temporal amplification rate ω_i of the first and second modes at $M_1 = 4.5$ as a function of the frequency ω_r for several wave angles. Three-dimensional first-mode waves are indeed more unstable than 2D waves, and second-mode 3D waves are more stable than the corresponding 2D waves. The latter result also holds for all of the higher modes. The most unstable first-mode wave is at an angle of close to 60°, with an amplification rate about twice the maximum 2D rate and with a frequency a little over one-half of the frequency of the most unstable 2D wave.

At $M_1 = 4.5$, the unstable regions of the first two modes are separated by a damped region for all wave angles. However, at $M_1 = 8.0$, Fig. 9.9 shows that for 2D waves the first three modes are merged into a single unstable region. If we look at Fig. 9.2 we see that at this Mach number the exceptional mode is the third mode. Thus we can note another feature of the neutral wavenumbers α_{sn} of these modes: They serve as the "end points" of the merged unstable regions of the modes lying below them. As the wave angle increases from zero and $\bar{M}_1$ decreases, the merging is still in general accord with Fig. 9.2 for $\bar{M}_1$, as is confirmed by the calculation of $\tilde{\alpha}_{sn}$. The same pattern of upward sloping exceptional wavenumbers is found for oblique waves as for 2D waves [Mack (1969)]. For $\psi = 60^\circ$, the second mode is stable; for $\psi = 56^\circ$, there are still second-mode unstable waves, as can be verified by examining the phase change across the boundary layer of the pressure fluctuations, even though no peak is visible on the curve of Fig. 9.9.

In Fig. 9.10, the maximum temporal amplification rate with respect to frequency is plotted against for the four Mach numbers 4.5, 5.8, 8.0 and 10.0. At all of these Mach numbers the most unstable first-mode wave is at an angle of between 50° and 60°, and has a maximum amplification rate that is roughly double the most unstable 2D wave. The effect of Mach number on the maximum first-mode amplification rate with respect to both frequency and wave angle is shown in Fig. 9.11. The wave angle of the most unstable wave is noted on the figure to within 5°, and the maximum 2D amplification rates are shown for comparison. An interesting change in the relationship between the 2D and 3D amplification rates takes place for $M_1 <$ 4. The 3D maximum amplification rate is no longer only double the 2D rate as at higher Mach numbers; instead, at $M_1 = 3.0$ the ratio of the 3D rate to the 2D rate is 5.8, at $M_1 = 2.2$ it is 33, and at $M_1 = 1.8$ it is 130. We recall from Fig. 9.1 that it is near $M_1 = 1.6$ that the difference $c_s - c_o$ is the smallest. Therefore, the sonic limit acts as a severe constraint on the amplification of 2D waves at low Mach numbers. When this constraint is removed, as it is for 3D waves, the amplification rates increase sharply. We may consider the 3D maximum amplification rate as the one that properly reflects the inherent instability of a given boundary-layer profile.

9.8 Effect of wall cooling

Perhaps the most celebrated result of the early stability theory for compressible boundary layers was the prediction by Lees (1947) that cooling the wall stabilizes the boundary layer. This prediction was made on the basis of the asymptotic theory, and a criterion was provided for the ratio of wall temperature to recovery temperature at which the critical Reynolds number becomes infinite. Although Lees's original calculations contained numerical errors, the temperature ratio for complete stabilization was later computed correctly by a number of authors. The most accurate calculations gave the result that complete stability can be achieved for $1 < M_1 < 9$ by sufficient cooling. These calculations can be criticized in three important respects: First, no indication is given as to how the amplification rate varies with wall temperature; second, the calculations are for 2D waves only; and third, no account is taken of the existence of the higher modes. In this Section we shall see that the current inviscid theory can remedy all of these deficiencies.

As the boundary layer is cooled a second generalized inflection point appears for $U < 1-1/M_1$. As the cooling progresses, this second inflection point moves towards the first one and then both disappear for highly cooled walls. The complete account, as given by Mack (1969), of how these two inflection points affect the instability of 2D and 3D waves is a lengthy one and also brings in unstable supersonic waves. The conclusion is that when the generalized inflection points disappear, so do the first mode waves, but the higher modes, being dependent only on a relative supersonic region, remain. Some results are shown in Fig. 9.12, where the ratio of the maximum temporal amplification rate to its uncooled value is plotted against the ratio of wall temperature T_w to recovery temperature T_r at $M_1 = 3.0$, 4.5., and 5.8 for 3D first-mode waves, and at $M_1 = 5.8$ for 2D second-mode waves. In each instance, the wave angle given in the figure is the most unstable. The first-mode waves, even when oblique, can be completely stabilized at the Mach numbers shown, just as originally predicted by Lees (1947). However, the second mode is not only not stabilized, it is actually destabilized, although if the amplification rate is based on the boundary-layer thickness, the increase in ω_i is just about compensated for by the reduction in y_δ and $\omega_i y_\delta$ is virtually unchanged by cooling.

As a final result on the effect of cooling, we give Fig. 9.13 which shows the temporal amplification rate at $M_1 = 10$ as a function of wavenumber for an insulated wall and a highly-cooled wall ($T_w/T_r = 0.05$). For the former, the first four modes are merged to form a single unstable region, and the limiting upper wavenumber is the exceptional wavenumber of Fig. 9.2. For the latter, the unstable regions of the four modes are separate, as is true at lower Mach numbers for an insulated wall, and the maximum amplification rate of each mode is about double the uncooled value.

10. COMPRESSIBLE VISCOUS THEORY

The early theoretical work on the viscous stability theory of compressible boundary layers was based on the asymptotic methods that had proven to be successful for incompressible flow. However, these theories, which were developed by Lees and Lin (1946), Dunn and Lin (1955), and Lees and Reshotko (1962), turned out to be valid only up to low supersonic Mach numbers. Some results for insulated-wall flat-plate boundary layers obtained with the asymptotic method are given in Fig. 10.1, and compared with direct numerical solutions of the eigenvalue problem. All numerical results in this Section are for the same family of flat-plate boundary layers used in Section 9. In Fig. 10.1 neutral-stability curves of frequency at $M_1 = 1.6$ and 2.2 as computed from the Dunn-Lin (1955) theory by Mack (1960) are compared with results obtained by numerical integration using both the sixth-order simplified equations of Dunn and Lin, and the sixth-order constant Prandtl number version of the complete stability equations of Appendix 1. At $M_1 = 1.6$, the three calculations are in good agreement for $R > 700$, but at $M_1 = 2.2$, the agreement between the Dunn-Lin theory and the numerical solution with the complete equations is poor at all Reynolds numbers. The asymptotic theory is supposed to solve the simplified equations with an error no larger than the error involved in dropping the missing viscous terms. It is evident from the numerical solutions of the Dunn-Lin equations in Fig. 10.1, that the equations are better than the method used to solve them, but even so at $M_1 = 2.2$ the differences compared to the complete equations are too large to permit their use. However, there is little reason in any case to use these equations in numerical work, because they are of the same order as the complete 2D equations, and for 3D waves the sixth-order approximation given in this Section is more accurate.

10.1 Effect of Mach number on viscous instability

The viscous theory must of course be used for all numerical calculations at finite Reynolds numbers. An important theoretical question that we are able to answer with the viscous theory is the influence of Mach number on viscous instability. The definition of viscous instability that we use here for classification purposes is that the maximum amplification rate increases as the Reynolds number decreases. The maximum is with respect to frequency, and also wave angle for 3D waves, at constant Reynolds number, and the amplification rate is referenced to L^* [Eq. (2.57)]. A neutral-stability curve with an upper-branch wavenumber which increases with decreasing Reynolds number, as for the Blasius boundary layer, is

an indicator of viscous instability. We start by examining the curves of neutral stability for 2D waves presented in Fig. 10.2, where at five Mach numbers the wavenumber is plotted against 1/R to emphasize the higher Reynolds number region. The neutral curve at $M_1 = 1.6$ is of the same general type as for a low-speed boundary layer with only viscous instability. The low values of the neutral wavenumbers reflect a drastic weakening of viscous instability compared to the Blasius boundary layer. We already know from Fig. 9.6 that the maximum inviscid amplification rate increases sharply for $M_1 > 2.2$. What we see in Fig. 10.2 is that as the Mach number increases above 1.6, viscous instability continues to weaken and the effect of the increasing inviscid instability extends to lower and lower Reynolds numbers. Finally, at $M_1 = 3.8$ the influence of inviscid instability is dominant at all Reynolds numbers, and no trace of viscous instability can be seen. Viscosity acts only to damp out the inviscid instability, just as for the low-speed Falkner-Skan boundary layers with a strong adverse pressure gradient. As a result, the instability characteristics of flat-plate boundary layers above $M_1 = 3$ are more like those of a free shear layer than of a low-speed zero pressure-gradient boundary layer.

We have learned in Section 9 that 2D amplification rates above $M_1 = 1$ are strongly influenced by the constraint of the sonic limit on the phase velocity, and do not represent the true instability of a boundary-layer profile. Therefore, to get a complete view of the influence of Mach number on viscous instability we must turn to 3D waves. The instability of 2D and 3D waves up to $M_1 = 3.0$ is summarized in Fig. 10.3, where the maximum temporal amplification rate is given at $M_1 = 1.3, 1.6, 2.2,$ and 3.0 as a function of Reynolds number up to R = 2000. The most unstable wave angles (to within 5°) of the 3D waves are shown in the figure. It is apparent that these angles differ little from the inviscid values except near the critical Reynolds number at $M_1 = 1.3$. We see that viscous instability, which at $M_1 = 1.3$ is totally responsible for both 2D and 3D instability at the Reynolds numbers of the figure, decreases with increasing M_1 for 3D as well as for 2D waves. However, there is little change in the maximum 3D amplification rate with increasing Mach number, in contrast to the large decrease in the maximum 2D amplification rate. At $M_1 = 3.0$, viscosity acts only to maintain the maximum amplification rate at about the same level down to low Reynolds numbers, rather than as the main source of instability as at lower Mach numbers.

There are unfortunately no calculations available between $M_1 = 3.0$ and 4.5, but the distribution with Reynolds number of the maximum temporal amplification rate is given in Fig. 10.4 at $M_1 = 4.5, 5.8,$ and 7.0 for wave angles that are approximately the most unstable. All of these waves are first-mode waves. At $M_1 = 10$ it is difficult to assign a maximum in the first-mode region as the single peak in the ω_i vs α curves for $\psi > 50^\circ$ occurs near the transition from the first to the second mode, and 55° has been rather arbitrarily selected as the most unstable angle. In any case, it is clear from Fig. 10.4 that in this Mach number range there is no viscous instability and the influence of viscosity is only stabilizing.

10.2 Second mode

The lowest Mach number at which the unstable second mode region has been located at finite Reynolds numbers is $M_1 = 3.0$, where the minimum critical Reynolds number R_{cr} is 13,900 [Mack (1984)]. As the Mach number increases, the inviscid second-mode maximum amplification rate increases, as shown in Fig. 9.6, and the unstable second-mode region moves rapidly to lower Reynolds numbers. At $M_1 = 3.8$, R_{cr} is 827; at $M_1 = 4.2$ it is 355; and at $M_1 = 4.5$ it is 235. Furthermore, the first and higher-mode unstable regions go through the same process of successive mergers as they do in the inviscid theory. The first merger, between the first and second-mode unstable regions, takes place at about $M_1 = 4.6$. Examples of neutral-stability curves of wavenumber just before merger ($M_1 = 4.5$), and just after merger ($M_1 = 4.8$), are shown in Fig. 10.5. The shapes of the neutral-stability curves, both before and after merger, are such as to suggest that viscosity is only stabilizing for all higher modes, and this is confirmed for the 2D second mode by Fig. 10.6, where the distribution of $(\omega_i)_{max}$ with Reynolds number is shown for $M_1 = 4.5, 5.8, 7.0,$ and 10.0.

The effect of wave angle on second-mode amplification rates is shown in Fig. 10.7, where $(\omega_i)_{max}$ is plotted against wave angle for the same Mach numbers as in Fig. 10.6. This figure is to be compared with the comparable inviscid results in Fig. 9.10. In both instances, increasing Mach number brings a reduction in the rapidity with which the maximum amplification falls off with increasing wave angle.

10.3 Effect of wall cooling and heating

Few results have been computed from the viscous theory for boundary layers with cooled and heated walls. One result, shown in Fig. 10.8, gives the effect of heating and cooling on the stability of a low-speed boundary layer ($M_1 = 0.05$). The x-Reynolds numbers of 2D normal modes for three constant values of the N factor, $\ln(A/A_o)_{max}$, are plotted against the wall temperature ratio T_w/T_r. We see that cooling has a strong stabilizing effect, and that heating has a strong destabilizing effect. The frequencies that correspond to the N factors are also strongly affected by the wall temperature. For example, at $T_w/T_r = 0.90$, the frequency for N = 9 is $F = 0.157 \times 10^{-4}$; at $T_w/T_r = 1.15$, it is $F = 0.445 \times 10^{-4}$.

As an example of the effect of wall cooling at hypersonic speeds, Fig. 10.9 shows 2D neutral curves at $M_1 = 5.8$ for $T_w/T_r = 1.0, 0.65, 0.25$ and 0.05. The freestream temperature is $50^\circ K$ except for the lowest wall temperature where it is $125^\circ K$. When the wall is cooled to $T_w/T_r = 0.65$, a noticeable stabilization takes place for the first-mode, but only a narrowing of the unstable wavenumber band can be detected in the second-mode region. At the other two temperature ratios, there is no unstable first-mode region. The lowest temperature ratio is of interest because there is no generalized inflection point in the boundary layer, and thus no α_{s2} to serve as the limit of the upper branch of the neutral curve. We may observe that the wavenumbers at the critical Reynolds numbers of the three cooled cases are in the inverse proportion 1.0:0.71:0.48, and the corresponding boundary-layer thicknesses are in the proportion 1.0:0.69:0.53. Consequently, the length scale is the controlling factor in the location of the second-mode unstable region in terms of wavenumber.

10.4 Use of sixth-order system for 3D waves

We have already noted in Section 8.5 that only a single dissipation term couples the energy equation [8.9e)] to the other equations for a 3D wave in either a 2D or 3D boundary layer, and mentioned the economy measure proposed by Mack (1969) of using the sixth-order system that results from neglecting this term for 3D waves. These equations are essentially the 2D equations in the direction of $\vec{k}$. In Table 10.1 the temporal amplification rates computed from the sixth- and eighth-order systems are compared for various wave angles and Reynolds numbers at five Mach numbers. In all cases the waves are close to the most unstable first-mode waves at the particular Mach and Reynolds numbers listed. We see that the sixth-order system is surprisingly good, and can be used at R = 1500 for all Mach numbers with a maximum error of less than 5%. The error of the sixth-order system, which depends not only on the Mach and Reynolds number, but also on the wave angle, is usually minimal up to about $\psi = 30°$ and can become large for $\psi >$ 70°.

Table 10.1. Comparison of temporal amplification rates for 3D waves as computed from sixth-order and eighth-order systems of equations at several Mach numbers.

M_1	R	α	ψ	$\omega_i \times 10^3$ 6th order	$\omega_i \times 10^3$ 8th order	% difference
1.3	500	0.075	45°	0.883	0.824	7.2
1.3	1500	0.060	45°	1.467	1.445	1.5
1.6	500	0.070	55°	0.974	0.874	11.4
1.6	1500	0.050	55°	1.384	1.346	2.8
2.2	500	0.055	60°	1.198	1.066	12.4
2.2	800	0.045	60°	1.391	1.300	7.0
2.2	1500	0.035	60°	1.325	1.273	4.1
4.5	500	0.045	60°	1.117	1.039	7.5
4.5	1500	0.050	60°	1.641	1.613	1.7
5.8	500	0.050	55°	0.790	0.736	7.3
5.8	1500	0.060	55°	1.403	1.384	1.4
10.0	1500	0.040	55°	0.444	0.434	2.3

There are three other dissipation terms in the energy equation besides the coupling term, and their effect on the amplification rate has also been examined by Mack (1969) at R = 1500 and M_1 = 2.2, 5.8 and 10.0. The wavenumbers were the same as in Table 10.1. At M_1 = 2.2, the coupling term has the largest influence on the amplification rate. However, at the two higher Mach numbers the other terms increase in importance. Since some terms are stabilizing and others destabilizing, the error with all dissipation terms zero is smaller at these two Mach numbers than with only the coupling term zero. It is not known how general this result is, but experience with the Dunn-Lin equations indicates that it is limited to waves with ψ well away from zero.

The small effect of the dissipation terms on the amplification rates of the 3D waves in the above-mentioned calculations is in distinct contrast to what happens when the Dunn-Lin equations are used for 2D waves. The sixth-order system with only the coupling term zero is exact for ψ = 0, unlike the Dunn-Lin equations where all of the dissipation terms are neglected along with a number of other terms that are supposed to be of the same order. The differences between the neutral-stability curves in Fig. 10.1 computed directly from the Dunn-Lin equations and those computed from the complete equations testify to the importance of the neglected terms. A calculation at M_1 = 2.2 and R = 600 for α = 0.045 gave the result that the maximum 2D amplification rate from the Dunn-Lin equations is 63% larger than when computed from the complete equations. A more favorable result is obtained at this Mach number for a 60° wave with α = 0.045 at R = 1000, where the Dunn-Lin equations give an amplification rate that is 15% too high. This is an improvement over the 2D results, but still not as good as the result obtained when only the coupling term is neglected. At M_1 = 4.5 and R = 1500, the amplification rate of the most unstable 3D first-mode wave computed from the Dunn-Lin equations is in error by 23%; the error for the most unstable (2D) second-mode wave is 14%. The conclusion to be drawn is that the Dunn-Lin approximation is too severe, and the equations are unsuitable for numerical work above about M_1 = 1.6. On the contrary, the sixth-order system with only the coupling term neglected can be used for numerical computations where high accuracy is not important, and they offer a substantial saving in computer time and expense.

10.5 Spatial theory

Both the theoretical and numerical aspects of the stability of compressible boundary layers were worked out almost completely on the basis of the temporal theory. In contrast, almost all stability calculations are now routinely done with the spatial theory. Two exceptions are the SALLY [Srokowski and Orszag (1977)] and COSAL [Malik and Orszag (1981)] codes for 3D boundary layer stability, which calculate eigenvalues from the temporal theory and use the 3D Gaster transformation to convert to spatial eigenvalues. This approach, which introduces a small error into the calculation has the advantage of allowing the use of powerful matrix methods. The COSAL code exploits this possibility by providing a global eigenvalue search which relieves the user from the necessity of making an initial eigenvalue guess.

Some of the extensive temporal calculations of Mack (1969) have been recalculated by El-Hady and Nayfeh (1979) using the spatial theory. All findings were in accord with the temporal calculations. A recent series of spatial calculations by Wazzan, Taghavi and Keltner (1984) found important differences with the calculations of Mack, but there is good reason to believe that the new calculations are not correct [Mack (1984b)].

As an example of the same calculation performed with the temporal and spatial theories, Figs. 10.10 and 10.11 give the respective maximum amplification rates of the most unstable first and second-mode waves at R = 1500 as a function of freestream Mach number. The differences between the temporal and spatial first-mode curves are due to the increase in the group velocity from about 0.4 at $M_1 = 0$ to near 1.0 at high Mach number. However, both curves reflect the fact that at first increasing Mach number brings a reduction in the maximum amplification rate because of the weakening of viscous instability, then the increasing inviscid instability becomes dominant, and finally the increasing boundary-layer thickness causes a proportionate reduction in the amplification rate. Furthermore, it is important to keep in mind that both the spatial theory and the temporal theory plus the Gaster transformation give almost identical values of the amplitude ratio, and so either can be used in transition-prediction calculations.

11. FORCING THEORY

11.1 Formulation and numerical results

The structure of linear stability theory allows the forced response of the boundary layer on a flat plate to a particular type of external disturbance field to be readily obtained [Mack (1971,1975)]. One of the independent solutions of the stability equations in the freestream is, for $\alpha_1 = 0$ and in the limit of large Reynolds number, the inviscid flow over an oblique wavy wall of wavelength $2\pi/\alpha$ moving with the velocity c. The time-independent part of the pressure fluctuation given by this solution is [Eq. (9.11)]

$$p = i\gamma M_1(\alpha-\omega)\exp\{i\alpha[x\mp(\overline{M}_1^2-1)^{1/2}y]\} \quad . \tag{11.1}$$

For a wave which is oblique to the freestream, α and $\overline{M}_1$ are taken in the direction normal to the constant phase lines in the x,z plane. It is seen from Eq. (11.1) that when $\overline{M}_1 > 1$, the constant phase lines in the x,y plane are Mach waves. With the negative sign in Eq. (11.1), the Mach waves are outgoing, i.e., energy is transported in the direction of increasing y; with the positive sign, the Mach waves are incoming. When $\overline{M}_1 < 1$, the solution with the upper sign decays exponentially upward, and the other solution increases exponentially upward. In stability theory, only solutions which are at least bounded as y→∞ are permitted, but no such restriction is present in the forcing theory where the incoming wave has been produced elsewhere in the flow. The full viscous counterpart of Eq. (11.1) for in incoming wave has a slow exponential increase upward, which is perfectly acceptable.

The incoming-wave solution bears some resemblance to a Fourier component of the sound field radiated from turbulent boundary layers at high supersonic speeds according to Phillips' (1960) theory. In this theory, each acoustic Fourier component α,β is produced by the same Fourier component of the frozen turbulent field moving at a supersonic source velocity c relative to the freestream. Thus the turbulent boundary layer is decomposed into oblique wavy walls moving supersonically, and the associated outgoing Mach waves are the incoming Mach waves of the receiving laminar boundary layer at y = 0. However, in Phillips' theory, the field is random, and each "wavy wall" exists for only a finite time related to the lifetime of an individual turbulent eddy. In the present theory, the incoming wave field is steady to an observer moving with c.

A solution for the boundary-layer response at each Reynolds number can be found for each α,β and c by using both inviscid solutions of the eighth-order system, Eqs. (8.11), together with the usual three viscous solutions which go to zero as y→∞ , to satisfy the boundary conditions as y = 0. The combined solution, in addition to giving the boundary-layer response which results from the incoming acoustic wave, also provides the amplitude and phase of the outgoing, or reflected, wave relative to the incoming wave. The combined, or response, wave is neutral in the sense of stability theory, but its amplitude in the boundary layer is a function of Reynolds number. If the local mass-flow fluctuation amplitude m(y) is chosen to represent the amplitude (a hot-wire anemometer measures primarily m), the ratio of m_p, the peak value of m(y), to m_i, the massflow fluctuation of the incoming wave, can be called A/A_1, and used in a manner similar to the amplitude ratio A/A_0 of an instability wave. An increase in m_p/m_i with increasing R represents an "amplification"; a decrease, a "damping".

The most important result of the forcing theory is shown in Fig. 11.1, where m_p/m_i from the viscous theory is plotted against Reynolds number for waves of six dimensionless frequencies in an insulated-wall, flat-plate boundary layer at $M_1 = 4.5$. The waves are 2D, and the phase velocity has been assumed to be c = 0.65. We see that the amplitude of each wave starts to grow at the leading edge, reaches a peak at a Reynolds number that varies inversely with frequency, and then declines. The lower the frequency, the higher the maximum value of m_p/m_i. This is the principal result of the forcing theory, and has been found to be true for all boundary layers and all waves regardless of the wave angle and the phase velocity (provided only that $\overline{M}_1 > 1$). As a consequence of this behavior, the forcing mechanism provides boundary-layer waves with amplitudes from 6-14 times as large as freestream sound waves without any instability amplification.

In the inviscid theory, once c and ψ have been specified the only remaining parameter is α. When the mass-flow fluctuation amplitude ratio is plotted against α for a 2D wave with c = 0.65 and the same boundary layer as in Fig. 11.1, the inviscid theory gives a result that is significantly different from the viscous theory. Since F = $\alpha c/R$, a wave of given dimensionless frequency F travelling downstream at a constant c will have its dimensionless wavenumber increase linearly with R. Consequently, the α axis is equivalent to the R axis in Fig. 11.1. What we find from the inviscid theory is that inviscid waves decrease in amplitude for $\alpha > 0.0075$. All of the amplitude peaks in Fig. 11.1 occur at an α larger than this except for the lowest frequency. Consequently, the initial growth of Fig. 11.1, which is just what is found in experiments in supersonic and hypersonic wind tunnels with turbulent boundary layers on the tunnel walls, is a purely viscous phenomenon. However, when the viscous response curves from Fig. 11.1

are also plotted against α, they show that the decrease in amplitude which follows the region of growth in Fig. 11.1 is described closely by the inviscid theory. This result is in contrast to stability theory, where the inviscid amplification and damping rates are only approached by the viscous theory in the limit $R \rightarrow \infty$. The higher the frequency, the lower the Reynolds number at which the viscous curve joins the inviscid curve.

11.2 Receptivity in high-speed wind tunnels

The quantity m_p/m_1, interpreted as A/A_1, is the most important result in supersonic and hypersonic wind tunnels. It provides an essential piece of information which has been missing up to now: the relation of the amplitude of a boundary-layer wave to the amplitude of the freestream wave which causes it. In other words, we now have a solution to one particular receptivity problem. Strictly speaking, m_p is equivalent to the A of stability theory only when the m distribution is self-similar, but such is not always the case. However, this situation is no different from the usual comparisons of the quasi-parallel stability theory with experiment, as in Section 7.5, where the peak m is followed downstream and identified with A even though the amplitude distributions are nonsimilar.

The major difficulty in using the forcing theory as a solution of the receptivity problem is that forced waves are distinct from free waves, and the process by which the former become the latter is unknown. An experiment by Kendall (1971) showed that, as measured by the phase velocity, a forced wave near the leading edge evolves into a free instability wave farther downstream. In the paper from which a portion of the text of this Section has been adapted [Mack (1975)], we assumed that the forcing theory applies up to the neutral-stability point of the particular frequency under consideration, and that stability theory applies downstream of that point. The conversion from one wave to the other would seem most likely to occur if the amplitude distribution through the boundary layer at the neutral-stability point matched the eigenfunction of the instability wave of the same frequency and wavelength. A limited number of calculations at $M_1 = 4.5$ show that the two distributions are indeed close together for the same F, α and R. With the only mismatch between the two waves a phase-velocity difference of 20%, conversion of forced into free waves can be expected to take place quickly.

Consequently, with the approach just outlined the forcing theory can be used to calculate A_0/A_1, the ratio of the instability-wave amplitude at the neutral point to the amplitude of the sound waves radiated by the turbulent boundary layer on the wind-tunnel wall. The subsequent ratio of the instability-wave amplitude to A_1 is found by multiplying A_0/A_1 by the usual amplitude ratio A/A_0 calculated from stability theory. Thus, with the forcing theory we can replace the previously unknown constant A_0 with a known frequency-dependent A_0.

11.3 Reflection of sound waves from a laminar boundary layer

A more straightforward use of the forcing theory is to calculate the reflection of a monochromatic sound wave from a boundary layer. Figure 11.2 gives the ratio of A_r, the amplitude of the reflected wave, to A_i, the amplitude of the incoming wave, as a function of α for c = 0.65 and the same $M_1 = 4.5$ boundary layer used previously. Figure 11.3 gives the ratio of $\hat{p}(0)$, the pressure fluctuation at the wall, to $\hat{p}_i(0)$, the pressure fluctuation of the incoming wave at the position of the wall with no boundary layer present. In each figure the upper curve is the inviscid result, and the other curves are the viscous results for a series of frequencies.

According to the inviscid theory, when $\alpha = 0$, $A_r/A_i = 1.0$ and $\hat{p}(0)/\hat{p}_i(0) = 2.0$; when $\alpha \rightarrow \infty$, $A_r/A_i = 1.0$ and $\hat{p}(0)/\hat{p}_i(0) = 0$. Thus for $\alpha = 0$, the boundary layer effectively has zero thickness and the sound wave reflects as from a solid surface in the absence of a boundary layer. The reflected wave has the same amplitude and phase at y = 0 as the incoming wave so that the wall pressure fluctuation is twice $\hat{p}_i(0)$. At the other limit, $\alpha \rightarrow \infty$, the boundary layer is infinitely thick compared to the wavelength, and the reflection is the same as from a constant-pressure surface. The amplitude of the reflected wave is again equal to that of the incoming wave, but its phase at y = 0 differs by $180°$ from the incoming wave. Thus the pressure fluctuation at the wall is zero. Between these two limits, the amplitude of the reflected wave is always greater than the amplitude of the incoming wave.

The viscous results are quite different. For small α, A_r is always less than A_i. Furthermore, a minimum exists in A_r for each frequency. A similar minimum exists in $\hat{p}(0)$, but it is located at a larger α than is the A_r minimum. If the A_r minimum were to reach zero, that particular α would constitute an instability eigenvalue for the family of incoming waves. However, in stability theory, this type of wave has not been encountered, either as a supersonic wave with c < $1-1/M_1$ as in the present example, or as a subsonic wave with c > $1-1/M_1$ where the amplitude increases exponentially with increasing y. Figure 11.2 indicates that if such an eigenvalue exists it would be at such a low Reynolds number to make the use of the quasi-parallel theory invalid.

When the incoming Mach waves of the external travelling sound field reflect from a solid surface in the absence of a boundary layer, there is no phase shift at the wall. Compression waves reflect as compression waves, and the reflected waves originate at the points where the corresponding incoming waves intersect the surface. However, when a boundary layer is present, there is a phase shift at the wall. Consequently, a reflected Mach wave of the same phase appears to originate at a distance Δ^* away from the point of intersection. This offset distance, expressed as a ratio to the boundary-layer thickness, is given by

$$\Delta^*/\delta = (c/FRy_\delta)[\theta_i(0) - \theta_r(0)] , \qquad (11.2)$$

where $\theta_i(0)$ is the phase (in radians) of the pressure fluctuation of the incoming wave at the wall, and $\theta_r(0)$ is the same quantity for the reflected wave. When the phase of the reflected wave lags the phase of the incoming wave, the reflected wave originates at a point downstream of the intersection point of the incoming wave. When the phase difference is an integer multiple of π, the incoming wave reflects as a wave of the opposite sign at the point of intersection.

In Fig. 11.5, the ratio Δ^*/δ is given at R = 600 as a function of frequency for the same conditions as in Figs. 11.3 and 11.4. At only one frequency, $F = 0.975 \times 10^{-4}$, is the offset distance zero. For all smaller frequencies, the phase of the reflected wave lags behind the phase of the incoming wave, and Δ^* is positive with a maximum of 4.5δ at $F = 0.08 \times 10^{-4}$. Because of the long wavelength at this frequency, this offset is only $0.077\lambda^*$, or 28° in phase. Offsets have been observed experimentally in unpublished measurements of Kendall. The measurements were made with a broad-band hot-wire signal, so no direct comparison with the single-frequency calculations is possible.

11.4 Table of boundary-layer thicknesses

As a final item in Part B, we append Table 11.1 which gives the three common dimensionless boundary-layer thicknesses as functions of the freestream Mach number for the family of insulated-wall, flat-plate boundary layers for which numerical results have been given in Sections 9, 10 and 11. These quantities may be used to convert the α, σ and R (all based on L^*) into, say, α_δ, σ_δ and R_δ, based on δ. The conversion is achieved by multiplying α, σ and R by y_δ.

Table 11.1 Dimensionless boundary-layer thickness (U = 0.999), displacement thickness and momentum thickness of insulated-wall, flat-plate boundary layers. (Wind-tunnel temperature conditions.)

M_1	y_δ	$y_\delta{}^*$	y_θ
0	6.0	1.72	0.664
0.7	6.2	1.92	0.660
1.0	6.4	2.13	0.656
1.6	7.0	2.77	0.648
2.0	7.6	3.37	0.644
2.2	8.0	3.72	0.643
3.0	9.8	5.48	0.642
3.8	12.1	7.83	0.644
4.2	13.5	9.22	0.645
4.5	14.6	10.34	0.646
4.8	15.8	11.55	0.646
5.8	20.0	15.73	0.636
6.2	21.7	17.49	0.629
7.0	25.4	21.19	0.616
7.5	27.8	23.62	0.607
8.0	30.3	26.13	0.598
8.5	32.9	28.72	0.590
9.0	35.5	31.38	0.581
9.5	38.2	34.10	0.573
10.0	41.0	36.88	0.565

PART C. THREE-DIMENSIONAL BOUNDARY LAYERS

12. ROTATING DISK - A PROTOTYPE 3D BOUNDARY LAYER

Up to this point we have been concerned in the numerical examples exclusively with two-dimensional boundary layers, although the formulations of Sections 2 and 8 are also valid for three-dimensional boundary layers. In the final three Sections we shall take advantage of this fact to present a number of results for 3D boundary layers. A fundamental difference between the stability of 3D and 2D boundary layers is that a 3D boundary layer is subject to crossflow instability. This type of instability, which cannot occur in a 2D boundary layer, is responsible for early transition on sweptback wings. Its essential features can best be introduced by studying the simple boundary layer on a rotating disk. This self-similar boundary layer of constant thickness was first used for this purpose by Gregory, Stuart and Walker (1955) in their classic paper on three-dimensional boundary-layer instability.

12.1 Mean boundary layer

The exact solution of the Navier-Stokes equations for a rotating disk was given by von Karman (1921), and later an accurate numerical solution was worked out by Cochran (1934) and is given in Schlichting's (1979) book. We use the coordinate system r^*, θ, z^*, where r^* is the radius, θ is the azimuth angle, and z^* is in the direction of the angular velocity vector $\vec{\Omega}$. The radial, azimuthal and axial velocity components can be written

$$U^*(r^*,z^*) = \Omega^* r^* U(\zeta) \ , \qquad V^*(r^*,z^*) = \Omega^* r^* V(\zeta) \ ,$$
$$W^*(z^*) = (\Omega^* \nu^*)^{1/2} W(\zeta) \ . \tag{12.1}$$

The dimensionless velocity components U, V and W are functions only of the axial similarity variable

$$\zeta = z^*/L^* \ , \tag{12.2}$$

where

$$L^* = (\nu^*/\Omega^*)^{1/2} \tag{12.3}$$

is the length scale. In terms of the length scale and the velocity scale $\Omega^* r^*$, the Reynolds number is

$$R = \Omega^* r^* L^*/\nu^* = r^*/L^* \ , \tag{12.4}$$

which is simply the dimensionless radial coordinate r. The Reynolds number based on the local azimuthal velocity and radius is

$$Re = \Omega^* r^{*2}/\nu^* = (r^*/L^*)^2 \ . \tag{12.5}$$

Thus $R = Re^{1/2}$, just as in the 2D boundary layers we have been studying. The displacement thickness of the rotating-disk boundary layer is $1.271L^*$.

The dimensionless azimuthal and radial velocity profiles in the coordinate system rotating with the disk are shown in Fig. 12.1. The azimuthal, or circumferential, profile is of the same type as in a 2D boundary layer with the velocity increasing monotonically from the surface to the outer flow, and it will be referred to as the streamwise profile. With the disk rotating in the direction of positive θ (counterclockwise), the outer flow relative to the disk is in the negative (clockwise) direction. The radial profile is of a type that cannot occur in a 2D boundary layer. The velocity, directed outward from the disk center, is zero both at the wall and in the outer flow, so that there is of necessity an inflection point, which is located at $\zeta = 1.812$, where U = 0.133 and V = -0.760. The radial velocity, being normal to the streamwise flow, is by definition the crossflow velocity. The maximum radial velocity of $U_{max} = 0.181$ is located at $\zeta = 0.934$, where V = -0.496.

12.2 Crossflow instability

The phenomenon of crossflow instability was discovered during early work on the flow over swept-back wings. Transition in flight tests was observed by Gray (1952) to occur near the leading edge at abnormally low Reynolds numbers compared to an unswept wing. Flow visualization revealed that the wing surface before transition was covered with closely-spaced parallel streaks in the direction of the local potential flow, as shown in Fig. IX.20 of the review article by Stuart (1963). The streaks were fixed to the wing, and, once formed, did not change with time. They were conjectured to be the result of stationary vortices in the boundary layer. This same phenomenon was demonstrated by Gregory, Stuart and Walker (1955) to exist on a rotating disk. The streaks were found by the china-clay technique to take on the form of logarithmic spirals at an angle of about 13° to 14° to the circumferential direction [see frontispiece of Rosenhead (1963)], with the radius of the spiral decreasing with increasing angle θ. As in the wing experiment, the streak pattern was fixed to the surface, and so could be photographed at the conclusion of the experiment with the disk at rest.

Stuart [Gregory et al. (1955)] used an order-of-magnitude argument to reduce the exact linearized Navier-Stokes equations for a rotating disk to the fourth-order Orr-Sommerfeld equation for the determination of eigenvalues. In this case, as we have already discussed in Section 2.4.1, the 3D stability problem reduces to a 2D stability problem for the velocity profile in the direction of the wavenumber vector. Since the velocity profile in a 3D boundary layer, unlike a 2D boundary layer, depends on the direction, there is a different stability problem to solve for each wave direction. The circumferential profile has only viscous instability, and is much too stable to have anything to do with the observed instability phenomena. The radial velocity profile, on the contrary, has inviscid instability because of the inflection point. As the inflection point is located well away from the disk surface, we can expect there to be a strong instability.

In addition to the inflectional radial profile, there is a whole family of profiles in directions close to the radial which also have inflection points. Stuart noted that for the velocity profile at an angle of $\epsilon = 13.2^\circ$, where ϵ is measured from the radius in the positive θ direction, the inflection point is located where the magnitude of the velocity is zero. Consequently, according to the Rayleigh theorem, which was shown to still be valid for this type of profile, a stationary neutral normal mode (phase velocity $c = 0$) can exist with a wave angle equal to ϵ. Stuart also showed by calculating streamlines in the plane of ζ and the wavenumber vector for the rotating disk with large suction that the stationary inviscid disturbance consists of a system of vortices close to the surface, all rotating in the same direction (clockwise, looking along the spiral towards the disk center) and spaced one wavelength apart, and a second system of vortices farther from the surface. Brown (1960) repeated this calculation for the rotating disk without suction using the viscous equations, and confirmed the vortices near the surface, but not those farther out. The vortices near the surface were in accord with conjectures made earlier. Thus the streaks and the spiral angle were explained as manifestations of inflectional instability associated with the crossflow, and the whole phenomenon was named crossflow instability.

This explanation, while very suggestive, left many questions unanswered. The azimuthal wavelength calculated by Stuart for the inviscid neutral wave, gave the result that there should be 113 vortices around the circumference at $R = 433$, whereas in the experiments only about 30 were observed. This discrepancy was attributed to the neglect of viscosity. Another reason for the discrepancy, not mentioned at the time, is that the theory dealt with neutral waves, while the waves that form in the china clay were unstable spatial waves, i.e., they were amplifying in the outward radial direction. Brown (1960) calculated a neutral-stability curve from the Orr-Sommerfeld equation for the velocity profile in the direction 11.5° [said to be measured from the photograph in Gregory et al. (1955)], and also determined the locus in α-R space of unstable stationary temporal waves with this wave angle. According to Brown's calculation, the number of vortices at $R = 433$ is 23.6, and at $R = 540$ is 31.5. These numbers are more in accord with experiment, but no explanation was given as to why these particular waves should be observed.

12.3 Instability characteristics of normal modes

The Orr-Sommerfeld calculations of Brown (1959,1960,1961) for various directional velocity profiles gave a critical Reynolds number of about 180. In none of the experiments were waves detected at anything approaching this low a Reynolds number. Malik, Wilkinson and Orszag (1981) derived a new system of equations in which all terms of order $1/r$ were retained. These equations are of sixth order for the determination of eigenvalues, rather than fourth order. With the sixth-order equations, the critical Reynolds number was computed to be 287 [later corrected to 275 by Malik (1983, private communication)]. This large difference between the fourth and sixth-order equations casts serious doubt on the use of the former in the rotating-disk problem.

The stability analysis is carried out in the polar coordinates r, θ, ζ. The wavenumber vector $\vec{k}$ at an angle ψ to the radial direction has components α in the radial direction and β_θ in the azimuthal direction. The wave angle ψ is measured from the radius and is positive counterclockwise as usual. In Fig. 12.2, the spatial amplification rate σ in the radial direction, computed as an eigenvalue with $(\beta_\theta)_i = 0$ from the sixth-order equations of Malik et al. (1981), is plotted against the azimuthal wavenumber $\beta_\theta = 2\pi/\lambda_\theta$, where λ_θ is the azimuthal wavelength in radians. This wavenumber expresses the number of wavelengths around a circumference, which, in the present case, is equivalent to the number of vortices. It is related to the wavenumber β based on L^* by $\beta = \beta_\theta/R$. The critical Reynolds number is seen to be about $R = 273$, in reasonable agreement with Malik's most recent value. For R greater than about 400, the maximum spatial amplification rate in Fig. 14.2 is larger than in any 2D Falkner-Skan boundary layer (for the separation profile, $\sigma_{max} = 48 \times 10^{-3}$). The group-velocity angle ϕ_r of the most unstable normal mode at $R = 500$ is -83° (measured from the radial direction), so that the amplification rate in that direction, $\sigma_g = \sigma\cos\phi_r$, is only 8.9×10^{-3}. The large values in the radial direction can be regarded as a consequence of the long spiral path length rather than a reflection of the inherent instability of the velocity profile.

The wave angle ψ is given in Fig. 12.3 at several Reynolds numbers as a function of β_θ. The interest in this figure is the prominent maximum in ψ that increases with R. To understand this behavior it is necessary to mention that the normal-mode solution represented in Figs. 12.2 and 12.3 is not unique. There is a second solution with larger wave angles that is completely damped for $R \lesssim 500$. At $R = 500$, the minimum wave angle of this solution is 18.3° at $\beta_\theta = 23.5$, and the minimum damping is 1.8×10^{-3} at $\beta_\theta = 22.2$. At a Reynolds number somewhere above 500, the two solutions exchange identities for certain β_θ, with consequences that have not yet been worked out.

The logarithm of the amplitude ratio A/A_0 obtained by integrating σ along the radius is given in Fig. 12.4 at $R = 350, 400, 450$ and 500. The reference amplitude A_0 is at $R = 250$, rather than at the lower-branch neutral point of each Fourier component. The wave angle at the maximum amplitude of each R is noted in the figure. These numerical results differ from those of Malik et al. (1981) because here the irrotationality condition, Eq. (2.55c), has been applied to the wavenumber vector of each Fourier component. For the disk, this condition is that the azimuthal wavenumber β_θ, or number of vortices, is constant. That is, in Fig. 12.2 the path of integration is parallel to the ordinate. In Fig. 12.4, $\ln(A/A_0)$ is given as a function of both β_θ and $(\beta_r)_0$, the value of β_r at the reference Reynolds number of 250. We observe that although the bandwidth of β_θ for which A is greater than A_0 increases with increasing R, the bandwidth for which A/A_0 is within $1/e$ of the maximum amplitude ratio decreases slightly. The values of $\ln(A/A_0)$ in this figure contrast with much higher values obtained by Cebeci and Stewartson (1980b) from the fourth-order system and the parallel-flow saddle-point criterion. Transition is usually observed to start at a Reynolds number in the vicinity of 500, so that the N factors of Fig. 12.4 are of the magnitude customarily associated with transition in 2D boundary layers. Thus we see that crossflow instability in the rotating-disk boundary layer is powerful enough to lead to transition at lower-than-normal Reynolds numbers where the streamwise profile is completely stable.

12.4 Wave pattern from a steady point source

The wave angles and number of vortices at the peak amplitudes of Fig. 12.4 are close enough to what is observed in the experiments to suggest that the normal modes which yield those values are the dominant modes of the stationary wave system that appears in the flow-visualization photographs. However, we are still left without any explanation of how only the most-amplified mode could be present at each radius. The filtering action of the boundary layer is not strong enough to accomplish this, and the constraints of constant F and β_0 do not allow any initial Fourier component to be the most-amplified normal mode at more than one radius. Besides, the experiment of Gregory et al. (1955) showed clearly that a band of circumferential wavelengths is present at each radius, not just the most amplified.

A definite step forward was accomplished by the experiment of Wilkinson and Malik (1983). These investigators used a hot-wire anemometer instead of flow visualization, and so could more accurately resolve the disturbance structure on the disk. Although it had been conjectured by Gregory et al. (1955) that minute roughnesses might play a role in fixing the vortex pattern with respect to the disk, the Wilkinson-Malik experiment revealed for the first time that the wave pattern responsible for the stationary vortex lines emanates from point sources randomly located on the disk. All of the observed properties of the waves can thus be explained as characteristic features of the interference wave pattern that results from the superposition of the entire azimuthal wavenumber spectrum of equal-phase zero-frequency normal modes produced by the point-source roughness element. The streaks of the flow-visualization photographs are the constant-phase lines of the wave pattern. The wave patterns from a number of sources eventually merge and cover the entire circumference of the disk. It is this merged wave pattern that appears in the flow visualization experiments. The much greater sensitivity of the hot wire compared to flow visualization techniques made it possible to detect the waves at small radii where the merger was not yet complete.

Wilkinson and Malik (1983) made the phhenomenon even clearer by placing an artificial roughness on the disk. The waves from this roughness were of larger amplitude than the waves from the naturally occurring minute roughnesses, and so offered an opportunity to study the essential phenomenon in a purer form. Figure 12.5, taken from Fig. 18 of their paper, shows the steady wave pattern from the single roughness, as well as others from unavoidable natural roughnesses. In this figure, which was obtained by forming an ensemble average of the amplitude measurements at every disk revolution, the amplitudes have been normalized to a constant value of the maximum amplitude at each radius.

The wave pattern of Fig. 12.5 is of the same type that we studied in Section 7 for a harmonic point source in a Blasius boundary layer, with due allowance made for the very different instability characteristics of 2D boundary layers and 3D boundary layers with crossflow instability. We therefore modified our calculation procedure for planar boundary layers to fit the different geometry of the rotating disk and the lack of an axis of symmetry, and have calculated the wave pattern produced by a zero-frequency point source located at the Reynolds number of the roughness element in the Wilkinson-Malik experiment [Mack (1984c)]. The wave forms, normalized to a constant value of the maximum amplitude as in Fig. 12.5, are shown in Fig. 12.6 along with the constant phase lines. The numbering of the constant-phase lines corresponds to the system used by Wilkinson and Malik. It is evident that the calculated wave pattern is in the closest possible agreement with the measured wave pattern as to the location of the constant-phase lines, the number of oscillations at each radius, and the azimuthal wavelength. The latter quantity varies with both radius and azimuth angle. The shift of the wave pattern to the right in Figs. 12.5 and 12.6 with respect to the constant-phase lines is because amplitude propagates essentially along group-velocity trajectories. The agreement between Figs. 12.5 and 12.6 conclusively demonstrates that the observed stationary waves on a rotating disk are the result of the superposition of the entire spectrum of normal modes, both amplified and damped.

The calculated amplitudes along the constant-phase lines are given in Fig. 12.7. Vortex No. 11 is the one that comes from the point source, and it is the only one with an amplitude minimum, which, it should be noted, is well beyond the critical Reynolds number of 273. The reference amplitude of this vortex was selected to fit the minimum amplitude of the experiment, and then used for all of the other vortices. A comparison is given in Fig. 12.8 of the calculated and experimental envelope amplitude distributions at $R = 400$ and 466. In this figure, the experimental amplitudes have been normalized to the arbitrary theoretical maximum amplitude at $R = 400$. At $R = 400$, the agreement is excellent except at the right-hand edge of the wave pattern, where a second wave pattern was present in the experiment. At $R = 466$, the influence of the second wave pattern has spread almost to the center of the principal wave pattern, and is the reason for the disagreement between theory and experiment in Fig. 12.8 to the right of the maximum amplitude.

13. FALKNER-SKAN-COOKE BOUNDARY LAYERS

13.1 Mean boundary layer

In order to more fully study the influence of three dimensionality in the mean flow on boundary-layer stability than is possible with the rotating disk, it is necessary to have a family of boundary-layers where the magnitude of the crossflow can be varied in a systematic manner. The two-parameter yawed-wedge flows introduced by Cooke (1950) are suitable for this purpose. One parameter is the usual Falkner-Skan dimensionless pressure-gradient parameter β_h; the other is the ratio of the spanwise and chordwise velocities. A combination of the two parameters makes it possible to simulate simple planar three-dimensional boundary layers.

The inviscid velocity in the plane of the wedge and normal to the leading edge in the direction x_c is

$$U_{c1}^* = C^*(x_c^*)^m , \qquad (13.1)$$

where the wedge angle is $(\pi/2)\beta_h$ and $\beta_h = 2m/(m+1)$ as in Eq. (2.62). We shall refer to this velocity as the chordwise velocity. The velocity parallel to the leading edge, or spanwise velocity, is

$$W_{s1}^* = \text{const.} \tag{13.2}$$

The subscript 1 refers to the local freestream. For this inviscid flow, the boundary-layer equations in the x_c direction, as shown by Cooke (1950), reduce to

$$f''' + ff'' + \beta_h[(m+1)/2 - f'^2] = 0 . \tag{13.3}$$

This equation is the usual Falkner-Skan equation for a two-dimensional boundary layer, and is independent of the spanwise flow. The dependent variable $f(y)$ is related to the dimensionless chordwise velocity by

$$U_c = U_c^*/U_{c1}^* = [2/(m+1)]f'(y) , \tag{13.4}$$

and the independent variable is the similarity variable

$$y = y^*(U_{c1}^*/\nu^* x_c^*)^{1/2} . \tag{13.5}$$

Once $f(y)$ is known, the flow in the spanwise direction z_s^* is obtained from

$$g'' + fg' = 0 , \tag{13.6}$$

where

$$W_s = W_s^*/W_{s1}^* = g(y) . \tag{13.7}$$

Both $f'(y)$ and $g(y)$ are zero at $y = 0$ and approach unity as $y \to \infty$. Tabulated values of $g(y)$ for a few values of β_h may be found in Rosenhead (1963, p. 470).

The final step is to use $f'(y)$ and $g(y)$ to construct the streamwise and crossflow velocity components needed for the stability equations. A flow geometry appropriate to a swept back wing is shown in Fig. 13.1. There is no undisturbed freestream for a Falkner-Skan flow, but such a direction is assumed and a yaw, or sweep, angle ψ_{sw} is defined with respect to it. The local freestream, or potential flow, is at an angle ψ_p with respect to the undisturbed freestream. It is the potential flow that defines the x,z coordinates of the stability equations. The angle of the potential flow with respect to the chord is

$$\theta = \tan^{-1}(W_{s1}^*/U_{c1}^*) , \tag{13.8}$$

and θ is related to ψ_{sw} and ψ_p by

$$\theta = \psi_{sw} + \psi_p . \tag{13.9}$$

With the local potential velocity, $U_1^* = (U_{c1}^{*2} + W_{s1}^{*2})^{1/2}$, as the reference velocity, the dimensionless streamwise and crossflow velocity components are

$$U(y) = f'(y) \cos^2\theta + g(y) \sin^2\theta , \tag{13.10a}$$

$$W(y) = [-f'(y) + g(y)] \cos\theta \sin\theta. \tag{13.10b}$$

These velocity profiles are defined by β_h, which fixes $f'(y)$ and $g(y)$, and the angle θ. We note from Eq. (13.10b) that for a given pressure gradient all crossflow profiles have the same shape; only the magnitude of the crossflow velocity changes with the flow direction. In contrast, according to Eq. (13.10a) streamwise profiles change shape as θ varies. For $\theta = 0$, $U(y) = f'(y)$; for $\theta = 90^\circ$, $U(y) = g(y)$; for $\theta = 45^\circ$, the two functions make an equal contribution.

When the Eq. (13.10) velocity profiles are used directly in the stability equations, the velocity and length scales of the equations must be the same as in Eq. (13.10). This identifies the velocity scale as U_1^*, the length scale as

$$L^* = (\nu^* x_c^*/U_{c1}^*)^{1/2} , \tag{13.11}$$

and the Reynolds number $U_1^* L^*/\nu^*$ as

$$R = R_c/\cos\theta , \tag{13.12}$$

where $R_c = (U_{c1}^* x_c^*/\nu^*)^{1/2}$ is the square root of the Reynolds number along the chord. For positive pressure gradients ($m > 0$), $\theta = 90^\circ$ at $x_c = 0$ and $\theta \to 0^\circ$ as $x_c \to \infty$; for adverse pressure gradients ($m < 0$), $\theta = 0^\circ$ at $x_c = 0$ and $\theta \to 90^\circ$ as $x_c \to \infty$. The Reynolds number R_c is zero at $x = 0$ for all pressure gradients, as is R with one important exception. The exception is where $m = 1$ ($\beta_h = 1$). For a 2D planar flow, $\beta_h = 1$ is the stagnation-point solution; here it is the attachment-line solution. In the vicinity of $x_c = 0$, the chordwise velocity is

$$U_{c1}^* = x_c^* (dU_{c1}^*/dx_c^*)_{x=0} . \tag{13.13}$$

The potential velocity along the attachment line is W_{s1}^*, and the Reynolds number is

$$R_{x=0} = W_{s1}^*/[\nu^*(dU_{c1}^*/dx_c^*)_{x=0}] , \tag{13.14}$$

a non-zero value.

For our purposes in this Section, we may regard θ as a free parameter, and use the velocity profiles of Eq. (13.10) at any Reynolds number. However, for the flow over a given wedge, θ can be set

arbitrarily at only one Reynolds number. If θ_{ref} is θ at $R_c = (R_c)_{ref}$, the θ at any other R_c is given by

$$\tan\theta = \tan\theta_{ref} \; [(R_c)_{ref}/R_c]^{m/(m+1)} \quad , \qquad (13.15)$$

For $m \ll 1$, the dependence on R_c is so weak that θ is constant almost everywhere. One way of choosing $(R_c)_{ref}$ within the present context is to make it the chord Reynolds number where $\psi_p = 0$; i.e., the local potential flow is in the direction of the undisturbed freestream. Then θ_{ref} is equal to the yaw angle ψ_{sw}.

Figure 13.2 shows the crossflow velocity profiles for $\theta = 45^\circ$ and four values of β_h. The inflection point and point of maximum crossflow velocity (W_{max}) are also noted on the figure. In Fig. 13.3, W_{max} for $\theta = 45^\circ$ is given as a function of β_h from near separation to $\beta_h = 1.0$. The crossflow velocity for any other flow angle is obtained by multiplying the W_{max} of the figure by $\cos\theta\sin\theta$. The maximum crossflow velocity of 0.133 is generated by the separation profile rather than by the stagnation profile, where W_{max} = 0.120. However, W_{max} varies rapidly with β_h in the neighborhood of separation, as do all other boundary-layer parameters, and for $\beta_h = -0.190$, W_{max} is only 0.102.

The function g(y) is only weakly dependent on β_h, and, unlike f'(y), never has an inflection point even for an adverse pressure gradient. Indeed it remains close to the Blasius profile in shape, as underlined by a shape factor H (ratio of displacement to momentum thickness) that only changes from 2.703 to 2.539 as β_h goes from -0.1988377 (separation) to 1.0 (stagnation). The weak dependence of g(y) on β_h has been made the basis of an approximate method for calculating boundary layers on yawed cylinders. For our purposes, it allows some of the results of the stability calculations to be anticipated. For waves with the wavenumber vector aligned with the local potential flow, we can expect the amplification rate to vary smoothly from its value for a two-dimensional Falkner-Skan flow to a value not too far from Blasius as θ goes from zero to 90°.

The stability results will be presented in terms of the Reynolds number R and the similarity length scale L^*. In order that the results may be converted to the length scales of the boundary-layer thickness, displacement thickness or momentum thickness, Table 13.1 lists the dimensionless quantities $y_\delta = \delta/L^*$, $y_{\delta^*} = \delta^*/L^*$ and and the shape factor H of the streamwise profile for several combinations of β_h and θ. Also listed are W_{max}, the average crossflow velocity $\overline{W} = (\int Wdy)/y$; y_{inf}, the y of the inflection point of the crossflow velocity profile; and ε_{inf}, the deflection angle of the streamline at $y = y_{inf}$. The quantity y_δ is defined as the point where $U = 0.999$.

TABLE 13.1 Properties of three-dimensional Falkner-Skan-Cooke boundary layers.

β_h	θ	y_δ	y_{δ^*}	H	W_{max}	$\overline{W}$	ε_{inf}	y_{inf}
SEP	2.2	8.238	3.495	4.024	0.0102	0.00476	0.487	4.306
	5.0	8.236	3.489	4.010	0.0231	0.01077	1.100	
	10.0	8.229	3.466	3.959	0.0455	0.02123	2.156	
	40.0	8.095	3.075	3.280	0.1310	0.06214	5.709	
	50.0	8.017	2.897	3.064	0.1310	0.06274	5.516	
-0.10	45.0	6.522	1.985	2.698	0.0349	0.01619	1.498	3.213
-0.02	45.0	6.098	1.763	2.609	0.0058	0.00267	0.249	2.940
0.02	45.0	5.931	1.682	2.578	-0.0054	-0.00248	-0.232	2.835
0.04	45.0	5.854	1.646	2.564	-0.0104	-0.00480	-0.449	2.787
0.10	45.0	5.646	1.551	2.529	-0.0239	-0.01094	-1.029	2.659
0.20	45.0	5.348	1.424	2.482	-0.0423	-0.01924	-1.823	2.478
1.0	2.4	3.143	0.6496	2.227	-0.0100	-0.00503	-0.406	1.524
	10.0	3.196	0.6603	2.226	-0.0410	-0.02021	-1.669	
	40.0	3.574	0.8050	2.275	-0.1181	-0.05204	-5.129	
	45.0	3.621	0.8378	2.301	-0.1191	-0.05217	-5.291	
	50.0	3.661	0.8706	2.332	-0.1181	-0.05081	-5.295	
	55.0	3.695	0.9024	2.366	-0.1127	-0.04804	-5.135	
	80.0	3.791	1.0153	2.524	-0.0410	-0.01704	-1.987	
	87.6	3.799	1.0260	2.542	-0.0100	-0.00416	-0.489	

13.2 Boundary layers with small crossflow

In a two-dimensional boundary layer, the most unstable wave is two dimensional. Therefore, we can expect that in three-dimensional boundary layers with small crossflow the most unstable wave will have its wavenumber vector nearly aligned with the local potential flow, and we can restrict ourselves to waves with $\psi = 0^\circ$ for the purpose of determining the maximum amplification rate. This procedure is equivalent to studying the two-dimensional instability of the streamwise profile provided that $\overline{\psi} = 0$ (amplification rate in streamwise direction). In the calculations of this Section, $\overline{\psi}$ was taken to be either zero or ϕ_r. In the latter case, σ_g is almost identical to σ, which we define as the amplification rate with $\overline{\psi} = 0^\circ$, and we shall ignore the difference.

The effect of the flow angle θ on the maximum spatial amplification rate of the waves with $\psi = 0^\circ$ is shown in Fig. 13.4 for $\beta_h = \pm 0.02$ and two Reynolds numbers. The amplification rate σ_{max} is expressed as a ratio to the Blasius value $(\sigma_b)_{max}$. It will be recalled that with $\beta_h = 0$, g(y) = f'(y), and the velocity profile remains the Blasius function for all flow angles. The effect of a non-zero flow angle with $\beta_h \neq 0$ is destabilizing for a favorable pressure gradient, and stabilizing for an adverse pressure gradient. Consequently, it reduces the pressure-gradient effect of 2D Falkner-Skan boundary layers. The reason for this result is easy to understand by reference to Eq. (13.10). We have already pointed out in Section

13.1 that the spanwise velocity profile g(y) is always close to the Blasius function. Thus as the flow angle increases from zero, the amplification rate must change from the two-dimensional Falkner-Skan value at $\theta = 0°$ to a value not far from Blasius at $\theta = 90°$.

As discussed previously, the only physically meaningful flow with $\theta = 90°$ and a non-zero Reynolds number is the attachment-line flow ($\beta_h = 1.0$). For all other values of β_h, R at this flow angle must be either zero ($\beta_h > 0$) or infinite ($\beta_h < 0$). With $\beta_h = 1.0$ and R = 1000 ($R_\theta = 404.2$, where R_θ is the momentum-thickness Reynolds number), $\sigma_{max}/(\sigma_b)_{max} = 0.766$. The minimum critical Reynolds number of this profile is $(R_\theta)_{cr} = 268$ (the parallel-flow Blasius value is 201), yet turbulent bursts have been observed as low as $R_\theta = 250$ for small disturbances by Poll (1977).

We must still show that the waves with $\psi = 0°$ properly represent the maximum instability of three-dimensional profiles with small crossflow. For this purpose a calculation was made of σ as a function of ψ for $\beta_h = -0.02$, $\theta = 45°$, R = 1000 and F = 0.4256 x 10^{-4}, the most unstable frequency for $\psi = 0°$ at this Reynolds number. It was found that the crossflow indeed introduces an asymmetry into the distribution of σ with ψ, and the maximum of σ is located at $\psi = -6.2°$ rather than at 0°. However, this maximum value differs from the σ_{max} of Fig. 13.4 by only 0.7%.

13.3 Boundary layers with crossflow instability only

The main advantage that the Falkner-Skan-Cooke boundary layers offer over the rotating-disk boundary layer for studying crossflow instability is that the maximum crossflow velocity is not constant, but is a function of β_h and θ. The crossflow velocity is a maximum at $\theta = 45°$ for a given β_h, and we can expect the crossflow instability to also be a maximum near this angle. Figure 13.5 shows the minimum critical Reynolds number R_{cr} at $\theta = 45°$ for the zero-frequency crossflow disturbances as a function of β_h. For comparison, R_{cr} for Tollmien-Schlichting waves in 2D Falkner-Skan crossflow boundary layers, as computed by Wazzan et al. (1968), is also given. For adverse pressure gradients, the steady crossflow disturbances become unstable at Reynolds numbers well above the R_{cr} of the 2D profiles. On the contrary, for $\beta_h > 0.07$ the reverse is true, and for most pressure gradients in this range the steady disturbances become unstable at much lower Reynolds numbers than the 2D R_{cr} (for $\beta_h = 1.0$, the 2D R_{cr} is 19,280 compared to $R_{cr} = 212$ for zero-frequency crossflow instability).

The distribution of R_{cr} with θ is shown in Fig. 13.6 for $\beta_h = 1.0$ over the complete range of θ, and for the separation profiles ($\beta_h = -0.1988377$) over the range $0° < \theta < 50°$. Near $\theta = 0°$ and $90°$, R_{cr} is very sensitive to θ; near, but not precisely at, $\theta = 45°$ R_{cr} has a minimum. This minimum occurs close to the maximum of the streamline deflection angle at $y = y_{inf}$, ε_{inf} (see Table 13.1), which, unlike W_{max}, is not symmetrical about $\theta = 45°$. Table 13.2 lists the critical wave parameters for a few combinations of β_h and θ. The extensive computations needed to fix these parameters precisely were not carried out in most cases, and so the values in the Table are not exact. It can be noted that the relation

$$\psi = (\beta_h/|\beta_h|)(90 - |\varepsilon|_{inf}) \qquad (13.16)$$

gives ψ_{cr} to within a degree for the separation profiles, and to within 0.1° for the other profiles of Tables 13.1 and 13.2. This result holds in general for the most unstable wave angle.

TABLE 13.2 Wave parameters at minimum critical Reynolds number of zero-frequency disturbances.

β_h	θ	R_{cr}	k_{cr}	ψ_{cr}
SEP	2.2	535	0.213	-89.41
	5.0	237	0.213	-88.68
	10.0	121	0.215	-87.44
	40.0	46.5	0.230	-83.54
	45.0	46.7	0.230	-83.57
	50.0	48.4	0.231	-83.81
-0.10	45.0	276	0.295	-88.42
-0.02	45.0	1885	0.310	-89.74
0.02	45.0	2133	0.322	89.76
0.04	45.0	1129	0.327	89.53
0.10	45.0	527	0.339	88.93
0.20	45.0	328	0.358	88.12
1.00	2.4	2755	0.553	89.60
	10.0	671	0.547	88.33
	40.0	219	0.545	84.88
	45.0	212	0.540	84.70
	50.0	212	0.540	84.70
	55.0	218	0.538	84.85
	80.0	563	0.532	88.00
	87.6	2325	0.532	89.51

As an example of a boundary layer which is unstable at low Reynolds number only as a result of crossflow instability, we select $\beta_h = 1.0$ and $\theta = 45°$, and present results for the complete range of unstable frequencies. Although this pressure gradient can only occur at an attachment line, Fig. 13.5 leads us to expect that all profiles with a strong favorable pressure gradient will have similar results. For this type of profile, the minimum critical Reynolds number of the least stable frequency is very close to the R_{cr} of Fig. 13.5. We therefore choose R = 400, which is well above R_{cr} and where the instability is fully developed, and present a summary of the instability characteristics in Fig. 13.7.

Figure 13.7a gives σ_{max} as a function of the dimensionless frequency F, and also shows the portion of the ψ-F plane for which there is instability. The unstable region is enclosed between the curves marked ψ_U and ψ_L. These curves represent either neutral stability points or extrema of ψ. The corresponding wavenumber magnitudes are shown in Fig. 13.7b. The negative frequencies signify that with ψ taken to be continuous through F = 0, the phase velocity changes sign. If we choose ψ so that the wavenumber and phase velocity are both positive, then it is ψ that changes sign at F = 0. Consequently, there are two groups of positive unstable frequencies with quite different wave angles. The first group, which includes the peak amplification rate, is oriented anywhere from 5° to 31° (clockwise) from the direction opposite to the crossflow direction. The second group is oriented close to the crossflow direction itself.

13.4 Boundary layers with both crossflow and streamwise instability

As an example of a boundary layer which has both crossflow and streamwise instability at low Reynolds numbers, we select $\beta_h = -0.10$ and $\theta = 45°$. In contrast to the previous case, the steady disturbances do not become unstable until a Reynolds number, R = 276, where the peak amplification rate is already 7.35 x 10^{-3}. [For $\beta_h = -0.10$ and $\theta = 0°$, $\sigma_{max} = 11.0$ x 10^{-3} at F = 2.2 x 10^{-4} according to Wazzan et al. (1968)]. The distribution of σ with ψ is shown in Fig. 13.8 for F = 2.2 x 10^{-4}, a frequency close to the most unstable frequency of F = 2.1 x 10^{-4}. We see that with a maximum crossflow velocity of 0.0349 (cf. Table 13.1), the distribution of σ about $\psi = 0°$ is markedly asymmetric, and the maximum amplification rate of 7.31 x 10^{-3} is located at $\psi = -29.4°$ rather than near zero. This asymmetry was barely perceptible for the small crossflow boundary layers of Fig. 13.4, where the crossflow is only one-sixth as large. The σ at $\psi = 0°$ of Fig. 13.8 (5.82 x 10^{-3}) is close to σ_{max} with respect to frequency of the $\psi = 0°$ waves (5.91 x 10^{-3}). Since this value is 20% below the peak amplification rate, the $\psi = 0°$ waves are no longer adequate to represent the maximum instability as with small crossflow boundary layers. Fig. 13.8 also gives the distribution with ψ of k and the real group-velocity angle, ϕ_r. The latter quantity remains within ± 7.5° of the potential-flow direction throughout the unstable region.

Because R = 276 is the minimum critical Reynolds number of the steady disturbances, the unstable region terminates in a neutral stability point at F = 0. We are particularly interested here in Reynolds numbers where F = 0 is also unstable, and as an example, Fig. 13.9 gives results for all unstable frequencies at R = 555. Figure 13.9a shows σ_{max} as a function of F (here, as in Fig. 13.7, σ_{max} is the maximum with respect to k), as well as the unstable region of the k-F plane; the unstable region of the ψ-F plane appears in Fig. 13.9b. These two unstable regions are quite different from those of Fig. 13.7 where there is only crossflow instability. The negative frequencies do resemble those of Fig. 13.7 in that the unstable range of ψ is small, the unstable range of k is large, and with ψ redefined so that F > 0, the orientations are close to the crossflow direction. However, for the higher frequencies, which are by far the most unstable, the unstable regions of Fig. 13.9 bear more of a resemblance to those of a 2D boundary layer than to Fig. 13.7. The main differences from the 2D case are the asymmetry about $\psi = 0°$ already noted in Fig. 13.8, the one-sidedness of ψ_{max}, and, for F < 0.4 x 10^{-4}, the replacement of a lower cutoff frequency for instability by a rapid shift with decreasing frequency to waves oriented opposite to the crossflow direction and which are unstable down to zero frequency. The instability shown in Fig. 13.9 represents primarily an evolution of the small crossflow boundary layers of Fig. 13.4 to larger crossflow. Only the lower frequencies, say F < 0.2 x 10^{-4}, have to do with the pure crossflow instability of Fig. 13.7. For frequencies near 0.4 x 10^{-4}, ψ varies little with k in one part of the unstable region, as with crossflow instability; in the other part, as with streamwise instability, the opposite is true. This behavior becomes more pronounced at high Reynolds numbers.

14. TRANSONIC INFINITE-SPAN SWEPT WING BOUNDARY LAYER

The 3D boundary layers that have received the most attention in aeronautical practice are those on transonic swept wings. The desirability of maintaining laminar flow on the wings of large transonic aircraft has led to the study of the instability of such boundary layer as a means of estimating the occurrence of transition and the effectiveness of various methods of laminar-flow control. The basic phenomenon of crossflow instability was encountered and its origin explained by the early investigators, as we have learned in Section 12, and means of coping with its adverse consequences were developed. However, interest in laminar-flow control was waning by the time computer-aided stability analysis became commonplace in the 1960's, and nothing more was done on the subject of 3D boundary-layer stability following Brown's work (1959,1960,1961) until the energy crisis of the mid-1970's. In response to the sudden need for an analysis tool, Srokowski and Orszag (1977) brought out the SALLY code. In spite of using the incompressible stability theory and a non-physical method of computing wave amplitude, this code has been widely used. It has since been superseded by COSAL, a compressible version of SALLY [Malik (1982)]. Work that was directed at developing more fundamental methods of stability analysis for swept-wing boundary layers was carried out by Cebeci and Stewartson (1980a,1980b), Lekoudis (1979,1980), Mack (1979a,1981), and Nayfeh (1980a,1980b).

Attention has so far been restricted to infinite-span swept wings. Even with this simplification, the nonsimilarity of the boundary layers has made it necessary to proceed on the basis of specific examples, and to try and glean a general understanding of the instability of this type of boundary layer on the basis of extensive numerical calculations. We shall follow this same practice in this Section. Detailed numerical results for a single example that were obtained by an application of methods already presented in this document [Mack (1979a)] are given in the hope that a careful study will yield some understanding of the instabilities that arise and the procedures to follow in analyzing them.

14.1 Mean boundary layer

The flow example used in this Section is the boundary layer on a 35° swept wing of infinite span with a supercritical airfoil section, distributed suction and a chord of $c^* = 2.0$ m (6.55 ft) normal to the leading edge. The undisturbed flow conditions are $M_\infty = 0.89117$, $T_\infty^* = 311°K$, and $P_\infty^* = 0.30663$ atm. The upper-surface pressure coefficient C_{p_e} is listed in Table 14.1 together with other properties of the potential flow as functions of s^*/c^*, where s^* is the arc length along the airfoil section. The coordinate system is shown in Fig. 14.1. The Reynolds number used in the stability calculations is R = $U_1^* L^*/\nu_1^*$, where U_1^* is the potential velocity. The length scale $L^* = (\nu_1^* s^*/U_{c1}^*)^{1/2}$ reduces to the usual

boundary-layer length scale when the flow is two dimensional, and is non-zero at the attachment line. The Reynolds number Re_s is $U_1^* s^* / \nu_1^*$. The velocity derivative which defines m and thus the Hartree β_h was evaluated by the numerical differentiation of U_{c1} as calculated from the pressure coefficient. The very large $-\beta_h$ near the trailing edge have been omitted from the Table.

Table 14.1 Properties of potential flow

N	s^*/c^*	M_1	C_p	β_h	ψ_p(deg)	$10^{-6} Re_s$	R	$10\ L^*$(cm)
1	0	0.4859	0.7652	1.0000	55.00	0	221	0.0560
2	0.0011	0.4934	0.7527	0.9770	45.23	0.009	224	0.0560
3	0.0033	0.5424	0.6680	0.9306	29.26	0.028	225	0.0593
4	0.0059	0.6261	0.5151	0.8753	16.96	0.056	301	0.0632
5	0.0087	0.7186	0.3375	0.7798	8.95	0.091	355	0.0682
6	0.0120	0.8033	0.1715	0.6721	3.91	0.132	412	0.0747
7	0.0157	0.8806	0.2051	0.6000	0.42	0.180	470	0.0818
8	0.0199	0.9487	−0.1104	0.5300	−2.06	0.235	529	0.0896
9	0.0246	1.0084	−0.2225	0.4759	−3.90	0.296	588	0.0978
10	0.0299	1.0623	−0.3206	0.4351	−5.34	0.363	647	0.1064
11	0.0358	1.1095	−0.4041	0.3900	−6.46	0.437	705	0.1153
12	0.0492	1.1863	−0.5338	0.2975	−8.06	0.604	823	0.1339
13	0.0651	1.2306	−0.6050	0.1583	−8.87	0.800	944	0.1535
14	0.0938	1.2462	−0.6295	−0.0137	−9.14	1.152	1131	0.1841
15	0.1281	1.2402	−0.6201	−0.0594	−9.03	1.573	1323	0.2152
16	0.1675	1.2316	−0.6066	−0.0558	−8.87	2.056	1513	0.2462
17	0.2113	1.2238	−0.5943	−0.0518	−8.75	2.595	1701	0.2767
18	0.2591	1.2180	−0.5850	−0.0449	−8.64	3.182	1884	0.3065
19	0.3101	1.2126	−0.5765	−0.0515	−8.55	3.809	2063	0.3354
20	0.3636	1.2071	−0.5676	−0.0721	−8.45	4.467	2235	0.3634
21	0.4190	1.1990	−0.5544	−0.1315	−8.30	5.146	2400	0.3903
22	0.4754	1.1864	−0.5339	−0.2205	−8.06	5.838	2559	0.4162
23	0.5132	1.1762	−0.5172	−0.2203	−7.86	6.300	2661	0.4329
24	0.5508	1.1704	−0.5076	−0.1231	−7.75	6.761	2758	0.4488
25	0.5882	1.1663	−0.5008	−0.1882	−7.67	7.218	2850	0.4640
26	0.6250	1.1558	−0.4831	−0.4625	−7.45	7.666	2940	0.4788
27	0.6610	1.1419	−0.4596	−0.6677	−7.17	8.101	3027	0.4933
28	0.6962	1.1257	−0.4320	−0.9785	−6.82	8.521	3109	0.5074
29	0.7302	1.1058	−0.3976	−1.6025	−6.38	8.919	3188	0.5213
30	0.7631	1.0826	−0.3568	−2.842	−5.84	9.293	3262	0.5351
31	0.7946	1.0553	−0.3080	−	−5.16	9.634	3333	0.5490
32	0.8246	1.0225	−0.2483	−	−4.29	9.933	3399	0.5636
33	0.8532	0.9820	−0.1732	−	−3.12	10.172	3461	0.5799
34	0.8803	0.9366	−0.0874	−	−1.65	10.345	3519	0.5982
35	0.9059	0.8960	−0.0094	−	−0.18	10.479	3573	0.6169

Table 14.2 lists some properties of the boundary-layer solution calculated for the potential flow of Table 14.1 and the suction distribution $C_Q(s^*)$ given in the last column. For comparison, the profile parameters of an insulated flat-plate boundary layer with no suction at $M_1 = 1.2$ are $y_\delta = 5.85$, $y_{\delta}^* = 2.31$ and $H = 3.54$. The maximum crossflow is $W_{max} = -0.115$, and it occurs at station $N = 4$ ($s^*/c^* = 0.0059$). This value is virtually identical to the maximum possible crossflow generated by the Falkner-Skan-Cooke profiles of Section 13, where $W_{max} = -0.119$ for $\beta_h = 1.0$ and $\psi_{sw} + \psi_p = 45^\circ$. Although the pressure gradient first becomes adverse at $N = 14$, W_{max} does not change sign until $N = 21$. For $N = 15$ to 26 ($s^*/c^* = 0.128$ to 0.625), there are two inflection points in the crossflow velocity profile. Up to $N = 20$ ($s^*/c^* = 0.364$), W has the same sign at both inflection points; for $N > 20$, W has opposite signs. There is reverse crossflow from $N = 17$ to 27 ($s^*/c^* = 0.211$ to 0.661). The angle ε_i is the angle of the velocity vector at the y of the inflection point of the crossflow velocity profile. When there are two inflection points, the listed ε_i is for the outer point when $W_{max} < 0$, and for the inner point when $W_{max} > 0$.

14.2 Crossflow instability

Surprisingly little crossflow is required for crossflow instability to occur. For example, it was found with the similar boundary layers of Section 13 that for $\beta_h = \pm 0.02$ and $\psi_{sw} + \psi_p = 45^\circ$ (the angle that generates the maximum crossflow for a given pressure gradient), the critical Reynolds number of crossflow instability for both boundary layers is close to 1100 even though W_{max} is only about 0.6%.

Figure 14.2 gives a comparison of the distribution of the amplification rate σ_g with the magnitude of the wavenumber vector $\vec{k}$ as computed at $N = 4$ from both the incompressible and sixth-order compressible stability theories. It is evident that the incompressible theory gives reasonably good results, with $\sigma_{max} = 7.30 \times 10^{-3}$ compared to 6.59×10^{-3} from the compressible theory, a difference of 10.8%. The eighth-order compressible equations give $\sigma_{max} = 6.51 \times 10^{-3}$, a difference of only 1.2% from the sixth-order system. Consequently, there is little reason to use the eighth-order system, and for a general study of crossflow instability near the leading edge the incompressible theory is adequate.

The angle ψ of the wavenumber vector as computed from the incompressible theory is also shown in Fig. 14.2. Almost identical results are given by the compressible theory. The narrow bandwidth of unstable and wide bandwidth of unstable k is characteristic of crossflow instability. The sharpness of the angular "tuning" increases as the crossflow decreases. For example, at $N = 17$ where $W_{max} = -0.0094$, the bandwidth of unstable k is about the same as in Fig. 14.2, but the bandwidth of unstable ψ is only 0.15°.

Table 14.2 Properties of mean boundary layer

N	y_δ	$y_{\delta*}$	H	R	W_{max}	ε_i(deg)	$10^3 C_Q$
1	3.847	1.0800	2.693	239	0	0	0
2	3.843	1.0428	2.603	234	-0.0408	-1.977	0
3	3.891	1.0157	2.538	259	-0.0936	-4.362	0
4	3.950	0.9914	2.506	299	-0.1146	-5.142	0
5	3.980	0.9511	2.480	338	-0.1116	-4.857	0.735
6	4.017	0.9372	2.513	386	-0.0984	-4.198	0.700
7	4.115	0.9819	2.614	462	-0.0866	-3.654	0.630
8	4.218	1.0274	2.689	544	-0.0783	-3.283	0.530
9	4.344	1.0921	2.787	642	-0.0717	-3.004	0.430
10	4.475	1.1590	2.870	749	-0.0669	-2.795	0.290
11	4.632	1.2468	2.974	879	-0.0633	-2.632	0.163
12	4.900	1.3860	3.106	1141	-0.0568	-2.341	0.155
13	5.141	1.5201	3.229	1435	-0.0485	-1.963	0.143
14	5.442	1.7004	3.352	1924	-0.0337	-1.317	0.143
15	5.635	1.8110	3.398	2395	-0.0215	-0.840	0.143
16	5.709	1.8341	3.371	2776	-0.0140	-0.520	0.143
17	5.732	1.8292	3.345	3112	-0.0094	-0.349	0.143
18	5.721	1.8030	3.306	3397	-0.0065	-0.242	0.143
19	5.706	1.7815	3.287	3675	-0.0046	-0.170	0.143
20	5.685	1.7603	3.265	3934	-0.0031	-0.117	0.143
21	5.685	1.7608	3.270	4226	0.0059	0.273	0.143
22	5.701	1.7754	3.279	4653	0.0113	0.637	0.143
23	5.708	1.7825	3.280	4743	0.0148	0.851	0.143
24	5.623	1.7076	3.184	4709	0.0155	0.853	0.214
25	5.494	1.6023	3.079	4567	0.0155	0.816	0.288
26	5.369	1.5099	2.997	4440	0.0191	1.011	0.370
27	5.217	1.4001	2.894	4238	0.0251	1.478	0.490
28	5.028	1.2685	2.770	3944	0.0309	1.873	0.610
29	4.827	1.1350	2.650	3618	0.0369	2.241	0.755
30	4.608	0.9964	2.523	3250	0.0432	2.601	0.930
31	4.392	0.8694	2.409	2898	0.0498	2.975	1.090
32	4.205	0.7671	2.317	2608	0.0579	3.441	1.215
33	4.062	0.6933	2.245	2399	0.0690	4.100	1.300
34	3.952	0.6344	2.172	2233	0.0816	4.854	1.380
35	3.853	0.5780	2.097	2065	0.0912	5.330	1.450

It is of interest to note that the angle $\psi = 84.8°$ at the maximum amplification rate is almost identical to the angle $90 - |\varepsilon_i| (= 84.9°)$, where ε_i is the angle defined in Section 14.1 and listed in Table 14.2. The near equality of these two angles has been found to be true in general for crossflow instability as long as $90 - |\varepsilon_i|$ is given the sign of W_{max}. When there are two inflection points and W has the same sign at each $(15 \le N \le 20)$, it is the outer point, where DW is a maximum, that is significant for instability. When W has opposite signs at the two inflection points $(21 \le N \le 26)$, it is the inner point, where DW is a minimum, that is significant. The above convenient relation between ψ and ε_i makes it easy to compute an initial eigenvalue for crossflow instability.

The real and imaginary parts of ϕ are also shown in Fig. 14.2. The real part, ϕ_r, has the same sign as W_{max}, and ϕ_r at k_{max}, the wavenumber for maximum amplification rate, is proportional to W_{max}. At k_{max}, $\psi - \phi_r = 88.6°$. Further back on the wing, this difference approaches $90°$ as the crossflow diminishes. The imaginary part of ϕ, ϕ_i, reverses sign at the point of maximum amplification rate, a behavior that is true at all stations.

Although crossflow instability has been defined as the existence of unstable steady disturbances, a whole band of frequencies becomes unstable at about the same critical Reynolds number. Figure 14.3 gives σ as a function of F at N = 4 as calculated from both the incompressible and sixth-order compressible theories for k = 0.520, the k_{max} of F = 0. It is apparent that the effect of compressibility is about the same for all frequencies as for F = 0. The values of $\sigma_{max} \times 10^3$ for k = 0.520 are: incompressible, 8.91; sixth-order compressible, 8.00; eighth-order compressible, 7.90.

There are both positive and negative unstable frequencies in Fig. 14.3. The negative frequencies simply mean that with the direction of $\vec{k}$ defined by the values of ψ shown in the figure, the phase velocity is negative. If, instead, the direction of $\vec{k}$ had been defined in the usual manner to be the direction of the phase velocity, there would be two groups of positive unstable frequencies. For the positive frequencies of Fig. 14.3, $\vec{k}$ is within $25°$ of the direction opposite to the crossflow; for the negative frequencies, $\vec{k}$ is within $5°$ of the direction of the crossflow. The sign convention of Fig. 14.3 has been adopted so that the maximum instability will always be associated with a positive frequency, and this nonstandard definition of $\vec{k}$ is used here, as in Section 13.3, to make it easier to plot the numerical results.

There is a wide band of unstable frequencies in Fig. 14.3. The dimensional frequency corresponding to $F = 2.0 \times 10^4$ is 57.8 khz, and the most unstable frequency is about 17 khz. The unstable bandwidth becomes much narrower further downstream as both the crossflow and maximum amplification rate decrease. It was found in Mack (1979b) that for a boundary layer with crossflow instability only, k_{max} does not vary

much with frequency for $F > 0$. For $F < 0$, k_{max} does change with frequency. It is estimated from Chap. 13 that the unstable region of negative frequencies at $N = 4$ extends to $F = -1.5 \times 10^{-4}$ with $\psi = 92°$, and that the maximum amplification rate of the wave with $\bar{k}$ in the crossflow direction is about one-half of that for the steady disturbance.

As crossflow instability is an example of inflectional instability, it is possible to deduce something about the stability characteristics from the location of the inflection point of the relevant velocity profile. It is not necessary for this purpose to consider the generalized inflection point of the compressible theory which is little different from the true inflection point at transonic Mach numbers. The relevant velocity profile is the one in the direction of $\bar{k}$. For the most unstable stationary wave ($\psi = 84.8°$), this profile has reverse flow, and the inflection point occurs almost at the zero velocity point in accordance with the theory of Stuart [Gregory et al.(1955)]. Inflectional profiles exist for ψ both greater and less than $84.8°$. The sign of the mean velocity at the inflection point determines the sign of the frequency (except very near $F = 0$ because of the finite Reynolds number). The profiles with $\psi > 84.8°$ give the negative frequencies; the profiles with $\psi < 84.8°$ the positive frequencies.

14.3 Streamwise instability

Along with crossflow instability, which is particular to three-dimensional boundary layers, there are also inflectional and viscous instabilities which are more like those of a two-dimensional boundary layer, but with modifications due to the crossflow. This type of instability will be called streamwise instability, and it refers to all instabilities that are not associated with a directional velocity profile of the type of the crossflow and reverse-flow profiles.

As suction is more effective at controlling streamwise than crossflow instability, only the latter instability is present over most of the wing chord in the present flow example. The region of streamwise instability starts at $N = 14$ ($s^*/c^* = 0.094$), according to the compressible theory, and extends to $N = 25$ ($s^*/c^* = 0.588$). Some stability characteristics at $N = 15$ ($s^*/c^* = 0.128$), where the edge Mach number of 1.24 is close to its maximum value, are shown in Fig. 14.4. Figure 14.4a gives the distributions of σ_{max} and F with wave angle from the incompressible and sixth-order compressible theories. The crossflow instability region ($\psi > 80°$) is not shown. The crossflow ($W_{max} = -0.0215$) has introduced an asymmetry into the distributions, but otherwise the results resemble what might have been expected from assuming that 2D results could be applied to 3D boundary layers. The two maxima in the amplification rate of the compressible theory contrast with the single maximum of the incompressible theory, and are in complete accord with 2D stability theory at $M_1 = 1.24$.

The reason that Fig. 14.4a resembles the results for a two-dimensional flat-plate boundary layer with no suction is that the shape factor H at $N = 15$ is almost the same as for such a boundary layer at the same Mach number, and the crossflow is not only small, but still in the direction associated with a favorable pressure gradient. The two inflection points of the directional velocity profiles, which exist for $-90° < \psi < -60°$, are unimportant except near $\psi = -90°$, because one is located near the wall and the other at the edge of the boundary layer. Consequently, what Fig. 14.4a shows is viscous instability, just as for a flat-plate boundary layer at the same Mach number.

The maximum amplification rate with respect to wavenumber is shown in Fig. 14.4b as a function of frequency for both crossflow and streamwise instability. It is evident that the incompressible theory gives a totally misleading result as to the importance of streamwise instability at this station. The two maxima of Fig. 14.4a are shown by two separate curves. The crossflow instability has the same general features as at $N = 4$, but with an unstable frequency band only about one-seventh as wide (cf. Fig. 14.3). Also the corresponding ψ are much closer to $90°$ for both positive and negative frequencies: $83.8° < \psi < 89.4°$ for $F > 0$; $89.4° < \psi < 90.4°$ for $F < 0$. It might also be observed that for $\psi = 90°$, the maximum amplification rate is about one-half of its $F = 0$ value, as surmised for $N = 4$.

The term streamwise instability covers such a wide variety of possibilities that it is worthwhile to give an additional example. Figure 14.5 is the counterpart at $N = 23$ ($s^*/c^* = 0.513$) to Fig. 14.4. At this station, the crossflow over the inner two-thirds of the boundary layer has reversed, but is even smaller than at $N = 15$ ($W_{max} = 0.0113$). The adverse pressure gradient is larger ($\beta_h = -0.22$), but because the suction is also larger there is still no inflection point in the streamwise velocity profile.

It is seen from Fig. 14.5a that the waves with $\psi < 0$ are much more unstable than those with $\psi > 0$ even though the maximum crossflow is positive. The reason is that for $\psi < -40°$ the directional velocity profiles have inflection points well out in the boundary layer (e.g., at $U = 0.30$ for $\psi = -70°$). A significant difference between Fig. 14.5 and Fig. 14.4 is that the smooth σ_{max} curves of the former do not permit a clear distinction to be made between crossflow and streamwise instability. The frequencies near zero (say, $F < 0.04 \times 10^{-4}$) have the characteristics of crossflow instability (wide band of unstable wavenumbers, narrow band of unstable angles); the larger frequencies (say, $F > 0.12 \times 10^{-4}$) have the characteristics of streamwise instability (narrow band of unstable wavenumbers, wide band of unstable angles). The intermediate frequencies, including the most unstable, have the characteristics of streamwise instability for a narrow band of small wavenumbers, and of crossflow instability for a wide band of larger wavenumbers.

The effect of compressibility is large and similar to that at $N = 15$ (Fig. 14.4) in the streamwise instability region, and is also a good deal larger in the crossflow instability region than at either $N = 4$ (Figs. 14.3 and 14.4) or $N = 15$. Indeed the peak amplification rate of the incompressible theory differs by 27% from the sixth-order compressible value and the corresponding wave angle by 15°, whereas the maximum incompressible amplification rate of the steady disturbances is in error by 40%. The latter difference decreases further back on the wing as the amplification rate increases (to 14% at $N = 35$), but is always larger than in the negative crossflow region on the forward part of the wing.

It is important to note the narrow bandwidth of unstable frequencies in Fig. 14.5b compared to Figs. 14.4b, and 14.3. The largest unstable frequency at $N = 23$ is only 5.2 khz, and the most unstable

frequency is 2.9 khz. Consequently, almost all unstable frequencies that exist upstream of $N = 23$ cannot persist to this station as amplified waves even when they are kinematically possible.

14.4 Wave amplitude

The wave amplitude rather than the local amplification rate is what is of interest in transition studies. In this Section, the irrotationality condition on $\vec{k}$ will be applied to the calculation of amplitude ratios of single Fourier components. The SALLY stability code of Srokowski and Orszag (1977) calculates $\ln(A/A_0)$ by what is called the envelope method, i.e., by integrating $(\sigma_g)_{max}$ along the trajectory defined by the real part of the group velocity. As a result, the amplitude ratio increases monotonically to the end of the instability region. Here, a band of initial wavenumbers with the same frequency is followed downstream starting at the first unstable station, $N = 3$ ($s^*/c^* = 0.0033$). The resulting amplification rates for seven initial wavenumbers with zero frequency are shown in Fig. 14.6 as computed from the incompressible theory. The listed initial wavenumbers are those at $N = 3$. For comparison, a portion of the $k_i = 0.35$ curve as computed from the sixth-order compressible theory is also shown.

For $R < 1000$, the different initial wavenumbers in Fig. 14.6 act much like different frequencies in a 2D boundary layer. The lower the initial wavenumber, the further downstream is its unstable region. For $R > 1000$, a rather different pattern is apparent in Fig. 14.6. The initial wavenumber of the wave component which has the maximum amplification rate at a given station becomes a slowly varying function of Reynolds number. In other words, a single Fourier component is nearly the most unstable over a wide range of Reynolds numbers. It is this pattern that prevails in the entire rear crossflow instability region. There the wave component with $k_i = 0.35$ at $N = 21$ ($R = 2400$, $s^*/c^* = 0.419$) is the most unstable from $R = 2600$ to at least $R = 3570$ ($s^*/c^* = 0.906$). Consequently, in this region the procedure we are using here gives the same result for the amplitude ratio as does the SALLY code.

The $\ln(A/A_0)$ values that correspond to the amplification rates of Fig. 14.6 are shown in Fig. 14.7 for six Fourier components along with the result given by the SALLY code (computed by Dr. A. Srokowski). The present method gives a peak in the envelope curve, $\ln(A/A_0)_{max}$ vs. R, at about $R = 1400$ ($s^*/c^* = 0.128$). In contrast, the curve from the SALLY code continues to rise to a value of $\ln(A/A_0) = 11.2$ at $R = 1880$ ($s^*/c^* = 0.259$). The peak with the irrotationality condition is a consequence of following Fourier components from a more unstable region to a less unstable region, and can also be encountered in 2D boundary layers with laminar-flow control.

Two additional curves included in Fig.14.7 give $\ln(A/A_0)$ for $k_i = 0.35$ as computed from the sixth- and eighth-order compressible equations. The peak $\ln(A/A_0)$ of the latter is about 6.9 compared to 7.8 from the incompressible theory and 11.2 from the SALLY program. Consequently, the method of integrating the maximum amplification rate overestimates the peak amplitude ratio by over 70 times.

As both Figs. 14.3 and 14.4b show that a non-zero frequency has the maximum amplification rate for crossflow instability, it is also a non-zero frequency that gives the maximum amplitude ratio. The possible importance of these frequencies is, however, counteracted by the narrowing of the unstable frequency bandwidth in the downstream direction. The result is that at $N = 15$ the frequency with the maximum amplitude ratio is the low frequency $F = 0.05 \times 10^4$ (1.4 khz), and the peak $\ln(A/A_0)$ of this frequency is only 2% larger than for zero frequency. Of course, larger differences than this exist upstream of $N = 15$ where higher frequencies are still unstable.

At station $N = 35$ in the rear crossflow instability region, the amplitude ratio of the most unstable zero-frequency wave component, $k_i = 0.35$, is 6.54 according to the incompressible theory, a result almost identical to the SALLY value of $n = 6.46$. However, compressibility cannot be neglected in this region as it was in the forward instability region. The sixth-order compressible theory gives $\ln(A/A_0) = 5.24$ at $N = 35$; thus the incompressible theory overestimates $\ln(A/A_0)$ by 25%.

Streamwise instability is limited to the region from $N = 15$ to $N = 25$ ($s^*/c^* = 0.588$) and leads to smaller amplitude ratios than does crossflow instability. As these waves travel downstream, their wave angle ψ remains very close (within about 1°) to its initial value, in contrast to the crossflow disturbances which are required by the dispersion relation to keep their angles within the narrow band set by the profile angle ε_i. According to Fig. 14.4b, $F = 0.375 \times 10^{-4}$ is the most unstable frequency for streamwise instability at $N = 15$. However, this and the neighboring unstable frequencies damp out quickly in the downstream direction. The frequencies which give the largest amplitude ratios are those which are unstable at $N = 23$ ($s^*/c^* = 0.513$), where the largest amplification rates of streamwise instability occur. For example, $F = 0.09 \times 10^{-4}$ becomes unstable at $N = 21$ and has a peak $\ln(A/A_0)$ of 2.3 at $N = 25$ for an initial wave angle of -70°; $F = 0.15 \times 10^{-4}$ becomes unstable at $N = 20$ and has a smaller peak at $N = 24$. Consequently, the maximum amplitude growth of streamwise-instability waves is only about 1% of that of the crossflow disturbances. Examples of amplification rates for a wing without suction may be found elsewhere [Mack (1981)].

APPENDIX 1.   COEFFICIENT MATRIX OF COMPRESSIBLE STABILITY EQUATIONS

There are 30 non-zero elements of the coefficient matrix $a_{ij}(y)$ of Eq. (8.11). The Z_1 equation has only one non-zero coefficient:

$$a_{12} = 1 \; . \tag{A1.1}$$

The Z_2 equation has six non-zero coefficients:

$$a_{21} = (iR/\mu T)(\alpha U+\beta W-\omega)+\alpha^2+\beta^2 \quad , \tag{A1.2a}$$

$$a_{22} = -(1/\mu)(d\mu/dT)DT \; , \tag{A1.2b}$$

$$a_{23} = (R/\mu T)(\alpha DU+\beta DW)-i(\alpha^2+\beta^2)(1/\mu)(d\mu/dT)DT$$
$$-i(1/3)(1+2d)(\alpha^2+\beta^2)(DT/T) \; , \tag{A1.2c}$$

$$a_{24} = (iR/\mu)(\alpha^2+\beta^2)-(1/3)(1+2d)(\alpha^2+\beta^2)\gamma M_1^2(\alpha U+\beta W-\omega) \; , \tag{A1.2d}$$

$$a_{25} = (1/3)(1+2d)(\alpha^2+\beta^2)(\alpha U+\beta W-\omega)/T-(1/\mu)(d\mu/dT)(\alpha D^2U+\beta D^2W)$$
$$-(1/\mu)(d^2\mu/dT^2)DT(\alpha DU+\beta DW) \quad , \tag{A1.2e}$$

$$a_{26} = -(1/\mu)(d\mu/dT)(\alpha DU+\beta DW) \tag{A1.2f}$$

The Z_3 equation has four non-zero coefficients:

$$a_{31} = -i \quad , \tag{A1.3a}$$

$$a_{33} = DT/T \quad , \tag{A1.3b}$$

$$a_{34} = -i\gamma M_1^2(\alpha U+\beta W-\omega) \quad , \tag{A1.3c}$$

$$a_{35} = (i/T)(\alpha U+\beta W-\omega) \; . \tag{A1.3d}$$

The Z_4 equation is the only one that requires a lengthy manipulation to derive. With

$$E = (R/\mu)+i(2/3)(2+d)\gamma M_1^2(\alpha U+\beta W-\omega) \quad , \tag{A1.4}$$

the six non-zero coefficients are

$$a_{41} = -(i/E)[(2/\mu)(d\mu/dT)DT+(2/3)(2+d)(DT/T)] \quad , \tag{A1.5a}$$

$$a_{42} = -(i/E) \; , \tag{A1.5b}$$

$$a_{43} = (1/E)[-(\alpha^2+\beta^2)+(2/3)(2+d)(DT^2/T)(1/\mu)(d\mu/dT)$$
$$+(2/3)(2+d)(D^2T/T)-(iR/\mu T)(\alpha U+\beta W-\omega)] \quad , \tag{A1.5c}$$

$$a_{44} = -(i/E)(2/3)(2+d)\gamma M_1^2[(\alpha U+\beta W-\omega)$$
$$X\cdot(1/\mu)(d\mu/dT)DT+\alpha DU+\beta DW+(DT/T)(\alpha U+\beta W-\omega)] \quad , \tag{A1.5d}$$

$$a_{45} = (i/E)\{(1/\mu)(d\mu/dT)(\alpha DU+\beta DW)+(2/3)(2+d)$$
$$X\;[(1/\mu)(d\mu/dT)(DT/T)(\alpha U+\beta W-\omega)+(\alpha DU+\beta DW)/T]\} \quad , \tag{A1.5e}$$

$$a_{46} = (i/E)(2/3)(2+d)(\alpha U+\beta W-\omega) \; . \tag{A1.5f}$$

The Z_5 equation has only one non-zero coefficient:

$$a_{56} = 1 \; . \tag{A1.6}$$

The Z_6 equation has six non-zero coefficients:

$$a_{62} = -2\sigma(\gamma-1)M_1^2(\alpha DU+\beta DW)/(\alpha^2+\beta^2) \quad , \tag{A1.7a}$$

$$a_{63} = (R\sigma/\mu)(DT/T)-i2\sigma(\gamma-1)M_1^2(\alpha DU+\beta DW) \quad , \tag{A1.7b}$$

$$a_{64} = -i(R\sigma/\mu)(\gamma-1)M_1^2(\alpha U+\beta W-\omega) \quad , \tag{A1.7c}$$

$$a_{65} = i(R\sigma/\mu T)(\alpha U+\beta W-\omega)+\alpha^2+\beta^2-(D^2T/\kappa)(d\kappa/dT) \tag{A1.7d}$$
$$-(DT^2/\kappa)(d^2\kappa/dT^2)-\sigma(\gamma-1)M_1^2(1/\mu)(d\mu/dT)(DU^2+DW^2)$$

$$a_{66} = -(2/\kappa)(d\kappa/dT)DT \quad , \tag{A1.7e}$$

$$a_{68} = -2\sigma(\gamma-1)M_1^2(\alpha DW-\beta DU)/(\alpha^2+\beta^2) \; . \tag{A1.7f}$$

The Z_7 equation has only one non-zero coefficient:

$$a_{78} = 1 \quad , \tag{A1.8}$$

The Z_8 equation has five non-zero coefficients:

$$a_{83} = (R/\mu T)(\alpha DW - \beta DU) \quad , \tag{A1.9a}$$

$$a_{85} = -(1/\mu)(d\mu/dT)(\alpha D^2 W - \beta D^2 U) - (1/\mu)(d^2\mu/dT^2)DT(\alpha DW - \beta DU) \quad , \tag{A1.9b}$$

$$a_{86} = -(1/\mu)(d\mu/dT)(\alpha DW - \beta DU) \quad , \tag{A1.9c}$$

$$a_{87} = (iR/\mu T)(\alpha U + \beta W - \omega) + \alpha^2 + \beta^2 \quad , \tag{A1.9d}$$

$$a_{88} = -(1/\mu)(d\mu/dT)DT \quad . \tag{A1.9e}$$

In these equations, the ratio of the second to the first viscosity coefficient

$$d = \lambda/\mu \tag{A1.10}$$

is taken to be a constant and equal to 1.2 (Stokes' assumption corresponds to $\lambda = 0$).

In the numerical computations, we use

$$\mu^* \times 10^5 = 1.458 T^{*3/2}/(T^* + 110.4) \quad , \qquad T^* \geq 110.4^\circ K \quad , $$
$$= 0.0693873\, T^* \quad , \qquad T^* < 110.4^\circ K \quad , \tag{A1.11}$$

for the viscosity coefficient in cgs units, and

$$\kappa^* = 0.6325 T^{*1/2}[1 + (245.4/T^*)10^{-12/T^*}]^{-1} \tag{A1.12}$$

for the thermal conductivity coefficient in cgs units. The Prandtl number $\sigma = c_p^* \mu^* / \kappa^*$ is computed as a function of temperature from μ^*, κ^* and a constant specific heat of $c_p^* = 0.24$.

APPENDIX 2. FREESTREAM SOLUTIONS OF COMPRESSIBLE STABILITY EQUATIONS

In the freestream $U = U_1$, $W = W_1$, $T = 1$, $\mu = 1$, $\kappa = 1/\sigma_1$, and all y derivatives of mean-flow quantities are zero. The first six of Eqs. (8.11) can be written as three second-order equations:

$$D^2 V_1 = b_{11} V_1 + b_{12} V_2 + b_{13} V_3 \quad , \tag{A2.1a}$$

$$D^2 V_2 = b_{22} V_2 + b_{23} V_3 \quad , \tag{A2.1b}$$

$$D^2 V_3 = b_{32} V_2 + b_{33} V_3 \quad , \tag{A2.1c}$$

where

$$V_1 = Z_1 \quad , \quad V_2 = Z_4 \quad , \quad V_3 = Z_5 \quad . \tag{A2.2}$$

The three coefficients of Eq. (A2.1a) are

$$b_{11} = \alpha^2 + \beta^2 + iR(\alpha U_1 + \beta W_1 - \omega) \quad , \tag{A2.3a}$$

$$b_{12} = i(\alpha^2 + \beta^2)[R + i(1/3)(1+d)\gamma M_1^2(\alpha U_1 + \beta W_1 - \omega)] \quad , \tag{A2.3b}$$

$$b_{13} = -(1+2d)(\alpha^2 + \beta^2)(\alpha U_1 + \beta W_1 - \omega) \quad . \tag{A2.3c}$$

The two coefficients of Eq. (A2.1b) are

$$b_{22} = \alpha^2 + \beta^2 - (R/E_1)[\gamma M_1^2 - (2/3)(2+d)\sigma(\gamma-1)M_1^2(\alpha U_1 + \beta W_1 - \omega)^2] \quad , \tag{A2.4a}$$

$$b_{23} = (R/E_1)[1 - (2/3)(2+d)\sigma](\alpha U_1 + \beta W_1 - \omega) \quad , \tag{A2.4b}$$

where E_1 is Eq. (A1.4) evaluated in the freestream. The two coefficients of Eq. (A2.1c) are

$$b_{32} = -i(\gamma-1)M_1^2\sigma(\alpha U_1 + \beta W_1 - \omega) \quad , \tag{A2.5a}$$

$$b_{33} = \alpha^2 + \beta^2 + i\sigma R(\alpha U_1 + \beta W_1 - \omega) \quad . \tag{A2.5b}$$

The six solutions of Eqs. (A2.1) have the form

$$V^{(i)}(y) = B^{(i)}\exp(\lambda_i y) \quad , \qquad (i = 1,6) \quad , \tag{A2.6}$$

where the $V^{(i)}$ are the six three-component solution vectors, the λ_i are the six characteristic values, and the $B^{(i)}$ are the six three-component characteristic vectors. Upon substituting Eq. (A2.6) into Eqs. (A2.1), the characteristic values are found to be

$$\lambda_{1,2} = \mp\left\{(1/2)(b_{22}+b_{33}) - [(1/4)(b_{22}-b_{33})^2 + b_{23}b_{32}]^{1/2}\right\}^{1/2} \quad , \tag{A2.7a}$$

$$\lambda_{3,4} = \mp (b_{11})^{1/2} \quad , \tag{A2.7b}$$

$$\lambda_{5,6} = \mp\left\{(1/2)(b_{22}+b_{33})+[(1/4)(b_{22}-b_{33})^2+b_{23}b_{32}]^{1/2}\right\}^{1/2} , \tag{A2.7c}$$

where the numbering has been arranged so that the first two of these will correspond to the first two of Eq. (2.49).

The last two of Eqs. (8.11) give a fourth uncoupled second-order equation

$$D^2Z_7 = [\alpha^2+\beta^2+iR(\alpha U_1+\beta W_1-\omega)]Z_7 , \tag{A2.8}$$

with the characteristic values

$$\lambda_{7,8} = \mp[\alpha^2+\beta^2+iR(\alpha U_1+\beta W_1-\omega)]^{1/2} , \tag{A2.9}$$

which are the same as the characteristic values $\lambda_{3,4}$.

The components of the characteristic vector corresponding to λ_3 are

$$B_1^{(3)} = 1 , \qquad B_2^{(3)} = 0 , \qquad B_3^{(3)} = 0 , \tag{A2.10}$$

and to λ_1 and λ_5 are,

$$B_1^{(j)} = [b_{12}(b_{33}-\lambda_j^2)-b_{13}b_{32}]/(\lambda_j^2-b_{11}) , \tag{A2.11a}$$

$$B_2^{(j)} = b_{33}-\lambda_j^2 , \tag{A2.11b}$$

$$B_3^{(j)} = -b_{32} . \tag{A2.11c}$$

The components of the characteristic vectors of the original solutions are:

$$A_1^{(j)} = B_1^{(j)} , \qquad A_2^{(j)} = \lambda_j B_1^{(j)} , \qquad A_4^{(j)} = B_2^{(j)} ,$$

$$A_5^{(j)} = B_3^{(j)} , \qquad A_6^{(j)} = \lambda_j B_3^{(j)} , \qquad (j = 1,6) , \tag{A2.12}$$

and the component $A_3^{(j)}$ is found from the continuity equation:

$$\lambda_j A_3^{(j)} = -iB_1^{(j)}-i(\alpha U_1+\beta W_1-\omega)[\gamma M_1^2 B_2^{(j)}-B_3^{(j)}] . \tag{A2.13}$$

REFERENCES

Bellman, R.E. and Kalaba, R.E. 1965 Quasilinearization and Boundary-Value Problems, American Elsevier, N.Y.

Betchhov, R. and Criminale, W.O. 1967 Stability of Parallel Flows, Academic Press, N.Y.

Bouthier, M. 1972 Stabilité linéaire des écoulements presque parallèles, J. de Mécanique, Vol. 11, pp. 599-621.

Bouthier, M. 1973 Stabilité linéaire des écoulements presque parallèles, Partie II, J. de Mécanique, Vol. 12, pp. 76-95.

Brown, W.B. 1959 Numerical Calculation of the Stability of Cross Flow Profiles in Laminar Boundary Layers on a Rotating Disc and on a Swept Wing and an Exact Calculation of the Stability of the Blasius Velocity Profile, Report No. NAI 59-5, Northrop Aircraft Inc., Hawthorne, CA.

Brown, W.B. 1960 Exact Numerical Solution of the Stability Equations of the Laminar Boundary Layer, Paper presented at International Congress of Applied Mechanics, Stresa, Italy.

Brown, W.B. 1961 A Stability Criterion for Three-Dimensional Laminar Boundary Layers, in "Boundary Layer and Flow Control" (G. V. Lachmann, ed.), Vol. 2, pp. 913-923, Pergamon Press, London.

Brown, W.B. 1962 Exact Numerical Solutions of the Complete Linearized Equations for the Stability of Compressible Boundary Layers, Norair Report No. NOR-62-15, Northrop Aircraft Inc., Hawthorne, CA.

Brown, W.B. and Sayre, P.H. 1954 An Exact Solution of the Orr-Sommerfeld Stability Equation for Low Reynolds Numbers, Report No. BLC-43, Northrop Aircraft Inc., Hawthorne, CA.

Cebeci, T. and Stewartson, K. 1980a Stability and Transition in Three-Dimensional Flows, AIAA J., Vol. 18, pp. 398-405.

Cebeci, T. and Stewartson, K. 1980b On the Prediction of Transition in Three-Dimensional Flows, in "Laminar-Turbulent Transition" (R. Eppler and H. Fasel, eds.), Springer Verlag, Berlin.

Cochran, W.G. 1934 The Flow due to a Rotating Disk, Proc. Cambridge Phil. Soc., Vol. 30, pp. 365-375.

Conte, S.D. and Miles, J.W. 1959 On the Numerical Integration of the Orr-Sommerfeld Equation, SIAM J., Vol. 7, pp. 361-366.

Cooke, J.C. 1950 The Boundary Layer of a Class of Infinite Yawed Cylinders, Proc. Cambridge Phil. Soc., Vol. 46, pp. 645-648.

Corner, D., Houston, D.T.R. and Ross, M.A.S. 1976 Higher Eigenstates in Boundary-Layer Stability Theory, J. Fluid Mech., Vol. 77, pp. 81-103.

Criminale, W.O. and Kovasnay, L.S.G. 1962 The Growth of Localized Disturbances in a Laminar Boundary Layer, J. Fluid Mech., Vol. 14, pp. 59-80.

Davey, A. 1973 A Simple Numerical Method for Solving Orr-Sommerfeld Problems, Quart. J. Mech. Appl. Math., Vol. 26, pp. 401-411.

Davey, A. 1977 On the Numerical Solution of Difficult Eigenvalue Problems, J. Comp. Phys. Vol. 24, pp. 331-338.

Davey, A. 1979 On the Removal of the Singularities from the Riccati Method, J. Comp. Phys., Vol. 30, pp. 137-144.

Davey, A. 1981 A Difficult Numerical Calculation Concerning the Stability of the Blasius Boundary Layer, in Proceedings of Numbrecht Conf.

Demetriades, A. 1977 Laminar Boundary Layer Stability Measurements at Mach 7 Including Wall Temperature Effects, AFOSR TR-77-1311.

Dougherty, N.S. and Fisher, D.F. 1980 Boundary Layer Transition on a 10° Cone: Wind Tunnel/Flight Data Correlations, AIAA Paper 80-0154; also see NASA TP 1971 1982.

Dryden, H. 1959 Transition from Laminar to Turbulent Flow, in "Turbulent Flows and Heat Transfer" (C.C. Lin, ed.), pp. 1-74, Princeton Univ. Press, Princeton.

Drazin, P.G. and Howard, L.N. 1966 Hydrodynamic Stability of Parallel Flow of Inviscid Fluid, in "Advances in Applied Mechanics" (G. Kuerti, ed.), Vol. 9, pp. 1-89, Academic Press, N.Y.

Drazin, P.G. and Reid, W.H. 1981 Hydrodynamic Stability, Cambridge Univ. Press, Cambridge.

Dunn, D.W. and Lin, C.C. 1955 On the Stability of the Laminar Boundary Layer in a Compressible Fluid, J. Aero. Sci., Vol. 22, pp. 455-477.

El-Hady, N.M. and Nayfeh, A.H. 1979 Nonparallel Stability of Compressible Boundary-Layer Flows, Report VPI-E-79-13, Virginia Polytechnic Institute and State Univ., Blacksburg, VA.

Fjortoft, R. 1950 Application of Integral Theorems in Deriving Criteria of Stability for Laminar Flows and for the Baroclinic Circular Vortex, Geofys. Publ., Vol. 17.

Foote, J.R. and Lin, C.C. 1950 Some Recent Investigations in the Theory of Hydrodynamic Stability, Quart. Appl. Math., Vol. 8, pp. 265-280.

Gallagher, A.P. and Mercier, A.M. 1962 On the Behavior of Small Disturbances in Plane Couette Flow, Part I, J. Fluid Mech., Vol. 13, pp. 91-100.

Gaster, M. 1962 A Note on a Relation between Temporally Increasing and Spatially Increasing Disturbances in Hydrodynamic Stability, J. Fluid Mech., Vol. 14, pp. 222-224.

Gaster, M. 1963 On the Stability of Parallel Flows and the Behavior of Separation Bubbles, Ph.D. Thesis, Univ. of London.

Gaster, M. 1965a On the Generation of Spatially Growing Waves in a Boundary Layer, J. Fluid Mech., Vol. 22, pp. 433-441.

Gaster, M. 1965b The Role of Spatially Growing Waves in the Theory of Hydrodynamic Stability, in "Progress in Aeronautical Sciences" (D. Küchemann and L.H.G. Sterne, eds.), Vol. 6, Pergamon Press, Oxford.

Gaster, M. 1968 The Development of Three-Dimensional Wave Packets in a Boundary Layer, J. Fluid Mech., Vol. 32, pp. 173-184.

Gaster, M. 1974 On the Effect of Boundary Layer Growth in Flow Stability, J. Fluid Mech., Vol. 66, pp. 465-480.

Gaster, M. 1975 A Theoretical Model of a Wave Packet in the Boundary Layer on a Flat Plate, Proc. Roy. Soc. A, Vol. 347, pp. 271-289.

Gaster, M. 1978 On the Application of Ray Mathematics to Non-Conservative Systems, Proceedings of NSF Regional Conference on Geophysical Fluid Dynamical Wave Mathematics, pp. 61-66, Univ. of Washington, Seattle, Wash.

Gaster, M. 1981a On Transition to Turbulence in Boundary Layers, in "Transition to Turbulence" (R.E. Meyer, ed.), Proceedings of Symposium, Univ. of Wisconsin 1980, Academic Press, N.Y.

Gaster, M. 1981b Propagation of Linear Wave Packets in Laminar Boundary Layers, AIAA J., Vol. 19, pp. 419-423.

Gaster, M. 1982a Estimates of Errors Incurred in Various Asymptotic Representations of Wave Packets, J. Fluid Mech., Vol. 121, p. 365-377.

Gaster, M. 1982b The Development of a Two-Dimensional Wave Packet in a Growing Boundary Layer, Proc. Roy. Soc. A, Vol. 384, pp. 317-332.

Gaster, M. and Davey, A. 1968 The Development of Three-Dimensional Wave Packets in Inviscid Parallel Flows, J. Fluid Mech., Vol. 32, pp. 801-808.

Gaster, M. Grant, I. 1975 An Experimental Investigation of the Formation and Development of a Wave Packet in a Laminar Boundary Layer, Proc. Roy. Soc. A, Vol. 347, pp. 253-269.

Gilev, V.M., Kachanov, Y.S. and Kozlov, V. V. 1981 Development of Spatial Wave Packets in a Boundary Layer, Preprint No. 34-81, Inst. of Theoretical and Appl. Math., USSR Acad. Sci., Novosibirsk.

Gill, A.E. 1965a A Mechanism for Instability of Plane Couette Flow and of Poiseuille Flow in a Pipe, J. Fluid Mech., Vol. 21, pp. 505-511.

Gill, A.E. 1965b Instabilities of "Top-Hat" Jets and Wakes in Compressible Fluids, Phys. Fluids, Vol. 8, pp. 1428-1430.

Godunov, S.K. 1961 On the Numerical Solution of Boundary Value Problems for Systems of Ordinary Differential Equations, Uspekhi Mat. Nauk, Vol. 16, pp. 171-174.

Gregory, N., Stuart J.T. and Walker, W.S. 1955 On the Stability of Three-Dimensional Boundary Layers with Application to the Flow Due to a Rotating Disk, Phil. Trans. Roy. Soc. A, Vol. 248, pp. 155-199.

Grosch, C.E. and Salwen, H. 1968 The Stability of Steady and Time-Dependent Plane Poiseuille Flow, J. Fluid Mech., Vol. 34, pp. 177-205.

Grosch, C.E. and Salwen, H. 1978 The Continuous Spectrum of the Orr-Sommerfeld Equation. Part I. The Spectrum and the Eigenfunctions, J. Fluid Mech., Vol. 87, pp. 333-54.

Hama, F.R., Williams, D.R. and Fasel, H. 1980 Flow Field and Energy Balance According to the Spatial Linear Stability Theory of the Blasius Boundary Layer, in "Laminar-Turbulent Transition" (R. Eppler and H. Fasel, eds.), pp. 73-85, Springer, Berlin.

Hefner, J.N. and Bushnell, D.M. 1979 Application of Stability Theory to Laminar Flow Control, AIAA Paper 79-1493.

Heisenberg, W. 1924 Uber Stabilität und Turbulenz von Flussigkeitsströmen, Ann. Phys.-Lpz. (4), Vol. 79, pp. 577-627 (also NACA TM No. 1291).

Jaffe, N.A., Okamura, T.T. and Smith, A.M.O. 1970 Determination of Spatial Amplification Factors and Their Application to Predicting Transition, Vol. 8, AIAA J., pp. 301-308.

Jordinson, R. 1970 The Flat Plate Boundary Layer. Part I. Numerical Integration of the Orr-Sommerfeld Equation, J. Fluid Mech., Vol. 43, pp. 801-811.

Jordinson, R. 1971 Spectrum of Eigenvalues of the Orr-Sommerfeld Equation for Blasius Flow, Phys. Fluids, Vol. 14, pp. 2535-2537.

Joseph, D.D. 1976 Stability of Fluid Motions, Springer Tracts on Natural Philosophy, Vol. 27 and 28, Springer, Berlin.

Karman, Th. von 1921 Laminare und turbulente Reibung, ZAMM, Vol. 1, pp. 233-252. (Also NACA TM No. 1092, 1946).

Kelvin, Lord 1880 On a Disturbing Infinity in Lord Rayleigh's Solution for Waves in a Plane Vortex Stratum, Math. and Phys. Papers, Vol. 8, pp. 186-187, Cambridge Univ. Press, Cambridge.

Kendall, J.M. 1967 Supersonic Boundary-Layer Stability Experiments, in Proceedings of Boundary Layer Transition Study Group Meeting (W.D. McCauley, ed.), Aerospace Corp. Report No. BSD-TR-67-213, Vol. II.

Kendall, J.M. 1971 JPL Experimental Investigations, in Proceedings of the Boundary-Layer Transition Workshop, Vol. IV, Aerospace Corp., San Bernardino, CA.

Kendall, J.M. 1975 Wind Tunnel Experiments Relating to Supersonic and Hypersonic Boundary-Layer Transition, AIAA J., Vol. 13, pp. 240-299.

Küchemann, D. 1938 Störungsbewegungen in einer Gasströmung mit Grenzschicht, ZAMM, Vol. 18, pp. 207-222.

Kümmerer, H. 1973 Numerische Untersuchungen zur Stabilität ebener laminarer Grenzschichtströmungen, Dissertation, Universität Stuttgart.

Kurtz, E.F., Jr. 1961 Study of the Stability of Parallel Flows, Ph.D. Thesis, Massachusetts Institute of Technology, Cambridge, MA.

Kurtz, E.F., Jr. and Crandall, S.H. 1962 Computer-aided Analysis of Hydrodynamic Stability, J. Math. Phys., Vol. 41, pp. 264-279.

Lakin, W., Ng, B. and Reid, W.H. 1978 Approximation to the Eigenvalue Relation for the Orr-Sommerfeld Equation, Phil. Trans. Roy. Soc. A, Vol. 289, pp. 147-371.

Landahl, M.T. and Kaplan, R.E. 1965 Effect of Compliant Walls on Boundary Layer Stability and Transition, AGARDograph 97, Part 1, pp. 363-394, NATO, Paris.

Laufer, J. and Vrebalovich, T. 1960 Stability and Transition on a Supersonic Laminar Boundary Layer on an Insulated Flat Plate, J. Fluid Mech., Vol. 9, pp. 257-299.

Lees, L. 1947 The Stability of the Laminar Boundary Layer in a Compressible Fluid, NACA Tech. Report No. 876.

Lees, L. 1952 Instability of Laminar Flows and Transition to Turbulence, Consolidated Aircraft Corp., San Diego, CA, Report No. ZA-7-006.

Lees, L. and Gold, H. 1964 Stability of Laminar Boundary Layers and Wakes at Hypersonic Speeds: Part I. Stability of Laminar Wakes, Inter. Symp. on Fundamental Phenom. in Hypersonic Flow, GALCIT Memo., California Institute of Technology, Pasadena, CA.

Lees, L. and Lin, C.C. 1946 Investigation of the Stability of the Laminar Boundary Layer in a Compressible Fluid, NACA Tech. Note No. 1115.

Lees, L. and Reshotko, E. 1962 Stability of the Compressible Laminar Boundary Layer, J. Fluid Mech., Vol. 12, pp. 555-590.

Lekoudis, S. 1979 Stability of Three-Dimensional Boundary Layers over Wings with Suction, AIAA Paper 79-0265.

Lekoudis, S. 1980 Stability of the Boundary Layer on a Swept Wing with Wall Cooling, AIAA J., Vol. 18, pp. 1029-1035.

Lighthill, M.J. 1963 Introduction. Boundary Layer Theory, in "Laminar Boundary Layers" (L. Rosenhead, ed.), pp. 46-113.

Lin, C.C. 1945 On the Stability of Two-Dimensional Parallel Flows, Parts I, II, III, Quart. Appl. Math., Vol. 3, pp. 117-142, 218-234, 277-301.

Lin, C.C. 1954 Some Physical Aspects of the Stability of Parallel Flows, Proc. Nat. Acad. Sci., Vol. 40, pp. 741-747.

Lin, C.C. 1955 The Theory of Hydrodynamic Stability, Cambridge Univ. Press, Cambridge.

Lin, C.C. 1961 Some Mathematical Problems in the Theory of the Stability of Parallel Flows, J. Fluid Mech., Vol. 10, pp. 430-438.

Mack, L.M. 1960 Numerical Calculation of the Stability of the Compressible Laminar Boundary Layer, Jet Propulsion Laboratory, Report No. 20-122, Pasadena, CA.

Mack, L.M. 1963 The Inviscid Stability of the Compressible Laminar Boundary Layer, in "Space Programs Summary," No. 37-23, p. 297, Jet Propulsion Laboratory, Pasadena, CA.

Mack, L.M. 1964 The Inviscid Stability of the Compressible Laminar Boundary Layer: Part II, in "Space Programs Summary," No. 37-26, Vol. IV, p. 165, Jet Propulsion Laboratory, Pasadena, CA.

Mack, L.M. 1965a Computation of the Stability of the Laminar Boundary Layer, in "Methods in Computational Physics" (B. Alder, S. Fernbach and M. Rotenberg, eds.), Vol. 4, pp. 247-299, Academic, N.Y.

Mack, L.M. 1965b Stability of the Compressible Laminar Boundary Layer According to a Direct Numerical Solution, in AGARDograph 97, Part I, pp. 329-362.

Mack, L.M. 1969 Boundary-Layer Stability Theory, Jet Propulsion Laboratory, Pasadena, CA, Document No. 900-277, Rev. A.

Mack, L.M. 1971 Progress in Compressible Boundary Layer Stability Computations, in Proceedings of the Boundary Layer Transition Workshop, Vol. 1, pp. 1-1 to 1-19, Aerospace Corp., San Bernardino, CA.

Mack, L.M. 1975 Linear Stability and the Problem of Supersonic Boundary-Layer Transition, AIAA J., Vol. 13, pp. 278-289.

Mack, L.M. 1976 A Numerical Study of the Temporal Eigenvalue Spectrum of the Blasius Boundary Layer, J. Fluid Mech., Vol. 79, pp. 497-520.

Mack, L.M. 1977 Transition Prediction and Linear Stability Theory, in AGARD Conference Proceedings No. 224, pp. 1-1 to 1-22, NATO, Paris.

Mack, L.M. 1979a On the Stability of the Boundary Layer on a Transonic Swept Wing, AIAA Paper No. 79-0264.

Mack, L.M. 1979b Three-Dimensional Effects in Boundary-Layer Stability, in Proceedings of Twelfth Symposium on Naval Hydrodynamics, pp. 63-70, National Academy of Sciences, Washington, D.C.

Mack, L.M. 1981 Compressible Boundary-Layer Stability Calculations for Sweptback Wings with Suction, AIAA J., Vol. 20, pp. 363-369.

Mack, L.M. 1984a Line Sources of Instability Waves in a Blasius Boundary Layer, AIAA Paper No. 84-0168.

Mack, L.M. 1984b Remarks on Disputed Results in Compressible Boundary-Layer Stability Theory, Phys. Fluids, Vol. 27, pp. 342-347.

Mack, L.M. 1984c The Stationary Wave Pattern Produced by a Point Source on a Rotating Disk, to be published.

Mack, L.M. and Kendall, J.M. 1983 Wave Pattern Produced by a Localized Harmonic Source in a Blasius Boundary Layer, to be published.

Mack, L.M. and Morkovin, M.V. 1971 High-Speed Boundary-Layer Stability and Transition, Recorded Lectures Series, AIAA, N.Y.

Malik, M.R. 1982 COSAL - A Black-Box Compressible Stability Analysis Code for Transition Prediction in Three-Dimensional Boundary Layers, NASA CR-165925.

Malik, M.R. and Orszag, S.A. 1981 Efficient Computation of the Stability of Three-Dimensional Boundary Layers, AIAA Paper No. 81-1277.

Malik, M.R., Wilkinson, S.P. and Orszag, S.A. 1981 Instability and Transition in Rotating Disk Flow, AIAA J., Vol. 19, pp. 1131-1138.

Morkovin, M.V. 1968 Critical Evaluation of Transition from Laminar to Turbulent Shear Layers with Emphasis on Hypersonically Travelling Bodies, Report AFFDL-TR-68-149, Wright-Patterson Air Force Base, Ohio.

Morkovin, M.V. 1978 Instability, Transition to Turbulence, and Predictability, AGARDograph No. 236, NATO, Paris.

Morkovin, M.V. 1983 Understanding Transition to Turbulence in Shear Layers, Report AFOSR-FR-83, Illinois Institute of Technology, Chicago, IL.

Morkovin, M.V. 1984 Guide to Experiments in Instability and the Laminar Turbulent Transition in Shear Layers, to be published.

Murdock, J.W. and Stewartson, K. 1977 Spectra of the Orr-Sommerfeld Equation, Phys. Fluids, Vol. 20, pp. 1404-1416.

Nachtsheim, P. 1963 Stability of Free-Convection Boundary Layer Flows, NASA Tech. Note No. D-2089.

Nachtsheim, P. 1964 An Initial Value Method for the Numerical Treatment of the Orr-Sommerfeld Equation for the Case of Plane Poiseuille Flow, NASA Tech. Note No. D-2414.

Nayfeh, A.H. 1980a Stability of Three-Dimensional Boundary Layers, AIAA J., Vol. 18, pp. 406-416.

Nayfeh, A.H. 1980b Three-Dimensional Stability of Growing Boundary Layers, in "Laminar-Turbulent Transition" (R. Eppler and H. Fasel, eds.), pp. 201-217, Springer, Berlin.

Nayfeh, A.H. and Padhye, A. 1979 The Relation between Temporal and Spatial Stability in Three-Dimensional Flows, AIAA J., Vol. 17, pp. 1084-1090.

Ng, B. and Reid, W.H. 1979 An Initial Value Method for Eigenvalue Problems Using Compound Matrices, J. Comp. Phys., Vol. 30, pp. 135-136.

Ng, B. and Reid, W.H. 1980 On the Numerical Solution of the Orr-Sommerfeld Equation: Asymptotic Initial Conditions for Shooting Methods, J. Comp. Phys., Vol. 38, pp. 275-293.

Noether, F. 1921 Das Turbulenzproblem, ZAMM, Vol. 1, pp. 125-138.

Obremski, H.T., Morkovin, M.V. and Landahl, M.T. 1969 A Portfolio of Stability Characteristics of Incompressible Boundary Layers, AGARDograph No. 134, NATO, Paris.

Orszag, S.A. 1971 Accurate Solution of the Orr-Sommerfeld Stability Equation, J. Fluid Mech., Vol. 50, pp. 689-703.

Osborne, M.R. 1967 Numerical Methods for Hydrodynamic Stability Problems, SIAM J. Appl. Math., pp. 539-557.

Pfenninger, W. 1977 Laminar Flow Control-Laminarization, in "Special Course on Concepts for Drag Reduction," AGARD Report No. 654, pp. 3-1 to 3-75, NATO, Paris.

Phillips, O.M. 1960 On the Generation of Sound by Supersonic Shear Layers, J. Fluid Mech., Vol. 9, pp. 1-28.

Poll, D.I.A. 1977 Leading Edge Transition on Swept Wings, in "Laminar-Turbulent Transition," AGARD Conference Proceedings No. 224, pp. 21-1 to 21-11, NATO, Paris.

Prandtl, L. 1921 Bemerkungen über die Enstehung der Turbulenz, ZAMM, Vol. 1, pp. 431-436.

Pretsch, J. 1942 Anfachung instabler Störungen in einer laminaren Reigungsschicht, Jb. deutsch. Luftfahrtfor., pp. 154-171.

Radbill, J.R. and Van Driest, E.R. 1966 A New Method for Prediction of Stability of Laminar Boundary Layers, AFOSR Report No. 66-0702.

Rayleigh, Lord 1880 On the Stability or Instability of Certain Fluid Motions, in "Scientific Papers," Vol. 1, pp. 474-487, Cambridge Univ. Press, Cambridge.

Rayleigh, Lord 1887 On the Stability or Instability of Certain Fluid Motions. II, in "Scientific Papers," Vol. 3, pp. 17-23, Cambridge Univ. Press, Cambridge.

Rayleigh, Lord 1892 On the Question of the Stability of the Flow of Fluids, in "Scientific Papers," Vol. 3, pp. 575-584, Cambridge Univ. Press, Cambridge.

Rayleigh, Lord 1895 On the Stability or Instability of Certain Fluid Motions. III, in "Scientific Papers," Vol. 4, pp. 203-219, Cambridge Univ. Press, Cambridge.

Rayleigh, Lord 1913 On the Stability of the Laminar Motion of an Inviscid Fluid, in "Scientific Papers," Vol. 6, pp. 197-204, Cambridge Univ. Press, Cambridge.

Reid, W.H. 1965 The Stability of Parallel Flows, in "Basic Developments in Fluid Dynamics" (M. Holt, ed.), Vol. 1, pp. 249-307, Academic Press, NY.

Reshotko, E. 1960 Stability of the Compressible Laminar Boundary Layer, GALCIT Memo. No. 52, California Institute of Technology, Pasadena, CA.

Reshotko, E. 1962 Stability of Three-Dimensional Compressible Boundary Layers, NASA Tech. Note D-1220.

Reshotko, E. 1976 Boundary Layer Stability and Transition, in "Annual Review of Fluid Mechanics" (M. Van Dyke, W.G. Vincenti and G.V. Wehausen, eds.), Vol. 8, pp. 311-349, Annual Reviews, Palo Alto.

Reynolds, O. 1895 On the Dynamical Theory of Incompressible Viscous Fluids and the Determination of the Criterion, Phil. Trans. Roy. Soc. A, Vol. 186, pp. 123-164.

Rosenhead, L. 1963 Laminar Boundary Layers, Oxford Univ. Press, Oxford.

Saric, W.S. and Nayfeh, A.H. 1975 Non-parallel Stability of Boundary Layer Flows, Phys. Fluids, Vol. 18, pp. 945-950.

Saric, W.S. and Nayfeh, A.H. 1977 Nonparallel Stability of Boundary Layers with Pressure Gradients and Suction, in AGARD Conference Proceedings No. 224, NATO, Paris.

Schlichting, H. 1933a Zur Entstehung der Turbulenz bei der Plattenströmung, Nachr. Ges. Wiss. Göttingen, Math.-phys. Klasse, pp. 181-208.

Schlichting, H. 1933b Berechnung der Anfachung kleiner Störungen bei der Plattenstromung, ZAMM, Vol. 13, pp. 171-174.

Schlichting, H. 1935 Amplitudenverteilung und Energiebilanz der kleinen Störungen bei der Plattengrenzschicht, Nachr. Ges. Wiss. Göttingen, Math.-phys. Klasse, Vol. 1, pp. 47-78.

Schlichting, H. 1940 Uber die theoretische Berechnung der kritischen Reynoldschen Zahl einer Reibungsschicht in beschleunigter ind verzögerter Stromung, Jb. deutsch. Luftfahrtfor. I, p. 97.

Schlichting, H. 1959 Entstehung der Turbulenz, in "Handbuch der Physik" (S. Flugge, ed.), Vol. VIII/I, pp. 351-450, Springer, Berlin.

Schlichting, H. 1979 Boundary Layer Theory (7th Ed.) McGraw-Hill, NY.

Schubauer, G.B. and Skramstad, H.K. 1947 Laminar Boundary Layer Oscillations and Transitions on a Flat Plate, J. Aero. Sci., Vol. 14, pp. 69-76; also NACA Report 909, 1948.

Scott, M.R. and Watts, H.A. 1977 Computational Solution of Linear Two-Point Boundary Value Problems and Orthonormalization, SIAM J. Numer. Anal., Vol. 14, pp. 40-70.

Shen, S.F. 1964 Stability of Laminar Flows, in "Theory of Laminar Flows" (F.K. Moore, ed.), pp. 719-853, Princeton Univ. Press, Princeton.

Smith, A.M.O. and Gamberoni, N. 1956 Transition, Pressure Gradient and Stability Theory, Report No. ES 26388, Douglas Aircraft Co., Inc., El Segundo, CA.

Squire, H.B. 1933 On the Stability of Three-Dimensional Disturbances of Viscous Flow between Parallel Walls, Proc. Roy. Soc. A, Vol. 142, pp. 621-628.

Srokowski, A. and Orszag, S.A. 1977 Mass Flow Requirements for LFC Wing Design, AIAA Paper No. 77-1222.

Stetson, K.F., Thompson, E.R., Donaldson, J.C. and Siler, L.G. 1983 Laminar Boundary Layer Stability Experiments on a Cone at Mach 8. Part 1: Sharp Cone, AIAA Paper 83-1761.

Stetson, K.F., Donaldson, J.C. and Thompson, E.R. 1984 Laminar Boundary Layer Stability Experiments on a Cone at Mach 8. Part 2: Blunt Cone, AIAA Paper 84-0006.

Stuart, J.T. 1963 Hydrodynamic Stability, in "Laminar Boundary Layers" (L. Rosenhead, ed.), pp. 629-670, Oxford Univ. Press, Oxford.

Tani, I. 1969 Boundary-Layer Transition, in "Annual Review of Fluid Mechanics" (W.R. Sears and M. Van Dyke, eds.), Vol. 1, pp. 169-196, Annual Reviews, Palo Alto.

Tani, I. 1981 Three-Dimensional Aspects of Boundary-Layer Transition, Proc. Indian Acad. Sci. (Engg. Br.), Vol. 4, Pt. 2, pp. 219-238.

Tatsumi, T. and Gotoh, K. 1971 in Instability of Continuous Systems (H. Leipholz, ed.), p. 368.

Taylor, G.I. 1915 Eddy Motion in the Atmosphere, Phil. Trans. Roy. Soc. A, Vol. 215, pp. 1-26.

Taylor, G.I. 1938 Some Recent Developments in the Study of Turbulence, Proceedings of 5th Inter. Congr. Appl. Mech., Cambridge, MA, pp. 294-310.

Thomas, L.H. 1953 The Stability of Plane Poiseuille Flow, Phys. Rev., Vol. 91, pp. 780-783.

Tollmien, W. 1929 Uber die Entstehung der Turbulenz, Nachr. Ges. Wiss. Göttingen, Math.-phys. Klasse, pp. 21-44.

Tollmien, W. 1935 Ein allgemeines Kriterium der Instabiltät laminarer Geschwindigkeitsverteilungen, Nachr. Ges. Wiss. Göttingen, Math.-phys. Klasse, Vol. 50, pp. 79-114.

Van Ingen, J.L. 1956 A Suggested Semi-Empirical Method for the Calculation of the Boundary Layer Transition Region, Univ. of Tech., Dept. Aero. Eng., Report VTH-74, Delft, Holland.

Van Stijn, T.L. and Van De Vooren, A.I. 1982 An Accurate Method for Solving the Orr-Sommerfeld Equation, J. Eng. Math., Vol. 14, pp. 17-26.

Van Stijn, T.L. and Van De Vooren, A.I. 1983 On the Stability of Almost Parallel Boundary-Layer Flows, Computers and Fluids, Vol. 10, pp. 223-241.

Wasow, W. 1948 The Complex Asymptotic Theory of a Fourth Order Differential Equation of Hydrodynamics, Ann. Math. (2), Vol. 49, pp. 852-871.

Wazzan, A.R. and Okamura, T.T. and Smith, A.M.O. 1968a Spatial and Temporal Stability Charts for the Falkner-Skan Boundary-Layer Profiles, Report No. DAC-67086, McDonnell-Douglas Aircraft Co., Long Beach, CA.

Wazzan, A.R., Okamura, T.T. and Smith, A.M.O. 1968b The Stability of Water Flow over Heated and Cooled Flat Plates, J. Heat Transfer, Vol. 90, pp. 109-114.

Wazzan, A.R., Taghavi, H. and Keltner, G. 1984 The Effect of Mach Number on the Spatial Stability of Adiabatic Flat Plate Flow to Oblique Disturbances, Phys. Fluids, Vol. 27, pp. 331-341.

Wilkinson, S.P. and Malik, M.R. 1983 Stability Experiments in Rotating-Disk Flow, AIAA Paper No. 83-1760.

Zaat, J.A. 1958 Numerische Beiträge zur Stabilitätstheorie der Grenzschichten, Grenzschichtforschung Symp., IUTAM, pp. 127-138, Springer, Berlin.

ACKNOWLEDGEMENT
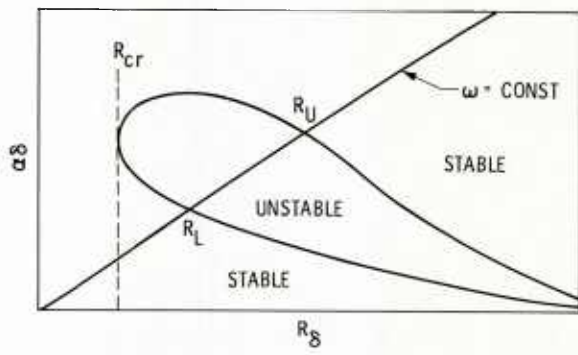
(a) VISCOUS INSTABILITY
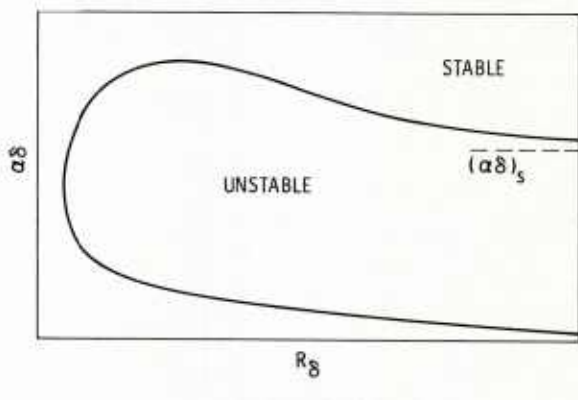
(b) INVISCID INSTABILITY

Fig. 1.1 Typical neutral-stability curves.

Fig. 3.2 Inviscid temporal damping rate vs. wavenumber for Blasius boundary layer.

Fig. 3.1 Alternative indented contours for numerical integration of inviscid equations.
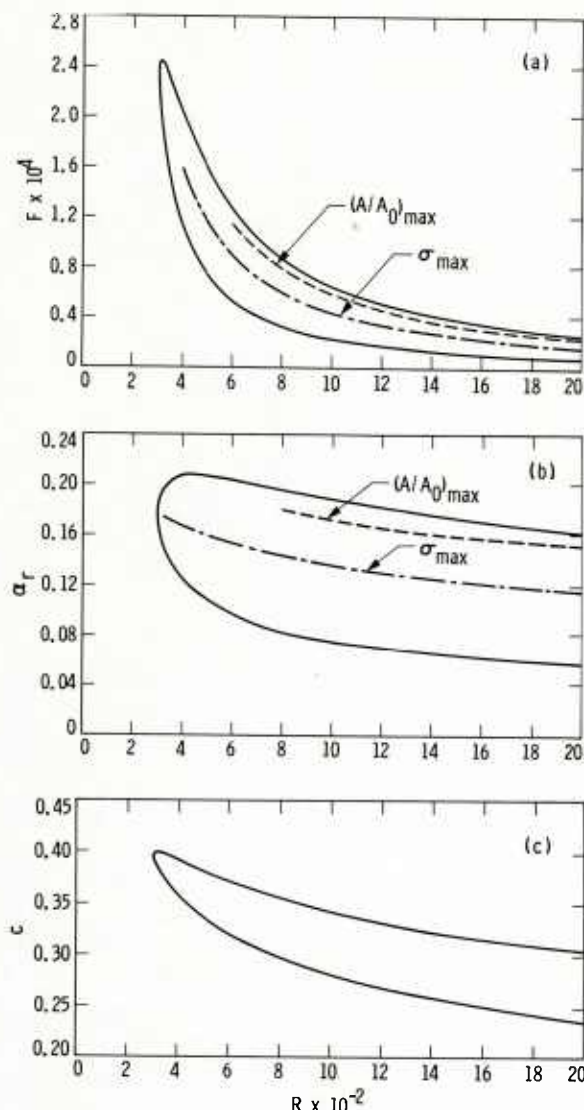
Fig. 6.1 Neutral-stability curves for Blasius boundary layer: (a) F vs. R; (b) α_r vs. R; (c) c vs. R; - -, σ_{max}; ---, $(A/A_0)_{max}$; both maxima are with respect to frequency at constant R.
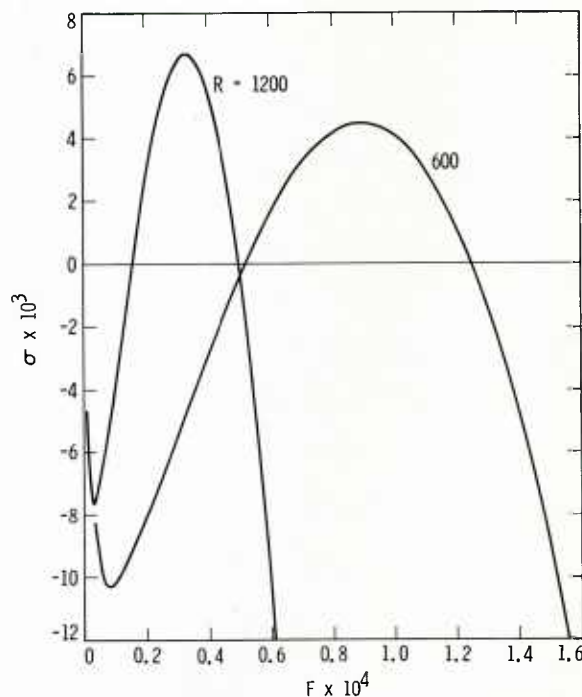
Fig. 6.2 Distribution of 2D spatial amplification rate with frequency in Blasius boundary layer at R = 600 and 1200.
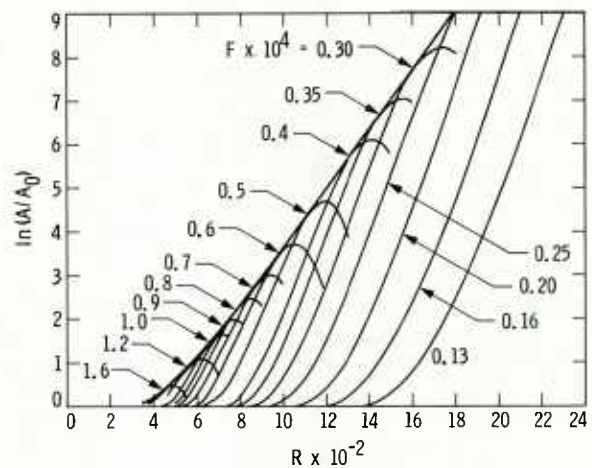
Fig. 6.4 2D $\ln(A/A_0)$ as function of R for several frequencies plus envelope curve; Blasius boundary layer.
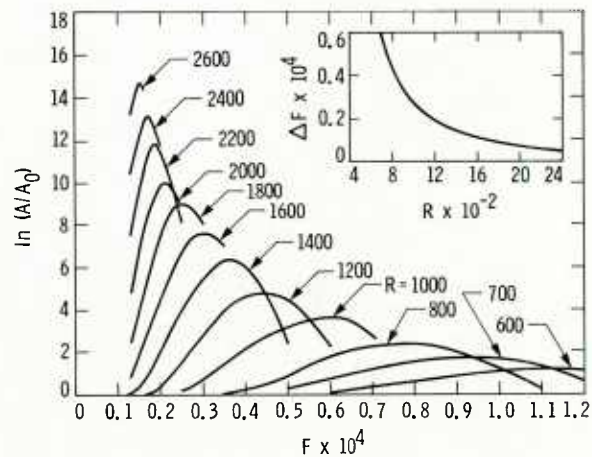
Fig. 6.5 Distribution of 2D $\ln(A/A_0)$ with frequency at several Reynolds numbers, and bandwidth of frequency response as a function of Reynolds number; Blasius boundary layer.
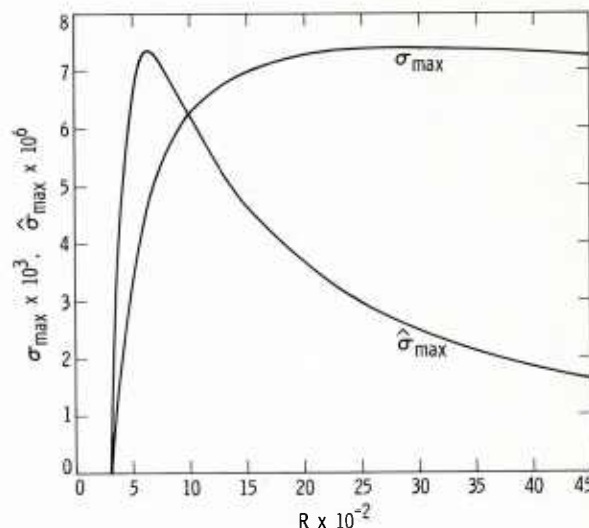
Fig. 6.3 Maximum 2D spatial amplification rates σ_{max} and $\hat{\sigma}_{max}$ as functions of Reynolds number for Blasius boundary layer.
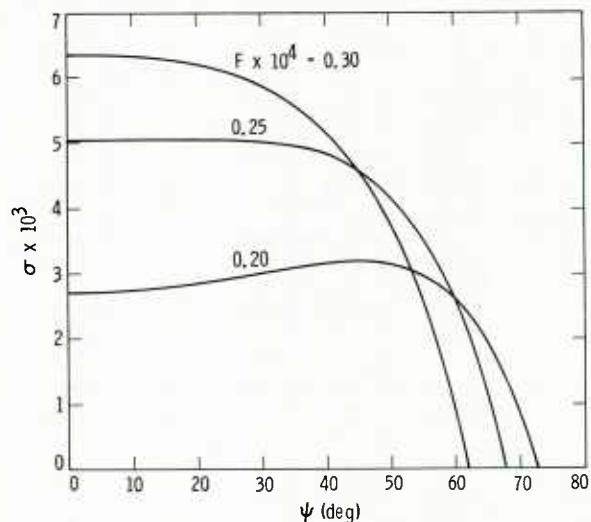
Fig. 6.6 Effect of wave angle on spatial amplification rate at R = 1200 for $F \times 10^4$ = 0.20, 0.25 and 0.30; Blasius boundary layer.
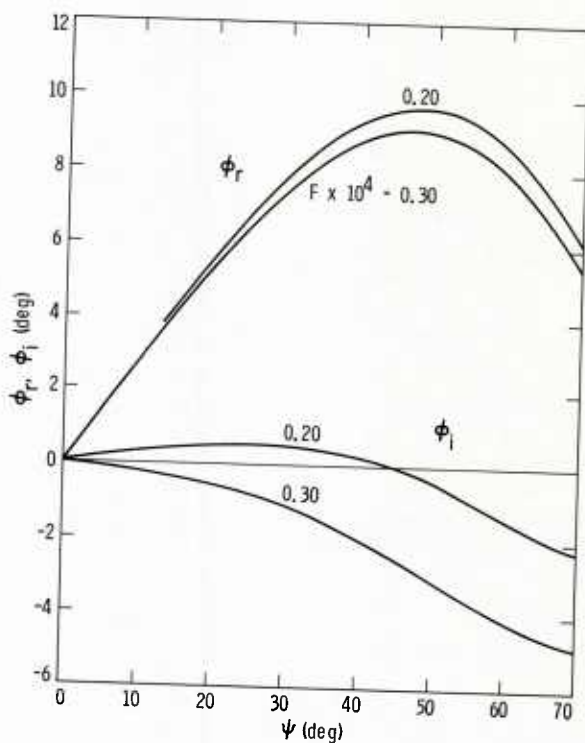
Fig. 6.7 Complex group-velocity angle vs. wave angle at $R = 1200$ for $F \times 10^4 = 0.20$ and 0.30; Blasius boundary layer.

Fig. 6.9 Eigenfunctions of $\hat{u}$ amplitude at $R = 800$, 1200 and 1600 for $F = 0.30 \times 10^{-4}$; Blasius boundary layer.
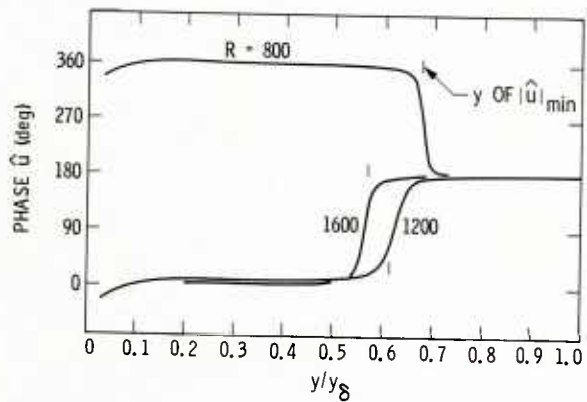
Fig. 6.10 Eigenfunctions of $\hat{u}$ phase at $R = 800$, 1200 and 1600 for $F = 0.30 \times 10^{-4}$; Blasius boundary layer.

Fig. 6.8 Effect of wave angle on $\ln(A/A_0)$ at several Reynolds numbers for $F = 0.20 \times 10^{-4}$; Blasius boundary layer.
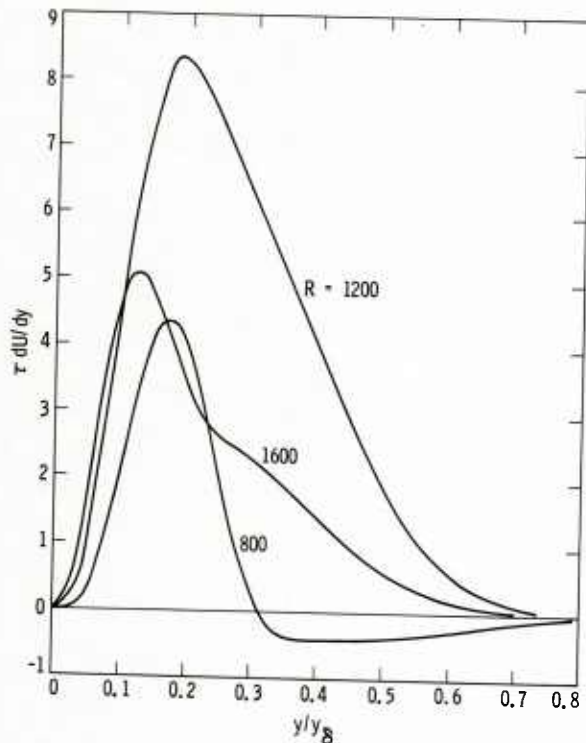
Fig. 6.11 Energy production term at $R = 800$, 1200 and 1600 for $F = 0.30 \times 10^{-4}$; Blasius boundary layer.
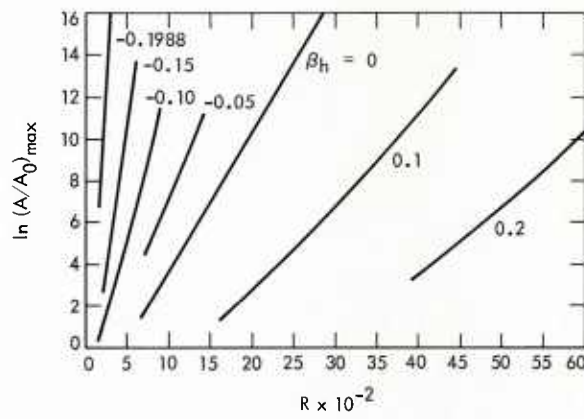
Fig. 6.12 2D envelope curves of $\ln(A/A_0)$ for Falkner-Skan family of boundary layers.
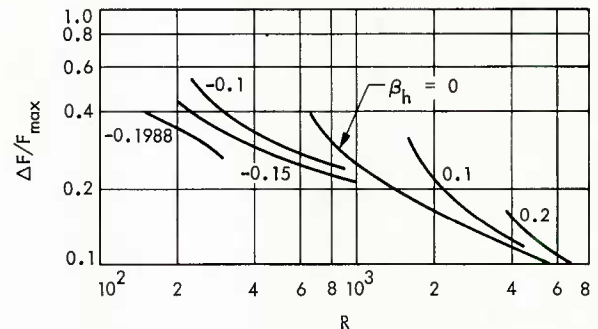
Fig. 6.14 Frequency bandwidth along 2D envelope curves for Falkner-Skan boundary layers.
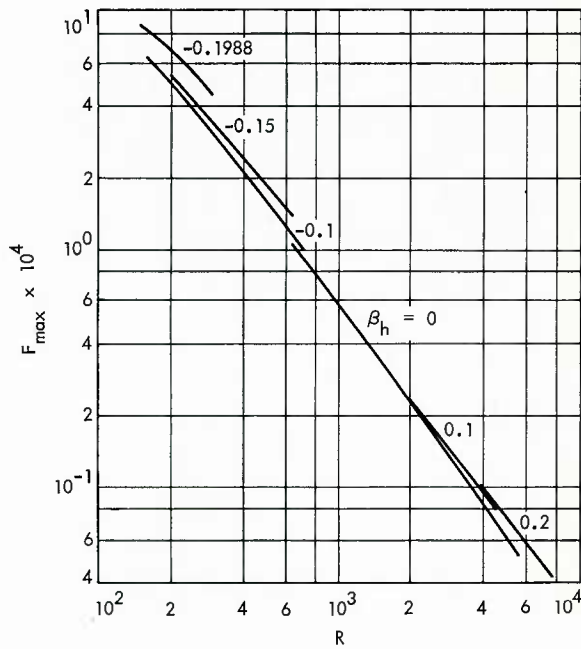
Fig. 6.13 2D envelope-curve frequencies of Falkner-Skan boundary layers.
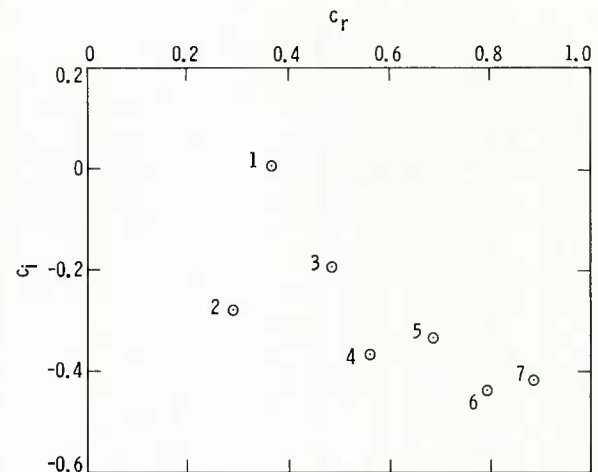
Fig. 6.15 Temporal eigenvalue spectrum of Blasius boundary layer for $\alpha = 0.179$, $R = 580$.
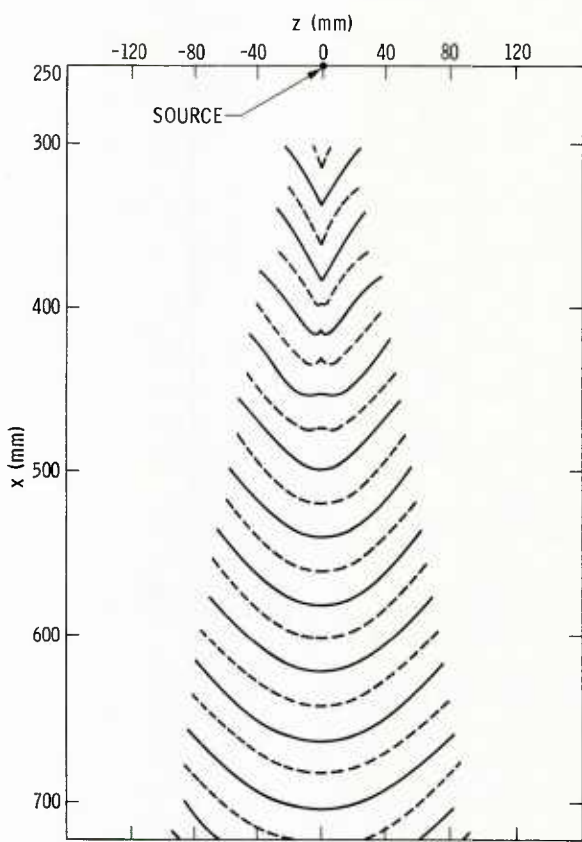
Fig. 7.1 Constant-phase lines of wave pattern from harmonic point source in Blasius boundary layer; $F = 0.92 \times 10^{-4}$, $R_s = 390$. [After Gilev et al. (1981)]

Fig. 7.3 Centerline phase distribution behind harmonic point source as calculated by numerical integration; $F = 0.60 \times 10^{-4}$, $R_s = 485$, Blasius boundary layer.
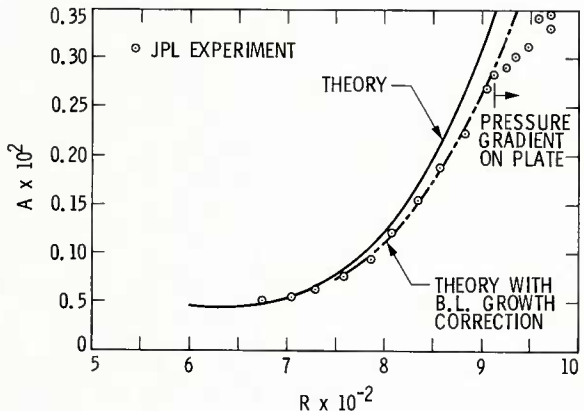
Fig. 7.4 Comparison of measured and calculated centerline amplitude distributions behind harmonic point source; $F = 0.60 \times 10^{-4}$, $R_s = 485$, Blasius boundary layer.

Fig. 7.2 Centerline amplitude distribution behind harmonic point source as calculated by numerical integration, and comparison with 2D normal mode; $F = 0.60 \times 10^{-4}$, $R_s = 485$, Blasius boundary layer.
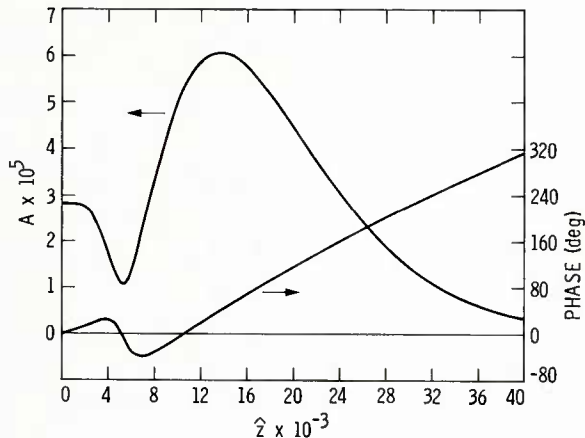
Fig. 7.5 Spanwise amplitude and phase distribution at $R = 700$ behind harmonic point source; $F = 0.60 \times 10^{-4}$, $R_s = 485$, Blasius boundary layer.
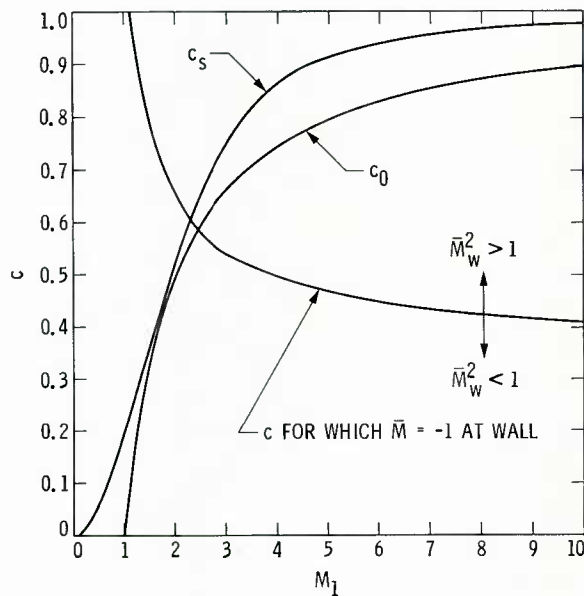
Fig. 9.1 Phase velocities of 2D neutral inflectional and sonic waves, and of waves for which relative supersonic region first appears. Insulated wall, wind-tunnel temperatures.

Fig. 9.4 Multiple wavenumbers of 2D noninflectional neutral waves (c=1). Insulated wall, wind-tunnel temperatures.

Fig. 9.2 Multiple wavenumbers of 2D inflectional neutral waves ($c=c_s$). Insulated wall, wind-tunnel temperatures.
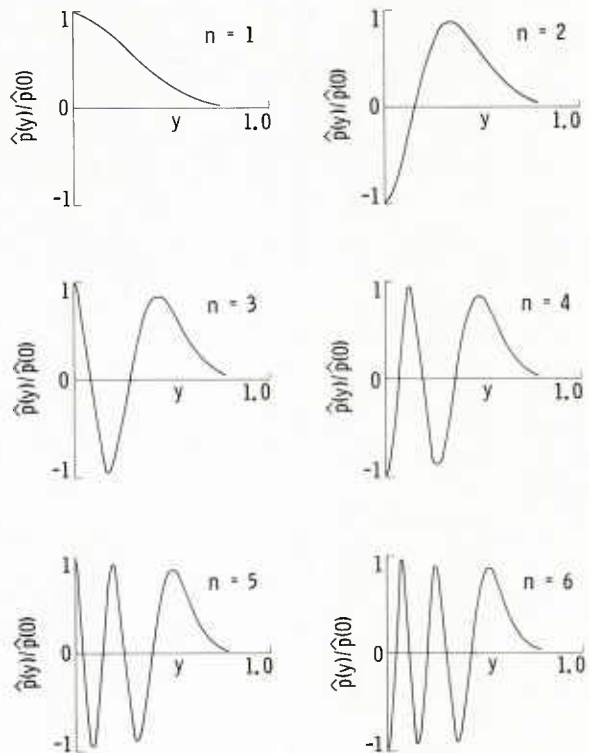
Fig. 9.5 Pressure-fluctuation eigenfunctions of first six modes of 2D noninflectional neutral waves (c=1) at $M_1 = 10$. Insulated wall, $T_1^* = 50^\circ K$.

Fig. 9.3 Pressure-fluctuation eigenfunctions of first six modes of 2D inflectional neutral waves ($c=c_s$) at $M_1 = 10$. Insulated wall, $T_1^* = 50^\circ K$.
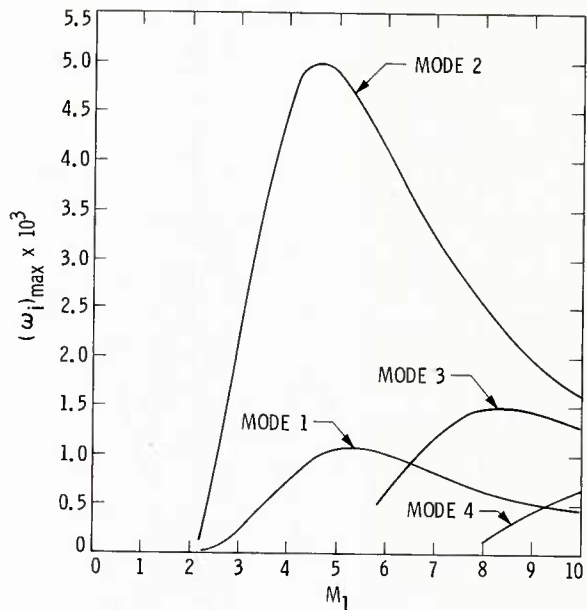
Fig. 9.6 Effect of Mach number on maximum temporal amplification rate of 2D waves for first four modes. Insulated wall, wind-tunnel temperatures.
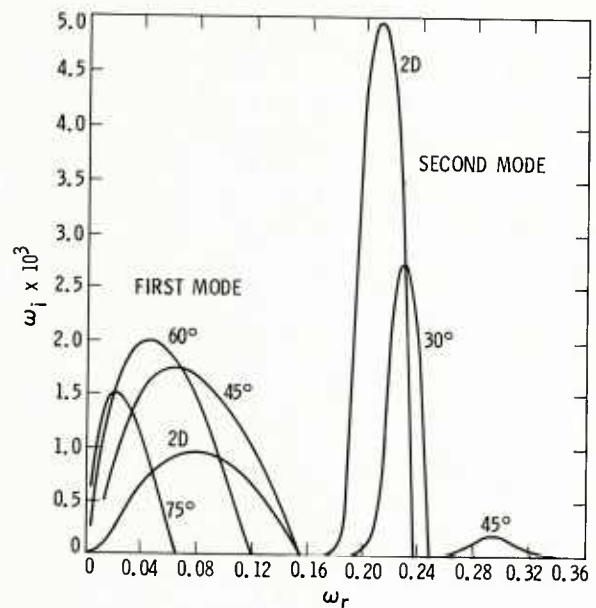
Fig. 9.8 Temporal amplification rate of first and second modes vs. frequency for several wave angles at $M_1 = 4.5$. Insulated wall, $T_1^* = 311^{\circ}$K.
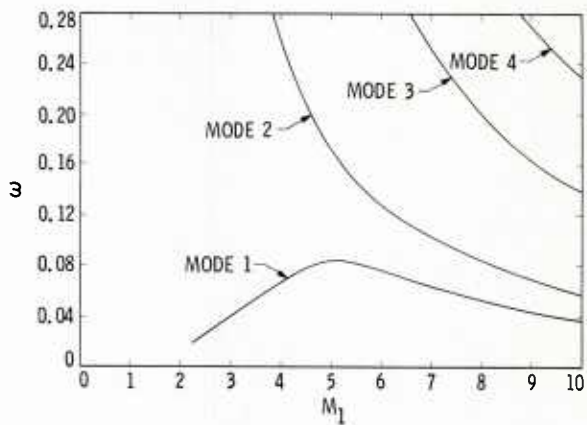
Fig. 9.7 Effect of Mach number on frequency of most unstable 2D waves for first four modes. Insulated wall, wind-tunnel temperatures.
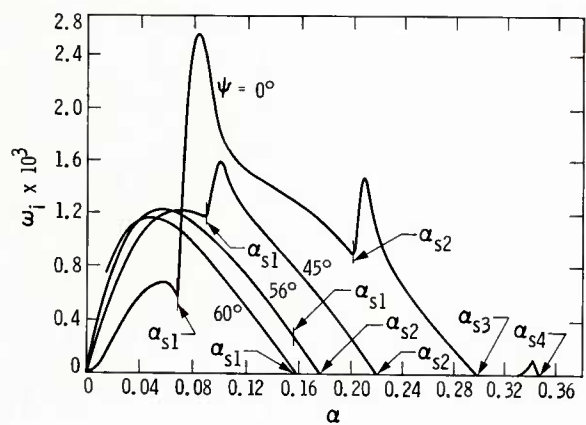
Fig. 9.9 Temporal amplification rate as function of wavenumber for 3D waves at $M_1 = 8.0$. Insulated wall, $T_1^* = 50^{\circ}$K.
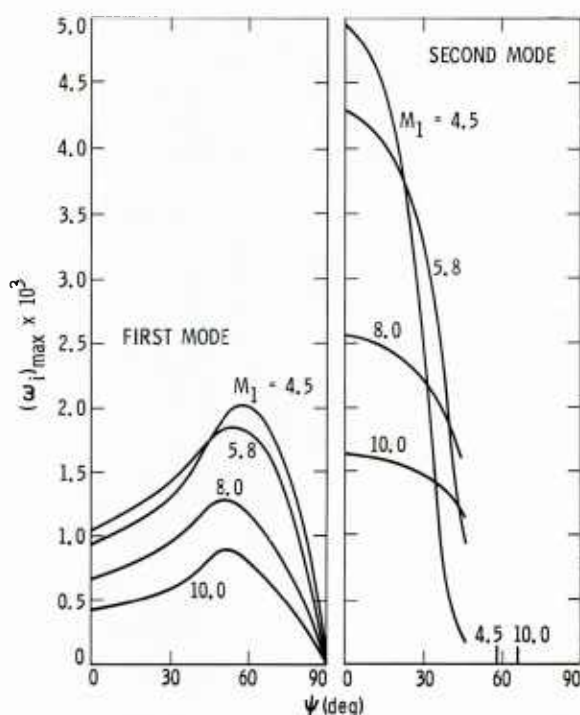
Fig. 9.10 Effect of wave angle on maximum temporal amplification rate of first and second-modes at M_1 = 4.5, 5.8, 8.0 and 10.0. Insulated wall, wind-tunnel temperatures.
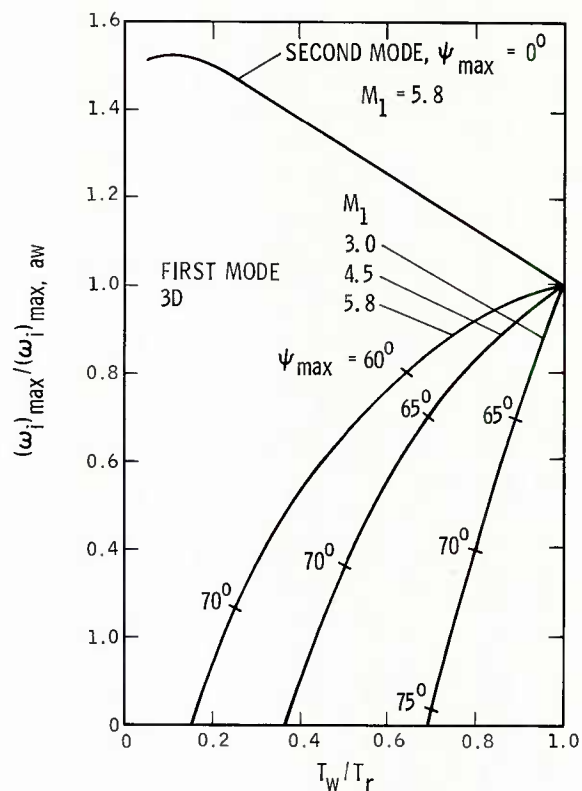
Fig. 9.12 Effect of wall cooling on ratio of maximum temporal amplification rate with respect to both frequency and wave angle of first and second modes at M_1 = 3.0, 4.5 and 5.8 to insulated-wall maximum amplification rate. Wind-tunnel temperatures.
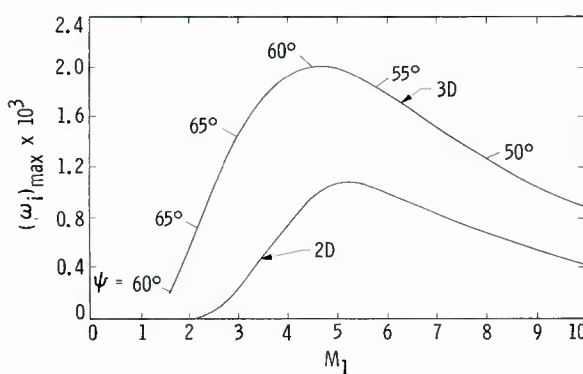

Fig. 9.11 Effect of Mach number on maximum temporal amplification rates of 2D and 3D first-mode waves. Insulated wall, wind-tunnel temperatures.
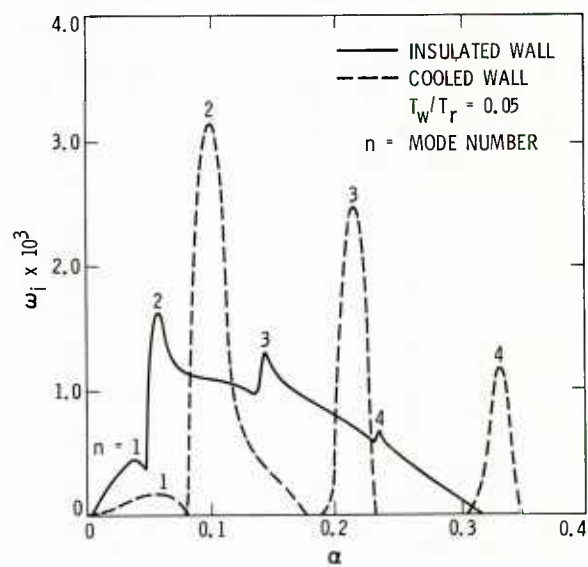
Fig. 9.13 Effect of extreme wall cooling on temporal amplification rates of 2D waves for first four modes at M_1 = 10, T_1^* = 50°K: ———, insulated wall; -----, cooled wall, T_w/T_r = 0.05.
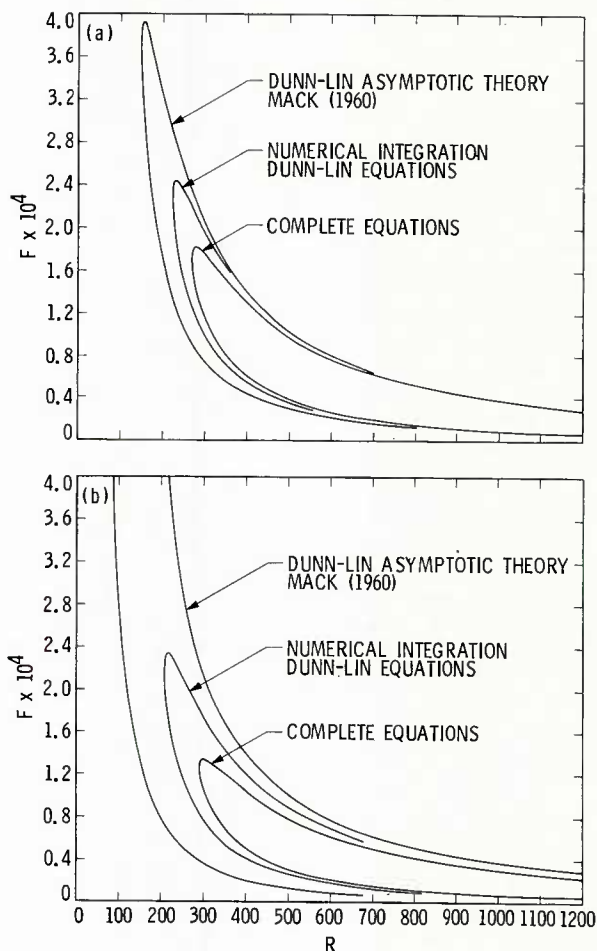
Fig. 10.1 Comparison of neutral-stability curves of frequency at (a) M_1 = 1.6 and (b) M_1 = 2.2. Insulated wall, wind-tunnel temperatures.
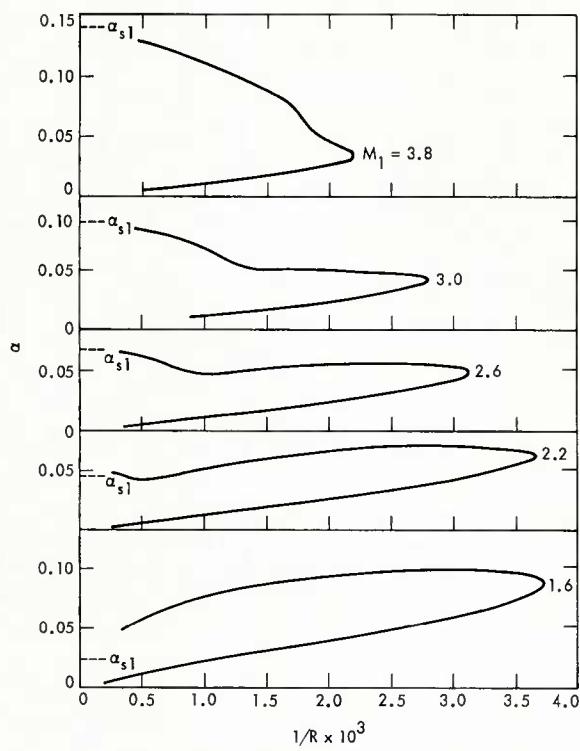

Fig. 10.2 Effect of Mach number on 2D neutral-stability curves of wavenumber. Insulated wall, wind-tunnel temperatures.
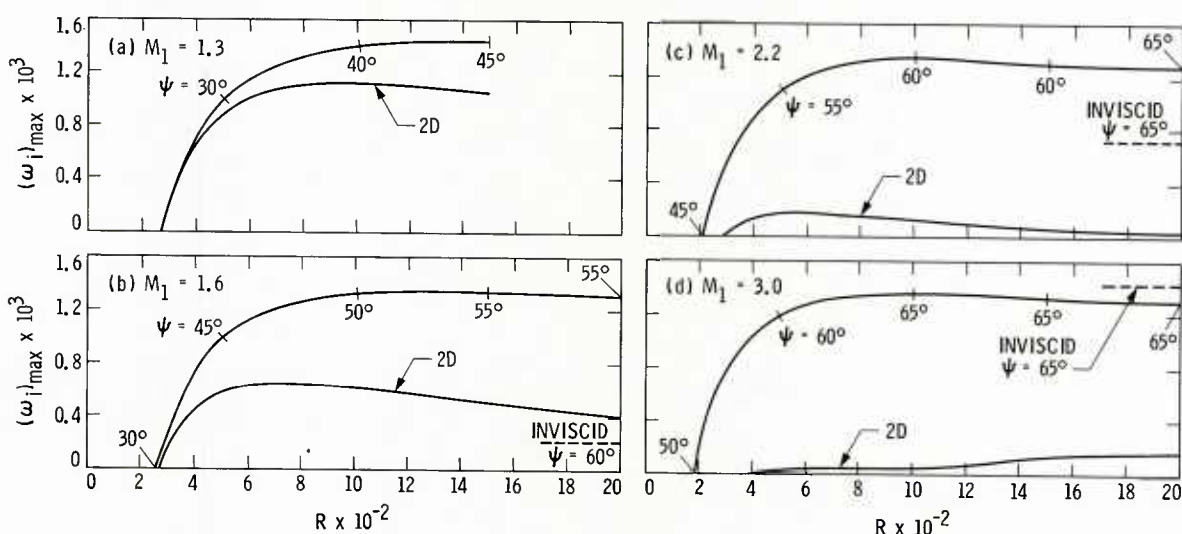

Fig. 10.3 Distribution of maximum temporal amplification rate with Reynolds number at (a) M_1 = 1.3, (b) M_1 = 1.6, (c) M_1 = 2.2 and (d) M_1 = 3.0 for 2D and 3D waves. Insulated wall, wind-tunnel temperatures.
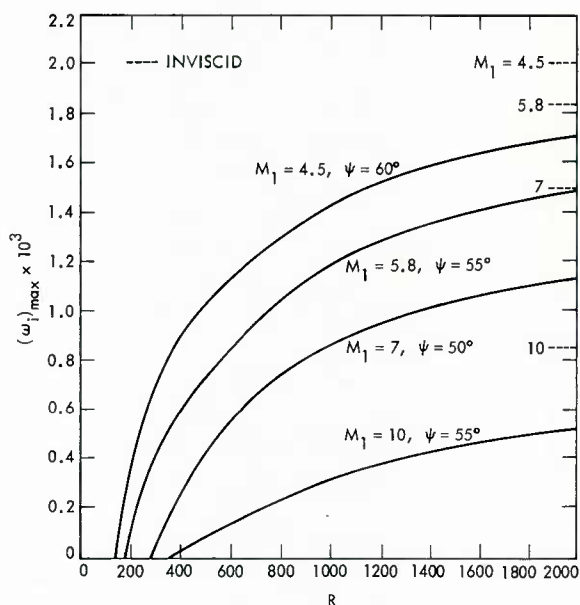
Fig. 10.4 Distribution of maximum first-mode temporal amplification rates with Reynolds number for 3D waves at M_1 = 4.5, 5.8, 7.0 and 10.0. Insulated wall, wind-tunnel temperatures.
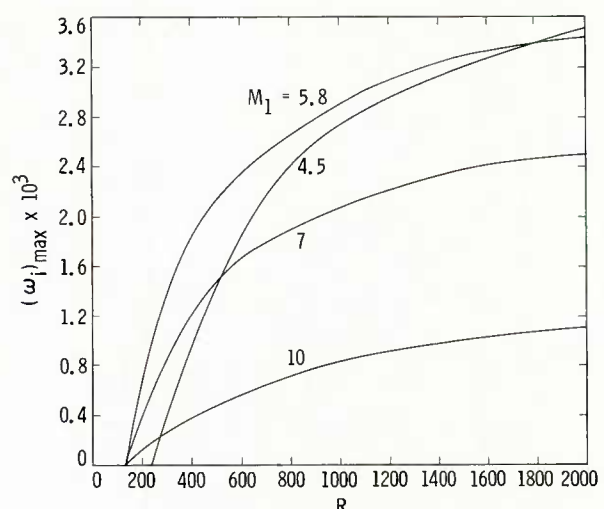

Fig. 10.6 Effect of Reynolds number on maximum second-mode temporal amplification rate at M_1 = 4.5, 5.8, 7.0 and 10.0. Insulated wall, wind-tunnel temperatures.
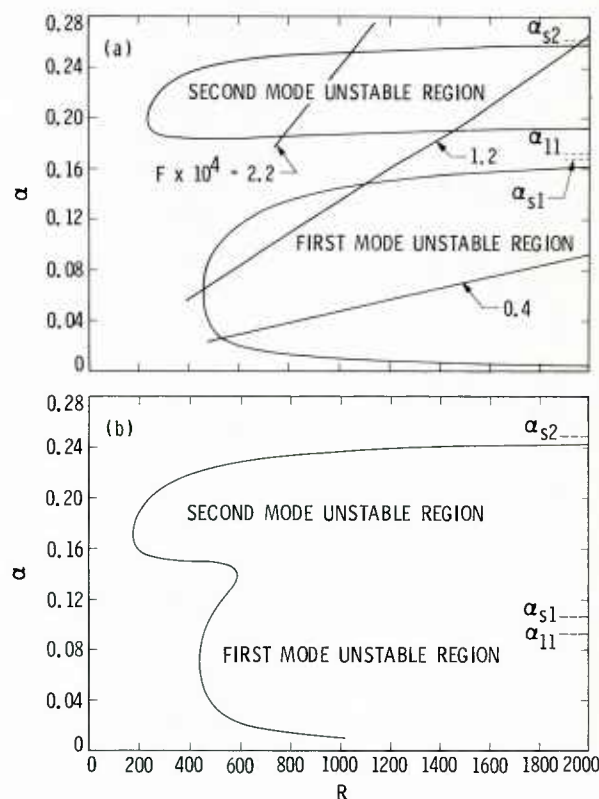

Fig. 10.5 Neutral-stability curves of wavenumber for 2D first and second-mode waves at (a) M_1 = 4.5 and (b) M_1 = 4.8. Insulated wall, wind-tunnel temperatures.
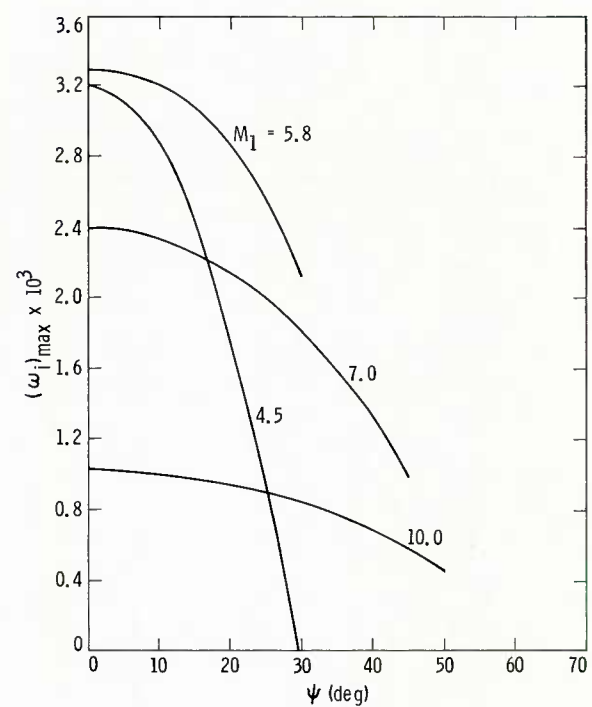

Fig. 10.7 Effect of wave angle on second-mode temporal amplification rates at R = 1500 and M_1 = 4.5, 5.8, 7.0 and 10.0 Insulated wall, wind-tunnel temperatures.
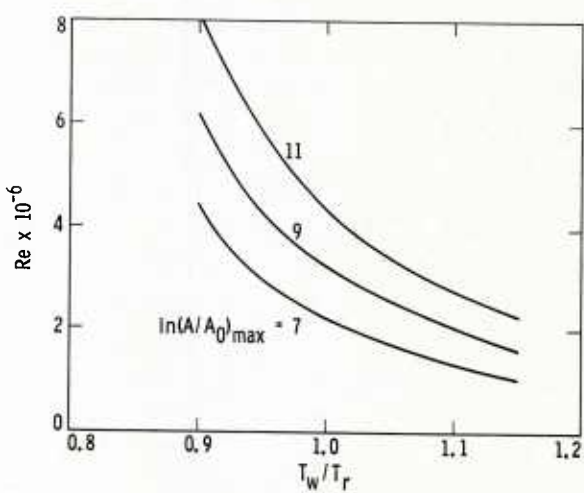
Fig. 10.8 Effect of wall cooling and heating on Reynolds number for constant $\ln(A/A_0)_{max}$ at M_1 = 0.05.
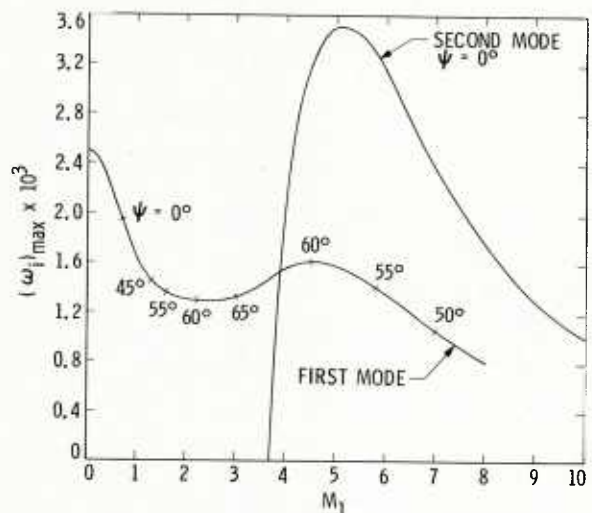
Fig. 10.10 Effect of Mach number on the maximum temporal amplification rate of first and second-mode waves at R = 1500. Insulated wall, wind-tunnel temperatures.
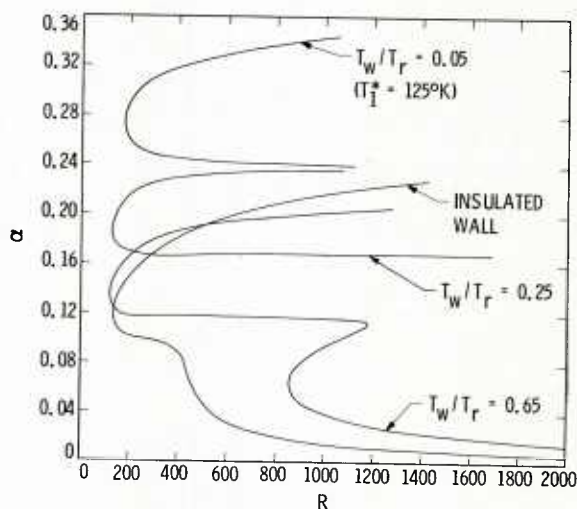
Fig. 10.9 Effect of wall cooling on 2D neutral-stability curves at M_1 = 5.8, T_1^* = 50°K.
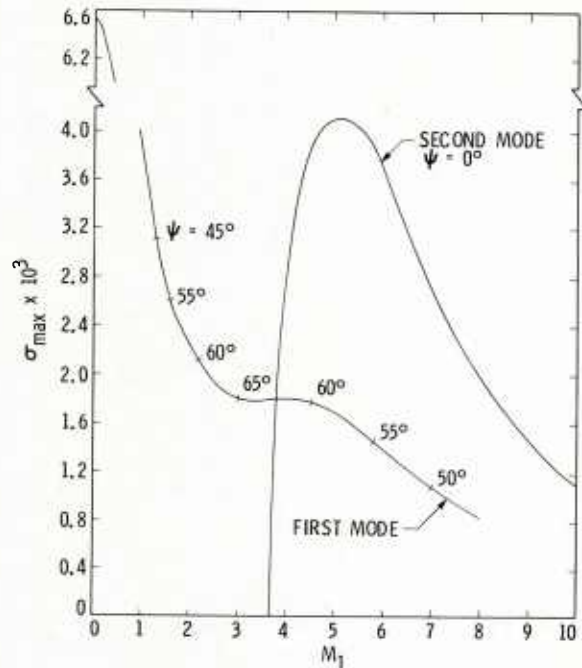
Fig. 10.11 Effect of Mach number on the maximum spatial amplification rate of first and second-mode waves at R = 1500. Insulated wall, wind-tunnel temperatures.
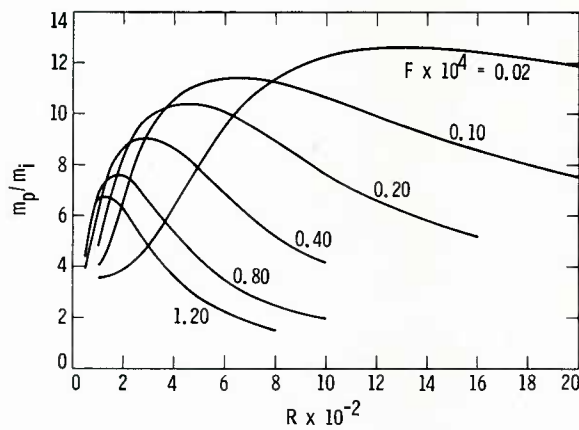
Fig. 11.1 Peak mass-flow fluctuation as a function of Reynolds number for six frequencies. Viscous forcing theory; $M_1 = 4.5$, $\psi = 0°$, $c = 0.65$, insulated wall.
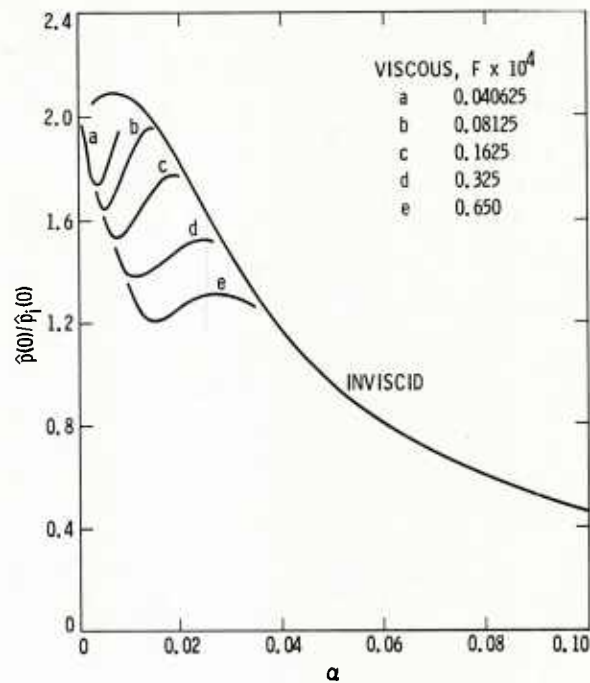
Fig. 11.3 Ratio of wall pressure fluctuation to pressure fluctuation of incoming wave; $M_1 = 4.5$, $\psi = 0°$, $c = 0.65$, insulated wall, $T_1^* = 311°K$.
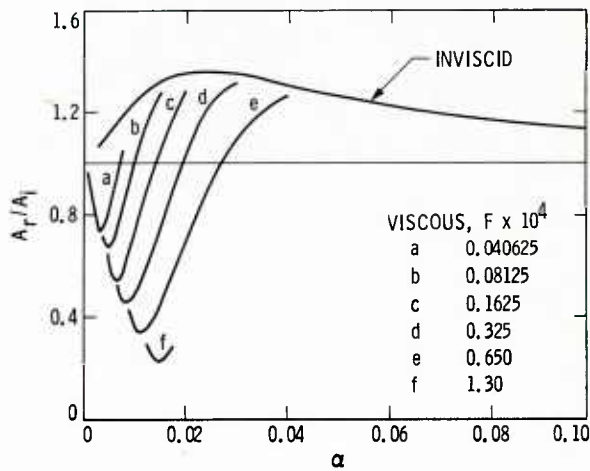
Fig. 11.2 Ratio of amplitude of reflected wave to amplitude of incoming wave as function of wavenumber from viscous and inviscid theories; $M_1 = 4.5$, $\psi = 0°$, $c = 0.65$, insulated wall, $T_1^* = 311°K$.
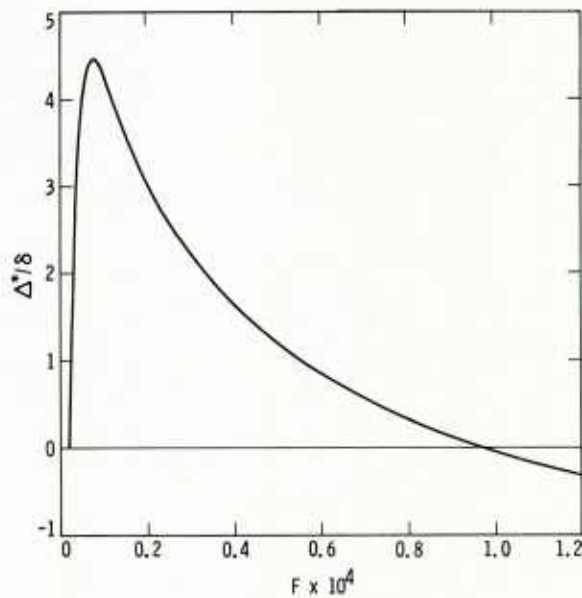
Fig. 11.4 Offset distance of reflected wave as function of frequency at $R = 600$; $M_1 = 4.5$, $\psi = 0°$, $c = 0.65$, insulated wall, $T_1^* = 311°K$.
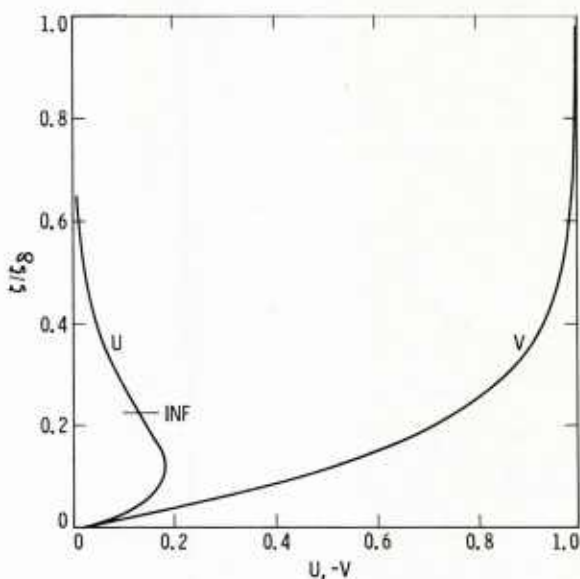
Fig. 12.1 Rotating-disk boundary-layer velocity profiles.
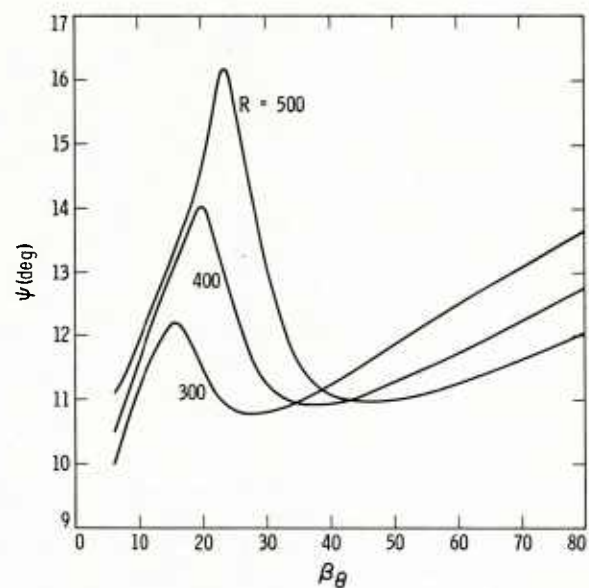
Fig. 12.3 Wave angle vs. azimuthal wavenumber at three Reynolds numbers for zero-frequency waves; sixth-order system.
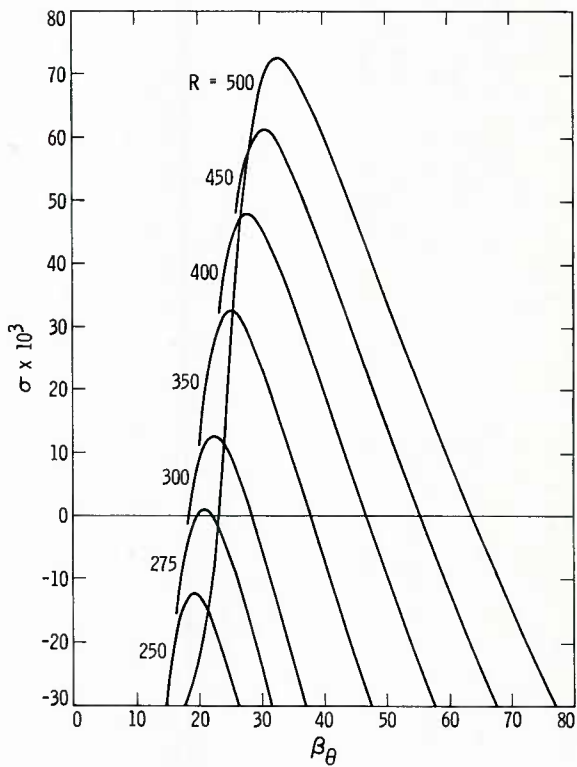
Fig. 12.2 Spatial amplification rate vs. azimuthal wavenumber at seven Reynolds numbers for zero-frequency waves; sixth-order system.
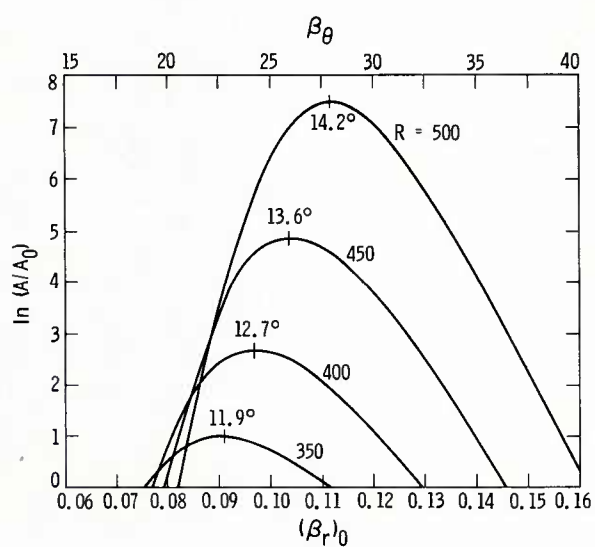
Fig. 12.4 $\text{Ln}(A/A)_0$ vs. azimuthal wavenumber at four Reynolds numbers for zero-frequency waves and wave angle at peak amplitude ratio; sixth-order system.
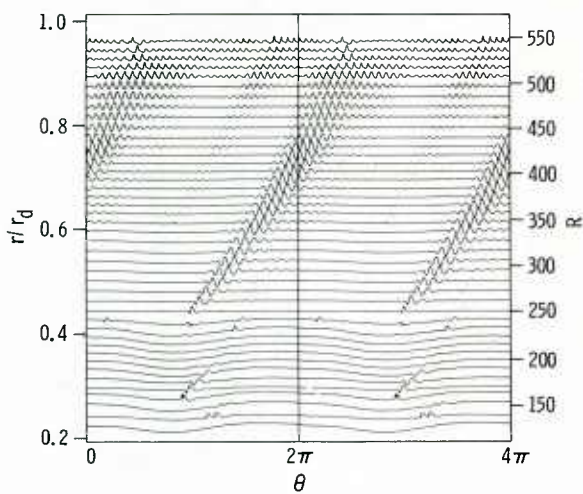
Fig. 12.5 Ensemble-averaged normalized velocity fluctuations of zero-frequency waves at $\zeta = 1.87$ on rotating disk of radius $r_d = 22.9$ cm. Roughness element at $R_s = 249$, $\theta_s = 173°$. [After Fig. 18 of Wilkinson and Malik (1983)]
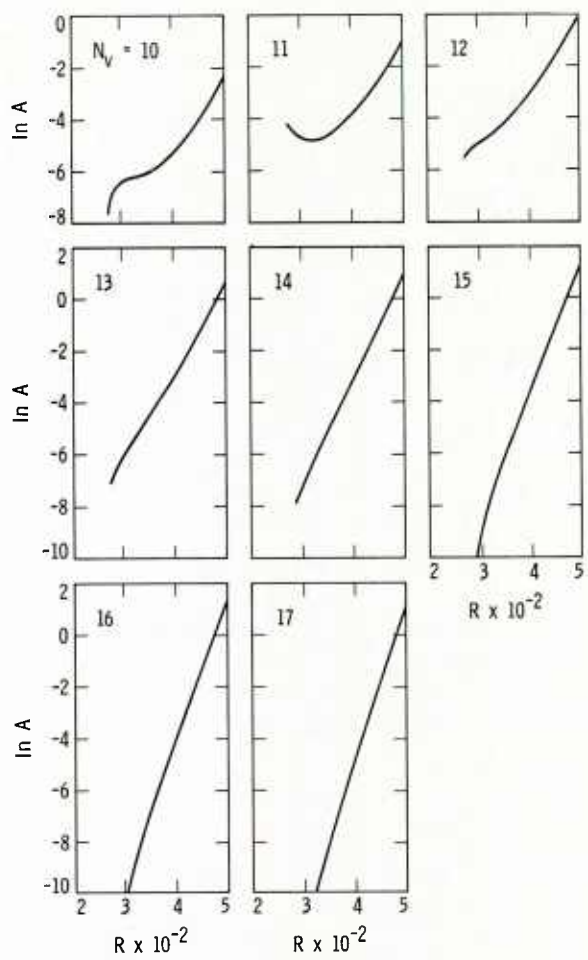
Fig. 12.7 Calculated amplitudes along constant-phase lines of wave pattern behind zero-frequency point source at $R_s = 250$ in rotating-disk boundary layer.
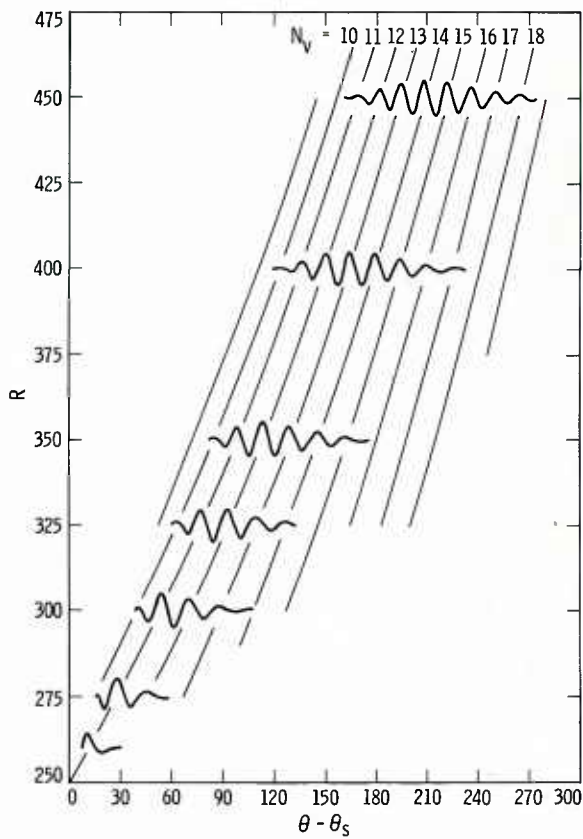
Fig. 12.6 Normalized wave forms and constant-phase lines of calculated wave pattern produced by zero-frequency point source at $R_s = 250$ in rotating-disk boundary layer.
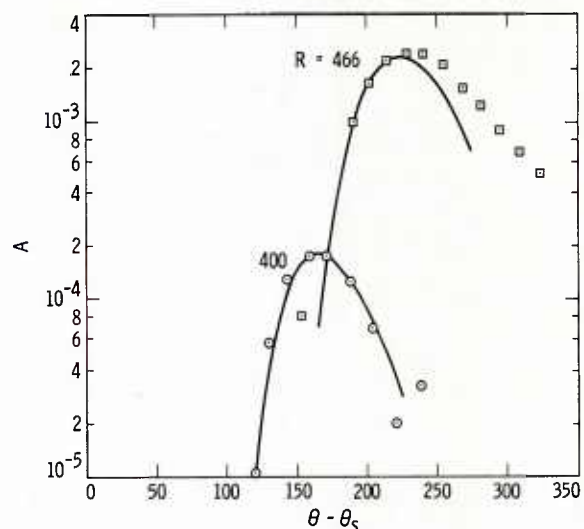
Fig. 12.8 Comparison of calculated envelope amplitudes at R = 400 and 466 in wave pattern produced by zero-frequency point source at $R_s = 250$ in rotating-disk boundary layer, and comparison with measurements of Wilkinson and Malik (1983) (○, R=397; □, R=466).
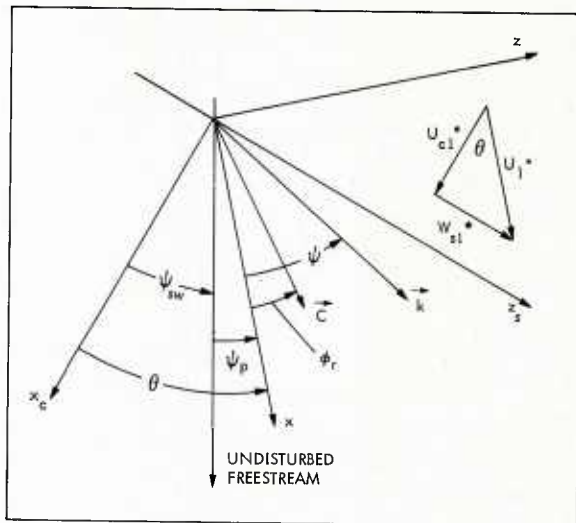
Fig. 13.1 Coordinate systems for Falkner-Skan-Cooke boundary layers.
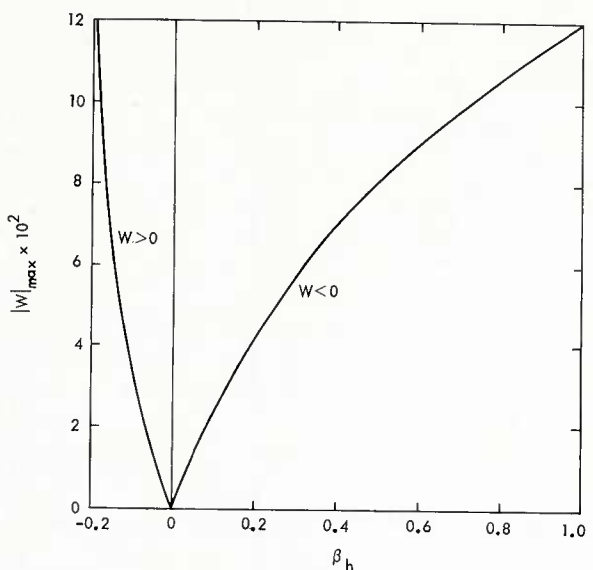
Fig. 13.3 Effect of pressure gradient on maximum crossflow velocity; Falkner-Skan Cooke boundary layers.
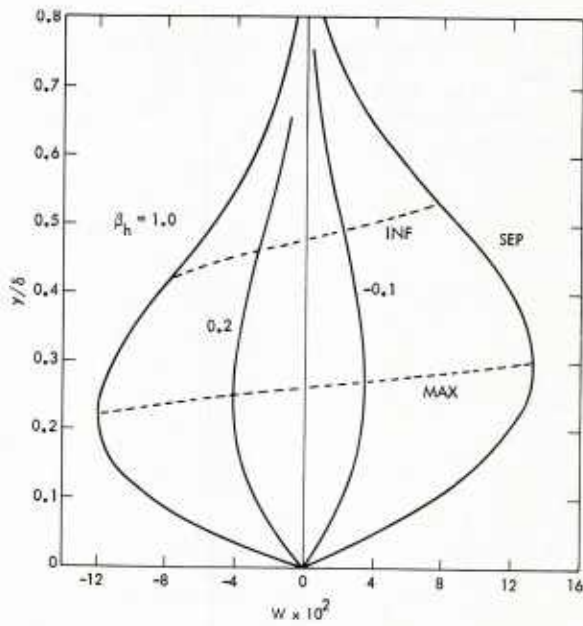
Fig. 13.2 Falkner-Skan-Cooke crossflow velocity profiles for β_h = 1.0, 0.2, -0.1 and SEP (separation, -0.1988377); INF, location of inflection point; MAX, location of maximum crossflow velocity.
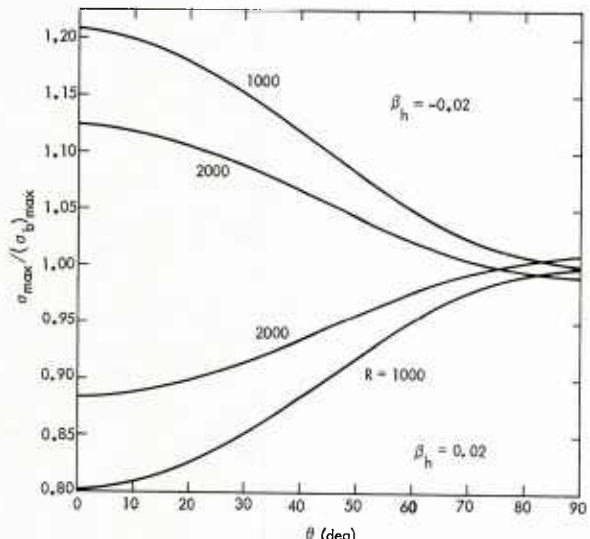
Fig. 13.4 Effect of flow angle on maximum amplification rate with respect to frequency of ψ = 0° waves at R = 1000 and 2000 in Falkner-Skan-Cooke boundary layers with β_h = ±0.02.
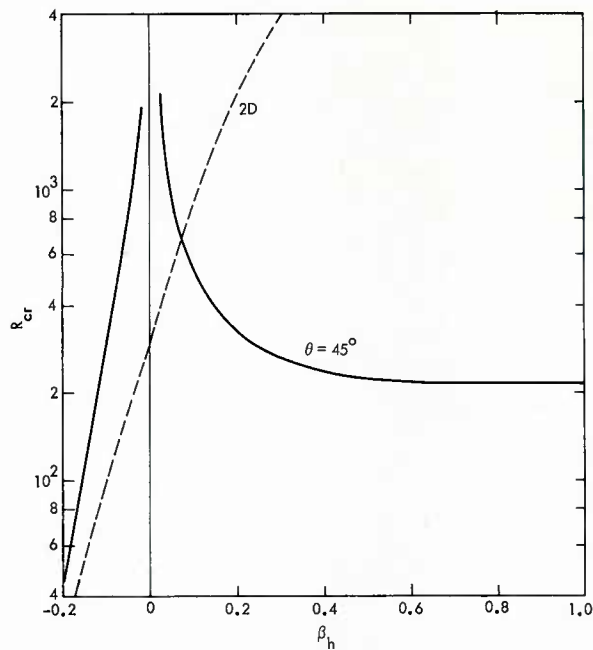
Fig. 13.5 Effect of pressure gradient on minimum
critical Reynolds number: ———, zero-frequency
crossflow instability waves in Falkner-Skan-
Cooke boundary layers with $\theta = 45°$; ———, 2D
Falkner-Skan boundary layers [from Wazzan et al.
(1968a)].
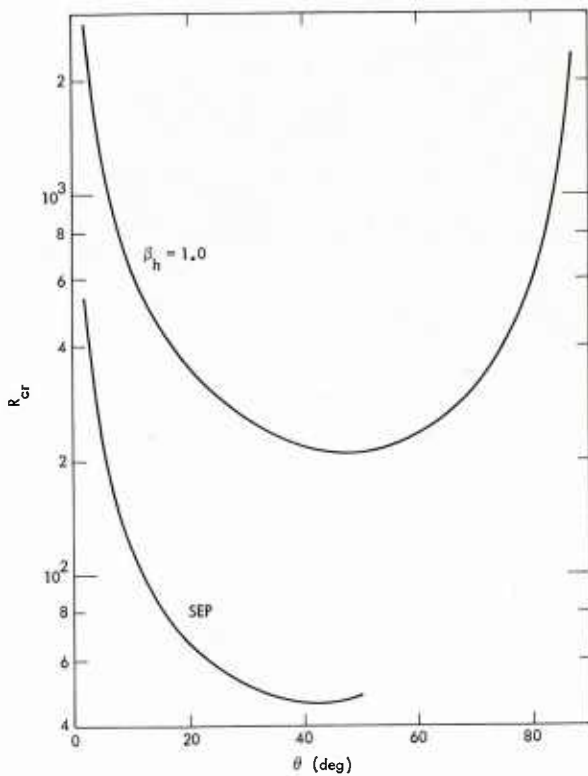
Fig. 13.6 Effect of flow angle on minimum
critical Reynolds number of zero-frequency
crossflow waves for β_h = 1.0 and -0.1988377
Falkner-Skan-Cooke boundary layers.
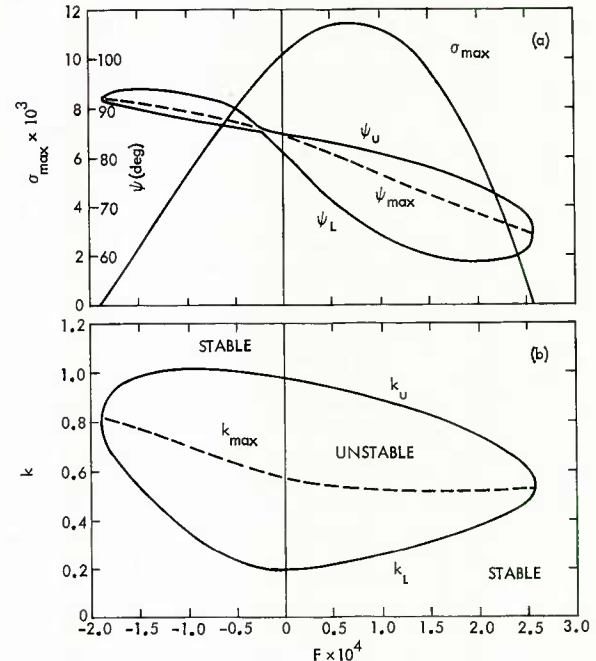
Fig. 13.7 Instability characteristics of β_h =
1.0, θ = 45° Falkner-Skan-Cooke boundary layers
at R = 400: (a) maximum amplification rate with
respect to wavenumber, and unstable ψ-F region;
(b) unstable k-F region.
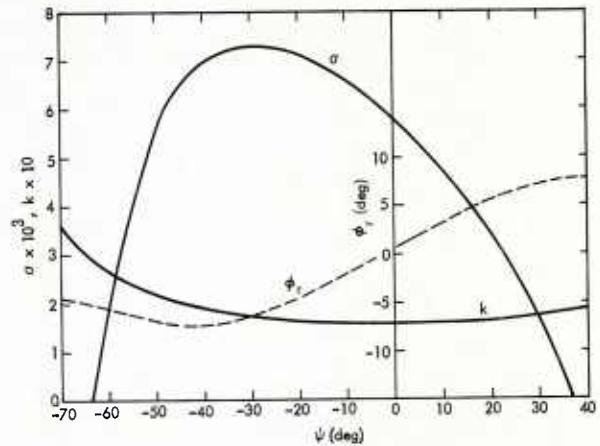
Fig. 13.8 Effect of wave angle on amplification
rate, wavenumber, and group-velocity angle for F
= 2.2 x 10⁻⁴ at R = 276; β_h = -0.10, θ = 45°
Falkner-Skan-Cooke boundary layer.
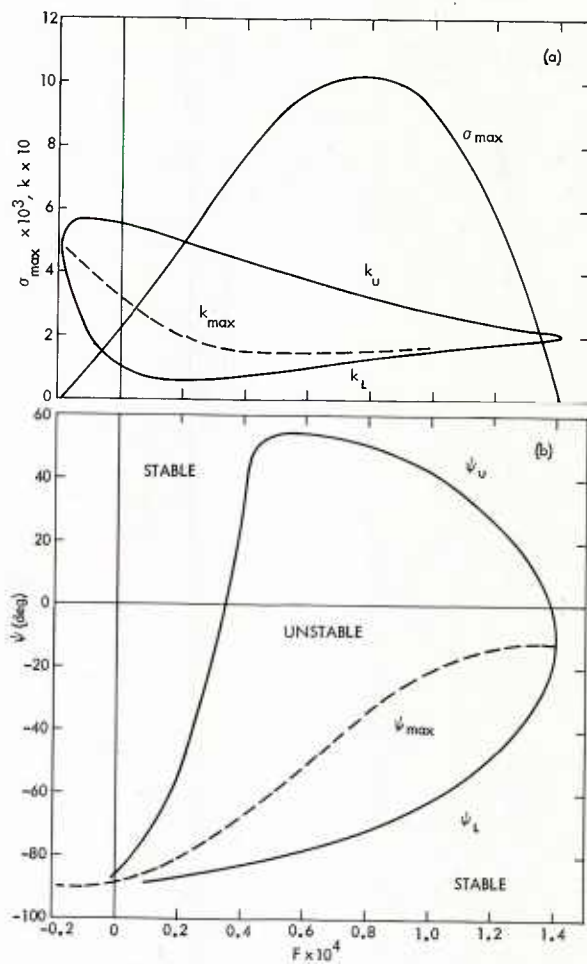
Fig. 13.9 Instability characteristics of $\beta_h =$ -0.10, $\theta = 45°$ Falkner-Skan-Cooke boundary layer at R = 555: (a) maximum amplification rate with respect to wavenumber, and unstable k-F region; (b) unstable ψ-F region.

Fig. 14.2 Amplification rate, wave angle, and group-velocity angle as functions of wavenumber at N = 4 (R=301) for F = 0: $-\cdot-$, incompressible theory; $-$, sixth-order compressible theory; 35° swept wing.
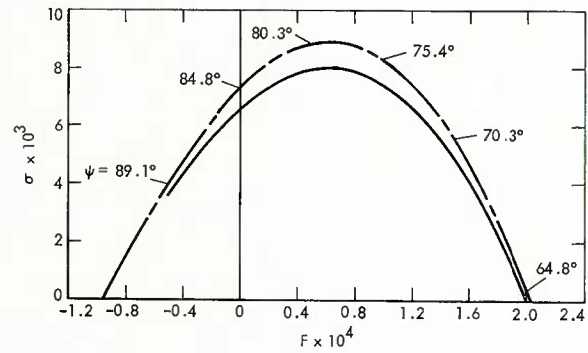
Fig. 14.3 Unstable frequency range at N = 4 (R=301) for k = 0.520: $-\cdot-$, incompressible theory, $-$, sixth-order compressible theory; 35° swept wing.

Fig. 14.1 Coordinate systems used for infinite-span swept wing.
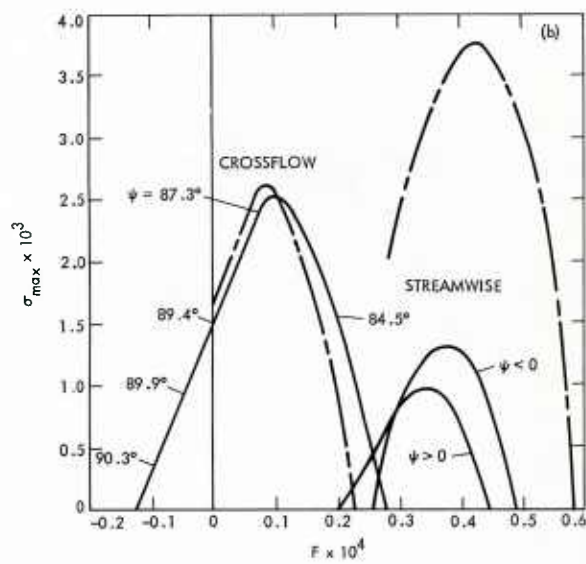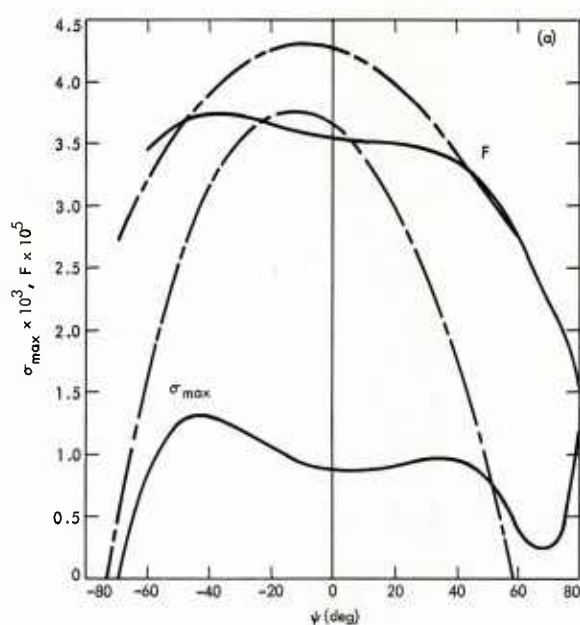
Fig. 14.4 Crossflow and streamwise instability at N = 15 (R=1323); (a) maximum amplification rate (with respect to frequency) and frequency as functions of wave angle; (b) maximum amplification rate (with respect to wavenumber) as function of frequency: – ·–, incompressible theory; ——, sixth-order compressible theory; 35° swept wing.
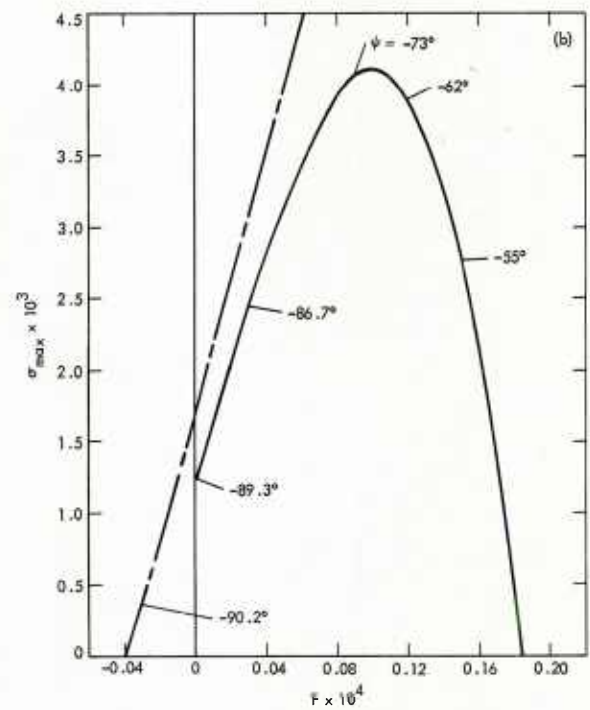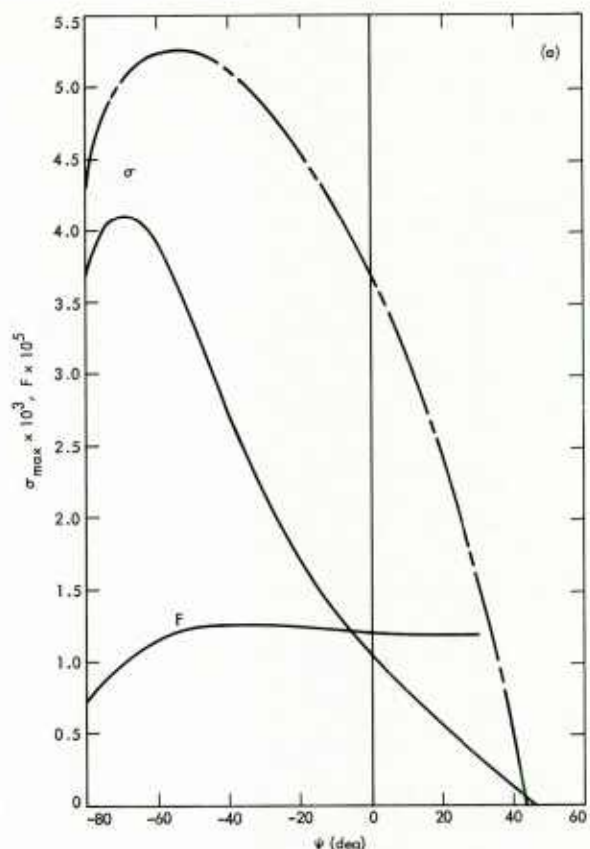
Fig. 14.5 Crossflow and streamwise instability at N = 23 (R=2661). (a) Maximum amplification rate (with respect to frequency) and frequency as function of wavenumber angle; (b) maximum amplification rate (with respect to wavenumber) as function of frequency: – ·–, incompressible theory; ——, sixth-order compressible theory; 35° swept wing.
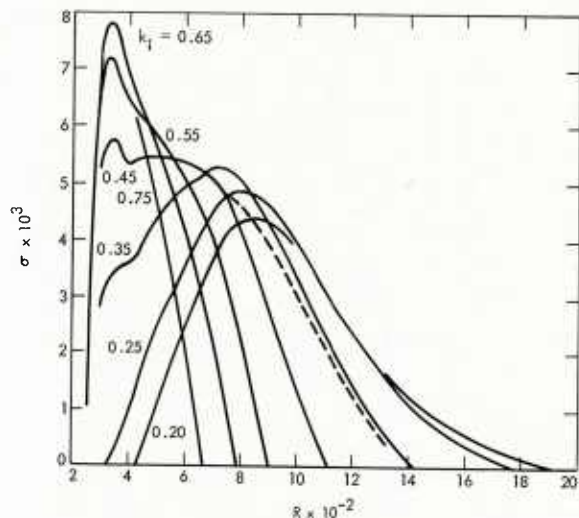
Fig. 14.6 Amplification rates of seven zero-frequency wave components in forward instability region of 35° swept wing with irrotationality condition applied to wavenumber vector: ———, incompressible theory; ———, sixth-order compressible theory for k_i = 0.35.
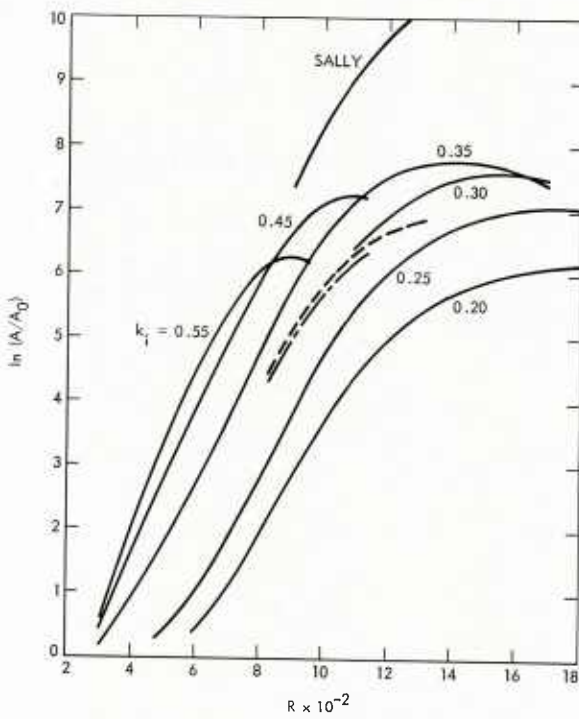
Fig. 14.7 Ln(A/A$_0$) of six zero-frequency wave components in forward instability region of 35° swept wing with irrotationality condition applied to wavenumber vector and comparison with SALLY code; ———, incompressible theory; ———, sixth-order compressible theory for k_i = 0.35; —·—, eighth-order compressible theory for k_i = 0.35.

ENVIRONMENT AND RECEPTIVITY

by

Professor E.Reshotko
Dept. of Mechanics & Aerospace Engineering
Case Western Reserve University
Cleveland, Ohio 44106, USA

SUMMARY

In an environment where initial disturbance levels are small, the transition Reynolds number of a boundary layer is very much dependent upon the nature and spectrum of the disturbance environment, the signatures in the boundary layer of these disturbances and their excitation of the normal modes ("receptivity"), and finally the linear and nonlinear amplification of the growing modes. This lecture reviews the progress in understanding receptivity to free stream vorticity and acoustic disturbances. It also outlines the technique of the initial value problem, which promises to be a significant additional tool for providing guidance toward the resolution of receptivity issues.

INTRODUCTION

Boundary Layer transition can be viewed as the consequence of the non-linear response of that very complicated oscillator, the laminar boundary layer to forcing disturbances. These disturbances are part of the environment in which the boundary layer develops and could include free-stream vorticity and entropy disturbances, radiated sound, surface vibrations, etc. or any combination of these.

As in any forced vibrations problem we must first determine and understand the free oscillations or normal modes of the oscillator. Then it would seem desirable to model transition in a way that simulates experiment - namely, to take a given initial disturbance spectrum (forcing function) and follow it forward in time. The response would depend on the receptivity (Morkovin 1969) of the boundary layer to the particular disturbance assumed, and the subsequent disturbance amplification.

By receptivity is meant the means by which a particular forced disturbance enters the boundary layer and the nature of its signature in the disturbance flow. If the initial disturbances are sufficiently large, they can grow by forcing mechanisms to non-linear levels and lead directly to turbulent flow. If they are small, they will tend to excite free disturbances in the boundary layer. These free disturbances are the aforementioned normal modes of the boundary layer and are often referred to as Tollmien-Schlichting (T-S) waves. The nature of each of these normal modes is determined from the solution of the eigenvalue problem arising from consideration of the linearized disturbance equations subject to appropriate boundary conditions. Boundary layer stability analyses have been generally restricted to studies of the normal modes. It is the means by which these normal modes are excited that will be developed in this lecture.

The questions that we address under the heading of receptivity have been asked for a very long time. It is however only within the last fifteen years or so that the serious study of this topic was undertaken. The present author's interest in this topic was stimulated in the middle 1960's by his dissatisfaction with use of the "unit Reynolds number" as one of the common correlating factors for transition. From simple dimensional analysis, it was shown (Reshotko 1969) that transition Reynolds numbers can be dependent on dimensionless forms of the frequency or wavelength and orientation spectra of the disturbance environment, and that this could in fact account for the so-called "unit Reynolds number effect." Mack (1975) has since demonstrated that by incorporating initial disturbance spectral information into a transition prediction method, the experimental variation of transition Reynolds number with unit Reynolds number is correctly reproduced. It follows directly that receptivity is an essential and important determinant in the transition process and worthy of special study.

The receptivity phenomenon differs from stability both physically and mathematically. Physically, it is the signature in the boundary layer of some externally imposed disturbance. Mathematically, the problem is no longer one of homogeneous equations with homogeneous boundary conditions, but one where either the

equations and/or the boundary conditions are non-homogeneous. Hence, in contrast to the normal modes stability calculations, the receptivity phenomenon is not an eigenvalue problem. The boundary layer is driven by the external forced oscillations, and its response is a `neutral' solution of the linearized disturbance equations having the same frequency as the particular forcing disturbance being considered. Each class of forcing disturbance has its own particular inhomogeneity.

Receptivity can of course be studied both experimentally and analytically. The combination of the two is clearly most desirable. The experiments are directed at understanding the receptivity to a particular class of environmental disturbance and much of the available analyses are attempts at direct modeling of the experiments. In the last several years, however, there has been a resurgence of interest in the technique of the initial-value problem as an additional means of studying receptivity. The initial-value formulation has the advantage of pointing out very clearly whether and how a given class of disturbance or else an alteration in boundary conditions excites the normal modes of the boundary layer. It is however not very useful for numerical computation. Once a relationship is defined through initial-value considerations, the character of the expected result is known, and numerical results are best obtained through direct modeling and computation.

The major portion of this lecture will be devoted to a somewhat detailed description of three receptivity phenomena for which there is some information. The lecture will conclude with a presentation of the initial-value problem technique and a discussion of some of the cases solved so far using this technique.

EXAMPLE RECEPTIVITY STUDIES

Receptivity to Free-Stream Turbulence

The signature in the flat plate boundary layer of the disturbances due to free-stream turbulence was measured by Klebanoff (1964). Some additional results of his from 1971 are shown in Fig. 1. For the low free-stream turbulence levels shown, the u' levels in the boundary layer peak at a Blasius η of about 2.3 and attain maximum levels of the order of 1% of free-stream velocity. Klebanoff noted that the signal through a low-pass filter at 12 Hz was almost identical in amplitude to the signal over all frequencies and hence concluded that most of the signal is at frequencies below 12 Hz. Similar results have been obtained by Leventhal and Reshotko (1981) and by Kendall (1982). Klebanoff's suggested modeling of this result is as the response to a low-frequency unsteadiness in free-stream velocity. His result is that the variation in u' should be as the product $\eta f''$ of the Blasius functions. This is an excellent simulation of the experimental results except that it approaches zero rather than the free-stream level at the edge of the boundary layer, and therefore does not relate the peak amplitude to the free-stream turbulence level.

To acquire further insight into the role of free-stream turbulence on transition, Rogler and Reshotko (1975) analytically and numerically studied the interaction between an incompressible boundary layer and a low intensity array of single-wave-number vortices convected at the mean free-stream velocity (Fig.2). The flow field is taken to be the sum of the steady laminar field (Blasius) plus a flow field ascribable to the effects of the vortex array. This latter flow field is further subdivided into the portion that exists in the absence of the plate (the vortex array itself) plus a flow field representing the alteration to that array due to the shearing mean flow and no-slip and impermeability conditions at the plate surface. This last portion of the flow field is described by a non-homogeneous Orr-Sommerfeld equation with dimensionless phase-speed unity and real wave number. The forcing function depends on the mean flow and on the free-stream disturbance array. It was found that amplitudes in the boundary layer grow in the downstream direction, with the maximum amplitude arising near the leading edge for small vortex diameters and further downstream for larger diameters (Fig. 3). Rogler and Reshotko further speculate that if initial turbulence levels are sufficiently large, the disturbances can grow by forcing mechanisms to nonlinear levels and lead to turbulent flows without resort to T-S amplification. This is an example of what Morkovin calls a "high intensity bypass."

A possible case in point is Poiseuille pipe flow. Wygnanski and Champagne (1973) observed that when their smooth pipe was carefully aligned (with a very good entrance section) turbulent slugs were observed at Re > 50,000, which they ascribed to the consequences of entrance-flow instability. Transition could be initiated at lower Re (2000 < Re < 2700) when a large disturbance was introduced into the inlet. Furthermore, their observed disturbance amplitude near the wall at Re = 2360 was greatly damped, consistent with the aforementioned calculations of Rogler and Reshotko (1975) for a flat plate. Hence the speculation that observed pipe flow transitions at Re ~ 2500 are due to large initial disturbances that grow to nonlinear levels by forcing mechanisms, since Poiseuille pipe flow is stable to T-S waves and the entrance flow does not become unstable until much larger values of Re are attained.

Another experiment related·to the Rogler-Reshotko work is that reported by Kachanov, Koslov and Levchenko (1978). These authors measured the disturbances in a flat-plate boundary layer due to a vibrating ribbon placed just ahead of the leading edge of the plate and at a height that is outside the boundary layer over most of the portion of the plate. The results are shown in Fig.4. The lower neutral point is at approximately 300 mm. from the leading edge.To be noted is the small response inside the boundary layer relative to the amplitudes outside the boundary layer, at least until the wake of the vibrating ribbon is ingested into the boundary layer. This compares well with the parallel-flow result from Rogler and Reshotko (1975) shown in Fig. 5. The implication is that free-stream disturbances initially outside the boundary layer have little influence on disturbance levels in the boundary-layer, and thus those disturbances that enter the boundary layer do so near the leading edge.

The above work has not yet established how the free-stream disturbances excite growing T-S waves. This latter question was addressed by Rogler (1977) who constructed a rudimentary initial-value analysis for this problem. His choice of initial condition is not consonant with the response to the forcing function, hence the eigenfunctions (normal modes) must be added in in some measure to satisfy the chosen initial condition. This analysis needs to be redone in a more formal way in order to validate Rogler's result.

In the absence of a complete receptivity model for free-stream turbulence, Mack (1977) developed an ad-hoc transfer function receptivity model in order to incorporate free-stream spectral information into his transition prediction procedure based on an amplitude criterion. This enabled him to come up with a rather successful e^n transition criterion where the exponent n is a function of the free-stream turbulence level.

Kendall (1984) has recently reported preliminary results of his experiments on receptivity of a flat-plate boundary layer to free stream turbulence. He observed that free stream turbulence produced large-amplitude, low frequency fluctuations in the boundary layer whose lateral width was only a few boundary layer thicknesses but whose length is estimated to be very much longer. Within the T-S band of frequencies, upstream of $Re_{\delta*} = 1000$, there was little amplitude in the region of the boundary layer where T-S eigenfunctions are prominent. The large amplitude, low-frequency mode responded almost linearly to the free stream fluctuation amplitude while the T-S mode seemed to respond in a faster than linear manner once detected. It is clear that more measurements are needed to clarify the issues.

Receptivity to Acoustic Disturbances

The sensitivity of transition Reynolds number to acoustic disturbances was studied by Spangler and Wells (1968) in a wind tunnel where they could closely control the characteristics of the settling chamber. Their results are shown in Fig. 6. For reference, the results of Schubauer and Skramstad (1948) are also shown on this figure. To be noted is that with decrease in turbulence level, Schubauer and Skramstad's transition Reynolds numbers increase until they reach their limiting value of about 2.8×10^6. By making their own settling chamber essentially anechoic, Spangler and Wells attained a transition Reynolds number of about 5.2×10^6. Acoustical excitation could diminish the transition Reynolds number at particular frequencies as could grids. This figure suggests also that the NBS tunnel was acoustically limited at turbulence levels below about 0.1%, a notion already put forward by Schubauer and Skramstad. The Spangler and Wells (1968) experiments did not at all examine receptivity issues so that the acoustic signatures in the boundary layer and the means of exciting growing T-S waves were not studied.

This was however done in an experiment by Shapiro (1977) on a flat plate boundary layer in a low turbulence wind tunnel, reported also by Leehey and Shapiro (1979). Fig. 7a shows the amplification and phase of a disturbance as measured in the boundary layer excited by an upstream loudspeaker mounted on the tunnel centerline. Upstream of the lower branch neutral point ($Re_{\delta*} = 1000$) a standing wave pattern appears with wavelength equal to that of the T-S wave at the excitation frequency. Downstream of the lower branch neutral point, the T-S growth is observed and the phase is that expected for the calculated phase speed of the T-S wave. Fig. 7b shows corresponding calculations made by Thomas and Lekoudis (1978) under the premise that the standing acoustic wave and T-S wave are independent in the region of the displayed measurements and so can be superimposed. The similarity between the calculated and experimental results supports the premise and the related argument by Leehey and Shapiro (1979) that by whatever mechanism, the acoustic wave excites the T-S wave in the immediate vicinity of the leading edge.

This matter was pursued further by Murdock (1979) who modeled the acoustic field by unsteady boundary layer solutions and then used these solutions as initial conditions for a Navier-Stokes computation of the boundary layer response. As long as the initial condition was applied very near the leading edge, a T-S wave resulted. However the amplitude of the T-S wave at the lower branch neutral point was very sensitive to the point at which the initial condition was applied. Hence the

receptivity condition was not yet clearly identified.

A more satisfactory resolution has come in the recent paper by Goldstein (1983) in which the method of matched asymptotic expansions was used. Goldstein's result is best understood with the aid of Fig. 8 taken from his paper. Near the leading edge, the motion is governed by the unsteady boundary layer equations. Farther downstream it is governed by the Orr-Sommerfeld equation with slowly varying coefficients. Goldstein shows that in between ($\omega x/U_\infty = \mathcal{O}(1)$) there is an overlap domain where the appropriate asymptotic forms of the Lam and Rott (1960) unsteady boundary layer solutions match, in a matched asymptotic sense, the T-S wave solutions to the Orr-Sommerfeld equation. The key element in the matching is that the asymptotic eigensolutions of Lam and Rott (1960) have wavelengths that decrease with downstream distance as $x^{-1/2}$. The matching is effected when the wavelength becomes that of the T-S wave at the excitation frequency. At the base of the boundary layer downstream of the overlap region is a Stokes shear layer of progressively decreasing amplitude. The T-S wave continues to decay until the lower branch neutral point is reached at which point it begins to grow.

Morkovin (1984) has also indicated that recent experiments at the Illinois Institute of Technology on the receptivity of laminar boundary layers to acoustic excitation have verified the essential features of the Goldstein (1983) model. Extensive hot-wire mapping of the streamwise velocity amplitude and phase resulting from a pulsating source showed streamwise variations of the amplitude of the acoustic pressure gradient. The T-S waves evolve from those length scales in the streamwise amplitude variation that are in the T-S band. H. Fasel has done confirming Navier-Stokes calculations at Morkovin's request.

Thus the conjectures of the prior investigators are all verified. The receptivity occurs near the leading edge through the mechanism whose details are supplied by Goldstein (1983). Downstream of the overlap region, the sound wave and T-S wave proceed independently with the latter growing in the T-S amplification region.

Response of Boundary Layer to a Moving Sound Wave

Measurements by Kendall (1970) on a flat plate at Mach number 4.5 in the JPL 20" supersonic tunnel with turbulent boundary layers on the tunnel walls show all frequencies to grow monotonically from the leading edge - well ahead of the minimum critical point - and the source of these disturbances has been identified as the sound field radiated from the tunnel wall boundary layers. Thus the sound field interacts with the boundary layer to provide growing disturbances in a region that is stable according to stability theory. In an attempt to account for these observations, Mack (1970,1971) altered his stability theory to include the response of a boundary layer to incoming sound waves. He in fact identified the radiated sound from the tunnel walls with incoming supersonic disturbances to the test boundary layer and proceeded to calculate the response of the boundary layer to this incoming forced disturbance. Satisfaction of the impermeability condition at the plate requires that there be a reflected sound field from the plate.

Fig. 9 compares mass-flow-fluctuation amplitudes due to an incoming sound field with the result from the most unstable eigensolution at the same frequency and Reynolds number. The ratio m'/m'_I is of the rms mass-flow fluctuation to that of the incoming wave in the free stream at $y = 0$. For the forced disturbance the peak amplitude in the boundary layer is 16 times that of the incoming wave, while in the freestream m'/m'_I of the combined incoming and reflected waves is less than 2. The peak m' of the eigensolution is scaled to the same peak as the forced curve. Note how close the two functions are over most of the boundary layer despite the mismatch in phase speed and direction of propagation. Fig. 10 gives the ratio of m'_p, the peak rms mass-flow fluctuation in the boundary layer, to m'_I. Disturbances of all frequencies are seen to grow rapidly with distance from the leading edge, reaching a peak in the vicinity of the region at which amplification due to instability begins. The magnitude of the peak is inverse to the frequency.

Mack then calculated the growth of disturbances at selected frequencies by using the forcing theory up to the neutral stability point and stability theory beyond the neutral point. The calculated results agree very well with measurements of disturbance amplitudes at three different frequencies as shown in Fig. 11 (Kendall 1975), lending some credence to the hypothesis. However, the mechanism by which the forced wave turns into the free wave is unknown and has been ignored by Mack, although the process most assuredly does take place, as seen in Fig. 12 (Kendall 1971). The measurements show the dimensionless wave speed, initially supersonic relative to the free stream, to accelerate during its streamwise travel, approaching a speed approximately equal to that predicted by stability theory.

The results in Fig. 11 are essentially the signature of disturbance growth triggered by tunnel sound and are representative of additional measurements by Kendall (1975) at Mach numbers 3 and 5.6. At Mach numbers 1.6, 2.2 and 8.5, the observed frequency response in the boundary layer shows definite peaks at the most

unstable frequencies of stability theory and little if any effect of tunnel sound. Hence the most pronounced contamination of the wind tunnel environment by radiated tunnel sound seems to be in the middle-Mach-number range that stretches from 2.5 to 7 or so. In the recent comparison of wind tunnel and flight transition results by Dougherty and Fisher (1980), the departure of the wind tunnel results from the flight trends occurs at a Mach number of about 1.7.

THE INITIAL VALUE PROBLEM

The use of the initial value formulation in hydrodynamic stability studies dates back at least to the work of Case (1960, 1961). Aside from the polemical content of those papers, Case pointed out that the eigenfunction representation of an arbitrary disturbance must include not only the discrete normal modes but also the continuous spectrum of modes even if they are only decaying modes. It has been pointed out by others since (Grosch and Salwen 1978 for example) that the continuous spectrum is essential in considering disturbances that move with the free-stream velocity and are non-decaying in the free stream outside the boundary layer. The work of Rogler and Reshotko (1975) involves direct computation of elements of the continuous spectrum.

An important early solution of an initial value problem is by Gaster (1965) where it was shown that an analytic representation of a vibrating ribbon does in fact lead to excitation of the growing discrete T-S wave. This was also shown using direct numerical computation by Nagel (1967).

Interest in the formal initial value problem has been recently revived. Gustavsson (1979) has formulated the temporal initial value problem, and Tsuge and Rogler (1983) have done the same for the case of spatial growth. The latter work will here be sketched out. The details that follow are adapted from an application of the Tsuge-Rogler formulation to a problem with a wavy wall boundary condition (Aldoss and Reshotko 1982). The wavy wall is here replaced by a straight wall.

The dimensionless two dimensional disturbance vorticity equation for incompressible parallel flow is

$$\left(\frac{\partial}{\partial t} + \bar{U}\frac{\partial}{\partial x}\right)\nabla^2 v - \bar{U}_{yy}\frac{\partial v}{\partial x} = \frac{1}{R}\nabla^4 v \tag{1}$$

where v is the dimensionless normal fluctuating velocity, and $R = \frac{U_\infty \ell}{\nu}$ is the Reynolds number. The boundary conditions at the wall from impermeability and no slip are

$$v(x, 0, t) = 0 \tag{2a}$$

$$\frac{\partial v}{\partial y}(x, 0, t) = 0 \tag{2b}$$

while v is bounded as y approaches infinity.

Applying a Fourier transform in time and a Laplace transform in space is appropriate to spatial growth formulations. The Fourier and Laplace transform pairs are as follows:

Fourier

$$\hat{v}(y; x, \omega) = \int_{-\infty}^{\infty} e^{i\omega t} v(y; x, t)\, dt \tag{3a}$$

$$v(y; x, t) = \frac{1}{2\pi}\int_{-\infty}^{\infty} e^{-i\omega t}\hat{v}(y; x, \omega)\, d\omega \tag{3b}$$

Laplace

$$\Phi \equiv \tilde{v}(y; s, \omega) = \int_{0}^{\infty} e^{-sx}\hat{v}(y; x, \omega)\, dx \tag{4a}$$

$$\hat{v}(y; x, \omega) = \frac{1}{2\pi i}\int_{p-i\infty}^{p+i\infty} e^{sx}\Phi(y; s, \omega)\, ds \tag{4b}$$

The disturbance equation (1) after successive forward transforms (3a) and (4a) becomes

$$\left[(\bar{U}-c)(D^2-\alpha^2) - \bar{U}'' - \frac{1}{i\alpha R}(D^2-\alpha^2)^2\right]\Phi = \frac{F_0}{i\alpha} \qquad (5)$$

where $D = d/dy$, $\alpha = -is$ and $c = \omega/\alpha$. The operator on the left side of (5) is the Orr-Sommerfeld operator while

$$F_0 = (-i\omega + s\bar{U})\left(s\hat{V}_{x=0} + \left.\frac{\partial \hat{V}}{\partial x}\right|_{x=0}\right) + \bar{U}\left.\widehat{\nabla^2 V}\right|_{x=0} - \bar{U}''\hat{V}_{x=0}$$

$$-\frac{1}{R}\left[s^3\hat{V}_{x=0} + s^2\left.\frac{\partial \hat{V}}{\partial x}\right|_{x=0} + s\left.\widehat{\nabla^2 V}\right|_{x=0} + \frac{\partial}{\partial x}\left.\widehat{\nabla^2 V}\right|_{x=0} + s\frac{\partial^2 V_{x=0}}{\partial y^2} - \frac{\partial^2}{\partial y^2}\left.\frac{\partial \hat{V}}{\partial x}\right|_{x=0}\right] \qquad (6)$$

is a function of the initial conditions evaluated at $x = 0^+$. The boundary conditions on Φ are

$$\Phi(0;\alpha,\omega) = \Phi'(0;\alpha,\omega) = 0 \qquad (7a)$$

$$\Phi, \Phi' \text{ are bounded as } y \to \infty \qquad (7b)$$

The solution of (5) is composed of the four complementary solutions of the Orr-Sommerfeld operator plus a particular solution.

The complementary solution can be written

$$\Phi_c = \sum_{j=1}^{4} c_j \phi_j(y) \qquad (8)$$

where the asymptotic forms (large y) of the ϕ_j's are

$$\phi_1 \sim e^{-\alpha y} \qquad \phi_2 \sim e^{-\mu y} \qquad \phi_3 \sim e^{\alpha y} \qquad \phi_4 \sim e^{\mu y} \qquad (9)$$

in which $\mu^2 = \alpha^2 + i\alpha R(1-c)$ with $\mathcal{R\ell}\,\mu > 0$.

The particular solution by variation of parameters is

$$\Phi_p = \sum_{j=1}^{4} \phi_j(y) \int_{y_j} \frac{R F_0 W_j(y)}{W} dy \qquad (10)$$

where W is the Wronskian of the complementary solutions and W_j is the cofactor of the Wronskian determinant with the sign reversed.

The solution can now be written

$$\Phi = \frac{R}{W}\left[\phi_1\left(a_1 + \int_0^y W_1 F_0\, dy\right) + \phi_2\left(a_2 + \int_0^y W_2 F_0\, dy\right) + \phi_3\int_\infty^y W_3 F_0\, dy + \phi_4\int_\infty^y W_4 F_0\, dy\right] \qquad (11)$$

where

$$a_1 = \frac{1}{\Delta}(b_3 E_{23} + b_4 E_{24})$$

$$a_2 = \frac{1}{\Delta}(b_3 E_{31} + b_4 E_{41})$$

$$b_j = \int_\infty^0 W_j F_0\, dy \qquad j = 3,4$$

$$W = 4\mu\alpha R^2 (\alpha - \omega)^2$$

$$\mathcal{E}_{mn} = \phi_{mo}\phi'_{no} - \phi'_{mo}\phi_{no}$$

and

$$\Delta = \mathcal{E}_{12} = \phi_{10}\phi'_{20} - \phi'_{10}\phi_{20}$$

Setting $\Delta = 0$ yields the dispersion relation for the discrete normal modes. The coefficients a_3 and a_4 in (11) must be zero from the boundedness condition.

The solution in physical variables is obtained by successive Laplace and Fourier inversions according to (4b) and (3b) respectively. The Laplace inversion involves summation of the contributions from the poles and branch cuts of (11) in the complex-s plane of the Laplace transformed variable (Fig. 13). The branch cuts indicate the contribution from the continuous spectrum while the poles arise from the discrete normal modes ($\Delta = 0$) and also possibly from the functional form of F_0, related to the initial disturbances at $x = 0^+$ (Tsuge and Rogler 1983).

The vibrating ribbon problem (Gaster 1965) is formulated by replacing boundary condition (2a) by

$$v(x,0,t) = \delta(x)\cos\beta t \tag{12}$$

where β is the ribbon circular frequency, and carrying through the rest of the analysis as indicated. As shown by Gaster (1965), the solution indicates excitation of the discrete T-S waves and ascertains the validity of the vibrating ribbon technique for experimental studies of stability.

The technique of the initial value problem is a most powerful analytic procedure for determining the prospective involvement of normal modes in any particular problem.

CONCLUDING REMARK

Although much progress has been made in identifying and understanding receptivity issues in the last ten years or so, much remains to be done. The detailed character of free stream turbulence as observed in wind tunnels has yet to be measured and the finer points of its signature in the boundary layer leading to excitation of T-S waves clarified. The receptivity to acoustic disturbances is in better shape.

Initial value analyses are an additional tool for providing guidance toward the resolution of receptivity issues.

REFERENCES

Aldoss, T.K. and Reshotko, E. 1982. Contribution of Roughness to Disturbances in a Boundary Layer. Bull. Amer. Phys. Soc. vol. 27 no. 9, Paper CB7, p. 1176 (Also PhD Dissertation of T.K. Aldoss at Case Western Reserve University, August 1982)

Case, K.M. 1960. Stability of Inviscid Plane Couette Flow. Phys. Fluids, vol. 3 no. 2, pp. 143-148

Case, K.M. 1961. Hydrodynamic stability and the inviscid limit. J. Fluid Mech. vol. 10 pt. 3, pp. 420-429

Dougherty, N.S. Jr. and Fisher, D.F. 1980. Boundary Layer Transition on a 10-Degree Cone: Wind Tunnel/Flight Data Correlation. AIAA Paper 80-0154

Gaster, M. 1965. On the generation of spatially growing waves. J. Fluid Mech. vol. 22 pt. 3, pp. 433-441

Goldstein, M.E. 1983. The evolution of Tollmien-Schlichting waves near a leading edge. J. Fluid Mech. vol. 127 pp. 59-81

Grosch, C.E. and Salwen, H. 1978. The continuous spectrum of the Orr-Sommerfeld equation. 1. The spectrum and the eigenfunctions. J. Fluid Mech. vol. 87 pt. 1 pp. 33-54

Gustavsson, L.H. 1979. Initial-value problem for boundary layer flows. Phys. Fluids vol.22 no. 9, pp. 1602-1605

Kachanov, Yu.S., Kozlov, V.V. and Levchenko, V.Ya. 1978. Isv. AN CCCP (Mechs. of Fluids and Gases) no.5, pp. 85-94

Kendall, J.M. 1970. JPL Space Prog. Summ. 37-62 III pp. 43 - 47

Kendall, J.M. 1971. JPL Experimental Investigations. Proc. Boundary Layer Transition Workshop, Aerospace Report TOR-0172 vol.IV pp. 2-1 - 2-16

Kendall, J.M. 1975. Wind Tunnel Experiments Relating to Supersonic and Hypersonic Boundary-Layer Transition. AIAA Jour. vol. 13 no. 3, pp.290-299

Kendall, J.M. 1982. Study of the Effect of Free-Stream Turbulence upon Disturbances in the Pre-Transitional Laminar Boundary Layer. AFWAL-TR-82-3002, Part I

Kendall, J.M. 1984. Experiments on the Generation of Tollmien-Schlichting Waves in a Flat Plate Boundary Layer by Weak Free Stream Turbulence. AIAA Paper 84-0011

Klebanoff, P.S. 1964. Private Communication. (Part presented at 11th Int. Cong of Appl. Mech. Munich, 1964)

Lam, S.H. and Rott, N. 1960. Theory of Linearized Time-Dependent Boundary Layers. AFOSR-TN-60-1100, Grad. School of Aeronautical Engineering, Cornell Univ.

Leehey, P. and Shapiro, P. 1979. Leading Edge Effect in Laminar Boundary Layer Excitation by Sound. Proc. IUTAM Symposium on Laminar-Turbulent Transition, Springer-Verlag 1980, pp. 321-331

Leventhal, L. and Reshotko, E. 1981. Preliminary Experimental Study of Disturbances in a Laminar Boundary-Layer due to Distributed Surface Roughness. AIAA Paper 81-1224

Mack, L.M. 1970. JPL Space Prog. Summ. 37-66, III pp. 13-16

Mack, L.M. 1971. Progress in Boundary Layer Stability Computations. Proc. Boundary Layer Transition Workshop, Aerospace Report TOR-0172 IV pp. 1-1 - 1-35

Mack, L.M. 1975. Linear Stability Theory and the Problem of Supersonic Boundary-Layer Transition. AIAA Jour. vol. 13 no. 3, pp.278-289

Mack, L.M. 1977. Transition Prediction and Linear Stability Theory. AGARD CP-224, pp. 1-1 - 1-22

Morkovin, M.V. 1969. Critical Evaluation of Transition from Laminar to Turbulent Shear Layers with Emphasisi on Hypersonically Traveling Bodies. AFFDL-TR-68-149, Air Force Flight Dynamics Lab., Wright-Patterson AFB, Ohio

Morkovin, M.V. 1984. Private Communication.

Murdock, J.W. 1969. The Generation of a Tollmien-Schlichting Wave by a Sound Wave. Proc. IUTAM Symposium on Laminar-Turbulent Transition, Springer-Verlag, 1980, pp. 332-338

Nagel, A.L. 1967. Stability of the Compressible Boundary Layer by Time Integration of the Navier-Stokes Equations. Boeing Sci. Res. Lab. Rept. DI-82-06555

Reshotko, E. 1969. Stability Theory as a guide to the Evaluation of Transition Data. AIAA Jour. vol. 7 no. 6, pp. 1086-1091

Rogler, H.L. 1977. The Coupling Between Freestream Disturbances, Driver Oscillations, Forced Oscillations and Stability Waves in a Spatial Analysis of a Boundary Layer. AGARD CP-224, pp. 16-1 - 16-14

Rogler, H.L. and Reshotko, E. 1975. Disturbances in a Boundary Layer Introduced by a Low Intensity Array of Vortices. SIAM J. Appl. Math. vol. 28 no. 2, pp.431-462

Schubauer, G.B. and Skramstad, H.K. 1948. Laminar Boundary Layer Oscillations and Transition on a Flat Plate. NACA Report 909

Shapiro, P.J. 1977. The Influence of Sound upon Laminar Boundary Layer Instability. Report No. 83458-83560-1, Acoustics and Vibrations Laboratory, MIT, Cambridge, Mass.

Spangler, J.G. and Wells, C.S. 1968. Effects of Free Stream Turbulence on Boundary Layer Transition. AIAA Jour. vol. 6 no. 3, pp.543-545

Thomas, A.S.W. and Lekoudis, S.G. 1978. Sound and Tollmien-Schlichting Waves in a Blasius Boundary Layer. Phys. Fluids vol. 21 no. 11, pp. 2112-2113

Tsuge, S. and Rogler, H.L. 1983. The two dimensional viscous boundary value problem for fluctuations in boundary layers. AIAA Paper 83-0044

Wygnanski, I.J. and Champagne, F.H. 1973. On transition in a pipe. Part 1. The origin of puffs and slugs and the flow in a turbulent slug. J. Fluid Mech. vol. 59 pt. 2 pp. 281-335
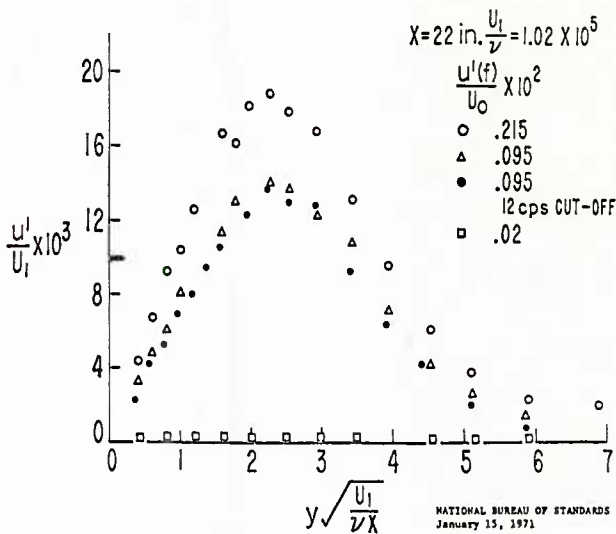
Fig. 1 - Measured rms u' fluctuations in a flat plate laminar boundary layer (Klebanoff)

$$U^{(a)} = -\cos(ky+y) \sin k(x-t)$$
$$V^{(a)} = \sin(ky+y) \cos k(x-t)$$
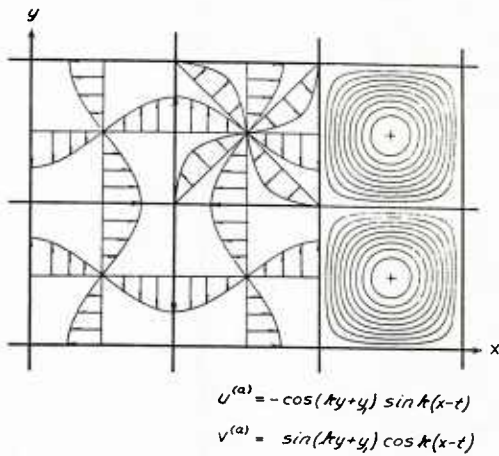
Fig. 2 - Convected array of counterrotating harmonic vortices (Rogler and Reshotko 1975)
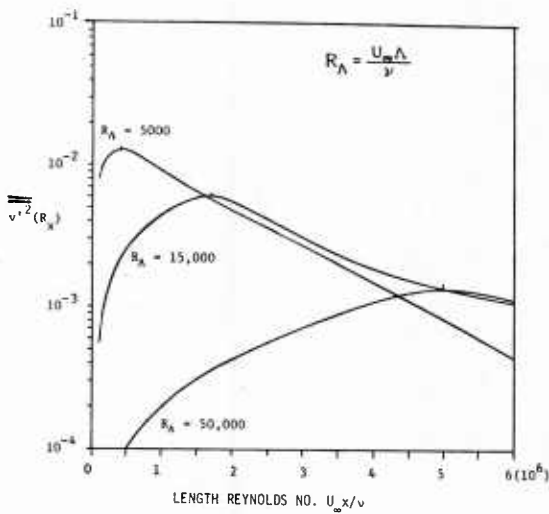
Fig. 3 - Variation of $\overline{v'^2}$ with length Reynolds number along the trajectory $\hat{\eta} = 4$ (Rogler and Reshotko 1975)
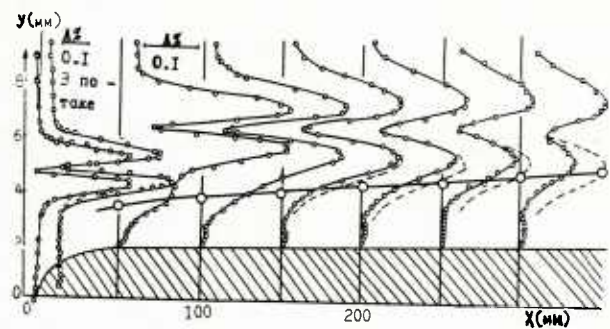
Fig. 4 - Response to a vibrating ribbon in the free-stream (Kachanov, Koslov and Levchenko, 1978)
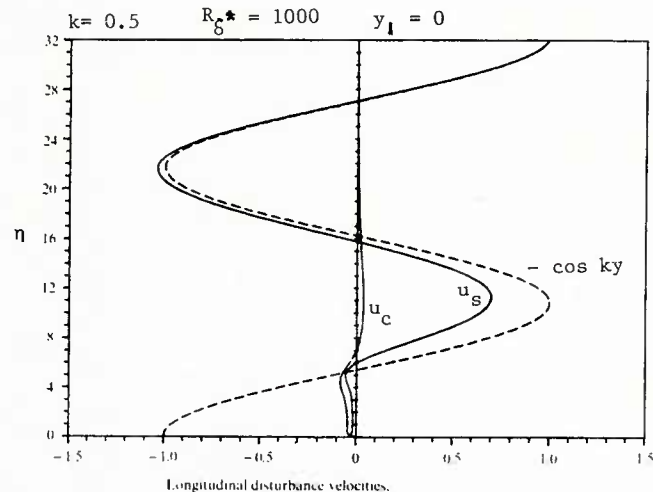
Fig. 5 - Response to array of vortices (Rogler and Reshotko, 1975)
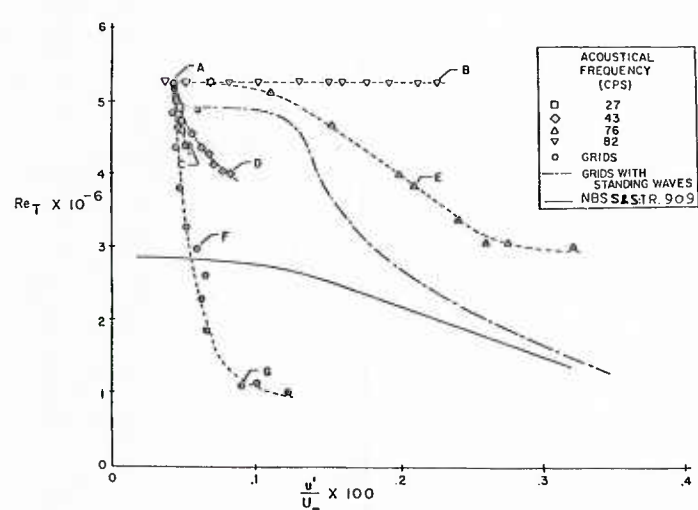
Fig. 6 - Dependence of flat plate transition Reynolds number on disturbance environment (Spangler and Wells 1968)
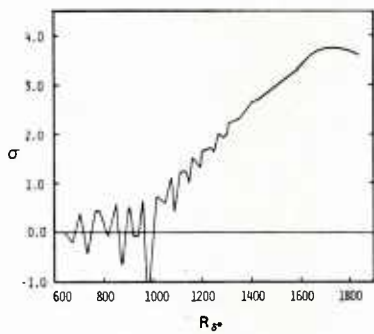
The variation of the measured growth of the wave amplitude with the displacement thickness Reynolds number for a frequency of $\omega\nu/U_0^2 = 56\times10^{-6}$ and $U_0 = 29$ m/sec (from Shapiro[1]).

The variation of the calculated growth of the wave amplitudes with the displacement thickness Reynolds number for a frequency of $\omega\nu/U_0^2 = 56\times10^{-6}$.
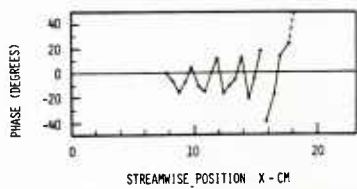
The variation of the measured phase angle of the wave relative to the signal driving the sound wave, with the distance from the leading edge (from Shapiro[1]).
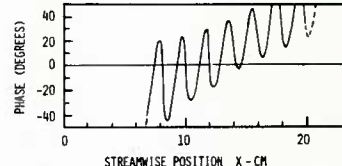
The variation of the calculated phase angle of the wave, relative to the sound wave, with the distance from the leading edge.

a) Experiment (Shapiro 1977)

b) Simulation (Thomas and Lekoudis 1978)

Fig. 7 – Sound and T-S waves in a Blasius boundary layer
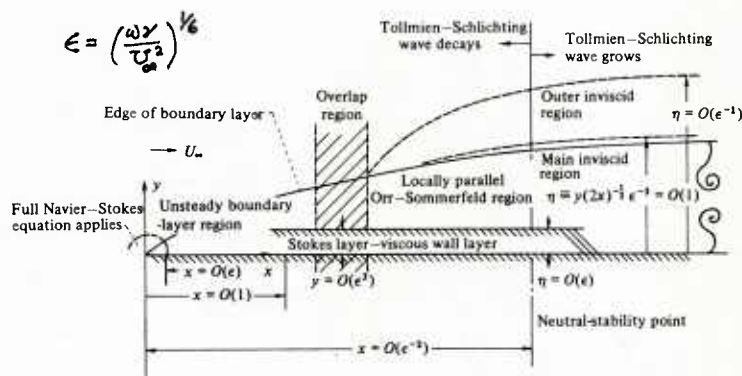
Fig. 8 – Asymptotic structure of unsteady boundary layer (Goldstein 1983)
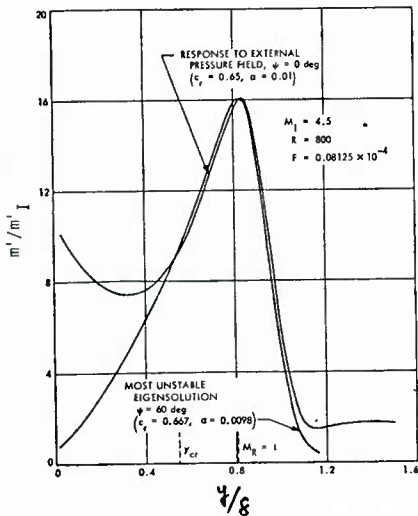
Fig. 9 – Distribution through boundary layer of mass-flow-fluctuation amplitude (Mack 1970)
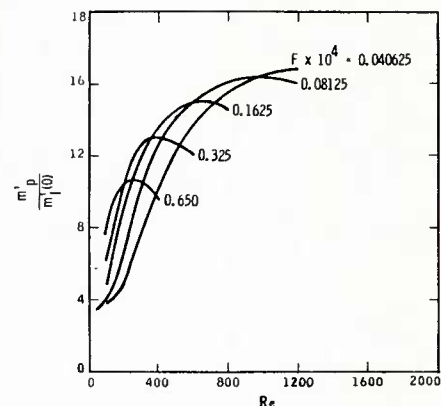
Fig. 10 – Effect of frequency on peak mass-flow fluctuation. $M_\infty = 4.5$, insulated wall, $\Psi = 0°$, $c_r = 0.65$ (Mack 1971)

Fig. 11 - Comparison with combined theory
(Kendall 1975)

Fig. 12 - Variation of wave speed with distance
along the plate. $M_\infty = 4.5$ (Kendall 1975)

The contour taken in the inverse transform, showing the branch lines and poles.
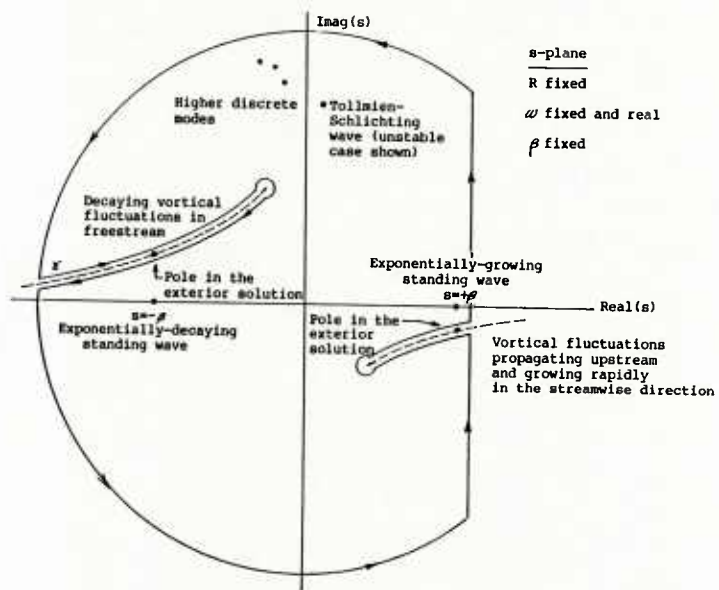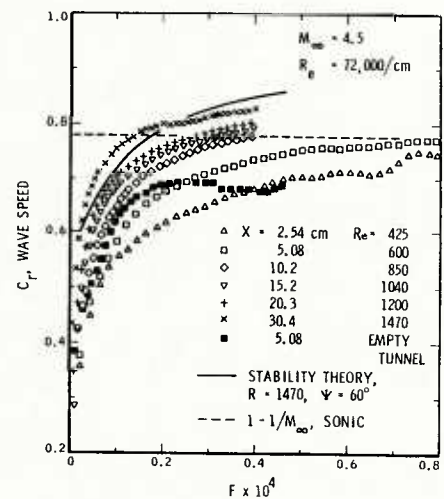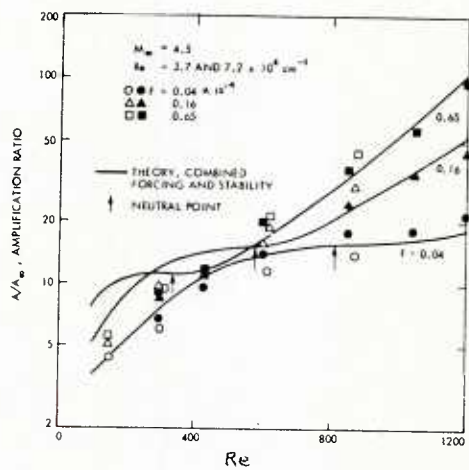
Fig. 13 - Laplace inversion (Tsuge and Rogler
1983)

'TRANSITION DESCRIPTION AND PREDICTION
IN THREE-DIMENSIONAL FLOWS'

by

D.I.A. Poll

Aerodynamics Division, College of Aeronautics,
Cranfield Institute of Technology, Cranfield,
Bedfordshire, MK43 0AL, England.

INTRODUCTION.

In situations where the phenomenon of boundary layer transition is important in an engineering sense the mean boundary layer flow is almost invariably highly three-dimensional. Therefore, from a purely practical point of view, an understanding, or at least an appreciation, of the implications of mean flow three-dimensionality must be assigned a high priority for those who wish to design engineering systems in which boundary layer transition is an important factor. At present there are two spectacular high technology projects under development which illustrate the importance of three-dimensional effects very clearly. These are the 'Swept Laminar Flow Wing' and the 'Space Shuttle' projects. Present generation civil transport aircraft have little or no laminar boundary layer flow on their wings and, consequently, operate at relatively high drag levels. The object of the 'Laminar Flow' project is to obtain a significant drag reduction on a swept-back wing by maintaining laminar flow over a much larger fraction of the surface area than has hitherto been the case. There are two ways in which this is being approached. The first is to tailor the geometry, and hence the pressure distribution, in such a way that the regions of natural laminar flow are increased - this could result in a modest drag reduction of between 5 and 10% in the cruise condition. In the second case the target is full chord laminar flow and to achieve this it is necessary to make use of tailored geometry (pressure distributions) plus active control systems such as distributed surface suction and possibly even surface cooling. With full chord laminar flow it is estimated that the total (2-D) profile drag coefficient of a wing section could be reduced from 0.005 to 0.001 at cruise conditions. However, each of the techniques proposed for the sustaining of laminar flow poses its own particular engineering problems. For example, the aerofoil geometry necessary for maintaining laminar flow in cruise may not produce the high lift coefficients required during take off and landing. This probably necessitates the use of a more effective flap system which in turn means extra weight and, therefore, extra induced drag. A similar situation occurs with the provision of a suction system which also involves extra weight. Clearly the success or failure of such a project rests squarely upon the designers ability to predict and, hence, avoid boundary layer transition. In the case of the Space Shuttle the problem is one of minimising the weight of the thermal protection system (TPS). During the re-entry phase the Shuttle has to loose a very large amount of kinetic energy and this is achieved by adopting a high drag attitude (incidences of order 30°-40°). Whilst this acts as a very effective braking mechanism it carries a penalty in the form of very large amounts of convective heat transfer to the windward face. Since the Shuttle is constructed primarily from metal it is clear that if mechanical integrity is to be maintained then the primary structure must be protected - hence the need for the TPS. On the current vehicle the TPS constitutes approximately 12% of the total structure weight (not including fuel or crew members) and this is equivalent to about 30% of the absolute maximum payload weight. Therefore, since the TPS serves no purpose other than that of passive insulation there are substantial payload improvements available if the weight of the TPS can be reduced. Over the years many studies have been conducted in this important area and, from these, it is abundantly clear that the choice of insulating material, its distribution over the surface and even the re-entry trajectory followed by the vehicle, are critically dependent upon the state of the boundary layer on the windward face. Therefore a truly optimum system can only be achieved through a complete understanding of the laminar to turbulent transition process.

The material to be presented in these lectures may be conveniently separated under two headings. The first is entitled 'leading edge problems' and in this section the consequences of three-dimensional mean flow will be discussed in the context of transition taking place in the immediate vicinity of the leading edge of a swept wing. This is an appropriate choice since most people will be familiar with the terminology and, more importantly, it is a situation where the transition process has particular engineering significance. The second heading is entitled 'More General Considerations' and here the mechanisms and principles discussed under the first heading will be re-examined in relation to more complex situations and also to transition in compressible flows with heat transfer.

NOTATION.

C	cross-flow velocity component
C_f	local skin friction coefficient
C_o	chord length measured normal to leading edge
d	trip wire diameter
H_{11}	streamwise shape factor
K	relaminarisation parameter (equation 13)
M	Mach number
p	static pressure
Q	resultant velocity $(U^2 + V^2)^{\frac{1}{2}}$
R	Reynolds number
$\bar{R}$	attachment line similarity parameter (equation 6)
R_d	trip wire Reynolds number (equation 7)
R_{δ_1}	displacement thickness Reynolds number
R_θ	momentum thickness Reynolds number
s	separation between trip and turbulence detector - measured along attachment line.
T	temperature
Tu	turbulence level
U_1	non-dimensional chordwise velocity gradient at the attachment line (equation 3)
U,V,W	velocity components outside the boundary layer
u,v,w	velocity components inside the boundary layer
x,y,z	orthogonal curvilinear coordinate system - see figure 1.
β	angle between the wall shear-stress vector and the velocity vector at the edge of the boundary layer.
Γ	intermittency factor for a transitional flow
δ_1	boundary layer displacement thickness in the streamwise direction
δ_2	boundary layer displacement thickness in the cross-flow direction
$\delta_{.99}$	height above the wall at which the velocity reaches $0.99Q_e$
ε	angle between the chordwise direction and the direction of disturbance propagation
η	attachment line characteristic length (equation 4)
θ	boundary layer momentum thickness
Λ	leading-edge sweep angle
μ	dynamic viscosity
ν	kinematic viscosity
ρ	density
τ	shear stress
θ	angle between the direction of disturbance wave propagation and the cross-flow direction.
χ	cross-flow characteristic Reynolds number (equation 10)

Subscripts.

AL   at   the attachment line

d   at   a distance d above the surface

e   at the edge of the boundary layer

MAX   at the maximum value

r   recovery conditions

T   at the onset of transition

w   at the wall

ϕ in the $\emptyset$ direction

*   at 'reference' conditions

∞ in the undisturbed free stream

0.01 C_{MAX} at the point where the velocity has dropped to 1% of its maximum value.

Part I - Leading Edge Problems.

Let us begin by considering a body with constant cross-section and of very large span, placed in a uniform flow such that the flow is everywhere normal to the spanwise generators. In this situation the boundary layer which forms on the body will be two-dimensional and it will begin at a stagnation line. From our experience of transition in two-dimensional mean flows we would always expect to find a region of laminar flow in the vicinity of the stagnation line. This is because all Reynolds numbers based upon local velocities tend to zero as the stagnation line is approached. We now modify the situation slightly by sweeping the body relative to the oncoming flow as shown in figure 1. Now the angle between the undisturbed free-stream velocity vector and the normal to the spanwise generators is no longer zero, but has some value Λ , where Λ is the leading edge sweep angle. If the free-stream Mach number is small enough for the flow to be everywhere subcritical ($M_e < 1$) then the chordwise pressure distribution will be unchanged provided that it is normalised with respect to the normal-to-leading-edge component of the free-stream dynamic pressure. This is known as the independence principle for the external flow and its validity can be demonstrated experimentally. Therefore, the flow outside the boundary layer is three-dimensional since it has velocity components U,V and W but these are functions of x and z only. The boundary conditions at the edge of the viscous region then take the form -

$$\frac{U_e}{U_\infty} = f(x) \qquad\qquad \frac{V_e}{V_\infty} = \text{constant} \qquad\qquad - \quad (1)$$

Under these conditions the steady laminar boundary layer equations also have a solution for which u, v and w are functions of x and z only. The governing equations for this situation are -

$$\frac{\partial u}{\partial x} + \frac{\partial w}{\partial z} = 0 \qquad\qquad\qquad\qquad \text{(continuity)}$$

$$u\frac{\partial u}{\partial x} + w\frac{\partial u}{\partial z} = U_e\frac{dU_e}{dx} + \nu\frac{\partial^2 u}{\partial z^2} \qquad \text{(x-momentum)} \quad - (2)$$

$$u\frac{\partial v}{\partial x} + w\frac{\partial v}{\partial z} = \nu\frac{\partial^2 v}{\partial z^2} \qquad\qquad \text{(y-momentum)}$$

Since the continuity equation and the equation for momentum in the x (chordwise) direction do not include terms containing spanwise velocity, v, we conclude that the boundary layer profile in the normal-to-leading-edge direction is independent of sweep. The equation for the spanwise flow component, however, can only be solved once the chordwise solution is known. Therefore, the application of sweep produces an additional velocity component, (v) without altering any of the other features of the flow. The question that is posed is what effect does sweep have on the transition behaviour for this flow?

(a)   Transition in the Attachment Line Boundary Layer.

Consider the flow about the body when the Reynolds number is very very large. In this limiting case we may consider the boundary layer to be vanishingly thin and the surface of the body can then be assumed to coincide with a particular stream surface of an inviscid flow.   This stream surface first encounters the body along a line AA.   At this line the stream surface divides with one branch following the upper surface of the body and the other branch following the lower surface.   The line AA is generally referred to as a line of attachment or simply 'attachment line'.   For the case of the body at zero sweep the attachment line is also a locus of two-dimensional stagnation points and as such is often called the 'stagnation line'.   However when the body is swept the term stagnation line is no longer appropriate since there is now a spanwise component of velocity Ve, (V_∞).   In situations when the boundary layer is not vanishingly thin the 'attachment line' AA is taken to be the projection of the dividing stream surface onto the surface of the body.

The flow near the leading edge of the swept body depicted in figure 1 is shown schematically in figure 2 and, in accordance with the above definition, the attachment line is represented by the line AA.   In the immediate neighbourhood of such a swept attachment line there is a region of sufficiently small chordwise extent where the flow at the edge of the boundary layer may be approximated to any desired degree of accuracy by the relations

$$\frac{Ue}{U_\infty} = U_1 \cdot \frac{x}{C_0} \quad \text{and} \quad Ve = V_\infty = \text{constant,}$$

$$- (3)$$

where $U_1 = \left[\frac{d(Ue/U_\infty)}{d(x/C_0)}\right]_{x=0}$

Under these conditions the boundary layer equations (2) have a similarity solution. The chordwise and spanwise velocity profile are, therefore, independent of x and y. This solution may be found in most standard texts on boundary layer theory e.g. Rosenhead[1] and the results are presented in figures 3 and 4.   The length scale for the solution is η where

$$\eta = \left[\frac{\nu}{(du_e/dx)_{x=0}}\right]^{\frac{1}{2}} \qquad - (4)$$

Since the solutions are independent of x and y the velocity profile shown in figure 4 is the attachment line velocity profile.   By integration of the profile it may be readily shown that

$$\delta_{.99} = 3.055 \eta \quad ,$$

$$\delta_1 = 1.026 \eta \quad , \qquad - (5)$$

and $$\theta = 0.404 \eta \quad .$$

Clearly, η itself serves as an entirely satisfactory boundary layer length and this may be used to form a characteristic Reynolds number $\bar{R}$, where -

$$\bar{R} = \frac{Ve.\eta}{\nu} = \left[\frac{Ve^2}{\nu U_\infty}\frac{Co}{U_1}\right]^{\frac{1}{2}} \qquad - (6)$$

This charactistic Reynolds number can also be derived simply on the basis of dimensional analysis - see Cumpsty and Head[2].   Consequently, $\bar{R}$ serves as a similarity parameter for the attachment-line boundary layer even when the flow is transitional or turbulent.

The transition characteristics of the swept attachment line were first encountered in the early 1960's during testing of the Northrop X-21A laminar flow aircraft - see Pfenninger[3].   The X-21A had a special wing which employed boundary layer suction through slots in the surface.   The suction was intended to stabilise the laminar boundary layer and, in this way, it was hoped that laminar flow could be maintained over the whole chord at cruise conditions.   However, early flight tests revealed that the boundary layer on the wing was turbulent at the attachment line in the cruise conditions - a result which apparently had not been anticipated!   This discovery was corroborated by flight test data from a Handley Page laminar flow wing which was undergoing trials at the College of Aeronautics[4] at the same time and, consequently, a number of wind-tunnel studies were performed in order to clarify the nature of the transition mechanism.   The experiments, which were performed by Pfenninger and his co-workers[3] (Northrop), Gregory[5] (National Physical Laboratory) and Gaster[6] (College of Aeronautics), demonstrated that, in the presence of large boundary layer tripping devices such as streamwise end-plates, boundary layer fences, isolated three-dimensional roughness elements or two-dimensional trip wires, transition at the attachment line began when $\bar{R}$ exceeded approximately 250.   When small tripping devices were used it was found that transition was delayed until much higher values of $\bar{R}$ were reached.   Similar results were also obtained in a later (1969) study performed by Cumpsty and Head[7].

Before embarking on a detailed description of the attachment-line transition process it is appropriate to present a visualisation of the transition at the attachment line. Figure 5 shows a series of surface oil-flow patterns which illustrate the process very clearly. For the visualisation a mixture of titanium dioxide and kerosene has been applied to the leading edge of a long cylinder swept at 63° relative to the oncoming flow. In the first picture the wind speed is 28 m/sec and the oil has moved back until a line of laminar separation is reached. The line of separation is, in fact, the leading edge of a swept separation bubble but, since oil was only applied to the leading edge region, the re-attachment line is not apparent. For the second picture the flow speed has been reduced to 24 m/sec and a short length of 0.3mm diameter wire has been fixed across the attachment line so that the wire axis lies in the x,z plane with the ends situated at x = ±6mm. The line of laminar separation is still clearly visible although it has been breached by a localised turbulent wedge which has its origin at the trip. Finally, in the third picture the wind speed has been increased to the original value of 28 m/sec. In this case the turbulence from the trip wire is no longer confined to a wedge but has spread along the span as witnessed by the disappearance of the laminar separation line - this is the manifestation of attachment-line transition or 'attachment-line contamination' as it is sometimes called.

To date the only comprehensive investigation of the transition behaviour of the swept attachment line is that conducted by Poll and which is described in references 8 - 11. This work was conducted at low speed (less than 60 m/sec) on a large swept cylinder model. The model was the same one used by Cumpsty and Head[7] for their attachment line studies and is fully described in references 7 - 11. In this work great care was taken to ensure that the laminar flow did not exhibit any significant dependence upon the spanwise coordinate y and that the values of $\bar{R}$ and η used in the data reduction were accurate. The state of the attachment line was determined by observing the output from hot-wire anemometers.

When the surface on which the attachment-line boundary layer forms is smooth and there are no sources of upstream disturbance, the transition will be the result of the amplification of the small scale fluctuations which are ever present in the free-stream. In such a case the laminar flow will first selectively amplify certain disturbances, characterised by their frequency and wave number, and 'wave packets' will appear in the boundary layer. For the swept attachment line these wave packets are observed at values of $\bar{R}$ in excess of 570 ($R_\theta > 230$) and typical examples are shown in figure 6. Similar results have also been obtained by Pfenninger and Bacon[12]. By observing the disturbance waves at various chordwise positions it has been found that the wavefronts corresponding to the oscillations shown in figure 6 are locally normal to the spanwise generators of the cylinder i.e. the disturbances are predominantly two-dimensional. As the wave packets are convected along the leading edge the disturbance amplitudes increase and eventually breakdown to form turbulent spots. The occurrence of turbulent spots or bursts marks the onset of transition. Clearly the process being described is similar to that which is observed in two-dimensional flows with low free-stream disturbances and, as such, might be expected to be in broad agreement with the predictions of linear stability theory. Figure 7 presents the results of such a calculation together with the experimental data from references 11,12 and 13. The stability characteristics have been computed from the Orr-Sommerfeld equation which means that the velocity component normal to the wall and the wall curvature have been omitted from the analysis. Transition onset has been predicted by an e^n model and the distance, s , represents the spanwise separation between the point of introduction of the disturbance and the point at which the disturbance breaks down to form a turbulent burst (both points being located on the attachment line). For the experimental data the distance s represents the spanwise distance between the upstream tip of the model and the point at which transition is first observed. It is apparent from the data that the use of R_θ (= 0.404 $\bar{R}$) correctly accounts for the combined effects of free-stream Reynolds number, model geometry and sweep angle. The data also indicate that the theoretical model produces the correct variation of $R_{\theta T}$ with s_T although the predicted value of $R_{\theta T}$ is about 10% greater than that observed in the experiments. It may also be noted that the infinite swept attachment-line velocity profile is more stable than the Blasius profile where the critical R_θ has a value of 201 and that for large values of s the results for e^6, e^{10} and e^{14} lie very close together. This latter piece of information suggests that the values of $\bar{R}$ (R_θ) for the onset of transition may not be sensitive to the initial disturbance level provided that it is still small enough for the linearised theory to remain valid. Therefore, despite the differences between theory and experiment, the results presented in figure 7 indicate that for s/θ_T greater than 20,000 an R_θ of 230 ($\bar{R}$ = 570) represents an upper limit for a laminar flow which is stable to small disturbances in the free-stream. If a laminar attachment-line boundary layer flow is to be maintained at values of $\bar{R}$ greater than 570 then some form of boundary layer control is necessary. This problem is addressed by Pfenninger and Bacon in reference 13.

In the flight work and experimental studies conducted up until 1975 it had been found that transition on the attachment line was occurring at values of $\bar{R}$ of about 250. Clearly, this observation cannot be explained in terms of the results presented in figure 7 i.e. in terms of linear stability theory. In order to examine this unusual behaviour the swept cylinder experiments were extended to investigate the response of the laminar attachment-line boundary layer to the presence of trip wires of various diameter arranged so that the wire axis lay in the x direction. In addition the trip wires were very long in the x direction so that the attachment-line boundary layer was encountering an effectively two-dimensional excrescence. The results of this exercise are summarised in figure 8 which shows the value of $\bar{R}$ necessary for the observation of the onset of transition (first bursts of turbulence) at a certain distance s from a

trip wire with a diameter d.   For very small values of d the results are
indistinguishable from the 'free' transition results presented in figure 7.   As
progressively larger trip wires are considered a critical value of d is encountered
at which the transition is just controlled by the trip wire - larger values of d
cause the transition onset location to move closer to the trip.   For trip wire
diameters smaller than this critical value transition is preceeded by the appearance
of wave packets.   When the trip wire is sized such that transition occurs between an
$\bar{R}$ of 600 and 400 (0.8 < d/η < 1.6) it is found that bursts of turbulence still occur
first at large spanwise distances downstream of the trip.   However the laminar
perturbation which preceeds the turbulent burst is no longer a packet of Tollmien -
Schlichting waves.   Instead the hot-wire reveals the presence of discreet disturbances
travelling along the attachment line.   Figure 9 gives a series of oscilloscope traces
which show the disturbance at various stages in its development.   If the trip diameter
is increased still further so that transition occurs at an $\bar{R}$ of between 400 and 250
(1.6 < d/η < 2.0) then the turbulent bursts originate at the trip-wire and then propagate
indefinitely along the span i.e. the onset of transition is observed at all spanwise
stations at the same value of $\bar{R}$.   Finally, when the trip size is such that transition
begins at an $\bar{R}$ of less than 250 (d/η > 2.0), the turbulent bursts still originate at the
trip wire but decay and ultimately disappear as they convect along the attachment line.

The results of figure 9 indicate that the transition behaviour of the infinite
swept attachment-line may be separated into four distinct regimes.   In the first
the values of $\bar{R}$ for transition onset are high and the turbulence is the result of an
instability of the laminar flow to the small disturbances present in the free stream.
This region is bounded by a critical value of d/η and for values of d/η greater than
this limiting level the transition location is determined by disturbances introduced by
the wire.   The behaviour is qualitatively similar to that observed in the flat plate
boundary layer where the concept of a 'maximum tolerable roughness height' is well
established - see for example Gibbings and Hall[14].   However, comparisons between the
tolerable heights for the flat plate and the attachment-line boundary layer indicate
that the attachment-line is much less sensitive to the presence of a two-dimensional
trip-wire.   In the second region disturbances from the trip are dominating the transition
process and the value of $\bar{R}$ for transition exhibits a strong dependence upon d/η .
The disturbance which is introduced by the trip wire is still essentially 'laminar'.
However, no wave packets or Tollmien-Schlichting like disturbances are found.   Instead
isolated perturbations (figure 9) are observed.   Although the precise nature of these
disturbances is not yet known the traces are consistant with the view that a laminar
vortex is being shed from the trip and this undergoes some kind of processing
(amplification ?) before breaking down to turbulence.   For the flat plate case it is
known that laminar vortex shedding can occur from a backward facing step for values of
R_{δ_1} and $d/_{\delta_1}$ greater than about 500 and 0.75 respectively - see Fasel et al (ref. 15).
From figure 8 and equations 5 it may be shown that the corresponding limits for attachment-
line flow are 410 and 0.8 - the similarity is obvious.   In the third region (250 < $\bar{R}$ < 400)
the tripwire is still dominating the transition behaviour but with the turbulent bursts
originating at the trip itself.   The data for this region suggest that the observed
variation of $\bar{R}$ with d/η is consistent with a constant trip-wire Reynolds number R_d where

$$R_d = \left[\frac{V_d \cdot d}{\nu} \right] \simeq 500 . \qquad - (7)$$

Corresponding transition behaviour in flat plate boundary layers indicates that R_d lies
between 150 and 400 - see Gibbins[16].   Once again we conclude that the attachment-line
boundary layer is less sensitive to the presence of two-dimensional trip wires.   The
fourth and final regime, however, is the one of most direct practical interest.   Here
very large trip wires are perturbing the flow but if $\bar{R}$ is less than 250 the turbulent
spots decay and ultimately disappear at some particular value of S/η .   It would appear
that an $\bar{R}$ of 250 represents a lower limit for the indefinite propagation of turbulence
along a swept attachment line when the boundary layer is subjected to a very large
disturbance.   This aspect of the transition behaviour does not appear to have a
counterpart in the flow over a flat plate.   Instead the behaviour is more in line with
that found in axisymmetric pipe flow with highly disturbed entry conditions - see
Wygnanski and Champagne[17].   In this situation burst of turbulence (puffs) originate at
the inlet and propagate indefinitely if the bulk flow Reynolds number exceeds
approximately 2000.   The puffs decay if the Reynolds number is less than 2000.

This lower transition bound for the attachment-line flow is clearly the one which was
found in the flight tests and studied experimentally in references 3 to 7.   For the
flight cases, however, there were no trip wires, as such, fixed to the wing.   Instead the
turbulent contamination was found to come from the wing/fuselage junction or boundary
layer fences.   To investigate this case in the experiment the attachment line was
contaminated by a turbulent boundary layer formed on a large streamwise end plate.   The
results of this test are presented in figure 10.   Also shown are the extrapolated trip
wire (d/η → ∞) results from figure 8.   It can be seen that the limiting value for
transition onset at large distances from the source of the disturbance is the same.
We, therefore, conclude that, at large distances downstream from the contamination
source, the lower bound for the existence of turbulent bursts on a swept attachment line
is given by a fixed value of $\bar{R}$ i.e. $\bar{R}$ equal to 250.

Thus far the description of the attachment line transition process has been limited
to the onset of transition i.e. the appearance of first bursts of turbulence.   In the
early work on this subject the development of the flow from the laminar to the fully
turbulent state received very little attention.   This was because the primary ojective
at that time was to avoid transition.   The transition to complete turbulence was however,

examined by Cumpsty and Head[7] and an attempt at computing Cumpsty and Head's transitional and turbulent velocity profiles was published by Cebeci[18]. At first sight it may appear that the transitional velocity profiles should be independent of spanwise position. However, this view cannot be correct since measurements carried out on isolated turbulent spots by Gaster[6] and also by Firmin and Cook[19] have shown that for values of $\overline{R}$ greater than 245 the spots expand in the y direction but shrink when $\overline{R}$ is less than 245. It follows that the turbulent intermittency must vary in the spanwise direction even when $\overline{R}$ is fixed. This problem has been examined by Poll[20] for the case where transition is the result of contamination by a large upstream disturbance. By using the Emmons[21] probalility theory for transition, a model of the attachment-line transition process, which is consistant with all the available experimental data - including the growth of individual turbulent spots, was developed. It was concluded that the intermittency at an infinite swept attachment line depends upon the parameters $\overline{R}$, η and s in such a way that

$$\Gamma = 1 - \mathrm{EXP}\left[-\left[\frac{\overline{R} - 245}{233}\right]^2 \left[\frac{s}{\overline{R}\eta} + 10\right]\right] \qquad - (8)$$

for

$$\frac{s}{\overline{R}\eta} > 8$$

Therefore, whilst under certain circumstances the onset of transition may be independent of spanwise position s, the completion of transition is always dependent upon s.

b) Transition due to Cross-Flow Instability.

Let us assume that the attachment-line boundary layer on the swept cylinder is laminar and stable to small amplitude free-stream disturbances (i.e. $R_\theta < 230$). In the region close to the attachment line the streamlines at the edge of the boundary layer are highly curved in planes drawn parallel to the surface - as shown in figure 2. The velocity profiles viewed in the chordwise and spanwise directions are very similar to those shown in figures 3 and 4. Along any of the external streamlines (except x = o) there is a favourable pressure gradient and one may expect that as a result of this the flow will be relatively stable to small disturbances. However, it turns out that this is not the case.

In order to assess the implication of the three-dimensionality of the boundary layer on the stability to small disturbances we make use of a piece of analysis which was performed over 30 years ago by Owen and Randall[22] and Stuart[23]. They showed that in situations where the disturbances are small (linearised theory), the mean flow component in the direction normal to the wall is everywhere small (parallel flow I), derivatives in the normal-to-wall coordinate are very much larger than derivatives in the other coordinate directions (parallel flow II) and, finally, the effects of curvature of the disturbance wavefronts and the body surface are small, then, in a localised region of a three-dimensional boundary layer, the velocity component in the direction of propagation of the disturbance may be regarded as a two-dimensional flow for stability purposes. Therefore, to determine the stability of a three-dimensional flow, at a given Reynolds number, it is necessary to examine all the possible directions available for disturbance propagation. To facilitate this consider the coordinate system sketched in figure 11. At a given position x_0 the inviscid streamline at the edge of the boundary layer makes an angle θ with the x direction such that -

$$\tan\theta = \frac{Ve}{Ue}. \qquad - (9)$$

The direction of propagation of the disturbance under consideration makes an angle ϵ with the x axis. Figure 12 shows the velocity profiles for the three-dimensional boundary layer when various values of ϵ are considered. When ϵ equals zero the profile is the chordwise velocity distribution shown in figure 3. Similarly for ϵ equal to $\Pi/2$ the profile is the spanwise velocity distribution shown in figure 4. These profiles are known to be stable (from the usual two-dimensional considerations). So too is the profile for ϵ equal to θ - the so called streamwise velocity profile. However, the significant feature of figure 12 is the appearance of the m and m' profiles. The m profiles are characterised by the existance of a point of inflection and having velocities which are all in the same direction whilst the m' profiles have the inflection point but have velocities which change sign. In stability theory (Stuart[23]) the existance of a point of inflection within the velocity profile is of particular importance since it is a sufficient condition for instability at very large Reynolds number. In practical terms this usually means that an instability to small amplitude disturbances is observed at very low Reynolds number. Therefore, by simply sweeping the cylinder shown in figure 1, it is possible to destabilise the boundary layer since the sweep leads directly to the formation of the m and m' profiles.

Experimental verification of the destabilising effect was first observed by Gray[24] and later by Anscombe and Illingworth[25] and Gregory and Walker[23,26]. In each of these investigations the location of the boundary layer transition front was determined by a surface visualisation technique such as the 'china-clay evaporation' method[27]. It was found that not only was the transition front location strongly affected by the angle of sweep but, in the laminar boundary layer immediately upstream from the transition front, the visualisation showed a series of closely spaced fine streaks almost aligned with the direction of the flow at the edge of the boundary layer. The pattern was very regular

and the streak spacing was observed to be of order $6.\delta_{99}$.   Moreover at the transition
front itself the demarkation line between laminar and turbulent flow had a distinct "saw-
tooth" form rather than the simple straight line normally observed for transition in
two-dimensional flow. These features are clearly visible in the 'china-clay' visualisation
of transition on the windward face of a swept cylinder shown in figure 13 - see Poll[28].
The appearance of the streaks was taken as evidence that the laminar boundary layer had
become unstable to a class of disturbance which had zero phase velocity i.e. one which
was fixed relative to the surface. It would appear that the major motivation for this
conclusion was that the surface evaporation visualisation techniques showed similar
streaks prior to transition in situations where a two-dimensional laminar boundary layer
was flowing over a concave surface.   In this situation the familiar 'Görtler instability'
(see reference 1) develops due to an imbalance between centifugal and inertia forces within the
fluid and contra-rotating vortices (Taylor-Görtler vortices) develope with their axis
aligned with the mean flow direction.   This observation had a very significant effect
upon the theoretical work which was performed at the time. The first attempt at correlating
the conditions necessary for the onset of transition and the 'appearance' of streaks was
conducted by Owen and Randall[29] (with a contribution by Squire[30]).   Owen and Randall
chose to characterise the three-dimensional nature of the swept wing boundary layer in
terms of the cross-flow velocity profile shown in Figure 14. This is the profile
corresponding to the case $\varepsilon = (\theta - \Pi/2)$ from figures 11 and 12. The characteristic local
Reynolds number associated with this profile may be taken to be

$$\chi = \frac{C_{max} \, Z_{0.01C_{max}}}{\nu} \qquad - (10)$$

Owen and Randall used χ as a parameter to correlate the data of Anscombe and Illingworth[25].
It was proposed that conditions necessary for the first appearance of streaks in the
evaporation pattern and also conditions necessary for the transition front to be located
very close to the leading edge (attachment line) could be represented by fixed values of χ
i.e.

$$\chi_{Streaks} = 145$$

and in the limit as $x/_{C_0} \rightarrow O$ $\qquad\qquad\qquad\qquad\qquad\qquad - (11)$

$$\chi_T = 200$$

(It should be noted that the numbers quoted here are not those originally quoted by Owen
and Randall - a small correction has been applied to allow for the fact that their
original definition of χ was slightly different from that given in equation 10.)   In
terms of the Anscombe and Illingworth experiment the proposed correlations were in fair
agreement with the observations.   However, it was not clear that the correlations were
unique.   In fact, a subsequent investigation conducted by Boltz, Kenyon and Allen[31] on
a different aerofoil section, but with the same range of sweep angles, indicated that the
value of χ at transition could vary from 200 to 250.   Further doubt was cast on the
validity of a transition criterion based upon a constant value of χ by experimental
investigations conducted on the flow over a disc rotating in a fluid which is at rest -
see Gregory, Stuart and Walker[23] and also Owen and Randall[22].   In this case the critical
values of X were found to be about 550 for the appearance of streaks, and 680, for
transition, - considerably different from those found on the swept wings.

   The most serious difficulty encountered in the interpretation of these early
investigations is that the situations considered experimentally were too complex.   In
order to answer some of the more important questions an experiment was conducted on a
'simple' shape by Poll.   The experiments, which are described in detail in references
9, 10 and 28, involved the observation of the movement of the transition front on the
windward face of the same long inclined cylinder used for the attachment-line transition
investigation described in the previous section.   Four different techniques were used
to observe the transition phenomenon.   These were china clay evaporation (see figure 13),
surface oil-flow, hot-wire anemometry and surface Pitot tube.   Of the two visualisation
techniques employed the surface oil-flow produced the clearest and most consistent results.
A typical sequence of oil flows is given in figure 15.   The oil-flow shows the streak
pattern which is characteristic of the disturbed laminar flow.   In the upper photograph
the flow is laminar, though perturbed, right up to a laminar separation line, whilst
in the lower photograph transition to turbulence is occurring in the attached flow
resulting in a suppression of the separation.   The oil-flow revealed streaks which had
the same spacing as those observed in the china clay evaporation tests - namely $6.\delta_{99}$.
By using transparent plastic tape it was possible to transfer the flow pattern onto a
flat surface.   This meant that accurate measurements could be made of the location of
the first appearance of the streaks and also of their orientation relative to the flow
direction at the edge of the boundary layer.   It was found that the Owen and Randall
parameter χ provided an excellent correlation for the first appearance of the streaks.
The results are shown in figure 16 from which it can be seen that

$$\chi_{Streaks} \approx 220$$

This is somewhat higher then the value of 145 quoted by Owen and Randall but the difference may be due to the fact that the china-clay evaporation responds to skin friction magnitude whilst the oil-flow responds to skin friction direction. It is not at all clear that the two visualisation techniques should produce streak indications under the same conditions. The orientation of the streaks relative to the x direction and also to the external streamline direction is given in figure 17. It can be seen that the streaks are not quite aligned with flow direction at the edge of the boundary layer, although the difference is never more than 6 degrees for the range of parameters covered. We note in passing that, since ϵ for the streaks is less than the streamline angle, the velocity profile in the direction of propagation is one of the $\bar{m}'$ set shown in figure 12. Since the boundary layer on the cylinder was always less than 1mm thick at the conditions necessary to produce transition on the forward face the hot-wire anemometer could only be used as a diagnostic tool. Nevertheless the hot-wire did reveal the presence of large amplitude travelling waves in the laminar flow ahead of transition. Example of the output signals are given in figure 18. Each shows two traces, the upper trace is the output from a hot-wire mounted 14 cms ($x/C_O = 0.31$) from the attachment-line i.e. at a location where the flow is perturbed by cross-flow instability. The lower trace gives the output from a hot-wire mounted on the attachment line itself ($x/C_O = 0$). In all the cases shown there are no detectable disturbances in the attachment-line boundary layer. For the first picture (a) the cross flow Reynolds number χ has a value of 257.

Therefore conditions are such that a surface oil-flow visualisation would indicate a streak pattern. The hot wire signal is clearly showing the presence of a large amplitude travelling disturbance which has frequency of about 1100 Hz. Moreover the disturbance is not quite a pure harmonic, like those shown in figure 6 for example. Instead it exhibits the kind of distortion which is characteristic of a basic tone being contaminated by higher harmonic components i.e. 2200 Hz, 3300 Hz etc.. In the second picture (b) the cross-flow Reynolds number has been increased to 295 and the highly perturbed signal now clearly shows the presence of patches of very high frequency disturbance which are typical of a flow in the latter stages of breakdown to form turbulent spots. Finally, for comparison, the last picture (c) shows the signal corresponding to turbulent flow (N.B. there is no turbulence or sign of instability at the attachment line. The bulk of the transition data obtained from this experiment was obtained by using the surface Pitot-tube technique for the determination of transition onset. Before the method was used, however, checks were made to verify that the different techniques employed in the experiment were in substantial agreement when it came to determining those conditions necessary for the onset of boundary layer transition at a fixed location on the model. The results obtained in the tests are summarised in figure 19 where the value of χ at the onset of transition is plotted against attachment-line momentum thickness Reynolds number $R\theta_{AL}$ at fixed values of x/C_O. This plot has some particularly interesting features. For fixed values of x/C_O a constant value of χ describes the data quite accurately, provided that the attachment line remains stable to small disturbances. i.e. provided $R\theta_{AL} < 240$. However, the critical value of χ displays a very strong dependence upon x/C_O. In particular, these results are considerably different from the Owen and Randall criterion given in equation (11). The most likely explanation for this discrepancy is that the limiting transition results ($x/C_O \to 0$) in the Anscombe and Illingworth[25] were in fact produced by the onset of attachment line contamination! Nevertheless it is perfectly clear that the use of a single value of χ for the correlation of the conditions necessary for the onset of transition cannot be considered satisfactory. However, following a suggestion of Arnal[32] (see also Coustols[33]), we find that an excellent correlation exists between the critical value of X and the streamwise shape factor, H_{11}, provided that situations in which the streamwise flow is unstable to small disturbances are excluded. This is shown in figure 20. Therefore, under certain rather restrictive circumstances, the problem of transition via cross-flow instability can be expressed in terms of two parameters but never in terms of one parameter as was previously supposed.

Part II - More General Considerations.

a) The possibility of relaminarisation.

The reversion of a turbulent boundary layer to the laminar state in regions of strong favourable pressure gradient is a well established phenomenon in two-dimensional and axi-symmetric flows. Experiments conducted in turbulent bounday layers have shown that when the pressure gradient is sufficiently large the characteristic 'inner region' breaks down and the fully turbulent laws cease to be valid. From the data which are currently available it appears that this breakdown occurs when the local pressure gradient drops below a critical level i.e. relaminarisation begins when

$$\frac{dp}{dx} < -0.024 \, \frac{\rho U_e^3}{\nu} \cdot \left[\frac{C_{fe}}{2}\right]^{3/2}$$

see for example Narasimha and Sreenivasan[34]. In the case of the infinite swept wing the corresponding expression is

$$\frac{dp}{dx} < -\frac{0.024}{\cos(\theta+\beta)} \cdot \frac{\rho Q_e^3}{\nu} \cdot \left[\frac{C_{fe}}{2}\right]^{3/2} \qquad - (12)$$

where β is the angle between the wall shear stress vector and the velocity vector at the edge of the boundary layer. For convenience this expression may be rearranged in the following way -

$$\frac{(U_e/U_\infty)^2}{R\cos^2\Lambda\,(Q_e/U_\infty)^4} \cdot \frac{d(U_e/U_\infty)}{d(X/C_O)} = K > \frac{0.024}{(\cos\beta - \sin\beta\tan\theta)} \cdot \left[\frac{C_{fe}}{2}\right]^{3/2} \quad - (13)$$

For typical aerofoil sections with streamwise incidences of less than 3° the chordwise velocity gradient is effectively constant in regions close to the attachment line. In such situations the variation of K with X/C_O exhibits a maximum where

$$K_{max} = \frac{1}{4\bar{R}^2} \quad \text{when} \quad \frac{Ue}{U_\infty} = \tan\theta$$

By noting that the minimum value of β is of order -20° and that for the turbulent attachment-line boundary layer the local skin friction coefficient is given by

$$C_{fe} \simeq \frac{0.0689}{\bar{R}^{0.42}}$$

- see Poll[35], the relaminarisation criterion expressed in equation (12) becomes simply

$$\bar{R} < 265.$$

This simplified analysis yields two important results. Firstly, the conventional relaminarisation parameter, K, reaches its peak value very close to the attachment line. Therefore turbulence resulting from cross-flow instability is unlikely to be relaminarised. Secondly, the relaminarisation criterion has been reduced to a critical value of the attachment-line similarity parameter $\bar{R}$ i.e. for relaminarisation $\bar{R}$ must be less than 265. However, even in situations where gross contamination is present, the attachment-line cannot support bursts of turbulence until $\bar{R}$ exceeds 245. Therefore we conclude that turbulence resulting from either attachment-line contamination or cross-flow instability is unlikely to be relaminarised in the strong favourable pressure gradients which exist near the leading edge of a swept wing.

b) The effects of compressibility and heat transfer.

In the case of attachment-line contamination the effects of compressibility were originally considered by Topham[36]. He concluded that for free-stream Mach numbers lying between 4 and 10 transition at the attachment-line began when $R_{\theta_{AL}}$ exceeded approximately 130. A later investigation conducted by Bushnell and Huffman[37] attempted to extend Topham's criterion to include the effects of heat transfer at the wall. However, they were forced to conclude that at transition onset the value of $R_{\theta_{AL}}$ was not a constant. Instead they observed that the critical value of $R_{\theta_{AL}}$ could lie anywhere between 100 and 300 depending upon the free-stream and wall conditions. The available data base has been re-examined recently by Poll[20]. In this study only those cases in which transition was clearly the results of gross upstream contamination were considered. It was found that all the available data could be correlated by a single value of the compressible attachment-line similarity parameter, $\bar{R}$, provided that the temperature dependent properties were evaluated at some intermediate, or reference, temperature i.e. the conditions necessary for the onset of transition are given by

$$\bar{R}_* = \left[\frac{Ve^2\,Co}{\nu_* U_\infty U_1}\right]^{\frac{1}{2}} = 245$$

where $T_* = Te + 0.10\,(Tw - Te) + 0.60\,(Tr - Te).$

(The reference temperature is the same as that determined by correlation of the turbulent attachment-line skin friction and heat transfer data - see reference 35.) In order to aid physical interpretation this criterion has been used to calculate the critical values of R_θ as a function of the edge Mach number, Me, and wall-to-recovery temperature ratio, Tw/T_r using the method described by Topham[36]. The results are presented in figure 21. It is apparent that there is a substantial edge Mach number dependence such that $R_{\theta_{AL}}$ increases with increasing Me. There is also a small increase in $R_{\theta_{AL}}$ as the wall temperature is reduced. Of particular interest is the tendency for the results at the higher edge Mach numbers that vary in such a way that

$$\frac{R_\theta}{Me} \simeq \text{constant}$$

This is the form of the boundary layer transition criteria which was employed in the design of the windward face thermal protection system for Space Shuttle - see for example Wurster[38]. In the case of attachment-line contamination R_θ/Me lies in the range 45 to 60 whereas for the windward plane of symmetry on the Space Shuttle R_θ/Me has values of between 225 and 319. This large difference is probably due to the fact that in the attachment-line case the boundary layer is tripped by large excresence whilst the values quoted by Wurster for the Space Shuttle refer to 'free transition' conditions.

The effects of compressibility and heat transfer on cross-flow instability have been studied experimentally by several groups e.g. Scott-Wilson and Capps[39], Dunning and Ulmann[40] and Jillie and Hopkins[41]. All observed the familiar streak pattern and characteristic 'sawtooth' transition fronts when surface exaporation, or sublimation, techniques were used. However, in each case, the models used were representative of geometrically complex situations such as wing/body combinations, delta wings and half wings. Consequently, there is little, or no, information concerning pressure distributions or boundary layer development near the swept leading edges. This means that it has not been possible to extract useful quantitative data and these experiments can only be used to provide qualitative evidence of transition via cross-flow instability in compressible flows. It should be noted, however, that an attempt to quantify the effects of compressibility on cross-flow instability was made by Chapman[42] in 1961. He applied the ideas of Owen and Randall[22,29] to the results of the swept cylinder experiments of Beckwith and Gallagher[43]. However, the transition phenomena reported by Beckwith and Gallagher[43] are now known to be consistent with the process of attachment-line contamination - see Poll[20,35]. Therefore Chapman's[42] conclusions are of little value. In addition to the experimental work there have also been some theoretical investigations of the effect of compressibility and heat transfer on cross-flow instability. It appears that this problem was first considered by Brown[44] who was able to show that for Mach numbers less than 2 the critical values of χ are almost independent of Mach number whilst cooling the wall raises the stability limit. For an example of more recent theoretical work the reader is referred to Mack[45].

c)   Prediction of transition location in general three-dimensional flows.

When conditions are such that the transition to turbulence does not take place in the immediate vicinity of the attachment line the problem of predicting the movement of the transition front in response to changing free-stream conditions becomes particularly difficult. For two-dimensional flows the state-of-the-art method for predicting transition is the 'e^N' technique - see Jaffe, Okamura and Smith[46]. This approach considers the spatial development of disturbances of fixed frequency and transition is supposed to occur when the amplitude of any frequency just exceeds about 22000 ($\approx e^{10}$) times its amplitude at first instability. Formal justification for this approach is not possible but it is clear that for reasonably accurate prediction the development of the actual disturbances must be in agreement with the predictions of linear stability theory over the greater portion of the distance between onset of instability and breakdown to turbulent spots. In recent years attempts have been made to extend the 'e^N' method to the three-dimensional flow situation, notably by Cebeci and Stewartson[47] and Neyfeh[48]. As was the case with the work of Stuart[23] attention has been focused upon the transition in the flow over the rotating disc. Cebeci and Stewartson calculated growth rates for disturbances in the flow over the disc but found that at the experimentally observed transition location the amplification factor was 5×10^8, or about e^{20}. At the time this cast considerable doubt on the validity of the 'e^N' method for general three-dimensional flows since the only justification for its use (is an engineering sense) lies in the fact that N should be approximately 10 in all cases. This problem was subsequently resolved by Malik, Wilkinson and Orszag[49]. They showed that the wave-front curvature and Coriolis forces had a considerable stabilising effect on the disturbances and that when the corrected amplification rates were used the amplification factor was found to be 60,000, or e^{11}, at the experimentally observed transition location. In the work of Cebeci and Stewartson[47] the growth rates for the disturbances were obtained from solutions of the Orr-Sommerfeld equation i.e. the effects of curvature and Coriolis coupling were ignored. One may conclude that the 'e^N' method appears to work in three-dimensional flows provided that the stability characteristics are generated by an appropriate theoretical model. In general the Orr-Sommerfeld equation will not produce accurate estimates of disturbance growth unless the effects of streamline curvature, body curvature and Coriolis forces are truely negligable. Clearly this is not the case in the rotating disc flow and it is probably not the case for the swept cylinder results described in Part I. However for certain aerofoil applications 'Orr-Sommerfeld plus e^{10}' may produce results which are sufficiently accurate for engineering purposes - see for example Srokowski and Orszag[50] and Hefner and Bushnell[51].

Whilst the linear stability theory plus the e^N transition criterion may represent a small forward step in the development of a satisfactory theory for boundary layer transition, it is already exceedingly expensive, in terms of the computer time, to obtain a prediction for transition position. For example, if we let the time taken to perform a inviscid pressure distribution prediction for an aerofoil be 1 unit, then it takes an additional unit of computer time to calculate the mean boundary layer flow to the degree of accurancy necessary for stability purposes i.e. using a accurate finite difference code. The transition prediction then takes typically 20 units if the appropriate stability characteristics can be obtained from the Orr-Sommerfeld equation and perhaps as many as 100 units if the effects of curvature and Coriolis forces must be included. By any standards the prediction of transition by this kind of method is both time consuming and, consequently, expensive. There is, therefore, a continuing need for the development of simple techniques for the prediction of transition. Some useful work has already been done in this important area. For determining the conditions necessary for the onset of instability in three-dimensional flow the stability characteristics of pure cross-flow velocity profiles (figure 14) have been investigated and correlated against certain important features in the mean flow. This was first attempted by Gregory (as reported in reference 52) who used the second derivative of the cross-flow velocity at the wall as the correlating parameter. However, Poll[9]

subsequently showed that this correlation was unreliable and suggested that the height of the point of inflection above the surface might be more successful. The proposed relation is shown in figure 22. An alternative correlation based upon a cross-flow profile shape factor has been proposed by Dagenhart[53]. For the prediction of transition two simple methods have been proposed recently by Coustols[33]. The first represents an extension of the correlation χ_T, versus H_{11} shown in figure 20. This is shown in figure 23 where it should be noted that χ has been replaced by the conventional cross-flow displacement thickness Reynolds number, R_{δ_2}. Whilst this represents a considerable improvement on the Owen and Randall "χ equal to constant" criterion it is evident that the data still exhibit a large amount of scatter. In an attempt to further reduce this scatter Coustols has proposed a second correlation which is based upon three parameters. This involves defining a new displacement thickness Reynolds number $R_{\delta_{1_\phi}}$ where ϕ is the angle between the disturbance wave propagation direction and the pure cross-flow direction ($\varepsilon = [\theta - \pi/2]$ in figure 11)

$$R_{\delta_{1_\phi}} = \frac{Q_e \sin\phi}{\nu} \int_0^\delta \left[1 - \frac{U_\phi}{U_{e_\phi}} \right] dz$$

For a given location, linear stability theory is used to determine that value of ϕ for which the ratio of the theoretical minimum critical Reynolds number $R_{\delta_1})$crit. to the actual Reynolds number, $R_{\delta_{1_\phi}}$ exhibits a local minimum value. Since this angle, ϕ'min, does not vary with free-stream unit Reynolds number the value of $R_{\delta_1})_{\phi-\phi min}$ may be obtained from the relation -

$$R_{\delta_1}\Big]_{(\phi = \phi_{min})} = \text{Constant} . R \qquad \qquad - (14).$$

The value of R necessary for transition at the fixed location is then determined by using equation (14) in conjunction with the correlation of $R_{\delta_{1T}}$ $(\phi = \phi \ min)$ versus H_{11} and turbulence level, Tu, shown in figure 24.

References.

1. Rosenhead, L.   Laminar Boundary Layers.
                                 Oxford University Press, 1963.

2. Cumpsty, N.A.   The calculation of three-dimensional turbulent boundary
    Head, M.R.   layers. Part II Attachment line flow on an infinite
                                swept wing.
                                The Aeronautical Quarterly Vol. XV111,
                                pp 150 - 164, May 1967.

3. Pfenninger, W.   Laminar Flow Control - Laminarisation,
                               Special course on concepts for drag reduction.
                               AGARD report 654, March 1977.

4. Landeryou, R.R.   Flight tests of a laminar flow swept wing with boundary
    Trayford, R.S.   layer control by suction.
                              College of Aeronautics Report 174, June 1964.

5. Gregory, N.   Laminar flow on a swept leading edge.
    Love, E.M.   National Physical Laboratory, Aerodynamics Department
                              Memorandum 26, 1965.

6. Gaster M.   On the flow along swept leading edges.
                              The Aeronautical Quarterly, Vol. XV111,
                              p.p. 165 - 184, May 1967.

7. Cumpsty, N.A.   The Calculation of the three-dimensional turbulent
    Head, M.R.   boundary layer. Part III. Comparison of attachment
                              line calculations with experiment.
                              The Aeronautical Quarterly, Vol. XX, pp 99 - 113
                              May 1969.

8.   Poll, D.I.A.   Leading edge transition on swept wings.
                                 AGARD Conference Proceedings number 224,
                                 Paper 21, May 1977.

9.   Poll, D.I.A.   Some aspects of the flow near a swept attachment line with
                                 particular reference to boundary layer transition.
                                 College of Aeronautics Report 7803, August 1978.

10. Poll, D.I.A.   Three dimensional boundary layer transition via the
                                 mechanisms of 'attachment line contamination'
                                 and "cross-flow instability".
                                 Proceedings of the IUTAM symposium on Laminar - Turbulent
                                 Transition, Stuttgart, Germany, September 1979 pp 253-262
                                 Springer - Verlag.

11. Poll, D.I.A.   Transition in the infinite swept attachment line
                                 boundary layer.
                                 The Aeronautical Quarterly, Vol XXX, pp 607 - 628,
                                 November 1979.

12. Pfenninger, W.   Amplified laminar boundary layer oscillations and
     Bacon, J.W.   transition at the front attachment line of a 45°
                                 swept flat-nosed wing with and without boundary
                                 layer suction.
                                 Proceedings of the Symposium on Viscous Drag Reduction,
                                 LTV Research Center, Dallas, Texas. September 1968,
                                 Plenum Press (ed. C.S. Wells).

13. Carlson, J.C.   Investigation of the laminar flow characteristics
                                 of a 33° swept suction wing at high Reynolds numbers
                                 in the NASA Ames 12' pressure wind tunnel.
                                 Northrop Report NOR - 66 - S8, January 1966.

14. Gibbins, J.C.   Criterion for tolerable roughness in a laminar
     Hall, D.J.   boundary layer.
                                 Journal of Aircraft, Vol.6, No.2, pp 171 - 173,
                                 1969.

15. Fasel, H.   Numerical simulation studies of transition phenomena
     Bestek, H.   in incompressible two-dimensional flows.
     Schefenacker, R.   AGARD Conference Proceedings 224, Laminar -
                                 Turbulent Transition, Copenhagen, Denmark, May 1977.

16. Gibbings, J.C.   On boundary layer transition wires.
                                 ARC CP 462, December 1958.

17. Wygnanski, I.J.   On transition is a pipe. Part I - The Origin of Puffs
     Champagne, F.H.   and Slugs and the flow in a turbulent slug.
                                 Journal of Fluid Mechanics, Vol 59, No.2,
                                 pp 281 - 335, 1973.

18. Cebeci, T.   Attachment-line flow on an infinite swept wing.
                                 AIAA Journal, Vol. 12, No. 2, pp 242 - 245,
                                 February 1974.

19. Firmin, M.C.P.   Unpublished work, RAE Farnborough, 1965.
     Cook, P.H.

20. Poll, D.I.A.   The development of intermittent turbulence on a
                                 swept attachment line including the effects of compressibility.
                                 The Aeronautical Quarterly, Vol. XXXIV, pp 1 - 23,
                                 February 1983.

21. Emmons, H.W.   The laminar-turbulent transition in a boundary layer -
                                 Part I.
                                 Journal of the Aeronautical Sciences, Vol.18.
                                 No.7, pp 490 - 498, July 1951.

22. Owen, P.R.   Boundary layer transition as a sweptback wing -
     Randall, D.G.   a further investigation.
                                 R.A.E. Technical Memorandum 330, 1953.

23. Gregory, N.   On the stability of three-dimensional boundary layers
     Stuart, J.T.   with application to the flow due to a rotating disc.
     Walker, W.S.   Philisophical Transactions of the Royal Society,
                                 Series A. No. 943, Vol. 248, pp 155 - 198, July 1955.

24. Gray, W.E.   The effect of wing sweep on laminar flow.
                                 R.A.E. Technical Memorandum 255, 1952.

25. Anscombe, A   Wind tunnel observations of boundary layer transition
     Illingworth, L.N.   on a wing at various angles of sweep back.
                            ARC Report and Memorandum 2968, May 1952.

26. Gregory, N.   Brief wind tunnel tests on the effect of sweep
     Walker, W.S.   on laminar flow.
                            ARC Paper 14,928 May 1952.

27. Richards, E.J.   The 'china clay' method of indicating transition.
     Burstall, F.H.   ARC Report and Memorandum 2126, August 1945.

28. Poll, D.I.A.   Some observations of the transition process on the
                            windward face of a long inclined cylinder.
                            (To be published).

29. Owen, P.R.   Boundary layer transition on a swept back wing.
     Randall, D.G.   R.A.E. Technical Memorandum 256, 1952.

30. Squire, H.B.   Private Communication to R.A.E. 1952.

31. Boltz, F.W.   Effects of sweep angle on the boundary layer
     Kenyon, G.C.   stability characteristics of an untapered wing
     Allen, C.Q.   at low speeds.
                            NASA TN D-338, July 1960.

32. Arnal, D.   Private communication
                            10th meeting of the Eurovisc Working Party
                            on Boundary Layer Transition, Cranfield
                            Institute of Technology, May 1982.

33. Coustols, E.   Stabilite et transition en ecoulement tridimensionnel
                            cos des ailes en fleche
                            These presentee a L'Ecole National Superieur
                            de l'Aeronautique et de l'Espace, Toulouse
                            France, Jun, 1983.

34. Narasimha, R   Relaminarisation in highly accelerated turbulent
     Sreenivasan, K.R.   boundary layers.
                            Journal of Fluid Mechanics, Vol.61,
                            No.3, pp 417-447, 1973.

35. Poll, D.I.A.   Skin friction and heat transfer at an infinite
                            swept attachment line.
                            The Aeronautical Quarterly, Vol. XXXll,
                            pp 299 - 318, November 1981.

36. Topham, D.R.   A correlation of leading edge transition and
                            heat transfer on swept cylinders in supersonic flow.
                            Journal of the Royal Aeronautical Society.
                            Vol. 69, pp 49-52, January 1965.

37. Bushnell, D.M.   Investigation of heat transfer to leading edge
     Huffman, J.K.   of a 76⁰ swept fin with and without chordwise slots
                            and correlations of swept-leading edge transition data
                            for Mach 2 to 8.
                            NASA TM X-1475, December 1967.

38. Wurster, K.E.   An assessment of the impact of transition on advanced
                            winged entry vehicle thermal protection system mass.
                            AIAA Paper No. 81-1090, 16th Thermphysics Conference,
                            Palo Alto, California, June 1981.

39. Scott-Wilson, J.B.   Wind tunnel observations of boundary layer transition
     Capps, D.S.   on two sweptback wings at a Mach number of 1.61.
                            R.A.E. TN Aero 2347, December 1954.

40. Dunning, R.A.   Effects of sweep and angle of attack on boundary
     Ulmann,E.F.   layer transition on wings at Mach number 4.04.
                            NACA TN 3473, March 1955.

41. Jillie, D.W.   Effects of Mach number, leading edge bluntness and sweep
     Hopkins, E.J.   on boundary layer transition on a flat plate.
                            NASA TN D-1071, 1961.

42. Chapman, G.T.   Some effects of leading edge sweep on boundary layer
                            transition at supersonic speeds.
                            NASA TN D-1075, 1961.

43. Beckwith, J.E.   Local heat transfer and recovery temperature
     Gallagher, J.J.   on a yawed cylinder at a Mach number of 4.15 and
                            high Reynolds numbers.
                            NASA TR R-104, 1961.

44. Brown, W.B.   Exact solution of the stability equations for
                                    laminar boundary layers in compressible flow.
                                    Published in 'Boundary Layer and Flow Control'
                                    Vol.2, edited by G.V. Lachmann; pp 1033-1048,
                                    Pergamon Press, 1961

45. Mack, L.M.   On the stabilization of three-dimensional
                                    boundary layers by suction and cooling.
                                    IUTAM Symposium on Laminar-Turbulent Transition,
                                    Stuttgart, West Germany, September 1979.
                                    pp 223-238, Springer-Verlag.

46. Jaffe, N.A.   Determination of spatial amplification factors and their
     Okamura, T.T.   application to predicting transition.
     Smith, A.M.O.   AIAA Journal, Vol.8, No.2, pp 301-308.
                                    February 1970.

47. Cebeci, T.   On stability and transition in three-dimensional
     Stewartson, K.   flows.
                                    AIAA Journal, Vol.18, No.4, pp 398-405,
                                    April 1980.

48. Neyfeh, Ali.H.   Stability of three-dimensional boundary layers.
                                    AIAA Journal, Vol.18, No.4, pp 406-416,
                                    April 1980.

49. Malik, M.R.   Instability and transition in rotating disc flow.
     Wilkinson, S.P.   AIAA Journal, Vol.19, No.9, pp 1131-1138,
     Orszag, S.A.   September 1981.

50. Srokowski, A.J.   Mass flow requirements for LFC wing design.
     Orszag, S.A.   AIAA paper 77-1222, Aircraft Systems and
                                    Technology Meeting, Seattle, Washington,
                                    August 1977.

51. Hefner, J.N.   Status of linear boundary layer stability
     Bushnell, D.M.   theory and the e^n method, with emphasis
                                    on swept-wing applications.
                                    NASA TP 1645, April 1980.

52. Brown, W.B.   A stability criterion for three-dimensional
                                    laminar boundary layers.
                                    Published in 'Boundary Layer and Flow Control',
                                    Vol.2, edited by G.V.Lachmann, pp 913-923,
                                    Pergamon Press, 1961.

53. Dagenhart, J.R.   Amplified cross-flow disturbances in the
                                    laminar boundary layer on swept wings
                                    with suction.
   NASA TP 1902, November 1981.
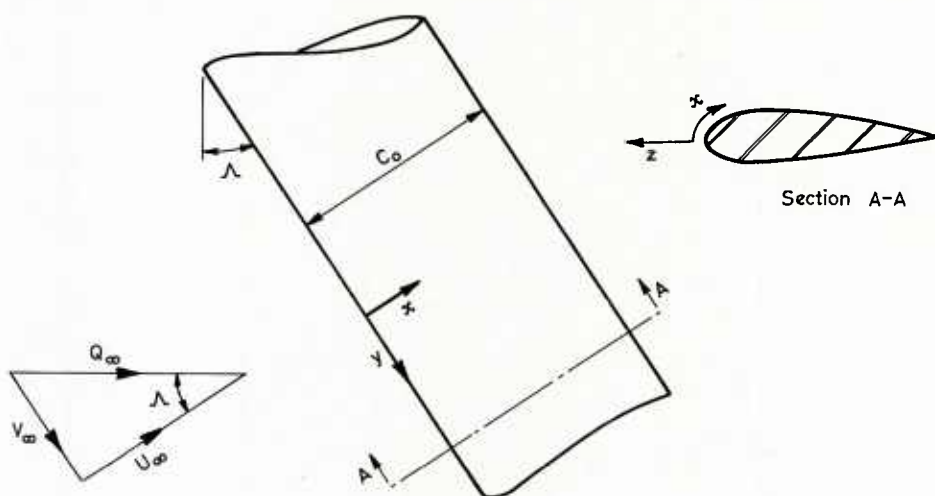
Figure 1.   Definition and notation for the infinite swept cylinder.
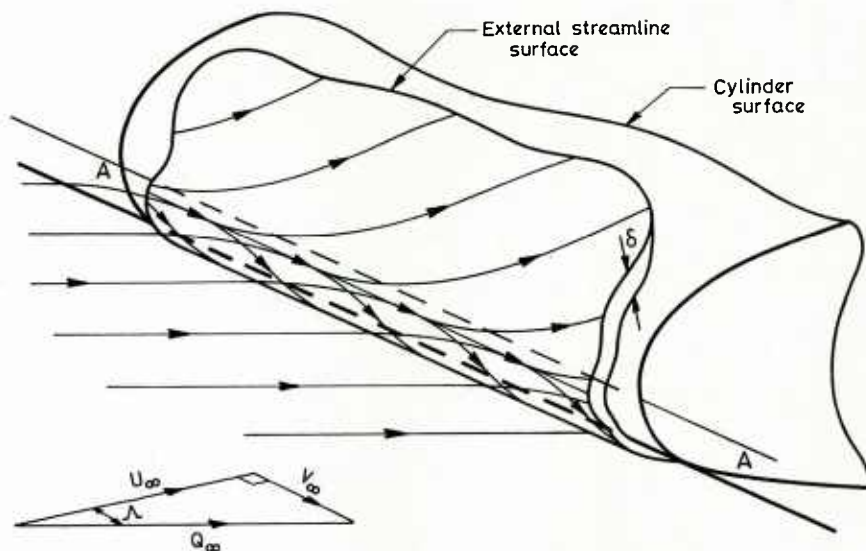
Figure 2.   Flow near the leading edge of a swept cylinder.
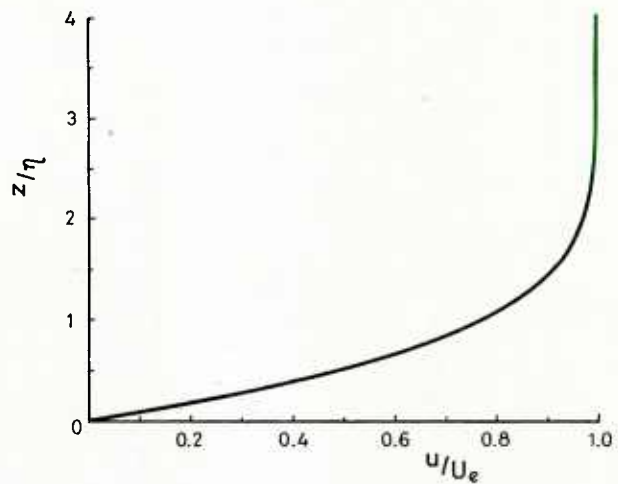
Figure 3.   Chordwise velocity profile in the immediate
vicinity of the attachment line.
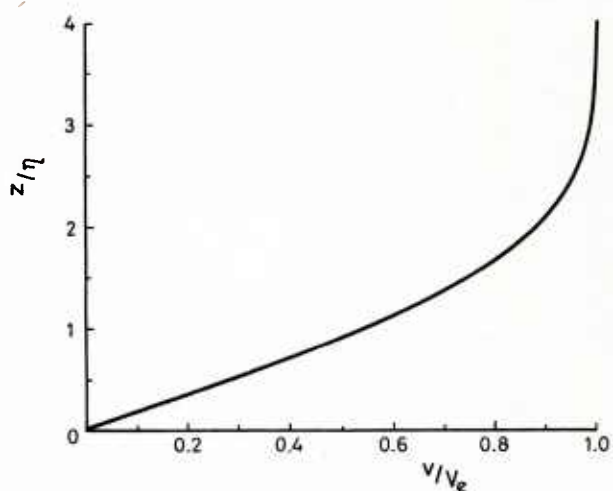
Figure 4.   Spanwise velocity profile in the immediate
vicinity of the attachment line.

a) Sweep = 63°, Speed = 28 m/sec , No trip

b) Sweep = 63°, Speed = 24 m/sec , Trip = 0.34 mm

c) Sweep = 63°, Speed = 28 m/sec , Trip = 0.34 mm
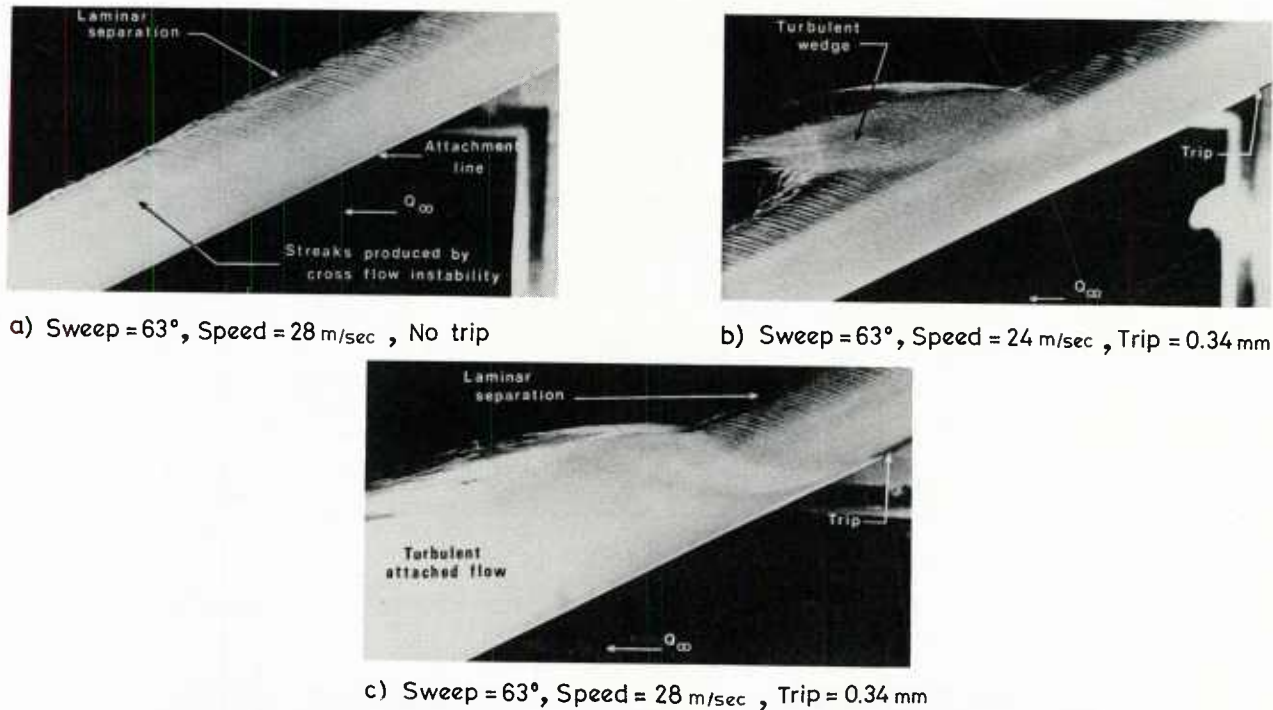
Figure 5.   Visualisation of the effect of transition via attachment-line contamination.

a)

b)
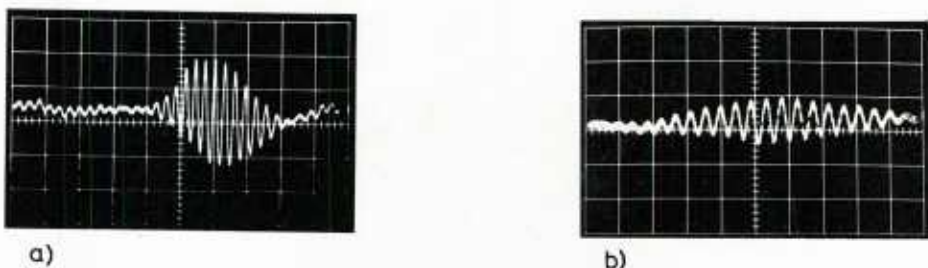
Figure 6.   Hot-wire signals showing the disturbances which preceed a turbulent burst when $\bar{R}$ exceeds 570 :-(a) $\bar{R} = 690$, $d/\eta = 0$, $z/\eta = 1.0$, (b) $\bar{R} = 590$, $d/\eta = 0.84$, $z/\eta = 0.9$. The horizontal scale = 1 m.sec/large division and the vertical scale = 0.02 volts/large division.

| Symbol	Sweep	Source
▽	64.5°	Poll (ref. 11)
○	68.0°	" "
×	71.0°	" "
□	45.0°	Pfenninger (ref.12)
◊	33.0°	Carlson (ref. 13)
– – –		Minimum critical R_{θ_L}
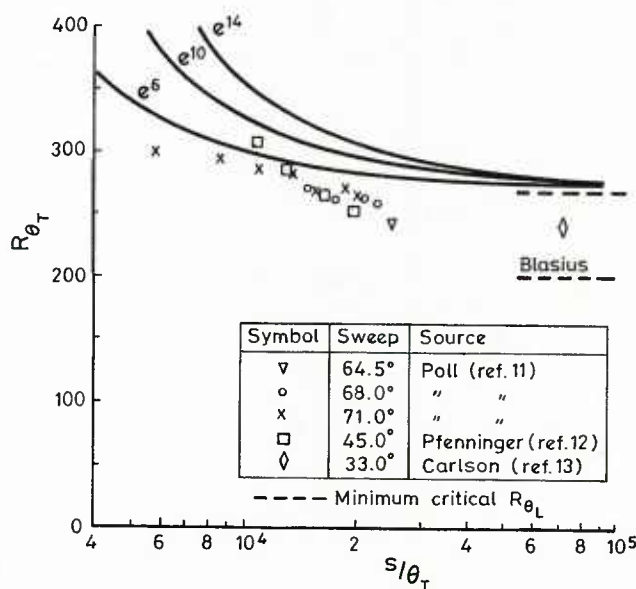
Figure 7.   A comparison between experimental 'free' transition results and a model based upon linear stability theory.
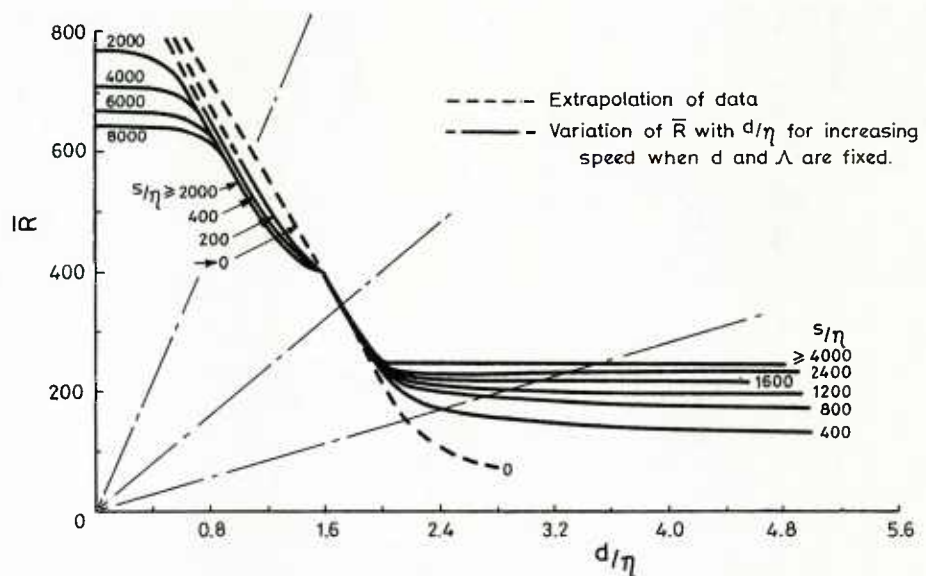
Figure 8. The variation of $\bar{R}$ with d/η and s/η for the appearance of first bursts of turbulence.
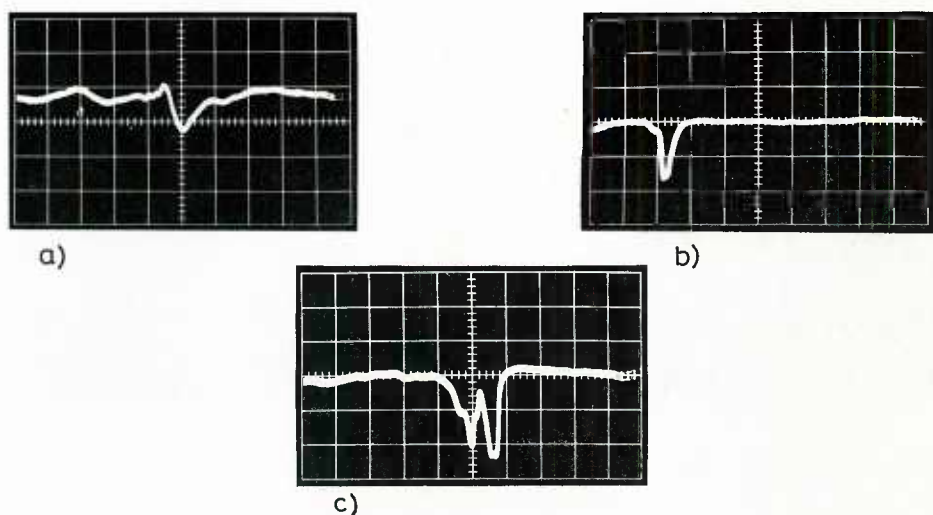
Figure 9. Traces showing the development of the disturbance which preceeds a turbulent burst when $\bar{R}$ lies between 570 and 400 :- (a) R = 465 , d/η = 1.15 , s/η = 1930 , z/η = 1.4 ; (b) $\bar{R}$ = 495, d/η = 1.23 , s/η = 2060 , z/η = 1.5; (c) R = 495 , d/η = 1.23 , s/η = 2060 , z/η = 1.5. In all cases the horizontal scale = 1 m sec/large division , in case (a) the vertical scale = 0.02 volts/large division and in cases (b) and (c) = 0.1 volts/large division .
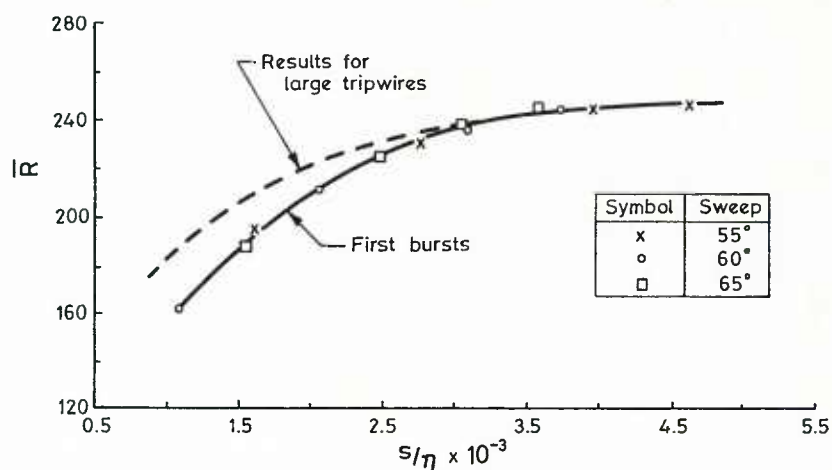
Figure 10. Transition characteristics for contamination by a flat-plate turbulent boundary layer.
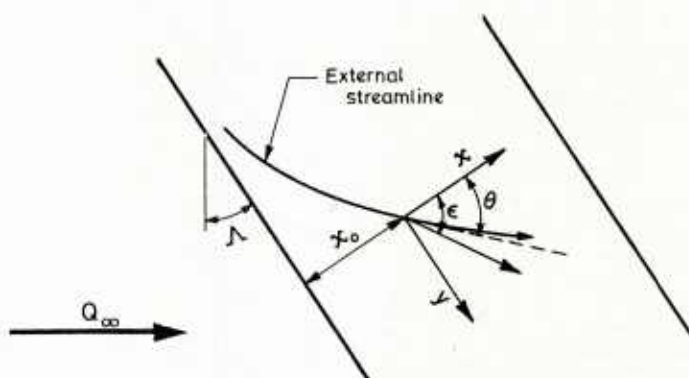
Figure 11. Co-ordinate system for investigating the stability of a three-dimensional boundary layer.
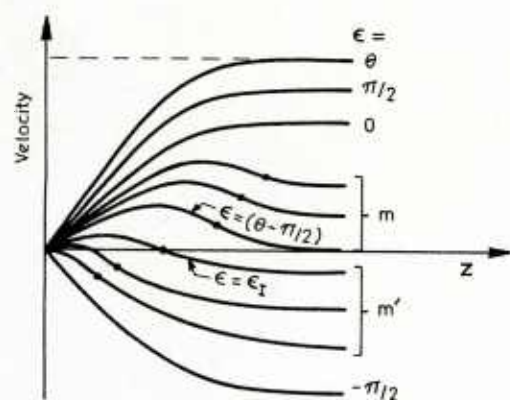
Figure 12. Variation of the velocity profile with the disturbance propagation angle.
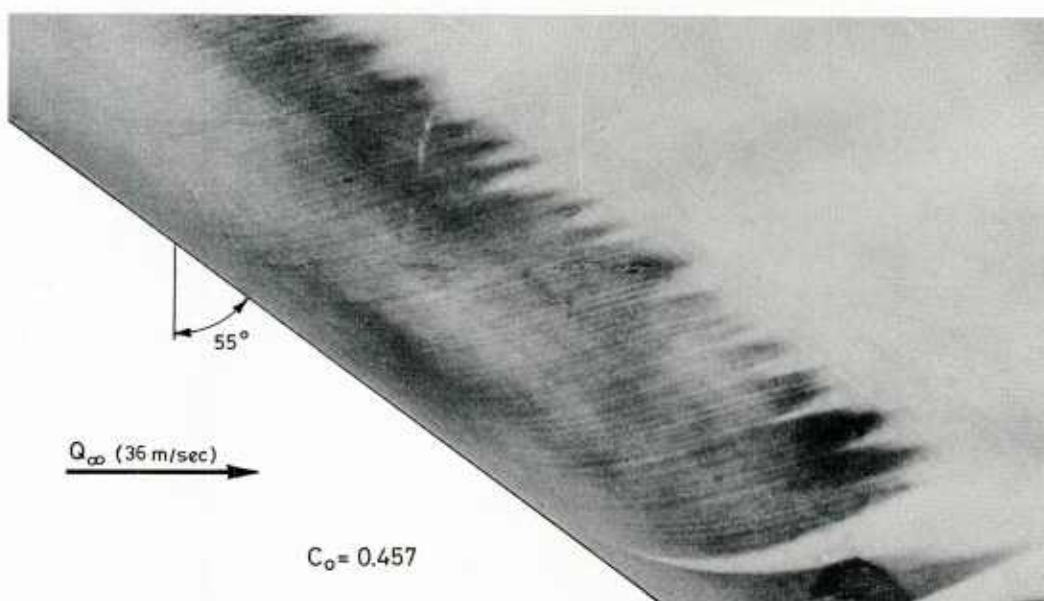
Figure 13. China-clay visualisation of the transition on the forward face of a swept cylinder. (Poll[28])
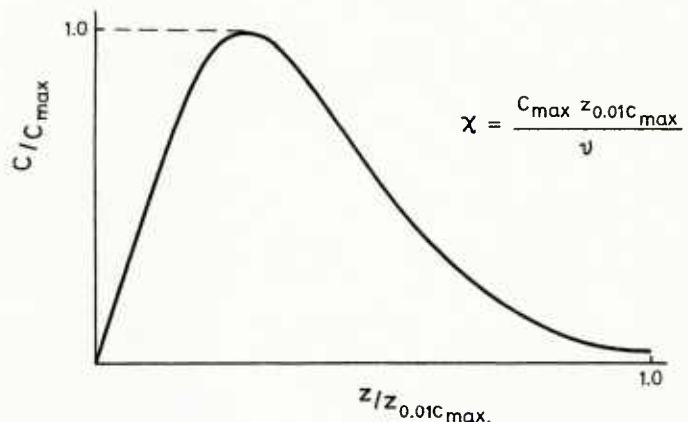
Figure 14.   Typical cross-flow velocity profile near the leading
edge of a swept wing.

$$\chi = \frac{C_{max}\, z_{0.01c_{max}}}{\upsilon}$$
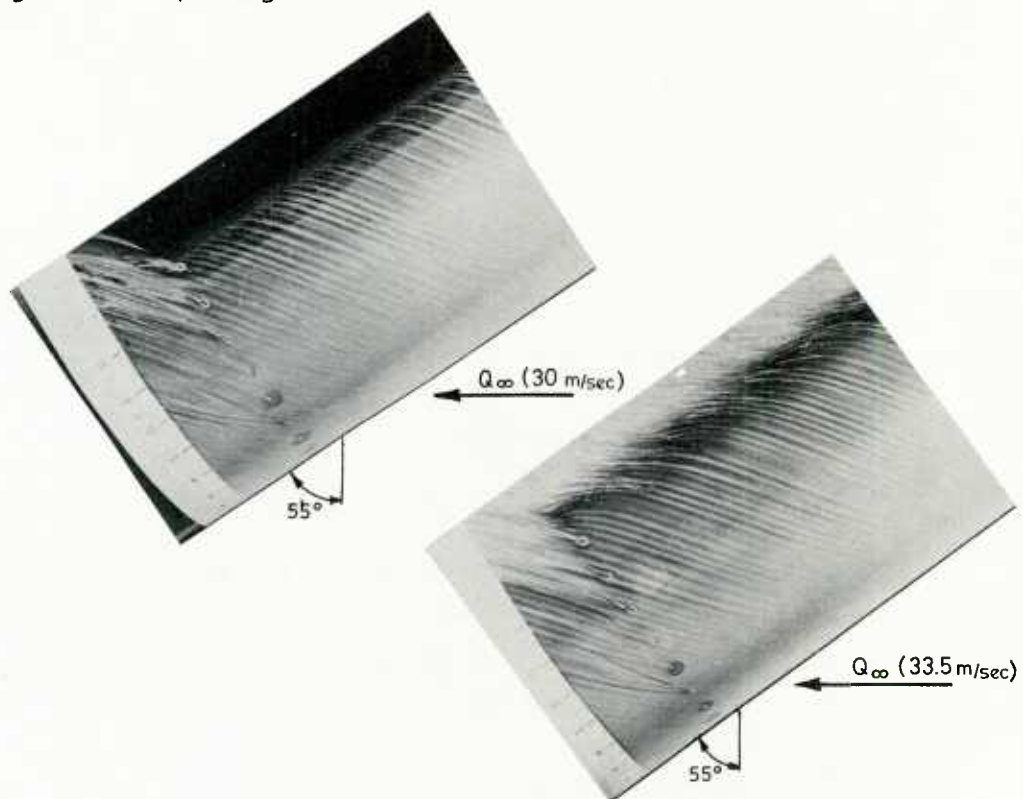
Figure 15.   Examples of the streak patterns
obtaind by surface oil-flow visualisation.

Symbol	Sweep
o	55°
x	63°
◊	71°
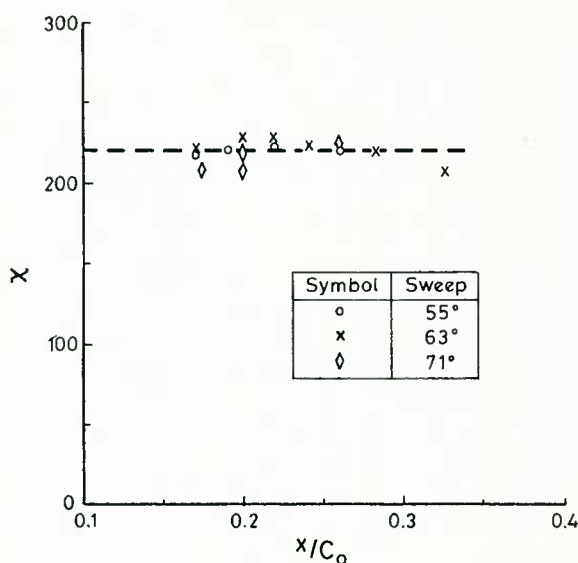
Figure 16.   Variation of χ with chordwise position and
sweep angle for the first appearance of streaks in the oil flow.
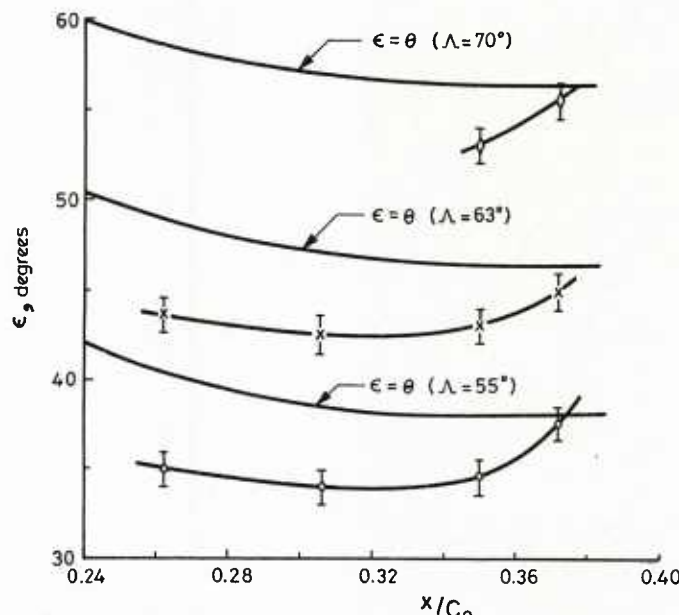
Figure 17. Orientation of the streaks relative to the normal-to-leading edge co-ordinate direction, x.
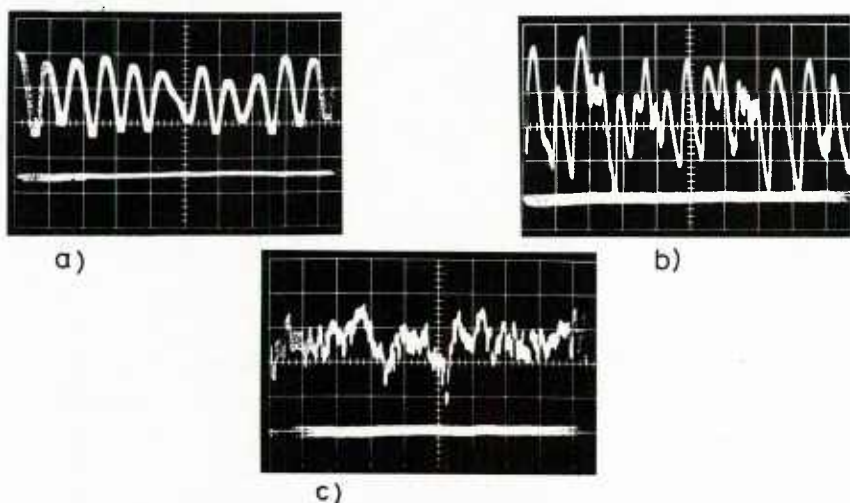
Figure 18. Traces showing the various stages of transition via cross-flow instability :- (a) disturbed laminar signal $\chi = 257$, (b) transitional $\chi = 295$, (c) fully turbulent $\chi = 348$. In each case $z = 0.25$ mm, horizontal scale = 1 m sec/large division and vertical scale = 0.1 volts/large division.

Symbol	x/C_o
x	0.394
o	0.372
▷	0.350
□	0.328
△	0.306
•	0.284
◁	0.262
◇	0.241
▽	0.219
⟡	0.197
+	0.175
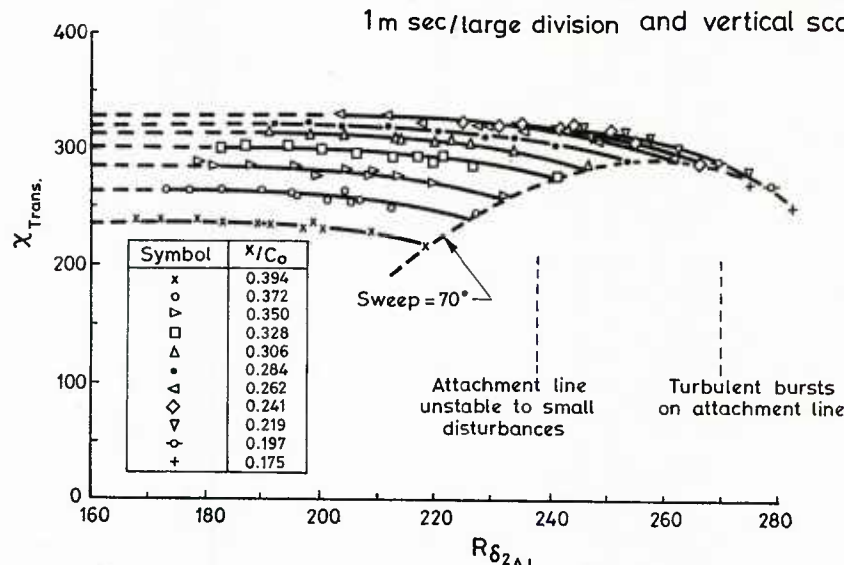
Figure 19. Variation of χ at transition with attachment-line momentum thickness Reynolds number and chordwise position.
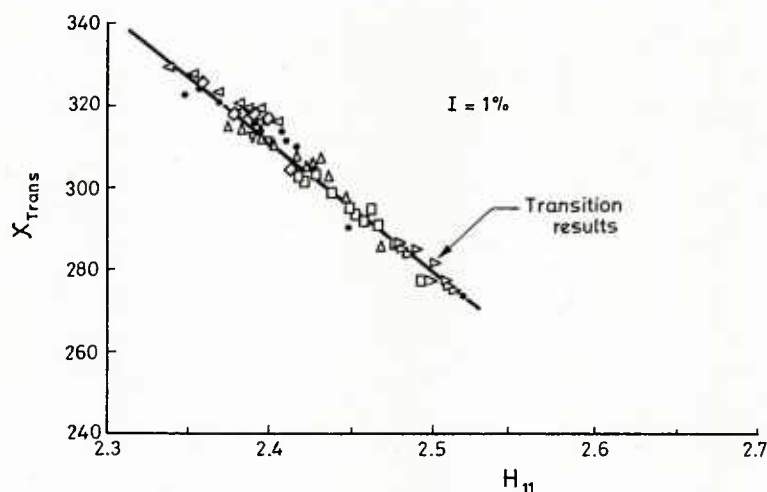
Figure 20.   Variation of the cross-flow Reynolds number at transition onset with streamwise shape factor.
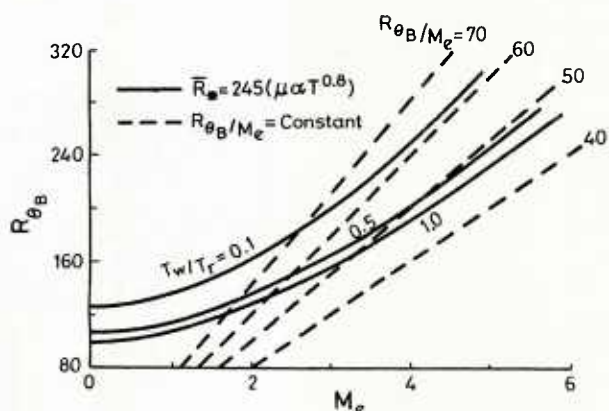
Figure 21.   Conditions necessary for the onset of transition in terms of R_θ, edge Mach number and wall-to-recovery temperature ratio.
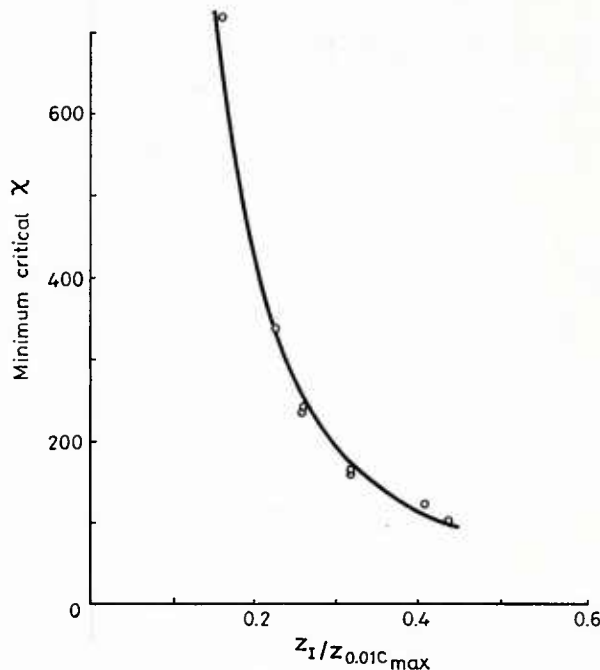
Figure 22.   Variation of X crit. with the position of the inflection point. (Poll[9])
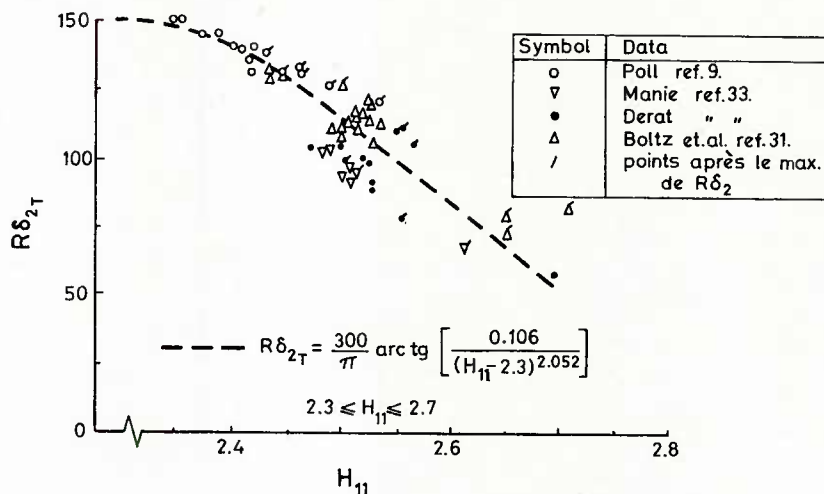
Figure 23.   Proposed cross-flow transition criterion $R\delta_{2T}$
versus H_{11} (Coustols[33])
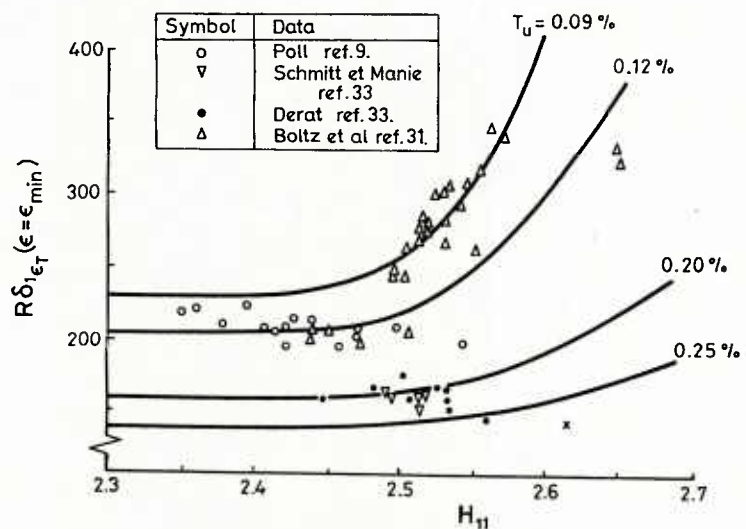
Figure 24. Alternative cross-flow transition criterion proposed
by Coustols[33].

NONLINEAR EFFECTS IN HYDRODYNAMIC STABILITY

Thorwald Herbert
Department of Engineering Science and Mechanics
Virginia Polytechnic Institute and State University
Blacksburg, Virginia 24061, U.S.A.

SUMMARY

The interest in the analysis of nonlinear effects is motivated by examples of insufficient agreement between observation and results of the linear theory for the prototypes of Taylor-Couette flow and plane Poiseuille flow. The principal methods for the analysis of nonlinear problems are characterized. The weakly nonlinear theory for a single normal mode and the calculation and use of high-order Landau constants is discussed. A survey is given on weakly nonlinear models of observed phenomena.

INTRODUCTION

The discussion on nonlinear effects is as old as the stability theory itself. Reynolds [1] suggested in 1883 for laminar-turbulent transition in pipe flow "that the condition might be one of instability for disturbances of a certain magnitude and stable for smaller disturbances". Ever since, nonlinear effects were employed as the prime candidate for explaining discrepancies between observation and the findings of the linear stability theory. This is often justified but not always. Beyond the neglect of nonlinear terms, the use of normal modes in all but one of the variables requires a simple basic flow, typically in an infinite pipe or between infinite plates or cylinders that are hardly realizable. Discrepancies may well be due to end effects, entrance effects, unsteadiness, or streamwise variation of the basic flow. Moreover, the results of the linear theory must always be seen in context with the background noise that is barely known in a specific experiment but provides the initial amplitudes for competing unstable modes in a band of wave numbers. On the other hand, the need for considering nonlinear terms is often suggested by results of the linear theory itself. In the Rayleigh-Bénard problem of convection in a horizontal fluid layer heated from below, the linear theory provides a critical Rayleigh number and wave number but leaves the form of the disturbances nonunique. Instead of two-dimensional convection rolls, linear solutions with different orientation of the wavenumber vector may be superposed to provide a variety of convection cells, e.g. hexagons. In any case, the exponential growth of an unstable mode will not indefinitely continue. Nonlinear effects will come into play and modify the form of the disturbances as well as the growth rate.

If nonlinearity acts stabilizing, an asymptotic equilibrium amplitude may be reached and the basic state may be replaced by a new stable motion that reflects the spatial structure of the linear normal mode. Such secondary motions are observable over a long time and occur as convection rolls or cells [2, Figs. 140-142] in the Rayleigh-Bénard problem or as Taylor vortices [2, Fig. 127] in the Couette flow between a fixed outer cylinder and a rotating inner cylinder. In all these figures, the relevant parameter (Rayleigh or Taylor number) exceeds the critical value and linear theory predicts instability in a broad band of wavenumbers (see Fig. 1 for a schematic stability diagram). One might well ask what happened to the other modes and what selected the observed wavelength? Obviously, with the given initial conditions (noise), some nonlinear mechanism preferred the observed mode and suppressed the others. As the relevant parameter is further increased, the steady secondary motion may itself become unstable. In thermal convection, the phenomena

Figure 1. Schematic stability diagram.

are very involved not only due to the different types of secondary motion but also by the dependence on the Prandtl number as a second parameter of this problem. The review by Busse [3] and his contribution to [4] are recommended for detailed information. In the Taylor-Couette flow the secondary instability leads to wavy Taylor vortices as shown in [2, Fig. 128]. The waves travel around the circumference and the new, tertiary motion can be characterized by the axial and azimuthal wavenumber. These tertiary motions sensitively depend on the history of the flow. Coles [5] produced as many as 25 different motions at the same Taylor number showing that preference for every single one is only marginal. As the Taylor number is varied, transitions from one state to another occur. It was earlier thought that these wavy vortices are the ultimate laminar motion before breakdown into turbulence. High-resolution power spectra of the time-dependent flow have shown, however, that the wavy vortices with only one characteristic frequency evolve into a quasi-periodic motion with two incommensurate frequencies, before broadening of the spectrum occurs at even higher Taylor numbers. The broadening of the spectrum is the widely accepted operational definition for the occurrence of turbulence. The turbulent motion [2, Fig. 131] exhibits chaotic, i.e. nonperiodic behavior with a superposed regular structure similar to the laminar Taylor vortices.

The experiments on the Taylor-Couette problem provide a particularly clear picture of the discrete steps in the transition to turbulence, and challenge theoretical explanation. Obviously, our description is incomplete and more detail can be found in the articles by DiPrima [6] and DiPrima and Swinney in [4]. More recent work is summarized in [7].

A completely different and rather sketchy picture of the nonlinear phenomena emerges from those cases where nonlinearity tends to enhance the growth predicted by the linear theory. No clue can be found for unstable disturbances. In the linearly stable region, however, weak decay of normal modes may be counterbalanced or outweighed by nonlinear destabilization in the presence of a finite-amplitude disturbance background. This nonlinear instability is held responsible for the occurrence of transition in plane Poiseuille flow at Reynolds numbers far below the critical value. If secondary motions exist in the stable domain, they must be unstable. No experimental evidence has been found for any stable secondary motion different from turbulent flow. It seems therefore that turbulence directly develops from linear or nonlinear instability at fixed Reynolds number. This evolution is radically different from the discrete steps of transition in the Rayleigh-Bénard or Taylor-Couette problem.

Nonlinear instability must also be employed for explaining the origin of turbulence in the Hagen-Poiseuille flow in a circular pipe and in plane Couette flow. Both these flows are stable for all Reynolds numbers according to linear stability theory. After 100 years of stability research, it is embarrassing to realize that little can be added to Reynold's suggestion (see above). This extreme example of pipe flow, however, shows the enormous difficulty of solving nonlinear stability problems and gives appreciation for the progress achieved in other fields.

This progress is due to a combination of experimental, analytical, numerical, and mathematical work. Development of a multitude of methods and application to the variety of nonlinear phenomena has produced an enormous body of scientific results that are scattered over the literature. Some basic concepts and results are discussed in the monograph [8] and with more emphasis on the mathematical bifurcation theory in [9,10]. The collection [4] of interdisciplinary contributions provides an excellent overview and up-to-date references. Complementary information on transition in shear flows is given in [11].

In the following, we briefly characterize the methods of approaching nonlinear problems: weakly nonlinear theory, computer simulation, bifurcation theory, and dynamical systems theory. The weakly nonlinear theory for extending the results of the linear theory for single modes is discussed in section 3. Models of weakly nonlinear interactions of modes are reviewed in section 4. The Taylor-Couette flow and plane Poiseuille flow are used as prototypes, with occasional reference to the Rayleigh-Bénard problem.

2. ANALYSIS OF NONLINEAR PROBLEMS

In view of the difficulties posed by the nonlinearity itself, it seems natural to avoid any additional complications of the problem. Therefore, the most powerful methods exist for the simplest problems: the temporal development of the motion in infinite geometry. Little can yet be done for the spatially developing boundary layers or mixing layers.

Historically, the "weakly nonlinear theory" of stability developed first. This theory is in fact a standard perturbation method [12] using expansions about the solution of the linear problem. Perturbation methods represent the solution $\underset{\sim}{f} = \underset{\sim}{f}(\underset{\sim}{x},\epsilon)$ of a nonlinear problem by an expansion

$$\underset{\sim}{f}(\underset{\sim}{x},\epsilon) = \sum_{m=0}^{\infty} \underset{\sim}{f}_m(\underset{\sim}{x})\epsilon^m = \underset{\sim}{f}_0(\underset{\sim}{x}) + \epsilon\underset{\sim}{f}_1(\underset{\sim}{x}) + \dots \tag{1}$$

in terms of some parameter (or variable) ϵ that appears naturally or artificially in the problem. After finding the solution $\underset{\sim}{f}_0(\underset{\sim}{x})$ of the equations for $\epsilon=0$, the functions $\underset{\sim}{f}_m(\underset{\sim}{x})$ are usually governed by a sequence of linear equations which can be solved sequentially. Normally, the series (1) is truncated after the first nonzero correction. This may provide valuable results on tendencies of the solution such as the gradient $\partial\underset{\sim}{f}/\partial\epsilon$ close to $\epsilon=0$ or on the solution for some range of ϵ. However, the validity of the results at finite values of ϵ can only be assessed with information on the convergence of the series (1). This information can be obtained by calculating higher-order terms in ϵ and applying techniques for the analysis and improvement of perturbation series [13].

In the weakly nonlinear stability theory, the (equilibrium or time-dependent) amplitude of a normal mode is used as expansion parameter ϵ while $\underset{\sim}{f}_0$ is the solution of the linear problem. Expansions in the equilibrium amplitude, $\epsilon=A_e$, are especially suited for obtaining the asymptotic secondary motions in the neighborhood of neutral solutions $\underset{\sim}{f}_0$. Expansions in the time-dependent amplitude, $\epsilon=A(t)$, provide as part of the solution a nonlinear ordinary differential equation ("Landau equation") for $A(t)$, typically of the form

$$\frac{dA}{dt} = a_0 A + a_1 A^3 + a_2 A^5 + \dots \tag{2}$$

with numerical coefficients ("Landau constants"). This equation yields the nonlinear growth of an unstable disturbance as well as the equilibrium amplitude A_e for $dA_e/dt = 0$. A detailed discussion of various methods, references, and improvements for expansions in $A(t)$ are given in [14].

The theory can also be applied for studying the secondary instability and nonlinear interaction of normal modes. In the latter case, expansions in time-dependent amplitudes provide coupled systems of

amplitude equations in just the form studied by mathematical theories. It is this link that makes the weakly nonlinear theory a particularly attractive tool. The selection of normal modes for the composition of relevant weakly nonlinear models, however, requires guidance by known results (e.g. observation) or physical intuition. In this sense, the weakly nonlinear theory cannot be considered a systematic method for analyzing nonlinear phenomena.

Except in rare cases [15], the solutions f_0 of the linear problem and the nonlinear contributions f_m in (1) can only be found numerically. One might therefore consider solving the whole problem by means of numerical methods. The analysis of secondary motions can be reduced to solving a nonlinear eigenvalue problem for the coefficients (functions) in a truncated Fourier expansion of the motion. The analysis of nonlinear growth and equilibration rests on an initial-value problem for a similar system of nonlinear equations. For some time, this approach was hampered by insufficient quality of the numerical methods. Especially when solving partial differential equations, effects of artificial (numerical) viscosity or phase errors in finite-difference methods may falsify the results even when sufficient resolution can be maintained. The use of improved finite-difference schemes, and in particular the application of spectral methods [16] made the computational approach a reliable tool for analyzing certain nonlinear phenomena without resort to prior modeling.

The solution of nonlinear eigenvalue problems for ordinary differential equations takes profit from the high resolution of spectral expansions with relatively few coefficients. These coefficients are governed by nonlinear algebraic equations that can be solved by standard iteration techniques (e.g. Newton's method in combination with an arc-length continuation method). Using these techniques, accurate solutions were obtained for finite-amplitude convection rolls [17], Taylor vortices [18] and secondary motions in plane Poiseuille flow [19]. Similar computations using finite-difference methods are reported in [20,21]. The nonlinear eigenvalue problem provides the secondary motion disregarding the stability or instability of the solution. The secondary motions provide a basis for the subsequent analysis of secondary instability [17,18,22].

Computational methods for the initial value problem seek in general for the solution of the full equations of motion in a finite size box limited by the physical walls in one direction. Periodicity of the solution is assumed in the variables parallel to the wall. Fourier expansions in these variables can be seen as a concept of the spectral method or as a nonlinear extension of the normal-mode concept. Obviously, the solution depends not only on the initial conditions but also on the size of the box. Since the computations (especially in three dimensions) are rather demanding, the box is usually chosen according to the wavelength of the normal mode under consideration. This prevents from the analysis of phenomena with scales larger than this wavelength, such as the occurrence of period-doubling or the nonlinear selection of the wavelength, e.g. of the Taylor vortices in [2, Fig. 127]. The use of a larger computational box, however, is only a matter of computer time and storage.

Numerous solutions of essentially two-dimensional problems have been reported. Numerical simulations in three dimensions - some of them with finite-difference methods - have been carried out for thermal convection [23], plane Poiseuille flow [24-26], and for the Taylor problem by Marcus and Moser, see [7]. To some extent, the results are like experimental data, but more quantities are recorded simultaneously at many points in space. The value of the numerical simulation depends largely on the post-processing of the raw data. The problem of retrieving from the overwhelming mass of data the essence of the mechanisms at work and an intelligible set of quantitative information is not a trivial task.

As expected from observations, simulations of convection flows or flows between rotating cylinders provide at fixed R the asymptotic equilibrium solution. Repeated runs are necessary in order to cover the different flow regimes at increasing values of R. In contrast, a single run for Poiseuille flow comprises all the stages of transition to turbulence at fixed R. After a finite time, the solution breaks down due to insufficient resolution for the fine scales that arise with the broadening of the spectrum. Computer experiments on Poiseuille flow are very valuable for bridging the gap between the temporal growth concept of the theory and the spatial development of disturbances in shear-flow experiments. The simulation of the spatial development is still hampered by the problem of formulating transparent boundary conditions at the exit of the computational box.

A third group of methods for the analysis of nonlinear phenomena is of a predominantly mathematical nature. The goal of these methods is obviously not the construction of solutions for the comparison with experiments, but increasing the insight into general properties of nonlinear systems and a classification of common patterns of solutions. Often, these methods use simple model equations that show properties similar to hydrodynamic systems, and even these simple equations usually must be solved numerically. The technical terms are sometimes difficult to comprehend for the non-mathematician and the relation between turbulence and the chaotic "strange attractor" is still a matter of controversial discussion [27]. The mathematical theories, however, have not only contributed the conceptual framework for a new generation of experiments, straightened out and enriched the terminology, but also revised various misconceptions of the behavior of deterministic nonlinear systems.

Stability analysis is, in other words, the struggle with the nonuniqueness of the solutions of nonlinear equations. How many solutions exist, which ones are stable, how are they connected as the parameter R varies? The bifurcation theory aims at answering these questions for abstract evolution equations of the form

$$\frac{d\underset{\sim}{u}}{dt} = \underset{\sim}{F}(\underset{\sim}{u}, R) \qquad (3)$$

where R is a parameter, $\underset{\sim}{F}$ some nonlinear function, and $\underset{\sim}{u}$ a vector field. The Navier-Stokes equations can be projected into this form and $\underset{\sim}{u}$ is considered the difference between the actual motion and the

basic flow which exists for all R. Typically, a first theorem states that $\underset{\sim}{u} \equiv 0$ is the only solution for sufficiently small R>0. Consequently, nonuniqueness of the solution at higher values of R must originate from the splitting, or bifurcation of solutions. These bifurcations can be studied using the simpler scalar problem

$$\frac{dA}{dt} = F(A,R) \tag{4}$$

where $A=A(t)$ can be interpreted as the amplitude of $\underset{\sim}{u}$. The classification of bifurcations and stable branches rests on the steady (or equilibrium) solutions of (4). The results can be given in the form of definitions and theorems but also as bifurcation diagrams. A small collection of such diagrams for the first bifurcation is shown in Fig. 2. Solid and dashed lines represent branches with stable and unstable solutions, respectively. The relation between stability diagram and bifurcation diagram is as follows: we extend the neutral curve (for A→0) in Fig. 1 into a "neutral surface" in the third dimension, amplitude A, and cut this surface at a fixed wavenumber α_0. The associated point R_0 of the neutral curve is the bifurcation point; α_0 is absorbed into the function F in (4). The case of "bifurcation to the right", or supercritical stability in Fig. 2a is obviously related to the observations in the Taylor-Couette problem: Couette flow is stable up to R_0 where stability is exchanged with Taylor vortices of amplitude A (the distinction between $\pm$A is redundant). For small A, the case of subcritical instability in Fig. 2b is characteristic for plane Poiseuille

Figure 2. Schematic bifurcation diagrams.

flow. The turning points into stable, large-amplitude motions (turbulent?) result from the uniqueness of the basic flow at low R. A tentative picture for pipe flow is given in Fig. 2c with a bifurcation point at infinity [28]. Note that the amplitude equation (2) has the form of equation (4) since the Landau constants depend on R. With the approximations $a_0 \sim (R-R_0)$, $a_1 \approx$ const. in the neighborhood of R_0, we obtain at lowest order for the steady solution $A_e \sim [-(R-R_0)/a_1]1/2$ which qualitatively agrees with Fig. 2a and 2b for $a_1 < 0$ and $a_1 > 0$, respectively. Fig. 2d is for an amplitude equation of the type $dA/dt = a_0A + a_1A^2 + a_2A^3$, with an unusual quadratic term. Fig. 2e shows a bifurcation similar to Fig. 2a in the presence of an imperfection, $dA/dt = a_0A + a_1A^3 + c$. This equation holds for the Taylor-Couette problem in finite-length cylinders [29] with c proportional to the ratio of gap width to cylinder length. Note that this realistic situation exhibits no bifurcation point. The abnormal solution (A<0) has been experimentally verified [30].

For stable branches, repeated bifurcation of the various types may occur at larger values of R. In mathematical terms, bifurcation is associated with the breaking of symmetries, i.e. with the dependence of the new solution on additional variables or the loss of regular properties such as simple periodicity. The question then arises how many steps (bifurcations) are necessary to convert the basic flow into the chaotic, turbulent motion. The early model of Landau [31] predicted an infinite number of steps that lead to a discrete spectrum with an enumerable set of lines. Fortunately, Landau's model seems not to be relevant to hydrodynamic systems. (Otherwise, any attempt to model this cascade would be condemned to fail.) Ruelle & Takens [32] showed that the cascade leads after a small number of bifurcations to nonperiodic, chaotic behavior of the solutions. In fact, these solutions with a continuous broad-band spectrum are less ordered or regular than Landau's model flows. Support to this more tractable cascade towards chaos was given by Ruelle's concept of "sensitivity to initial conditions" [33] that shed new light on deterministic systems. According to this concept, the nonrepeatable nature of solutions typical for turbulent motions can be understood without resorting to statistical methods.

Important contributions in this field were provided by the qualitative theory of ordinary differential equations, or dynamical systems theory. Simple systems with ⩾ 3 degrees of freedom show a variety of solutions with properties corresponding to the observations in thermal convection or in the flow between concentric cylinders. The Lorenz equations [34] are meanwhile a classical example (see also Yorke & Yorke in [4]):

$$\frac{dx}{dt} = -\sigma x + \sigma y,$$

$$\frac{dy}{dt} = -xz + rx - y, \tag{5}$$

$$\frac{dz}{dt} = xy - bz.$$
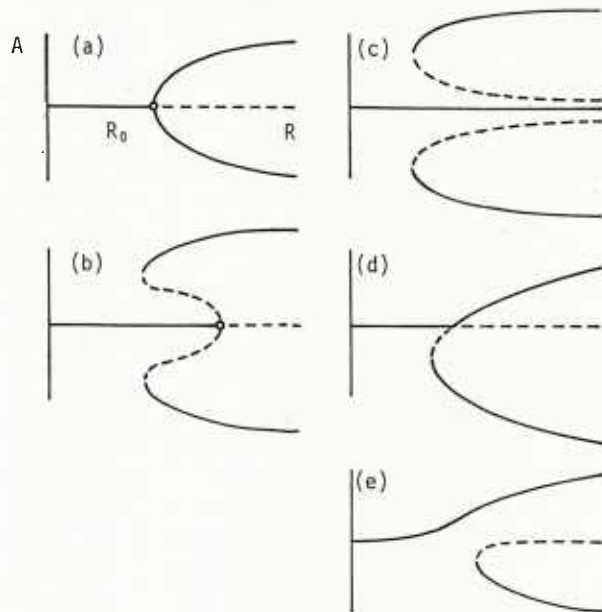
Depending on the values of the parameters σ, r and b, this system exhibits a basic state (x=y=z=0), steady solutions, time-periodic and nonperiodic solutions. When solving equations (5) numerically, extreme care is required due to the sensitivity of the solution to round-off and truncation errors. Solutions that start very close to each other may be far apart at later times. More detail about the Lorenz system and similar systems as well as graphs of spectra and "strange attractors" can be found in [35].

The interest in systems as "simple" as (5) is not surprising; such systems can be considered as coupled amplitude equations as they are obtained from weakly nonlinear models. In fact, the Lorenz equations represent a model for a convection problem (see Yorke & Yorke [4]) and Busse [36] found another interesting system that describes his observations on weakly turbulent convection in a rotating fluid layer. However, for those working with shear flows, the chaotic motion lacks the violence of the observed turbulent motions, and some important ingredient seems to be missing in the nonlinear systems currently studied. The trajectories of the solutions in the phase space are too smooth for the strange attractor to be a generally accepted model of shear flow turbulence.

3. WEAKLY NONLINEAR ANALYSIS OF A SINGLE MODE

In view of the important role of systems of amplitude equations in the analysis of nonlinear effects, it is surprising to find rather few thorough investigations. Often, only asymptotic estimates of the Landau coefficients are given. Usually the equations are truncated at the lowest possible order. Obviously, the formulation of higher-order terms for solutions of the Navier-Stokes equations can be very tedious when done by hand. However, this work can be delegated to the computer. Simultaneously, the computer program generates the formal expansion, collects the terms that appear in the equations, and finally solves these equations. Once this program is written, it can be easily adapted to other flows, other equations with quadratic nonlinearity, other expansion parameters, or extended for the analysis of secondary instability or the interaction of modes.

As an example, we consider the nonlinear growth of a two-dimensional T-S wave in plane Poiseuille flow. The disturbance can be written in terms of a single scalar streamfunction ψ. This case also shows the nonlinear effect on the phase velocity that is missing in the Taylor-Couette problem. We expand in the amplitude $A(t)$ in a similar way as Stuart [36] and Watson [37]. However, the formulation given here [14] avoids the nonuniqueness that appeared in Watson's method and is not restricted to the neighborhood of the neutral curve.

With x in the streamwise direction and the channel walls at $y=\pm1$, the linear theory provides normal modes in the form

$$\psi(x,y,t) = e^{a_0 t}\phi_{10}(y)e^{i(\alpha x - \omega_0 t)}, \tag{6}$$

where α is the wavenumber, a_0 the amplification rate and ω_0 the frequency. For given values of R and α, $\lambda_0 = a_0 - i\omega_0$ is the principal eigenvalue of the Orr-Sommerfeld problem and $\phi_{10}(y)$ the related eigenfunction. If nonlinear terms are taken into account, the disturbance reacts with itself, with its complex conjugate, and with the mean flow - which results in the generation of harmonics, a mean-flow distortion, and a distortion of the fundamental, respectively. Moreover, the frequency and amplification rate will change with the finite size of the disturbance. Therefore it seems natural to represent the nonlinear disturbance as the Fourier series

$$\psi(x,y,t) = \sum_{n=-\infty}^{\infty} \psi_n(y,t)e^{in\theta}, \quad \theta = \alpha x - \gamma(t). \tag{7}$$

With real $\gamma(t)$ any growth of the disturbance is absorbed into the Fourier coefficients ψ_n. For a real solution, we must satisfy $\psi_{-n}=\psi_n^\dagger$, where $\dagger$ denotes the complex conjugate. We define the (real) amplitude by

$$A(t) = |\psi_1(0,t)| \tag{8}$$

A straightforward expansion procedure [14] then provides

$$\psi_n(y,t) = A^{|n|}\phi_n(y,t), \tag{9}$$

$$\phi_n(y,t) = \sum_{m=0}^{\infty} \phi_{nm}(y)A^{2m}, \quad \phi_{00}\equiv 0, \tag{10}$$

$$\lambda = \sum_{m=0}^{\infty} \lambda_m A^{2m}, \quad \lambda_m = a_m - i\omega_m. \tag{11}$$

where

$$\lambda = \frac{1}{A} \frac{dA}{dt} - i \frac{d\gamma}{dt} \tag{12}$$

The λ_m and ϕ_{nm} for $n,m > 0$ are governed by the equations

$$\{L_n - (2ma_0 + n\lambda_0)D_n\} \phi_{nm} = g_{nm} + f_{nm} \tag{13}$$

where

$$L_n = \frac{1}{R} D_n^2 - in\alpha(UD_n - U''), \quad D_n = \frac{d^2}{dy^2} - n^2\alpha^2 \tag{14}$$

$$g_{nm} = \sum_{(1)} (2\ell a_\mu + n\lambda_\mu)D_n\phi_{n\ell} \tag{15}$$

$$f_{nm} = i\alpha \sum_{(2)} (k\phi'_{\nu\mu} - \nu\phi_{\nu\mu} \frac{d}{dy}) D_k\phi_{k\ell}. \tag{16}$$

$U=U(y)$ is the basic flow and the prime denotes d/dy. The summations will be defined shortly. The boundary conditions are

$$\phi'_{0m} = \phi''_{0m} = \phi'_{nm} = \phi_{nm} = 0, \quad n > 0 \quad \text{at } y = \pm 1 \tag{17}$$

The conditions on ϕ''_{0m} originate from the assumption of a fixed mean-pressure gradient. The ϕ_{0m} are determined to within an arbitrary constant, as usual for the streamfunction. For the fundamental, we obtain with (8) the additional conditions

$$\phi_{10}(0) = 1, \quad \phi_{1m}(0) = 0, \quad m > 0. \tag{18}$$

The ordinary differential equations can be solved in the sequence of ascending order in A of the terms. The solution proceeds line by line from left to right in Table 1.

	ψ_0	ψ_1	ψ_2	ψ_3	ψ_4	ψ_5 $\cdots$
A		λ_0, ϕ_{10}				
A^2	ϕ_{01}		ϕ_{20}			
A^3		λ_1, ϕ_{11}		ϕ_{30}		
A^4	ϕ_{02}		ϕ_{21}		ϕ_{40}	
A^5		λ_2, ϕ_{12}		ϕ_{31}		ϕ_{50}
$\cdots$		$\cdots\cdots\cdots$				

Table 1.

At any order, summation (1) collects the terms containing the Landau constants λ_μ, $\mu \neq 0$ that appear up to and including this order such that $\mu + \ell = m$. Summation (2) collects all the terms containing lower-order functions $\phi_{\nu\mu}$, $\phi_{\nu\mu}^T (= \phi_{-\nu,\mu})$ such that $\nu + k = n$, $\mu + \ell = m$. At first order, both summations are empty, and (13) - (17) reduce to the homogeneous Orr-Sommerfeld problem for λ_0, ϕ_{10} subject to the normalization (18). We assume that a boundary-value method is available (e.g. spectral collocation with Chebyshev polynomials) for converting the Orr-Sommerfeld problem into an algebraic eigenvalue problem. With an initial guess for λ_0, we find λ_0, ϕ_{10} by using standard iterative procedures. At order A^2, summation (1) is still empty, but summation (2) provides inhomogeneous terms. ϕ_{01} and ϕ_{20} are obtained by solving inhomogeneous algebraic systems. At order A^3, summation (2) provides f_{11} and summation (1) contains the yet unknown λ_1 multiplied with a known function. We augment the algebraic system in a similar way as for the linear problem with λ_0, ϕ_{10}: introduce an extra column for the unknown λ_1 and an extra row in order to satisfy (18). Solving the augmented inhomogeneous system is straightforward. No adjoint function is needed nor is any distinction to be made between the different definitions of the Landau constant [14]. At this level we have already exceeded (by solving for ϕ_{11}) the usual level of approximation. However, completing the line with ϕ_{30} and continuing to higher order is bare routine. The only new step comes with the equation for ϕ_{12}: the part of g_{12} that depends only on the lower-order Landau constants is added to f_{12} on the right-hand side. In a modular program, the now existing modules can be cyclically called over and over up to arbitrary order. Apart from computer time and storage, the change from the lowest truncation to the high-order approach requires little extra effort. Based on the principle that higher-order terms arise from products of lower-order terms, the summations (1) and (2) can be automatically performed using tables of the already available parts of the solution. As a rule of thumb, solving up to λ_2, ϕ_{12} requires twice the computer time for solving the linear problem. Our program consists of about 250 Fortran statements, including input/output, eigenvalue search, and a special routine for solving algebraic systems.

The question on the validity arises in two respects: for the solution and for the expansion procedure itself. Obviously, the solution in form of the series (10) - (11) converges only for sufficiently small values of A^2. The radius ρ of convergence in the complex plane is limited by the singularity nearest to the origin. If the amplitudes of physical interest are inside this radius, $A^2 < \rho$, the series provides a valid approximation. If the nearest singularity appears on the positive real axis, it may have physical meaning and requires further consideration. Often, however, the singularity is located somewhere in the complex plane or on the negative real axis and has no physical meaning since $A^2 > 0$ and real. These nonphysical singularities can restrict ρ to very small values and in fact to $\rho = 0$. Outside this small radius, the series produces useless results no matter how many terms are taken into account. Nevertheless, the information concealed in the higher-order terms can be profitable. Techniques are available [13] for estimating the radius of convergence, for studying the location and nature of the nearest singularity, and for recasting the series in a more suitable form.

Invalidity of the expansion procedure is indicated by resonance in the equations (13) for ϕ_{nm}, $n \neq 1$. Resonance occurs whenever $2ma_0 + n\lambda_0$ coincides with an eigenvalue of the homogeneous problem for ϕ_{nm}, $n \neq 1$. In this case the inhomogeneous problem cannot be solved, except if an orthogonality condition can be satisfied by varying a free Landau constant. Such constants are not available for $n \neq 1$. A serious case of invalidity occurs when expansions in $A(t)$ are used in the stable domain, $a_0 < 0$, due to resonance for $n=0$ [14]. For $a_0 > 0$, resonance with unstable harmonics, $n>1$, can sometimes occur. This case is of physical interest and can be analyzed by using a model with two (or more) interacting modes.

The main result of the weakly nonlinear analysis based on $A(t)$ is the series (11) with known numerical coefficients λ_m. According to (12), the real part provides the amplitude equation (2) while the imaginary part describes the nonlinear changes of the frequency. The amplitude A_e of the equilibrium states which may asymptotically evolve from a growing mode can be found from (2) by letting $dA/dt = 0$, if $A_e^2 < \rho$. The expansion in $A(t)$ is for fixed R, α and provides only the values of A_e at this point. If the analysis aims only at the equilibrium states, an expansion in powers of A_e can be used. The formalism is very similar to that given above. Insteady of the series for $dA/dt \, (\equiv 0)$, a series $R = R_0 + R_1 A_e^2 + \ldots$ is obtained, where R_0, α is a point on the neutral curve. This series directly describes the branches of the bifurcation diagram as long as $A_e^2 < \rho$.

A survey of applications to our prototype flows and references are given in [14]. A study on Poiseuille flow with emphasis on the convergence problem appeared recently [38]. The results verify the subcritical instability of plane Poiseuille flow and the supercritical stability of convection cells and Taylor vortices in the neighborhood of the critical point. Results from higher approximations often agree with computational results for a considerable range of amplitudes. However, ongoing work [39] on expansions for equilibrium states in the Poiseuille flow has also shown that the radius of convergence can indeed be zero.

4. WEAKLY NONLINEAR MODELS

For a given flow and a supercritical value of R, the linear theory often predicts instability or very weak stability for many different normal modes. Weakly nonlinear models are formed by superposing different modes for the purpose of deriving amplitude equations and finding simple mechanisms of observed phenomena. Any number of such models can be constructed by choosing members from the pool of normal modes and ordering their amplitudes. In the following, we discuss a selection of well established models, noting that in some cases the final proof of relevance is still missing.

In the Taylor-Couette problem, the existence of finite-amplitude Taylor vortices for R slightly above the critical value R_c can be established for single modes in a band of wavenumbers. However, the observed vortices [4, Fig. 6.5, p. 155] have wavenumbers very close to the critical value α_c. An explanation could arise from the model of side-band instability: a finite amplitude Taylor vortex of amplitude A_e and wavenumber α could be unstable with respect to disturbances of wavenumbers $\alpha + \Delta\alpha$, $\alpha - \Delta\alpha$ and small (background noise) amplitudes B, C, respectively, where B, $C \ll A_e$. At lowest order, B and C are governed by the amplitude equations

$$\frac{dB}{dt} = b_0 B + (b_1 B + b_2 C)A_e^2, \quad \frac{dC}{dt} = c_0 C + (c_1 C + c_2 B)A_e^2 \tag{19}$$

where b_0, c_0 are the linear growth rates and $A_e^2 = -a_0/a_1$ from eq. (2). Estimates in the neighborhood of the critical point provide $b_1 \approx c_1 \approx 2a_1$, $b_2 \approx c_2 \approx a_1$ and therefore

$$\frac{dB}{dt} \approx (b_0 - 2a_0)B - a_0 C, \quad \frac{dC}{dt} \approx (c_0 - 2a_0)C - a_0 B \tag{20}$$

Considering the constant coefficients, the solution can be sought in the form B, $C \sim e^{\lambda t}$. With a parabolic approximation for the growth rate as a function of α, one finds instability of the Taylor vortex, $\lambda > 0$, outside a band $(1/3)^{1/2}$ times the unstable band predicted by the linear theory centered at α_c. The band width for stable Taylor vortices shrinks if a more accurate approximation (5th order terms in (2)) for the Taylor vortices is used [40], but there still remains a significant difference between theoretical and experimental results.

In a more general framework [41], the side-band instability was studied using the nonlinear Schrödinger equation

$$\frac{\partial A}{\partial t} - b \frac{\partial^2 A}{\partial z^2} = a_0 A + a_1 |A|^2 A \qquad (21)$$

where z is the coordinate of spatial periodicity (axial in the Taylor-Couette problem). This equation for the complex amplitude $A(z,t)$ governs the weakly nonlinar development of a wave packet in the neighborhood of the critical point. This study established the relation between side-band instability and the Benjamin-Feir instability of water waves and extended the theory for wave disturbances which are associated with complex eigenvalues. A survey on applications of (21) to hydrodynamic stability problems is given in [42].

Once the existence of finite-amplitude Taylor vortices with $\alpha \approx \alpha_c$ is established, the onset and formation of wavy vortices can be studied. Especially attractive is the case of small gap width, where waviness appears at rather small amplitude of the Taylor vortices. The physical model seems obvious since the linear theory predicts instability of the Couette flow with respect to nonaxisymmetric modes at supercritical values of R. These modes can be characterized by the number m of azimuthal waves, with m=0 for Taylor vortices. The model currently in use studies the interaction of six modes, and accordingly, the amplitude equations are somewhat lengthy. Some equations and the main results are given in [6]. The model predicts the onset and characteristics (e.g. the torque) of wavy vortices for given m in reasonable agreement with experimental and computational results. However, a new selection problem arises since wavy vortices with different may occur as R increases. Our preliminary results have shown that the instability of a wavy vortex with α_1, m_1 with respect to another wavy vortex with α_2, m_2 can be studied with an extended model. The increasing complexity of the amplitude equations poses no problem if these equations are generated by a computer program. The dramatic increase in the number of terms, however, restricts the analysis to relatively low order.

Attempts have also been made [43] to derive the quasi-periodic and chaotic motion between rotating cylinders from large systems of amplitude equations for a finite number of Fourier components in the axial and azimuthal direction. Although some aspects of the observations are reproduced, the model has not given a quantitative description of the flow phenomena.

For shear flows, weakly nonlinear models were primarily developed in order to explain the spanwise periodic, three-dimensional phenomena in the transition region of boundary layers. Little experimental guidance has been available on the choice of modes. A discussion of the principal models is given in [44] which is here complemented by recent results. For a shorter notation, we denote the modes by $A\{\alpha,\beta\}$, where A is the complex amplitude and α,β are the streamwise and spanwise wavenumber, respectively. We also understand that the complex conjugate mode is included when necessary, as well as the mode $A\{\alpha,-\beta\}$ for $\beta \neq 0$. All modes are principal modes of the Orr-Sommerfeld problem.

The Benney-Lin model considers the interaction between a two-dimensional wave $A\{\alpha,0\}$ and an oblique wave $B\{\alpha,\beta\}$ with arbitrary β. This model yields the amplitude equations

$$\frac{dA}{dt} = A(a_0 + a_1 |A|^2 + a_2 |B|^2) + a_3 B^2 A^\dagger, \qquad \frac{dB}{dt} = B(b_0 + b_1 |B|^2 + b_2 |A|^2) + b_3 A^2 B^\dagger. \qquad (22)$$

In the light of resonant wave interactions, the case of synchronization between the waves is of special interest. The linear theory predicts phase velocities of the waves which typically differ by 15%. Itoh [45] has shown that nonlinear synchronization can occur at reasonable finite amplitudes. However, the results are not fully conclusive regarding the relevance of this model in plane Poiseuille flow. Results for the boundary layer [46] seem to support the Benney-Lin mechanism. The analysis of the secondary instability based on a Floquet system [47], however, has clearly revealed that the principal mode of three-dimensional instability in Poiseuille flow does not originate from the Benney-Lin mechanism.

The Craik model of a resonant triad between $A\{\alpha,0\}$ and a subharmonic mode $B\{\alpha/2, \beta\}$ leads to two equations with a second-order interaction,

$$\frac{dA}{dt} = a_0 A + a_1 B^2, \qquad \frac{dB}{dt} = b_0 B + b_1 A B^\dagger. \qquad (23)$$

Resonance or synchronization between the waves can occur at the linear level for a specific wavenumber $\beta = \beta^*$. In Poiseuille flow, this mechanism is inactive by reasons of symmetry. Subharmonic three-dimensional instability in Poiseuille flow [22] originates from a near-resonant triad between $A\{\alpha,0\}$ and eigensolutions of the Squire equation for the vorticity component normal to the wall. In the boundary layer, this mechanism acts in cooperation with Craik's mechanism [48]. In other words, Craik's model is relevant but incomplete.

A similar statement holds for the model [44] of a parametrical excitation of streamwise vortices $B\{0,\beta\}$ by two-dimensional waves. For $B<<A$ this provides an amplitude equation

$$\frac{dB}{dt} = B(b_0 + b_1 |A|^2) \qquad (24)$$

and the weak decay b_0 can be outweighed if $b_1 > 0$. The results for the threshold amplitude $|A_t| = (-b_0/b_1)^{1/2}$ given in [44] reveal the pitfalls of the weakly nonlinear modeling. Independent analysis of the parametrical secondary instability [47] shows that these threshold amplitudes are a reasonable approximation only for $\beta \approx 1$. At lower β, the results suffer from the low order of

truncation. At larger β, the use of (24) fails to provide low threshold amplitudes since a second spanwise periodic mode is important for the instability mechanism but is not included in the model.

The analysis of the three-dimensional phenomena in shear flows as an instability of a streamwise periodic flow will be discussed in the next lecture. This analysis provides for the first time a catalogue of the normal modes which are crucial for the various types of resonant wave interaction in shear flows. This catalogue can be utilized for constructing improved weakly nonlinear models.

ACKNOWLEDGMENT

REFERENCES

[1] Reynolds, O., "An experimental investigation of the circumstances which determine whether the motion of water shall be direct or sinuous, and of the law of resistance in parallel channels," Phil. Trans. R. Soc. 174, 935-982 (1883).

[2] VanDyke, M. (ed.), Album of Fluid Motion, Parabolic Press (1982).

[3] Busse, F. H., "Non-linear properties of thermal convection," Rep. Prog. Phys. 41, 1929-1967 (1978).

[4] Swinney, H. L. & Gollub, J. P., Hydrodynamic instabilities and the Transition to Turbulence, Springer-Verlag (1981).

[5] Coles, D., "Transition in circular Couette flow," J. Fluid Mech. 21, 385-425 (1965).

[6] DiPrima, R. C., "Transition in flows between circular cylinders," in: Transition and Turbulence (ed. R. E. Meyer), 1-23, Academic Press (1981).

[7] Park, K. & Donnelly, R. J. (eds.), Summary of the Workshop,"60th Anniversary Taylor Vortex Flow," June 12-15, 1983, Eugene, Oregon.

[8] Drazin, P. & Reid, W. Hydrodynamic Stability, Cambridge University Press (1981).

[9] Joseph, D. D., Stability of Fluid Motions, Vol. I & II, Springer-Verlag (1976).

[10] Iooss, G. & Joseph, D. D., Elementary Stability and Bifurcation Theory, Springer-Verlag (1980).

[11] Morkovin, M. V., "Understanding transition to turbulence in shear layers - 1983," AFOSR Final Report AD-A134796 (1983).

[12] Nayfeh, A. H., Perturbation Methods, Wiley (1973).

[13] VanDyke, M., "Computer-extended series," Ann. Rev. Fluid Mech. 16, 287-309 (1984).

[14] Herbert, Th., "On perturbation methods in nonlinear stability theory," J. Fluid Mech. 126, 167-186 (1983).

[15] Kuo, H. L., "Solution of the non-linear equations of cellular convection and heat transport," J. Fluid Mech. 10, 611-634 (1961).

[16] Orszag, S. A. & Israeli, M., "Numerical simulation of viscous incompressible flows," Ann. Rev. Fluid Mech. 6, 281-318 (1974).

[17] Clever, R. M. & Busse, F. H., "Transition to time-dependent convection," J. Fluid Mech. 65, 625-645 (1974).

[18] Jones, C. A., "Nonlinear Taylor vortices and their stability," J. Fluid Mech. 102, 249-261 (1981).

[19] Herbert, Th., "Finite-amplitude stability of plane parallel flows," AGARD CP-224, 3/1-10 (1977).

[20] Zahn, J.-P., Toomre, J., Spiegel, E. A. & Gough, D. O., "Nonlinear cellular motions in Poiseuille channel flow," J. Fluid Mech. 64, 319-345 (1974).

[21] Meyer-Spasche, R. & Keller, H. B., "Computation of the axisymmetric flow between rotating cylinders," J. Comp. Phys. 35, 100-109 (1980).

[22] Herbert, Th., "Secondary instability of plane channel flow to subharmonic three-dimensional disturbances," Phys Fluids. 26, 871-874 (1983).

[23] Lipps, F. B., "Numerical simulation of three-dimensional Bénard convection in air," J. Fluid Mech. 75, 113-148 (1976).

[24] Orszag, S. A. & Kells, L. C., "Transition to turbulence in plane Poiseuille flow and plane Couette flow," J. Fluid Mech. 96, 159-206 (1980).

[25] Kleiser, L., "Spectral simulations of laminar-turbulent transition in plane Poiseuille flow and comparison with experiments," Springer Lecture Notes in Physics 170, 280-287 (1982).

[26] Biringen, S., "A numerical simulation of transition in plane channel flow," AIAA Paper No. 83-0047 (1983).

[27] Tatsumi, T. (ed.), Proc. IUTAM Symposium "Turbulence and Chaotic Phenomena in Fluids," 5-10 Sept. 1983, Kyoto, Japan.

[28] Rosenblat, S. & Davis, S. H., "Bifurcation from infinity," SIAM J. Appl. Math. 37, 1-19 (1979).

[29] Hall, P., "Centrifugal instabilities in finite containers: a periodic model," J. Fluid Mech. 99, 575-596 (1980).

[30] Benjamin, T. B., "Bifurcation phenomena in steady flows of a viscous fluid," Proc. Roy. Soc. London A 359, 1-43 (1978).

[31] Landau, L. D., "On the problem of turbulence," C. R. Acad. Sci. URSS 44, 311-314 (1944).

[32] Ruelle, D. & Takens, F., "On the nature of turbulence," Comm. Math. Phys. 20, 167-192 and 23, 343-344 (1971).

[33] Ruelle, D., "Dynamical systems with turbulent behavior," in: Mathematical Problems in Theoretical Physics," Lecture Notes in Physics 80, 341-360, Springer-Verlag (1978).

[34] Lorenz, E. N., "Deterministic nonperiodic flow," J. Atmos. Sci. 20, 130-141 (1963).

[35] Helleman, R. H. G. (ed.), Nonlinear Dynamics, Ann. New York Acad. Sci. 357 (1980).

[36] Stuart, J. T., "On the non-linear mechanics of wave disturbances in stable and unstable parallel flows," Part 1, J. Fluid Mech. 9, 353-370 (1960).

[37] Watson, J., "On the non-linear mechanics of wave disturbances in stable and unstable parallel flows," Part 2, J. Fluid Mech. 9, 371-389 (1960).

[38] Sen, P. K. & Venkateswarlu, D., "On the stability of plane Poiseuille flow to finite-amplitude disturbances, considering high-order Landau coefficients," J. Fluid Mech. 133, 179-206 (1983).

[39] Sethuramalingam, K., "High-order parameter expansions for equilibrium states in plane Poiseuille flow," forthcoming Ph.D. thesis, VPI&SU.

[40] Nakaya, C., "Domain of stable periodic vortex flows in a viscous fluid between concentric circular cylinders," J. Phys. Soc. Japan 36, 1164-1173 (1974).

[41] Stuart, J. T. & DiPrima, R. C., "The Eckhaus and Benjamin-Feir resonance mechanisms," Proc. Roy. Soc. London A 362, 27-41 (1978).

[42] Stewartson, K., "Some aspects of nonlinear stability theory," Fluid Dyn. Trans. 7, 101-128 (1975).

[43] Yahata, H., "Temporal development of the Taylor vortices in a rotating fluid," Prog. Theor. Phys. Suppl. 64, 176-185 (1978), Part II, Prog. Theor. Phys. 61, 791-800 (1979), Part III, Prog. Theor. Phys. 64, 782-793 (1980).

[44] Herbert, Th. & Morkovin, M. V., "Dialogue on bridging some gaps in stability and transition research," in: Laminar-Turbulent Transition (eds. R. Eppler & H. Fasel), 47-72, Springer-Verlag (1980).

[45] Itoh, N., "Three-dimensional growth of finite wave disturbances in plane Poiseuille flow," Trans. Japan Soc. Aeron. Space Sci. 23, 91-103 (1980).

[46] Nakaya, C., "Three-dimensional waves in a boundary layer," in: Laminar-Turbulent Transition (eds. R. Eppler & H. Fasel), 239-242, Springer-Verlag (1980).

[47] Herbert, Th., "Modes of secondary instability in plane Poiseuille flow," to appear in [27].

[48] Herbert, Th., "Subharmonic three-dimensional disturbances in unstable plane shear flows," AIAA Paper No. 83-1759 (1983).

SECONDARY INSTABILITY OF SHEAR FLOWS

Thorwald Herbert
Department of Engineering Science and Mechanics
Virginia Polytechnic Institute and State University
Blacksburg, Virginia 24061, U.S.A.

SUMMARY

A survey is given on the appearance of secondary instability in shear flows. The mixing layer, the flat-plate boundary layer, and plane Poiseuille flow are considered as prototype flows. The computational and analytical work which produced conceptual enlightenment is discussed. A theory of secondary instability is presented: the (almost) periodic flow that develops in the presence of finite-amplitude traveling waves is used as a basic flow for a linear stability analysis with respect to spanwise periodic, three-dimensional disturbances. The Hill-type stability equations with periodic coefficients allow for various classes of normal modes that are associated with different types of resonance. A numerical method for solving the secondary stability problem is discussed. Results for fundamental and subharmonic modes in plane Poiseuille flow are reviewed briefly. The present scope of the theory and its potential for future extensions are discussed.

1. INTRODUCTION

One of the most challenging objectives of the nonlinear stability theory is ultimately the understanding, prediction, and control of transition in shear flows such as duct flows, boundary layers, mixing layers, jets, and wakes. Over the past decades, considerable progress has been achieved in developing a consistent picture of transition in Rayleigh-Benard convection [1], Taylor-Couette flow [2], and similar problems. This success was due to the combination of new observations, numerical, and analytical results as well as mathematical concepts. In shear flows, however, a rather incomplete picture evolved primarily from experimental evidence [3] while theoretical support has been widely lacking. The key experiments, especially in boundary layers and Poiseuille flow, are intrinsically difficult to conduct. The phenomena run away in space since they sensitively depend on the ever-changing, unmeasurable details of the upstream flow conditions. Often, certain stages of the transition process are bypassed owing to the high background noise [4] as witnessed by the controversy on the linear stability of plane Poiseuille flow that lasted until 1975, when Nishioka et al. [5] obtained for the first time laminar flow at supercritical Reynolds numbers.

The mathematical tools - bifurcation theory and the analysis of dynamical systems - are here less powerful. Two general properties seem to be the key to the present theories: separability of the stability problem in order to reduce it to nonlinear ordinary differential equations, and the existence of a critical parameter. These requirements are not satisfied by the weakly nonparallel shear flows, $\underset{\sim}{v} = \underset{\sim}{v}(\epsilon x, y)$, where $\epsilon = 1/R$ expresses the weakness of the variation in the streamwise direction x. For these flows, the Reynolds number R is introduced artificially by using a local length scale, say x_0, and therefore changes with the independent variable x. This Reynolds number together with the local parallel flow assumption provides an ad-hoc solution to the non-separability of the stability equations but lacks the meaning of the critical parameter in a bifurcation problem. Even in plane Poiseuille flow, where the key requirements are satisfied, the detailed analysis of the cascade towards turbulence has only one step: once the flow becomes unstable to finite or infinitesimal disturbances, it "snaps through" to the fully turbulent motion. In view of the sequence of discrete events observed between onset of primary instability and ultimate breakdown [6,7], this result may raise some doubts. These are unjustified, however, since bifurcation theory uses the temporal growth concept, whereas most experiments on shear flows study the spatial development. In a strictly temporal experiment - as illustrated by the work of Thorpe [8] on Kelvin-Helmholtz instability in stratified liquids - the unstable plane Poiseuille flow at fixed Reynolds number would in fact directly develop into the turbulent motion over the full length and width of the channel. The term "snap through" simply denotes the lack of stable motions (such as Benard cells or Taylor vortices) different from the turbulent flow. It is the lack of these intermediate stages and of their step-by-step bifurcation into motions of increasing complexity, that makes the experimental and theoretical analysis of the transition process in shear flows a rather difficult task.

Nevertheless, experiments with reduced background noise level and carefully controlled disturbance environment have revealed important details of the transition process. Computer simulations of the temporal disturbance growth in a streamwise and spanwise periodic box have added insight. As a result of analytical and computational efforts, a theory of the secondary instability in shear flows evolved which can be characterized as a stability theory of streamwise periodic flows. The theory yet lacks the maturity of other tools, but it has been proven powerful enough for devoting one lecture of this course to its discussion.

In the following we consider the secondary instability of three generic model flows: (i) the free shear layer, or mixing layer, (ii) the Blasius boundary layer along a flat plate, and (iii) the plane Poiseuille flow in a channel. For a detailed discussion of free shear layers, the reader is referred to the recent article by Ho & Huerre [9]. A survey on Poiseuille flow, presenting the 1981 state-of-the-art, appeared recently [10].

2. APPEARANCE OF SECONDARY INSTABILITY

In all three model flows, primary instability occurs with respect to traveling waves. In the free shear layer, the inviscid inflexional (or vortical) instability is governed by the Rayleigh equation. The spatial growth of the disturbances on a fast convective time scale redistributes the vorticity into almost periodically spaced lumps. "In the simplest terms one might think of the vortical lumps being rolled along by the difference in velocity across the mixing layer" [11]. A particularly clear visualization of the roll-up into vortices in the cat's eyes has been made by Roberts et al. [12]. Secondary instability occurs as vortex pairing, i.e., pairs of vortical lumps start to roll around each other and ultimately merge into a new structure of larger lumps with about twice the original spacing. Hot-wire signals show a changeover from the fundamental to the subharmonic frequency. Often, the pairing process repeats itself and governs the streamwise growth of the shear-layer thickness. Although small-scale three-dimensional effects appear simultaneously with the first pairing [13], the large-scale structure remains essentially two-dimensional.

In the Blasius boundary layer, the primary instability with respect to T-S waves is governed by the Orr-Sommerfeld equation. Due to the viscous nature of the instability mechanism, the spatial growth on a viscous time scale is feeble at the large Reynolds numbers of concern. The small growth rates allow the use of Gaster's transformation [14] for relating to the simpler temporal growth concept. For a long period of time, the sequence of processes that lead from T-S waves to transition was derived solely from the vibrating ribbon experiments of Klebanoff et al. [15] and is now called K-breakdown. According to this pattern, a three-dimensional structure evolves whenever the T-S amplitude exceeds a certain threshold value. This structure is characterized by spanwise alternating "peaks" and "valleys", i.e., regions of enhanced and reduced wave amplitude. A system of counter-rotating streamwise vortices occurs simultaneously with the peaks and valleys. The growth rate at the peak positions is essentially larger than the primary T-S growth and leads rapidly to the formation of an intense shear layer at the peak. The highly inflexional, instantaneous velocity profiles become unstable with respect to high-frequency disturbances indicated by "spikes" in the hot-wire signals. The appearance of spikes is considered the onset of ultimate breakdown of the laminar into the turbulent flow.

Originally, the occurrence of spikes has been denoted as secondary instability, whereas the peak-valley splitting has been attributed to a spanwise-differential amplification of the T-S wave. A revised sequence has been introduced in 1979 [4,16] considering the peak-valley splitting as the manifestation of secondary instability. It has also been suggested [4] that this instability originates from parametric excitation of three-dimensional disturbances in the streamwise periodic flow created by the T-S wave. Moreover, recent experiments [17,18] have shown that the route to transition in boundary layers is non-unique and sensitively depends on the experimental conditions. The difference is in the nature and scale of the three-dimensional disturbances that generate different characteristic patterns of Λ-shaped vortex loops in flow visualizations, as sketched in Fig. 1. In the K-breakdown, the Λ vortices are aligned along the peaks and repeat with the wavelength λ_x of the T-S wave (Fig. 1a). At lower levels of the T-S amplitude, a staggered arrangement of Λ vortices is observed (Fib. 1b). This pattern repeats itself with wavelength $2\lambda_x$ and a fixed hot-wire records subharmonic signals. The spanwise wavelength λ_z may be larger or less than λ_x, depending on the T-S amplitude.

The portrait of transition in boundary layers fits very well to the observations in plane Poiseuille flow [10]. The only evident differences seem to be the possibility of subcritical disturbance growth in Poiseuille flow, the symmetry of the parabolic profile, and the constant Reynolds number. The K-breakdown has been studied, and supplemented by detailed results on the later stages of transition [6,7,20]. Flow visualizations [21,22] show the patterns of Λ vortices typical for the fundamental and subharmonic modes. (The flow visualizations are considered conclusive, although the facility used is too short for the parabolic profile to fully develop.)

Figure 1. Pattern of Λ vortices in flow visualizations after onset of secondary instability. (a) In-line peak-valley structure for fundamental modes. (b) Staggered structure for subharmonic modes. The flow is from left to right.

Evaluation of the observations for the various shear flows clearly shows that secondary instability occurs whenever the primary waves exceed a certain threshold amplitude. It is tempting, therefore, to consider the secondary instability as the instability of an almost periodic flow. For an observer moving with the phase velocity, the two-dimensional flow appears almost periodic in x, with a slowly varying amplitude. The disturbances originating from secondary instability may have the streamwise wavelength λ_x (fundamental modes) or $2\lambda_x$ (subharmonic modes). The unstable fundamental modes are likely to be always three-dimensional, whereas subharmonic modes can be two-dimensional (vortex pairing) or three-dimensional. One may also speculate that the secondary instability is somehow related to the periodically spaced vortical lumps created by the primary wave. Morkovin [3] considers the behavior of redistributed vorticity as key to the mechanisms in the transition process.

3. THEORETICAL APPROACH

From the foregoing, the theoretical approach suggests itself. In the first step, we establish the two-dimensional flow in the presence of finite amplitude primary disturbances. In general, this flow will not be strictly periodic. However, strictly periodic equilibrium states exist in Poiseuille flow [28,24], and these will serve for the formulation of the theory in section 4 in order to keep the mathematical treatment as clean as possible. Results for equilibrium states can be used as a benchmark for checking those assumptions necessary in the more general cases. Analysis of the linear stability of the streamwise periodic flow with respect to three-dimensional disturbances provides a system of stability equations with periodic coefficients called a Floquet system. Well-known properties of such systems [25,26] are exploited in order to identify classes and form of solutions.

Various aspects of this approach have been applied in earlier work on stability of flows. Clever & Busse [27] calculated nonlinear steady convection rolls and performed an analysis of the secondary instability of these rolls. Much of the basic concepts is concealed in the semi-analytical technique of solution. Maseev [28] studied the occurrence of three-dimensional disturbances in the boundary layer by using a Floquet system, but neither his method nor his results on peak-valley splitting received particular attention. Kelly [29] found the vortex pairing in an inviscid shear layer "due to a secondary instability associated with the nearly periodic flow which arises from the finite-amplitude growth of the fundamental disturbance", and related the subharmonic pairing mode to principal parametric resonance in a Floquet system. His weakly nonlinear method of solution provided results consistent with observations. Without resort to Floquet theory, Craik [30] developed a weakly nonlinear model of a resonant wave triad in the boundary layer. Chapter 48.2 of the monograph by Drazin & Reid [31] reviews some concepts for the analysis of periodic flows. The chapter closes with an example on gravity waves, where using Floquet theory led to an important discovery that was beyond the limitations of what was thought to be an equivalent weakly nonlinear theory. Floquet theory has also widely been applied in the stability analysis of time-periodic flows, as reviewed by Davis [32]. The major problem areas in this field, however, are quite different from the case considered here.

With the advent of increasingly powerful computers, considerable progress has been made in simulating the transition process in unstable shear flows on the basis of the Navier-Stokes equation. The concept of secondary instability is inherent in these simulations but not always discernible. Some computational work was directed toward this problem. Pierrehumbert & Widnall [33] performed a linear stability analysis of an array of finite-size vortices in a shear layer with respect to fundamental and subharmonic disturbances. Beyond the pairing mode, they found three-dimensional modes of instability [33, Figs. 6, 9] that result in the patterns sketched in Fig. 1. Of the various numerical studies [9] of mostly spatially periodic and temporally growing shear layers, the work of Brachet & Orszag [34] bears the closest relation to our topic. The secondary and tertiary instability of a plane shear layer with a cubic profile as it occurs in an inclined fluid layer heated from above have been studied by Nagata & Busse [35]. However, the concepts of the stability analysis are difficult to extract from the semi-analytical method of solution. Orszag & Patera [36] emphasized the universality of secondary instability based on results for plane Poiseuille flow, plane Couette flow, pipe flow and a model of the boundary layer flow. The analysis was made at large amplitudes of the periodic flow in order to explain the observed low transition Reynolds numbers. Light was shed on the vortical nature of the secondary instability and on the energy transfer showing the catalyst role of the primary wave in the parametrical excitation of three-dimensional disturbances. This, as well as earlier work of Orszag and coworkers also showed some drawbacks of the numerical approach. With a computational box having the fundamental wavelength, no indication of a subharmonic instability could be obtained. The spanwise wavelength was imprinted by choosing the computational box. The choice of different initial conditions in the earlier [37] and later work [38, 39] led unintentionally to different modes of instability. Finally, the computational expense prevents a systematic analysis of the parametrical dependence. Simulations of secondary instability and transition in a spatially periodic, temporally growing boundary layer are currently performed by Spalart [40] at NASA Ames using a larger computational box. Preliminary results on fundamental and subharmonic instability and on the selected wavelengths agree favorably with experiments.

A rudimentary theory of secondary instability based on a Floquet system has been simultaneously developed by Orszag & Patera [38,39] and Herbert [10,41] for equilibrium states in Poiseuille flow. The former work was motivated by the exponential growth of small three-dimensional disturbances observed in the numerical simulations, indicating the activity of a linear instability mechanism. The theory was only utilized for verifying the growth rate of the observed mode of instability for a large-amplitude equilibrium state. Numerical simulation was continued to be used as the main tool for analyzing the secondary instability [36]. The work of Herbert aimed at verifying the parametrical excitation of three-dimensional disturbances through T-S waves of small but finite amplitude [4]. He developed the theory [41-45] as a self-supporting tool for systematically identifying classes and modes of disturbances. The applications were oriented toward the onset of instability at low amplitudes and a comparison with experimental results. The limit of vanishing amplitude was studied as the key to evaluating existing weakly nonlinear models and to the construction of improved models.

In the next section, the theory is first formulated for a strictly periodic situation using equilibrium states in Poiseuille flow as an example. Various steps in the derivation of the equations are sketched rather than described in detail. After reviewing the main results for Poiseuille flow, approximations are introduced that lead to a simpler formulation applicable to a wider variety of stability problems.

4. THEORY OF SECONDARY INSTABILITY

We consider the flow of an incompressible fluid of density ρ and viscosity μ between parallel plates of distance $2h$. The flow is driven by a constant mean-pressure gradient in the x' direction. We denote with y the coordinate normal to the plates measured from the channel center, z is normal to the x', y plane and t the time. Velocity field $\underset{\sim}{v}(x',y,z,t) = (u,v,w)$ and pressure $p(x',y,z,t)$ are governed by the Navier-Stokes equations

$$\frac{\partial \underset{\sim}{v}}{\partial t} + (\underset{\sim}{v} \cdot \nabla)\underset{\sim}{v} = -\nabla p + \frac{1}{R} \nabla^2 \underset{\sim}{v}, \quad \nabla \cdot \underset{\sim}{v} = 0 \tag{1}$$

where R is the Reynolds number. All quantities are nondimensional using h and the mid-channel velocity U_0 in steady flow for reference. The boundary conditions require

$$\underset{\sim}{v}(x',y,z,t) = 0 \quad \text{for} \quad y = \pm 1. \tag{2}$$

From (1) we derive the transport equation for the vorticity $\underset{\sim}{\omega} = \nabla \times \underset{\sim}{v} = (\xi, \eta, \zeta)$,

$$\frac{\partial \underset{\sim}{\omega}}{\partial t} + (\underset{\sim}{v} \cdot \nabla)\underset{\sim}{\omega} - (\underset{\sim}{\omega} \cdot \nabla)\underset{\sim}{v} = \frac{1}{R} \nabla^2 \underset{\sim}{\omega} \tag{3}$$

and note that the pressure is eliminated by taking the curl of the momentum equation.

We consider a two-dimensional basic flow $\underset{\sim}{v}_2 = (u_2, v_2, 0)$, p_2 subject to small three-dimensional disturbances $\underset{\sim}{v}_3 = (u_3, v_3, w_3)$, p_3 according to

$$\underset{\sim}{v}(x',y,z,t) = \underset{\sim}{v}_2(x',y,t) + \varepsilon \underset{\sim}{v}_3(x',y,z,t) \tag{4}$$

$$p(x',y,z,t) = p_2(x',y,t) + \varepsilon p_3(x',y,z,t)$$

and assume ε being sufficiently small for linearization. Substitution into (1) - (2) and comparison of like powers of ε provide two sets of equations for the basic flow and disturbances, respectively.

We compose the basic flow in the form

$$v_2(x',y,t) = \underset{\sim}{v}_0(y) + A\underset{\sim}{v}_1(x',y,t) \tag{5}$$

$$p_2(x',y,t) = p_0(x') + Ap_1(x',y,t)$$

where $\underset{\sim}{v}_0, p_0$ represent plane Poiseuille flow,

$$\underset{\sim}{v}_0(y) = (u_0, 0, 0), \quad u_0 = 1 - y^2, \quad p_0 = -2x'/R. \tag{6}$$

The steady parallel flow v_0, p_0 satisfies equations (1) - (2) for all values of R. The component v_1, p_1 is considered in the form of a wave, i.e. periodic in t, periodic in x' with wavelength $\lambda_x = 2\pi/\alpha$, and traveling with the phase velocity c_r in the x' direction. In a Galilean frame moving with the wave, we obtain

$$\underset{\sim}{v}_1(x',y,t) = \underset{\sim}{v}_1(x,y) = \underset{\sim}{v}_1(x + \lambda_x, y), \quad x = x' - c_r t \tag{7}$$

and consequently, $\underset{\sim}{v}_1$ and $\underset{\sim}{v}_2$ are steady and streamwise periodic. The amplitude A in (5) is assumed to be constant and will be defined shortly.

We express $\underset{\sim}{v}_1 = (u_1, v_1, 0)$ and the vorticity $\nabla \times \underset{\sim}{v}_1 = (0, 0, \zeta_1)$ in terms of a streamfunction $\psi_1(x,y)$ such that

$$u_1 = \partial \psi_1/\partial y, \quad v_1 = -\partial \psi_1/\partial x, \quad \zeta_1 = -\nabla^2 \psi_1. \tag{8}$$

Equation (3) for the basic flow then reduces to the nonlinear partial differential equation

$$[\frac{1}{R} \nabla^2 - (u_0 - c_r) \frac{\partial}{\partial x} - A \frac{\partial \psi_1}{\partial y} \frac{\partial}{\partial x} + A \frac{\partial \psi_1}{\partial x} \frac{\partial}{\partial y}]\zeta_1 + \frac{\partial \zeta_0}{\partial y} \frac{\partial \psi_1}{\partial x} = 0 \tag{9}$$

with boundary conditions $\partial\psi_1/\partial x = \partial\psi_1/\partial y = 0$ at $y=\pm1$. The x-periodic streamfunction can be represented by the Fourier series

$$\psi_1(x,y) = \sum_{n=-\infty}^{\infty} \phi_n(y)e^{in\alpha x}. \tag{10}$$

For a real solution, we require $\phi_{-n} = \phi_n^\dagger$, where $\dagger$ denotes the complex conjugate. The functions $\phi_n(y)$, $n \geqslant 0$ are governed by a nonlinear system of ordinary differential equations,

$$\{\frac{1}{R} D_n^2 - in\alpha[(u_0 - c_r)D_n - u_0'']\}\phi_n = \sum_{m=0}^{n} P_{m,n-m} + \sum_{m=1}^{\infty} (P_{-m,n+m} + P_{n+m,-m})\}, \tag{11}$$

$$P_{n,m} = -i\alpha\{\phi_m' n D_n\phi_n - m\phi_m D_n\phi_n'\}$$

where $D_n = d^2/dy^2 - n^2\alpha^2$ and the prime denotes d/dy. The boundary conditions are

$$\phi_0' = \phi_0'' = 0, \quad \phi_n = \phi_n' = 0, \quad n > 0 \quad \text{for} \quad y = \pm1 \tag{12}$$

The condition on ϕ_0'' expresses the constant mean-pressure gradient. Note that the left-hand side of (11) has the form of the Orr-Sommerfeld equation for a two-dimensional T-S wave of wavenumber $n\alpha$ with the complex eigenvalue c replaced by c_r. The nonlinear coupling terms on the right-hand side vanish as $A \rightarrow 0$. With a suitable normalization of ϕ_1, solutions of the system (11) - (12) exist for certain combinations of parameters that satisfy a nonlinear dispersion relation $F(R,\alpha,A,c_r)=0$. This relation implicitly represents the neutral surface of plane Poiseuille flow [23,24]. Accurate approximations to these equilibrium solutions (whose amplitude A neither grows nor decays) can be obtained by numerically solving a truncated version $(n < N)$ of the system (11) - (12). In the computations, the amplitude is usually defined by a local normalization of ϕ_1, e.g. $\phi_1(0) = 1$ which also fixes the phase of the periodic basic flow. For a more convenient comparison with experimental data, however, we introduce a posteriori the normalization

$$\max_{0 \leqslant y < 1} \sum_{n=1}^{\infty} |\phi_n'(y)|^2 = \sum_{n=1}^{\infty} |\phi_n'(y_m)|^2 = \frac{1}{2}, \tag{13}$$

$$\max_{0 \leqslant x < \lambda_x} u_1(x,y_m) = u_1(0,y_m).$$

Hence, the amplitude A measures the maximum streamwise r.m.s. fluctuation of the basic flow (usually denoted as u_m') and the streamwise fluctuation velocity assumes a maximum at $x=0$. The search for a maximum is restricted to the half-channel $y \geqslant 0$ owing to the symmetry properties

$$\phi_n(-y) = (-1)^{n+1}\phi_n(y) \tag{14}$$

of the periodic equilibrium solutions.

For the three-dimensional disturbances $\underset{\sim}{v}_3, p_3$ in (4) we obtain from (1) after linearization in ε

$$(\frac{1}{R}\nabla^2 - \frac{\partial}{\partial t})\underset{\sim}{v}_3 - (\underset{\sim}{v}_2 \cdot \nabla)\underset{\sim}{v}_3 - (\underset{\sim}{v}_3 \cdot \nabla)\underset{\sim}{v}_2 = \nabla p_3, \quad \nabla \cdot \underset{\sim}{v}_3 = 0 \tag{15}$$

However, we use the momentum equation only for retrieving p_3. The analysis of the velocity field $\underset{\sim}{v}_3$ is based on the vorticity equation

$$(\frac{1}{R}\nabla^2 - \frac{\partial}{\partial t})\underset{\sim}{\omega}_3 - (\underset{\sim}{v}_2 \cdot \nabla)\underset{\sim}{\omega}_3 - (\underset{\sim}{v}_3 \cdot \nabla)\underset{\sim}{\omega}_2 + (\underset{\sim}{\omega}_2 \cdot \nabla)\underset{\sim}{v}_3 + (\underset{\sim}{\omega}_3 \cdot \nabla)\underset{\sim}{v}_2 = 0 \tag{16}$$

We follow the usual procedure for deriving the stability equations: (i) substitute the basic flow $\underset{\sim}{v}_2$, (ii) take the derivative $\partial/\partial z$ of the equation (16) for η_3, (iii) take the derivative $\partial/\partial x$ of the equation for ζ_3 and subtract the derivative $\partial/\partial z$ of the equation for ξ_3, and (iv) eliminate w_3 by using the continuity equation (15). This procedure provides the following stability equations

$$[\frac{1}{R}\nabla^2 - (u_0 - c_r)\frac{\partial}{\partial x} - \frac{\partial}{\partial t}]\frac{\partial\eta_3}{\partial z} + \zeta_0\frac{\partial^2 v_3}{\partial z^2}$$

$$+ A\{(-\frac{\partial\psi_1}{\partial y}\frac{\partial}{\partial x} + \frac{\partial\psi_1}{\partial x}\frac{\partial}{\partial y} - \frac{\partial^2\psi_1}{\partial x\partial y})\frac{\partial\eta_3}{\partial z} + \frac{\partial^2\psi_1}{\partial x^2}(\frac{\partial^2 u_3}{\partial x\partial y} + \frac{\partial^2 v_3}{\partial y^2}) - \frac{\partial^2\psi_1}{\partial y^2}\frac{\partial v_3}{\partial z^2}\} = 0, \tag{17}$$

$$[\frac{1}{R}\nabla^2 - (u_0 - c_r)\frac{\partial}{\partial x} - \frac{\partial}{\partial t}]\nabla^2 v_3 - \frac{d\zeta_0}{dy}\frac{\partial v_3}{\partial x} + A\{(-\frac{\partial\psi_1}{\partial y}\frac{\partial}{\partial x} + \frac{\partial\psi_1}{\partial x}\frac{\partial}{\partial y})\nabla^2 v_3$$

$$+ \frac{\partial^2\psi_1}{\partial x^2}(\frac{\partial\zeta_3}{\partial y} + \frac{\partial\eta_3}{\partial z}) - \frac{\partial^2\psi_1}{\partial x\partial y}(\frac{\partial\zeta_3}{\partial x} + \frac{\partial\xi_3}{\partial z}) - \frac{\partial\zeta_1}{\partial x}(2\frac{\partial u_3}{\partial x} + \frac{\partial v_3}{\partial y})$$

$$- \frac{\partial\zeta_1}{\partial y}\frac{\partial v_3}{\partial x} - (u_3\frac{\partial}{\partial x} + v_3\frac{\partial}{\partial y})\frac{\partial\zeta_1}{\partial x}\} = 0. \tag{18}$$

Since $\partial\eta_3/\partial z$ and $\partial\xi_3/\partial z$ can be expressed in terms of u_3, v_3, these two coupled differential equations determine u_3, v_3 subject to the boundary conditions

$$u_3 = v_3 = v_3' = 0 \quad \text{for} \quad y = \pm 1. \tag{19}$$

The properties of these equations can now be exploited in order to specify the form of the disturbances in more detail.

We note that the equations are linear in u_3, v_3. Boundary conditions (19) and the coefficients in (17) - (18) are independent of z and t. Therefore, we can apply the normal-mode concept [31, p.11] in these variables and write

$$\underset{\sim}{v}_3 = e^{\sigma t}e^{i\beta z}\underset{\sim}{v}(x,y) \tag{20}$$

These disturbances are spanwise periodic with wavelength $\lambda_z = 2\pi/\beta$. We consider β as real, whereas $\sigma = \sigma_r + i\sigma_i$ is in general complex. Separability and exponential behavior in time follows directly from our assumption of a constant amplitude A. For $A \to 0$, the system (17) - (19) reduces to the equations for primary instability of the parallel flow $\underset{\sim}{v}_0$ with respect to three-dimensional disturbances.

For $A \neq 0$, the characteristic feature of the system (17) - (19) is the occurrence of x-periodic coefficients. Insight into classes of solutions and their streamwise structure can be obtained from the Floquet theory of ordinary differential equations. Although the system is complicated by the y-dependence of the coefficients, high order, and numerous terms, Hill's equation or even Mathieu's equation with damping can be considered as relevant models. Various types of resonance can occur in such a Floquet system [26]. With a streamwise periodicity of wavenumber α, primary resonance may lead to unstable solutions having the same periodicity in the streamwise direction. In a system with quadratic nonlinearity, principal parametric resonance is associated with subharmonic solutions of wavenumber $\hat{\alpha}=\alpha/2$. A glance at the Strutt diagram and the effect of damping [26, Figs. 5-6, 5-9] shows that subharmonic instability may occur at the lowest levels of excitation. Moreover, instability may occur for wavenumbers in a band centered at $\hat{\alpha}$ or α. These cases of combination resonance, $\alpha_1 + \alpha_2 = \alpha$ or $\alpha_1 - \alpha_2 = \alpha$, are presently under study but will not be discussed in the following.

For our system, Floquet theory [25] provides solutions with $\underset{\sim}{v}(x,y) = e^{\gamma x}\underset{\sim}{f}(x,y)$, where $\underset{\sim}{f}$ is x-periodic with wavelength λ_x or $2\lambda_x$, and γ is a characteristic exponent. As in the primary stability problem, at this point a choice must be made between the concepts of spatial or temporal growth. In the following, we use the temporal growth concept with complex $\sigma = \sigma_r + i\sigma_i$. Since σ absorbs the characteristic exponents γ, we can seek for solutions with $\gamma=0$, i.e. in the form (20) with $\underset{\sim}{v}(x,y)$ periodic in x with $2\lambda_x$,

$$\underset{\sim}{v}_3 = e^{\sigma t}e^{i\beta z}\sum_{n=-\infty}^{\infty}\underset{\sim}{\hat{v}}_n(y)e^{in\hat{\alpha}x}, \quad \hat{\alpha} = \pi/\lambda_x = \alpha/2 \tag{21}$$

Substitution into the disturbance equations (17) - (19) and comparing terms in like exponentials provides the following system of ordinary differential equations for the Fourier coefficients

$$[\frac{1}{R}\hat{D}_n - in\hat{\alpha}(u_0 - c_r) - \sigma](k_n^2\hat{u}_n - in\hat{\alpha}\hat{v}_n') - \beta^2 u_0'\hat{v}_n + A\sum_{\ell=-\infty}^{\infty}Q_{\ell,n-2\ell} = 0, \tag{22}$$

$$\{(\frac{1}{R}\hat{D}_n - in\hat{\alpha}(u_0 - c_r) - \sigma)\hat{D}_n + in\hat{\alpha}u_0''\}\hat{v}_n + A\sum_{\ell=-\infty}^{\infty}R_{\ell,n-2\ell} = 0, \tag{23}$$

where $\hat{D}_n = d^2/dy^2 - k_n^2$, $k_n^2 = \beta^2 + n^2\hat{\alpha}^2$, and with $m = n - 2\ell$,

$$Q_{\ell,m} = -in\hat{\alpha}k_m^2\hat{u}_m\phi_\ell' + 2i\ell\hat{\alpha}(\beta^2 + nm\hat{\alpha}^2)\hat{u}_m'\phi_\ell - \beta^2\hat{v}_m\phi_\ell'' - nm\hat{\alpha}^2\hat{v}_m'\phi_\ell' + 2n\ell\hat{\alpha}^2\hat{v}_m''\phi_\ell,$$

$$R_{\ell,m} = (2\ell\hat{\alpha}k_n^2)^2\hat{u}_m\phi_\ell + (m^2 - n^2)\hat{\alpha}^2\hat{u}_m\phi_\ell'' - 4\ell m\hat{\alpha}^2\hat{u}_m'\phi_\ell' + (2\ell\hat{\alpha})^2\hat{u}_m''\phi_\ell$$

$$+ i\hat{\alpha}\hat{v}_m[(m - 2\ell)k_n^2\phi_\ell' + n\phi_\ell'''] + 2i\ell\hat{\alpha}\hat{v}_m'(\phi_\ell'' - k_n^2\phi_\ell) + (2\ell - m)i\hat{\alpha}\hat{v}_m''\phi_\ell' + 2i\ell\hat{\alpha}\hat{v}_m'''\phi_\ell.$$

The boundary conditions are

$$\hat{u}_n = \hat{v}_n = \hat{v}_n' = 0 \quad \text{for} \quad y = \pm 1 \tag{24}$$

and $\hat{w}_n$ is obtained from continuity,

$$in\hat{\alpha}\hat{u}_n + \hat{v}_n' + i\beta\hat{w}_n = 0. \tag{25}$$

The homogeneous equations (22) - (24) represent an eigenvalue problem with the eigenvalue σ and an associated eigensolution that consists of a sequence of functions $\{\hat{u}_n, \hat{v}_n\}$. The system determines the solution for given α, β, R and given basic flow (u_0, A, ϕ_n). For $A\equiv 0$, equations (23) reduce to Orr-Sommerfeld equations for three-dimensional disturbances of wavenumbers $n\alpha, \beta$ and with eigenvalues $c_n = c_r + i\sigma/(n\alpha)$. Equations (22) reduce to the equations for the y-component of vorticity first derived and studied by Squire [46] in his analysis of three-dimensional primary disturbances. We therefore suggest that these equations be called Squire equations. Note that these equations support a separate set of eigensolutions if $\hat{v}_n\equiv 0$. These Squire modes cannot lead to primary instability [46] but are important for the resonant interactions that lead to secondary instability. The link between modes of secondary and primary instability can easily be traced by varying the amplitude $A\to 0$.

At closer inspection of the system (22) - (24), it becomes obvious that the equations uncouple into two systems of equations for the Fourier coefficients $\underset{\sim}{v}_n$ with n even and odd, respectively. The two separate classes of solutions take the form

$$\underset{\sim}{v}_f = e^{\sigma t} e^{i\beta z} \sum_{n=-\infty}^{\infty} \hat{\underset{\sim}{v}}_{2n}(y) e^{in\alpha x} \tag{26}$$

$$\underset{\sim}{v}_s = e^{\sigma t} e^{i\beta z} \sum_{n=-\infty}^{\infty} \hat{\underset{\sim}{v}}_{2n+1}(y) e^{i(2n+1)\hat{\alpha}x} \tag{27}$$

The <u>fundamental</u> modes $\underset{\sim}{v}_f$ have wavelength λ_x and originate from primary resonance. The <u>subharmonic</u> modes $\underset{\sim}{v}_s$ have wavelength $2\lambda_x$ and arise from principal parametric resonance.

The characteristics of the modes (26) - (27) are formally consistent with observations. The fundamental modes are doubly periodic with λ_x and λ_z as the ordered pattern of Λ vortices in Fig. 1a that is characteristic for peak-valley splitting. The aperiodic term $\underset{\sim}{v}_0$ in (26) represents a spanwise periodic mean-flow distortion $(\hat{u}_0)$ and a longitudinal mean-vortex system $(\hat{v}_0, \hat{w}_0)$ that are known [15] to accompany the peak-valley splitting. The aperiodic term is absent in the subharmonic modes (27). These modes are doubly periodic with $2\lambda_x$ and λ_z, and invariant under the translation $(x,y) \to (x + \lambda_x, z + \lambda_z/2)$ that is characteristic for the staggered pattern of Λ vortices in Fig. 1b. In frequency spectra from a laboratory-fixed probe, the subharmonic modes contribute peaks at frequencies $f/2$, $3f/2$,.. but not at the fundamental frequency $f=\alpha c_r$ and its harmonics.

For both classes of modes, the eigenvalues σ are in general complex. Exploiting the fact that ψ_1 must be real, however, it can be shown that the spectrum consists of either real eigenvalues or complex conjugate pairs. If σ_1 is a complex eigenvalue and the sequence $\{\hat{u}_\nu, \hat{v}_\nu\}$, the associated eigensolution, then a second solution is $\sigma_2 = \sigma_1^*$, $\{\hat{u}_\nu, \hat{v}_\nu\}_2 = \{\hat{u}_{-\nu}, \hat{v}_{-\nu}\}_1^\dagger$. If the system supports real eigenvalues $\sigma=\sigma_r$, the eigensolution satisfies $\{\hat{u}_\nu, \hat{v}_\nu\} = \{\hat{u}_{-\nu}, \hat{v}_{-\nu}\}^\dagger$ to within a redundant complex factor (that can be suppressed by proper normalization). In this case, the aperiodic terms $\hat{u}_0$, $\hat{v}_0$ in $\underset{\sim}{v}_f$ are real, whereas $\hat{w}_0$ is purely imaginary.

The coefficients of the stability equations (22) - (23) are in general complex, except for n=0. However, as suggested by the symmetry of the spectrum about the real axis, a formulation can be found with real coefficients by rewriting the Fourier series (26) - (27) in trigonometric form, i.e. by introducing

$$\underset{\sim}{v}_n^+ = \frac{1}{2}(\hat{\underset{\sim}{v}}_n + \hat{\underset{\sim}{v}}_{-n}), \quad \underset{\sim}{v}_n^- = \frac{1}{2i}(\hat{\underset{\sim}{v}}_n - \hat{\underset{\sim}{v}}_{-n}), \quad n \geqslant 0 \tag{28}$$

and rearranging the equations accordingly. The new functions $u_n^\pm$, $v_n^\pm$ are governed by a system of equations with real coefficients. The solution however is only real for real σ. Although mathematically equivalent to (22) - (23), use of the real system is advantageous for the numerical work. The numerical solution requires drastic truncation of the Fourier series. The lowest approximation (N=1) takes ϕ_n, $|n| \leqslant N=1$ into account and provides $v_0 = v_0^+$, $v_2^\pm$ for fundamental modes, $v_1^\pm$ for the subharmonic modes. The next approximation (N=2) provides $v_4^\pm$ in $\underset{\sim}{v}_f$ and $v_3^\pm$ in $\underset{\sim}{v}_s$. Accordingly, truncation at N requires the simultaneous solution of $4N + 2$ equations of the Orr-Sommerfeld or Squire type for the fundamental modes, $4N$ equations for the subharmonic modes.

5. RESULTS FOR EQUILIBRIUM STATES

A detailed report on the results for equilibrium states in plane Poiseuille flow is in preparation [47]. Some results are given in [42-44]. The analysis concentrated on the range of subcritical Reynolds numbers $5000 < R < 5772$, with wavenumbers $\alpha \approx 1$ and amplitudes $A < 0.025$. Experiments [5-7] and computational [48] studies concentrated on the same range. The peculiar y-symmetry of plane Poiseuille flow and of the coefficients ϕ_n of the equilibrium states provides two groups of modes with different y-symmetry of the v_n. Symmetric and antisymmetric fundamental modes have similar but not identical character whereas symmetric and antisymmetric subharmonic modes are complex conjugate to each other. Instability with respect to fundamental modes occurs typically at amplitudes in the range of $A=0.01$. The principal (most amplified) mode is associated with real σ, i.e. the disturbance is synchronized with the basic flow. The amplification rate σ_r increases approximately with the square of the amplitude, $\sigma_r \approx O(A^2)$. The instability is strong in the sense that for $A=0.025$ the disturbance grows by a factor of 100 within about five cycles of the basic flow. The strong growth on a fast convective (rather than viscous) time scale originates from the strong mechanism of combined vortex tilting and stretching [36]. Instability can occur in a broad band of spanwise wavenumbers β, with maximum growth in the range $1.2 < \beta < 2$. Superposition of the disturbances to the basic flow provides the distributions of the streamwise velocity fluctuations that are typical for peak-valley splitting.

Instability with respect to subharmonic modes occurs at even lower amplitudes in the range of $A=0.005$. The principal mode is complex but the value of σ_i is rather small except at small β. The amplification rate increases almost linearly with the amplitude, $\sigma_r \approx O(A)$ and reaches at $A=0.025$ a value comparable to that for the fundamental modes. Onset of subharmonic instability occurs in a small band of wavenumbers centered at $\beta \approx 0.75$. A broad-band character develops at larger amplitudes, with a sharp cutoff at low β indicating suppression of the two-dimensional ($\beta=0$) pairing mode in the presence of walls.

All these results are qualitatively and (whenever comparable data exist) quantitatively consistent with experimental and computational results. Striking similarity also exists with the more detailed experimental data for the Blasius boundary layer. This similarity is less surprising in view of the origin of the secondary instability. At sufficiently large amplitude, the primary wave produces an array of vorticity concentrations near the centers of the cat's eyes, at the edge of the viscous layers near the walls. Secondary instability originates from bending the distributed vortices into regions of different streamwise velocity. Therefore, secondary instability can be considered a generic phenomenon in flows with primary T-S wave instability.

6. APPROXIMATIONS

The application of the above theory is restrained by the use of equilibrium states as a strictly periodic flow. These nonlinear states may be unavailable or may not exist in the parameter range of interest. The finite amplitude A plays a dual role in the theory. First, it appears in the equations (11) for the basic flow and generates harmonics (ϕ_n, $n>1$), a mean-flow distortion (ϕ_0), and a distortion of the fundamental (ϕ_1). Second, the amplitude multiplies the periodic terms in equations (22) - (23) and directly controls the parametrical excitation of secondary modes. Extensive numerical studies using results for N=2 as a benchmark have shown that the neglect of nonlinear terms in the basic flow has a slightly stabilizing but insignificant effect [43]. For practical purpose, the shape assumption [49] can be applied, i.e. the nonlinear solution ψ_1 can be replaced by

$$\psi_1(x,y) = \phi(y)e^{i\alpha x} + \phi^\dagger(y)e^{-i\alpha x} \tag{29}$$

where $\phi(y)$ is the eigenfunction associated with the principal mode $c^* = c_r + ic_i$ of the Orr-Sommerfeld equation for given R and α, and $\beta=0$. In physical terms, the use of (29) requires that for the amplitudes of concern the nonlinear effects on the y-distribution of vorticity (ζ_1) can be neglected. As a by-product, the amplitude is no longer restricted by the nonlinear dispersion relation for equilibrium states, and can be arbitrarily chosen.

One of the crucial prerequisites of the theory is the constant amplitude A. When using linear T-S waves in (29), however, the amplitude varies exponentially, $A \sim e^{\alpha c_i t}$. In order to overcome this problem, we make the quasi-static assumption, i.e. the basic flow is assumed to vary so slowly compared to the disturbances that it can be considered as steady. This assumption requires

$$|\alpha c_i| << |\sigma_r|. \tag{30}$$

Obviously, this assumption blurs the onset of secondary instability in a basic flow of varying amplitude. In view of the feeble (viscous) T-S growth and the strong (convective) growth of three-dimensional disturbances, however, the quasi-static approach can be justified for the situations of practical interest.

The use of the shape assumption essentially simplifies the stability equations. In order to obtain equations with real coefficients, we consider fundamental modes in the form

$$v_f = e^{\sigma t}e^{i\beta z}[v_0^+(y) + 2v_2^+(y)\cos\alpha x - 2v_2^-(y)\sin\alpha x] \tag{31}$$

The u and v components are governed by the equations

$$(\tfrac{1}{R}\hat{D}_0 - \sigma)\,u_0^+ - u_0'v_0^+ - 2A\{\alpha[(u_2^+)'\phi_i - (u_2^-)'\phi_r] + v_2^+\phi_r'' + v_2^-\phi_i''\} = 0 \tag{32}$$

$$(\tfrac{1}{R}\hat{D}_0 - \sigma)\hat{D}_0 v_0^+ + 2A\{\alpha^2[(u_2^+)''\phi_r + (u_2^-)''\phi_i + 2(u_2^+)'\phi_r' + 2(u_2^-)'\phi_i'$$

$$+ u_2^+(\phi_r'' + \beta^2\phi_r) + u_2^-(\phi_i'' + \beta^2\phi_i)] - \alpha[(v_2^+)'''\phi_i - (v_2^-)'''\phi_r$$

$$+ 2(v_2^+)''\phi_i' - 2(v_2^-)''\phi_r' + (v_2^+)'(\phi_i'' - \beta^2\phi_i) - (v_2^-)'(\phi_r'' - \beta^2\phi_r)$$

$$- 2\beta^2(v_2^+\phi_i' - v_2^-\phi_r)]\} = 0 \tag{33}$$

$$(\tfrac{1}{R}\hat{D}_2 - \sigma)k_2^2 u_2^+ + \alpha k_2^2(u_0 - c_r)u_2^- - \alpha^2(u_0 - c_r)(v_2^+)' + \alpha(\tfrac{1}{R}\hat{D}_2 - \sigma)(v_2^-)'$$

$$- \beta^2 u_0'v_2^+ - A\{\alpha\beta^2[(u_0^+)'\phi_i - u_0^+\phi_i'] - \alpha^2(v_0^+)''\phi_r + \beta^2 v_0^+\phi_r''\} = 0 \tag{34}$$

$$(\tfrac{1}{R}\hat{D}_2 - \sigma)\hat{D}_2 v_2^+ + \alpha[(u_0 - c_r)\hat{D}_2 - u_0'']v_2^- + \alpha A\{\alpha[(u_0^+)''\phi_r + u_0^+(\phi_r'' - k_2^2\phi_r)$$

$$+ (v_0^+)'''\phi_i + (v_0^+)''\phi_i' + (v_0^+)'(\phi_i'' - k_2^2\phi_i) + v_0^+(\phi_i''' - k_2^2\phi_i')\} = 0 \tag{35}$$

$$(\tfrac{1}{R}\hat{D}_2 - \sigma)k_2^2 u_2^- - \alpha k_2^2(u_0 - c_r)u_2^+ - \alpha^2(u_0 - c_r)(v_2^-)' - \alpha(\tfrac{1}{R}\hat{D}_2 - \sigma)(v_2^+)'$$

$$- \beta^2 u_0'v_2^- + A\{\alpha\beta^2[(u_0^+)'\phi_r - u_0^+\phi_r'] + \alpha^2(v_0^+)''\phi_i - \beta^2 v_0^+\phi_i''\} = 0 \tag{36}$$

$$(\tfrac{1}{R}\hat{D}_2 - \sigma)\hat{D}_2 v_2^- - \alpha[(u_0 - c_r)\hat{D}_2 - u_0'']v_2^+ + \alpha A\{\alpha[(u_0^+)''\phi_i - u_0^+(\phi_i'' - k_2^2\phi_i)$$

$$+ (v_0^+)'''\phi_r + (v_0^+)''\phi_r' + (v_0^+)'(\phi_r'' - k_2^2\phi_r) + v_0^+(\phi_r''' - k_2^2\phi_r')\} = 0 \tag{37}$$

where $\phi = \phi_r + i\phi_i$, $\hat{D}_n = d^2/dy^2 - k_n^2$, $k_n^2 = \beta^2 + (n\hat{\alpha})^2$. The boundary conditions are

$$u_0^+ = v_0^+ = (v_0^+)' = u_2^\pm = v_2^\pm = (v_2^\pm)' = 0 \quad \text{for} \quad y = \pm 1, \tag{38}$$

and the w components are obtained from

$$w_0^+ = \tfrac{i}{\beta}(v_0^+)', \quad w_2^\pm = \tfrac{i}{\beta}[(v_2^\pm)' \mp \alpha u_2^\mp] \tag{39}$$

Note that the six equations (32) - (37) are coupled and need to be solved simultaneously.

The <u>subharmonic modes</u> take the form

$$\underset{\sim}{v}_s = 2e^{\sigma t}e^{i\beta z}[\underset{\sim}{v}_1^+(y)\cos\hat{\alpha}x - \underset{\sim}{v}_1^-(y)\sin\hat{\alpha}x] \tag{40}$$

The u and v components are solutions to the equations

$$(\tfrac{1}{R}\hat{D}_1 - \sigma)k_1^2 u_1^+ \pm \hat{\alpha}k_1^2(u_0 - c_r)u_1^\mp - \hat{\alpha}^2(u_0 - c_r)(v_1^+)' \pm (\tfrac{1}{R}\hat{D}_1 - \sigma)\hat{\alpha}(v_1^\mp)'$$

$$- \beta^2 u_0'v_1^\pm - A\{\hat{\alpha}k_1^2[u_1^\mp\phi_r' \mp u_1^+\phi_i'] + 2\hat{\alpha}(\hat{\alpha}^2 - \beta^2)[(u_1^\mp)'\phi_r \mp (u_1^\pm)'\phi_i]$$

$$+ \beta^2[v_1^\mp\phi_i'' \pm v_1^\pm\phi_r''] - \hat{\alpha}^2[(v_1^\mp)'\phi_i' \pm (v_1^\pm)'\phi_r'] - 2\hat{\alpha}^2[(v_1^\mp)''\phi_i \pm (v_1^\pm)''\phi_r]\} = 0, \tag{41}$$

$$(\tfrac{1}{R}\hat{D}_1 - \sigma)\hat{D}_1 v_1^\pm \pm \hat{\alpha}[(u_0 - c_r)\hat{D}_1 - u_0'']v_1^\mp + A\{4\hat{\alpha}^2 k_1^2[u_1^\mp\phi_i \pm u_1^+\phi_r]$$

$$+ 4\hat{\alpha}^2[(u_1^\mp)'\phi_i' \pm (u_1^\pm)'\phi_r'] + 4\hat{\alpha}^2[(u_1^\mp)''\phi_i \pm (u_1^\pm)''\phi_r] + \hat{\alpha}[v_1^\mp(\phi_r'' - 3k_1^2\phi_r)'$$

$$\mp \; v_1^{\pm}(\phi_i'' - 3k_1^2\phi_i)'] + 2\hat{\alpha}[(v_1^{\mp})'(\phi_r'' - k_1^2\phi_r) \mp (v_1^{\pm})'(\phi_i'' - k_1^2\phi_i)]$$

$$+ 3\hat{\alpha}[(v_1^{\mp})''\phi_r' \mp (v_1^{\pm})''\phi_i'] + 2\hat{\alpha}[(v_1^{\mp})'''\phi_r \mp (v_1^{\pm})'''\phi_i]\} = 0, \qquad (42)$$

where either the upper or lower signs are used throughout. The boundary conditions are

$$u_1^{\pm} = v_1^{\pm} = (v_1^{\pm})' = 0 \quad \text{for} \quad y = \pm 1, \qquad (43)$$

and the w components are obtained from

$$w_1^{\pm} = \frac{i}{\beta}\,[(v_1^{\pm})' \mp \hat{\alpha}u_1^{\mp}]. \qquad (44)$$

In the subharmonic case, four coupled equations must be solved simultaneously.

The eigenvalues σ are in general complex (complex conjugate pairs). However, the case of the real eigenvalues $\sigma=\sigma_r$ is of particular interest since synchronization between basic flow and disturbances offers an optimum chance for energy transfer. At larger amplitudes, the principal modes of fundamental and subharmonic instability are likely to be associated with real eigenvalues. As a consequence of the shape assumption, the amplitude appears linearly in the stability equations. As long as $\sigma(A)$ is real, this enables an inverse eigenvalue search for $A(\sigma)$, i.e. to find the amplitude that produces a given amplification rate.

For A=0, the stability equations reduce to Orr-Sommerfeld equations and Squire equations written for the real and imaginary parts. Although the equations are lengthy, they can be considered as a straightforward extension of the primary stability problem. The secondary level of the stability analysis is obviously more involved but tractable with essentially the same numerical techniques suited for solving the Orr-Sommerfeld equation.

The stability equations (32) - (38) have been utilized for analyzing fundamental modes in plane Poiseuille flow. In applications for boundary layers, the equations (32) - (33) for the aperiodic terms may require modification owing to the nonparallelism of the flow [4]. Equations (41) - (43) were used for Poiseuille flow and for the analysis of the subharmonic instability of the Blasius boundary layer.

7. NUMERICAL METHOD OF SOLUTION

In our numerical work, little or no guidance was available on the eigenvalues of the secondary instability problem. In this case, solving the boundary value problem is clearly preferable to shooting methods on the basis of artificial initial value problems. With proper methods of discretization, boundary value methods provide access to the spectrum of eigenvalues that we found extremely helpful in the initial orientation period for any new problem under consideration. Spectra were also helpful in tracing the intricate crossings of eigenvalues at low amplitudes. On the other hand, the sole use of a global procedure is expensive in terms of computer time. Therefore it is recommended to combine the use of spectra with local procedures for tracing single eigenvalues and pairs of eigenvalues. We have primarily used Wielandt's method [50] for this purpose.

Global and local procedures are based on an algebraic substitute for the differential equations. The algebraic equations were obtained by employing a spectral collocation method [23,24] based on Chebyshev polynomials. Accurate solutions can be obtained with relatively small numbers of collocation points. In plane Poiseuille flow, we have exploited symmetry and used typically 18 collocation points in the half-channel. In the analysis of boundary-layer flow, we have used an algebraic transformation of the semi-infinite y-domain to a finite domain $0\leqslant\eta\leqslant 1$ and employed only odd Chebyshev polynomials [45] with typically 30 collocation points. The accuracy of the results is mainly governed by the accurate representation of the basic flow. Otherwise, the results on the secondary instability are rather insensitive to the number J of collocation points. The M x M real algebraic systems with M = 6J + 18 for fundamental modes and M = 4J + 12 for subharmonic modes are rather large, but tractable. More efficient methods of solving the secondary stability equations are currently being developed.

8. FINAL REMARKS

After a glance at the tedious equations of sections 5 and 6, and in view of the typically 100-200 unknowns in the algebraic eigenvalue problem, the reader may be discouraged to ever use this method of analysis. He may change his attitude, however, when viewing the comparison of theoretical and experimental [17] results for the subharmonic instability in the Blasius boundary layer shown in Figs. 2 and 3. (For a more detailed discussion see [45].) The amplitude growth curves for the T-S wave and the subharmonic disturbance in Fig. 2 verify the growth rates predicted by the present theory. An adjustment had only to be made by choosing the initial (background) amplitude of the subharmonic disturbance that could not be obtained from the experiment. Fig. 3 is representative for the correct prediction of the spatial structure of the disturbances, that extends over all available experimental data. Perhaps the most important conclusion from Fig. 2 is the ability of the theory to predict the onset of signi-

ficant three-dimensionality for a given disturbance background. Due to the rapid growth of the three-dimensional disturbances and subsequent breakdown, this seems to be a more rational approach to predicting transition Reynolds numbers than the methods currently used, e.g. the e^n criterion.
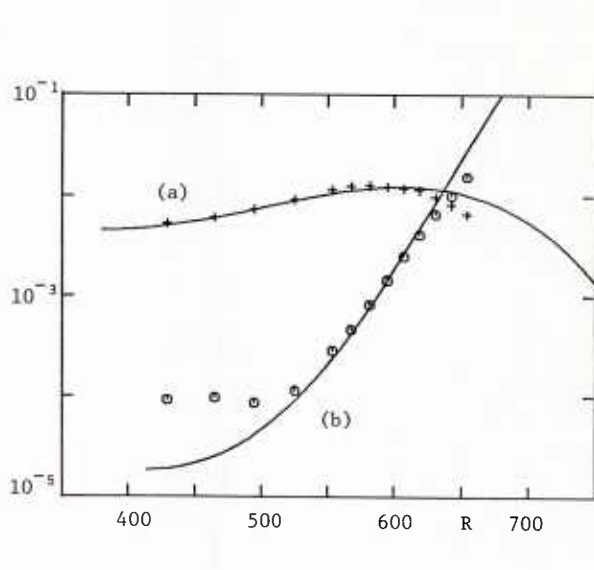

Figure 2. Amplitude variation with $R=R_x^{1/2}$ for (a) the T-S wave with an initial amplitude $A_0=0.0044$ and (b) the subharmonic disturbance of wavenumber $\beta/R = 3.3 \cdot 10^{-4}$ with an initial amplitude $B_0 = 1.86 \cdot 10^{-5}$. Comparison between (———) theory and $(+,o)$ experiment [17, Fig. 22a] at frequency $\alpha c_r/R = 1.24 \cdot 10^{-4}$.

Figure 3. Distribution of the streamwise r.m.s. velocity of a subharmonic disturbance at $R=608$, $\beta/R = 3.3 \cdot 10^{-4}$, $\alpha c_r/R = 1.24 \cdot 10^{-4}$. Displacement thickness and position of the critical layer are shown as δ^* and y_c, respectively. Comparison of (———) theory and (o) experiment [17, Fig. 21].

The theory of section 6 can be applied to a variety of stability problems. However, the theory is also open for improvements and extensions. The spatial growth concept can be applied, and corrections can be made for the yet neglected amplitude variation of the T-S wave. This seems to be of particular importance for the analysis of free shear layers and boundary layers with strong adverse pressure gradients. Improved techniques for solving the equations will also help to develop the analysis of secondary instability into a common tool for understanding and predicting the three-dimensional stages of the transition process in shear flows.

REFERENCES

[1] Busse, F. H., "Transition to turbulence in Rayleigh-Benard convection," in: Hydrodynamic Instabilities and the Transition to Turbulence (eds. H. L. Swinney & J. P. Gollub), 97-137, Springer-Verlag (1981).

[2] DiPrima, R. C. & Swinney, H. L., "Instabilities and transition in flow between concentric rotating cylinders," in: Hydrodynamic Instabilities and the Transition to Turbulence (eds. H. L. Swinney & J. P. Gollub), Springer-Verlag, 139-180 (1981).

[3] Morkovin, M. V., "Understanding transition to turbulence in shear layers - 1983," AFOSR Final Report AD-A134796 (1983).

[4] Herbert, Th. & Morkovin, M. V., "Dialogue on bridging some gaps in stability and transition research," in: Laminar-Turbulent Transition (eds. R. Eppler & H. Fasel), 47-72, Springer-Verlag (1980).

[5] Nishioka, M., Iida, S. & Ichikawa, J., "An experimental investigation on the stability of plane Poiseuille flow," J. Fluid Mech. 72, 731-751 (1975).

[6]   Nishioka, M., Asai, M. & Iida, S., "An experimental investigation of secondary instability," in: Laminar-Turbulent Transition (eds. R. Eppler & H. Fasel), 37-46, Springer-Verlag (1980).

[7]   Nishioka, M., Asai, M. & Iida, S., "Wall phenomena in the final stage of transition to turbulence," in: Transition and Turbulence (ed. R. E. Meyer), 113-126, Academic Press (1981).

[8]   Thorpe, S. A., "Experiments on the instability of stratified shear-flows: miscible fluids," J. Fluid Mech. 46, 299-319 (1971).

[9]   Ho, C. M. & Huerre, P., "Perturbed free shear layers," Ann. Rev. Fluid Mech. 16, 365-424 (1984).

[10] Herbert, Th., "Stability of plane Poiseuille flow - theory and experiment," Fluid Dyn. Trans. 11, 77-126 (1983).

[11] Winant, C. D. & Browand, F. K., "Vortex pairing: the mechanism of turbulent mixing-layer growth at moderate Reynolds number," J. Fluid Mech. 63, 237-255 (1974).

[12] Roberts, F. A., Dimotakis, P. E. & Roshko, A., "Kelvin-Helmholtz instability of superposed streams," in: Album of Fluid Motion (ed. M. VanDyke), 85, Parabolic Press (1982).

[13] Breidenthal, R., "Structure in turbulent mixing layers and wakes using a chemical reaction," J. Fluid Mech. 109, 1-24 (1981).

[14] Gaster, M., "A note on the relation between temporally-increasing and spatially-increasing disturbances in hydrodynamic stability," J. Fluid Mech. 14, 222-224 (1962).

[15] Klebanoff, P. S., Tidstrom, K. D. & Sargent, L. M., "The three-dimensional nature of boundary-layer instability, J. Fluid Mech. 12, 1-34 (1962).

[16] Blackwelder, R. F., "Boundary-layer transition," Phys. Fluids 22, 583-584 (1979).

[17] Kachanov, Yu. S. & Levchenko, V. Ya, "Resonant interactions of disturbances in transition to turbulence in a boundary layer" (in Russian), Preprint No. 10-82, I.T.A.M., USSR Academy of Sciences, Novosibirsk (1982).

[18] Saric, W. S. & Thomas, A. S. W., "Experiments on the subharmonic route to turbulence in boundary layers," Proc. IUTAM Symposium "Turbulence and Chaotic Phenomena in Fluids," Kyoto, Japan (1983).

[19] Saric, W. S., Kozlov, V. V. & Levchenko, V. Ya., "Forced and unforced subharmonic resonance in boundary layer transition," AIAA Paper No. 84-0007 (1984).

[20] Nishioka, M. & Asai, M., "Evolution of Tollmien-Schlichting waves into wall turbulence," Proc. IUTAM Symposium "Turbulence and Chaotic Phenomena in Fluids," Kyoto, Japan (1983).

[21] Kozlov, V. V. & Ramasanov, M. P., "Development of finite-amplitude disturbance in Poiseuille flow," Izv. Akad. Nauk SSSR, Mekh. Zhidk. i Gaza, 43-47 (1983).

[22] Kozlov, V. V. & Ramasanov, M. P., "Formation of three-dimensional structures in Poiseuille flow by resonant interaction," Preprint No. 11-83, I.T.A.M., USSR Acad. Sci., Novosibirsk (1983).

[23] Herbert, Th., "Finite-amplitude stability of plane parallel flows," AGARD CP-224, 3/1-10 (1977).

[24] Herbert, Th., "Die neutrale Fläche der ebenen Poiseuille-Stromung," Habilitationsschrift, Universität Stuttgart (1978).

[25] Coddington, E. A. & Levinson, N., Theory of Ordinary Differential Equations, "McGraw-Hill (1955).

[26] Nayfeh, A. H. & Mook, D. T., Nonlinear Oscillations, Wiley (1979).

[27] Clever, R. M. & Busse, F. H., "Transition to time-dependent convection," J. Fluid Mech. 65, 625-645 (1974).

[28] Maseev, L. M., "Occurrence of three-dimensional perturbations in a boundary layer," Fluid Dyn. 3, 23-24 (1968).

[29] Kelly, R. E., "On the stability of an inviscid shear layer which is periodic in space and time," J. Fluid Mech. 27, 657-689 (1967).

[30] Craik, A. D. D., "Nonlinear resonant instability in boundary layers," J. Fluid Mech. 50, 393-413 (1971).

[31] Drazin, P. & Reid, W., "Hydrodynamic Stability," Cambridge University Press (1981).

[32] Davis, S. H., "The stability of time-periodic flows," Ann. Rev. Fluid Mech. 8, 57-74 (1976).

[33] Pierrehumbert, R. T. & Widnall, S. E., "The two- and three-dimensional instabilities of a spatially periodic shear layer," J. Fluid Mech. 114, 59-82 (1982).

[34] Brachet, M. E. & Orszag, S. A. "Secondary instability of free shear flows," J. Fluid Mech., to appear.

[35] Nagata, M. & Busse, F. H., "Three-dimensional tertiary motions in a plane shear layer," J. Fluid Mech. 135, 1-28 (1983).

[36] Orszag, S. A. & Patera, A. T., "Secondary instability of wall-bounded shear flows," J. Fluid Mech. 128, 347-385 (1983).

[37] Orszag, S. A. & Kells, L. C., "Transition to turbulence in plane Poiseuille flow and plane Couette flow," J. Fluid Mech. 96, 159-206 (1980).

[38] Orszag, S. A. & Patera, A. T., "Subcritical transition to turbulence in plane channel flows," Phys. Rev. Lett. 45, 989-993 (1980).

[39] Orszag, S. A. & Patera, A. T., "Subcritical transition to turbulence in plane shear flows," in: Transition and Turbulence (ed. R. E. Meyer), 127-146, Academic Press (1981).

[40] Spalart, P. R., Personal communication, January 1984.

[41] Herbert, Th., "A secondary instability mechanism in plane Poiseuille flow," Bull. Amer. Phys. Soc. 26, 1257 (1981).

[42] Herbert, Th., "Secondary instability of plane channel flow to subharmonic three-dimensional disturbances," Phys. Fluids 26, 871-874 (1983).

[43] Herbert, Th., "Modes of secondary instability in plane Poiseuille flow," Proc. IUTAM Symposium, "Turbulence and Chaotic Phenomena in Fluids," Kyoto, Japan (1983).

[44] Herbert, Th., "Subharmonic three-dimensional disturbances in unstable shear flows," AIAA Paper No. 83-1759 (1983).

[45] Herbert, Th., "Analysis of the subharmonic route to transition in boundary layers," AIAA Paper No. 84-0009 (1984).

[46] Squire, H. B., "On the stability for three-dimensional disturbances of viscous fluid between parallel walls," Proc. Roy. Soc. London Ser. A, 142, 621-628 (1983).

[47] Herbert, Th., "Three-dimensional instability of periodic secondary motions in a plane channel," in preparation for J. Fluid Mech.

[48] Kleiser, L., "Numerische Simulationen zum laminar-turbulenten Umschlagsprozess der ebenen Poiseuille-Strömung," Dissertation, Universität Karlsruhe (1982).

[49] Stuart, J. T., "On the non-linear mechanics of hydrodynamic stability," J. Fluid Mech. 4, 1-21 (1985).

[50] Zurmühl, R., Matrizen, Springer-Verlag (1961).

LAMINAR FLOW CONTROL – VISCOUS SIMULATION

by

Professor E.Reshotko
Dept. of Mechanics & Aerospace Engineering
Case Western Reserve University
Cleveland, Ohio 44106, USA

SUMMARY

Laminar flow control offers the possibility of major reductions in aircraft drag. This lecture provides the theoretical background for the possible stabilizations of the laminar boundary layer due to shaping, suction and cooling. It comments also on the effects of vehicle and environmental factors on the implementation of that technology.

Viscous simulation is the name given to the technology of adjusting boundary-layer conditions on a wind tunnel model so that results can be reliably extrapolated to flight conditions. This lecture will discuss the need for an underlying simulation methodology, will describe some alternate methodologies, will discuss the needed boundary-layer controls/trips for implementation , and finally the process of scaling wind-tunnel results to flight conditions.

INTRODUCTION

This lecture comes virtually at the end of this course and is to be viewed as a presentation of applications of our stability and transition knowledge. The two special applications to be developed herein are a) transition delay as a means of developing a low drag technology for aircraft and underwater vehicles, and b) transition control as a factor in developing a wind tunnel testing technology that is extrapolable to flight conditions.

In each case, the general topic will be outlined. The information related to stability and transition will enter as needed in the exposition.

LAMINAR FLOW CONTROL

The drag of an airplane at cruise flight conditions is about 60% friction drag for present day transport aircraft with turbulent boundary layers on their wetted surfaces; most of the balance is induced drag. For underwater vehicles, the friction drag is more like 90% of total drag. In each case therefore, there is significant opportunity for performance improvement through drag reduction.

More specifically, the drag reduction opportunities lie in stabilizing the laminar boundary layer as much as possible so that more of the friction drag is at laminar rather than turbulent levels. There can additionally be reduction of the turbulent friction drag of those portions of the vehicle that cannot be laminarized. Some of the techniques envisioned for turbulent friction drag reduction are polymer additions, riblets, large eddy break-up devices (LEBU) and microbubble additions. These will not be discussed in this lecture. It will rather be devoted to application of the transition modifiers (which are really stability modifiers) to increasing the extent of laminar flow on the vehicle surfaces.

The Transition Modifiers

As already pointed out in the stability lectures, from the Rayleigh theorem, an inflected velocity profile is inviscidly unstable. The flat plate (Blasius) boundary layer is not inflected and hence is inviscidly stable. Incompressible boundary layers under adverse pressure gradient are inflected while those under favorable pressure gradient are not. More generally, even including viscous effects, the stability of a velocity profile improves as its second derivative near the wall becomes more negative.

Thus the transition modifiers can be nicely identified by examining the boundary layer momentum equation in the near vicinity of a wall:

$$\left(\rho v_w - \frac{d\mu}{dT}\frac{\partial T}{\partial y}\right)\frac{\partial u}{\partial y} + \frac{dp}{ds} = \mu_w \frac{\partial^2 u}{\partial y^2}$$

It is readily seen that suction ($v_w < 0$), cooling in air ($\frac{d\mu}{dT} > 0$, $\frac{\partial T}{\partial y} > 0$), heating in water ($\frac{d\mu}{dT} < 0$, $\frac{\partial T}{\partial y} < 0$), and favorable pressure gradient all tend to make ($\frac{\partial^2 u}{\partial y^2}$)$_w$ more negative. The stabilizing effect of all of these factors has been demonstrated through direct computation involving the appropriate systems of disturbance equations and boundary conditions. From the above reasoning, the effects of these techniques should be additive. This has also been confirmed in the limited studies to date of combined effects.

The drag reduction capabilities of all of the above transition modifiers have been examined. They will each be described.

Favorable Pressure Gradient - "Shaping"

The exploitation of favorable pressure gradient for stabilizing laminar boundary layers dates back to the 1930's and led to the development of the NACA 6-series airfoils. This technique has also been used extensively for low Reynolds number airfoils such as found on sailplanes. Because this stabilization technique requires no "active" system, it is often referred to as "natural laminar flow." On any shaped surface, whether an airfoil or a body, the favorable pressure gradient extends to the longitudinal location of the pressure minimum. Beyond that point the pressure gradient becomes adverse. If the flow remains laminar over the entire favorable pressure gradient region, then beyond the pressure minimum, it either shortly undergoes transition, or else proceeds to laminar separation followed by transition. Which of these occurs depends on many factors including the shape itself, angle-of-attack, Reynolds number, surface roughness, etc.

The objective in design is to have as extensive a region of favorable pressure gradient as possible followed by some means of maintaining attached flow in the adverse pressure gradient region.

A design example for a body of revolution is shown in Fig. 1. It is seen that shifting the pressure minimum downstream leads to a downstream shift in the estimated transition point.

A second very recent example applies shaping to turbofan nacelles. Younghans and Lahti (1984) indicate that the reshaped nacelle shown in Fig. 2 should have lower drag than a conventional nacelle. Wind tunnel tests of an installed (wing-pylon-nacelle) shaped nacelle show an effective drag reduction of about 92% of the predicted value of 13 counts.

Suction

Laminar Flow Control by suction (LFC) also dates back to the late 1930's and early 1940's. Pfenninger (1946) developed the use of suction slots for this application and showed in his initial experiments in Zurich that for small suction rates (C_Q = 0.0014 to 0.0018), full chord laminarization could be obtained on both sides of a 17%-thick airfoil over a range of angles of attack. It was also realized in these studies that the results were dependent on the turbulence and acoustic disturbance levels in the wind tunnel.

The interest of the United States Air Force in this technique is described by Antonatos (1966). Following studies at NACA - Langley of using suction to increase the extent of laminar flow on airfoils, the USAF entered into a program with Northrop Corp. to study the feasibility of laminar flow control in flight and to establish design criteria for laminar flow control. The program included flight tests of an unswept suction glove on an F-94 airplane and culminated in the successful X-21 flight tests of a swept LFC wing using a large number of fine suction slots designed by Pfenninger. Measured performance at a chord Reynolds number of 47 million (Whites, Sudderth and Wheldon 1966) indicated nearly complete laminarization of the upper wing surface and about 75% of the lower surface. This resulted in a 20% reduction in airplane drag and removed any doubt that extensive laminarization could be achieved in flight. There were nevertheless practical concerns about the operational feasibility of such an aircraft that are being investigated to this day. These concerns included the maintenance of clean slots - free from clogging, the loss of

laminar flow in flying through rain or ice, effects of leading edge icing and contamination by insects, among others.

Pfenninger and Reed (1966) have summarized the stability issues for laminar flow control by suction on swept wings. These include stabilization of the chordwise flow on the major portion of the wing, stabilization of the crossflow in the leading and trailing edge regions of the wing, and the criteria for avoiding transition through leading edge contamination.

The phenomenon of leading edge contamination is as follows: For a swept wing attached to a fuselage, turbuent flow from the fuselage boundary layer can spread along the wing stagnation or attachment lines. Such contamination can also occur if the spanwise flow at the attachment line is tripped by excessive surface roughness. Leading edge contamination can be avoided by keeping the momentum thickness Reynolds

number on the attachment line below 90 or 100. ($\mathrm{Re}_{\theta_{a.\ell.}} = W_{\infty}\theta/\gamma$ where θ is the

momentum thickness of the laminar spanwise boundary layer along the attachment line.) Poll (1977) confirmed these findings, namely that leading edge contamination can be avoided by shielding the attachment-line flow from disturbances, reducing sweep angle and leading-edge radius.

Interest in laminar flow control for aircraft was revived in the late 1970's as part of NASA's Aircraft Energy Efficiency (ACEE) Program. The recent developments are described by Wagner and Fischer (1984). They include the development and testing of specially designed supercritical airfoil shapes for this application, the development and testing of slotted suction surfaces for such airfoils as well as surfaces made of electron beam perforated titanium sheets. The supercritical airfoil is especially attractive for this application because of its mildly favorable pressure gradient over most of the airfoil surface. This tends to reduce the suction requirement. Wagner and Fischer also describe the concurrent developments in structural technology for such LFC wings and the design of leading edge systems that keep the leading edges free of the residue of insect impacts and of icing formation.

The goal for such LFC wings is shown in Fig. 3, while a more realistic objective may be as shown in Fig. 4. In any case, friction drag coefficients of up to twice the laminar level are envisioned – well below the level for turbulent flow. The early work in Laminar Flow Control is summarized in the Lachmann (1961) volumes while Bushnell and Tuttle (1979) provide a comprehensive bibliography of all but the most recent work.

Heating or Cooling

Many authors have confirmed that surface heating stabilizes water boundary layers (Wazzan, Okamura and Smith 1968, 1970; Lowell and Reshotko 1974; Strazisar, Reshotko and Prahl 1977). The effects of heating on stability carry through to transition as evidenced in the results of Barker and Jennings (1977) (Fig. 5) where in the entrance flow boundary layer of a constant diameter pipe there was considerable increase in transition Reynolds number with heating.

The stabilizing effect of cooling in air was indicated even earlier (Lees 1947) than the above results for water. The effect of cooling on transition was demonstrated dramatically in the flight transition tests of a cone by Dougherty and Fisher (1980), who observed the transition Reynolds number to vary approximately as T_w^{-7} (Fig. 6). The use of cooling in air for drag reduction is a possibility only for an aircraft using a cryogenic fuel such as hydrogen. Reshotko (1979) has shown in his study that drag reductions of the order of 20-25% are within reason by cooling 75% of the wing surfaces and about 20% of the fuselage length.

Vehicle and Environmental Factors

The realization of increased lengths of laminar flow by exploiting the stabilization techniques discussed above depends on several additional factors. The factors identified as "vehicle factors" relate to the character of the vehicle surface, vibrations and noise. The environmental factors have all been mentioned earlier and include those studied in connection with receptivity as well as ice crystals, rain, insects, dirt, etc. Our knowledge about most of these factors suffers from a very poor data base. What can be done at best is to present some general considerations and rules-of-thumb that will have to do until they are replaced by something more substantial.

Surface Roughness

Surfaces of low drag vehicles are designed to be nominally smooth, therefore surface roughnesses should be small. A measure of surface roughness effects is through the parameter $Re_k = u_k k / \nu_k$ where k is the roughness height, u_k is the velocity at height k in the laminar boundary layer and ν_k is the kinematic viscosity evaluated at height k. Distributed roughnesses with $Re_k < 25$ should behave as smooth surfaces. This is in fact the criterion for a hydraulically smooth surface in turbulent flow. If a surface is prepared with abrasives, the above specification should apply to the deepest scratches rather than to the rms value.

For a slotted suction surface, the suction slot design must be such that the suction flow is predictable, stable and uniform along the length of the slot, and free from such surface defects that would interfere with laminarization. Any surface corrosion or slot clogging would have to be considered as a contribution to roughness. More detailed considerations are given by Pfenninger (1977).

Surface Waviness

Surface waviness can result either from manufacture or else from surface deformation under load. The surface waviness criterion that is prevalent in laminar flow technology is based on a data correlation by Carmichael (1959)

$$\frac{h}{\lambda} = \left[\frac{59000 \; c \; \cos^2 \Lambda}{\lambda \; (Re_c)^{3/2}} \right]^{1/2}$$

where

h is the full amplitude over wavelength λ

c is the wing chord, or body length

Λ is the sweep angle in the case of a wing

The allowable waviness amplitude is of course less than h. Common wisdom indicates that a proper waviness criterion could be obtained from stability considerations to T-S waves or in the case of a concave waviness also to Gortler instability. These stability studies have however not yet been done.

Surface Vibrations

Linear vibrations reasoning dictates that these will be important only in situations where the surface vibrations spectrum overlaps the T-S growth frequency bands of the boundary layer.

Vehicle Maneuvers

If vehicle maneuvers are such that the characteristic period of a maneuver is comparable to the flow time, then the vehicle boundary layer is unsteady. Very little of a definitive nature has been done on the stability and transition of unsteady boundary layers. For the most part, vehicle maneuvers are slow enough so that the flow is quasi-steady.

Ice Crystals

Intermittent or partial loss of laminarization can occur on an aircraft when ice crystals are ingested into the boundary layer and trigger turbulent events. Similar effects can occur for underwater vehicles due to suspended ocean particulate. It is estimated (Chen, Goland and Reshotko 1979) that ingested particles must be of the order of half the boundary layer thickness or larger to serve as an effective trip, and of course the degree of intermittency or loss of laminarization depends on the particle flux.

Insects, Dirt, Dust, etc.

The leading edge of the aircraft wing must be protected at low altitudes from insects, dirt, dust, etc. since any roughening or residue will behave as a roughness at higher altitudes. In slotted wing designs, the slots near the leading edge can be used for keeping the leading edge clean at low altitudes by blowing through them. An alternative protection is to use a Krueger leading flap as an insect shield backed up with a spray system to keep the leading edge clean (Wagner and Fischer 1984).

Concluding Remark

It has been demonstrated beyond any doubt that the stability modifiers - shaping, suction, heating in water and cooling in air, can lead to significant runs of laminar flow on aircraft and underwater vehicles. The practical use of these techniques depends on overcoming any problems arising from the vehicle and environmental factors that have been described. Of course, the resulting low drag vehicle must be able to fulfil its mission reliably and economically. There is a definite possibility that vehicles will be built in the near future that make use of laminar flow technology.

VISCOUS SIMULATION

While wind tunnels have now been used for about a century to obtain performance data for vehicles to be used in atmospheric flight, there are still numerous uncertainties and ambiguities in the interpretation of the data and in reliably extrapolating them to flight conditions. The problem can be divided into two parts - far field and near field.

The first of these recognizes the finiteness of the wind tunnel as compared to the infinity of the flight domain. Techniques have been proposed for assessing the blockage and interference effects due to the finite dimensions of the wind tunnel. More recently, much attention has been given to the adaptive wind tunnel - a facility in which through bleed at the wind tunnel walls, the pressure distribution far from the model can be set equal to that in the infinite flow field corresponding to the pressure distribution on the model. This requires on-line potential flow or Euler computation of the inviscid far-field flow. The recent status of work on wind tunnel interference and adaptive wind tunnels is as found in the proceedings of the recent AGARD Specialists Meeting on Wall Interference in Wind Tunnels (AGARD CP-335, 1982). The near-field simulation is referred to as viscous simulation since it involves adjusting the boundary layer conditions on a model in such a way that the results can be reliably corrected to flight Reynolds numbers. This is usually done by some form of boundary layer tripping since transition locations in flight are likely to occur at smaller fractions of chord or fuselage length than in the wind tunnel.

The topic of viscous simulation has not been formally addressed in recent years and perhaps never. Rather, the matter has been handled by a body of folklore based on years of experience in relating wind tunnel to flight tests. The folklore includes where and how to trip the boundary layer; and how to scale wind tunnel results to that for the full scale vehicle in flight. There are many such folklores, a large portion of them proprietary.

Because of the sensitivity of wind tunnel results in the transonic regime in particular to tunnel operating conditions, there is a special interest at present in trying to give viscous simulation a more scientific basis and thus to replace folklore with a set of well-thought-out procedures. This may be a bit more difficult than apparent because the aforementioned folklores are complemented by significant data bases, and so their proprietors may find it difficult to part with them in favor of some other scheme, however reasonable, that has no data base.

Nevertheless, for all the good reasons to develop sensible ideas on viscous simulation, the Fluid Dynamics Panel of AGARD has set up a Working Group on Viscous Simulation that will make an approximately two year study of the topic beginning in May 1984. Pending the results of these studies, what follows are the author's own views on viscous simulation.

Developing a Simulation System

There is in all liklihood some flexibility in developing a simulation system. But overall, this would consist of the following elements:

1. Choosing a Simulation Methodology

    A simulation methodology is the underlying rationale for relating wind tunnel results to flight conditions. Such methodologies are not unique, and are in someways dependent on the phenomenon being simulated. It could be different for unsteady phenomena such as buffeting than for steady phenomena.

2. Applying the Needed Boundary-Layer Controls/Trips

    Implementation of the simulation methodology often requires fixing of the transition point at a location upstream of where it would occur without a trip. Aside from physical trips, such tripping can be accomplished by exploiting the turbulence and acoustic levels in a facility or even by augmenting them.

3. Scaling of Wind-Tunnel Results to Full Scale Vehicle in Flight

    This is accomplished within the dictates of the simulation methodology. Use should be made of computational fluid dynamics (CFD) capabilities to facilitate scaling.

It is of course to be recognized that the methodologies, trips and scaling procedures would have to be developed separately for each flight regime - subsonic, transonic, supersonic and hypersonic.

Example Simulation Methodologies

The following is a suggested simulation methodology. The testing in the wind tunnel should be done at the flight Mach number whose correct value is established with the aid of the far field simulations and/or corrections alluded to earlier. The near field simulation can be effected by requiring exact scaling of the geometrical shape of the component being studied together with the correct geometric reproduction (as a fraction of chord or body length) of transition and separation locations as would be encountered at flight Reynolds numbers. This would give a correct picture of the viscous-inviscid interactions, and therefore nearly correct pressure distributions. The only scaling then required is of the surface shear. The measured wall shear effects would have to be scaled to flight Reynolds numbers either from established data bases or else using CFD.

The "correct" location of the transition point implies knowledge of the transition Reynolds number in flight. The latter of course is not known and must be estimated in some standard manner. One can argue that just as we design for a standard atmosphere, why not also assume a "standard environment." For low Mach numbers possibly into the transonic range this could be an "e^9 environment," as substantiated in high flow quality wind tunnel tests and in some flight tests. e^9 transition locations are readily calculated by a variety of available programs. This standard environment or standard transition criterion can of course be changed in favor of a better one when such an improved criterion is identified. Standard criteria would also have to be developed for the supersonic and hypersonic regimes.

An alternative methodology relies more heavily on CFD. Using experiment to refine a CFD procedure, including the turbulence modeling, that procedure together with a transition prediction procedure can be used to calculate the flowfield at flight conditions.

In the first methodology, as much as possible of the simulation is done experimentally and only Reynolds number scaling is used. In the second methodology, the experiment is used to develop a reliable computational method, and then the computation is used to determine flight pressure distributions as well as shears. For the present state of development of CFD, the first methodology is more tractable.

Tripping Techniques

This lecture is too short for a review of tripping practices. However, the properties of a desirable trip can be easily stated. A tripping device should cause transition close to the device and in a predictable manner. The drag of the device should be minimal. Finally, the turbulent boundary layer resulting from tripping

should be a member of the extrapolable family of turbulent boundary layers.

Many wind tunnel groups employ tripping techniques in accordance with the suggestions of Braslow and co-workers at NACA/NASA (Braslow and Knox 1958, Braslow, Hicks and Harris 1966). It is however very possible as mentioned earlier to exploit a poor tunnel environment as a tripping device. Just those features that cause a particular tunnel to be a poor facility for transition research may make it very suitable for viscous simulation. Such environmental trips can be rather desirable because they have no inherent drag and the resulting turbulent boundary layers tend to be of the extrapolable family. It is suggested that studies be made of techniques to control the location of transition due to an environmental trip, either by augmenting the turbulence or acoustic disturbance levels in the tunnel or else by adding a mechanical trip.

A Subsonic Example

Consider the case of an airfoil at a low subsonic Mach number whose chord Reynolds number in flight is 35×10^6. This is to be studied by wind tunnel tests at the same Mach number as in flight on a geometrically similar shape in a wind tunnel model whose chord Reynolds number is 5×10^6. Since the e^9 transition Reynolds number at low flight speeds is about 3.5×10^6, this indicates transition on the airfoil in flight at 0.1 chord. Transition on the wind tunnel model should also be effected at 0.1 chord or at a transition Reynolds number of 500,000. This can be done either by tripping or else by running the tests in a wind tunnel whose turbulence level is about 1.3% (Mack 1977). The measured friction drag coefficient can then be extrapolated to the flight Reynolds number by standard techniques.

Problems at Transonic, Supersonic and Hypersonic Speeds

The preferred simulation methodology referred to above requires the ability to predict transition locations for a standard environment as well as shock wave and separation locations. This is not presently possible in all flight regimes. In the transonic regime, transition might be estimated by an e^9 criterion but shock locations are very sensitive to far field tunnel conditions. In the supersonic and hypersonic regimes, while shock locations and shock-induced separations are fairly predictable, there is little guidance with respect to the transition Reynolds number in atmospheric flight.

Concluding Remark

It is clear that there is much work to be done on the important topic of viscous simulation. Success in this area will depend in a significant way on the extent to which the understanding of the elements of the laminar-turbulent transition process can be exploited. It is of particular interest to see if present tripping technology can be augmented by successful use of "non-intrusive" environmental trips.

REFERENCES

Antonatos, P.P. 1966. Laminar Flow Control – Concepts and Applications. Astronautics and Aeronautics vol.4 no.7 pp. 32 – 36

Barker, S.J. and Jennings, C.G. 1977. The Effect of Wall Heating on Transition in Water Boundary Layers. AGARD CP-224, pp. 19-1 – 19-9

Braslow, A.L. and Knox, E.C. 1958. Simplified Method for Determination of Critical Height of Distributed Roughness Particles for Boundary Layer Transition at Mach Numbers From 0 to 5. NACA TN 4363

Braslow, A.L., Hicks, R.M. and Harris, R.V. Jr. 1966. Use of Grit-Type Boundary-Layer-Transition Trips on Wind-Tunnel Models. NASA TN D-3579

Bushnell, D.M. and Tuttle, M.H. 1979. Survey and Bibliography on Attainment of Laminar Flow Control in Air Using Pressure Gradient and Suction. NASA Reference Publication 1035

Carmichael, B.H. 1959. Surface Waviness Criteria for Swept and Unswept Laminar Suction Wings. Norair Report NOR-59-438 (BLC-123)

Chen, C.P., Goland, Y. and Reshotko, E. 1979. Generation Rate of Turbulent Patches in the Laminar Boundary Layer of a Submersible. Proceedings Symposium on Viscous Drag Reduction. In Hough, G.R., ed., Viscous Drag Reduction, Progress in Astronautics and Aeronautics, vol. 72, AIAA, 1980, pp. 73-89

Dougherty, N.S. Jr. and Fisher, D.F. 1980. Boundary Layer Transition on a 10-Degree Cone. AIAA Paper 80-0154

Lachmann, G.V. ed. 1961. Boundary Layer and Flow Control, vols. I and II, Pergamon Press

Lees, L. 1947. The Stability of the Laminar Boundary Layer in a Compressible Fluid. NACA Report 876

Lowell, R.L. and Reshotko, E. 1974. Numerical Study of the Stability of a Heated Water Boundary Layer. Report FTAS/TR-73-93, Case Western Reserve University

Mack, L.M. 1977. Transition Prediction and Linear Stability Theory. AGARD CP-224, pp. 1-1 - 1-22

Pfenninger, W. 1946. Untersuchingen uber Reibungs vermin-derungen an Tragflugeln, insbesondere mit Hilfe von Grenz-schichtabsaugung. Mitteilung No 13 des Inst. fur Aerodynamik, E.T.H., Zurich

Pfenninger, W. 1977. Special Course on Concepts for Drag Reduction, Chapter 3 - Laminar Flow Control Laminarization, AGARD Report No. 654

Pfenninger, W. and Reed, V.D. 1966. Laminar-Flow Research and Experiments. Astronautics and Aeronautics vol. 4 no. 7 pp. 44 - 50

Poll, D.I.A. 1977. Leading Edge Transition on Swept Wings. AGARD CP-224, pp. 21-1 - 21-11

Reshotko, E. 1979. Drag Reduction by Cooling in Hydrogen-Fueled Aircraft. Jour. Aircraft, vol. 16 no. 9, pp. 584-590

Strazisar, A.J., Reshotko, E. and Prahl, J.M. 1977. Experimental Study of the Stability of Heated Flat Plate Boundary Layers in Water. J. Fluid Mech. vol. 83 pt. 2, pp. 225-247

Wagner, R.D. and Fischer, M.C. 1984. Fresh Attack on Laminar Flow. Aerospace America vol. 22 no. 3, pp. 72-76

Wazzan, A.R., Okamura, T.T. and Smith, A.M.O. 1968. Spatial and Temporal Stability Charts for the Falkner-Skan Boundary Layer Profiles. Douglas Aircraft Co. Report No. DAC-6708

Wazzan, A.R., Okamura, T.T. and Smith, A.M.O. 1970. The Stability and Transition of Heated and Cooled Incompressible Laminar Boundary Layers. Proc. 4th Int. Heat Transfer Conf., ed. U. Grigull and E. Hahne, vol. 2, FC 1.4, Elsevier

Whites, R.C., Sudderth, R.W. and Wheldon, W.G. 1966. Laminar Flow Control on the X-21. Astronautics and Aeronautics, vol. 4 no.7, pp. 38-43

Younghans, J.L. and Lahti, D.J. 1984. Experimental Studies on Natural Laminar Flow Nacelles. AIAA Paper 84-0034.
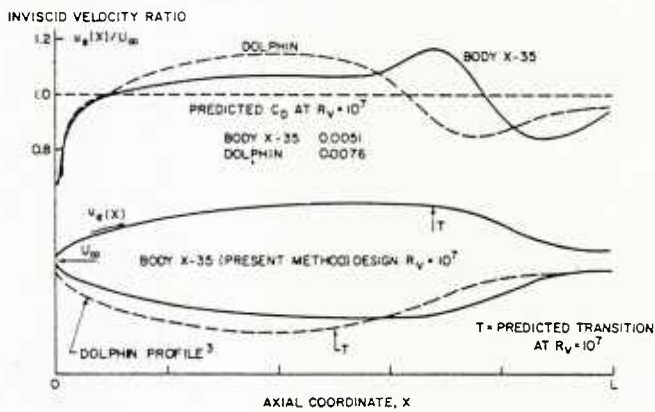
Fig. 1. Effect of reshaping on transition and drag of a
body of revolution.

a) Conventional Nacelle

b) Natural Laminar Flow Nacelle
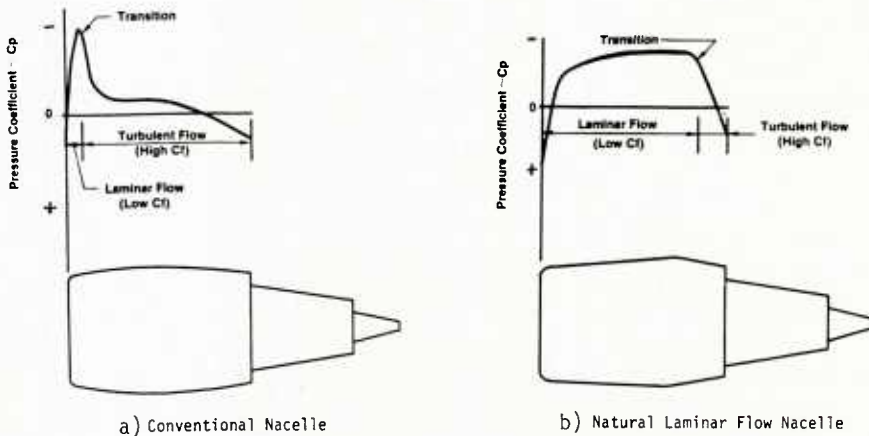
Fig. 2. Effect of shaping on transition for a turbofan
nacelle (Younghans and Lahti, 1984).
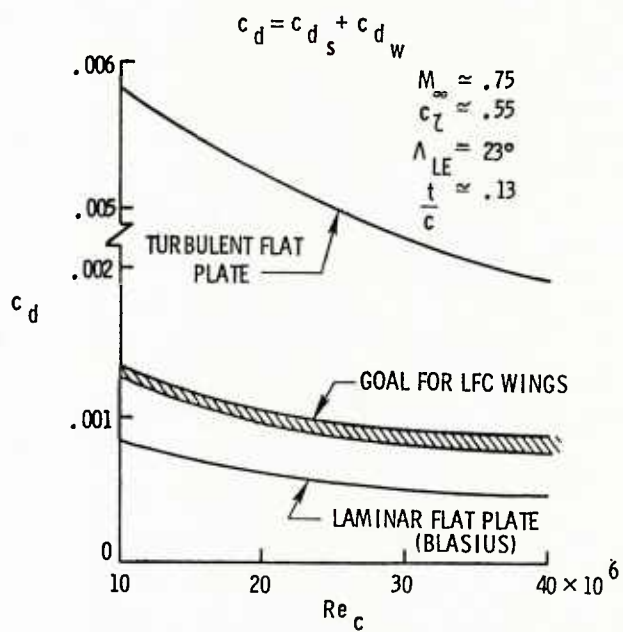
Fig. 3. Estimated variation of supercritical LFC wing
drag with Reynolds number.

SWEEP 30 DEG, $C_L = 0.5$, $M_\infty \cong 0.8$
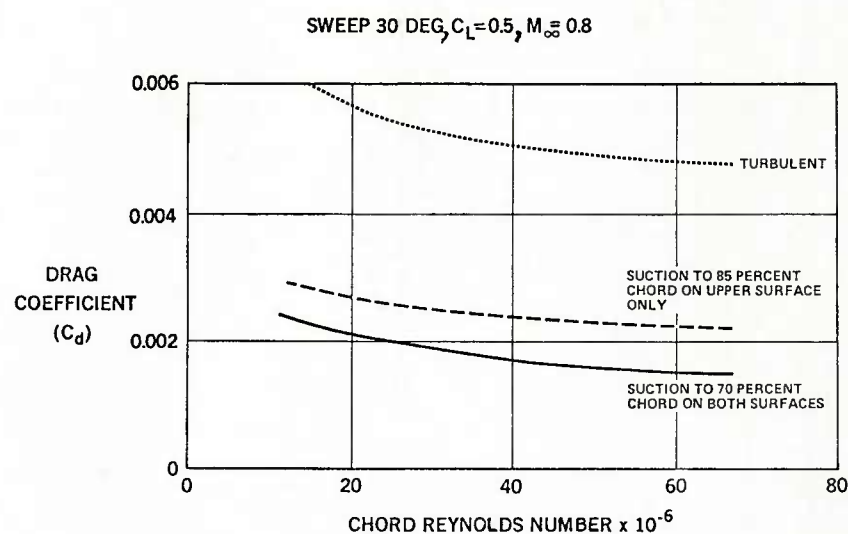
Fig. 4. Effect of LFC extent on wing drag.
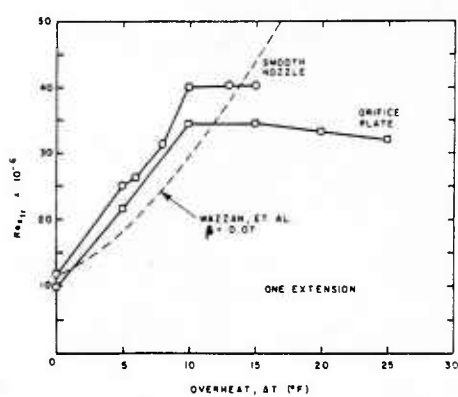
Fig. 5. Effect of heating on transition Reynolds number in a water boundary layer (Barker and Jennings 1977).
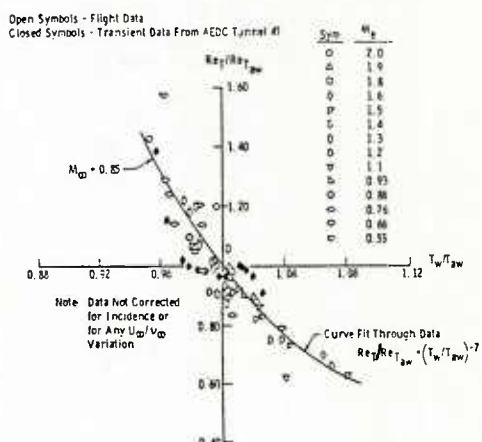

Fig. 6. Effect of T_w/T_{aw} on transition on a cone (Dougherty and Fisher, 1980).

AGARD Report No.709 Advisory Group for Aerospace Research and Development, NATO SPECIAL COURSE ON STABILITY AND TRANSITION OF LAMINAR FLOW Published June 1984 232 pages The aim of the Special Course on Stability and Transition of Laminar Flows was to present the knowledge of laminar-turbulent transition. Incompressible two-dimensional and compressible flows in transonic, supersonic, and hypersonic regimes were covered, as well as available results for three-dimensional flows. The course notes consist of material presented and discussed at the Special Course held at the von Kármán P.T.O.	AGARD-R-709 Boundary layer transition Laminar flow Stability Aerodynamics	AGARD Report No.709 Advisory Group for Aerospace Research and Development, NATO SPECIAL COURSE ON STABILITY AND TRANSITION OF LAMINAR FLOW Published June 1984 232 pages The aim of the Special Course on Stability and Transition of Laminar Flows was to present the knowledge of laminar-turbulent transition. Incompressible two-dimensional and compressible flows in transonic, supersonic, and hypersonic regimes were covered, as well as available results for three-dimensional flows. The course notes consist of material presented and discussed at the Special Course held at the von Kármán P.T.O.	AGARD-R-709 Boundary layer transition Laminar flow Stability Aerodynamics
AGARD Report No.709 Advisory Group for Aerospace Research and Development, NATO SPECIAL COURSE ON STABILITY AND TRANSITION OF LAMINAR FLOW Published June 1984 232 pages The aim of the Special Course on Stability and Transition of Laminar Flows was to present the knowledge of laminar-turbulent transition. Incompressible two-dimensional and compressible flows in transonic, supersonic, and hypersonic regimes were covered, as well as available results for three-dimensional flows. The course notes consist of material presented and discussed at the Special Course held at the von Kármán P.T.O.	AGARD-R-709 Boundary layer transition Laminar flow Stability Aerodynamics	AGARD Report No.709 Advisory Group for Aerospace Research and Development, NATO SPECIAL COURSE ON STABILITY AND TRANSITION OF LAMINAR FLOW Published June 1984 232 pages The aim of the Special Course on Stability and Transition of Laminar Flows was to present the knowledge of laminar-turbulent transition. Incompressible two-dimensional and compressible flows in transonic, supersonic, and hypersonic regimes were covered, as well as available results for three-dimensional flows. The course notes consist of material presented and discussed at the Special Course held at the von Kármán P.T.O.	AGARD-R-709 Boundary layer transition Laminar flow Stability Aerodynamics

Institute, Belgium, on 26–30 March 1984 under the joint sponsorship of the Institute and the AGARD Fluid Dynamics Panel.

Institute, Belgium, on 26–30 March 1984 under the joint sponsorship of the Institute and the AGARD Fluid Dynamics Panel.

Institute, Belgium, on 26–30 March 1984 under the joint sponsorship of the Institute and the AGARD Fluid Dynamics Panel.

Institute, Belgium, on 26–30 March 1984 under the joint sponsorship of the Institute and the AGARD Fluid Dynamics Panel.

U214957

AGARD

NATO ⊕ OTAN

7 RUE ANCELLE · 92200 NEUILLY-SUR-SEINE

FRANCE

Telephone 745.08.10 · Telex 610176

**DISTRIBUTION OF UNCLASSIFIED
AGARD PUBLICATIONS**

AGARD does NOT hold stocks of AGARD publications at the above address for general distribution. Initial distribution of AGARD publications is made to AGARD Member Nations through the following National Distribution Centres. Further copies are sometimes available from these Centres, but if not may be purchased in Microfiche or Photocopy form from the Purchase Agencies listed below.

NATIONAL DISTRIBUTION CENTRES

BELGIUM
Coordonnateur AGARD — VSL
Etat-Major de la Force Aérienne
Quartier Reine Elisabeth
Rue d'Evere, 1140 Bruxelles

CANADA
Defence Science Information Services
Depar…
Ottaw…

DENMARK
Danis…
Øster…
Cope…

FRANCE
O.N.…
29 A…
9232…

GERMAN…
Fach…
Phy…
Ker…
D-7…

GREECE
Hel…
Res…
Ho…

ICELAN…
Direc…
c/o Flugrad
Reykjavik

ITALY
Aeronautica Militare
Ufficio del Delegato Nazionale all'AGARD
3, Piazzale Adenauer
Roma/EUR

LUXEMBOURG
See Belgium

NETHERLANDS
…

…R
…lishment
…lopment (ARGE)
…kara
…ntre

Orpington, Kent BR5 3RE

UNITED STATES
National Aeronautics and Space Administration (NASA)
Langley Field, Virginia 23365
Attn: Report Distribution and Storage Unit

THE UNITED STATES NATIONAL DISTRIBUTION CENTRE (NASA) DOES NOT HOLD
STOCKS OF AGARD PUBLICATIONS, AND APPLICATIONS FOR COPIES SHOULD BE MADE
DIRECT TO THE NATIONAL TECHNICAL INFORMATION SERVICE (NTIS) AT THE ADDRESS BELOW.

PURCHASE AGENCIES

Microfiche or Photocopy
National Technical
Information Service (NTIS)
5285 Port Royal Road
Springfield
Virginia 22161, USA

Microfiche
ESA/Information Retrieval Service
European Space Agency
10, rue Mario Nikis
75015 Paris, France

Microfiche or Photocopy
British Library Lending
Division
Boston Spa, Wetherby
West Yorkshire LS23 7BQ
England

Requests for microfiche or photocopies of AGARD documents should include the AGARD serial number, title, author or editor, and publication date. Requests to NTIS should include the NASA accession report number. Full bibliographical references and abstracts of AGARD publications are given in the following journals:

Scientific and Technical Aerospace Reports (STAR)
published by NASA Scientific and Technical
Information Branch
NASA Headquarters (NIT-40)
Washington D.C. 20546, USA

Government Reports Announcements (GRA)
published by the National Technical
Information Services, Springfield
Virginia 22161, USA

SPS

*Printed by Specialised Printing Services Limited
40 Chigwell Lane, Loughton, Essex IG10 3TZ*